

Guoqing Zhang  
Bin Xu  
YanJun Lu  
Suet To *Editors*

# Fabrication of Micro/Nano Structures via Precision Machining

Modelling, Processing and Evaluation

 Springer

# Fabrication of Micro/Nano Structures via Precision Machining

Guoqing Zhang · Bin Xu · Yanjun Lu · Suet To  
Editors


# Fabrication of Micro/Nano Structures via Precision Machining


Modelling, Processing and Evaluation

 Springer

*Editors*

Guoqing Zhang  
College of Mechatronics and Control  
Engineering  
Shenzhen University  
Shenzhen, Guangdong, China

Bin Xu   
College of Mechatronics and Control  
Engineering  
Shenzhen University  
Shenzhen, Guangdong, China

YanJun Lu   
College of Mechatronics and Control  
Engineering  
Shenzhen University  
Shenzhen, Guangdong, China

Suet To  
Department of Industrial and Systems  
Engineering  
The Hong Kong Polytechnic University  
Hung Hom, Kowloon, Hong Kong

ISBN 978-981-99-1337-4

ISBN 978-981-99-1338-1 (eBook)

<https://doi.org/10.1007/978-981-99-1338-1>

© The Editor(s) (if applicable) and The Author(s), under exclusive license to Springer Nature Singapore Pte Ltd. 2023

This work is subject to copyright. All rights are solely and exclusively licensed by the Publisher, whether the whole or part of the material is concerned, specifically the rights of translation, reprinting, reuse of illustrations, recitation, broadcasting, reproduction on microfilms or in any other physical way, and transmission or information storage and retrieval, electronic adaptation, computer software, or by similar or dissimilar methodology now known or hereafter developed.

The use of general descriptive names, registered names, trademarks, service marks, etc. in this publication does not imply, even in the absence of a specific statement, that such names are exempt from the relevant protective laws and regulations and therefore free for general use.

The publisher, the authors, and the editors are safe to assume that the advice and information in this book are believed to be true and accurate at the date of publication. Neither the publisher nor the authors or the editors give a warranty, expressed or implied, with respect to the material contained herein or for any errors or omissions that may have been made. The publisher remains neutral with regard to jurisdictional claims in published maps and institutional affiliations.

This Springer imprint is published by the registered company Springer Nature Singapore Pte Ltd. The registered company address is: 152 Beach Road, #21-01/04 Gateway East, Singapore 189721, Singapore

# Preface

Micro/nano structures, inspired from nature, have some unique properties such as friction reduction, structural color, self-cleaning, etc., whereby have been widely employed in the fields of optics, aerospace, electronics, and communication. These unique functions of micro/nano structures originate from their complex and uniform surface structures or textures, and depend on the employed fabrication methods to a large extent. Therefore, their fabrications have received extensive attentions, becoming a research hot topic. Precision machining, as a machining method with deterministic geometry, has become an ideal method for the preparation of micro/nano structures. This book will introduce the cutting-edge technology of micro/nano structure fabrication from precision machining, electrical discharge machining (EDM) and precision grinding and injection molding, and the contents of the presented book include micro/nano structure modeling, tool path generation, machining process, and surface evaluation. The purpose of this book is to provide a variety of feasible machining methods and advanced manufacturing techniques for the precision fabrication of micro/nano structures, especially for complex micro/nano structures. Since the book focuses on the micro/nano structure fabrication methods, including hierarchical micro/nano structures, graduate students, engineering technicians, and researchers in the related fields will benefit from this book, and also someone in related application fields such as biomedicine, communication, optics, etc. may be inspired from this book.

We are thankful to all the authors for their chapter. We also thank the publisher for their guidance and support.

Shenzhen, China  
Shenzhen, China  
Shenzhen, China  
Hong Kong, China

Guoqing Zhang  
Bin Xu  
Yanjun Lu  
Suet To

# Contents

<b>Part I Fabrication of Micro/Nano Structures via Precision Mechanical Machining</b>	
<b>1 Introduction to Precision Machining Micro/Nano Structures</b> .....	3
Yuting Ma, Guoqing Zhang, and Shuaikang Cao	
<b>2 Tool Offset Flycutting Straight-Groove-Type Microstructures</b> .....	15
Jianpeng Wang, Guoqing Zhang, and Jiankai Jiang	
<b>3 Tool Offset Flycutting Multi-layer Hierarchical Microstructures</b> ...	41
Jianpeng Wang, Guoqing Zhang, and Jiankai Jiang	
<b>4 Tool Offset Flycutting Micro-optics Arrays with High-Aspect-Ratio</b> .....	79
Zhanwen Sun, Suet To, and Sujuan Wang	
<b>5 Diamond Milling System for Fabricating Infrared Micro-optics Arrays</b> .....	103
Zhanwen Sun, Suet To, and Sujuan Wang	
<b>6 Cutting Force and Energy Modelling in Ultra-Precision Machining of Micro-structures</b> .....	129
Zejia Zhao and Yiji Liang	
<b>Part II Fabrication of Micro/Nano Structures via Electrical Discharge Machining (EDM)</b>	
<b>7 Introduction to Electrical Discharge Machining Micro/Nano Structures</b> .....	165
Weitong Liu, Yuping Li, and Bin Xu	
<b>8 Fabrication of 3D Micro-electrode and Its Application in Micro-EDM</b> .....	177
Yangquan Liu, Weitong Liu, and Bin Xu	

<b>9</b>	<b>Fabrication of Micro-structures by Applying Cu-Sn 3D Micro-electrode</b> .....	195
	Zhaozhi Wu and Xiaoyu Wu	
<b>10</b>	<b>Fabrication of Micro-grooves by Applying Laminated Disc Electrodes</b> .....	217
	Weijie Pan, Jianguo Lei, and Xiaoyu Wu	
<b>11</b>	<b>Fabrication of Blind Multi-microgrooves by Applying Long-Laminated Electrode</b> .....	239
	Huiyong Wu, Jianguo Lei, and Xiaoyu Wu	
<b>12</b>	<b>Geometric Evolution of Microstructures in EDM with Composite Laminated Electrode</b> .....	261
	Kai Jiang, Xiaoyu Wu, Jianguo Lei, and Bin Xu	
<b>Part III Fabrication of Micro/Nano Structures via Precision Grinding and Injection Molding</b>		
<b>13</b>	<b>Introduction to Precision Grinding and Injection Molding Micro/Nano Structures</b> .....	287
	YanJun Lu, Yuming Huang, and Jiangxiu Ouyang	
<b>14</b>	<b>Precision Dressing and Truing of Diamond Grinding Wheel with V-tip</b> .....	301
	YanJun Lu, Jiangxiu Ouyang, and Yuming Huang	
<b>15</b>	<b>Precision Grinding of Micro-structures of Hard-Brittle Material Surfaces</b> .....	319
	YanJun Lu, Yuming Huang, HaoJun Huang, and Long Zhang	
<b>16</b>	<b>Precision Grinding and Polishing of Optical Micro-structured Surface</b> .....	337
	Chunjin Wang, Xingyu Mou, Wang Luo, and YanJun Lu	
<b>17</b>	<b>Fabrication of Micro-structured Polymer Via Precision Grinding and Injection Molding</b> .....	361
	YanJun Lu, Xingyu Mou, and Fumin Chen	
<b>18</b>	<b>Fabrication of Micro-structured LED Diffusion Plate Via Precision Grinding and Injection Molding</b> .....	379
	YanJun Lu, Xingyu Mou, Wang Luo, and Chunjin Wang	

## About the Editors



**Guoqing Zhang** was born in June 1982. He received his Bachelor's Degree in Mechanical Engineering from Northeast Petroleum University, China in 2005. In 2009, he received his Master's Degree in Mechanical Engineering from Harbin Institute of Technology, China. And he received his Ph.D. Degree from The Hong Kong Polytechnic University in 2014. Now, he is a Research Professor at Shenzhen University and selected for the Shenzhen Peacock Program for Overseas/Professional High-Level Talents. He serves as a Deputy Director of Guangdong Key Laboratory of Electromagnetic Control and Intelligent Robots, Deputy Director of Shenzhen Key Laboratory of High Performance Nontraditional Manufacturing, Committee Member of Chinese Mechanical Engineering Society Design Branch, and Member of Advanced Optical Manufacturing Young Expert Committee of Chinese Optical Engineering Society.

His research interests include ultra-precision machining technology and equipment, robots and intelligent equipment, etc. Until now, he has hosted more than 10 research projects including 4 NSFC (National Natural Science Foundation of China) projects, published more than 70 peer-reviewed papers, and has been granted 14 US patents and 26 CN patents. He co-edited 2 books published by Springer. He now serves as an Academic Editor for the international journal "Shock and Vibration" and reviewer for more than 10 international journals. He has won more than



5 prizes which includes the China Industry-University-Research Cooperation Promotion Award (individual) and the second prize of innovation achievement.



**Bin Xu** was born in February 1985. He received his Bachelor's Degree in Mechanical Engineering from Naval Aeronautical University, China in 2007. In 2009, he received his Master's Degree in Mechanical Engineering from Shenzhen University, China. And he received his Ph.D. Degree from Shenzhen University in 2013. Now, he is an Associate Professor at Shenzhen University. He serves as a Director of Department of Mechanical and Electronic Engineering.

His research interests include micro-electrical discharge machining, micro-electrochemical machining, laser beam machining, etc. Until now, he has hosted more than 8 research projects including 1 NSFC (National Natural Science Foundation of China) project, published more than 50 peer-reviewed papers, and has been granted 10 CN patents. He has won more than 5 prizes which includes the Science and Technology Award of Guangdong Province, the Science and Technology Award of Shenzhen, the China Machinery Industry Science and Technology Award, and the Science and Technology Award of Chinese Optical Engineering Society.



**Yanjun Lu** was born in July 1987. He received his Bachelor's Degree in Mechanical Engineering from Wuhan Institute of Technology, China in 2009. In 2012, he received his Master's Degree in Mechanical Fault Diagnosis from Wuhan Institute of Technology, China. He received his Ph.D. Degree from South China University of Technology of China in 2015. Now, he is an Assistant Professor at Shenzhen University and serves as the Director of the Joint Training Postgraduate Demonstration Base of Guangdong Province, selected as Science and Technology Commissioner of Guangdong Province, 100 innovative Doctoral and Post-Doctoral Fellows in Guangdong Province, Shenzhen High-Level Talents, "Pilot Talents" in Nanshan District, expert in Shenzhen Science and Technology Expert Database, and senior member of China Mechanical Engineering Society.

His research interests include dressing and truing of coarse diamond grinding wheel and micro-structure

manufacture; mirror grinding of carbide alloy and optical glass; micro-array structure grinding machining of glass, ceramics, and composites; and application researches on micro-injection molding of LED light guide plate and biomedical microfluidic chip; etc.

Until now, he has more than 20 peer-reviewed papers published in top science magazines, such as “International Journal of Machine Tools and Manufacture”, “Journal of Mechanical Engineering”, and has been granted more than 40 patents and 16 invention patents (including 2 US patents). He has hosted more than 10 research projects including NSFC (National Natural Science Foundation of China) project and China Post-doctoral Science Foundation and has hosted 5 enterprise projects. He has won the eighth “Innovation Leader Award” of the 2018 Jinbo Awards.



**Prof. Suet To** is a Full Professor of the Department of Industrial and Systems Engineering of The Hong Kong Polytechnic University, Associate Director of State Key Laboratory of Ultra-precision Machining Technology and Advanced Optics Manufacturing Centre. She graduated from Kunming University of Science and Technology with Bachelor Degree in Mechanical Engineering and obtained her M.Phil. Degree in Materials Science from Brunel University in UK and Ph.D. in Ultra-precision Machining Technology from The Hong Kong Polytechnic University. She started her academic career as Assistant Professor in 2005 and promoted to Associate Professor and Professor in 2010 and 2018, respectively. She is an active researcher who focuses on Ultra-precision Machining and Material Science. Her research interests include ultra-precision machining, advanced optics manufacturing technology, ultra-precision machining of micro/nano-structure, and effect on materials. She has published 3 research books, more than 300 international SCI refereed journal papers, and over 200 international conference papers, as well as obtained more than 20 patents in China and USA. She has secured more than 20 external projects as Principal Investigator (PI)/Project Coordinator (PC) and successfully obtained over HK\$55 million of research grants.

Prof. To holds various honorary positions in professional bodies including Board Member of the Asian

Society for Precision Engineering and Nanotechnology (ASPEN), Committee Member of the Production Engineering Division of the Chinese Society for Mechanical Engineers (CSME), and Associate Member of the International Academy for Production Engineering (CIRP). She also serves as Editorial Board member in several international journals, such as International Journal of Machine Tools and Manufacturing, Journal of Applied Optics, Journal of Nano-manufacturing and Metrology, International Journal of Extreme Manufacturing, and Chinese Journal of Mechanical Engineering.

**Part I**  
**Fabrication of Micro/Nano Structures**  
**via Precision Mechanical Machining**

# Chapter 1

## Introduction to Precision Machining Micro/Nano Structures



Yuting Ma, Guoqing Zhang , and Shuaikang Cao

**Abstract** Micro/nano structures have many functions and are widely used in engineering field. As an important machining method for micro/nano structures, ultra-precision machining has advantages in surface roughness, shape control accuracy, geometric consistency of micro/nano structures, and machining efficiency. As a member of ultra-precision machining, ultra-precision fly cutting has high flexibility and suitable for the machining of complex micro and nano structures. In fly cutting, the constant cutting speed of raster milling and tool offset fly cutting provides uniform high surface quality, solving the problems of workpiece size limitation, insufficient dynamic response, and inconsistent geometry of micro/nano structures that exist in diamond turning. This section discusses the preparation of micro/nano structures using ultra-precision fly cutting. Based on the summary of the characteristics of several methods of ultra-precision machining, this section focuses on the combination of ultra-precision fly cutting combined with slow/fast tool servo to produce multi-scale complex micro/nano structures, and the analysis of the force and energy signals during machining to optimize the machining process. This section will provide guidance for the the application of ultra-precision fly cutting and provide theoretical reference for the preparation of multi-scale complex micro/nano structures.

## 1 Micro/Nano Structures Fabrication Methods

Micro/nano structures refer to the surface overlying with micro/nano-scale structures and carrying special functions, which is a ubiquitous biological surface form in nature. It has been widely applied in opto-mechatronics, bionics, biomedicine, aerospace and defense engineering [1]. For example, pyramid array structures can enhance the optical performance of photovoltaic devices such as solar light guide plate; lotus leaf biomimetic structures have superhydrophobicity; compound eye

---

Y. Ma · G. Zhang (✉) · S. Cao

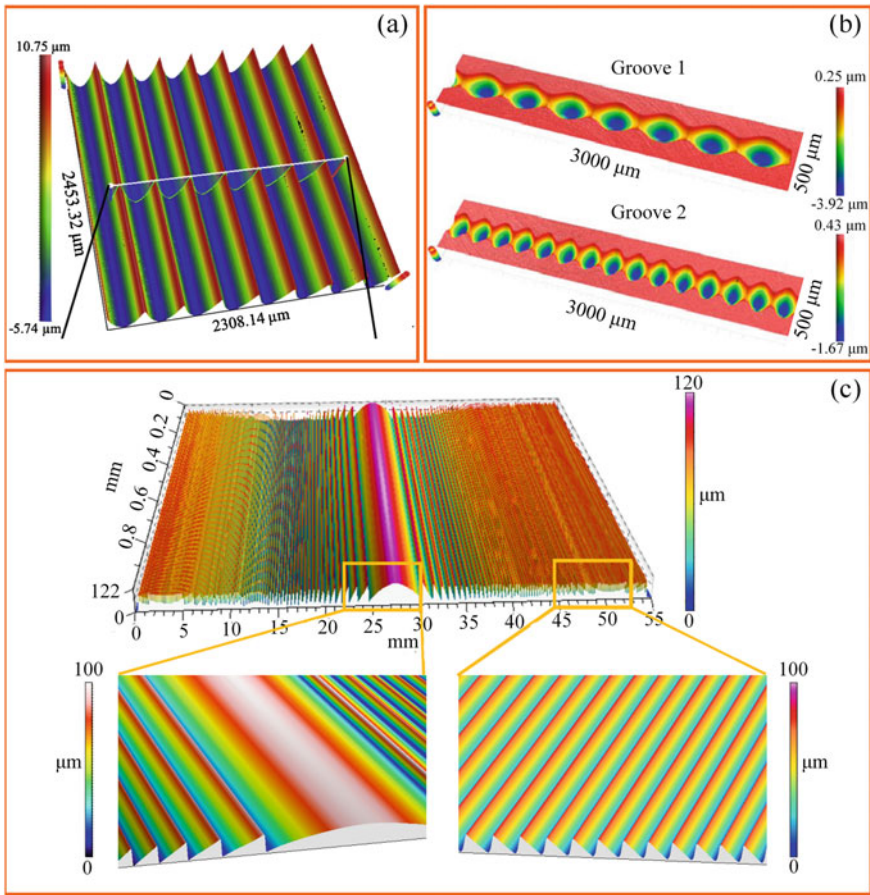
Shenzhen Key Laboratory of High Performance Nontraditional Manufacturing, College of Mechatronics and Control Engineering, Shenzhen University, Nan-hai Ave 3688, Shenzhen 518060, Guangdong, China  
e-mail: [zhanggq@szu.edu.cn](mailto:zhanggq@szu.edu.cn)

biomimetic structures can prevent atomization phenomenon. Cui et al. referred three kinds of biological structure to propose a novel microstructure on tool surface for more sufficient lubrication, efficiently reduce energy consumption [2]. Kong et al. designed and fabricated self-cleaning surfaces using simplified 3D patterned microstructures to simulate the lotus effect [3]. Yue et al. found that the freezing time of the droplets on the layered surface was four times longer than the ordinary surface, which showed great potential in antifreezing applications [4]. Therefore, it is of great practical significance to study the fabrication technology functional surfaces with micro/nano structures, which is the current research focus.

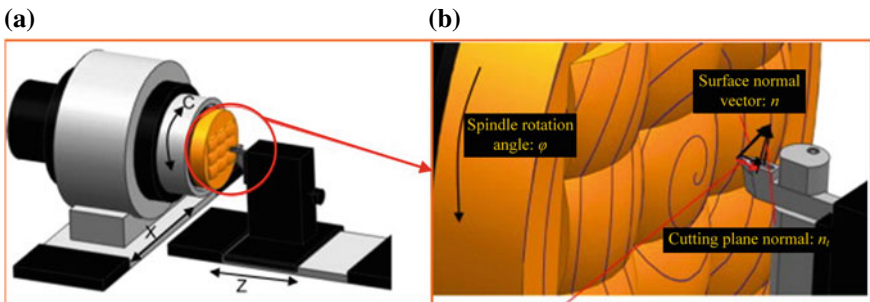
Ultra-precision machining, as a deterministic geometric shape machining method, has advantages in surface roughness, shape control accuracy, surface geometric consistency and machining efficiency, which is an ideal method for machining multi-scale complex micro/nano structures. Typical micro/nano structures fabricated by ultra-precision machining as shown in Fig. 1 [5]. Ultra-precision machining refers to the machining technology of submicron dimensional accuracy and nanometer surface roughness. According to the different machining principles, the ultra-precision machining methods of micro/nano structures are mainly classified into the following two categories: micro/nano structured surface machining based on tool pre-processing and motion control of machine tool axis.

The micro/nano structured surface machining based on tool pre-processing uses the pre-processing technology (such as focused ion beam, micro-grinding, laser cutting, etc.) to process the micro/nano structure on the cutting edge of the tool. Then, structured cutting tools are used to cut the workpiece so as to realize the copy of the micro/nano structure of the cutting edge [9, 10]. This method is easy to realize large-scale manufacturing of micro/nano structured surfaces without special processing technology. However, the process of pre-processing cutting edge is complicated and the cost is high; the shape and size of the micro/nano structures cannot be flexibly adjusted; the structured cutting edge makes the tool easier to wear, which affects the geometric consistency and dimensional accuracy of the micro/nano structures.

The micro/nano structured surface machining based on motion control of machine tool axis is the most direct and widely used machining method. It is mainly based on the relative motion between diamond tool and workpiece to realize the machining and manufacturing of ideal micro/nano structures. One of the most widely used technologies is single-point diamond turning, in which the workpiece is mounted on a spindle and rotates with the spindle, and is applicable to the machining of rotationally symmetrical surfaces. The schematic diagram of single-point diamond turning as represented in Fig. 2. However, as the tool feeds toward the center of the workpiece, the tool linear speed decreases, leading to sampling point conflicts that affect surface quality. Also, inconsistencies in cutting speed and spindle speed can lead to inconsistent surface quality.



**Fig. 1** **a** 15  $\mu\text{m}$  deep micro-raster composed by arc-shaped micro-grooves [6], **b** 3D surface topographies of the micro-grooves and the corresponding micro-topographies [7], **c** the hexagon cube corner array [8]



**Fig. 2** **a** Single-point diamond turning, **b** turning tool path [11]

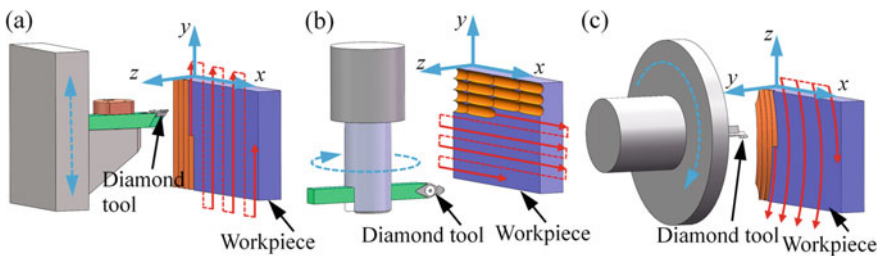
## 2 Principal Cutting Movement in Micro/Nano Structures Machining

When the spindle does not provide a rotary motion but a feed motion in the Y-axis direction is called linear scraping, as depicted in Fig. 3a. Linear scraping technology is an effective method to achieve linear micro-groove machining. In the linear scraping cutting tool movement, the linear micro-groove cross texture surface can be fabricated with the servo vibration of one-dimensional or multi-dimensional workpiece. However, limited by the linear axis feed speed of the lathe, the efficiency of linear scraping is low.

In contrast, fly cutting not only avoids the limits of turning but also provides a higher degree of flexibility for machining micro/nano structures. The motion of the tool rotating with the spindle for machining is called fly cutting. According to the different positions of the tool and spindle, fly cutting could be categorized into raster milling and tool offset fly cutting.

When the tool position is perpendicular to the spindle it is called raster milling as shown in Fig. 3b. Raster milling realizes precise raster scanning movement of the tool on the workpiece surface through three straight axes with high resolution, and the tool is positioned on the high-speed axis of rotation to remove material on the workpiece surface intermittently. Raster milling is suitable for the machining of linear micro-grooves and their intersecting forming arrays. In raster milling, the surface creation needs the combination of high speed rotation of the tool and linear movement of the cutting spindle. The kinematic mapping model of the motion axis to the machining surface needs to be established to clarify the surface creation mechanism, and the influence of machining errors on the surface creation during cutting needs to be studied. The tool path optimization and surface topography prediction can be realized by constructing the raster milling strategy and the tool geometry projection model along the tool path [12–14]. At the same time, the influence mechanism of material slip, spindle error, size effect, tool wear and other factors on the machining surface quality should be comprehensively considered in the study of machining surface mechanism, so as to improve the machining surface quality [15–18].

Tool offset fly cutting is called when the tool position is parallel to the spindle, as shown in Fig. 3c. In tool offset fly cutting, the rotation radius of the tool partially



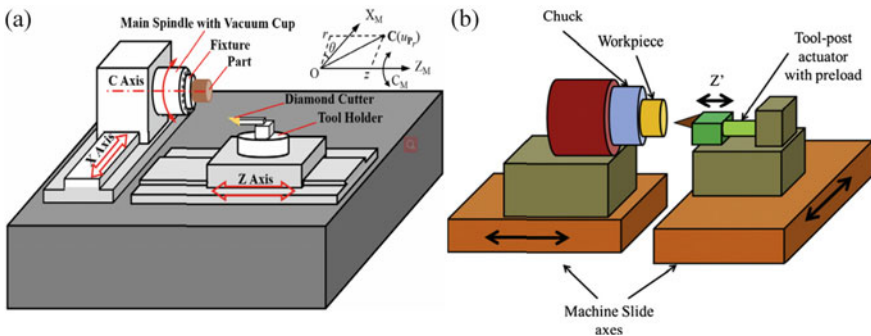
**Fig. 3** a Linear scraping, b raster milling, c tool offset fly cutting



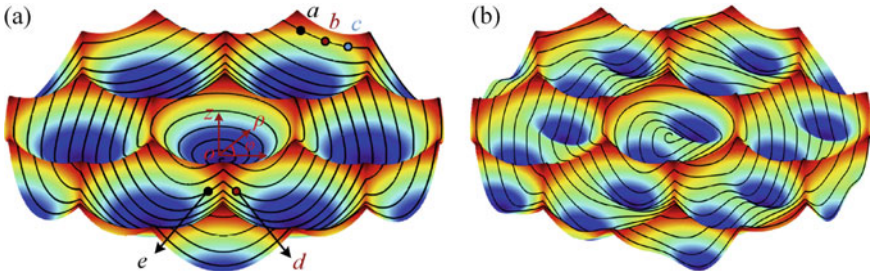
covers the workpiece surface to achieve uniformly surface machining. Compared with linear scraping and raster milling, tool offset fly cutting can achieve the integration of interval trajectory and high cutting speed. As an independent lathe configuration, tool offset fly cutting is mainly used in plane machining [19, 20]. Zhu et al. designed a novel ultra-precision fly cutting method to generate large-scale of micro-lens array [21]. Zhu et al. proposed a novel biaxial servo-assisted fly cutting method, which can achieve active control of residual tool marks of micro/nano structures [22]. The constant cutting speed of fly cutting in the machining process provides uniform surface quality, and solves the problems of workpiece size limitation, insufficient dynamic response, and the inconsistency of micro/nano structure geometry in diamond turning.

### 3 Asisted Cutting Movement in Micro/Nano Structures Machining

Micro/nano structured surface machining based on motion control of machine tool axis is usually applied in combination with slow/fast tool servo systems to expand the machining application [23, 24]. Slow tool servo (STS) uses the X, Z, C axis position servo linkage of commercial lathe to realize non-rotary symmetric surface machining in polar or cylindrical coordinate system. Since the Z-axis motion frequency that drives the tool motion is only tens of Hertz, it can only be used for the smooth surfaces machining. A typical schematic of a STS system as shown in Fig. 4a. Yin et al. used STS diamond turning technology to realize the machining of off-axis aspheric surface [25]; Nagayama and Yan used the STS diamond turning technology to realize the freeform surface machining with nanoscale surface shape accuracy [23]; Huang et al. used STS diamond turning technology to fabricate complex surface optical lenses [26]. Zhang et al. proposed a new machining method of rotating tool turning based on the STS technology to machine the prism in one setting [27].



**Fig. 4** **a** A typical schematic of a STS system [28], **b** a typical schematic of a FTS system [29]

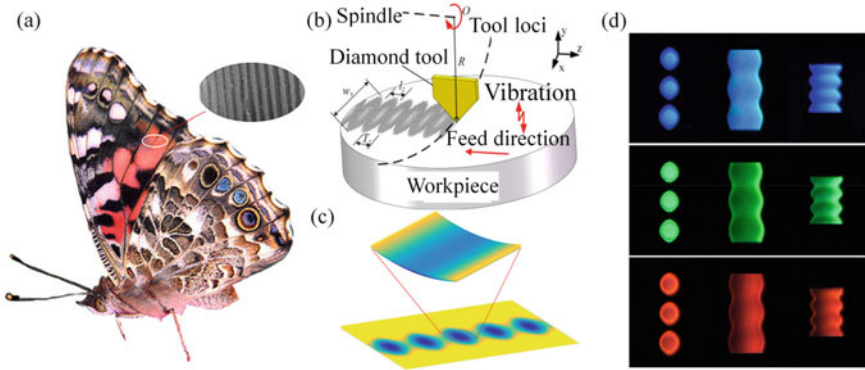


**Fig. 5** Conventional spiral path based fast tool servo diamond cutting of **a** micro-sphere lens array, **b** micro-freeform lens array [34]

Different from STS, the fast tool servo (FTS) system is based on the T-shaped layout of lathe, the machining complex shape surface is decomposed into rotary surface and microstructures, and composite machining is carried out based on the dependence relationship of motion axis [30, 31]. FTS has the advantages of controllable machining accuracy, high frequency response and large flexibility of machining system, so it is widely used in the machining and manufacturing of micro/nano structures with limited stroke [32, 33]. A typical schematic of a FTS system as shown in Fig. 4b. The fast tool servo diamond turning is limited by the bandwidth and resolution requirements, and it is affected by vibration when machining the discontinuous complex lens array such as Fig. 5, which leads to the deterioration of surface quality. Zhu et al. proposed a new diamond machining method with consistent machining capability and the ability to guarantee good accuracy in the preparation of complex lens arrays [34].

FTS system can be designed as different degree-of-freedom (DOF) to satisfy various requirement. Single-DOF FTS system is mainly used to fabricate simple micro/nano structures. Multi-DOF FTS system extends the system application, it can output complex tool trajectory to fabricate multi-scale complex micro/nano structures [30, 35]. Zhu et al. designed a piezo-driven 2-DOF FTS cutting tool motion mechanism for fabricating micro-structured surfaces with scattering homogenization [36]. Liu et al. designed a 2-DOF piezo-actuated FTS system that could generate sinusoidal wavy surface uniformly [37]. Li et al. proposed a 3-DOF piezo-driven FTS mechanism with high natural frequency and decoupling property, which effectively reduced the surface error of the microstructures [38].

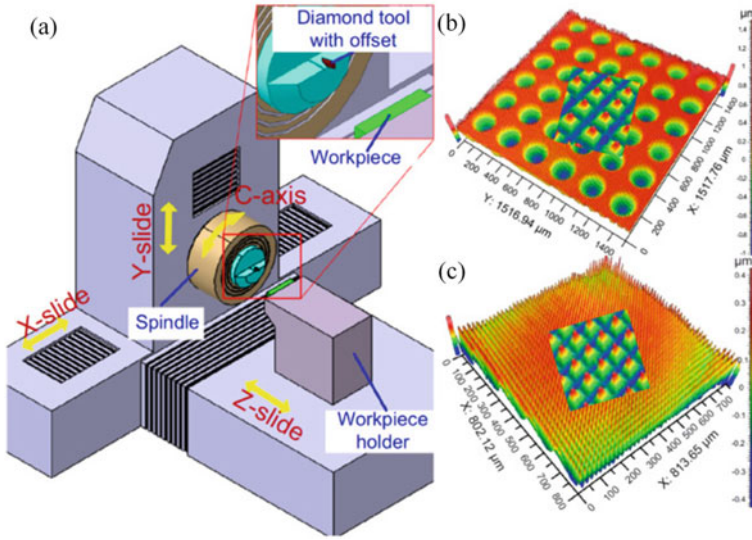
Work directly with the FTS device is difficult to raster milling due to the short contact time between the cutting tool and the workpiece. The machining of simple micro/nano structures can be realized by controlling the rotation speed of the raster milling tool to match the servo vibration device. For example, Duan et al. achieved the periodic microstructured optical surface machining by controlling the cutting speed of the raster milling and modulating the cutting arc trajectory combined with the one-dimensional FTS device [39, 40]; Zhou et al. took a different approach, using the high-speed cutting characteristics of raster milling to achieve high spatial frequency micro-groove structure, combined with the medium frequency vibration



**Fig. 6** Multi-layer structure color micro grooves array fabricated by raster milling and servo vibration device: **a** structured coloration, **b** vibration-assisted fly cutting for two-level structures, **c** created two-level iridescent structures, **d** high-saturation iridescent pattern [40]

of the workpiece to achieve the basic surface shape, and comprehensively realize the combined machining of multi-layer structure color micro-groove array, as shown in Fig. 6 [40]. These innovation methods verified the feasibility of the raster milling combined with FTS device for micro/nano structure machining. However, due to the raster milling servo axis usually has a small radius arc space trajectory and high speed, it is unable to realize straight track compensation and cooperation with multi-dimensional servo vibration platform. Thus raster milling is unable to meet the requirement of micro/nano grooved surface machining.

Combined with STS/FTS system also extends the applicability for tool offset fly cutting to realize the preparation of multi-scale micro/nano structures. Zhu et al. designed the novel end-fly-cutting-servo system combined with STS/FTS technology to realize the machining of freeform surface, micro-lens array and micro-pyramid multi-layer composite structures [21, 41, 42]. The configuration of the proposed novel end-fly-cutting-servo system structure and the fabricated micro/nano structures are shown in the Fig. 7. In the following study, they used the spindle integrated three-dimensional servo vibration device to realize the dual excitation vibration of different planes, and fabricated micro/nano structures with constant amplitude and spatial frequency [43]. However, in the above machining methods, the main cutting motion of the tool is not compensated in a straight line, and the cutting trajectory is still a circular arc trajectory, which cannot realize the fabrication of high-quality micro/nano groove surface.



**Fig. 7** **a** The configuration of the proposed novel end-fly-cutting-servo system, **b** micro-aspheric array with nano-pyramids, **c** F-theta freeform surface with nano-pyramids [44]

## 4 Summary and Outlook

This part mainly discusses the fabrication of micro/nano structures by ultra-precision fly cutting. Based on the summary of the characteristics of several methods of ultra-precision machining, this section focuses on ultra-precision fly cutting combined with STS/FTS system to prepare multi-scale complex micro-nano structure, and analyzes the force signal and energy signal in machining, so as to optimize the machining process. In this chapter, different methods of fabricating micro/nano structures by ultra-precision machining are reviewed and the related application progress is introduced, and the limitations of different machining processes are summarized. In particular, the potential applications of tool offset fly cutting as an effective method of machining micro/nano structures in combination with STS/FTS are introduced. However, no matter turning or fly cutting, it is difficult to achieve straight grooves because of the specific tool path. Chapter 2 effectively solves the problem that the circular arc tool trajectory in fly cutting cannot fabricate straight grooves, and introduces the breakthrough in machining straight grooves by tool offset fly cutting. Chapter 3 introduces the fabrication of multi-layer hierarchical micro/nano structures by tool offset fly cutting. In Chap. 4, the method of machining micro-optics arrays with high-aspect-ratio by tool offset fly cutting is presented. It can avoid the destruction of tool interference and tool vibration to the surface, and realize smoother and more uniform surface quality of micro/nano structures. In Chap. 5, the method of raster milling on monocrystalline silicon to fabricate infrared micro-optics

arrays is proposed, which can effectively avoid the non-uniform fracture of work-piece surface, reduce the surface roughness and improve the machining efficiency. In Chap. 6, from the perspective of energy signal and force signal, a theoretical model is established to analyze the material removal mechanism in ultra-precision machining process, which provides guidance for optimizing machining performance. This part will provide guidance for the expansion and application of ultra-precision fly cutting, and provide theoretical reference for the preparation of multi-scale complex micro/nano structures.

**Acknowledgements** The work described in this chapter was supported by the National Natural Science Foundation of China (Grant No. 52275454), and the Shenzhen Natural Science Foundation (Grant No. 20200826160002001, JCYJ2022053103614032).

## References

1. Chen H, Zhang P, Zhang L, Liu H, Jiang Y, Zhang D, Han Z, Jiang L (2016) Continuous directional water transport on the peristome surface of *Nepenthes alata*. *Nature* 532(7597):85–89
2. Cui X, Sun N, Guo J, Ma J, Ming P (2022) Green multi-biomimetic spontaneous oil-transport microstructure and its effects on energy consumption in sustainable intermittent cutting. *J Cleaner Prod* 367:133035
3. Kong LB, Cheung CF, To S (2012) Design, fabrication and characterization of three-dimensional patterned microstructured surfaces with self-cleaning properties from hydrophilic materials. *Proc Inst Mech Eng, Part B: J Eng Manuf* 226(9):1536–1549
4. Yue X, Liu W, Wang Y (2018) Freezing delay, frost accumulation and droplets condensation properties of micro- or hierarchically-structured silicon surfaces. *Int J Heat Mass Transf* 126:442–451
5. Zhang S, Zhou Y, Zhang H, Xiong Z, To S (2019) Advances in ultra-precision machining of micro-structured functional surfaces and their typical applications. *Int J Mach Tools Manuf* 142:16–41
6. Sun Z, To S, Yu KM (2019) Feasibility investigation on ductile machining of single-crystal silicon for deep micro-structures by ultra-precision fly cutting. *J Manuf Processes* 45:176–187
7. Sun Z, To S, Wang S (2019) An analytical force model for ultra-precision diamond sculpturing of micro-grooves with textured surfaces. *Int J Mech Sci* 160:129–139
8. Zhang X, Liu K, Shan X, Liu Y (2014) Roll-to-roll embossing of optical linear Fresnel lens polymer film for solar concentration. *Opt Express* 22(25):A1835–A1842
9. Wang Y, Fan P, Luo X, Geng Y, Goel S, Wu W, Li G, Yan Y (2021) Fabrication of three-dimensional sin-shaped ripples using a multi-tip diamond tool based on the force modulation approach. *J Manuf Processes* 72:262–273
10. Sharma V, Pandey PM (2016) Recent advances in turning with textured cutting tools: a review. *J Cleaner Prod* 137:701–715
11. Liu X, Zhang X, Fang F, Zeng Z, Gao H, Hu X (2015) Influence of machining errors on form errors of microlens arrays in ultra-precision turning. *Int J Mach Tools Manuf* 96:80–93
12. Wang SJ, To S, Chen X, Chen XD (2014) An investigation on surface finishing in ultra-precision raster milling of aluminum alloy 6061. *Proc Inst Mech Eng, Part B: J Eng Manuf* 229(8):1289–1301
13. Cheng MN, Cheung CF, Lee WB, To S, Kong LB (2008) Theoretical and experimental analysis of nano-surface generation in ultra-precision raster milling. *Int J Mach Tools Manuf* 48(10):1090–1102

14. Kong LB, Cheung CF, To S, Lee WB (2009) An investigation into surface generation in ultra-precision raster milling. *J Mater Process Technol* 209(8):4178–4185
15. Zhang G, Ran J, To S, Wu X, Huang P, Kuz'min MP (2020) Size effect on surface generation of multiphase alloys in ultra-precision fly cutting. *J Manuf Processes* 60:23–36
16. Zhang G, To S, Zhang S (2016) Evaluation for tool flank wear and its influences on surface roughness in ultra-precision raster fly cutting. *Int J Mech Sci* 118:125–134
17. Zhang G, To S, Xiao G (2014) A novel spindle inclination error identification and compensation method in ultra-precision raster milling. *Int J Mach Tools Manuf* 78:8–17
18. Zhang G, To S, Zhang S, Zhu Z (2016) Case study of surface micro-waves in ultra-precision raster fly cutting. *Precis Eng* 46:393–398
19. Zhang S, Zong W (2021) FE-SPH hybrid method to simulate the effect of tool inclination angle in oblique diamond cutting of KDP crystal. *Int J Mech Sci* 196:106271
20. Li C, Piao Y, Hu Y, Wei Z, Li L, Zhang F (2021) Modelling and experimental investigation of temperature field during fly-cutting of KDP crystals. *Int J Mech Sci* 210:106751
21. Zhu Z, To S, Zhang S (2015) Large-scale fabrication of micro-lens array by novel end-fly-cutting-servo diamond machining. *Opt Express* 23(16):20593–20604
22. Zhu Z, To S, Zhang S (2015) Active control of residual tool marks for freeform optics functionalization by novel biaxial servo assisted fly cutting. *Appl Opt* 54(25):7656–7662
23. Nagayama K, Yan J (2021) Deterministic error compensation for slow tool servo-driven diamond turning of freeform surface with nanometric form accuracy. *J Manuf Processes* 64:45–57
24. Yang S, Yu D, Yang H, Feng Y, Liu X, Yin Z (2021) Hybrid tool servo diamond turning of multiscale optical surface based on spectral separation of tool path. *Int J Adv Manuf Technol* 116(1):145–157
25. Yin ZQ, Dai YF, Li SY, Guan CL, Tie GP (2011) Fabrication of off-axis aspheric surfaces using a slow tool servo. *Int J Mach Tools Manuf* 51(5):404–410
26. Huang P, Wu X, To S, Zhu L, Zhu Z (2020) Deterioration of form accuracy induced by servo dynamics errors and real-time compensation for slow tool servo diamond turning of complex-shaped optics. *Int J Mach Tools Manuf* 154:103556
27. Zhang X, Gao H, Guo Y, Zhang G (2012) Machining of optical freeform prisms by rotating tools turning. *CIRP Ann* 61(1):519–522
28. Qin F-Z, Ma J-W, Jia Z-Y, Li G-L, Zhang J-Z (2022) Estimation and compensation for deviation of contour in slow tool servo precision turning for complicated curved surface. *J Mech Sci Technol* 36(8):4185–4196
29. Senthil Kumar A, Aravind Raghavendra MR, Neo WK, Rahman M (2014) 11.04—Fast and fine tool servo for ultraprecision machining. In: Hashmi S, Batalha GF, Van Tyne CJ, Yilbas B (eds) *Comprehensive materials processing*. Elsevier, Oxford, pp 61–88
30. Zhao D, Zhu Z, Huang P, Guo P, Zhu L, Zhu Z (2020) Development of a piezoelectrically actuated dual-stage fast tool servo. *Mech Syst Signal Process* 144:106873
31. Yoshioka H, Kojima K, Toyota D (2020) Micro patterning on curved surface with a fast tool servo system for micro milling process. *CIRP Ann* 69(1):325–328
32. Huang W-W, Li L, Zhu Z, Zhu L-M (2022) Modeling, design and control of normal-stressed electromagnetic actuated fast tool servos. *Mech Syst Signal Process* 178:109304
33. Zhou X, Zhu Z, Zhao S, Lin J, Dou J (2011) An improved adaptive feedforward cancellation for trajectory tracking of fast tool servo based on fractional calculus. *Procedia Eng* 15:315–320
34. Zhu W-L, Duan F, Zhang X, Zhu Z, Ju B-F (2018) A new diamond machining approach for extendable fabrication of micro-freeform lens array. *Int J Mach Tools Manuf* 124:134–148
35. Tong Z, Zhong W, To S, Zeng W (2020) Fast-tool-servo micro-grooving freeform surfaces with embedded metrology. *CIRP Ann* 69(1):505–508
36. Zhu Z, Zhou X, Liu Z, Wang R, Zhu L (2014) Development of a piezoelectrically actuated two-degree-of-freedom fast tool servo with decoupled motions for micro-/nanomachining. *Precis Eng* 38(4):809–820
37. Liu Y, Zheng Y, Gu Y, Lin J, Lu M, Xu Z, Fu B (2019) Development of piezo-actuated two-degree-of-freedom fast tool servo system. *Micromachines* 10 (5)

38. Li H, Tang H, Li J, Chen X (2021) Design, fabrication, and testing of a 3-DOF piezo fast tool servo for microstructure machining. *Precis Eng* 72:756–768
39. Duan F, Zhu W-L, Sun A, Ju B-F (2020) Systematic modeling and rapid control for diamond machining of periodical optical surface. *J Manuf Processes* 56:451–462
40. He Y, Zhou T, Dong X, Liu P, Zhao W, Wang X, Hu Y, Yan J (2020) Generation of high-saturation two-level iridescent structures by vibration-assisted fly cutting. *Mater Des* 193:108839
41. To S, Zhu Z, Zeng W (2015) Novel end-fly-cutting-servo system for deterministic generation of hierarchical micro–nanostructures. *CIRP Ann* 64(1):133–136
42. Zhu Z, To S, Zhang S (2015) Theoretical and experimental investigation on the novel end-fly-cutting-servo diamond machining of hierarchical micro-nanostructures. *Int J Mach Tools Manuf* 94:15–25
43. Zhu Z, To S, Ehmann KF, Xiao G, Zhu W (2016) A novel diamond micro-/nano-machining process for the generation of hierarchical micro-/nano-structures. *J Micromech Microeng* 26(3):035009
44. Zhang SJ, To S, Zhu ZW, Zhang GQ (2016) A review of fly cutting applied to surface generation in ultra-precision machining. *Int J Mach Tools Manuf* 103:13–27

# Chapter 2

## Tool Offset Flycutting

### Straight-Groove-Type Microstructures



Jianpeng Wang, Guoqing Zhang, and Jiankai Jiang

**Abstract** Optical microstructure arrays with regular geometry, like micro groove arrays, pyramid arrays, triangular pyramid arrays, etc., are commonly employed in optical components because of their distinctive special optical characteristics. Machining these microstructure arrays requires the collaboration of several linear axes of the ultra-precision machine tool (UPMT), but the machining ability of UPMT is constrained by the absence of some linear axes, such as the Y-axis. This study describes the development of a novel offset-tool-servo end flycutting (OTSEF) system integrating slow tool servo (STS) technology to fabricate microstructure arrays with straight-groove type using a UPMT with three axes (X-, Z-, and C-axis) configuration. This study developed a compensation mathematical model to linearize tool arc trajectory. After that, cutting experiments for micro groove arrays, pyramid arrays, and triangular pyramid arrays were performed by the machine tool and the machining quality was evaluated. Theoretical and experimental results demonstrate the high accuracy of these machined microstructure arrays with RMS (root mean square) error of less than 1  $\mu\text{m}$ , which confirms the effectiveness of the proposed method to fabricate straight-groove type microstructure arrays only using three axes UPMTs. The proposed method not only offers a technological innovation for machining straight-groove-type microstructure arrays but also serves as a theoretical guide for more complex microstructure array machining.

---

J. Wang · G. Zhang (✉)

Shenzhen Key Laboratory of High Performance Nontraditional Manufacturing, College of Mechatronics and Control Engineering, Shenzhen University, Nan-hai Ave 3688, Shenzhen 518060, Guangdong, People's Republic of China  
e-mail: [zhanggq@szu.edu.cn](mailto:zhanggq@szu.edu.cn)

J. Jiang

Jiangmen Vocational and Polytechnic College, Chao-lian Ave 6, Jiangmen 529090, Guangdong, People's Republic of China



## 1 Introduction

Microstructure arrays can improve photovoltaic parts' optical performance like solar light guide plates, which are widely utilized in biomedical, aerospace, and defense industries, among other disciplines. Non-mechanical machining and mechanical machining are the two main categories of machining techniques for these microstructure arrays. The main non-mechanical machining methods are electrical etching, laser etching, 3D printing, etc. [1–3]. But most of these methods are not appropriate for microstructure arrays machining in the optics field and usually with a huge cost and time consumption.

Ultra-precision machining, a mechanical machining technology, is an efficient, high-accuracy, and low-cost method to fabricate microstructure arrays, especially using non-ferrous metals as the workpiece such as aluminum, copper, and brittle materials. Flycutting is a typical ultra-precision machining technology, which uses diamond tools as the cutting tool and is often used to fabricate macrostructures. Diamond tools combining with UPMTs can achieve mirror-level surface machining at a low cost and can be further used in the manufacturing of high-accuracy microstructure arrays relying on tool path planning.

Usually, ultra-precision flycutting needs to combine with two assistance technologies, fast tool servo (FTS) and slow tool servo (STS), to fabricate various microstructure arrays. FTS is a useful technique for cutting complex microstructure arrays because the cutting tool is mounted on an FTS holder with high-frequency vibration. In recent years, Zhu et al. developed an FTS device with multiscale productivity in both spatial and time domains employed in diamond cutting [4]. Using FTS, Li et al. successfully fabricated rectangular freeform surfaces with form errors on micro- and nano-level [5]. However, while cutting microstructure arrays, the displacement response of the FTS restricts the workpiece size. Also, it is challenging to satisfy the machining demands of microstructure arrays with some sharp edges like the cone shape. Additionally, the shock and vibration of the FTS system induced by the fast forth and back of the diamond tool will destroy the fabricated microstructure and even the FTS system. STS is another advanced technology used in ultra-precision machining and accomplished by the linkage control of the machine tool's motion axes under a lower frequency (tens of hertz). Based on STS, Xu et al. proposed a novel rotary ultrasonic turning to fabricate micro groove structures [6]; Yan and Fang studied a novel wheel grinding with a fillet-end grinding wheel to limit the wheel error transfer [7]. Combining with flycutting and F/STS, To et al. combined the concepts of end-face fly-cutting and F/STS to create a novel end-fly-cutting-servo system with 4-axis servo motions [8]; Zhu et al. machined overlapping lens array using a 4-axis UPMT by combining end flycutting and FTS [9]; Combining end flycutting and STS, Zhu et al. machined a secondary pyramid array also using a 4-axis UPMT [10].

In ultra-precision machining, machining microstructure arrays like the typical pyramid arrays and triangular pyramid arrays are fabricated by the profile-imprinting method. The surface of the workpiece is imprinted with the shape of the diamond tool cutting edge, and the required feed is performed during cutting using the machine

tool's multi-axis linkage. The linking of multi-axis (at least three linear axes) machine tools are the mainstay of the mechanical machining of microstructure arrays. For instance, Zhu et al. fabricated a pyramid array using a 4-axis linkage machine tool [10]; Zhang et al. achieved online machining and monitoring of V-groove arrays by employing a 5-axis machine tool [11]. A diamond tool with V-shaped sharp and a 5-axis UPMT were used by Huang et al. to fabricate grayscale micro figures on metal surfaces using diamond micro lithography [12]. However, it is a challenge to fabricate the straight-groove-type microstructures using a common configuration of a 3-axis UPMT due to the lack of a linear axis (Y-axis).

This chapter proposed a novel offset-tool-servo end flycutting (OTSEF) system integrating STS technology that enables the machining of straight-groove microstructure arrays, such as pyramid arrays and triangular pyramids, on a conventional UPMT with only 3-axis (X-, Z-, and C-axis). First, a mathematical model for the linearization of the arc tool trajectory was developed. The model was used to fabricate the groove, pyramid, and triangular pyramid arrays independently. The impacts of machining error and tool posture on the micro grooves' form accuracy were then discussed. The distribution and amplitude of machining errors were analyzed by comparing the experimental results with the simulation results. This method is an economical and effective method for the fabricating of straight-groove type microstructure arrays, and also provides technical and theoretical references of complex microstructure arrays fabrication, such as hierarchical microstructure arrays, using 3-axis (X-, Z-, and C-axis) UPMTs.

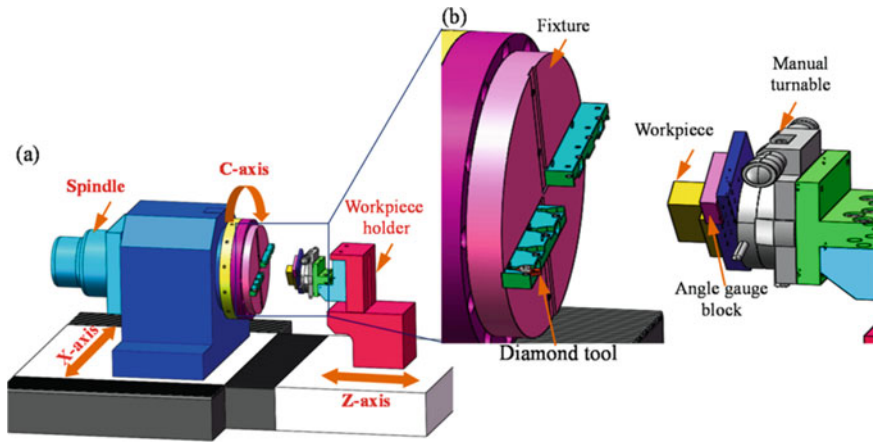
## 2 Machining System

### 2.1 The OTSEF System

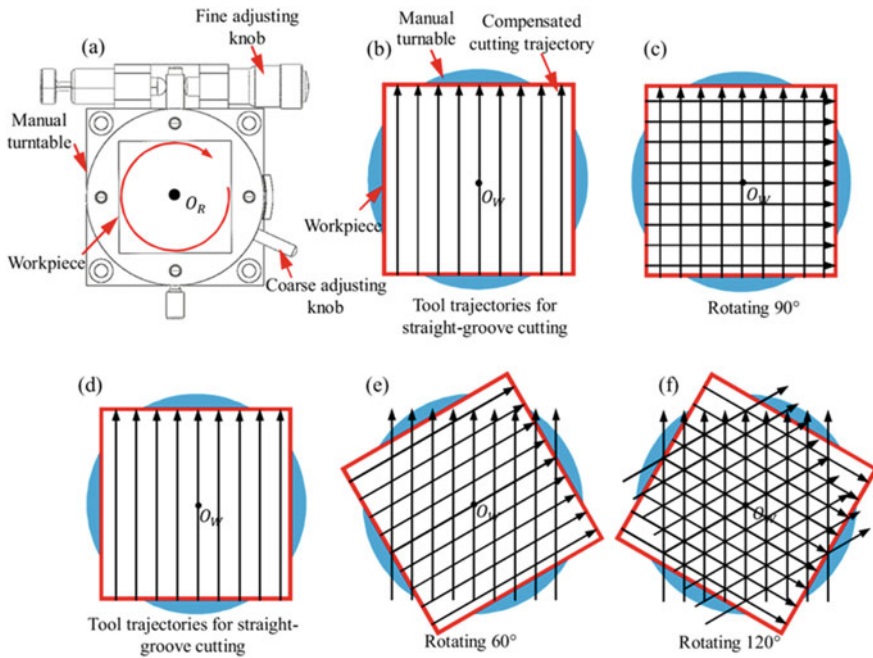
The configuration of the OTSEF system is based on a 3-axis (X-, Z-, and C-axis) servo motions UPMTs, as shown in Fig. 1a. In contrast to traditional F/STS assisted diamond turning, the workpiece is clamped to a manual turntable and further secured to a holder using a special clamp to realize the workpiece rotates in lockstep with the manual turntable, as illustrated in Fig. 1b. The rotation angle of the workpiece is calibrated using a high-accuracy angle gauge block to guarantee rotation accuracy.

The tool trajectory used to fabricate different straight-groove types of microstructure arrays, including pyramid and triangular pyramid arrays, is shown in Fig. 2.  $O_R$  stands for the manual turntable's rotating center, and  $O_W$  represents the workpiece's center. In Fig. 2a, it is stated that the workpiece is mounted on the turntable, and it can follow the turntable to rotate at an angle. Two adjusting knobs are used to operate the manual turntable: one is coarse and another is fine to assure rotation precision.

In the microstructure arrays fabrication process, the designed fundamental array (DFA) can be machined using the straight cutting method, whereas other microstructure arrays are fabricated by the intersection of DFA. Figure 2b shows that a group of



**Fig. 1** Schematic of **a** the configuration of the OTSEF system and **b** the relative positions of the diamond tool and workpiece



**Fig. 2** Schematic of tool trajectories used in microstructure arrays fabrication: **a** the workpiece rotates following the manual turntable; **b** and **c** tool trajectories used in pyramid arrays fabrication; **d–f** tool trajectories used in triangular pyramid arrays fabrication

straight cutting is used to fabricate the well-defined DFA. A micro pyramid array can be overlapped on the original DFA to be further fabricated, as illustrated in Fig. 2c. Similarly, a triangular pyramid array can be machined by the overlapping DFAs two times by rotating the original DFA  $60^\circ$  and  $120^\circ$  respectively of, as shown in Fig. 2d–f.

## 2.2 Tool Path Planning

Because the diamond tools have a regular geometry, machining accuracy can be directly influenced by the diamond tools' installation position. Therefore, a description of tool posture and an examination of its effects on machining accuracy is very important. The rotation tool path following the spindle is illustrated in Fig. 3a, where  $R_d$  is the tool rotation radius,  $O_W-X_W Y_W Z_W$  and  $O_S-X_S Y_S Z_S$  stand for the workpiece and spindle's Cartesian coordinate systems, respectively. When a tool is mounted to a fixture, the install tool portion of the fixture is turned horizontal using an electronic gauge probe to align the tool's rake face with the spindle axis. In the OTSEF system, the spindle coordinate system  $O_S-X_S Y_S Z_S$  is chosen as a global reference, therefore, the flycutting tool trajectory can be expressed as:

$$X^2 + Y^2 = R_d^2 \quad (1)$$

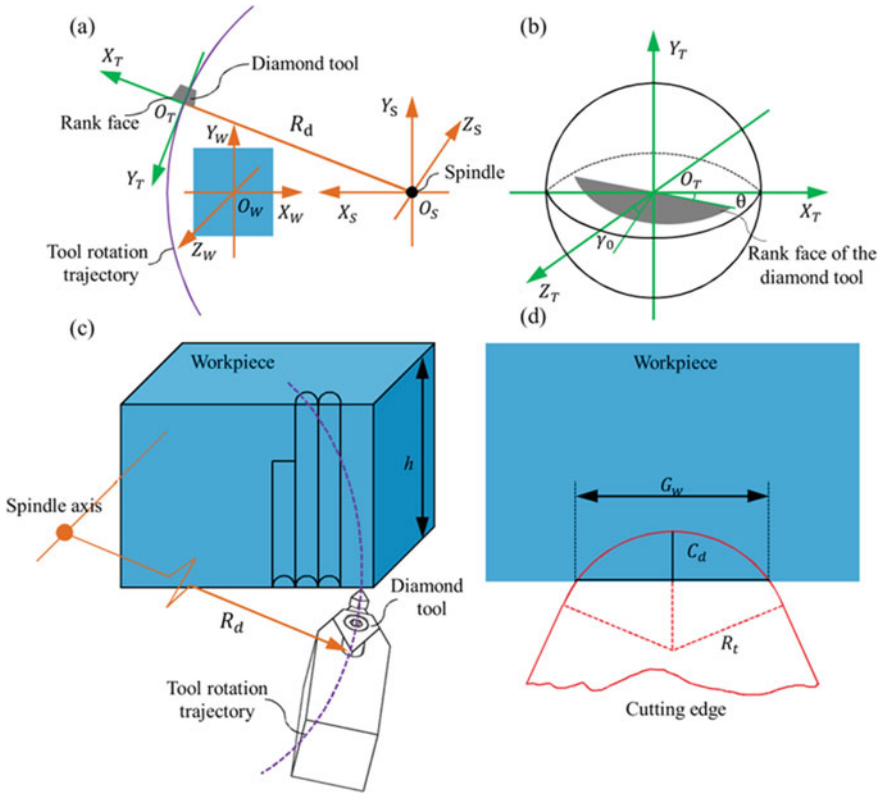
Additionally, as illustrated in Fig. 3b, a tool coordinate system  $O_T-X_T Y_T Z_T$  is established. The tool rake angle is represented by the symbol  $\gamma_0$  and the tool nose radius is given as  $R_t$ . An angle error  $\theta$  inevitably exists since the tool rotates around the  $O_T Y_T$  axis during its installation. The equation for the cutting edge in the tool coordinate system can be expressed as follows:

$$\begin{cases} X_T = R_t \cos \theta \\ Y_T = R_t \sin \theta \sin \gamma_0, \theta_\epsilon [\theta_{\min}, \theta_{\max}] \\ Z_T = R_t \sin \theta \cos \gamma_0 \end{cases} \quad (2)$$

Where  $\theta_{\min}$  and  $\theta_{\max}$  stand for the cutting edge's minimum and maximum deflection angles, respectively.

## 2.3 Mathematical Modeling

The arc tool trajectory of end flycutting is not suited to fabricate straight-groove type microstructures. To accurately fabricate straight-groove type microstructure arrays, a compensation algorithm is provided to linearize the arc tool trajectory using the

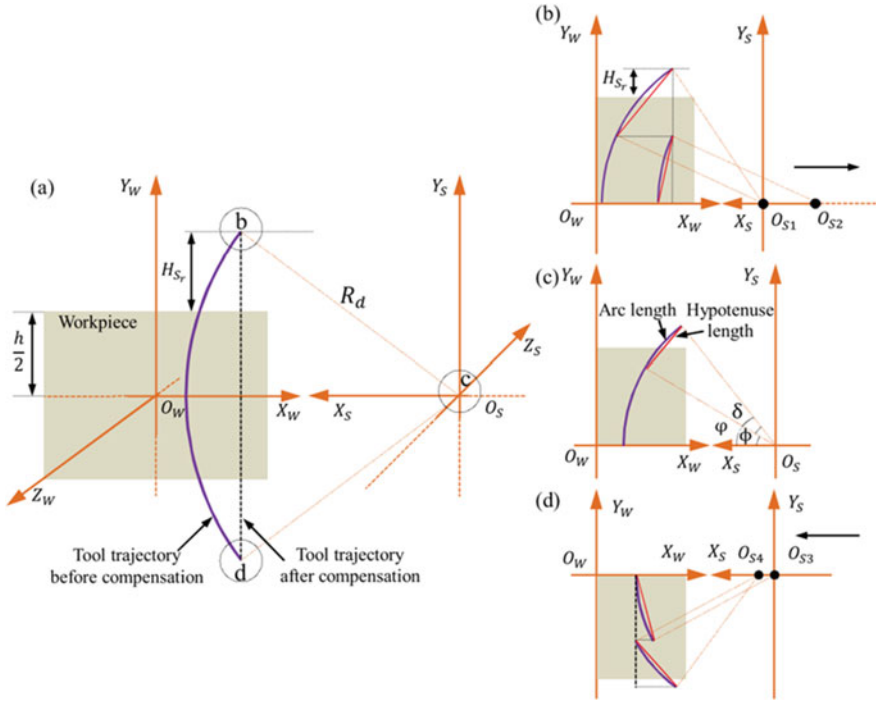


**Fig. 3** Schematic of diamond tool flycutting: **a** tool trajectory; **b** tool coordinate system; **c** flycutting straight groove array; **d** parameters of diamond tool cutting edge

linkage servo motion of the Z- and C-axis of the UPMT. The linearization tool path modeling in this section mainly comes from our published work [13].

Combining the iterative and differential methods is fundamental to achieving a compensation algorithm. Each difference element's distance to be compensated needs to be computed by the mathematical model, and the subsequent compensation distance is determined by adding the previous compensation result to the computation. Two steps make up the mathematical modeling process: first, the arc tool path used for cutting is discretized into linear differential elements to fit C-axis; second, according to the relative motion relation between the machine tool and the workpiece, the mathematical model of compensating the tool arc trajectory to a linear trajectory is derived.

Figure 4 illustrates a case of the end flycutting that an arc trajectory is interpolated to a linear trajectory.  $\delta$  stands for the spindle rotation angle in each differential element. The arc length of the differential element corresponding to the  $\delta$  can be solved to get the compensation distance. Therefore, we utilize the equivalent linear length rather



**Fig. 4** Schematic of linearization arc tool trajectory: **a** tool trajectory from b to d; **b** small differential element in right compensation stage; **c** parameters of a differential element; **d** small differential element in left compensation stage

than the arc length to decrease the calculated amount based on differential theory. Based on Eq. (1), the derivative of Y can be derived as follows:

$$Y' = \frac{dY}{dX} = \mp \frac{X}{\sqrt{R_d^2 - X^2}} \tag{3}$$

When the spindle rotates at an angle  $\delta$ ,  $\varphi$  and  $\phi$  stand for included angles between the bottom and top boundaries of angle  $\delta$  and the  $O_S X_S$  axis, respectively, the related expression of these angles can be derived as:

$$\varphi - \phi = \delta \tag{4}$$

Based on the calculation formula of arc length, the arc length corresponding to angle  $\delta$  in the flycutting trajectory, whose rotation radius is defined as  $R_d$  in the  $O_S-X_S Y_S$  plane, can be expressed by:

$$L_a = \int_{R_d \cos \phi}^{R_d} \sqrt{1 + Y'^2} dx \quad (5)$$

Combining Eqs. (3) and (5), and considering Eq. (4) yields:

$$L_a = R_d \int_{R_d \cos \phi}^{R_d} \frac{1}{\sqrt{R_d^2 - X^2}} dx = \frac{R_d \pi \delta}{180} \quad (6)$$

The hypotenuse length corresponding to angle  $\delta$  can be calculated as shown in Fig. 4c by:

$$L_h = 2R_d \sin\left(\frac{\delta}{2}\right) \quad (7)$$

The error between the hypotenuse length and arc length, taking into account both Eqs. (6) and (7) is derived as:

$$\delta L_e = L_a - L_h = \frac{R_d \pi \delta}{180} - 2R_d \sin\left(\frac{\delta}{2}\right) \quad (8)$$

The error between the hypotenuse length and arc length is determined as  $10^{-6}$  nm by substituting frequently used machining parameters  $\delta = 0.004^\circ$  and  $R_d = 15$  mm into Eq. (8). The computed error is substantially small than the feedback resolution of the UPMT (0.01 nm linear/0.0000001° rotary), so the error value in between could be disregarded. The hypotenuse length can thus be used in place of the equivalent arc length when the C-axis rotates at a reasonably modest angle.

As is shown in Fig. 4a, when the coordinate planes of  $O_W-X_W Y_W$  and  $O_S-X_S Y_S$  coincide, the flycutting tool arc trajectory (before compensation) is compensated as a linear trajectory (after compensation). The flycutting tool with the spindle rotation intermittent cutting on the workpiece surface. The spindle rotation cycle covering the workpiece is evenly discretized into  $N_s$ , where the number of real tool positions is numbered from 1 to  $2n$ . As for the  $l$  point ( $l \in [1, 2n]$ ) in the  $k$ th spindle rotation cycle, the rotation angle  $\varepsilon_{k,l}$  about point  $l$  can be expressed as follows:

$$\varepsilon_{k,l} = 2\pi k + \frac{2\pi l}{N_s} \quad (9)$$

When  $l \in [1, 2n]$  and  $\varepsilon_{k,l} \in \left[\frac{\varepsilon_{k,1}}{2\pi}, \frac{\varepsilon_{k,2n}}{2\pi}\right]$ , it represents that the workpiece is cut, otherwise, it represents tool air cutting.

In addition, when the tool positions are within the range of  $[1, n]$  and  $[n + 1, 2n]$ , the arc trajectory of the flycutting tool is compensated for linear trajectory, as shown in Fig. 4b, d. In Fig. 4b, the  $h$  and  $H_{Sr}$  are defined as the workpiece's height and the tool trajectory's reserved height to guarantee that the tool trajectory completely covers the workpiece surface, respectively. When  $H_{Sr}$  was given the proper numerical value,

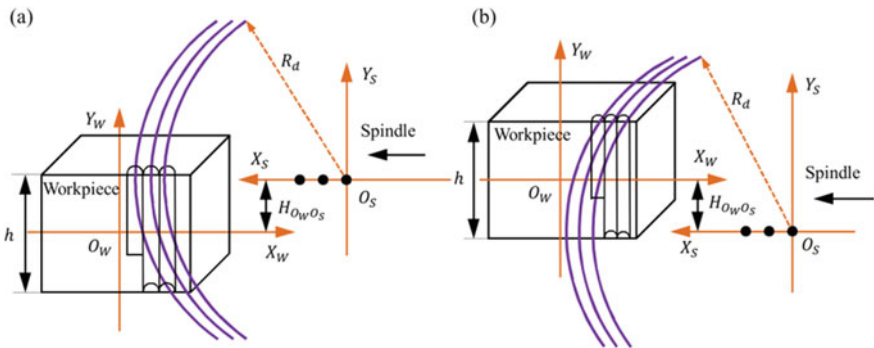
the compensation procedure started. At that moment,  $O_{S1}$  represents the spindle center. Actually, the spindle rotation angle  $\delta$  is a given parameter and therefore can calculate the corresponding X-axis feed distance, i.e. spindle center moves from  $O_{S1}$  to  $O_{S2}$ . When the vertical height  $H_{S_r} + h/2$  was iteratively subtracted to zero, the compensation procedure for tool position within  $[1, n]$  came to an end. This process is named right compensation because X-axis moves to the right throughout the compensation stage.

Similar to the right compensation stage, when the tool position is within  $[n + 1, 2n]$ , X-axis moves to the left throughout the compensation stage and therefore this process is named left compensation, as shown in Fig. 4d. Clearly, when the spindle moves an angle  $\delta$ , the spindle center moves from  $O_{S3}$  to  $O_{S4}$ .

Noted that the coordinate plane  $O_S-X_S Z_S$  of the spindle coordinate system is fixed during the machining process, but the coordinate plane  $O_W-X_W Z_W$  of the workpiece coordinate system changes depending on how the workpiece is installed. When  $O_S$  is higher or lower than  $O_W$ ,  $H_{O_W O_S}$  stands for the vertical error. These are illustrated in Fig. 5. Clearly, the  $H_{O_W O_S}$  exists inevitable and should be suppressed to guarantee machining accuracy. Actually, the right and left compensation stage shown in Fig. 5 is similar to that in Fig. 4. The difference is that the iterative decrement of right compensation from  $H_{S_r} + h/2 + H_{O_W O_S}$  to 0, as shown in Fig. 5. And in the left compensation stage, the vertical error is an iterative increase from 0 to the absolute value of  $H_{S_r} + h/2 - H_{O_W O_S}$ .

In the compensation mathematical model,  $R_d^k$  denotes the radius of the flycutting tool trajectory,  $\delta X_S^{k,l}$  stands for the X-axis compensation distance when the C-axis rotates an angle  $\delta$ , and  $\delta Y_S^{k,l}$  represents the Y-axis translation following the C-axis. All of these parameters are operated in the  $O_S-X_S Y_S Z_S$  system.

During the right compensation stage, the starting point's compensation distance for the X- and Y-axis during right compensation is calculated by:



**Fig. 5** Schematic of vertical error between  $O_S$  and  $O_W$  when the tool trajectory covers workpiece surface: **a**  $O_S$  higher than  $O_W$  and **b** lower than  $O_W$



$$\begin{cases} \delta X_S^{k,1} = -2R_d^k \sin\left(\frac{\delta}{2}\right) \sin\left[\sin^{-1} \frac{H_{Sr}+h/2+H_{Ow}O_S}{R_d^k} - \frac{\delta}{2}\right] \\ \delta Y_S^{k,1} = 2R_d^k \sin\left(\frac{\delta}{2}\right) \cos\left[\sin^{-1} \frac{H_{Sr}+h/2+H_{Ow}O_S}{R_d^k} - \frac{\delta}{2}\right] \end{cases} \quad (10)$$

where  $R_d^k \in [R_d - X_T, R_d + X_T]$ .

Replacing  $\delta Y_S^{k,1}$  into Eq. (10), the new equation can be used to calculate the corresponding variable distance  $\delta X_S^{k,2}$  and  $\delta Y_S^{k,2}$  for the second compensation procedure, which is derived by the following:

$$\begin{cases} \delta X_S^{k,2} = -2R_d^k \sin\left(\frac{\delta}{2}\right) \sin\left[\sin^{-1} \frac{(H_{Sr}+h/2+H_{Ow}O_S - \delta Y_S^{k,1})}{R_d^k} - \frac{\delta}{2}\right] \\ \delta Y_S^{k,2} = 2R_d^k \sin\left(\frac{\delta}{2}\right) \cos\left[\sin^{-1} \frac{(H_{Sr}+h/2+H_{Ow}O_S - \delta Y_S^{k,1})}{R_d^k} - \frac{\delta}{2}\right] \end{cases} \quad (11)$$

Repeating the iteration process, until the tool position covers the range  $[1, n]$ . The general expressions are given by:

$$\begin{cases} \delta X_S^{k,n} = -2R_d^k \sin\left(\frac{\delta}{2}\right) \sin\left[\sin^{-1} \frac{(H_{Sr}+h/2+H_{Ow}O_S - \delta Y_S^{k,1} - \delta Y_S^{k,2} - \dots - \delta Y_S^{k,n-1})}{R_d^k} - \frac{\delta}{2}\right] \\ \delta Y_S^{k,n} = 2R_d^k \sin\left(\frac{\delta}{2}\right) \cos\left[\sin^{-1} \frac{(H_{Sr}+h/2+H_{Ow}O_S - \delta Y_S^{k,1} - \delta Y_S^{k,2} - \dots - \delta Y_S^{k,n-1})}{R_d^k} - \frac{\delta}{2}\right] \end{cases} \quad (12)$$

During the left compensation stage, the compensation distances for the X- and Y-axis at the initial tool position  $n + 1$  are derived as:

$$\begin{cases} \delta X_S^{k,n+1} = 2R_d^k \sin\left(\frac{\delta}{2}\right) \sin\left(\frac{\delta}{2}\right) \\ \delta Y_S^{k,n+1} = -2R_d^k \sin\left(\frac{\delta}{2}\right) \cos\left(\frac{\delta}{2}\right) \end{cases} \quad (13)$$

By substituting  $\delta Y_S^{k,n+1}$  into Eq. (13), the compensation distance of the X- and Y-axis into the subsequent compensatory procedure can be expressed by:

$$\begin{cases} \delta X_S^{k,n+2} = 2R_d^k \sin\left(\frac{\delta}{2}\right) \sin\left[\sin^{-1} \frac{|\delta Y_S^{k,n+1}|}{R_d^k} + \frac{\delta}{2}\right] \\ \delta Y_S^{k,n+2} = -2R_d^k \sin\left(\frac{\delta}{2}\right) \cos\left[\sin^{-1} \frac{|\delta Y_S^{k,n+1}|}{R_d^k} + \frac{\delta}{2}\right] \end{cases} \quad (14)$$

Repeating the iteration process, until the tool position covers the range  $[n + 1, 2n]$ . The general expressions are given by:

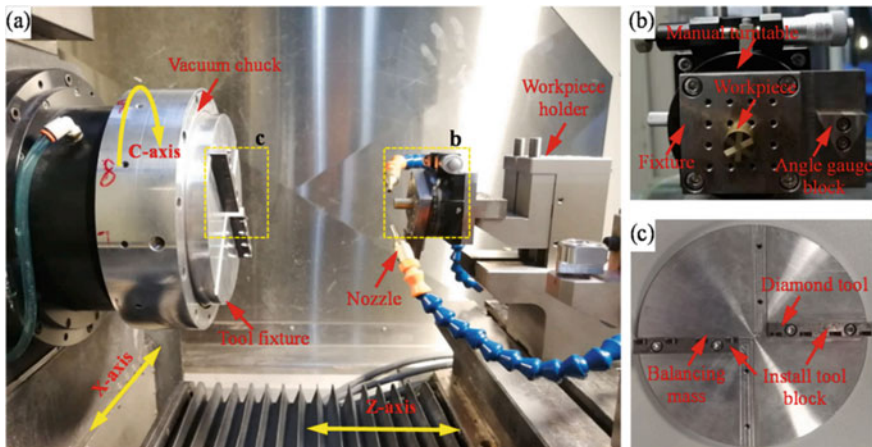
$$\begin{cases} \delta X_S^{k,2n} = 2R_d^k \sin\left(\frac{\delta}{2}\right) \sin\left[\sin^{-1} \frac{|\delta Y_S^{k,n+1} + \delta Y_S^{k,n+2} + \dots + \delta Y_S^{k,2n-1}|}{R_d^k} + \frac{\delta}{2}\right] \\ \delta Y_S^{k,2n} = -2R_d^k \sin\left(\frac{\delta}{2}\right) \cos\left[\sin^{-1} \frac{|\delta Y_S^{k,n+1} + \delta Y_S^{k,n+2} + \dots + \delta Y_S^{k,2n-1}|}{R_d^k} + \frac{\delta}{2}\right] \end{cases} \quad (15)$$

### 3 Experiments and Results Analysis

#### 3.1 Experiment Setup

Three typical straight-groove type microstructure arrays, including micro groove, pyramid, and triangular pyramid arrays, were machined on a 3-axis (X-, Z- and C-axis) UPMT to test the effectiveness of the proposed cutting method. Figure 6a illustrates how the vacuum chuck adsorbed the flycutting tool fixture on the spindle while the workpiece is mounted on a precision manual turntable (RPG60, MISUMI, Japan). The turntable is mounted to the tool holder. Figure 6b shows that the workpiece was fixed on the turntable through a specialized fixture. Although the turntable has a resolution of roughly 55 s, manual operation still causes significant machining errors. An angle gauge block was used to correct the rotation accuracy of the workpiece, and an electronic probe was used to measure the block, which was about  $0.02^\circ$ . Figure 6c illustrated that the diamond tool was fixed on the tool block. For the machining, a small nose radius diamond tool (natural single-crystal material) was used; the tool rotation radius is location dependent. The radius of tool rotation ( $R_d$ ) varies in [15, 35, 55, 75 mm]. During end flycutting, a balancing mass was employed to dynamically balance the diamond tool's weight. Furthermore, the workpiece surface needs to finish machined directly by flycutting to obtain a mirror surface before microstructure fabrication, which was aimed to correct the surface inclination issue.

Table 1 contains a list of the experimental tool and cutting parameters. The employed diamond tool, which has a nose radius of 0.1 mm, rake and included angles of  $0^\circ$  and  $120^\circ$ , respectively. And the C-axis rotating speed of 1 revolution



**Fig. 6** Hardware configuration of OTSEF system: **a** experimental setup, **b** a precision manual turntable, and **c** diamond tool fixture used in flycutting

**Table 1** Experimental parameters

Parameter	Value
Tool radius $R_t$	0.1 mm
Tool rake angle	$0^\circ$
Tool include angle	$120^\circ$
Cutting depth $C_d$	0.02 mm
Rotation speed	1 r/min

per minute, was used to fabricate microstructure arrays. In the experimental process, choosing a minimum tool rotation radius of 15 mm can highlight the efficiency of linear path interpolation.

According to Fig. 3c, d,  $C_d$  stands for the cutting depth and  $G_w$  represents the width of the micro groove. So, based on the geometric relationship shown in Fig. 3d,  $G_w$  can be expressed as follows:

$$G_w = 2\sqrt{R_t^2 - (R_t - C_d)^2} \quad (16)$$

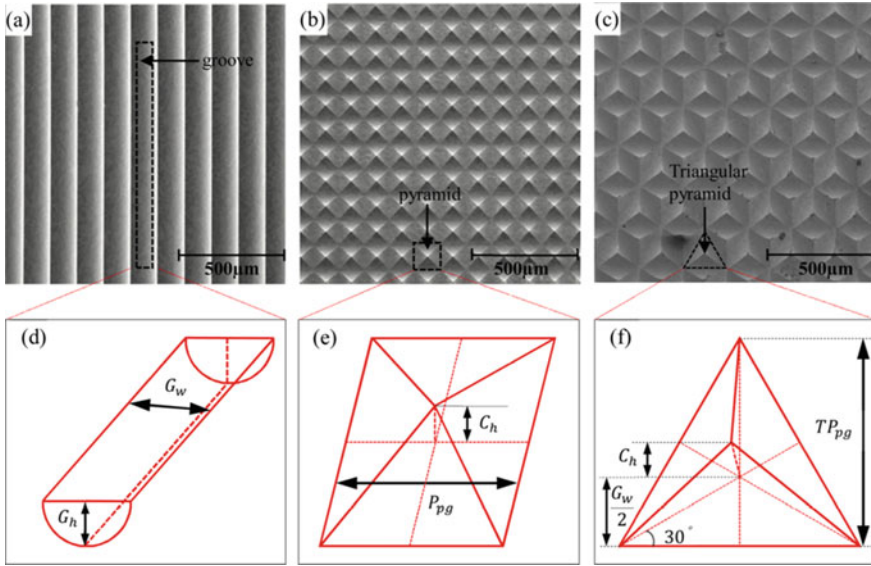
The spatial height is set at 20  $\mu\text{m}$  for the machining of three typical structures to assess the reliability of the machining system. Figure 7d, e illustrate that  $G_h$  stands for the micro groove's spatial height,  $P_{pg}$  represents the spacing between neighboring grooves, and  $C_h$  is defined as the pyramid microstructure's spatial height. Especially, when  $P_{pg}$  equals  $G_w$ ,  $C_h$  equals the  $C_d$  correspondingly. Figure 7f illustrates some geometry parameters of triangular pyramid microstructures, where  $TP_{pg}$  stands for the distance of neighboring grooves. To acquire the spatial height  $C_h$  (equal to the  $C_d$ ),  $TP_{pg}$  can be derived as:

$$TP_{pg} = \frac{G_w}{2} + \left( \frac{G_w}{2} / \sin 30^\circ \right) = \frac{3G_w}{2} \quad (17)$$

Some geometric parameters of three types machined microstructures are listed in Table 2. Moreover, brass was chosen as the cutting material due to its excellent cutting ability and material properties in ultra-precision machining.

### 3.2 Results and Discussion

The machined microstructure arrays are shown in Figs. 7 and 8. Figure 7a–c illustrates the machined microstructure arrays captured by an environmental scanning electron microscope (FEI Quanta 450 FEG). Clearly, the micro groove array was discovered to have good width consistency and straightness, while the micro pyramid array and micro triangular pyramid array both possess a single geometry shape and are distributed uniformly. An optical microscope module of a white light



**Fig. 7** Morphology of machined microstructure arrays: **a** micro groove array, **b** micro pyramid array, **c** micro triangular pyramid array; **d–f** their geometric characteristic. (Captured by SEM)

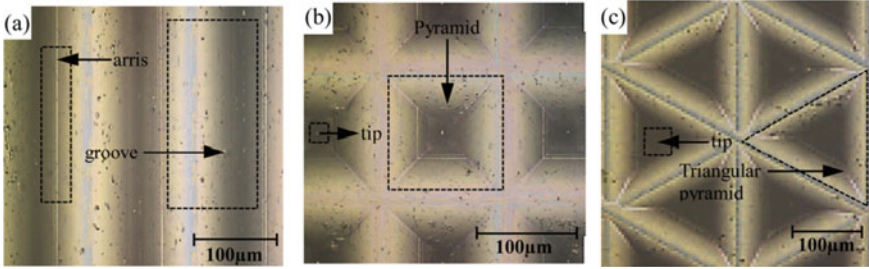
**Table 2** Microstructure parameters

Microstructures	Height $h$ ( $\mu\text{m}$ )	Spacing $G_w$ ( $\mu\text{m}$ )
Groove	20	120
Pyramid	20	120
Triangular pyramid	20	180

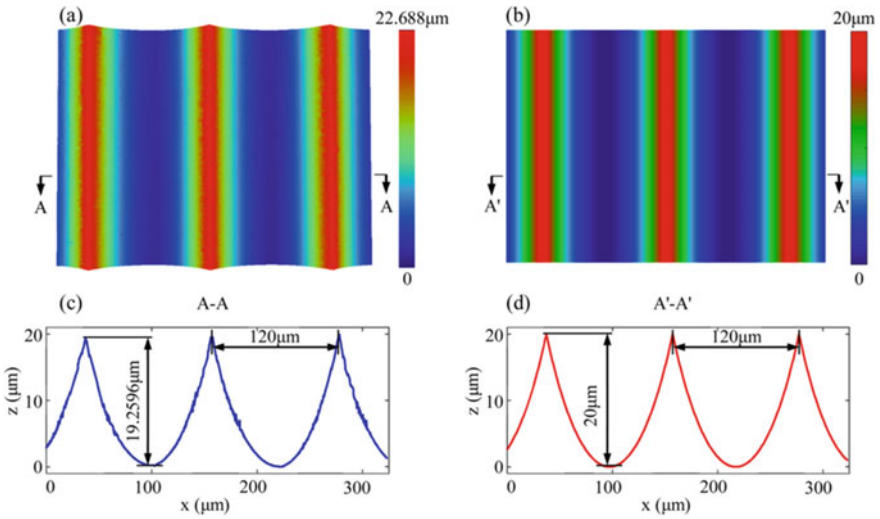
interferometer (Bruker Contour GT-X) was utilized to examine the geometry of the machined microstructure arrays to further analyze their geometrical features. Figure 8 shows a diagram of the three microstructure arrays. It is discovered that the machined microstructure arrays have good geometric consistency, with the sides of the microgroove array being straight and parallel to one another and the sides of the micro pyramid array and micro triangular pyramid array being the same length.

To evaluate the machining accuracy of these microstructures, the designed morphology of the three microstructure arrays was simulated using MATLAB® 2018, as shown in Figs. 9b, 11b and 13b, respectively. First, the equation for the surface array unit is established using the tool geometry and path. Second, cutting parameters are used in the equation to produce the array’s data point sets. Finally, MATLAB software is used to display the data clouds to generate a simulation model.

The in-depth analysis for each microstructure array is provided below combining the measured and simulated results.



**Fig. 8** Morphology characteristic of **a** micro groove array; **b** micro pyramid array; **c** micro triangular pyramid array. (Captured by Bruker Contour GT-X)



**Fig. 9** Comparison of measured and simulated micro groove array: **a** measured morphology; **b** simulated morphology; **c** measured sectional profile A-A; **d** simulated sectional profile B-B

### 3.2.1 Micro Groove Array

Figure 9a illustrates the measured three-dimensional (3D) morphology of the machined micro groove array, and its sectional curve is shown in Fig. 9c. Figure 9b, d illustrate the simulated 3D morphology and its sectional curve of the micro groove array, respectively

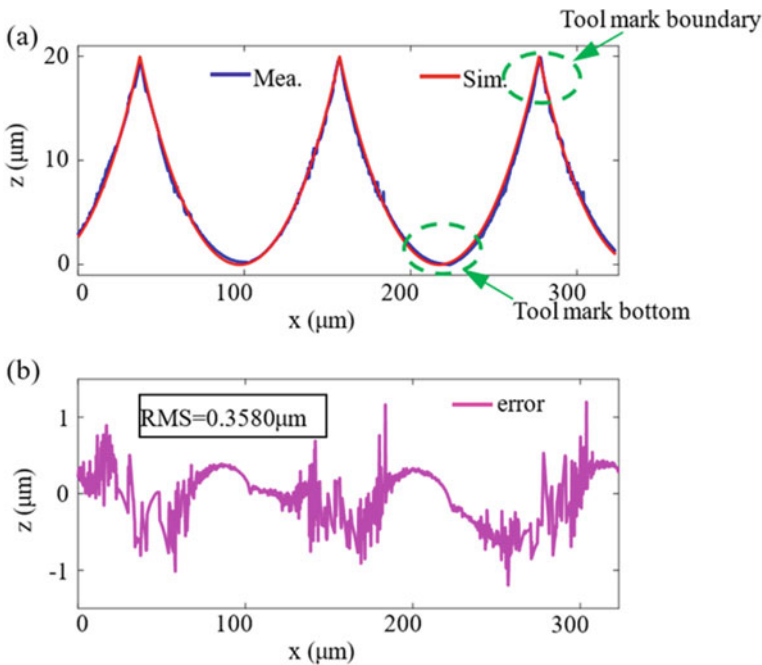
Clearly, the measured micro groove array’s groove width is 120  $\mu\text{m}$ , which is the same as the designed value shown in Fig. 9d. Moreover, the measured micro groove array’s groove depth is 19.2596  $\mu\text{m}$ , while the designed value is 20  $\mu\text{m}$ . The deviation in groove depth between the measured and designed is 0.7404  $\mu\text{m}$ , which may be caused by the material rebound and feed error. Comparing the measured and

simulated results, the machined micro groove array has good consistency with the simulated one, demonstrating the efficiency of the OTSEF system.

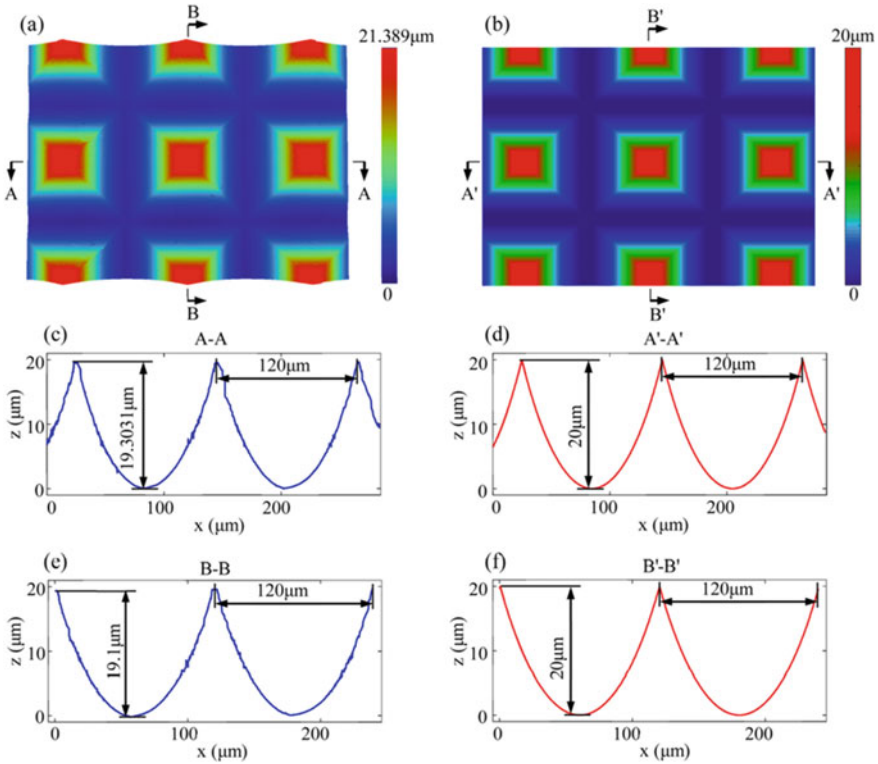
By comparing the measured sectional curve of the micro groove array with the simulation curve, the machining accuracy of the micro groove array using the OTSEF system can be further evaluated, as shown in Fig. 10a. Figure 10b illustrates their form error, and the overlapping two curves are discovered to be fine coincident. To access the curve error between the simulated and measured micro groove structures, root mean square (RMS) is used here, which can be calculated by:

$$\text{RMS} = \sqrt{\frac{\sum_1^n (h_{\text{Exp}} - h_{\text{Des}})^2}{n}} \quad (18)$$

Based on the error data in Fig. 10b and calculated by Eq. (18), the value of RMS is  $0.3580 \mu\text{m}$ , which is less than  $1 \mu\text{m}$ . There are a few point values that are still larger than  $1 \mu\text{m}$ , which is assumed to cause by the material rebound and burr on the workpiece surface. Additionally, the RMS error is bigger at the tool mark boundary of the curve but smaller at the tool mark bottom. This difference is assumed with material deformation during cutting since the residual tool mark boundary on the workpiece is thinner and more prone to deformation when subjected to tool force.



**Fig. 10** Machining error analysis for micro groove array: **a** fitting curves of A–A (see Fig. 9c) and B–B (see Fig. 9d) and **b** error curve

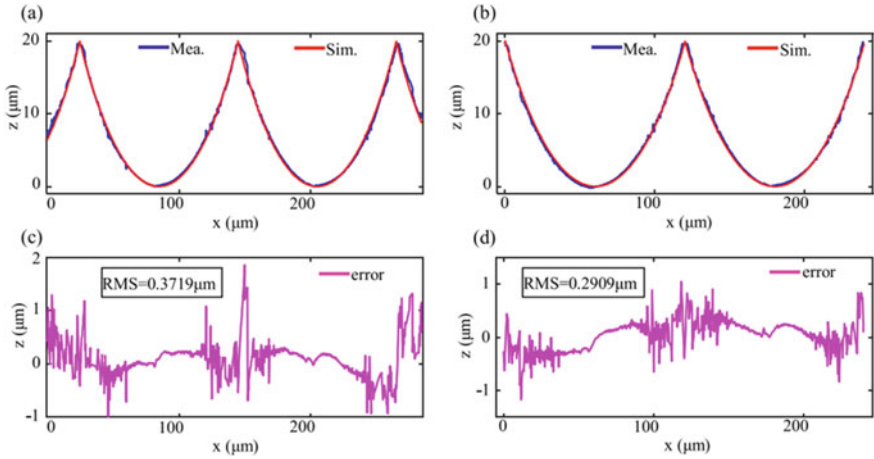


**Fig. 11** Comparison of measured and simulated micro pyramid array: **a** measured morphology; **b** simulated morphology; **c** measured sectional profile A-A; **d** simulated sectional profile A'-A'; **e** measured sectional profile B-B; **f** simulated sectional profile B'-B'

### 3.2.2 Micro Pyramid Array

A micro pyramid array was machined further based on the finished micro groove array. The machined micro pyramid array's measured 3D morphology is shown in Fig. 11a, and its two contour curves in sectional planes A-A and B-B are shown in Fig. 11, e. The simulated 3D morphology of the micro pyramid array is shown in Fig. 11b. The measured 3D morphology was discovered to be well consistent with the simulated one. The simulated micro pyramid array's measured 3D morphology is shown in Fig. 11b, and its two section curves in sectional planes A-A and B-B are shown in Fig. 11d, f. It is discovered that the spacing between two neighboring pyramids is equal to the desired spacing, and the height error is less than 1  $\mu\text{m}$  between the simulated and measured pyramids. The height error during cutting is inevitable due to the mechanical error of a manual turntable and the repeatability error of machine tools.

Figure 12a, b illustrate the fitting curves for the micro pyramid array's sectional curve in the A-A and B-B sectional planes, respectively. Clearly, the curves are



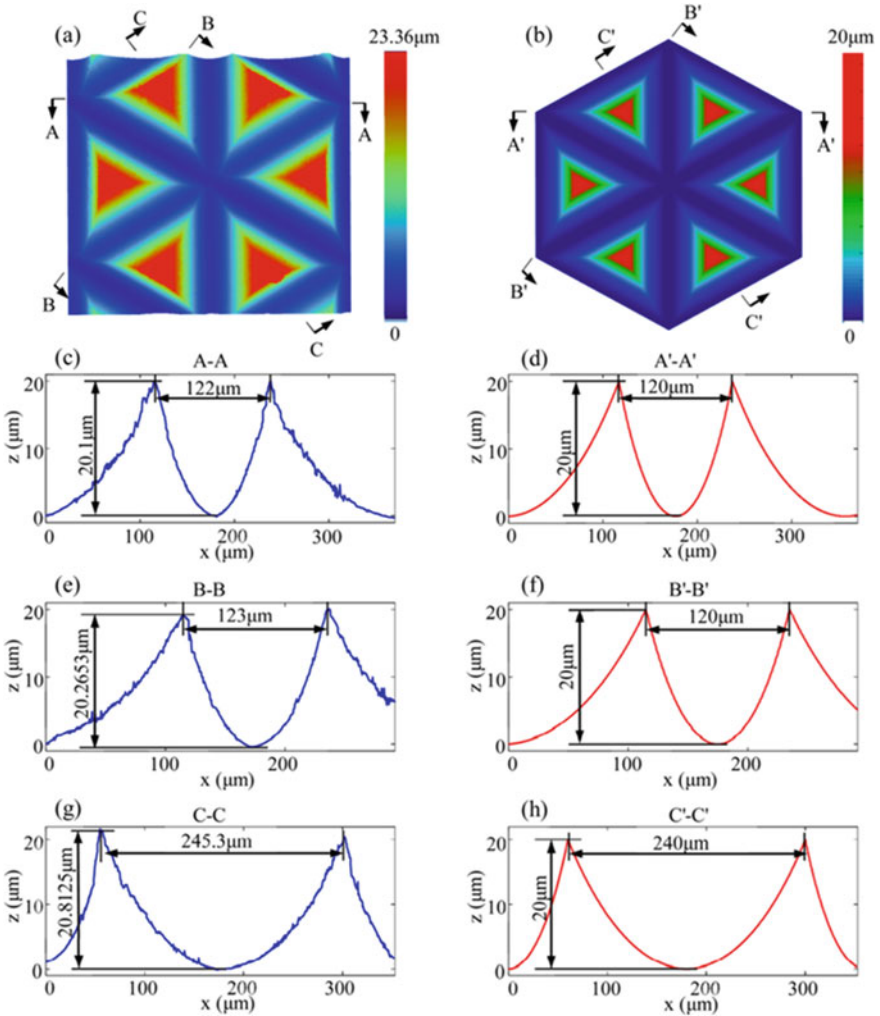
**Fig. 12** Machining error analysis for micro pyramid array: **a** fitting curves of A–A (see Fig. 11c) and A'–A' (see Fig. 11d), **b** fitting curves of B–B (see Fig. 11e) and B'–B' (see Fig. 11f), **c**, **d** error curves corresponding to (a) and (b), respectively

well-fitting on both sectional planes, and the measured profile's curve fluctuations may be because of the tool wear or burr. The error curves in Fig. 12c, d have RMS values of  $0.3719 \mu\text{m}$  and  $0.2909 \mu\text{m}$ , respectively. Also, there are large deviations of the error curve existing near the tool mark boundary, where the material is prone to form burrs and deform. The error curve deviation is also demonstrated that the material is easily deformable and prone to form burrs around the tool mark boundary in machining.

### 3.2.3 Micro Triangular Pyramid Array

As shown in Fig. 2f, when fabricating the micro triangular pyramid array, the third cutting trajectory must pass the intersection point of the previous two trajectories with a  $120^\circ$  gap in between. It can be machined by measuring the separation between the third tool trajectory and the intersection point of the previous two in trial cutting and then compensated. After compensation, a micro triangular pyramid array with less error can be fabricated. Figure 13a illustrates the 3D morphology of the measured micro triangular pyramid array. A regular hexagonal region contains six triangular pyramidal structures that are evenly distributed. To obtain the sectional curves, three sectional planes of A–A, B–B, and C–C in Fig. 13a are employed. In the A–A, B–B, and C–C section planes, the height differences between the simulated and measured sectional curves are  $0.1 \mu\text{m}$ ,  $0.2653 \mu\text{m}$ , and  $0.8125 \mu\text{m}$ , respectively. These errors can be suppressed by decreasing the groove cutting times because these error is caused by the lathe error during cutting. The deviations of the two adjacent curve peaks in A–A, B–B, and C–C sectional planes are  $2 \mu\text{m}$ ,  $3 \mu\text{m}$ , and  $5.3 \mu\text{m}$ ,

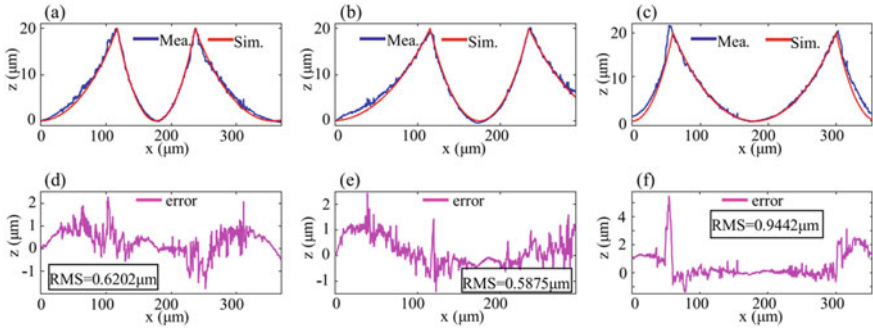




**Fig. 13** Comparison of measured and simulated micro triangular pyramid array: **a** measured morphology; **b** simulated morphology; **c** measured sectional profile A-A; **d** simulated sectional profile A'-A'; **e** measured sectional profile B-B; **f** simulated sectional profile B'-B'; **g** measured sectional profile C-C; **h** simulated sectional profile C'-C'

respectively, which is assumed to be caused by the turntable's rotation error. These errors can be reduced by using an electric turntable with high accuracy and good rigidity.

Figure 14a-c show the simulated and measured sectional curves in A-A, B-B, and C-C sectional planes that are fitted. The middle region between the two curve peaks of the sectional curves on the three sectional planes exhibits good coincidence. The variations near the curve peaks, however, are greater than others. The



**Fig. 14** Machining error analysis for micro triangular pyramid array: **a** fitting curves of A–A (see Fig. 12c) and A′–A′ (see Fig. 12d), **b** fitting curves of B–B (see Fig. 12e) and B′–B′ (see Fig. 12f), **c** fitting curves of C–C (see Fig. 12g) and C′–C′ (see Fig. 12h) and **d–f** error curves corresponding to (a–c), respectively

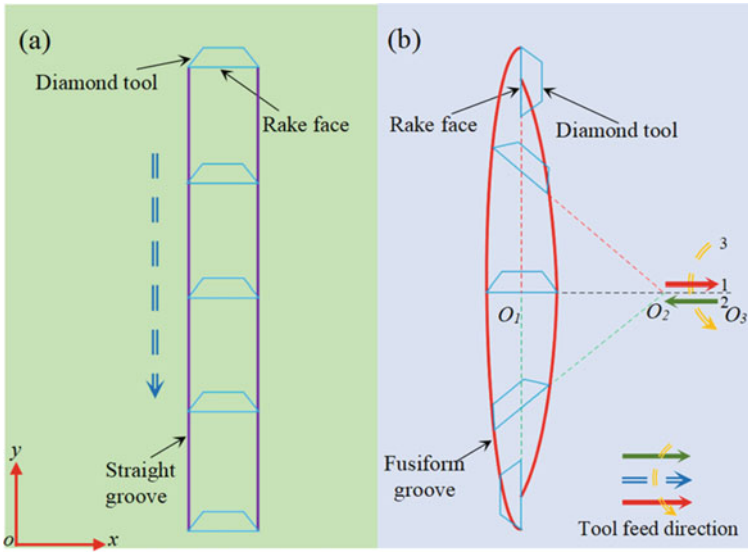
three error curves are shown in Fig. 14d–f with the corresponding RMS values of  $0.6202 \mu\text{m}$ ,  $0.5875 \mu\text{m}$ , and  $0.9442 \mu\text{m}$ , respectively. Due to the burrs existence and the turntable’s error influence, the error curve’s amplitude was larger than  $2 \mu\text{m}$  only in a tiny area and greater than  $3 \mu\text{m}$  only at a very special point in the C–C sectional plane

The above discussion and analysis about three kinds of straight-groove type microstructure arrays have demonstrated that the OTSEF system can truly and successfully process the straight-groove type microstructure arrays even in the absence of linear axes. The machined microstructure shows good morphological properties and form accuracy, demonstrating the efficiency of the OTSEF system. And this system can be used to fabricate more kinds of microstructure arrays, especially the straight-groove type microstructure arrays.

### 3.2.4 The Machining Error Evaluation of the Fusiform Groove

Note that the tool pose inclination could distort the morphology of the straight-groove (see Fig. 15a) into the fusiform groove (see Fig. 15b). Therefore, a machining error evaluation for the machined groove (fusiform groove) using the OTSEF system is still needed. The evaluation model of machining error for the fusiform groove in this section mainly comes from our published work [14].

Developing a mathematical model of the theoretical boundary for a fusiform groove is important to assess its machining error. To conveniently derive the model, a diamond tool is equalized as line AB in the machining of the fusiform groove, as shown in Fig. 16a. To produce a linearization tool trajectory, the diamond tool (line AB) needs to rotate a designed angle and shift the predetermined distance. As a result, the covering path of points A and B can serve as the boundary of the fusiform



**Fig. 15** Schematic of groove boundary and tool pose machined by different machining strategies: **a** conventional vertical scratching for straight groove machining and **b** the proposed linearized tool path for fusiform groove machining

groove if the midpoints of line AB at various locations are translated to be a vertical line, as shown in Fig. 16b.

Actually, the translation of the point coordinates can be used to create a boundary mathematical model of the fusiform groove. For convenience, the coordinates of several points shown in Fig. 16b need to be defined:  $A_1 (x_1, y_1)$ ,  $N (x_0, y_0)$ ,  $B_1 (x_2, y_2)$ ,  $A_2 (r, 0)$ ,  $B_2 (r_1, 0)$ , and  $N_1 (0, y_0)$ .

In  $\triangle O_S FM$ , the Pythagorean theorem can be used to express the following geometric relationship:

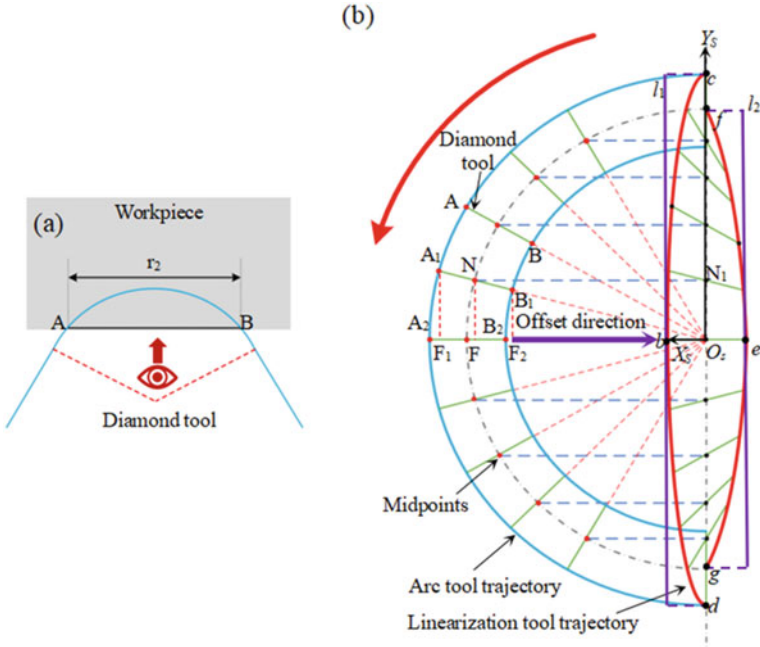
$$x_0^2 + y_0^2 = (r_1 + r_2/2)^2 \quad (19)$$

where  $x_0 \geq 0$ ,  $y_0 \geq 0$ .

Given that  $\triangle O_S FM$ ,  $\triangle O_S F_1 A_1$ , and  $\triangle O_S F_2 B_1$  are similar, some geometric relations can be deduced as follows:

$$\begin{cases} x_0/x_1 = y_0/y_1 = (r_1 + r_2/2)/r_1 + r_2 \\ x_0/x_2 = y_0/y_2 = (r_1 + r_2/2)/r_1 \end{cases} \quad (20)$$

The tool position is changed owing to the translation of the tool path. Based on the coordinate translation rule, when translating  $N (x_0, y_0)$  to  $N_1 (0, y_0)$ , the coordinates of points  $A_1 (x_1, y_1)$  and  $B_1 (x_2, y_2)$  can be derived using Eqs. (19) to (20) as:



**Fig. 16** Schematic of the fusiform groove formation in tool path linearization: **a** the equivalence line (AB) of diamond tools in groove machining and **b** the translation and rotation trajectory of AB in the generation of fusiform groove boundary

$$\begin{cases} (x_1, y_1) = \left( x_0(r_1 + r_2)/(r_1 + r_2/2) - x_0, (r_1 + r_2)\sqrt{(r_1 + r_2/2)^2 - x_0^2}/(r_1 + r_2/2) \right) \\ (x_2, y_2) = \left( x_0r_1/(r_1 + r_2/2) - x_0, r_1\sqrt{(r_1 + r_2/2)^2 - x_0^2}/(r_1 + r_2/2) \right) \end{cases} \quad (21)$$

Defining  $\begin{cases} r_1 + (r - r_1)/2 = R \\ r_1 + r_2 = r \\ x_0 = t \end{cases}$  in Eq. (21), the parametric coordinate expression of line bc belonging to the fusiform groove boundary can be conveniently expressed as:

$$\begin{cases} x_{bc}(t) = rt/R - t \\ y_{bc}(t) = r/R\sqrt{R^2 - t^2} \end{cases} \quad (22)$$

where  $\begin{cases} r - R \cos \varepsilon \leq t \leq R \\ 0^\circ \leq \varepsilon \leq 90^\circ \end{cases}$ .

Since lines bd and bc are symmetric about the X-axis, therefore, the parametric coordinate expression of line bd is given by

$$\begin{cases} x_{bd}(t) = x_1(t) \\ y_{bd}(t) = -y_1(t) \end{cases} \quad (23)$$

$$\text{where } \begin{cases} r - R \cos \varepsilon \leq t \leq R \\ 0^\circ \leq \varepsilon \leq 90^\circ \end{cases}.$$

Like the derivation of Eq. (22), the parametric coordinate expression for line ef is given by

$$\begin{cases} x_{ef}(t) = r_1 t / R - t \\ y_{ef}(t) = r_1 / R \sqrt{R^2 - t^2} \end{cases} \quad (24)$$

Similarly, according to the symmetry, the parametric coordinate expression of line eg is given by

$$\begin{cases} x_{eg}(t) = x_2(t) \\ y_{eg}(t) = -y_2(t) \end{cases} \quad (25)$$

$$\text{where } \begin{cases} r - R \cos \varepsilon \leq t \leq R \\ -90^\circ \leq \varepsilon \leq 0^\circ \end{cases}.$$

The theoretical models of fusiform groove boundary are given by Eqs. (23) to (25). To access its machining error, the straight-groove boundary is also needed to compare. Therefore, a boundary mathematical model of the straight-groove structure is need to be derived.

As shown in Fig. 16b, clearly, the straight-groove structure boundary is composed of two straight lines  $l_1$  and  $l_2$ . The left half of the straight-groove structure boundary can be represented as follows:

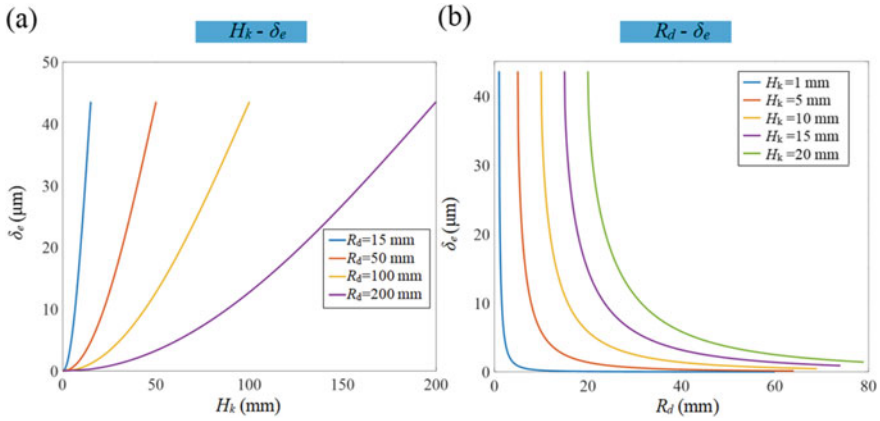
$$\begin{cases} x_{l1} = r_1 - R \\ -r_1 \leq y_{l1} \leq r_1 \end{cases} \quad (26)$$

Similarly, the right half is given by

$$\begin{cases} x_{l2} = R - r_1 \\ -r_2 \leq y_{l2} \leq r_2 \end{cases} \quad (27)$$

As a result, by comparing the straight-groove and fusiform groove, the boundary machining error can be determined based on Eqs. (22) to (27) as:

$$\begin{cases} \Delta x_{bc}(t) = x_{bc}(t) - (r - r_1)/2 & r - R \cos \varepsilon \leq t \leq R & 0^\circ \leq \varepsilon \leq 90^\circ \\ \Delta x_{bd}(t) = x_{bd}(t) - (r - r_1)/2 & r - R \cos \varepsilon \leq t \leq R & -90^\circ \leq \varepsilon \leq 0^\circ \\ \Delta x_{ef}(t) = (r - r_1)/2 - x_{ef}(t) & r - R \cos \varepsilon \leq t \leq R & 0^\circ \leq \varepsilon \leq 90^\circ \\ \Delta x_{eg}(t) = (r - r_1)/2 - x_{eg}(t) & r - R \cos \varepsilon \leq t \leq R & -90^\circ \leq \varepsilon \leq 0^\circ \end{cases} \quad (28)$$



**Fig. 17** Machining error for fusiform groove compared with straight groove: **a** the relation between  $\delta_e$  and  $H_k$  at different  $R_d$  (15, 50, 100, and 200 mm) and **b** the relation between  $\delta_e$  and  $R_d$  at different  $H_k$  (1, 5, 10, 15, and 20 mm)

The machining error can be connected to the  $t$  and  $r$  variables by analyzing Eq. (28).  $t$  and  $r$  are the functions of  $\varepsilon$  and  $R_d$ . However,  $\varepsilon$  is determined by the given parameter  $H_k$  (length of the groove) in the tool path modeling process. Therefore, the parameters  $R_d$  and  $H_k$  determine the machining error of the fusiform.

Figure 17 illustrates the relationship between the machining error  $\delta_e$  and  $R_d$  and  $H_k$ . Clearly, the curvature of the arc tool trajectory decreases as the tool offset distance increases, which allows for the suppression of the linear tool path's machining error. However, the machining error follows the length of the linear tool path as  $R_d$  is constant. This suggests that the machining accuracy of the fusiform groove can be improved by reducing  $H_k$  or increasing  $R_d$ .

## 4 Conclusions

In this chapter, a novel offset-tool-servo end flycutting (OTSEF) system was developed to fabricate straight-groove type microstructure arrays by combining the concepts of end fly cutting and STS. Some bullet points are drawn as follows:

- (1) By exchanging the position of the tool and workpiece, a novel OTSEF system was developed. The arc trajectory of the flycutting tool could be compensated into a linear trajectory. Multiple straight-groove-type microstructure arrays can be fabricated by actively controlling the intersection and overlap of tool imprints with the aid of a precision turntable to rotate the workpiece at a particular angle.
- (2) A tool path interpolation algorithm and a mathematical model are established to linear the arc trajectory flycutting tool. Multiple straight-groove-type

microstructure arrays could be simulated by Matlab based on the tool path planning.

- (3) The simulated results and the experimental results are discovered to be in strong agreement. The machined three kinds of straight-groove-type microstructure arrays have micron-level form precision, and the error curve's root mean square (RMS) value is less than 1  $\mu\text{m}$ , demonstrating the feasibility of OTSEF in fabricating straight-groove-type microstructure arrays.
- (4) The tool inclination will distort the straight groove shape into a fusiform groove. The machining error model of straight groove structure is established. Based on the machining error evaluation and analysis, two methods to reduce the machining error of straight groove structures are further proposed.
- (5) Compared with the traditional STS and FTS, the OTSEF could machine large-scale microstructure arrays, which are not constrained by tool feed frequency. The OTSEF system has promising application potential in machining complex micro/nano structures.

**Acknowledgments** The work described in this chapter was supported by the National Natural Science Foundation of China (Grant No. 52275454, 51827901), and the Shenzhen Natural Science Foundation (Grant No. 20200826160002001, JCYJ2022053103614032).

## References

1. Zhu H, Zhang Z, Xu J, Xu K, Ren Y (2018) An experimental study of micro-machining of hydroxyapatite using an ultrashort picosecond laser. *Precis Eng* 54:154–162
2. Chen XL, Fan GC, Lin CH, Dong BY, Guo ZN, Fang XL, Qu NS (2020) Investigation on the electrochemical machining of micro groove using masked porous cathode. *J Mater Process Technol*, 276
3. Madhukar YK, Mullick S, Nath AK (2016) A study on co-axial water-jet assisted fiber laser grooving of silicon. *J Mater Process Technol* 227:200–215
4. Zhu ZW, To S, Zhang SJ, Zhou XQ (2016) High-throughput generation of hierarchical micro/nanostructures by spatial vibration-assisted diamond cutting. *Adv Mater Interfaces* 3(4):1500477
5. Li Z, Fang F, Zhang X, Liu X, Gao H (2017) Highly efficient machining of non-circular freeform optics using fast tool servo assisted ultra-precision turning. *Opt Express* 25:25243–25256
6. Xu S, Shimada K, Mizutani M, Kuriyagawa T (2014) Fabrication of hybrid micro/nano-textured surfaces using rotary ultrasonic machining with one-point diamond tool. *Int J Mach Tool Manu* 86:12–17
7. Yan GP, Fang FZ (2019) Fabrication of optical freeform molds using slow tool servo with wheel normal grinding. *Cirp Ann-Manuf Techn* 68:341–344
8. To S, Zhu ZW, Zeng WH (2015) Novel end-fly-cutting-servo system for deterministic generation of hierarchical micro-nanostructures. *Cirp Ann-Manuf Techn* 64:133–136
9. Zhu WL, Duan F, Zhang XD, Zhu ZW, Ju BF (2018) A new diamond machining approach for extendable fabrication of micro-freeform lens array. *Int J Mach Tools Manu* 124:134–148
10. Zhu Z, To S, Zhang S (2015) Theoretical and experimental investigation on the novel end-fly-cutting-servo diamond machining of hierarchical micro-nanostructures. *Int J Mach Tool Manu* 94:15–25

11. Zhang X, Jiang L, Zeng Z, Fang F, Liu X (2015) High angular accuracy manufacture method of micro v-grooves based on tool alignment by on-machine measurement. *Opt Express* 23:27819–27828
12. Huang R, Zhang X, Neo WK, Kumar AS, Liu K (2018) Ultra-precision machining of grayscale pixelated micro images on metal surface. *Precis Eng* 52:211–220
13. Jiang JK, Luo T, Zhang GQ, Dai YQ (2020) Novel tool offset fly cutting straight-groove-type micro structure arrays. *J Mater Process Technol* 288:116900
14. Zhang GQ, Ma S, Wang JP, Jiang JK, Luo T, Wang HT (2022) Offset-tool-servo diamond end flycutting multi-layer hierarchical microstructures. *Int J Mech Sci* 233:107645



# Chapter 3

## Tool Offset Flycutting Multi-layer Hierarchical Microstructures



Jianpeng Wang, Guoqing Zhang, and Jiankai Jiang

**Abstract** The industries of optics, electronics, aerospace, and communication, inspired by nature, have all made extensive use of microstructural functional surfaces. These functions are not only derived from a single layer of microstructures, but they also mainly depend on the joint effects of hierarchical microstructures (HMs). Generally, overlapping two or more layers could generate functional combined and complementary HM. Slow/fast tool servo (S/FTS) technology is commonly used to fabricate micro/nanostructures. However, fabricating HMs with sharp edges is still a challenge when relying on only a commercial 3-axis ultra-precision machine tool (UPMT). In this chapter, the offset-tool-servo end flycutting (OTSEF) system was further developed to fabricate HMs integrating STS and FTS, respectively. Considering the installation and geometry shape of the diamond tool, a tool path based on the OTSEF system was planned. Furthermore, the mathematical modeling of HMs tool path generation was established and different HMs with high quality and precision were successfully machined. The theoretical and experimental results show that the OTSEF system has unique advantages to fabricate HMs. The current study presents a deep insight into tool path modeling and method for HMs using only a 3-axis UPMT.

### 1 Introduction

The biomimetic microstructure has promising application value and has caught researchers' attention [1]. Some well-known hierarchical microstructures (HMs) examples are the shark skin, which motivated people to fabricate riblet structures on aircraft wings to reduce air resistance [2]; the butterfly wings, which motivated

---

J. Wang · G. Zhang (✉)

Shenzhen Key Laboratory of High Performance Nontraditional Manufacturing, College of Mechatronics and Control Engineering, Shenzhen University, Nan-hai Ave 3688, Shenzhen 518060, Guangdong, People's Republic of China  
e-mail: [zhanggq@szu.edu.cn](mailto:zhanggq@szu.edu.cn)

J. Jiang

Jiangmen Vocational and Polytechnic College, Chao-lian Ave 6, Jiangmen 529091, Guangdong, People's Republic of China

humans to create periodic micro/nanostructures to control the optical absorption properties [3]; the lotus leaf, which served as the basic theory for superhydrophobic [4], self-cleaning [5] and low adhesion [6] materials; the moth-eye, which inspired people to use micro-lens arrays to carry out specific focusing tasks on optical applications [6]. Of course, machining these functional surfaces is basic for their applications. Several machining techniques have been used to fabricate HM function surfaces [7]. Based on the type of material removed, fabrication techniques for HM function surfaces can be categorized into physical [8], chemical [9], and mechanical [10]. Although physical and chemical methods are thought to be efficient for HMs, they frequently have limitations due to the properties of materials and lengthy processing durations. Additionally, there are still challenges for the majority of these methods to fabricate HMs with certain geometry morphology and high form accuracy.

Ultra-precision machining technology (UPMT) has great potential for machining finely shaped HMs. Because it can machine surfaces with nanometer-scale roughness and submicron form accuracy on most materials [11]. Among UPMT, single-point diamond turning, assisted by slow tool servo (STS) [12] or fast tool servo (FTS) [13], is regarded as a promising technique for the flexible fabrication of HMs. Note that the applications and mechanisms of these two machining methods are entirely different. In STS, complex microstructures are fabricated using diamond tools at a lower frequency under the linkage control of the machine tool's motion axes [14]. In FTS, an extra fast servo system drives a diamond tool with a high frequency to work with the lathe's feed [15]. Both STS and FTS have some typical applications of high-performance HMs machining [16]. Such as, Li and Yi successfully fabricated a 3D artificial compound eye, a micropillar array on a curved spherical surface, using the STS diamond turning. [17]; Prasad et al. fabricated a hierarchical textured surface, overlapping rectangular sub-micron second-layer pillars on the top surface of the first-layer pillars, using STS diamond turning [18]; Scheiding et al. fabricated micro-optical lenses on a surface of the steeply curved substrate based on a novel voice coil driven FTS system into diamond turning [19]. However, the cylindrical coordinate system, which is used by default for S/FTS diamond turning, has some basic flaws that result in inconsistent cutting quality, inconsistent azimuth sampling, and constrained tracking bandwidth [20]. Therefore, S/FTS diamond turning is constrained by these inherent problems in the fabrication of complex micro/nanostructures.

End flycutting is a relatively excellent technique for microstructure fabrication and it also belongs to UPMT. Due to its distinctive surface generation mechanism, which includes constant cutting speed, uniform sample length, and uniform tracking bandwidth, it can not only ensure surface quality uniformity but also offer flexibility for machining complex microstructures [21]. Especially combined with S/FTS is considered an efficient and flexible method for HMs machining [22, 23]. Such as To et al. first proposed a novel end-fly-cutting-servo system combining STS technology to fabricate HMs [24]; Zhu et al. successfully machined a multi-layer overlapping lens array by combining end flycutting and FTS technology [25]. It is worth mentioning that the complex microstructure fabrication based on end flycutting combined with S/FTS mainly rely on the UPMT with at least three linear axes. Therefore, HMs

machining only uses an UPMT with a common configuration (X-, Z- and C-axis) is meaningful and challenging.

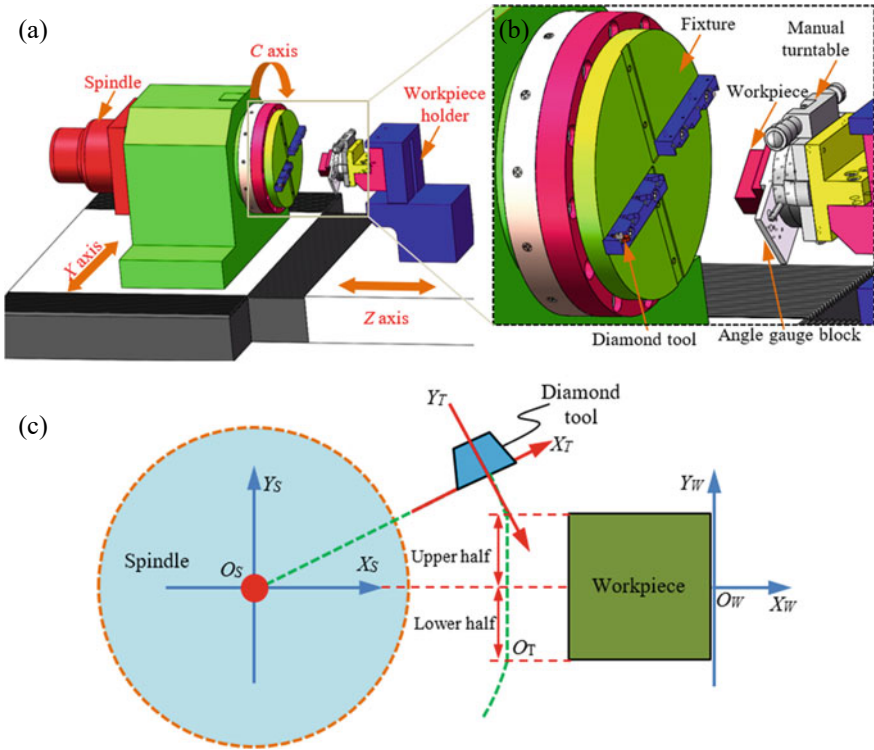
In the last chapter, we proposed an OTSEF system integrating STS to fabricate straight-groove type microstructures using a 3-axis UPMT. In this chapter, on one hand, we will further study the HMs fabrication based on the proposed system; on the other hand, we also proposed a method to fabricate HMs based on the OTSEF system integrating FTS. Micro-lenses are a representative microstructure commonly applied in the field of optics. So, overlapping nanostructures on the micro-lens surface to compose diverse HMs have the potential to obtain additional special functions, such as antireflection, hydrophobicity, and diffraction, to strengthen the functionality of the micro-lens [26]. This chapter, however, mainly focuses on the tool path planning and HMs machining using the OTSEF system, and microstructures machining error evaluation. The present research provides two novel and effective methods for machining HMs on a machine tool with a common configuration (X-, Z-, and C-axis).

## 2 Fabrication of HMs Using OTSEF System Integrating STS

This section focused on the fabrication of HMs using the OTSEF system integrating STS and the content is mainly from our published paper [27]. In this section, firstly, tool path modeling for single micro-lens unit machining is established, and then using the coordinate translation method to extend the model in the micro-lens arrays machining. After the fabrication of the micro-lens basal surface, the nanostructure is machined further on the micro-lens surface based on the intersection of the tool path and then overlaps a smaller micro-lens on the basal surface to generate some more complex HMs. Finally, the machining error is analyzed and discussed in detail.

### 2.1 Tool Path Modeling for Micro-lens Unit Machining

The configuration of the OTSEF system is shown in Fig. 1a, b. Clearly, a diamond tool is fixed on a specialized fixture, which was absorbed on a vacuum chuck to follow the spindle rotation. As a result, the tool trajectory that covers the workpiece surface is made up of a series of concentric circles with equal offsets and radii, which is actually the tool trajectory of end flycutting to remove materials. We still used the linearized arc tool trajectory, proposed in the last chapter, to fabricate micro-lens microstructures, as shown in Fig. 1c, because this method is convenient to fabricate HMs using the intersection of the tool path. Excepting the tool trajectory linearization, a micro-lens unit fabrication also needs a linkage motion of the Z-axis, which is employed to provide changeable cutting depth following the tool linear trajectory.

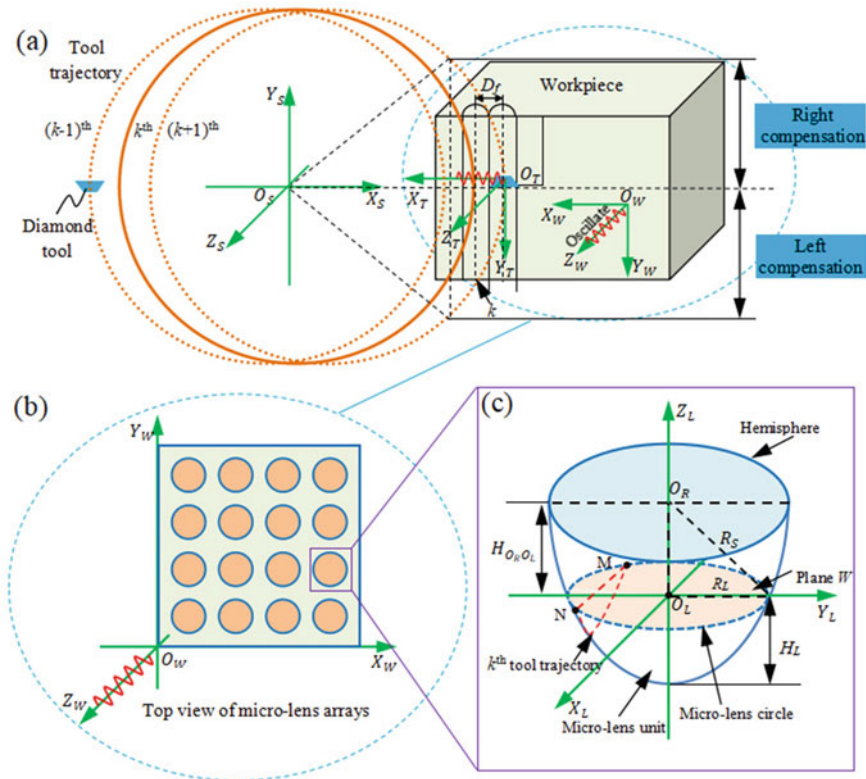


**Fig. 1** Schematic of **a** the configuration of the OTSEF system, **b** the relative positions of diamond tool and workpiece, and **c** the tool trajectory of rotation and linear in flycutting

Moreover, the spindle coordinate system  $O_S-X_S Y_S Z_S$  and the work coordinate  $O_W-X_W Y_W Z_W$  are still used as the reference coordinate system, respectively, which is as same as the definition in the last chapter.

Figure 2 illustrates a diagram of a micro-lens unit generation using linearization tool trajectories. Figure 2a illustrates the tool arc trajectory spanning the workpiece surface. The tool arc trajectory can be compensated to linear trajectory using tool servo motion in the  $X_T$  axis. The top view of the micro-lens array is illustrated in Fig. 2b in the workpiece coordinate system  $O_W-X_W Y_W Z_W$ , while the geometry of a micro-lens unit and some geometry parameters used to calculate tool path modeling are illustrated in Fig. 2c. In the present study, a concave spherical micro-lens unit was selected to be machined. The parameter of the micro-lens has the following definition:  $R_L$  is the radius, and  $H_L$  is the depth. Moreover, the hemisphere radius is defined as  $R_S$ , and the distance from  $O_R$  to  $O_L$  is defined as  $H_{O_R O_L}$ .

Indeed, the inputting geometric parameters associated with the micro-lens unit and the outputting various cutting depths corresponding to the spindle rotation angle is the meaning of the tool path model for the machining of micro-lens units. The  $k$ th tool trajectory is represented here as a tool trajectory, therefore the superscript



**Fig. 2** Schematic of micro-lens fabrication using linearization tool trajectory: **a** tool path linearization using the OTSEF system, **b** micro-lens distribution in an array, and **c** geometry parameters using in tool path modelling for a micro-lens unit machining

or subscript  $k$  of one parameter indicates any tool trajectory to derive the general tool path model for fabricating micro-lens units. In addition, the micro-lens circle represents the circle located on plane  $W$ , as shown in Fig. 2c.

Based on the micro-lens unit's geometric parameters shown in Fig. 2c, the following geometric relation exists.

$$R_S^2 - R_L^2 = H_{O_R O_L}^2 = (R_S - H_L)^2 \quad (1)$$

The distance between  $O_R$  and  $O_L$  (see Fig. 3c) can be derived using Eq. (1) as follows:

$$H_{O_R O_L} = \frac{R_L^2 - H_L^2}{2H_L} \quad (2)$$



the coordinate position relationship between micro-lens units. To cover the micro-lens unit, the micro-lens circle enclosed area is divided into  $m$  segments with a fixed distance between them. In this case,  $m$  here represents the tool path counting, whereby the feed distance  $D_f$  between neighboring tool paths is calculated by:

$$D_k = R_L - \left(k - \frac{1}{2}\right)D_f \quad (3)$$

As shown in Fig. 3a, the distance between the  $k$ th tool trajectory and  $O_L$  also can be computed as:

$$D_f = \frac{2R_L}{m} \quad (4)$$

As shown in Fig. 3a,  $H_k$  stands for the distance between  $M$  and  $D$ . Based on the Pythagorean theorem, the following geometric relation exists:

$$H_k^2 + D_k^2 = R_L^2 \quad (5)$$

Therefore, the following geometric relation can be derived from Eqs. (3) to (5).

$$H_k = \sqrt{R_L^2 - \left[R_L - \left(k - \frac{1}{2}\right)D_f\right]^2} = \sqrt{R_L^2 - \left[R_L - (2k - 1)\frac{R_L}{m}\right]^2} \quad (6)$$

Actually,  $H_k$  is the only unknown parameter to calculate the changeable cutting depth, but it can be derived as a series of given parameters in Eq. (6). Moreover, the  $k$ th tool trajectory was evenly discretized into  $N_s$  segments for the current research, numbered from 1 to  $N_s$ , to conveniently derive the general mathematic model calculating the changeable cutting depth. The tool positions within the BF and MN segments (see Fig. 3a) are numbered  $n$  to  $m$  and  $n_1$  to  $m_1$  respectively,  $i$  ( $i \in [1, N_s]$ ) denotes one point of the  $k$ th tool trajectory. Also as indicated in Fig. 3a, the  $A$  represents the beginning cutting position, and the spindle rotation angle here is  $0^\circ$ .

Based on the geometric relation illustrated in Fig. 3a,  $MD$  represents a micro-lens unit formation stage, and the corresponding cutting depth is not 0. This stage is actually called right compensation stage, and the range of spindle rotation angle can be derived as:

$$\frac{\pi}{2} - \arctan \frac{H_k}{D_{ks}} \leq \epsilon_{MD}^{k,i} < \frac{\pi}{2}, i \in [n_1, N_s/2] \quad (7)$$

where  $D_{ks} = \sqrt{R_d^2 - H^2}$  is indicated in Fig. 3a.

The changeable cutting depth can be calculated according to the geometric relation within this range illustrated in Fig. 3b as:

$$Z_{CD}^{k,i} = \sqrt{R_k^2 - (H_k - \Delta y_r)^2} - H_{O_R O_L} \quad (8)$$

where  $\Delta y_r = \Delta Y_S^{k,n_1} + \Delta Y_S^{k,n_1+1} + \dots + \Delta Y_S^{k,N_s/2}$  could be derived using Eq. (12) given in the last chapter, and  $R_k$  is the  $k$ th sectional semicircle radius, which actually can be derived by the Pythagorean theorem illustrated in Fig. 3b:

$$R_k = \sqrt{H_{O_R O_L}^2 + H_k^2} \quad (9)$$

Similarly, in DN segment (left compensation stage), the spindle rotation angle  $\epsilon_{DN}^{k,i}$  and the corresponding cutting depth  $Z_{DN}^{k,i}$  are:

$$\begin{cases} \frac{\pi}{2} \leq \epsilon_{DN}^{k,i} \leq \frac{\pi}{2} + \tan^{-1} \frac{H_k}{\sqrt{R_d^2 - H^2}}, i \in [N_s/2, m_1] \\ Z_{DN}^{k,i} = \sqrt{R_k^2 - (\Delta y_1)^2} - H_{O_R O_L} \end{cases} \quad (10)$$

where  $\Delta y_1 = \Delta Y_S^{k,N_s/2} + \Delta Y_S^{k,N_s/2+1} + \dots + \Delta Y_S^{k,m_1}$  could be derived by Eq. (15) given in the last chapter.

## 2.2 Tool Path Modeling for Micro-lens Array Machining

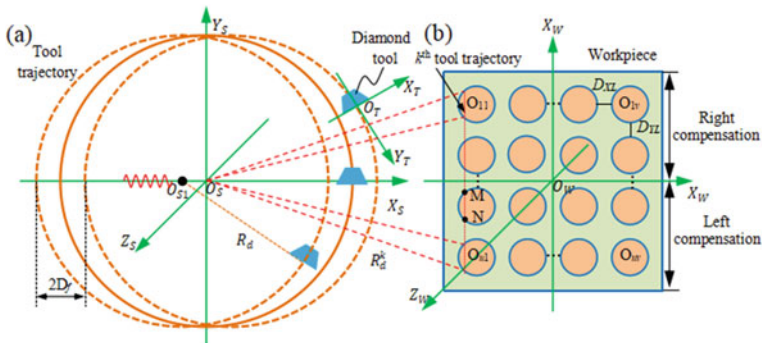
In this part, the tool path model is further deduced to fabricate a micro-lens array according to the model derivation of a micro-lens unit. Figure 4a illustrates the tool trajectory covering the micro-lens array area and the coordinate relation of micro-lens units. The rows and columns of the micro-lens array are represented using variables  $u$  and  $v$  respectively to convenient derive the tool path model for the micro-lens array machining. Since the parameters described in Sect. 2.1 have the same physical significance in different micro-lens unit machining, they can be conveniently defined by adding a superscript or subscript variables  $u$  and  $v$  to stand for different micro-lens units.

As shown in Fig. 4b, in the  $O_S-X_S Y_S$  coordinate system,  $(X_0, Y_0)$  stands for the coordinate of  $O_{11}$ , where  $O_{11}$  actually could be used to represent the micro-lens unit position in the array.  $D_{XL}$  stands for the neighboring distance between the boundary of two micro-lens units along the  $X$ -axis, while  $D_{YL}$  is that along the  $Y$ -axis.  $R_L$  stands for the micro-lens circle radius. Therefore, based on the geometric relation shown in Fig. 4b, the center coordinate of a micro-lens unit can be expressed as:

$$O_{uv}(X_{uv}, Y_{uv}, Z_{uv}) = [X_0 + (v - 1) \times (2R_L + D_{XL}), Y_0 - (u - 1) \times (2R_L + D_{YL}), -H_L] \quad (11)$$

Similar to the derivation of Eq. (5) in Sect. 2.1, in the micro-lens array's tool path modeling, their geometric relation is given by:





**Fig. 4** Schematic of a micro-lens array machining: **a** tool feeds of the OTSEF system and **b** micro-lens units distribution in a micro-lens array and their geometry relation

$$(H_k^{uv})^2 + (D_k^{uv})^2 = R_L^2 \quad (12)$$

A micro-lens circle's point coordinates are defined as  $(X_{uv}^{k,i}, Y_{uv}^{k,i}, Z_{uv}^{k,i})$ , while its center coordinates are defined as  $(X_{uv}, Y_{uv}, Z_{uv})$ . Therefore, Eq. (12) can be further derived as:

$$(X_{uv}^{k,i} - X_{uv})^2 + (Y_{uv}^{k,i} - Y_{uv})^2 = R_L^2 \quad (13)$$

Solving Eq. (13), yields:

$$Y_{uv}^{k,i} = Y_{uv} \pm \sqrt{R_L^2 - (X_{uv}^{k,i} - X_{uv})^2} \quad (14)$$

where  $Y_{uv}^{k,i}$  is employed to compute the angle of spindle rotation to cover one micro-lens in the array.

Clearly, Eq. (14) can be divided into the following two expressions:

$$\begin{cases} Y_{uv1}^{k,i} = Y_{uv} + \sqrt{R_L^2 - (X_{uv}^{k,i} - X_{uv})^2} \\ Y_{uv2}^{k,i} = Y_{uv} - \sqrt{R_L^2 - (X_{uv}^{k,i} - X_{uv})^2} \end{cases} \quad (15)$$

which is actually the boundary points of micro-lens machining.

Similar to Eq. (7), in the right compensation stage, the angle range of spindle rotation to cover one micro-lens unit can be derived using the geometry relation shown in Fig. 4 as:

$$\frac{\pi}{2} - \arcsin \frac{Y_{uv1}^{k,i}}{R_d^k} \leq \epsilon_r^{k,i} \leq \frac{\pi}{2} - \arcsin \frac{Y_{uv2}^{k,i}}{R_d^k}, \quad i \in [n_1, m_1] \quad (16)$$

In this range, the changeable cutting depth can be derived using Eq. (8) as:

$$Z_{MN}^{k,i} = \sqrt{(R_k^{uv})^2 - (H_{uv}^k - \Delta y_{uv}^r)^2} - H_{O_R O_L} \quad (17)$$

where  $\Delta y_{uv}^r = \Delta Y_S^{k,n_1} + \Delta Y_S^{k,n_1+1} + \dots + \Delta Y_S^{k,m_1}$  still could be derived based on Eq. (12) given in the last chapter, and  $R_k^{uv}$  was derived using Eq. (9):

$$R_k^{uv} = \sqrt{H_{O_R O_L}^2 + (H_k^{uv})^2} \quad (18)$$

Similarly, in the left compensation stage, the angle of spindle rotation  $\varepsilon_1^{k,i}$  and cutting depth  $Z_{MN}^{k,i}$  can be expressed as:

$$\begin{cases} \frac{\pi}{2} + \arcsin \frac{|Y_{uv1}^{k,i}|}{R_d^k} \leq \varepsilon_1^{k,i} \leq \frac{\pi}{2} + \arcsin \frac{|Y_{uv2}^{k,i}|}{R_d^k}, & i \in [n_1, m_1] \\ Z_{MN}^{k,i} = \sqrt{(R_k^{uv})^2 - (\Delta y_{uv}^l)^2} - H_{O_R O_L} \end{cases} \quad (19)$$

where  $\Delta y_{uv}^l = \Delta Y_S^{k,n_1} + \Delta Y_S^{k,n_1+1} + \dots + \Delta Y_S^{k,m_1}$  also could be derived based on Eq. (15) given in the last chapter.

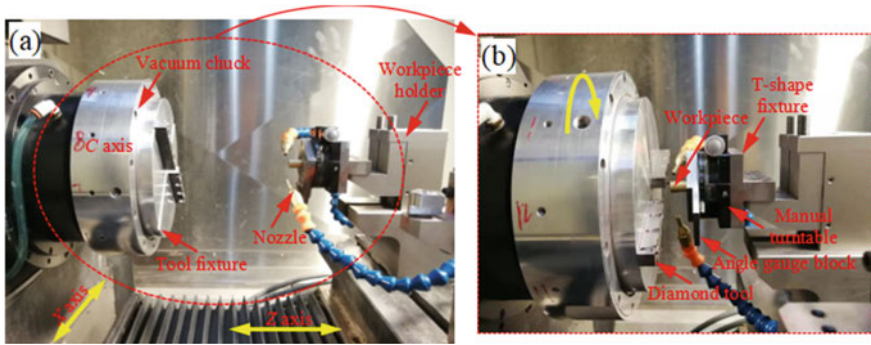
### 2.3 Fabrication of Micro-lens Unit and Array

According to the tool path model established in Sects. 2.1 and 2.2, a 3-axis UPMT (Moore Nanotech 450UPL, USA) was used to perform experiments fabricating a micro-lens unit and array. The experimental setup is shown in Fig. 5, where a diamond tool (Contour Fine Tooling, UK) is mounted on a tool fixture using a specialized tool block. On the block, there are 4 V-shaped grooves to guarantee the accurate offset position, i.e. tool rotation radius  $R_d$ , varies in the range of [15, 35, 55, 75] mm. We still used a manual turntable (MISUMI, RPG60, Japan) to provide rotational freedom for the workpiece to realize the tool path intersection. Actually, the experimental setup is the same as that of the last chapter.

In the experiments, brass was used as the workpiece material. Table 1 lists the parameter for micro-lens machining.

Using MATLAB® software to solve the model can generate the tool trajectory's point cloud for a micro-lens unit (Radius: 0.5 mm; depth: 10  $\mu$ m), as shown in Fig. 6a. These point can be read and performed by the UPMT. After machining, the micro-lens unit was measured by white light interferometer (Bruker Contour GT-X, USA), and its morphology is shown in Fig. 6b. Figure 6c illustrates the sectional contour curve of the micro-lens unit, whereas a portion of the amplified contour curve is illustrated in Fig. 6d. The measurement results show that the machined micro-lens unit has a high machining accuracy and a uniform contour curve.

Based on a micro-lens unit machined, a micro-lens array was fabricated further. A cloud map for the micro-lens array's machining points is shown in Fig. 7a. Using



**Fig. 5** Hardware configuration of OTSEF system: **a** experimental setup and **b** relative position between the workpiece and diamond tool

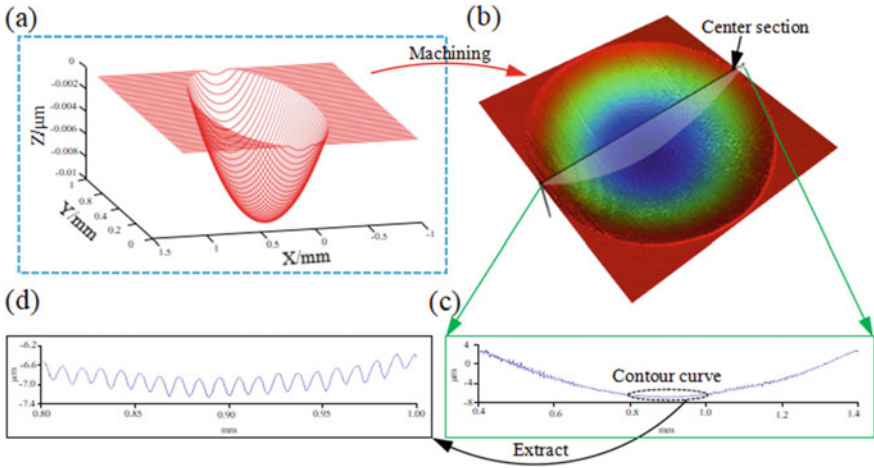
**Table 1** Experimental parameters for machining a micro-lens unit and an array

	Parameter	Value
Diamond tool	Tool radius $R_t$	0.102 mm
	Tool rake angle	0°
	Tool included angle	120°
UPMT	Cutting depth $Z$	0–0.01 mm
	Feed rate $D_f$	20.833 $\mu\text{m}/\text{rev}$
	Rotation speed	1 r/min
Micro-lens	Depth $H_L$	0.01 mm
	Radius $R_L$	0.5 mm
	Tool feed number	48

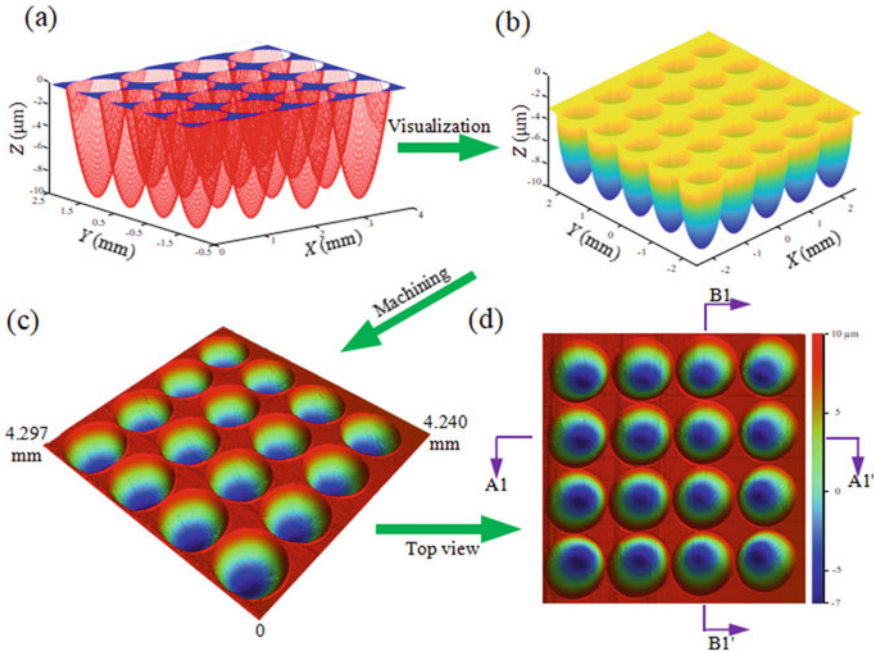
MATLAB®, the simulated 3D morphology of the micro-lens array is shown in Fig. 7b, which could serve as micro-lens array machining analysis. The captured morphology of the machined micro-lens array is shown in Fig. 7c, while Fig. 7d shows the top view of Fig. 7c. According to the measurement results, the micro-lens unit was consistently aligned into an array with very clear micro-lens boundary.

The root mean square (RMS) error was still used to assess the machining accuracy of micro-lens array. In order to get the contour curve, cross sections A1–A1' and B1–B1' were chosen, as shown in Fig. 7d. The obtained contour curve was then compared to the simulated ones with RMS errors 0.4188  $\mu\text{m}$  and 0.5266  $\mu\text{m}$ , respectively, as shown in Fig. 8, which shows a high form accuracy and demonstrates the effectiveness using the OTSEM system to fabricate micro-lens arrays.

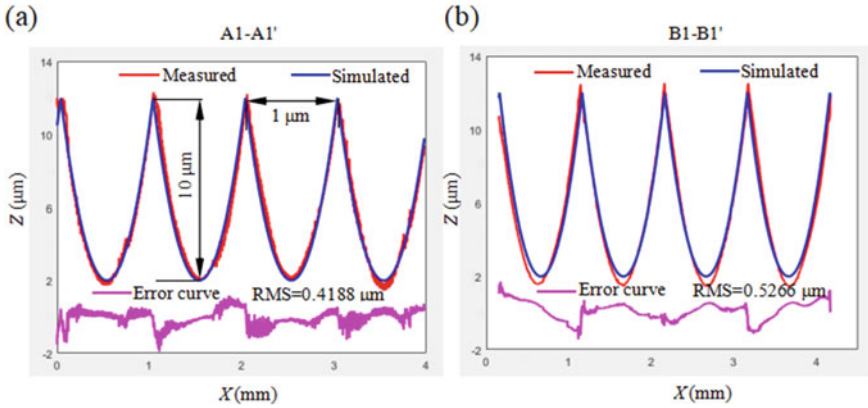
Furthermore, according to the machined basal surface (micro-lens) and the OTSEF system, three types of HMs can be fabricated further by machining secondary pyramid microstructures (SPMs) on the basal surface, including micro-lens unit with SPMs (MLU-SPM), lenslet with 1-layer SPMs (L-1SPM), and lenslet with 2-layer SPMs (L-2SPM).



**Fig. 6** Surface characterizations for a micro-lens unit: **a** a cloud map of a micro-lens unit’s tool trajectory points, **b** a measured 3D morphology of the micro-lens unit (captured by a white light interferometer), **c** a sectional contour curve of (b), and **d** an amplified view of the sectional contour curve



**Fig. 7** A micro-lens array’s simulation and machining: **a** a cloud map of a micro-lens array’s tool trajectory points, **b** the micro-lens array’s simulated 3D morphology, **c**, **d** measured 3D morphology of the micro-lens array (captured by a white light interferometer)



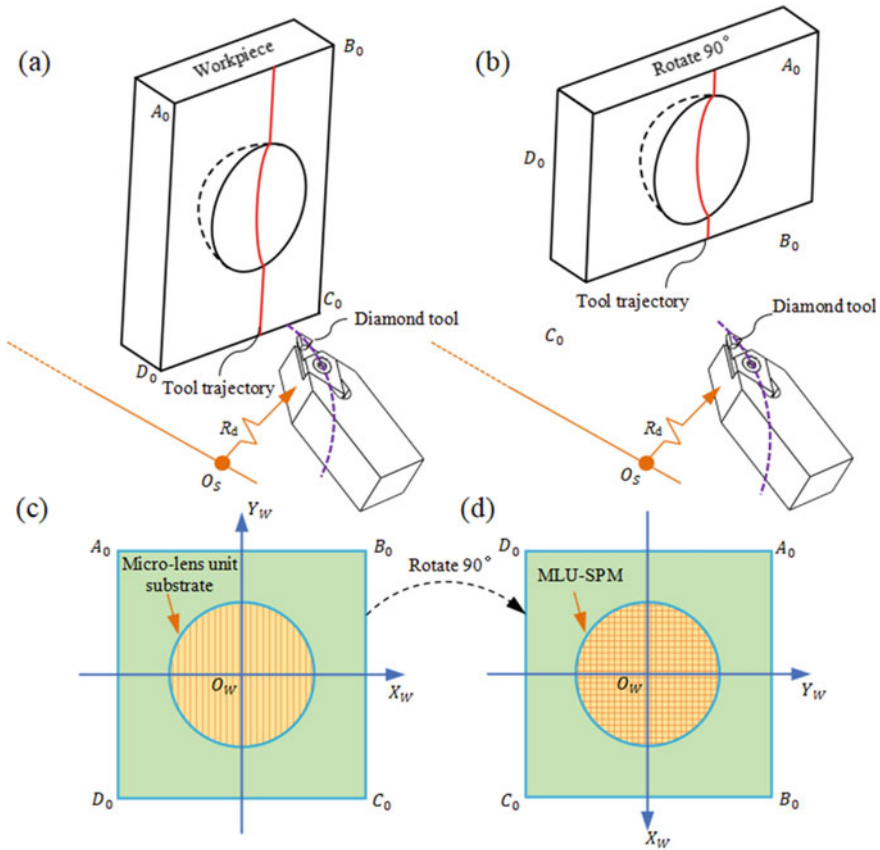
**Fig. 8** Comparison of simulated and measured sectional contour curves: **a** the simulated and measured fitting results for A1–A1′ (see Fig. 7d) sectional contour curves and their error curves, and **b** the simulated and measured fitting results for B1–B1′ (see Fig. 7d) sectional contour curves and their error curves

## 2.4 Tool Path Planning and Fabrication of MLU-SPM

Figure 9 shows the tool path for the machining of the MLU-SPM. For the MLU-SPM machining, a micro-lens basal surface need to be machined for the first step, as shown in Fig. 9a; then rotate the workpiece by  $90^\circ$  for the secondary machining, as shown in Figs 9b. Figure 9c, d illustrate the tool path for the fabrication of the micro-lens basal surface and MLU-SPM, respectively. The micro-lens' depth and radius here are 10 mm and  $0.5 \mu\text{m}$ , respectively.

The machined results are shown in Fig. 10. The captured morphology of the machined MLU-SPM is illustrated in Fig. 10a, which has an ordered SPM array on the micro-lens surface. Because the SPMs on the micro-lens surface as strong noises and significantly deteriorate the basal morphology, we used a zero-order Gaussian regression filter to separate the micro-lens surface and the SPM [28]. As shown in Fig. 10b, the micro-lens basal surface can be obtained by the filter. Moreover, a magnified view of the zone marked in Fig. 10a is shown in Fig. 10c aimed to get a clear view of the SPMs. Clearly, the machined SPMs featured round connections and sharp spires, which corresponded to the edge profiles and intersection of the diamond tool, respectively.

As shown in Fig. 10d, e, the contour curves get from cross sections of A2–A2′ and B2–B2′ respectively are used for the further analysis the machined microstructure. The SPM's width and depth are 25 and  $1.5 \mu\text{m}$ , respectively, which corresponds to the SPM's designation accuracy. The result shows that the OTSEF system can realize high-accuracy microstructure fabrication. Furthermore, the SPMs with various feature sizes can be machined through flexibly choosing the feed rates and geometries of diamond tools.



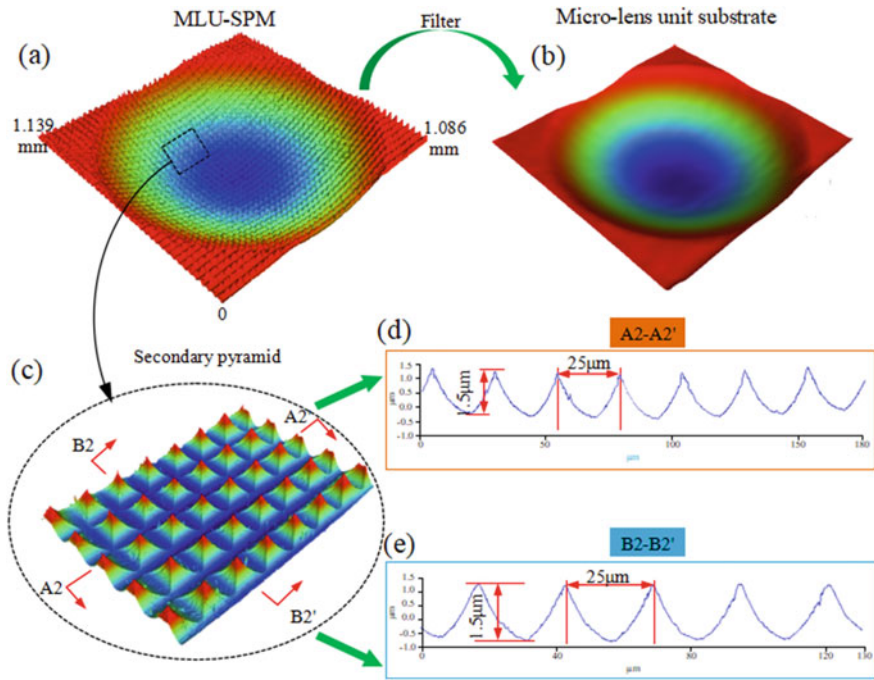
**Fig. 9** Schematic of tool path planning for MLU-SPM machining: **a** tool path for a micro-lens unit machining, **b** tool path for the micro-lens unit secondary machining with workpiece rotation  $90^\circ$ , **c** a micro-lens unit basal surface machined by the tool path planning in (a), and (d) a MLU-SPM machined by the tool path planning in (a) and (b)

## 2.5 Machining Error Compensation and Analysis

### 2.5.1 The Feature Matrix of Machining Error

Actually, machining errors, including translation errors and rotation errors, are inevitable during the fabrication of HMs; therefore, error identification and compensation are crucial to guarantee machining accuracy.

Inevitable manual tool setting causes the center of workpiece and spindle deviation during the machining, which is the main translation error. Generally, the translation error can be described in 9 cases as shown in Fig. 11a, where  $C_{p,q}$  stands for the translation error; p and q stand for the errors in X- and Y-direction, respectively; 0, 1, and



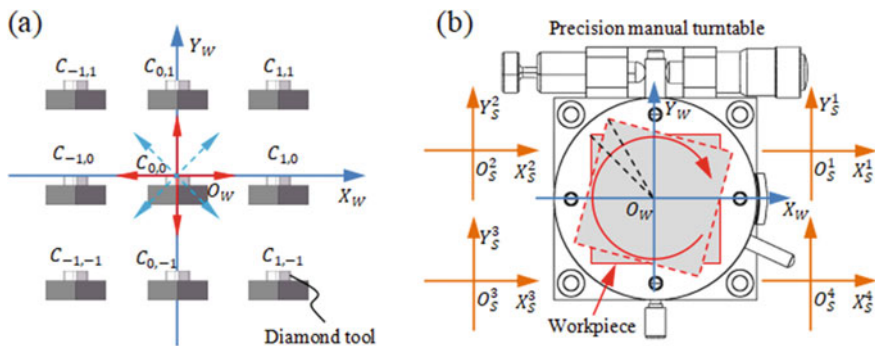
**Fig. 10** Surface characterizations for a MLU-SPM: **a** a measured 3D morphology of the MLU-SPM, **b** basal surface of micro-lens unit after zero-order Gaussian regression filter, **c** a magnified view of partial secondary pyramid microstructure in (a), **(d)** and **e** sectional contour curves for A2–A2' and B2–B2' in (c)

–1 denote no, positive and negative errors, respectively. Therefore, a homogeneous matrix can be used to characterize the translation error as follows:

$$C_{p,q} = \begin{bmatrix} 1 & 0 & 0 & p \\ 0 & 1 & 0 & q \\ 0 & 0 & 1 & 0 \\ 0 & 0 & 0 & 1 \end{bmatrix} \quad (20)$$

Moreover, manual operation of the turntable can cause a nonnegligible rotation error, as shown in Fig. 11b. Similar to the translation error, the rotation error can be expressed as a homogeneous matrix:

$$R_E^{\pi/2+\eta} = \begin{bmatrix} \cos(\pi/2 + \eta) & -\sin(\pi/2 + \eta) & 0 & 0 \\ \sin(\pi/2 + \eta) & \cos(\pi/2 + \eta) & 0 & 0 \\ 0 & 0 & 1 & 0 \\ 0 & 0 & 0 & 1 \end{bmatrix} = \begin{bmatrix} \mp \sin \eta & -\cos \eta & 0 & 0 \\ \cos \eta & \mp \sin \eta & 0 & 0 \\ 0 & 0 & 1 & 0 \\ 0 & 0 & 0 & 1 \end{bmatrix} \quad (21)$$



**Fig. 11** Schematic of machining errors: **a** translation error and **b** rotation error

where  $\eta$  ( $\eta \in \mathbb{R}$ ) is the angle error when the turntable is rotated by  $90^\circ$ .

$(x_{uv}, y_{uv}, z_{uv})$  stands for the micro-lens' circle center coordinate, which can be expressed as a homogeneous vector:

$$\mathbf{O}_{uv} = \begin{bmatrix} x_{uv} \\ y_{uv} \\ z_{uv} \\ 1 \end{bmatrix} \quad (22)$$

Therefore, the main machining error can be integrated using Eqs. (20) to (22), and the feature matrix of the machining error can be derived as:

$$\mathbf{R}_E^{\frac{\pi}{2}+\eta} \mathbf{T}_E \mathbf{O}_{uv} - \mathbf{R}_E^{\frac{\pi}{2}} \mathbf{O}_{uv} = \begin{bmatrix} \mp(x_0 + p) \sin \eta - (y_0 + q) \cos \eta + y_0 \\ (x_0 + p) \cos \eta \mp (y_0 + q) \sin \eta - x_0 \\ 0 \\ 0 \end{bmatrix} \quad (23)$$

where  $\mathbf{T}_E$  and  $\mathbf{R}_E^{\pi/2}$  stands for the axial error and without rotation error when the turntable is rotated by  $90^\circ$ , respectively, and they can be expressed as a homogeneous matrix:

$$\mathbf{T}_E = \begin{bmatrix} 1 & 0 & 0 & p \\ 0 & 1 & 0 & q \\ 0 & 0 & 1 & 0 \\ 0 & 0 & 0 & 1 \end{bmatrix}, \mathbf{R}_E^{\pi/2} = \begin{bmatrix} \cos(\pi/2) & -\sin(\pi/2) & 0 & 0 \\ \sin(\pi/2) & \cos(\pi/2) & 0 & 0 \\ 0 & 0 & 1 & 0 \\ 0 & 0 & 0 & 1 \end{bmatrix} = \begin{bmatrix} 0 & -1 & 0 & 0 \\ 1 & 0 & 0 & 0 \\ 0 & 0 & 1 & 0 \\ 0 & 0 & 0 & 1 \end{bmatrix} \quad (24)$$



### 2.5.2 Error-Oriented Identification of Tool Deviation in Y-direction

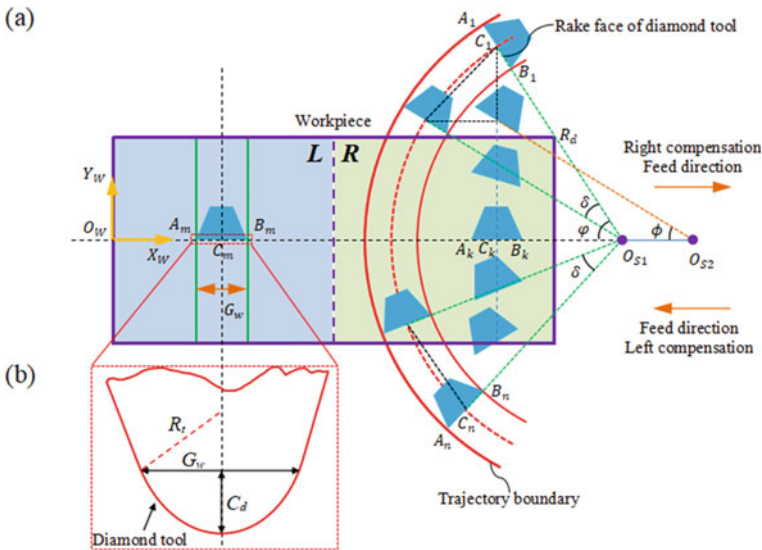
Clearly, tool deviation caused a significant translation error; therefore, the tool deviation direction should be identified first and then compensate it. We proposed an error-oriented method to identify tool deviation direction, which utilizes the machining error of the microstructure to judge the tool deviation direction. Actually, in the last chapter, we found that a fusiform groove is machined by the linearization tool path. That implies that the width of the machined groove and the tool deviation in the Y-direction are related. Therefore, the width of the machined groove can be used to determine the tool deviation direction.

Here, we modeled the width of the machined groove. As shown in Fig. 12a, during the machining process, the width of the machined groove varies following the diamond tool's rake face. But in conventional vertical scratching (see Fig. 12a L part), the width of the scratch groove is uniform and exists the following geometry relation:

$$G_w = 2\sqrt{R_t^2 - (R_t - C_d)^2} \tag{25}$$

where  $G_w$  is the width of the scratch groove,  $R_t$  is the tool radius, and  $C_d$  is the cutting depth.

In the right compensation stage, since a certain angle exists between the diamond tool's rake face and the  $O_W-X_WZ_W$  coordinate plane (see Fig. 12a R part), the width of the machined groove here can be derived as:



**Fig. 12** Strategies of straight groove machining: **a** vertical scratching (see L part) and the linearization tool path machining (see R part), and **b** diamond tools' geometry parameters

$$G_w^e = 2\sqrt{R_t^2 - (R_t - C_d)^2} \sin(\delta_e) \tag{26}$$

where  $e \in [n, N_S/2]$  and  $\delta_e = \sin^{-1} \frac{H_{sr}+h/2+H_{ow}o_s - \Delta Y_s^{k,1} - \Delta Y_s^{k,2} - \dots - \Delta Y_s^{k,e}}{R_d^k}$  could be derived based on Eq. (12) given in the last chapter.

Similarly, in the left compensation stage, the width of the machined groove here can be derived as:

$$G_w^f = 2\sqrt{R_t^2 - (R_t - C_d)^2} \cos(\delta_f) \tag{27}$$

where  $f \in [N_S/2, m]$  and  $\delta_f = \sin^{-1} \frac{\delta Y_s^{k,N_S/2} + \delta Y_s^{k,N_S/2+1} + \dots + \delta Y_s^{k,m}}{R_d^k}$  could be derived based on Eq. (15) given in the last chapter.

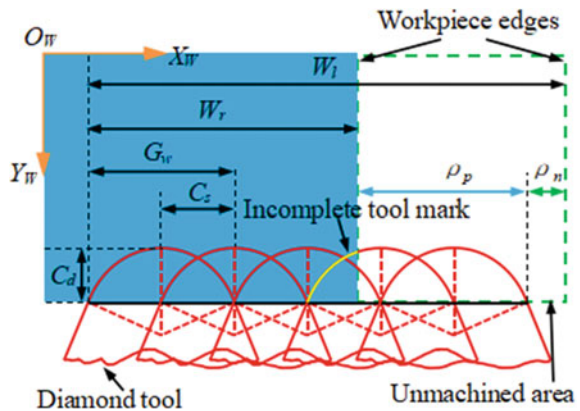
Evidently, according to Eq. (26), the maximum width of the machined groove exists when the spindle rotates  $90^\circ$ , which coincides with the machined groove's center line. Actually, the center of the machined groove does not coincide with the workpiece's center due to the translation error of the Y-direction. Therefore, comparing the center position of the machined groove and the workpiece can identify the tool deviation direction and distance in the Y-direction and then compensate for it.

### 2.5.3 Error-Oriented Identification of Tool Deviation in X-direction

The translation error in the X-direction causes the workpiece's edge to fall into two cases: over-machining and under-machining. As illustrated in Fig. 13, usually, incomplete tool marks remain in over-machining, whereas under-machining results in unmachined areas.

Multiple linearization tool trajectories are used to determine whether the edge of the workpiece has been over- or under-machining, because a linearization tool mark

**Fig. 13** Geometry parameters employing in X-axis error calculation



is not wide enough to cover and further establish the edge of the workpiece, as shown in Fig. 13. By measuring the multiple linearization tool marks' width, the error in the X-direction can be calculated. According to the geometric relation in Fig. 13, the theoretical width between neighboring linearization tool marks can be derived as follows:

$$G_W = 2C_S = \sqrt{R_t^2 - (R_t - C_d)^2} \quad (28)$$

It appears that the theoretical width of multiple linearization tool marks can be given by:

$$G_{TW} = aG_W \quad (29)$$

where  $a$  is the number of the linearization tool marks.

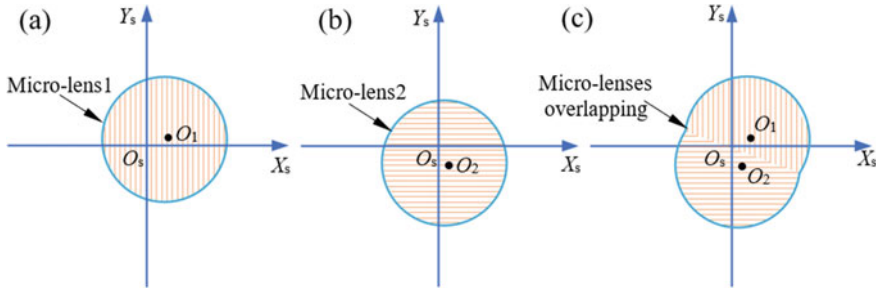
According to the geometric relations illustrate in Fig. 13, translation error  $\rho_p$  for over-machining and  $\rho_n$  for under-machining in the X-direction can be derived as follows:

$$\begin{cases} \rho_p = G_{TW} - W_r \\ \rho_n = W_l - G_{TW} \end{cases} \quad (30)$$

where  $W_r$  and  $W_l$  stand for the distances from the first linearization tool path to the edge of the workpiece in over- and under-machining, respectively.

According to Eq. (30), the translation error in the X-direction can be calculated, which can be used to identify the tool deviation in the X-direction as  $C_{1,0}$  and  $C_{-1,0}$  as indicated in Fig. 11a, and then compensation it.

Actually, if without the proposed tool deviation identification and compensation in the X- and Y-direction, some HMs, like the secondary pyramid microstructures by two micro-lenses overlapping, cannot be well-formed. Figure 14 illustrates this process. With the finish of the first-layer machining, the fabricated micro-lens1 could be generated and illustrated by Fig. 14a. By following, the workpiece rotates  $90^\circ$  and the micro-lens2 is then fabricated by the second-layer machining, as is illustrated by Fig. 14b. However, if the tool deviations exist, the pyramid microstructures (formed by overlapping the micro-lens1 and micro-lens2) fail to well generate, as illustrated by Fig. 14c. Obviously, if without the tool deviation identification, a significant center deviation between the two micro-lenses will be caused and cannot well overlap the secondary pyramid microstructures. Therefore, the successful machining of some HMs, especially some overlapping microstructures, must rely on the proposed tool deviation identification of X- and Y-direction to align with the center of the micro-lens.



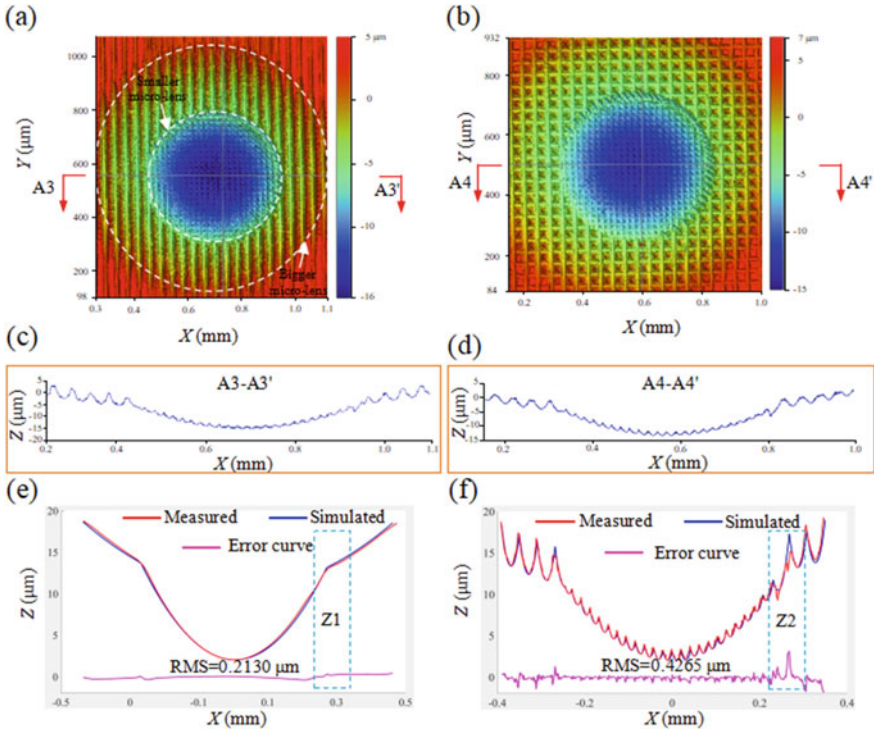
**Fig. 14** Two micro-lenses overlapping to form the secondary pyramid microstructure: **a** the first-layer machining to form micro-lens1; **b** the second-layer machining to form micro-lens2; **c** pyramid microstructures fails to be formed by these two micro-lenses overlapping

## 2.6 Fabrication of L-1SPM and L-2SPM

After the machining error identification and compensation, two types of HMs, including L-1SPM and L-2SPM, were machined successfully, as shown in Fig. 15a, b, respectively. Taking L-1SPM as the example, a bigger micro-lens (radius: 0.5 mm) and a smaller micro-lens (radius: 0.25 mm) compose a lenslet basal surface, on which has ordered secondary microstructures. To access the machining quality for the L-1SPM (see Fig. 15a), the contour curve was extracted using cross section of A3–A3', as shown in Fig. 15c. Obviously, the shape of the SPM perfectly follows the diamond tool's edge, which demonstrates the effectiveness of the proposed method. Furthermore, the machined result of L-2SPM is similar to the L-1SPM and both show high form accuracy.

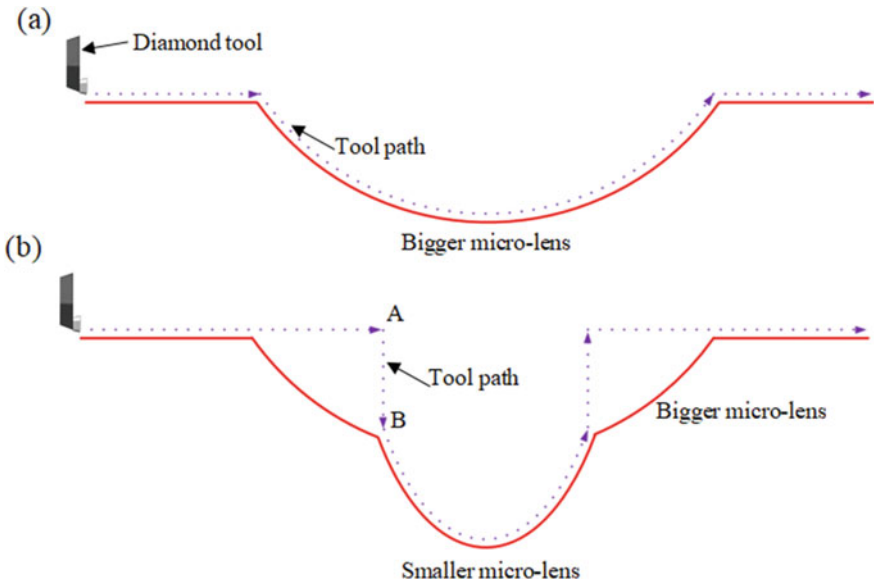
RMS values are still employed to perform quantitative error analysis of the L-1SPM. Figure 15e illustrates the error curve obtained by comparing the measured and simulated curves of the lenslet. Using MATLAB® to compare the two curves to calculate the RMS value of the error curve is 0.2130  $\mu\text{m}$ . Figure 15f shows the error curve obtained by comparing the measured and simulated curves of L-1SPM. Similarly, the error curve's RMS value also can be calculated by that of L-1SPM, which is 0.4256  $\mu\text{m}$ . Both are within 1  $\mu\text{m}$  and have achieved the submicron level, confirming the effectiveness of the proposed method.

Further analysis, Z1 and Z2 areas exhibit clear poor form accuracy, as shown in Fig. 15e, f. Actually, these areas are the boundaries of the bigger and smaller micro-lenses. Different tool feed strategies of the tool path are the main potential reason for this, as illustrated in Fig. 16. Figure 16a shows that the tool path changes steadily in the process of machining bigger micro-lenses. However, there are abrupt changes of the tool path in the case of smaller micro-lenses, especially in the AB section shown in Fig. 16b, which cause tool vibration and impact stress and further lead to a large material flow.

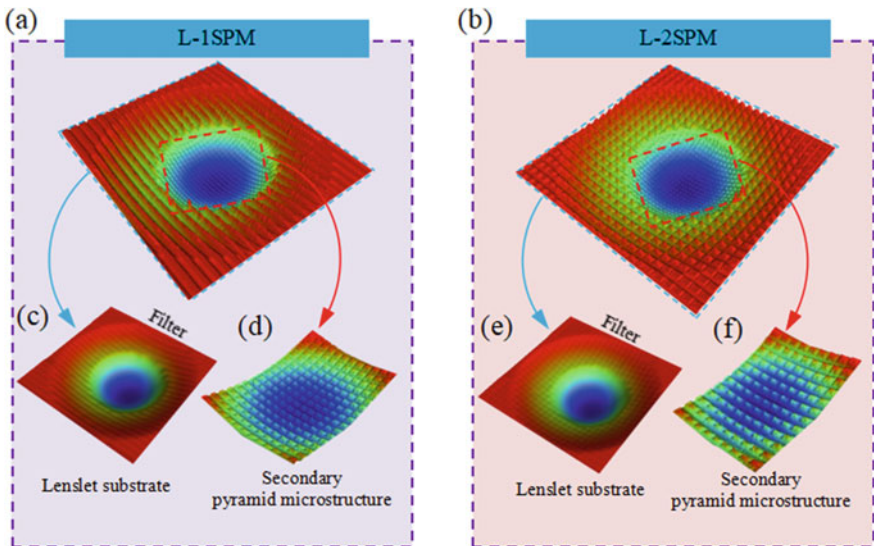


**Fig. 15** Surface characterizations and machining errors analysis for HMs: **a, b** a measured 3D morphology of the L-1SPM and L-2SPM, respectively, **c, d** sectional contour curves for A3–A3' and A4–A4' in **(a)** and **(b)**, respectively, **e, f** comparison between the simulated and measured curves of the lenslet and L-1SPM, respectively

The captured morphologies of the L-1SPM and L-2SPM are detailed shown in Fig. 17a, b, respectively. The basal of the HMs can be extracted by zero-order Gaussian regression filtering, which presents a lenslet structure as shown in Fig. 17c, e. Figure 17d, f show the captured morphologies of the inner secondary pyramid microstructure of L-1SPM and L-2SPM, respectively. The extracted surface morphology shows the high quality of the machined microstructures and demonstrates the feasibility and sufficiency of the OTSEF system in the machining of HMs. Therefore, the OTSEF system integrating STS is a powerful scheme for the efficient fabrication of complex microstructures using a three-axis (X-, Z-, and C-axes) UPMT.



**Fig. 16** Tool feed strategy for one tool path: **a** the tool path for a bigger micro-lens formation, and **b** for a smaller micro-lens formation



**Fig. 17** Decomposition characteristics for HMs: **a, b** measured 3D morphologies of the L-1SPM and L-2SPM, respectively, **c, e** lenslet basal surface after filtering, **d, f** measured 3D morphologies of inner secondary pyramid microstructures

### 3 Fabrication of HMs Using the OTSEF System Integrating FTS

Using the OTSEF system integrating STS can fabricate some low curvature variation surface with micro/nanostructures. However, it is difficult to fabricate surfaces with high curvature variation and dense micro/nanostructures due to the low-frequency movement of each servo axis of the machine tool. Consequently, it is essential to add auxiliary mechanisms to achieve high-frequency movement.

This section focused on the fabrication of HMs using the OTSEF system integrating FTS. We construct an FTS system (a vibration platform) driven with piezoelectric ceramic and flexible structures to realize the high-frequency vibration of workpieces. It can combine with the main rotary motion of the end flycutting tool to generate a surface morphology with high curvature characteristics. We established a tool path modeling of end flycutting for micro-lens array machining. After the fabrication of micro-lens basal surface, the nanometer microstructure was further fabricated on the micro-lens surface using the vibration platform. Finally, the machining error is analyzed and discussed in detail.

#### 3.1 Tool Path Modeling for Micro-lens Array Machining

To fabricate micro-lens arrays via end flycutting, a tool path modeling for micro-lens array machining is necessary. We use a rectangular area of length  $W$  and height  $H$  as a workpiece. This area must meet the condition that half of the height value is less than the rotation radius of the diamond tool ( $R_d$ ). The cutting edge of the diamond tool used in this mathematical model is arc-shaped, and the rake/clearance angle is  $0^\circ/10^\circ$ . To conveniently describe the coordinates of the tool point, the origin of the workpiece coordinate system  $O_W-X_W Y_W$  located in the middle of the left boundary line of the workpiece was planned, as shown in Fig. 18a. To describe the relationship between the motion process of the diamond tool and lens array formation, some parameters need to be defined, including the distance from the tool rotation center to the left boundary line of the workpiece  $S$ , feed speed  $f_d$  in the  $X$ -direction of the workpiece coordinate system  $O_W-X_W Y_W$ , spindle revolutions  $n$ , and each revolution arc is divided into  $l$  points with a constant angle. All defined parameters are shown in Fig. 18. Moreover, the center point of the tool cutting-edge arc  $O_r$  is used to replace the position of the diamond tool. According to the arc trajectory of the tool rotation, the tool points of the entire lens array are divided, and the diamond tool machines each lens unit evenly, as shown in Fig. 18b. Because the rake face of the tool is always in contact with the workpiece during machining, the direction of spindle rotation needs to be noted. The front face of the tool shown in Fig. 19a is oriented downward and exhibits counterclockwise rotation when projected onto the workpiece coordinate system.

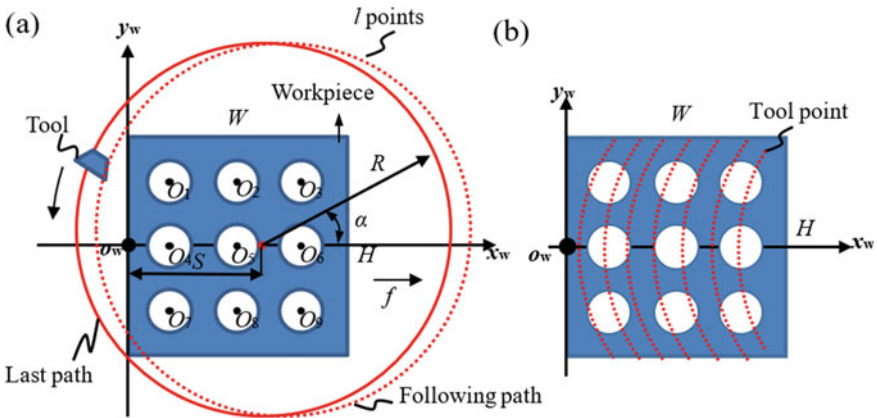


Fig. 18 Schematics of **a** tool rotation and feed, and **b** tool path covering the lens array

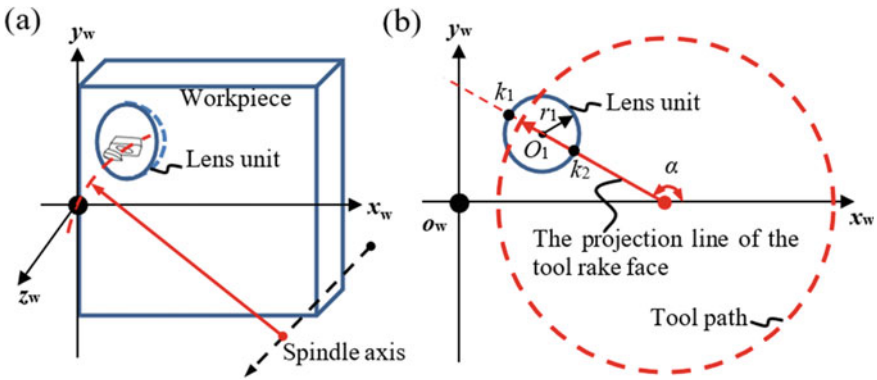


Fig. 19 Schematics of **a** lens unit formation in single tool path, and **b** geometric relation between the projection line of the tool rake face and the tool path on the  $O_W-X_WY_W$  coordinate plane

To obtain the tool points for machining the circular boundary, a corresponding mathematical model was established and then simulations were performed using MATLAB® 2018 to obtain the required tool points. A single lens was used for analysis. First, the workpiece coordinate system was set up, and the tool-point coordinates  $(X_d, Y_d)$  were calculated on the workpiece coordinate system. Subsequently, the boundary equation of the lens unit on the workpiece coordinate system was established. Because the plane where the tool front face intersects the lens unit produces a circular cross-section, a coordinate system  $O_n-X_nZ_n$  was established in the plane where the circular cross section was located. The theoretical cutting depth of the tool point can then be calculated in this coordinate system.

The purpose of establishing the mathematical model of the lens array was to determine the compensated cutting depth. The cutting depth needs to be solved first



for the angle the tool has turned, the distance the tool has fed in the X-direction, and the radius of the lens unit.

The current tool points are defined as  $k$ , and the coordinates  $(X_s, Y_s)$  of the tool edge arc rotation center projected on the workpiece coordinate system  $O_W-X_W Y_W$  can be expressed as follows:

$$\begin{cases} x_s = R \times \cos \bar{\alpha} + n \times f_d + s \\ y_s = R \times \sin \alpha \end{cases} \quad (31)$$

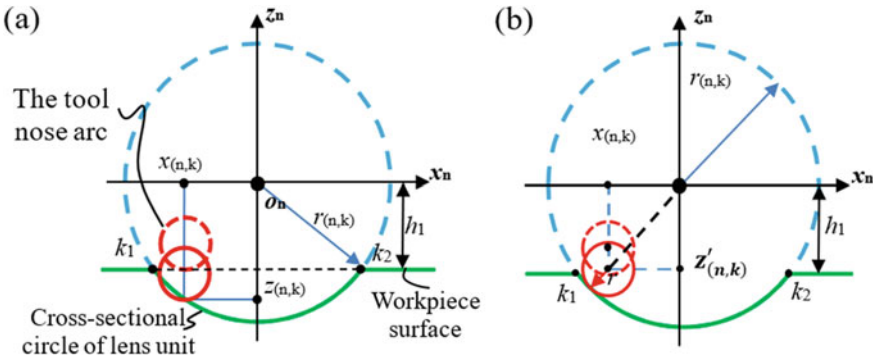
where  $\alpha = k \times \frac{2\pi}{T}$ ,  $n$  denotes the spindle revolutions,  $R$  denotes the rotation radius of the diamond tool, and  $\alpha$  denotes the tool rotation angle.

Although the lens units are distributed in different areas of the workpiece, the tool points of the lens array can be obtained by modeling and calculating the cross-sectional circle of the lens unit and tool nose arc. When the tool point is located on the lens unit, the diamond tool must be fed in the direction of cutting depth. Therefore, by obtaining the current tool-point coordinates and the tool rotation angle, the tool path of the entire lens array can be obtained by continuous iteration through geometric calculations.

Based on the analysis above, one of the lens units was used to establish a mathematical model for calculating a single tool point. For lens unit  $O_1$  of radius  $r_1$  shown in Fig. 20, the equation of the circle boundary projected on the workpiece coordinate system  $O_W-X_W Y_W$  is:

$$(x - x_{O_1})^2 + (y - y_{O_1})^2 = r^2 \quad (32)$$

When the tool points move to the lens unit area, the plane of the rake face can intercept the unit lens to obtain a circular section, and the plane where the rake face is projected onto the  $O_W-X_W Y_W$  coordinate system is a straight line, which can be derived as:



**Fig. 20** Schematics of **a** interference between the rake face's tool nose arc and the lens unit's cross-sectional circle and **b** its compensation

$$y = \tan \alpha \cdot (x - n \cdot f_d - s) \quad (33)$$

The projection of the tool points in the  $O_W-X_W Y_W$  coordinate system is on the ray emitted from the center of the coordinate system. During the machining process, the fixture is screwed to the tool, which causes the tool's radius of rotation at the tool position to deviate from the theoretical design value. In addition, because the tool height is not a constant value, when using different tools, the tool points will change in the mathematical model; therefore, the rake face must be compensated in the model. Angle compensation is performed on the angle  $\alpha$ , and the actual value of the compensation angle  $\alpha'$  can be written as:

$$\alpha' = \alpha + \arcsin\left(\frac{h_w - h_d}{R}\right) \quad (34)$$

where  $\alpha'$  is the angle after compensation,  $h_d$  is the actual tool height, and  $h_w$  is the tool slot depth.

By substituting the angle  $\alpha$  in Eq. (33) with  $\alpha'$ , and combining Eqs. (32) and (33), simultaneously, the coordinates of points  $k_1(x_1, y_1)$  and  $k_2(x_2, y_2)$  can be obtained. These are the boundary points of the current cross-sectional circle of the lens unit.

$$\begin{cases} (x_1, y_1) = \left( \frac{-b - \sqrt{(b^2 - 4ac)}}{2a \tan \alpha} + n f_d + s, \frac{-b - \sqrt{(b^2 - 4ac)}}{2a} \right) \\ (x_2, y_2) = \left( \frac{-b + \sqrt{(b^2 - 4ac)}}{2a \tan \alpha} + n f_d + s, \frac{-b + \sqrt{(b^2 - 4ac)}}{2a} \right) \end{cases} \quad (35)$$

$$\text{where } \begin{cases} a = \frac{1}{(\tan \alpha')^2} + 1 \\ b = 2(n \times f_d + s) - x_{o1} - y_{o1} \\ c = (x_{o1} - n \times f_d - s)^2 + y_{o1} - r^2 \end{cases}.$$

We assumed that the distance from the horizontal plane of the lens unit center to the surface of the workpiece is  $h_1$  and established the coordinate system of the cross-sectional circle with the boundary points. As shown in Fig. 20, the coordinate system  $O_n-X_n Z_n$  between the cutting depth and feed directions was determined for the lens unit. The radius  $r_{(n,k)}$  of the cross-sectional circle of the lens unit can be calculated by:

$$r_{(n,k)} = \sqrt{h_1^2 + \frac{|k_1 k_2|}{2}} \quad (36)$$

$$\text{where } |k_1 k_2| = \sqrt{(x_2 - x_1)^2 + (y_2 - y_1)^2}.$$

Based on the radius of the cross-sectional circle of the lens unit calculated using Eq. (35), the projection equation of the cross-sectional circle can be expressed as:

$$x_{(n,k)}^2 + z_{(n,k)}^2 = r_{(n,k)}^2 \quad (37)$$

where  $x_{(n,k)}$  and  $y_{(n,k)}$  are the coordinate values of the tool point.

Based on the two points  $k_1(x_1, y_1)$  and  $k_2(x_2, y_2)$  calculated above, the abscissas of the tool points  $x_{(n,k)}$  are expressed in the cross-sectional circular coordinate system as:

$$x_{(n,k)} = \sqrt{(x_s - x_1)^2 + (y_s - y_1)^2} - \frac{|k_1 k_2|}{2} \quad (38)$$

Combining Eqs. (36) and (37),  $z_{(n,k)}$  can be calculated, which is the current tool point feed value.

$$z_{(n,k)} = \sqrt{r_{(n,k)}^2 - \left( \sqrt{(x_s - x_1)^2 + (y_s - y_1)^2} - \frac{|k_1 k_2|}{2} \right)^2} \quad (39)$$

The tool-nose arc cuts into the lens according to the  $z_n$  direction, as shown in Fig. 20. When the tool tip is fed in the Z-direction, the tool nose arc overcuts the cross-sectional circle of the lens, resulting in tool interference, and thus affecting the accuracy of the lens unit. Therefore, interference compensation must be applied at this point. As shown in Fig. 20, the tangency between the tool nose arc, the cross-sectional circle of the lens unit, and the compensated point coordinates in this coordinate system are given by:

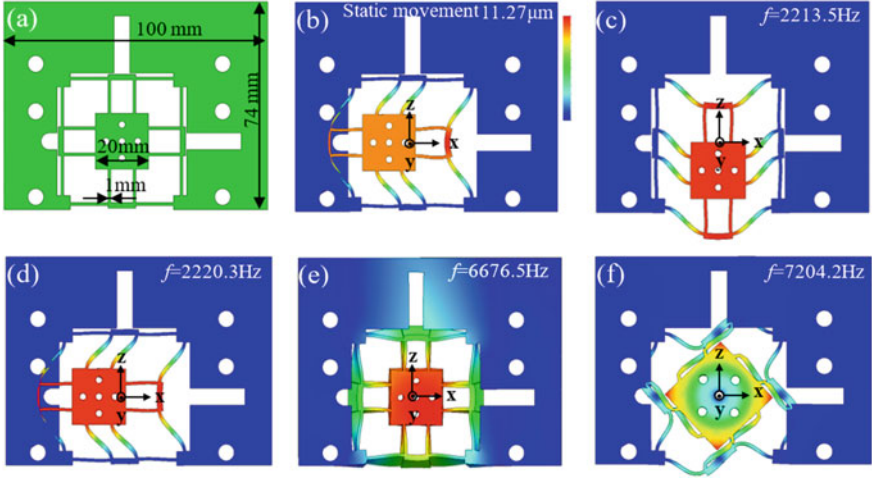
$$z'_{(n,k)} = -\sqrt{(r_{(n,k)} - r)^2 - x_{(n,k)}^2} \quad (40)$$

### 3.2 Simulation and Prediction of Path Planning

The constructed FTS system (a vibration platform) is driven by piezoelectric ceramic and flexible structures. For the flexible hinges, the symmetrical parallelogram flexible structures have great orthogonal decoupling characteristics to ensure the accuracy of movement in two directions.

The specific structure is shown in Fig. 21a and its thickness is 11 mm. It's a 2-DOF (two degree of freedom) micro-displacement platform. The spring steel 65Mn was selected as the material. Figure 21b shows that the center platform can output displacement of 11.27  $\mu\text{m}$  in the X-direction under a thrust of 78 N. Figure 21c–f show the first four vibration modes and their resonant frequency of the micro-displacement platform, respectively. Its vibration model of first-, second-, and third-order mode along the Z-, X-, and Y-direction are with the frequency of 2213.5, 2220.3, and 6676.5 Hz, respectively; its vibration model of fourth-order mode is torsion along the Y-axis with the frequency of 7204.2 Hz. The frequencies of the first two models have exceeded 2000 Hz, which can meet the requirements of fabricating structures with high curvature variation.

Vibration excitation in the direction of 1-DOF is applied to the workpiece, and the cutting marks left by the tool after machining on the surface of the workpiece can



**Fig. 21** 2-DOF micro-displacement platform **a** Schematic diagram of structural layout; **b** static analysis diagram in X-direction; **c** first-order mode; **d** second-order mode; **e** third-order mode; **f** fourth-order mode

change regularly. Figure 22 shows the surface profile of a single cutting path left by the tool on the surface of the workpiece when the diamond arc cutting edge tool is rotating. The trajectory profile of a single tool path is represented by Eq. (41), where  $\theta \in [\pi, 2\pi]$ ,  $\beta \in [0, 2\pi]$ ,  $R_d$  is the tool rotation radius of gyration, and  $a$  is the depth of cut. Based on the geometric relationship shown in Fig. 23, the coordinate value of any point on the arc tool path can be expressed as follows:

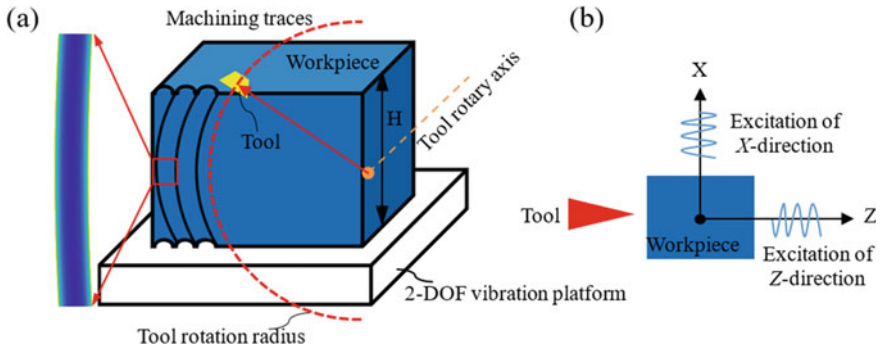
$$\begin{cases} x = (R_d + a \cos(\theta)) \sin(\beta) \\ y = (R_d + a \cos(\theta)) \cos(\beta) \\ z = a \sin(\theta) \end{cases} \quad (41)$$

Moreover, the sinusoidal excitation signal can be expressed as follows:

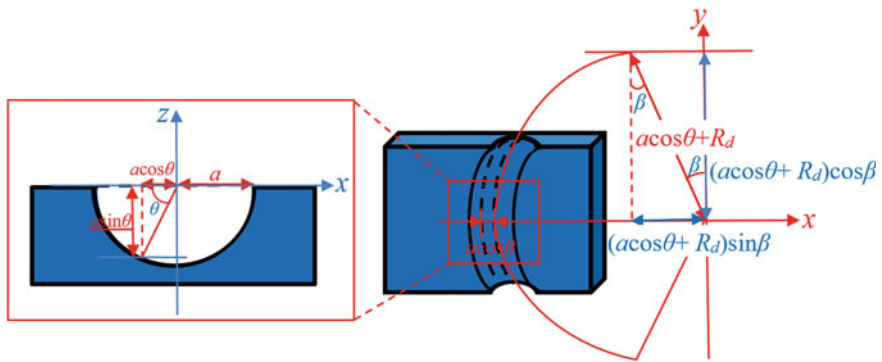
$$v = A \sin(2\pi ft) \quad (42)$$

where  $A$  is the amplitude of the sine excitation,  $f$  is the vibration frequency, and  $t$  is the time.

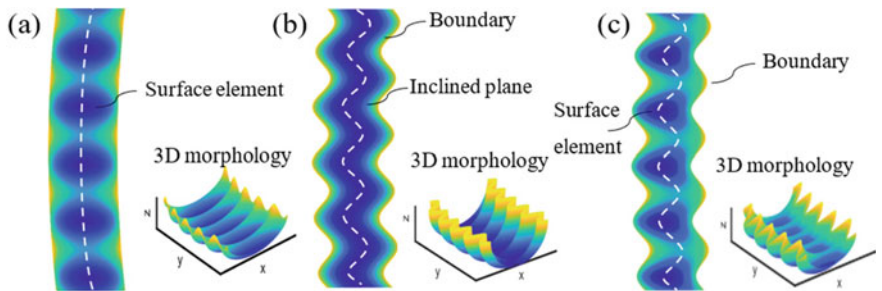
Using Eq. (42) superimposed on the coordinates of  $X$  and  $Z$  of Eq. (41), respectively, the shapes of the cutting path with sinusoidal excitation characteristics can be obtained, as shown in Fig. 24. Figure 24a, b illustrate the simulated 3D morphology of the tool path under the excitation vibration of the sinusoidal in the X- and Z-direction, respectively. Clearly, the simulated 3D morphology of a tool path machined in the X-direction is with various cutting depth and still maintain the arc tool path, whereas that in the Z-direction is with constant cutting depth and sinusoidal machined boundary.



**Fig. 22** **a** Tool edge traces cut by the rotary path; **b** schematic diagram of the workpiece with two-degree-of-freedom vibration excitation



**Fig. 23** Geometric relationship between radius of gyration and depth of tangent in ideal coordinate system



**Fig. 24** Schematic diagram of simulation results of tool trajectory remaining surface under single-DOF excitation **a** sinusoidal excitation applied in Z-direction; **b** sinusoidal excitation applied in X-direction; **c** in phase superposition of excitation in two directions

The changed complex morphology of a tool path machined is the basis to fabricate HMs. Furthermore, a more complex microstructure can be simulated by changing the phase starting point of sinusoidal excitation both in the X- and Z-direction, and also can further change the vibration phase of these two directions to generate various more complex microstructures. Here, we only simulated the microstructure surface of combined paths in the X- and Z-direction under double excitation with the same phase, as shown in Fig. 24c.

### 3.3 Fabrication of Micro-lens Array

According to the tool path model established in Sect. 3.1, we still used the OTSEF system to fabricate micro-lens arrays. The experimental setup is illustrated in Fig. 25. Moreover, to fabricate some micro/nanostructures with high curvature variation, the OTSEF system needs to integrate FTS. The integrated FTS is constituted of a 2-DOF high-frequency motion platform and piezoelectric ceramic. The workpiece is clamped on the platform and driven by the low-voltage piezoelectric ceramic stack (PSt150/5 × 5/20). Moreover, a power amplifier (Piezo Drive PX200) is used to amplify the waveform generated by the signal generator (Tekrtonix AFG1022), and the output voltage is applied to the piezoelectric stack to produce micro-displacement deformation, resulting in high-frequency motion of the workpiece.

For the basal surface (micro-lens) machining, the selected machining parameters are summarized in Table 2. The most suitable diamond tool in the fabrication of

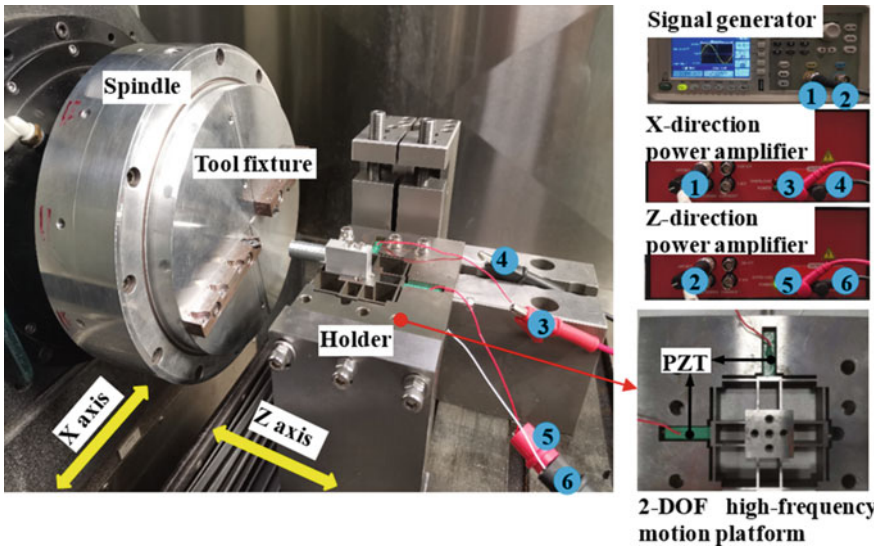


Fig. 25 Experimental setup for microstructures machining

**Table 2** Cutting parameters employed in the fabrication of micro-lens array

Parameter	Value
Tool radius	0.1 mm
Rake angle	0°
Include angle	100°
Rotating radius	15 mm
Cutting depth	10 $\mu\text{m}$
Rotation speed	4 r/min
Feeding	1.229 mm

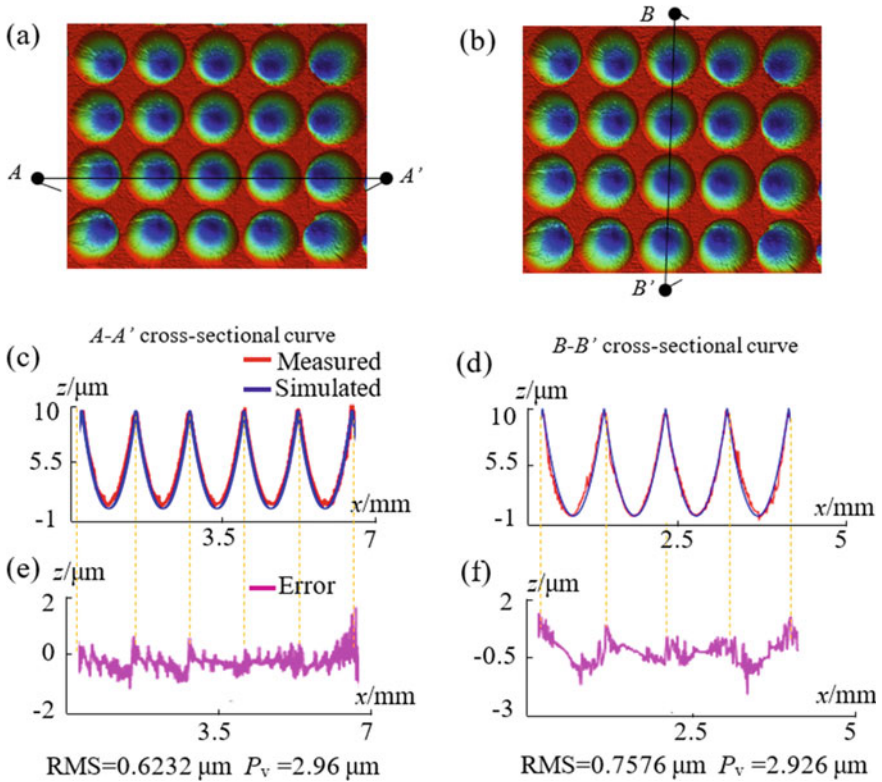
microstructures is the S-point diamond tool, whereas it more easily has fracture wear and usually uses a small tool radius to substitute it. We use a diamond tool with a tool radius of 0.1 mm. Moreover, the workpiece's material is aluminum alloy 6061.

Figure 26a, b illustrate the captured 3D morphology of the machined micro-lens array. Clearly, each micro-lens unit is distributed uniformly with clear boundary shape and good morphology characteristics, proving the effectiveness of the proposed method. RMS is still employed to evaluate the machining quality of the micro-lens array by comparing the simulated and measured cross-sectional curves. To analyze the machining accuracy of the micro-lens array, the simulated cross-sectional curve was fitted with that of measured, which have a great coincidence, as shown in Fig. 26c, d. Figure 26e, f illustrate the form errors in the direction of horizontal and vertical axis, which are 0.6232 and 0.7576  $\mu\text{m}$ , respectively. Furthermore, the  $P_v$  value are less than 3  $\mu\text{m}$  in both these two directions. There are many subtle fluctuations in the cross-sectional curve, caused by residual burrs and material flow.

### 3.4 Fabrication of Microstructures Using Sinusoidal Excitation

The machining parameters of the sub-layer microstructures are listed in Table 3. Considering the material flow and rebound, an excessively large tool radius of the diamond tool will make the micro-structures generation inconspicuous and affect the machining efficiency. Therefore, it is suitable to choose a smaller tool radius (13  $\mu\text{m}$ ), and the cutting depth should not be too large (5  $\mu\text{m}$ ) in the fabrication of these sub-layer microstructures. Moreover, the excitation frequency chosen by us is 300 Hz.

Using 1-DOF sinusoidal excitation in the Z- and X-direction to fabricate sub-layer microstructures, the captured 3D morphology of the machined surfaces are shown in Fig. 27a, b respectively. Comparing the simulation structure of Fig. 24, they have great consistency in morphology. Affected by machining accuracy, ambient noise and open-loop motion accuracy of the micro-displacement high-frequency motion

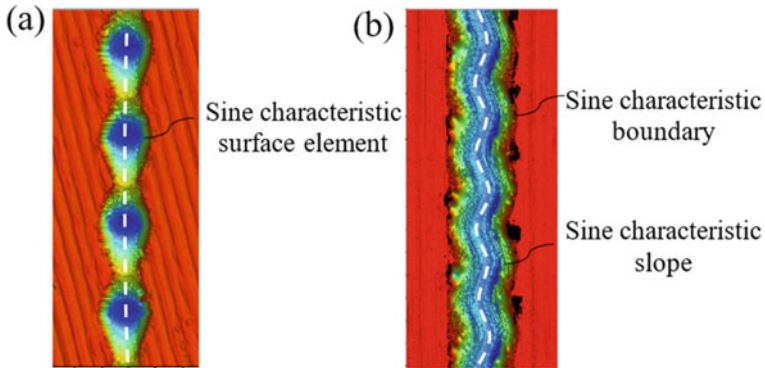


**Fig. 26** a, b 3D morphology of circular boundary lens array; Comparison of measured c A–A’ and d B–B’ cross-sectional curves with simulated results; Error curves for the cross-sectional curves on e A–A’ and f B–B’ section planes

**Table 3** Cutting parameters employed in the fabrication of microstructures using sinusoidal excitation

Parameter	Value
Tool radius	13 μm
Rake angle	0°
Include angle	100°
Rotating radius	15 mm
Cutting depth	5 μm
Rotation speed	60 r/min
Feed rate	1.229 mm/min
Excitation frequency	300 Hz
Voltage	40 V

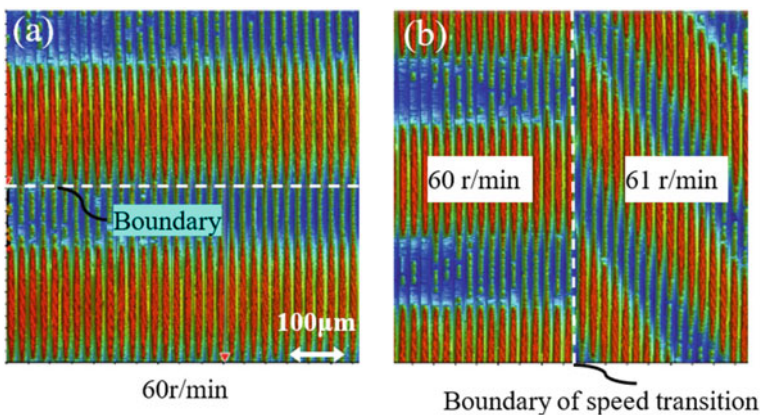




**Fig. 27** Schematic diagram of measurement results of tool path remaining surface profile machining under 1-DOF **a** Sinusoidal excitation applied in the Z-direction; **b** Sinusoidal excitation applied in the X-direction

platform, the motion waveform of tool paths has changed slightly. However, it does not affect the formation of sublayer surface microstructure arrays.

Note that there is a mapping relationship between spindle speed and excitation frequency. When the spindle rotation speed is 60 r/min and the sinusoidal excitation frequency is 300 Hz, the morphology of the machined surface is shown in Fig. 28a. However, when the rotation speed is changed to 61 r/min, the machined microstructure array under the same excitation is shown in Fig. 28b. Clearly, using different excitation frequencies with a common spindle rotation speed, the excitation phase of the neighboring tool has changed and the convex position has moved back relative to the previous tool path. Consequently, it can be seen that the dislocation microstructure can be realized by changing the rotation speed at some excitation frequency.



**Fig. 28** 1-DOF in the Z-direction under 300 Hz sinusoidal excitation vibration, 60 r/min and 61 r/min speed affect the micro-structure layout and the machining measurement results

**Fig. 29** The relationship between speed and frequency under 180° phase difference

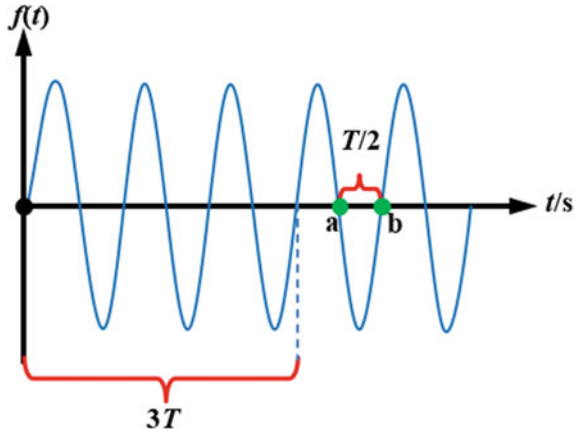


Figure 29 shows the relationship between excitation frequency and spindle rotation speed. In a sinusoidal excitation with a frequency of  $f$ , the time of a single sinusoidal wave is  $T$ , and  $T$  is equal to the reciprocal of the frequency, which is  $1/f$ . The phase difference of a single sinusoidal wave corresponding to two points  $a$  and  $b$  is  $180^\circ$ , and the time difference between the two is  $T/2$ . Between two adjacent rotations of the spindle, if the switching point of the spindle is at point  $b$ , that is, the time of one rotation is  $nT + 2/T$ . Then the two tool paths repeated machining will fabricate a characteristic surface microstructure with a phase difference of  $180^\circ$ .

The relation between the speed and frequency can be expressed as follows:

$$\frac{60}{n_s} = nT + \frac{T}{2} \quad (43)$$

where  $n_s$  is the spindle rotation speed and  $n$  is a positive integer.

Since the 3-axis UPMT used in the experiment is in the non-C-axis mode to fabricate the sub-layer microstructures, the recognized speed is an integer. Therefore, Eq. (43) can be simplified as:

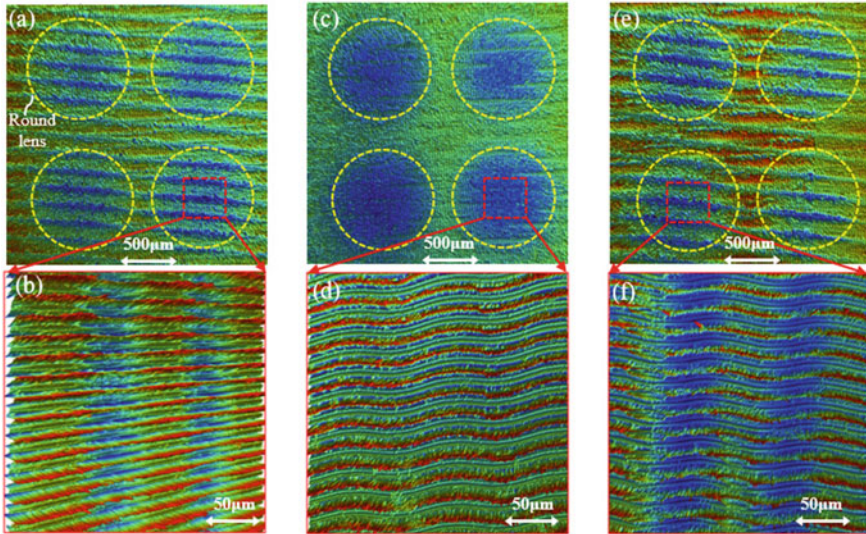
$$\frac{f}{n_s} 60 = n + 0.5 \quad (44)$$

Substituting  $f = 300$  Hz into Eq. (44), it can be calculated that the minimum speed value that satisfies the equation is 32 r/min. Other speeds that form a multiple of 3 or 5 with 32 r/min can also meet the conditions, but the maximum speed is 36000 r/min. However, considering that the machining area occupies about one-tenth of the rotating arc, the lowest speed is the best choice to achieve high-frequency characteristics of the machined surface.

### 3.5 Fabrication of Multi-scale Microstructure

Based on the mathematical model in Sects. 3.1 and 3.2 and the experimental test in Sects. 3.3 and 3.4, three kinds of multi-scale microstructures have been fabricated, as shown in Fig. 30. In the experiment, we used a diamond tool with a radius of  $13\ \mu\text{m}$  to fabricate the micro-lens array (using slow servo in Z-direction of the machine tool) and the sub-layer microstructures on the basal surface (using 300 Hz sinusoidal excitation of the 2-DOF vibration platform) simultaneously.

Figure 30a, b show the captured 3D morphology of the micro-lens array and sub-layer microstructures fabricated using 1-DOF excitation vibration in the Z-direction with no phase difference, while Fig. 30c, d show that in X-direction. Unfortunately, with the influence of the secondary vibration, the shape of the basal micro-lens array is partially distorted in the direction of cutting depth, but the sub-layer structure can be uniformly arranged and shows the characteristic of sinusoidal. Figure 30e–f show the captured 3D morphology of micro-lens array and sub-layer microstructures fabricated using 2-DOF excitation vibration both in the X- and Z-direction with no phase difference. The shape of the basal micro-lens array still has partially distorted in the direction of cutting depth, but the sub-layer structure can be uniformly arranged and shows the characteristic of sinusoidal both in two directions. The experimental results show a huge machining error combined with the self-constructed FTS system and the UPMT. The main reason is that the FTS system is open-loop control, so it



**Fig. 30** Schematic diagrams of multi-level structure **a** Z-direction single excitation-lens laminated structure; **b** Z-direction single excitation sub-layer structure; **c** X-direction single excitation-lens laminated structure; **d** X-direction single excitation sub-layer structure; **e** double excitation-lens laminated structure; **f** double excitation sub-layer structure

is unable to identify, feedback and compensate for the displacement of the machine tool, resulting in the loss of accuracy. Therefore, an FTS system with closed-loop control may guarantee machining accuracy to ensure the realization of these multi-layer microstructures machining. And this is the following study point focused on us.

## 4 Conclusions

In the present study, an OTSEF system was developed, and integrated STS and FTS into it to fabricate HMs, respectively. To conclude, some bullet points are as follows:

- (1) A tool path planning model for the fabrication of the micro-lens unit and micro-lens array using linear trajectory is established, whereby the RMS error of the machined micro-lens unit and a micro-lens array is less than  $1\ \mu\text{m}$  as compared to the theoretical morphology.
- (2) An error-oriented identification method for tool deviation in X- and Y-directions was proposed, by which the misalignment between the diamond tool and the workpiece can be identified and then compensated to improve the machining accuracy of microstructures.
- (3) The multi-layer HMs, L-1SPM, and L-2SPM, were fabricated further by employing the OTSEF system integrating FTS. Machining results not only showed the fine morphology accuracy of the HMs but also demonstrated the effectiveness and high accuracy of OTSEF in machining HM surfaces.
- (4) A tool path planning model for the fabrication of the micro-lens array using arc trajectory is established, whereby the RMS error of the machined micro-lens array is less than  $1\ \mu\text{m}$  as compared to the theoretical morphology.
- (5) An FTS system was constructed using a 2-DOF high-frequency motion platform and piezoelectric ceramic. The machining characteristics of the sublayer structure were tested and verified, and the HMs microstructure was fabricated employing the OTSEF system integrating STS.

**Acknowledgements** The work described in this chapter was supported by the National Natural Science Foundation of China (Grant No. 52275454, 51827901), and the Shenzhen Natural Science Foundation (Grant No. 20200826160002001, JCYJ2022053103614032).

## References

1. Brinksmeier E, Karpuschewski B, Yan J, Schnemann L (2020) Manufacturing of multiscale structured surfaces. *CIRP Ann-Manuf Techn* 69:717–739
2. Pu X, Li GJ, Huang HL (2016) Preparation, anti-biofouling and drag-reduction properties of a biomimetic shark skin surface. *Biol Open* 5:389–396

3. Liu XY, Zhang SS, Zhang HB (2016) Microstructure of butterfly wing scale and simulation of structural color. *Optik* 127:1729–1733
4. Bhushan B, Jung YC, Koch K (2009) Micro-, nano- and hierarchical structures for superhydrophobicity, self-cleaning and low adhesion. *Philos Trans A Math Phys Eng* 367:1631–1672
5. Cheng YT, Rodak DE, Wong CA, Hayden CA (2006) Effects of micro- and nano-structures on the self-cleaning behavior of lotus leaves. *Nanotechnol* 17:1359–1362
6. Koch K, Bhushan B, Jung YC, Barthlott W (2009) Fabrication of artificial Lotus leaves and significance of hierarchical structure for superhydrophobicity and low adhesion. *Soft Matter* 5:1386–1393
7. Zhu ZW, To S, Zhang SJ (2015) Large-scale fabrication of micro-lens array by novel end-fly-cutting-servo diamond machining. *Opt Express* 23:20593–20604
8. Fudouzi H, Hariyama T, Yamahama Y, Yoshioka S, Uodu Y (2013) Opal Films with Dome-Shaped Structures Fabricated by Hot Embossing. *Kōbunshi rombun shū* 70:227–231
9. Wang LQ, Lin JP, Zhang X (2013) Hierarchical microstructures self-assembled from polymer systems. *Polymer* 54:3427–3442
10. Zhu ZW, To S, Tong Z, Zhuang ZX, Jiang XQ (2019) Modulated diamond cutting for the generation of complicated micro/nanofluidic channels. *Precis Eng* 56:136–142
11. Ikawa N, Donaldson RR, Komanduri R, König W, Aachen TH, Mckeown PA, Moriwaki T, Stowers IF (1991) Ultraprecision metal cutting—the past, the present and the future. *CIRP Ann-Manuf Techn* 40:587–594
12. Chang KM, Cheng WT, Liu YT (2019) Development of non-axisymmetric aspheric ultraprecision machining using FPGA-based piezoelectric FTS. *Sensor Actuat A-Phys* 291:99–106
13. Gao W, Araki T, Kiyono S, Okazaki YC, Yamanaka M (2003) Precision nano-fabrication and evaluation of a large area sinusoidal grid surface for a surface encoder. *PreciS Eng* 27:289–298
14. Yi A, Li L (2005) Design and fabrication of a microlens array by use of a slow tool servo. *Opt Lett* 30:1707–1709
15. Zhou M, Zhang HJ, Chen SJ (2010) Study on diamond cutting of nonrationally symmetric Microstructured surfaces with fast tool servo. *Mater Manuf Process* 5:488–494
16. Yuan YJ, Zhang DW, Jing XB, Zhu HY, Zhu WL, Cao J, Ehmann KF (2019) Fabrication of hierarchical freeform surfaces by 2D compliant vibration-assisted cutting. *Int J Mech Sci* 152:454–464
17. Li L, Yi A (2010) Development of a 3D artificial compound eye. *Opt Express* 18:18125–18137
18. Prasad KK, Roy T, Vinod GMM, K, Vinod M, (2021) Diamond turned hierarchically textured surface for inducing water repellency: analytical model and experimental investigations. *Int J Mech Sci* 193:106140
19. Scheiding S, Yi AY, Gebhardt A, Li L, Risse S, Eberhardt R, Tünnermann A (2011) Freeform manufacturing of a microoptical lens array on a steep curved substrate by use of a voice coil fast tool servo. *Opt Express* 19:23938–23951
20. Tong Z, Zhong WB, To S, Zeng WH (2020) Fast-tool-servo micro-grooving freeform surfaces with embedded metrology. *CIRP Ann-Manuf Techn* 69:505–508
21. Zhang SJ, To S, Zhu ZW, Zhang GQ (2016) A review of fly cutting applied to surface generation in ultra-precision machining. *Int J Mach Tool Manu* 103:13–27
22. Zhu ZW, To S, Zhang SJ, Zhou XQ (2016) High-throughput generation of hierarchical micro/nanostructures by spatial vibration-assisted diamond cutting. *Adv Mater Interfaces* 3:1500477
23. Zhu ZW, To S, Ehmann KF, Xiao GB, Zhu WL (2016) A novel diamond micro-/nano-machining process for the generation of hierarchical micro-/nano-structures. *J Micromech Microeng* 26:035009
24. To S, Zhu Z, Zeng W (2015) Novel end-fly-cutting-servo system for deterministic generation of hierarchical micro-nanostructures. *CIRP Ann-Manuf Techn* 64:133–136
25. Zhu WL, Duan F, Zhang XD, Zhu ZW, Ju BF (2018) A new diamond machining approach for extendable fabrication of micro-freeform lens array. *Int J Mach Tools Manu* 124:134–148
26. Ko DH, Tumbleston JR, Henderson KJ, Euliss LE, Lopez DJM, R, Samulski ET, (2011) Biomimetic microlens array with antireflective “moth-eye” surface. *Soft Matter* 7(14):6404–6407

27. Zhang GQ, Ma S, Wang JP, Jiang JK, Luo T, Wang HT (2022) Offset-tool-servo diamond end flycutting multi-layer hierarchical microstructures. *Int J Mech Sci* 233:107645
28. Zhu ZW, To S, Zhang SJ (2015) Theoretical and experimental investigation on the novel end-fly-cutting-servo diamond machining of hierarchical micro-nanostructures. *Int J Mach Tools Manu* 94:15–25

# Chapter 4

## Tool Offset Flycutting Micro-optics Arrays with High-Aspect-Ratio



Zhanwen Sun, Suet To , and Sujuan Wang 

**Abstract** Micro-optical arrays (MOAs) with high aspect ratios (AR) provide special benefits when it comes to minimising system of optics by lowering the focus range. It is commonly accepted that fast or slow tool servo (F/STS) is superior for creating MOAs with great form accuracy. However, the Non-smooth cutting track of F/STS causes intense the fluctuation of the tool and the conflict between the side face of the tool and the finished surface when processing MOAs with high AR, which deteriorates surface coarseness. In order to realize flexible manufacture of miniature liberal form lenticles arrays with high AR, this paper proposes a new offset-tool-servo (OTS) diamond processing method and its accompanying cutting tool trail generating method of calculation is suggested in this work. In order to solve the problem of tool conflict caused by rapid tool descent in F/STS system, a four-axis servo mechanism was used to establish the helical path of tools of per lenticles on OTS. Furthermore, the suggested processing approach efficiently prevents the degradation of the surface quality brought on by tool fluctuations by ensuring the flatness of the produced cutting tool trail for every lenticles. This technique is used by creating various MOAs with aspheric and freeform forms. It is shown that the OTS approach may provide smoother and more uniform surface quality while achieving AR values that are two times bigger than those of the F/STS method.

## 1 Introduction

Because of its excellent vision and small size, micro-optical arrays (MOAs) with multiple lenticles cellular have been broadly applied in videos, transducers, and optoelectronic equipment [1, 2]. The lenticles was first intended for aspheric and

---

Z. Sun · S. Wang (✉)

State Key Laboratory of Precision Electronic Manufacturing Technology and Equipment,  
Guangdong University of Technology, Guangzhou, China  
e-mail: [grace.wangsj@gdut.edu.cn](mailto:grace.wangsj@gdut.edu.cn)

S. To

State Key Laboratory in Ultra-Precision Machining Technology, Department of Industrial and Systems Engineering, The Hong Kong Polytechnic University, Kowloon, Hong Kong

spheric surfaces [3]. These days, with the quick advancement of optical and electronic technology, it is challenging for basic surfaces to meet the demands of sophisticated multi-function integrated system of optics [4, 5]. Contrarily, MOAs with complex constructions have drawn increasing amounts of attention, for instance miniature Fresnel lenticles arrays [5], composite eye construction [6], miniature lenticular arrays [7], and reflective arrays [4]. These MOAs typically have discontinuous constructions with extremely high shape accuracy and aspect ratios (AR). High AR MOAs and complex architectures enable optical designers to achieve multifunctional integration and reduced system of optics in unimaginable ways. Nevertheless, the high AR of lenticles and complicated forms present significant obstacles for the worthwhile production of such MOAs with ultra-high form accuracy and smooth surface coarseness using current processing processes.

Numerous micro manufacturing processes, which can be loosely categorized into machinery' and non-machinery' processing, have been proposed to meet the criteria of MOAs. MOAs can be manufactured on a large scale using non-machinery' methods, namely chemical etching [8, 9] and laser lithography [10, 11]. However, these methods frequently call for pricey infrastructure and expensive, time-consuming processes, and they can only handle a limited number of materials with simple geometrical constructions [12, 13]. Because of its superiorities in producing ultra-high shape accuracy, machinery' processing with diamond tools is usually viewed neatly manufacturing has a broader prospect MOAs with intricate constructions on various engineering materials. Machinery' processing can be classified into two types: Fast and Slow Tool Servo (F/STS) and Diamond Crumbling, according to the tool configuration method [14–16]. Ball crumbling cutter mounted on rapid axle for diamond crumbling. The rotational diamond tool is capable of producing individual rotationally symmetric lenticles. One lenticles Cellular at a time can be machined throughout the entire fabricated parts surface using three translational servo motions. Since per lenticles is cut under the same conditions, an even surface quality can be obtained across the entire MOA's surface. Diamond crumbling, however, can create only massive sparse arrays with spherical or aspheric shapes [17]. Satisfying the increasing demand for high AR and arbitrary MOAs is challenging.

The best method for fabricating MOAs with extremely high form accuracy is F/STS diamond swirling [15, 18]. High-frequency servo motion along the Z-axis enables the flexible fabrication of lenticles with aspheric or freeform forms on various technical materials. However, the inevitable path of tool discontinuity in MOA's F/STS diamond swirling process will cause serious tool fluctuations, which will worsen the surface coarseness and indigent surface quality [18, 19]. Due to the diamond tool's sharp descending and rising movements, tool fluctuations may be particularly noticeable while processing MOAs with high AR [20]. Furthermore, the flank face of the diamond tool will invariably interfere with the completed surface when swirling MOAs with high AR because of the rough cutting tool track's excessive slope angle [21]. Although F/STS is an encouraging way to create microscopic structures, the problems mentioned above prevent it from being used to fabricate MOAs with high AR and intricate architectures.



Several diamond processing techniques developed from F/STS have been suggested for producing MOAs with particular forms. For instance, Neo DWK et al. [22] created polygonal Fresnel lenses arrays utilizing a cutting-brink diamond micro chiselling technique. Brinksmeier et al. [4] suggested using guilloche processing technology to create retroreflective arrays. The flexibility of these approaches is severely constrained because they can only be used to create MOAs with the shapes mentioned above. Zhu et al. [23] have suggested an end-fly-cutting-servo method to fabricate MOAs on a wide scale. This technique can be used to create hybrid MOAs and effectively guarantees uniform surface quality over a large area [19]. However, similarly to traditional F/STS, the cutting tool track of the end-fly-cutting-servo system is not smooth when generating MOAs. Therefore, this way is also restricted to manufacturing MOAs with high AR because of tool fluctuation and conflict.

Zhu et al. [20] have suggested a virtual axle-based tool servo diamond swirling method that enables flexible production of discontinuously organized micro-optics arrays. In virtual axle swirling, the diamond tool is mounted on a tool holder and subsequently secured on the Z translational slide, while the fabricated parts are coupled to the axle while it rotates around the C-axis. This technique allows for creating arrayed microscopic structures with consistent surface quality by essentially building the rotation axis at the centres of per lenses cellular in turn. The X- and Y-axes must, however, to assign harmonic oscillations at the same frequency as the rotation of the axle, to make sure that the positions of the individual lenses cellular always match the virtual axle that has already been created. Because the fabricated parts are fixed on the axle when the virtual axle is turned, the processing of large aperture MOA s requires very high amplitude of X-axes and Y-axes oscillation. This poses a significant challenge to the dynamic responsiveness of the processing tools. Additionally, a low-efficient oscillation frequency should be reduced using a very slow axle rotation rate.

In various optical applications, the aspect ratio of MOAs typically varies from 0.02 to 0.23 [18, 19, 24]. A clear definition of the high and low AR for MOAs does not yet exist because of the diverse processing processes. For instance, the aspect ratio is often less than 0.06 for MOAs produced by machinery' processing techniques for instance sculpturing, crumbing, and F/STS, to avoid the tool and the lenses Cellular conflict [21]. Non-machinery' processing techniques like LIGA and laser processing are needed to produce MOAs with an AR greater than 0.06 [24, 25]. These non-machinery' methods, however, are typically confined to processing a small number of materials with low geometrical intricacy and form precision. They also frequently involve complex processes with low efficiency. Based on the current most advanced processing technology, 0.06 AR can be marked as a threshold between high and low AR of processing technology.

The processing of multi-level microscopic structures with extreme precision frequently uses ultra-precision fly cutting. Since the axle velocity and the tool's swing radius (the range from the tool tip to the axle axis) are constant, this method runs with a constant cutting velocity. It is typically used to cut huge, flat surfaces. The production of microscopic structures functional surfaces is also possible with

servo fly cutting [26]. It has been used to fabricate microscopic structures functional surfaces in combination with slow tool servo or rapid tool servo due to its consistency in cutting velocity, sampling length, and quality. It guarantees consistent surface quality due to its constant cutting velocity, continuous sample period, and tracking bandwidth. Zhu et al. [27] have studied end-flying cutting servo (EFCS), a unique ultra-precision diamond cutting technique, was employed in this investigation. And the production of micro-lenticles arrays on a massive scale. The shape and mounting position of the diamond tool was taken into consideration when developing the best path of tool-generating approach for EFCS. Experimentally, a sizable portion of a typical aspheric MLA was created. And the correctness of the produced shapes, the surface micromorphology, and the processing effectiveness were carefully examined. The findings demonstrate that the MLA is consistent over the whole region. Subsequently, Zhu et al. [28] created a brand-new biaxial servo-assisted fly-cutting (BSFC) technique for flexible control of RTM in creating freeform optical components as a functional micro/nano texture. For primary surface creation and RTM control, dual-axis servo movements along the z-axis and lateral feed direction are primarily employed in the BSFC system. By creating two functional microscopic structures with secondary phase gratings that have integrated reflection and diffraction functions and a standard F-theta free-form surface with scattering uniformity.

In the current chapter, a novel offset-tool-servo (OTS) diamond processing approach is presented to address the challenges conventional diamond-cutting technologies face in manufacturing MOAs with high AR. In the first section, ball crumbing and F/STS ideas are combined to form the core of OTS. Spiral cutting tool tracks are created for per lenticles Cellular using four-axis servo movements, efficiently avoiding tool conflict and fluctuation during the processing of MOAs with high AR. The second section, the processing strategy also provides significant flexibility for producing MOAs with complex structural designs. The introduction of the cutting tool track assurance technique takes into account the special processing concept of OTS. In the third section, in order to verify the correctness of OTS, two MOAs models, namely aspherical MOAs and miniature free-form surface MOAs, are also presented in this paper. The results are compared with those obtained by conventional methods.

## 2 Rules for Flexible MOAs Creation

In diamond swirling, in order to avoid the conflict of the tool side surface and the processing surface, it is necessary to make the gap corner of the tool greater than the maximum Angle of the path of tool. As result, to prevent tool conflict when F/STS turn MOAs with high AR, a diamond tool with a large gap corner is typically used [29]. However, the huge gap corner significantly lowers the tool tip's rigidity, leading to significant tool fluctuations, particularly during the repeated quickening and slackening movements in F/STS. In the suggested offset-tool-servo (OTS) system, a foreign method is chosen: individually crumbing per lenticles using

a different spiral cutting tool track. This is done without lowering the tool stiffness. The basic concept of OTS is to combine the superiorities of F/STS with ball end crumbing by means of multiple axes, including the X-, Y-, Z-, and C-axis.

Figure 1a shows the OTS system’s schematic configuration. In contrast to conventional F/STS, the diamond cutter is connected to the axle by the tool holder. In order to realize the translation servo movement along the Z axis, the work piece is fixed to the fixture installed on the Z slide. Tool forward has the freedom to change the direction to perpendicular to the projection of the cutting tool track by the rotating movement of the axle. Rotating the axle forms a circular trail of the diamond tool, since there is a predetermined deviation range between the tool tip and the mannered axis, it is represented by a yellow dotted line in Fig. 1b. Using collaborative servo motion along the x and y axes, the circular trail can be changed into a series of helical path of tools per lenticles, similarly to ball end crumbing. Similar to F/STS, the required lenticles are arising by the translation servo of the fabricated parts on the Z-axis forms deterministically and compensate for tool brink radius. The whole MOAs may be obtained by independently constructing per lenticles cellular at various positions on the fabricated parts. In OTS, the X-, Y-, and C-axis servo motions work together to control the spiral cutting tool track and modify the diamond tool’s cutting direction. In contrast, the Z-axis servo motion creates the required lenticles surface.

The following benefits are obtained in the manufacturing of MOAs thanks to OTS’s distinctive processing strategy:

- (i) Prevent tool conflict when crumbing MOAs with high AR. The lenticles is individually machined in the OTS system using a spiral cutting tool track. According to Fig. 1b, the centre of per spiral cutting tool track intersects with analogous to the centre of the lenticles. In this instance, the cutting tool track’s curvature changes rather than the aspect of lenticles ratio determines the cutting tool track’s slope angle. From a cross-sectional direction, Fig. 2a depicts the location of the diamond tool concerning the created lenticles in the OTS system.

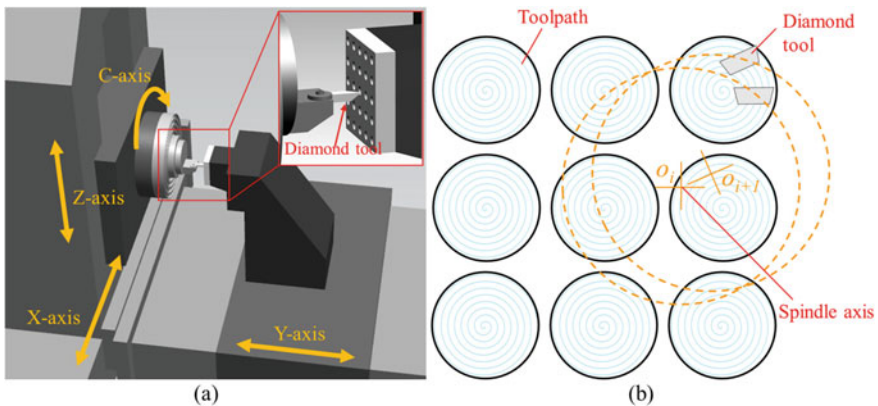
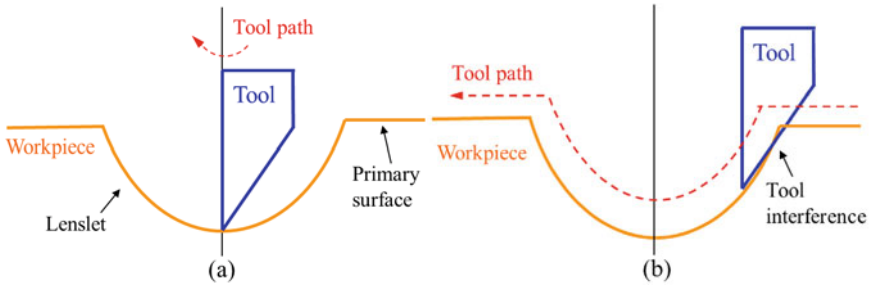


Fig. 1 a OTS construction diagram b Basic processing rule diagram



**Fig. 2** The position of the diamond cutter relative to the lenticles **a** was arising by the OTS system and **b** the F/STS system

It can be shown that the cutting tool track's slope angle is  $0^\circ$  at the cutting spot and has no bearing on the AR of the lenticles. In contrast, the fabricated parts of centre are where the helical cutting tool track of F/STS process is determined. Therefore, as illustrated in Fig. 2b, at the position where the diamond tool cutting the lenticles from the main surface, a very significant bevel Angle can be produced; when processing MOA with high AR, this extremely large tilt angle causes the tool to be affected on one side.

The maximum allowable AR for an OTS lenticles may be calculated as, for example, a diamond cutter clearance with respect to tool conflict at the base of the lenticles. To prevent conflict from the tool flank face, the maximum permitted AR for the lenticles produced by F/STS must be few than  $1/\sin(\alpha) - 1/\tan(\alpha)$  [19]. For instance, by employing the diamond tool with a  $7^\circ$  gap corner, it is possible to produce MOAs with  $\text{AR} \tan(7^\circ) = 0.122$  by OTS. However, the tool conflict prevents fabrication using the traditional F/STS. The high AR obtained by F/STS with the same diamond tool is only  $1/\sin(7^\circ) - 1/\tan(7^\circ) = 0.061$ .

- (ii) Steer clear of tool fluctuation. The tool fluctuations are successfully reduced in the OTS system because the path of tool is glossy, continuous and does not need to be quickened or slowed down. Additionally, because per lenticles of cutting velocity is consistent, the whole optic array may have a uniform surface quality. In contrast, as the tool cuts internal and outside of the lenticles in the F/STS system, it will certainly result in a discontinuous cutting tool track with impulse excitations, which will cause severe tool fluctuations and ruin the surface quality. This will be demonstrated analytically below.
- (iii) The ability to machine MOAs with big apertures with flexibility. The  $X$ - and  $Y$ -axis oscillation amplitudes in OTS are fixed and unrelated to the fabricated parts aperture because the compensation range of the diamond tool from the axle's rotating centre is fixed. As a result, the suggested OTS approach may be used to create optic components with a very large aperture without changing the machine tools' dynamic reaction. To improve the efficiency of the processing process, a very short compensation range and high rotation velocity rate might be chosen.

Overall, the proposed OTS system's unique cutting technique gives this processing approach an brink when it comes to manufacturing micro-optic arrays with high AR and miniature liberal form optics with intricate constructions. The stated benefits will be moreover illustrated in the section that follows.

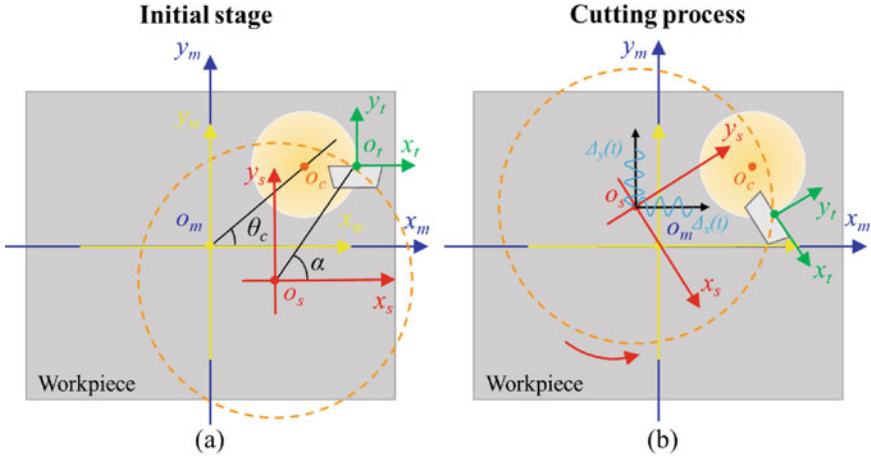
### 3 The Assurance of OTS Cutting Tool Track

Complete lenticles arrays can be created by repeating the basic cutting process for one lenticles cellular at the respective positions of the lenticles fields, as per micro-lenticles cellular is created individually in OTS. The helical cutter position of a individual lenticles element is decomposed into four servos movements throughout the processing process, comprising three translational and rotating motions. In addition, the diamond tool's rake face shall be perpendicular to the anticipated cutting tool track. A cutting tool track-generating approach is suggested once the OTS system's Athletics are examined.

#### 3.1 Athletics of the OTS

Without losing versatility, Fig. 3 depicts the OTS's athletics during a individual lenticles Cellular processing. The fabricated parts and machine tool are given the correlative systems  $O_m-x_m y_m z_m$  and  $O_w-x_w y_w z_w$ , respectively. As illustrated in Fig. 3a, the  $x_w$ - and  $x_m$ -axis are set in the horizontal direction, and the two correlatives initially overlap.  $O_m-x_m y_m z_m$  remains constant and serves as the spatial reference during the processing process. The cutter location spot (CLP) serves as the fixed correlative system known as  $O_t-x_t y_t z_t$ , with the  $y_t$ -axis placed perpendicular to the tool rake face. With the aid of the linear variable differential transformer, the tool rake face is adjusted to horizontal before the processing operation. The diamond tool and the axle's rotational centre are offset by a fixed compensation range  $\rho$  and a fixed angle discrepancy  $\alpha$ , respectively. The axle's correlative system is  $O_s-x_s y_s z_s$ , with the original spot  $O_s$  assigned to the centre of the axle. As a result, the correlatives  $O_t-x_t y_t z_t$  and  $O_s-x_s y_s z_s$ , which rotate with the rotational axle, do not move relative to one another.

Using translational motions on the X- and Y-axis, the CLP is initially moved to the right side of the lenticles cellular as shown in Fig. 3a, during the initial step of processing. As illustrated in Fig. 3b, the axle rotates at a constant velocity during the cutting operation. At the same time, the X- and Y-axes oscillate at the same frequency to produce a local circular trail with the spot  $O_c$  as its fixed centre. The X-axis can then be fed to generate a local spiral cutting tool track with a fixed feeding velocity per revolution for the lenticles cellular. The production of the lenticles is



**Fig. 3** Athletic diagram of OST processing for one lenticles unit during (a) start-up phase and (b) cutting procedures

required shape and the tool brink correction is accomplished via servo movement along the Z-axis. The entire MOAs can be obtained by performing the procedures for producing a individual lenticles cellular repeatedly at various spots on the fabricated parts.

### 3.2 Determining the Cutting Tool Track

It is supposed that the desired lenticles unit has a radius of  $r_c$  and that the correlatives of the fabricated parts correlative system at its centre spot  $o_c$  is  $(a, b)$ , in Fig. 3a. The shaft rotating angle is uniformly discretized into  $(N_s + 1)$  spots for per revolution, following the constant angle sampling approach. The axle’s rotation angle for the  $n$ th spot of the  $m$ -th revolution can be written as:

$$\varphi_{m,n} = 2\pi m + \frac{2\pi n}{N_s}$$

The rake surface of the diamond tool must remain perpendicular to the planned cutting tool track in order for the line of the  $x_t$ -axis to continue passing through the centre of the lenticles cellular  $O_c$  during the processing. This geometric relationship allows us to may express the correlative of the CLP analogous to  $\varphi_{m,n}$  in the system  $o_m$ - $x_m y_m z_m$  as follows:

$$\begin{cases} x_{CLP}^{(m,n)} = -d_c \cos(\theta_c + \varphi_{m,n}) - d_c + \frac{\varphi_{m,n} f_c}{2\pi} \\ y_{CLP}^{(m,n)} = -d_c \sin(\theta_c + \varphi_{m,n}) \end{cases} \quad (1)$$

where, as shown in Fig. 3a,  $f_e$  is the feeding velocity,  $d_c$  and  $\theta_c$  are the range from  $o_c$  to  $o_m$  and the angle between the line  $o_c o_m$  and  $x_m$ -axis, respectively, and these values can be written as follows:

$$\begin{cases} d_c = \sqrt{a^2 + b^2} \\ \theta_c = \tan^{-1}(b/a) \end{cases} \quad (2)$$

The cutter brink contour associated with swirling angle  $\varphi_{m,n}$  can be described in the system  $o_m-x_m y_m z_m$  by: Assuming a diamond tool with rake angle of  $0^\circ$  and brink radius of  $R_t$  is used:

$$\begin{cases} x_T^{(m,n)} = -x_{CLP}^{(m,n)} + l \times \cos(\varphi_{m,n}) \\ y_T^{(m,n)} = -y_{CLP}^{(m,n)} + l \times \sin(\varphi_{m,n}), l = [-R_t \cos(\delta), R_t \cos(\delta)] \\ z_T^{(m,n)} = z_0 - \sqrt{R_t^2 - l^2} \end{cases} \quad (3)$$

where the diamond tool's wrap angle is  $\delta$ . To do a numerical calculation, the cutting brink is then unevenly discretized into  $(N_0 + 1)$  spots. It is possible to write the tangent line of the  $i$ -th spot  $(x_{T,i}^{(m,n)}, y_{T,i}^{(m,n)}, z_{T,i}^{(m,n)})$  as follows:

$$\begin{aligned} \vec{T}_i &= \left( \frac{\partial x_T^{(m,n)}}{\partial l}, \frac{\partial y_T^{(m,n)}}{\partial l}, \frac{\partial z_T^{(m,n)}}{\partial l} \right) | l = l_i \\ l_i &= -R_t \cos(\delta) + (i + 1) \frac{2R_t \cos(\delta)}{N_0} \end{aligned} \quad (4)$$

The  $o_w-x_w y_w z_w$  mechanism allows for the expression of  $z_w = F_w(x_w, y_w)$  on the surface of the lenticles cellular. The normal line analogous to the surface at the  $i$ -th position of the cutting brink can be expressed as:

$$\vec{V}_i = \left( \frac{\partial F_w}{\partial x}, \frac{\partial F_w}{\partial y}, -1 \right) | x = x_{T,i}^{(m,n)}, y = y_{T,i}^{(m,n)} \quad (5)$$

As shown in Fig. 4, the cutter contact spot (CCS) can be found by locating the tool's blade perpendicular to the lenticles surface. As a result, CCS can be roughly estimated by computing the least value of the tow lines numerically [30]:

$$d_T^{(m,n)} = \arg \min_i \left\{ \left| \vec{V}_i \times \vec{T}_i \right|, \forall i \in [1, N_0 + 1] \right\} \quad (6)$$

The following equations can be used to represent the correlative of CLP in the  $o_m-x_m y_m z_m$  system at rotation angle  $\varphi_{m,n}$ :

$$\begin{cases} x_{CLP}^{(m,n)} = -d_c \cos(\theta_c + \varphi_{m,n}) - d_c + \frac{\varphi_{m,n} f_e}{2\pi} \\ y_{CLP}^{(m,n)} = -d_c \sin(\theta_c + \varphi_{m,n}) \\ z_{CLP}^{(m,n)} = \sqrt{R_t^2 - l_i^2} + F_w \left[ -x_{CLP}^{(m,n)} + l_i \times \cos(\varphi_{m,n}), -y_{CLP}^{(m,n)} + l_i \times \sin(\varphi_{m,n}) \right] \end{cases} \quad (7)$$

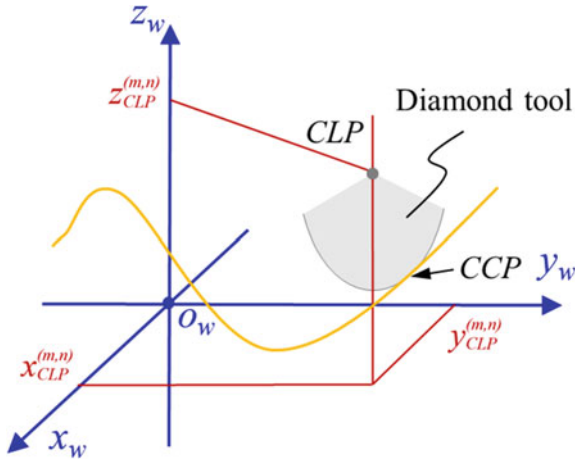


Fig. 4 Measurement—schematic diagram of CCP in the  $o_w-x_w y_w z_w$  system

Because the diamond tool is fixed to the axle and has a predetermined deviation from the centre of rotation, there is no relative movement between  $o_t-x_t y_t z_t$  and  $o_s-x_s y_s z_s$  and  $o_s-x_s y_s z_s$ . In this way, the CLP enables projection with a conscious change of the correlatives  $o_s$  of the axis centres. The correlative of the spot  $o_s$  in the  $o_m-x_m y_m z_m$  can be written as follows using the matrix for correlative transform:

$$\begin{pmatrix} x_s^{(m,n)} \\ y_s^{(m,n)} \\ z_s^{(m,n)} \\ 1 \end{pmatrix} = \begin{pmatrix} 1 & 0 & 0 & -\rho \cos(\alpha) \\ 0 & 1 & 0 & -\rho \sin(\alpha) \\ 0 & 0 & 1 & 0 \\ 0 & 0 & 0 & 1 \end{pmatrix} \times \begin{pmatrix} x_{CLP}^{(m,n)} \\ y_{CLP}^{(m,n)} \\ z_{CLP}^{(m,n)} \\ 1 \end{pmatrix} \quad (8)$$

The cutting tool track may be found by performing the above computations for all  $m$  and  $n$ . The Main shaft rotation at a steady velocity throughout crumbing. In servo state, the X-, Y-, and Z-axes move following the spots  $x_s^{(m,n)}$ ,  $y_s^{(m,n)}$ , and  $z_s^{(m,n)}$ , Separately. This method is repeated at the analogous positions in the small lenticles array to obtain the MOAs of the desired shape.

### 3.3 Features of the Cutting Tool Track

The cutting tool track for a typical MOA is created to give an intuitive instructions of processing features of the OTS system, as illustrated in Fig. 5a. Per lenticles Cellular has a circumradius of  $150 \mu\text{m}$  and a depth of  $17 \mu\text{m}$ , respectively. As can be seen, the cutting tool track for OTS is described as a collection of distinct spiral trajectories with a fixed interval between revolutions. Per spiral trail's centre corresponds to the centre of the analogous MOA lenticles. Tool fluctuation is efficiently avoided



by OTS's independent cutting process, which also improves the consistency of per surface of lenticles quality. The cutting tool track for F/STS, in contrast, is depicted in Fig. 5b It is an individual helical rail which is centre near the centre of the MOAs. In this situation, one axle revolution covers many lenticles cellular. A steep slope descent is required as the diamond tool cuts from the main surface to the individual per of the lenticles, which causes violent fluctuation of the tool and conflict between the tool and the sides. As more lenticles cellular are covered every revolution at the place with an high radial range, the tool fluctuations may be stronger there.

The commonly anticipated tool processing trail in the  $XOY$  plane when crumbing miniature lenticles arrays using the slow tool servo technique. When crumbing micro-lenticles arrays using the slow tool servo approach, the generally anticipated tool processing trail in the  $XOY$  plane is projected as an equidistant thread line. Based on this spiral line, the processing trail is discretized following predetermined guidelines to determine the correlatives of the processing spot in the  $XOY$  plane, and the correlatives of the processing spot in the  $Z$  direction are then determined following various mathematical descriptions equations of the array surface to produce the machine tool motion trajectory and processing code. The slow tool servo processing machine's topology allows calculating the processing spots in the cylindrical correlative system. The correlative values  $(\theta, r, h)$  obtained for per discrete spot correspond to the machine's axle angle,  $X$ -axis feed position, and  $Z$  -axis feed position, separately [31, 32].

Equal angle discretization and equal angle and equal arc length combination discretization methods are frequently used for trail discretization. The equal angle discretization method divides per circle's processing trail into fixed equal polar angle intervals because the processing process axle rotates uniformly, and the instruction execution time is typically constant. However, the machine tool's interpolation chord length will increase with the range between the cutting spot and axle rotation centre, which increases the processing error away from the target. The number of identical circumferential sections must be increased to increase the machining precision of the fabricated workpiece's outside. However, doing so will result in a high number of codes and indigent efficiency. The interpolation arc length in the processing track can be kept constant using the rule of equal arc length for discrete processing tracks. However, this programming calculation is relatively large, and the angle between the cutting spots is large in the vicinity of the axle rotation centre. The axle velocity

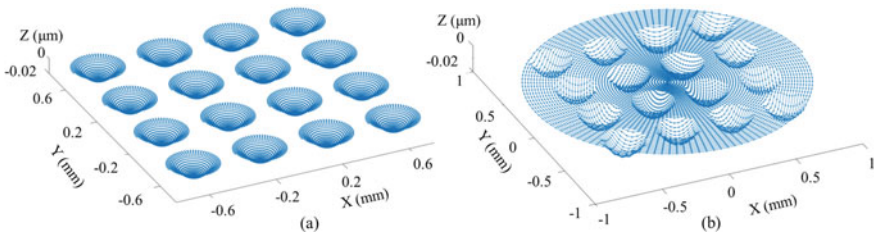
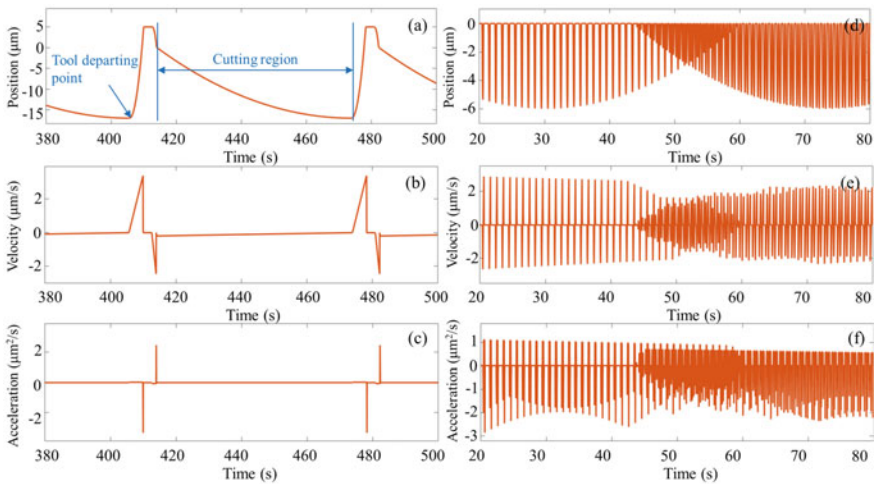


Fig. 5 Features of the cutting tool track for a OTS and b F/STS

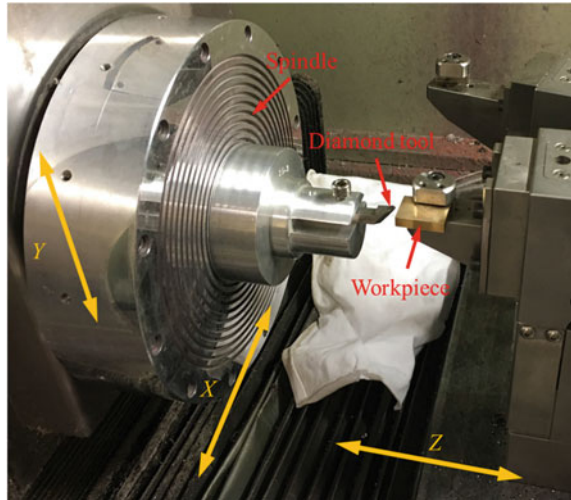
will be too high when crumbing the fabricated workpiece’s centre. By restricting the maximum discretization angle and applying equal-angle discretization at the place near the axle rotation centre, the combination of equal-angle and equal-arc-length discretization methods is frequently employed to prevent this issue. The tool is fed into the fabricated workpiece’s centre using the combined discrete technique, which also progressively raises the axle velocity from a low velocity to the greatest velocity in the equal-angle discrete region and completes the equal-angle discrete at a constant velocity. The equiangular discretization’s central region is machined at a constant pace.

Figure 6 the dynamics of the motion of the proposed OTS and F/STS knives on the Z-axis was showed in terms of location, speed, and the quickening rate. When seen in Fig. 6a, OTS involves periodic contacts and separations between the diamond tool and the fabricated parts, although the cutting tool track in the cutting zone is extremely smooth. There are no changes in velocity or quickening rate during the cutting process, as demonstrated in Fig. 6b, c. As demonstrated in Fig. 6e, f, the cutting process in F/STS involves intense changes in the tool’s speed and quickening rate while it is still in contact with the fabricated parts. Thus, in the F/STS system, the diamond tool can be used as a pulse excitation for per shot. Violent tool shocks caused by intermittent pulses can compromise surface quality. On the whole, OTS technology improves AR over conventional F/STS and is effective in suppressing tool fluctuation.



**Fig. 6** Dynamic features of the tool actions in Z-axis for OTS: **a** position, **b** velocity and **c** quickening rate and for F/STS **d** position, **e** velocity and **f** accelerated velocity

**Fig. 7** Hardware setup for OTS systems



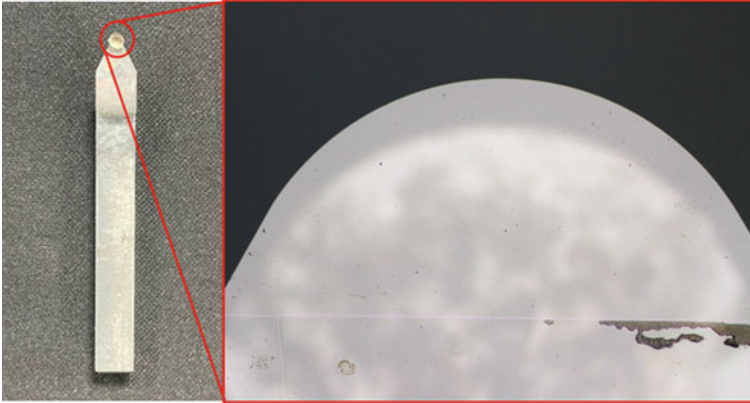
## 4 Experimental Setup

The trials are conducted using a four-axis hyper precision lathe (Moore 350FG, USA), as depicted in Fig. 7. Three translational slides and an axle are included in the swirling apparatus. By fixing the diamond tool on the tool holder and attaching it to the axle with a suction cup, the fabricated parts will be stuck on the Z guide. On this basis, the machine's axle and three translating slides work in servo drive mode during the processing process. Copper makes up the fabricated parts. The company contour provides a diamond tool which is used. The rake and gap corners are  $0^\circ$  and  $7^\circ$ , respectively, and the tool nose radius is 0.28 mm, as shown in Fig. 8. Contactless optical equipment for measurement (Zygo Nexview) is utilized with the appropriate magnification to see the shape and micro-topographies of the machined surface. In order to record the topographies of the machined constructions, optical microscope from Olympus BX60 was also applied.

Micro-aspheric arrays were produced utilizing the proposed OTS, and compared with the array produced by F/STS in order to approve the superiorities of the recommended OTS in processing MOAs with high AR values. The micro-aspheric lenses express themselves as [33]:

$$z(x, y) = \frac{sCR_0^2}{4+4\sqrt{1-(1+k)C^2R_0^2}} - \frac{sC\rho^2(x,y)}{4+4\sqrt{1-(1+k)C^2\rho^2(x,y)}} \quad (9)$$

where  $R_0$  stands for the aspheric radius, while  $C$  and  $k$  govern the curvature and conicity, separately, and  $s$  stands for the shape coefficient. As was previously mentioned, traditional F/STS can only achieve an AR of 0.061, while OTS can obtain a maximum AR of 0.122 utilizing a tool with a  $7^\circ$  gap corner. To allow for margin, slow tool servo (STS) with the coefficients indicated in Table 1, was used to create



**Fig. 8** Diamond tool for OST

**Table 1** Coefficients of the microspheres surface from atmospheric OTA and STS propagations

Coefficient	OTS	STS
Shape coefficient (s)	-1	-1
Array radius $R_0$ (mm)	0.15	0.15
Conical constant (k)	-0.6	-0.6
Curvature (C)	5.7	2.5
Aspect ratio	0.11	0.04

a miniature aspheric array with a value of 0.04 AR., and OTS is used to fabricate those with an AR of 0.11. Table 2 lists the processing specifications in detail.

The fabricated parts measures  $40 \times 10 \text{ mm}^2$ . Since per lenticles Cellular has a basic dimension of  $0.35 \times 0.35 \text{ mm}^2$ , These pieces are large enough to hold several hundred lenticles. The size of the entire MOAs in the current study is  $3.5 \times 3.5 \text{ mm}^2$  and they cover 100 lenticles cellular.

**Table 2** OTS and STS processing process specifications

Processing specifications	Hybrid micro-aspheric surface	Hybrid sinusoid surface
Axle rotation rate (rpm)	15	30
Feeding velocity ( $\mu\text{m/r}$ )	2	2
Bottom of cut ( $\mu\text{m}$ )	5	5
Offset radius (mm)	5.45	None

**Table 3** Coefficients of the Radiant micro-construction arrays

Coefficient	Radiant micro-construction arrays
Spheric radius $R_{ball}$ (mm)	0.22
Radius of the array $R_l$ (mm)	0.18
Amplitude $A$ (mm)	0.002

To illustrate further the superiorities of the OTS technology, microscopic free-form optical elements with more complex configurations, for instance arrays of radial microscopic structures, were fabricated with the identical process specifications. The arrangement of radiating micro-constructions can be considered as a spherical radiating microscopic structures in a local columnar correlative system:

$$z(\rho, \varphi) = \sqrt{R_{ball}^2 - \rho^2} - \sqrt{R_{ball}^2 - R_l^2} + A \sin(6\varphi) \quad (10)$$

where  $A$  is the amplitude of the radiating microscopic structures,  $R_l$  stands for the radius of lenticles, and  $R_{ball}$  is radius of the surface of the sphere. Table 3 displays the radiant micro-construction array coefficients.

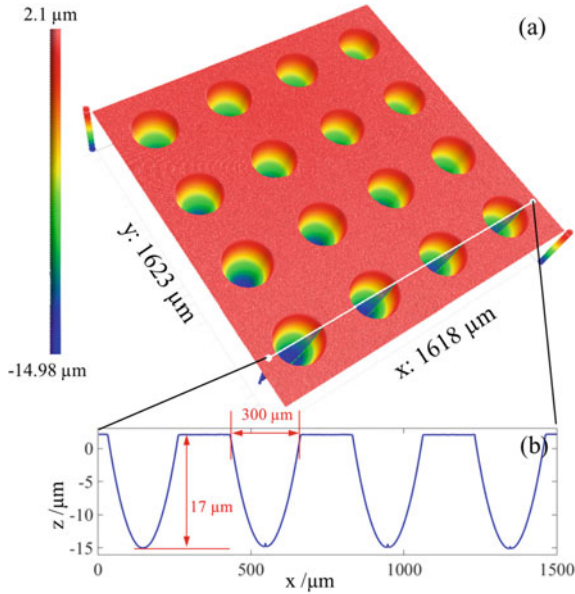
## 5 Results and Discussion

Miniature spherical arrays are created using the proposed OTS system, and the outcomes are Contrast-ed to those achieved using the traditional F/STS to confirm the suggested OTS's viability in processing MOAs with hyper AR. To further demonstrate OTS's benefit in producing MOAs with intricate constructions, it is also used to build miniature liberal form lenticles arrays with radiant microscopic structures.

### 5.1 Miniature Spherical Arrays

The features of the OTS-arising miniature spherical lenticles arrays are depicted in Fig. 9. Figure 9a displays a schematic of the developed  $4 \times 4$  lenticles arrays. It can be seen that the lenticles Cellular are evenly spaced apart, with an identical gap between per succeeding lenticles Cellular. Figure 9b displays a cross-sectional view through the centre of a small lenticles in the  $X$  direction. Both the two-dimensional contour map and the three-dimensional contour show that per lenticles cellular has homogeneous properties in terms of size and shape.

The circumradius of lenticles and depth are  $150 \mu\text{m}$  and  $17 \mu\text{m}$ , respectively, as illustrated in Fig. 9b. The AR of lenticles was computed using the definition of AR and came out to 0.113, which is the ideal AR value as indicated in Table 1. As mentioned above, to avoid the disturbance of the tool, the conventional F/STS

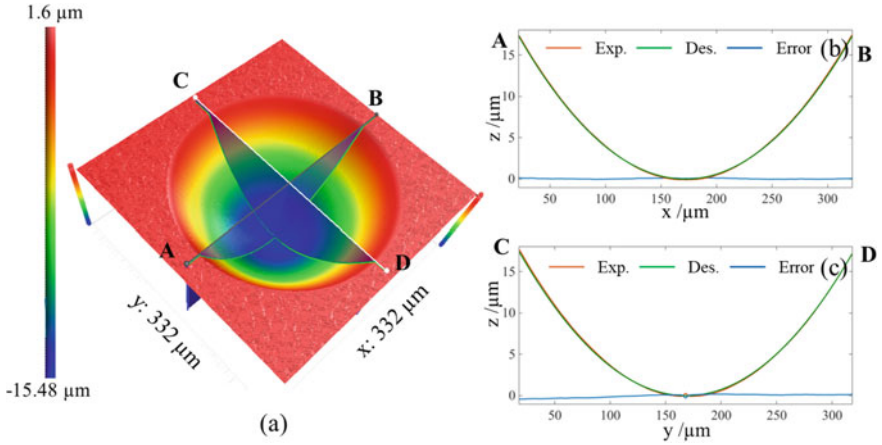


**Fig. 9** **a** A three-dimensional structural view of a miniature spherical array, and a **b** contour map in the X-direction

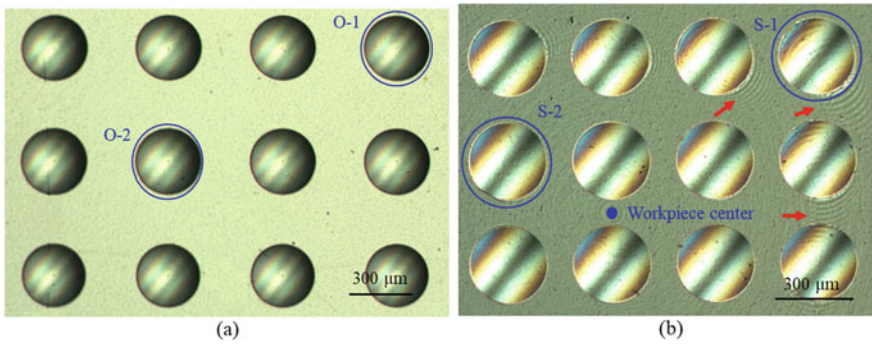
uses a  $7^\circ$  drilling tool with a maximum AR of only 0.06. Due to tool conflict, the miniature spherical arrays produced by the proposed OTS with an AR of 0.113 cannot be produced by the traditional F/STS, demonstrating the effectiveness of the proposed OTS. Due to its distinctive cutting method, in which per lenticles cellular is uniquely manufactured by a screw cutting tool track similar to spherical grinding, OTS can achieve higher AR than F/STS. In contrast to F/STS, this special processing technique results in a completely different relative location among the diamond tools and lenticles units, as seen in Fig. 2. With OTS, the cutting tool track is smooth and free of repeated downward motions of the diamond tool, leaving a significant gap between the completed surface and the diamond tool's side face.

A random lenticles Cellular from the produced lenticles arrays is chosen, and its form properties are displayed in Fig. 10, allowing for further examination of the shape distortion of the MOAs. Fig. 10b, c illustrates that its sectional views in the X and Y orientations are retrieved, and compared with the intended contour maps of the lenticles. The experimentally achieved contour map (in orange color) is nearly identical to the desired contour maps, as illustrated in Fig. 10b, c (in green color). The contour map shapes of the arising small lenticles in the X and Y axes are consistent with the desired small lenticles contour maps and their shape deviations do not exceed  $\pm 50$  nm. In some cases, it is generally feasible to generate high AR and high forming accuracy MOAs with the OTS.

Microscopic images of the microsphere lenticles arrays fabricated from the OTS and STS are displayed in Fig. 11a, b. In Fig. 11a, the entire array has a smooth and



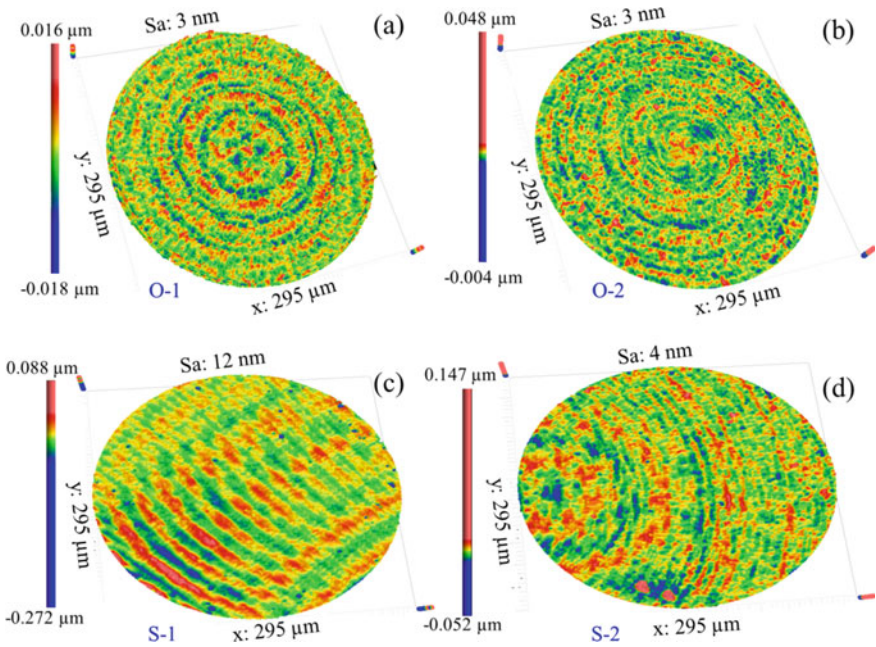
**Fig. 10** a Three-dimensional construction of the resulting lenslets cavity, and b and c sectional views in the X and Y orientations



**Fig. 4.11** The microscope pictures of MOA produced with a OTS and b STS

uniform characteristic with the absence of distortion in shape and size, due to per OTS being cut individually under the same conditions. The microscopic morphology of the lenslets cellular assigned as O-1 and O-2 in Fig. 12a are depicted in Fig. 4.12a, b with the spherical surface removed from the lenslets. Although the two lenslets cellular were taken from various locations inside the lenslets arrays, their surface microscopic morphology are remarkably analogous and share a 3 nm level of coarseness. Fig. 12a, b show the residual circumferential tool scars with their centres superimposed with the centres of lenslets, which are the outcome of the special cutting procedure of OTS as described above.

However, on the microscope array of lenslets images arising by STS, clear changes the variation is visible around the cutting orientation, as shown in Fig. 11b. The fluctuations of the tooltips in F/STS are the main culprits for these undesirable



**Fig. 12** The microscopic morphological images of lenticles cellular at per of the different sites produced by OTS are (a) and (b) while (c) and (d) are produced by STS

fluctuations [18]. According to F/STS, per lenticles can be considered as an excitation of the pulse of the diamond tool, which can cause the diamond tool to accelerate and decelerate in an impulse-like manner as it cuts into and out of per lenticles, as seen in Fig. 6f. As shown determined by the microscopic contour of the lenticles S-1 in Fig. 12c, tool fluctuations can significantly damage the created micro-contour of lenticles and cause a significant increase in surface coarseness. The lenticles S-2, located nearer to the fabricated centre of parts than S-1, has significantly smoother micro-contour than S-1, as illustrated in Fig. 12d. Radially dependent cutting requirement of the F/STS is responsible for the various microscopic appearance of S-1 and S-2. It is confirmed that, compared to F/STS, the suggested OTS efficiently reduces tool fluctuations during MOA processing and improves evenness of surface.

A prerequisite for the operation of the OTS system is that the X and Y axes amicably oscillate back and forth at the identical frequency, resulting in a local spiral orbit that is aligned with the centre of the nearest lenticles unit. In contrast to the traditional swirling with virtual axle [20], the OTS method clamps the diamond tool to the axle with a predetermined compensation of range. As a result, the compensation range of the diamond tool determines t harmonic motion amplitude on the sine or cosine, and the amplitudes have no bearing on the aperture of MOAs. The axle rotation frequency is the same as the frequencies of the harmonic motions. Therefore, even



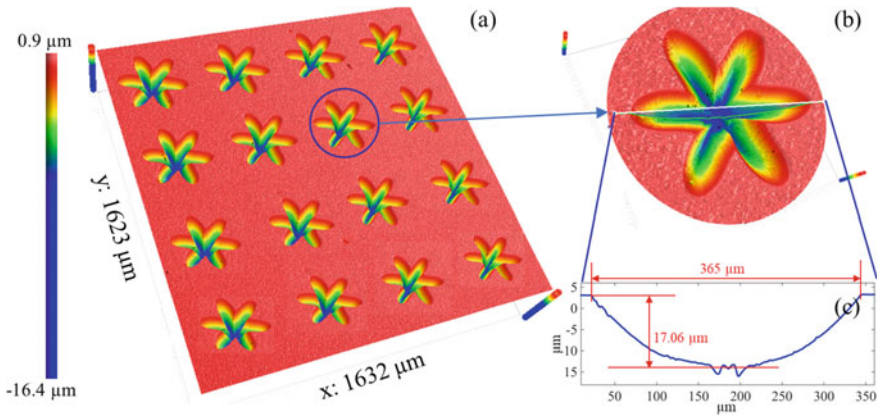
when crumbing optics with large apertures, the axle velocity in the OTS system may remain constant.

The MOAs with an area of  $3.5 \times 3.5 \text{ mm}^2$  require a total cutting time of roughly 4.5 h. It is well known that the data transmission rate from the control system is the main reason for the restriction of axle velocity with the servo processing technologies [33]. Many control spots are necessary to ensure the precision of per lenticles form of cellular, especially for lenticles with freeform geometries and high aspect ratios, which furthermore slows down the axle velocity [34]. This is the problem that both the traditional F/STS and the suggested OTS technique share. OTS has a substantially lower number of regulating spots than traditional F/STS because of the repeated cutting process, which results in relatively more high processing efficiency. For instance, using the same feeding velocity and the appropriate sampling rates, it is expected to take about eight hours to cut with a normal slow-tool servo for a given area and a small lenticles density. [19, 35]. You can choose a higher axle velocity by using a faster data transfer rate control system.

## 5.2 Miniature Free-Form Lenticles Array

Due to the rapid growth of optical and electrical facilities, simple spherical MOAs struggle to meet the requirement for multifunctional integration in complicated system of optics [4, 5]. Miniature liberal form lenticles arrays with complex shapes and high aspect ratios, for instance, micro-Fresnel lenticles arrays [5] and anti-reflection arrays [4], are becoming increasingly necessary to meet the functional integration and minimization requirements of the optical system. It is challenging for traditional F/STS to build miniature liberal form lenticles arrays with high form accuracy due to tool conflict and restricted dynamic responsiveness. Radiant micro-construction arrays are created to verify the adaptability of the suggested OTS technique in the processing of miniature liberal form lenticles arrays. Figure 13a displays an overview of the created radiant micro-construction arrays. The six radiant lobes that distinguish per lenticles are the same for all. The arrays are used to extract an arbitrary lenticles, whose two-dimensional transverse section contour map and three-dimensional contour are displayed in Fig. 13b, c, separately. The diameter of lenticles and depth are  $365 \mu\text{m}$  and  $17.06 \mu\text{m}$ , separately, and its AR is 0.09. With just a 1.3% deviation, the shape of the created construction closely resembles the required construction as given in Eq. (10), demonstrating the viability of the proposed OTS for producing MOAs with almost unlimited construction with high shape precision and without tool conflict.

Notably, the luminous micro-construction arrays created by OTS are distinguished by their discontinuous forms and high aspect ratio. Even though it can occasionally be simple for F/STS to build intricately curved surfaces, doing so when employing a spiral cutting tool track is frequently quite challenging [20]. The discontinuous spiral cutting tool track In the MOA of F/STS diamond rotation can cause strong tool fluctuations, which worsen coarseness of surface and lead to the surface quality is



**Fig. 13** **a** Contour and **b** random lenticles voxels and **c** cross-sectional contour maps of the array of radiative microscopic structures produced by the OTS

inferior [18, 19]. Due to the diamond tool’s sharp descending and rising motions, tool fluctuations may be particularly noticeable while cutting MOAs with high AR [20]. Additionally, when swirling MOAs with high AR, the non-smooth cutting tool track with a significant slope angle invariably interferes between the completed surface and the side face of the diamond tool.

## 6 Conclusions

In this chapter, a brand-new offset-tool-servo (OTS) diamond processing technique for flexible fabrication of micro-optical arrays (MOA) with high aspect ratio (AR) has been proposed. Unlike conventional fast-small tool servo systems (F/STS), the diamond tool has a predetermined deviation from the center of rotation. With three translations and one axis of rotation for servo drive, individual processing of the lenticles is achieved using a spiral path of tool. This process ensures uniformity of shape and surface of the MOA and effectively avoids tool conflict and fluctuation while achieving a high AR MOA using conventional fast-slow tool servo (F/STS). A new method of calculation for determining the tool track based on the deviation of the diamond tool from the axle rotation center is given. The key findings may be summed up as follows:

- (1) For per lenticles, OTS generates a spiral cutting tool track whose center overlaps the center of the associated lenticles. Even when cutting MOAs with a high AR, the cutting tool track, in this instance, is smooth and continuous without any sharp downward movements of the tool. As a result, OTS is able to produce MOAs twice as high as conventional F/STS using the same diamond tools as conventional F/STS.

- (2) The diamond tool in OTS occasionally comes into contact with the fabricated parts surface. It then moves away from it, but there are no variations in the diamond tool's velocity or quickening rate while the fabricated parts is being machined. The glossiness of superficial surface and homogeneity of the created MOAs are guaranteed by the special cutting method used by OTS wells.
- (3) An array of microspheres with AR of 0.113 was established utilizing a diamond tool with a gap corner of  $7^\circ$  to demonstrate the OTS. In contrast, the highest AR that F/STS can obtain is just 0.06, which is significantly less than that of OTS. OTS achieves a more consistent and smoother surface quality than F/STS, with a coarseness of 3 nm, thanks to its uniform cutting condition.
- (4) In order to demonstrate the potential of the suggested OTS in the manufacturing of MOAs with complicated shapes and high AR, radial constructions of MOAs are a type of freeform lenticles arrays that are also produced by OTS. The robust agreement between the surface that was created and the surface that was sought supports the versatility of OTS in the processing of MOAs with intricate features.

**Acknowledgements** This work described in this chapter was supported by the National Natural Science Foundation of China (NSFC Project No. 52005110, No. 51975128), the Natural Science Foundation of Guangdong Province (Project No. 2022A1515011055) and Guangzhou Basic and Applied Basic Research Project (No. 202201010233).

## References

1. Zuo H, Choi D, Gai X, Luther-Davies B, Zhang B (2017) CMOS compatible fabrication of micro, nano convex silicon lenticles arrays by conformal chemical vapor deposition. *Opt Express* 25:3069–3076
2. Li K, Yöntem AÖ, Deng Y, Shrestha P, Chu D, Zhou J, Yao J (2017) Full resolution auto-stereoscopic mobile display based on large scale uniform switchable liquid crystal micro-lenticles array. *Opt Express* 25:9654–9675
3. Suzuki H, Moriwaki T, Yamamoto Y, Goto Y (2007) Precision cutting of aspherical ceramic molds with micro PCD crumbing tool. *CIRP Ann* 56:131–134
4. Brinksmeier E, Schönemann L (2014) Propagation of discontinuous microscopic structures by diamond micro chiseling. *CIRP Ann* 63:49–52
5. Jasinevicius R, Duduch J, Cirino G, Pizani P (2013) Diamond swirling of small Fresnel lenticles array in individual crystal. In *Sb. J Micromech Microeng* 23:055025
6. Chen J, Lee HH, Wang D, Di S, Chen S-C (2017) Hybrid imprinting process to fabricate a multi-layer compound eye for multispectral imaging. *Opt Express* 25:4180–4189
7. Fattal D, Peng Z, Tran T, Vo S, Fiorentino M, Brug J, Beausoleil RG (2013) A multi-directional backlight for a wide-angle, glasses-free three-dimensional display. *Nature* 495:348
8. Wang C, Cheung CF, Liu M, Lee WB (2017) Fluid jet-array parallel processing of optical microscopic structures array surfaces. *Opt Express* 25:22710–22725
9. Zhang F, Yang Q, Bian H, Li M, Hou X, Chen F (2020) Fabrication of chalcogenide glass based hexagonal gapless microlentiles arrays via combining femtosecond laser assist chemical etching and precision glass molding processes. *Materials* 13:3490

10. He Z, Lee Y-H, Chanda D, Wu S-T (2018) Adaptive liquid crystal micro lenses array enabled by two-photon polymerization. *Opt Express* 26:21184–21193
11. Low MJ, Lee H, Lim CHJ, Sandeepa CSS, Murukeshan VM, Kim S, Young J (2020) Laser-induced reduced-graphene-oxide micro-optics patterned by femtosecond laser direct writing. *Appl Surf Sci* 526:146647
12. Shao J, Ding Y, Wang W, Mei X, Zhai H, Tian H, Li X, Liu B (2014) Propagation of fully-covering hierarchical micro-/nano-structures by nanoimprinting and modified laser swelling. *Small* 10:2595–2601
13. Sun Z, To S, Yu K (2018) One-step propagation of hybrid micro-optics with high-frequency diffractive structures on infrared materials by ultra-precision side crumpling. *Opt Express* 26:28161–28177
14. Dutterer BS, Lineberger JL, Smilie PJ, Hildebrand DS, Harriman TA, Davies MA, Suleski TJ, Lucca DA (2014) Diamond crumpling of an Alvarez lenses in germanium. *Precis Eng* 38:398–408
15. Li Z, Fang F, Chen J, Zhang X (2017) Processing approach of freeform optics on infrared materials via ultra-precision swirling. *Opt Express* 25:2051–2062
16. Sun Z, To S, Zhang S (2018) A novel ductile processing model of individual-crystal silicon for freeform surfaces with large azimuthal height variation by ultra-precision fly cutting. *Int J Mach Tools Manuf* 135:1–11
17. Davis GE, Roblee JW, Hbrinks AR (2009) Comparison of freeform manufacturing techniques in the production of monolithic lenses arrays. In: *Optical manufacturing and testing VIII*. International Society for Optics and Photonics, 742605
18. Zhu Z, To S, Zhu WL, Huang P (2017) Feasibility study of the novel quasi-elliptical tool servo for fluctuation suppression in the swirling of micro-lenses arrays. *Int J Mach Tools Manuf* 122:98–105
19. Zhu Z, To S, Zhang S (2015) Large-scale fabrication of micro-lenses array by novel end-fly-cutting-servo diamond processing. *Opt Express* 23:20593
20. To S, Zhu Z, Wang H (2016) Virtual axle based tool servo diamond swirling of discontinuously structured microoptics arrays. *CIRP Ann* 65:475–478
21. Huang P, To S, Zhu Z (2018) Diamond swirling of micro-lenses array on the roller featuring high aspect ratio. *Int J Adv Manuf Technol* 1–7
22. Neo DWK, Kumar AS, Rahman M (2015) An automated Guilloche processing technique for the fabrication of polygonal Fresnel lenses array. *Precis Eng* 41:55–62
23. Zhu Z, To S, Zhang S (2015) Theoretical and experimental investigation on the novel end-fly-cutting-servo diamond processing of hierarchical micro-nanostructures. *Int J Mach Tools Manuf* 94:15–25
24. Zhou X, Weng Y, Peng Y, Chen G, Lin J, Yan Q, Zhang Y, Guo T (2018) Design and fabrication of square micro-lenses array for integral imaging three-dimensional display. *Optik* 157:532–539
25. Chiu CC, Lee YC (2011) Fabricating of aspheric micro-lenses array by excimer laser micromachining. *Opt Lasers Eng* 49:1232–1237
26. To S, Zhu Z, Zeng W (2015) Novel end-fly-cutting-servo system for deterministic propagation of hierarchical micro-nanostructures. *CIRP Ann Manuf Technol* 64:133–136
27. Zhu ZW, To S, Zhang SJ (2015) Large-scale fabrication of micro-lenses array by novel end-fly-cutting-servo diamond processing. *Optic Express* 23:20593–20604
28. Zhu Z, To S, Zhang S (2015) Active control of residual tool marks for freeform optics functionalization by novel biaxial servo assisted fly cutting. *Appl Optics* 54:7656–7662
29. Li L, Allen YY (2009) Microfabrication on a curved surface using three-dimensional micro lenses array projection. *J Micromech Microeng* 19:105010
30. Zhu Z, Zhou X, Luo D, Liu Q (2013) Development of pseudo-random diamond swirling method for fabricating freeform optics with scattering homogenization. *Opt Express* 21:28469–28482
31. Wang XS, Fu XQ, Li CL, Kang M (2015) Path of tool propagation for slow tool servo swirling of complex optical surfaces. *Int J Adv Manuf Technol* 79:437–448

32. Li D, Qiao Z, Walton K, Liu YT, Xue JD, Wang B, Jiang XQ (2018) Theoretical and experimental investigation of surface contour propagation in slow tool servo ultra-precision processing of freeform surfaces. *Materials* 11:2566
33. Yu D, Wong Y, Hong G (2011) Ultraprecision processing of micro-constructed functional surfaces on brittle materials. *J Micromech Microeng* 21:095011
34. Zhu Z, To S (2015) Adaptive tool servo diamond swirling for enhancing processing efficiency and surface quality of freeform optics. *Opt Express* 23:20234–20248
35. Gao W, Araki T, Kiyono S, Okazaki Y, Yamanaka M (2003) Precision nano-fabrication and evaluation of a large area sinusoidal grid surface for a surface encoder. *Precis Eng* 27:289–298

# Chapter 5

## Diamond Milling System for Fabricating Infrared Micro-optics Arrays



Zhanwen Sun, Suet To , and Sujuan Wang 

**Abstract** A growing variety of sophisticated infrared optic systems need infrared micro-optic arrays (MOAs) with several micro-freeform lenticles. High-form-accurate MOA fabrication has been accomplished using a variety of ultra-precision diamond cutting processes. Because of the poor fracture toughness, the high anisotropy of the infrared materials, and the variable thickness of the chip due to the constant change in the height and gradient of the desired MOAs, the nonhomogeneous fractured surface of infrared MOAs may be readily caused by the current technologies. In this chapter, a unique self-tuned diamond milling (STDM) approach is presented, which can improve the surface homogeneity and the processing efficiency of infrared MOAs and develops a matching tool path programming algorithm. Based on the local surface morphology, a double-axial rapid servo movement platform is incorporated into the raster milling system of STDM system, so that the maximum chip thickness of each rotation tool cycle can be matched with the critical cut deepness of infrared material, improving the surface homogeneity of the lens, and do not produce cracks. To prove the feasibility of the proposed cutting method, micro-aspheric MOAs without cracks have been successfully processed on a typical infrared material on single-crystal silicon. The proposed STDM has advantages over standard diamond milling in that it can prevent uneven fractures without decreasing the feed speed, leading to a surface roughness of only 4 nm and approximately double processing efficiency.

---

Z. Sun · S. Wang (✉)

State Key Laboratory of Precision Electronic Manufacturing Technology and Equipment,  
Guangdong University of Technology, Guangzhou, China  
e-mail: [grace.wangsj@gdut.edu.cn](mailto:grace.wangsj@gdut.edu.cn)

S. To

State Key Laboratory in Ultra-Precision Machining Technology, Department of Industrial and Systems Engineering, The Hong Kong Polytechnic University, Kowloon, Hong Kong, China

## 1 Introduction

Infrared low-level array (MOA) is widely used in infrared optic systems, photonic devices and sensors because of its high sensitivity, high reducibility and wide field of view [1, 2]. Generally speaking, these infrared MOAs are discrete microscopic surfaces that consist of lenticle cells at regular intervals. To achieve the specialized functionalities of diverse applications, at present, the shape of the lens has been developed from the basic sphere to the aspheric surface, even the tiny free surface [3, 4]. Nevertheless, a large proportion of infrared optic material, including silicon and germanium, exhibit considerable anisotropy and relatively low fracture toughness. The existing processing techniques face new challenges in realizing the flexible production of infrared MOAs with smooth and homogeneous quality of surface and increased processing efficiency due to the growing complication of the micro-structured lenticle and the solid-and-fragile characteristics of infrared materials. It is well known that to prevent image distortion and unwanted scattering effects, and infrared optic elements need have not only smoothness of the surface with high shape precision, but also excellent surface evenness [5, 6].

For the time being, MOAs on infrared materials have been produced using mechanical and non-mechanical methods. The capacity to produce many lenticle cells is a frequent benefit of non-mechanical methods, which mostly include lithographic techniques and chemical etching [7, 8]. However, the majority of these techniques are confined to producing lenticles on certain materials with fixed feature sizes and geometries, and complicated processes are often needed to achieve sufficient surface quality. In order to meet the growing demand for infrared MOAs, a barrier has been created by the non-mechanical technologies' lack of flexibility and uncontrolled elements.

The fabrication of infrared MOAs with complicated micro-freeform surfaces and high form precision is made possible by mechanical processing techniques, which are adopted to multi axis diamond milling technology and fast and slow tool servo (FTS/STS) diamond turning. These methods are more flexible and certainty than non-mechanical methods. With translational servo movements along the z-axis, FTS/STS diamond cutting—developed from diamond turning—generates the dimensional accuracy and surface roughness of aspheric surface and miniature free-form lens are up to submicron [9, 10]. Even though FTS/STS is a superior process, it is still difficult to fabricate infrared MOAs without crack and homogeneous quality of surface, which can be attributed to some of the technique's intrinsic flaws. In particular, because in FTS/STS, a columnar coordinate system is used, whose tangential direction changes constantly with the crystal orientation of the single crystal infrared material. As a result, infrared lenticles are more likely to develop nonhomogeneous cracks and radial-spoke marks, negatively affecting optic performance [11, 12]. Moreover, leaving tool traces on the completed lenticle surfaces and the unavoidable tool vibrations brought on the discontinuity of tool path applied in the FTS/STS turning of MOAs will significantly reduce the surface roughness [13]. The tool vibrations can get more intense, particularly as the lenticle's complexity

and aspect ratio increase. The significant responsiveness of the completed surface mass at the location of the small lens on the MOAs, however, can be caused by the constantly fluctuating the velocity of the cut, cutting pressures, and the conflicts of azimuth sampling caused by the time-changing radial range of the cutting point in FTS/STS [14, 15]. Extremely low feed speed must be chosen for tool vibration suppression of the FTS/STS and ensure malleable removal of IR materials, making in poor processing efficiency, to increase the homogeneity of the surface and to prevent cracks on the finished surface.

According to how the diamond tool is installed, multi-axis diamond milling may be split into two primary categories: ball end milling and raster milling [16–18]. In ball end milling, three sides of the conversion drive a rotating tool to produce lenticle cells one at a time, producing the whole MOAs. Ball end milling can offer a consistent process of the cutting from the perspective of the entire MOAs. However, this way struggles to ensure homogeneousness and smoothness of the surface in the lens cell because it is simple for friable fractures to occur at each lenticle's bottom surface where the critical value is less than the instant cutting deepness. In contrast, an insert diamond or a diamond turning tool is used in raster milling, also known as fly cutting, in place of a ball milling tool with a rational axis parallel to the work piece surface. Raster milling, which has a completely distinct malleable processing model from F/STS and ball end milling [19], is more advantageous for the malleable processing of infrared materials for microstructure surfaces. This is due to its two key superiorities: (i) By producing very thin chips, the intermittent cutting method effectively suppresses the fractures of infrared material [20]; (ii) the continuation of the cutting direction reduces undesirable radial-spoke markings generated by single crystal infrared material FTS/STS [16]; (iii) the multi-axis cutting property of the milling process effectively eliminates tool vibrations even when processing complex geometry MLAs. The ability to produce infrared optics with micro-structured or even micro-freeform surfaces using multi-axis raster milling has garnered significant interest due to the above advantages and its high flexibility and form precision.

During raster milling of MOAs, the maximum chip thickness per tool rotation period is determined by the local inclination of the desired MOAs, in addition to the criteria for cutting planer surfaces, e.g., cutting deepness, feed speed, and tool geometry. Two key requirements must be met in order to achieve smooth surfaces: the infrared materials are detached in the fully malleable mode, which can be achieved by strictly limiting the critical deepness of cut (DoC) is greater than chip thickness, which is the cutting deepness of transition origination from toughness to friability; or (ii) the cracks produced at lightly higher feed speeds are completely removed by the following tool passes without expansion. Although the tool rake angle and cutting orientations affect the critical DoC of infrared materials, the value is often in the sub-micrometer range [21]. In order to ensure the total smoothness of the infrared lenticle, which applies to the lenticle with basic forms and mild gradient change, an exceptionally low input rate is often needed. However, as micro-freeform surfaces and micro-structured become more complex, the process of cutting becomes inconsistent, resulting in constantly shifting chip thickness from one location to another, which is a surefire way to produce a uneven surface quality with partial fractures of the processed



surfaces. Additionally, it is challenging to precisely predict the fractured sites and choose the proper processing settings since a micro-freeform surface's height and partial gradient are constantly changing. The currently used method of employing a suitably low feed speed to prevent fractures at a micro-freeform surface's biggest DoCs is overly low efficiency for the regions with lower DoCs, thus decreasing the processing efficiency. Infrared MOA ball milling and FTS/STS have a similar constraint.

Numerous techniques, including vibration-assisted cutting [22], laser-assisted cutting [23], and ion implantation modification [24], have been presented to improve the critical DoC of infrared materials since it is a crucial element in surface homogeneity and processing effectiveness. Vibration-assisted and laser-assisted cutting are efficient in boosting the plastic deformation of infrared materials and friable fractures can be restrained even at slightly deeper cutting deepness to increase their machinability. Additionally, it has been claimed that altering a tiny layer of the workpiece surface with ions helps to raise the essential DoC of infrared materials. The incorporation of these methods does not improve the inherent process inconsistency of the current technologies into ultra-precision diamond cutting technologies because they neglect the geometric characteristics of the micro-freeform lenticle and are unable to self-adaptively adjust the chip thickness according to the partial surface morphology of the micro-freeform.

Faced with the problems mentioned above, the creation of novel self-tuning processing systems is required to ensure the smoothness and consistency of the whole infrared MOAs, improving surface homogeneity and processing effectiveness. In this chapter, the flexible creation of infrared MOAs with excellent surface homogeneity and improved processing efficiency is achieved by combining a dual-axial rapid servo movement platform into a raster milling system. This system is called a self-tuned diamond milling (STDM) system. In the first section introduces the STDM, which adopts the double-axial rapid servo movement, to flexibly adjust the thickness of the chip according to the local surface morphology. In contrast, the existing diamond cutting techniques only consider the shape accuracy of the micro-freeform surface needed. This ensures process consistency. In the subsequent section, the appropriate tool path programming method is also presented, fully considering the tool geometry, infrared material property, and special STDM system kinematics. In order to validate the proposed STDM, in the final section, the experimental results were compared with the results obtained with the conventional raster milling method when the micro-aspheric MOAs were processed on single crystal silicon.

## 2 Processing Principle for Self-tuned Diamond Milling

The most reliable approach is to remove the infrared material in the malleable mode in order to avoid friable fracture of infrared MOAs during diamond milling. This is made possible by capping the maximum chip thickness at the crucial DoC of the infrared material for each tool spinning cycle. During diamond milling of

MOAs with complex micro-freeform surfaces, the maximum chip thickness per tool rotation period is dependent not only on the processing parameters of the cutting planer surface, including the DoC and feed speed, but also on the partial gradients of desired MOAs. Therefore, the micro-freeform surfaces' geometric complication necessarily results in the chip thickness varying with cutting locations, making it difficult to choose the right processing settings for traditional milling and facilitating the easy production of friable fractures. The existing method will drastically decrease processing efficiency, which uses extremely low feed speeds. In order to overcome this problem, a double-axial rapid servo movement platform was introduced in the raster milling system, and developed a self-tuned diamond milling (STDM) system.

A schematic representation of the STDM system's hardware configuration is shown in Fig. 1a. The workpiece is attached to the end effector of a three-degree-of-freedom (DoF) rapid servo movement platform, and then placed on the y-axis slide, and the diamond tool is attached to the tool holder and fixed to the aerostatic bearing spindle. The proposed STDM system uses only servo movements in the input (x axis) and the DoC (z axis) directions, despite the three-DoF movement platform's ability to product rapid movements along the x-, y-, and z-axis. Figure 1b shows a schematic of the cutting movements. The diamond tool that periodically cuts in and out of the work piece as the spindle rotates and feeds along the x-axis at a constant moving speed to remove the material. The work piece follows a rapid servo movement along the z-axis, similar to the rapid FTS, with the aid of the three-DoF movement platform to produce the appropriate micro-structured surfaces. In order to obtain crack-free micro-freeform surfaces with high homogeneity and to increase processing efficiency, a simultaneous Ultra rapid servo movement is also applied along the feed (x) direction to the work piece. This is done to strictly match the maximum thickness of chip with the critical DoC in line with the partial surface morphology. The whole workpiece may be covered while obtaining the appropriate MOAs by repeating this cutting process by stepping a movement along the Y-axis, much like raster milling. Rather than cutting individual lenticle cells, the entire lens array is generated by several grating cutting cycles on a flat surface, as seen in Fig. 1b.

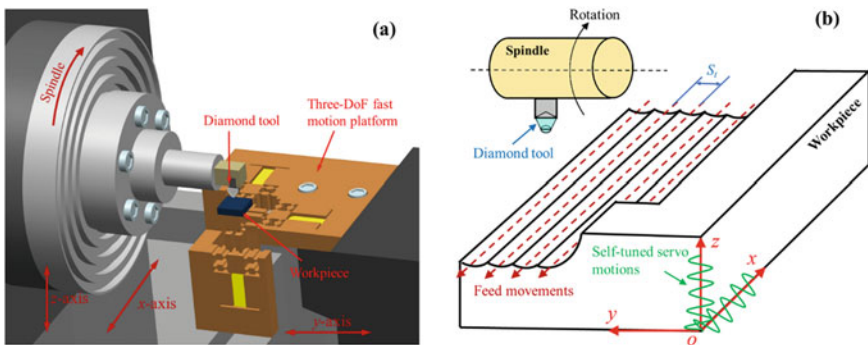
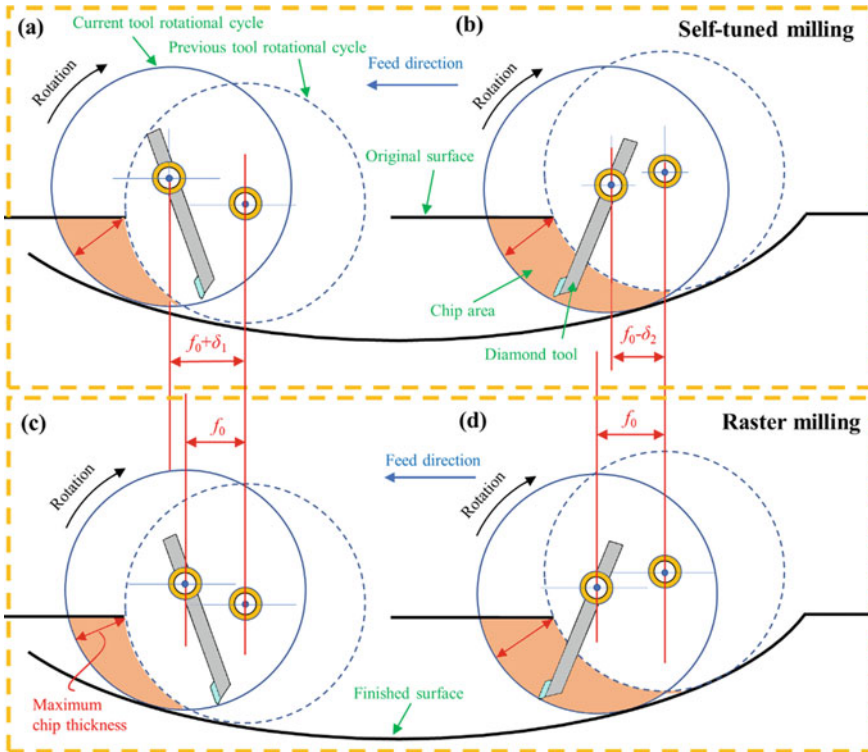


Fig. 1 Schematic of a hardware configuration and b cutting mechanism of STDM

Along with the typical benefits of diamond milling for producing MOAs, such great flexibility and consistent cutting speed, the STDM system’s special processing concept additionally offers the following benefits:

- (i) Prevent local fractures while creating infrared MOAs with intricate micro-freeform surfaces. As shown in Fig. 2a, b, the maximum thickness of chip for each rotational tool cycle is constant in the STDM system due to the deliberate control of the additional servo movement along the x-axis, which enables real-time adjustment of the instant feed speed to follow the local shape characteristics of the required micro-freeform surfaces. By actively adjusting the maximum thickness of the chip to a value not exceeding the critical DoC, it is possible to successfully avoid friable fractures across MOAs. As seen in Fig. 2b, c, the maximum thickness of chip differs from location to location with conventional milling because the feed speed is non-adjustable and constant during the cutting process. This is the primary cause of the unevenly distributed friable fractures of infrared MOAs;



**Fig. 2** Schematic of the chip formation under **a** and **b** STDM and **c** and **d** conventional raster milling

- (ii) Increasing processing effectiveness. Tiny feed speeds severely constrain the existing processing efficiency for traditional diamond milling to ensure malleable material detach from the maximum DoC of a micro-freeform surface. In contrast, the self-tuned STDM chip thickness modification permits a substantially greater average speed of feed while preventing breakdown, increasing the processing efficiency.

### 3 Toolpath Decision for STDM

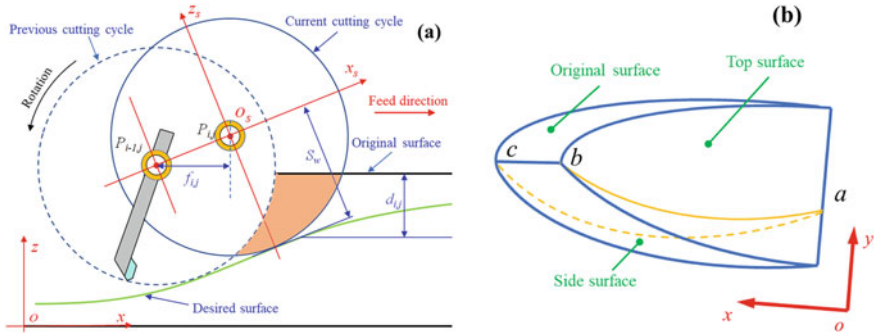
#### 3.1 Toolpath Programming Algorithm

The proposed STDM uses an additional rapid servo movement along the x-axis to actively adjust the maximum thickness of the chip based on the partial surface morphology, which requires a more complex toolpath programming algorithm than standard diamond milling, which only uses three-axis servo movements. Based on the STDM processing theory, a set of swing centre points (SCPs) of the spindle are numerically determined to create the toolpath programming algorithm while adhering to limitations on the required micro-freeform surface's form accuracy and the relationship between the critical DoC and maximum thickness of chip. The rapid movement platform's servo movements along the x- and z-axes are then computed following the established SCP coordinates.

STDM, the rotary spindle moves along the feed (x-axis) and the grating (y-axis) axes. Assuming the infrared material's initial surface is flat, a coordinate system with the x- and y-axes pointing in the direction of the feed and the grating is constructed on the workpiece, as illustrated in Fig. 1b. The workpiece is homogeneously split into  $N$  pieces along the grating direction using the equal interval-based discretization. The projection tool path in the  $o-xy$  plane is a collection of parallel straight lines dispersed along the grating direction with a set interval of  $S_t$ , as illustrated in Fig. 1b. As a result, in the workpiece coordinate system, the y coordinate of the  $i$ -th SCP situated in the  $j$ -th feed movement cycle can be represented as follows:

$$y_{i,j}^{(w)} = j \cdot S_t \quad (1)$$

As shown in Fig. 3a), two adjacent cycles of tool rotation along the direction of feed intermittently create the chips in STDM. In contrast to milling flat surfaces, the maximum thickness of chip for milling micro-freeform surfaces is influenced by the partial gradients of the required surface, the location of the SCP in the primary tool cycle of rotation, and other factors as well, such as the location of  $P_{i-1,j}$  in Fig. 3a. Each chip element is encircled by four surfaces, including top, bottom, the original, and side surfaces, as depicted by the three-dimensional schematic morphology of the chip created by STDM in Fig. 3b. The study found that the thickness of chip fluctuates between the zero at the contact point a of the tool work piece and the maximum value at point b before returning to zero at point c. As a result, the maximum thickness of



**Fig. 3** Schematic of **a** STDM viewed from y-axis and **b** 3D morphology of the chip

chip may be calculated by measuring the range from the point  $c$  to the place at which the bottom surface of the chip intersects with the straight line connecting the points  $c$  and  $p$ .

As illustrated in Fig. 3a, a different coordinate system  $o_s-x_s y_s z_s$  with the  $x_s$ -axis parallel to the required surface is constructed on the swing center of the spindle. The computation is made simpler by assuming that the spindle would not move during chip production since the time between adjacent cutting cycles is so short, making it possible to ignore the gradients change. In STDM, the cutting period for each tool rotation is also very brief. By resolving the above equations as follows, in the spindle coordinate system, the coordinate  $(x_b^{(s)}, y_b^{(s)}, z_b^{(s)})$  of the point  $b$  may be found according to the geometrical relation:

$$\begin{cases} x_b^{(s)} = \sqrt{\left(\sqrt{R_t^2 - \left(y_b^{(s)}\right)^2} + S_w - R_t\right)^2 - \left(z_b^{(s)}\right)^2} - f_{i,j} \\ y_b^{(s)} = \frac{z_b^{(s)} \cos \theta_{i,j} - d_{i,j} + S_w \cdot \cos \theta_{i,j}}{\sin \theta_{i,j}} \\ z_b^{(s)} = R_t - S_w + S_t \sin \varphi_{i,j} - \sqrt{R_t^2 - \left(y_b^{(s)} - S_t \cos \varphi_{i,j}\right)^2} \end{cases} \quad (2)$$

where  $d_{i,j}$  is the instant deepness of cutting,  $S_w$  is the swing radius of tool, and  $R_t$  is the nose radius of tool. Where  $\theta_{i,j}$  and  $\varphi_{i,j}$  stand for the desired surface's inclination angle along the  $x_s$ - and  $y_s$ -axes, respectively.

$$\begin{cases} \theta_{i,j} = \tan^{-1} \left( \frac{z_{i,j}^{(w)} - z_{i-1,j}^{(w)}}{f_{i,j}} \right) \\ \varphi_{i,j} = \tan^{-1} \left( \frac{z_{i,j}^{(w)} - z_{i-1,j}^{(w)}}{S_t} \right) \end{cases} \quad (3)$$

The straight line's expression between the points  $c$  and  $P_{i,j}$  is as follows:

$$\frac{x}{x_b^{(s)}} = \frac{y}{y_b^{(s)}} = \frac{z}{z_b^{(s)}} \quad (4)$$

Equations (2) and (3) can be used to calculate the coordinates of the intersection point  $(x_t^{(s)}, y_t^{(s)}, z_t^{(s)})$  between the straight line and the bottom surface of the chip as follows:

$$\begin{cases} x_t^{(s)} = x_b^{(s)} \cdot k \\ y_t^{(s)} = y_b^{(s)} \cdot k \\ z_t^{(s)} = z_b^{(s)} \cdot k \end{cases}, k = \frac{(S_w - R_t) \sqrt{(x_b^{(s)})^2 + (y_b^{(s)})^2} + \sqrt{R_t^2 (x_b^{(s)} + z_b^{(s)})^2 + (y_b^{(s)})^2} S_w (S_w - 2R_t)}{(x_b^{(s)})^2 + (y_b^{(s)})^2 + (z_b^{(s)})^2} \quad (5)$$

The maximum thickness of chip  $h_{max}$  for the  $i$ -th SCP situated in the  $j$ -th feed movement cycle is designated as follows based on Eqs. (2) and (5):

$$h_{max} = \sqrt{(x_b^{(s)} - x_i^{(s)})^2 + (y_b^{(s)} - y_i^{(s)})^2 + (z_b^{(s)} - z_i^{(s)})^2} \quad (6)$$

As is known to all that the critical DoC is the cut off value that separates the removal of friable and malleable material. Thus, by substituting the infrared material's critical DoC in Eq. (6) for the maximum chip thickness  $h_{max}$ , it is possible to ensure that the created MOAs are generally smooth and free of friable fractures while also significantly increasing the processing efficiency.

It is known from Eqs. (2)–(6) that there are two unsuspected variables in these equations, namely  $f_{i,j}$  and  $z_{i,j}$ , and that the location of  $P_{i,j}$  is determined repeatedly by the points of  $P_{i-1,j}$  and  $P_{i,j-1}$ . Another equation representing the tangent line between the surface created by the rotation of tool at  $P_{i,j}$  and the required micro-freeform surface must be constructed to calculate specifically  $f_{i,j}$  and  $z_{i,j}$ . By homogeneously cutting the tool edge into  $2 N_t$  pieces and the tool rotational trajectory into  $2 N_s$  pieces. So the surface produced by the rotation of tool at  $P_{i,j}$  may be represented as:

$$z_{m,n}^{(s)} = \sqrt{\left( R_t \sqrt{1 - \left( \frac{n}{N_t} \right)^2} + S_w - R_t \right)^2 - \left( \frac{m S_w}{N_s} \right)^2}, m \in [-N_s, N_s], n \in [-N_t, N_t] \quad (7)$$

The minimum range between the surface provided by Eq. (7) and the required surface can be utilized to simplify the tangency condition. As a consequence, the other mathematical relationship between the two unsuspected variables,  $f_{i,j}$  and  $z_{i,j}$  can be as follows:

$$\begin{aligned} z_{i,j} = \min & \left| z_{m,n}^{(s)} - F \left( f_{i,j} + x_{i-1,j} + \frac{m S_w}{N_s}, y_{i,j}^{(w)} + \frac{n}{N_t} R_t \right) \right| \\ & + z_0, \forall m \in [-N_s, N_s], \forall n \in [-N_t, N_t] \end{aligned} \quad (8)$$

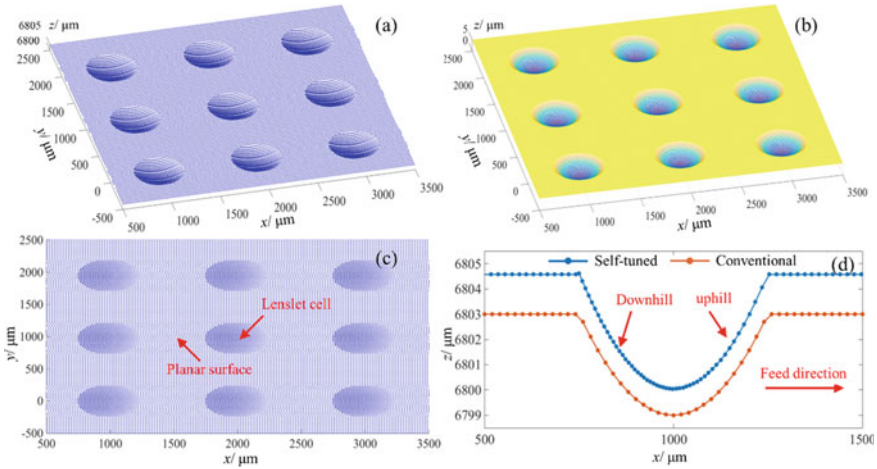
where  $z_0$  represents the imaginary range, and  $F(\cdot)$  represents the function of the required lenticle surface. The locations of all SCPs may be iteratively determined by solving Eqs. (6) and (8) while considering the material nature, particular shape

precision of the required surface, kinematics, and the geometry of tool. A constant feed speed is utilized to identify the initial SCP at the top and right corner of the workpiece. These SCPs are used as the fundamental information for the subsequent iterative computation. Although the transition zone between the lenticle and the flat surface is discontinuous, it is important to keep in mind that the tangency condition in Eq. (8) can still provide a seamless transition that without overcutting.

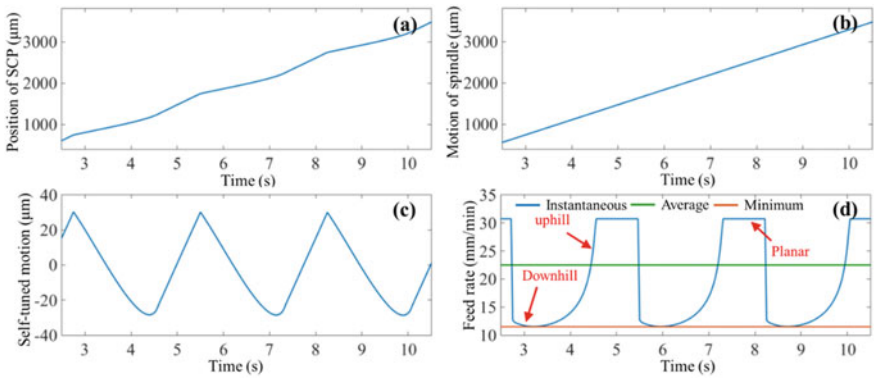
### 3.2 Characteristics of the Toolpath

The toolpath of typical micro-aspheric MOAs is decided using the programming algorithm mentioned above to define the STDM processing process, as illustrated in Fig. 4a. The form characteristic of the MOAs is depicted in Fig. 4b. Each lenticle cell has an aperture of  $500\ \mu\text{m}$  and a height of  $4\ \mu\text{m}$ , respectively. The projected image of the tool path on the  $x$ - $y$  plane is displayed in Fig. 4c for clarity. In comparison to the flat surface, it is shown that SCPs are scattered significantly more densely in the regions corresponding to lenticle cells. In the Figures, the period between two adjacent spots is fixed, which denotes lower feed speeds while milling lenticle cells. The SCP distribution of the centreline of any lenticle along the feed direction is compared for the self-tuned and conventional raster milling, which shown in Fig. 4d to better characterize the STDM toolpath. The density of SCPs for STDM varies depending on the partial gradients of the lenticle and the instant cutting deepness where the density of the SCPs on the downward gradients is obviously greater than that at the upward gradients, even when the cutting deepness is identical. In terms of adaptively adjusting the speed of feed to match the maximum thickness of chip with the crucial DoC, this verifies the efficiency of the suggested toolpath programming method. Contrarily, with traditional raster milling, the range between two adjoining SCPs remains constant during the processing process, making it more likely to cause friable lenticle fractures in the downward and deep sections.

The relative movement between the the workpiece and the SCP along the direction of feed during a grating cutting cycle is shown in Fig. 5a to illustrate the movement characteristics of STDM. It has a propensity to increase linearly with periodic variations imposed. This is because, as seen from the STDM processing principle, the rapid movement platform's self-tuned servo movement and the spindle's homogeneous movement, as shown in Fig. 5b, c, severally, combine to produce the movement of the SCP relative to the workpiece. The blue line in Fig. 5d depicts how the instant speed of feed of the STDM changes periodically at various places along the  $x$ -axis due to the self-tuned movement. The speed of feed is determined by multiplying the range between two nearby SCPs by a predetermined time interval. The STDM is estimated to have an average feed speed of  $22.4\ \text{mm/min}$  and an estimated minimum feed speed of  $11.3\ \text{mm/min}$  with a spindle speed of  $6000\ \text{rpm}$  and a required DoC of  $100\ \text{nm}$ . To prevent friable fractures in the biggest DoC area under the identical cutting circumstances, the maximum speed of feed permitted in traditional raster



**Fig. 4** Schematic of **a** toolpath and **b** shape of micro-aspheric arrays, **c** toolpath in  $x$ - $y$  plane and **d** distribution of SCPs for the central line of one lenslet



**Fig. 5** **a** Location of the SCPs along feed direction, movements of the **b** spindle and **c** self-tuned platform in  $x$ -axis and **d** feed speed

milling must be below than 11.3 mm/min. As a result, STDM has roughly double the processing efficiency of traditional milling.

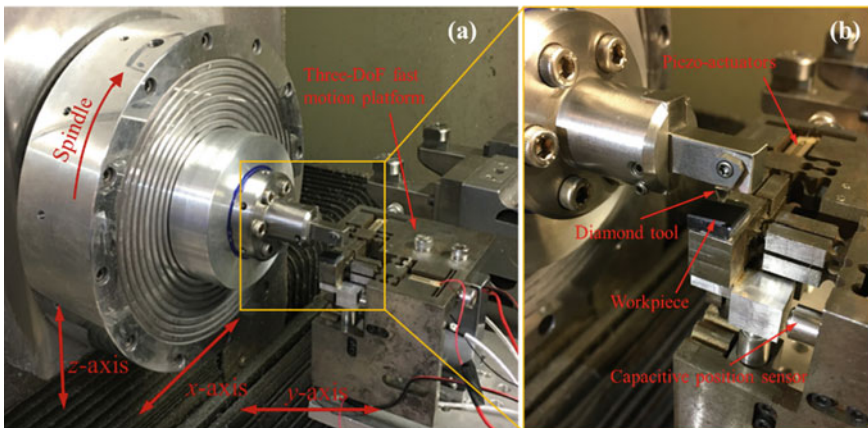
### 4 Growth of STDM System and Experimental Setup

Following Fig. 1a, the STDM system is created by combining a three degree of freedom piezoelectric driven movement platform with three translational movement slides and a rotating spindle on a CNC ultra-precision lathe (Moore nanotech 350FG),



as illustrated in Fig. 6a. Three piezo-actuators control the three-DoF movement platform in Fig. 6b, and three orthogonally arranged unidirectional compliant mechanisms are employed to precisely guide the movements in each direction. In Sect. 2, the STDM processing principle is described in deepness. To ensure movement of synchronization between the piezo-actuated movement platform and the CNC lathe, the CNC lathe is controlled during the processing process, analogous to raster milling a flat surface. The locations of the  $x$ - and  $y$ -slides are continuously surveillanced and send it to a multi-axis card of the movement control (Power PMAC). The PMAC control card then generates control signals based on the acquired locations and the intended toolpath, which amplified by power amplifier and input into the piezoelectric actuator. PMAC collects, for feedback control, the end-effector's displacement in the directions of the feed and DoC using a capacitive location sensor. As a result, the synchronized domination of the piezoelectric driving movement platform and the multi-axis CNC lathe will enable the STDM of infrared MOAs.

Micro-aspheric MOAs were produced on the surface of single-crystal silicon, which verified the feasibility of the STDM. In modern infrared optic systems, silicon is the most commonly used infrared material. The key DoC utilized in toolpath design in this work is 100 nm to ensure the malleable material removal mode because the monocrystalline silicon's critical DoC along the  $\langle 110 \rangle$  direction of crystal is determined to be at or below 120 nm [25] on the basis of the taper cutting experiment. In the studies, a diamond tool with a round edge and a 0.5 mm nose radius is used. The tool has a rake angle of  $-25^\circ$  and a clearance angle of  $7^\circ$ , respectively. The optic microscopy apparatus also recorded the microscopy images of the processed MOAs (Olympus BX60). The form precision and topographies of the created MOAs are captured using a non-contact optic surface profiler (Nexview, Zygo). The micro-aspheric lenticle cell is mathematically described as follows [26]:



**Fig. 6** **a** Hardware configuration of the STDM system and **b** an enlarged view of the three-DoF rapid movement platform

**Table 1** Coefficients defining the shape of the micro-aspheric lenslet

Shape coefficient ( $s$ )	-1
Radius of the array $R_0$	2.5 mm
Conic constant ( $k$ )	-0.8
Curvature ( $C$ )	$0.05 \text{ mm}^{-1}$

**Table 2** Processing parameters used for STDM and conventional raster milling

Processing parameters	STDM	Raster milling
Swing radius (mm)	7.1	7.1
Spindle rotation rate (rpm)	6000	6000
Step range ( $\mu\text{m}$ )	15	15
Tool nose radius (mm)	0.2	0.2
Material	Single-crystal silicon	Single-crystal silicon
Cutting direction	<100>	<100>
Deepness of cut ( $\mu\text{m}$ )	2	2
Feed speed (mm/min)	22	12,22

$$z(x, y) = \frac{sCR_0^2}{4 + 4\sqrt{1 - (1+k)C^2R_0^2}} - \frac{sC\rho^2(x,y)}{4 + 4\sqrt{1 - (1+k)C^2\rho^2(x,y)}} \quad (9)$$

When  $C$  is a constant governing the curvature, the each lenslet's radius is  $R_0$ , the conical surface is defined by  $k$ , the convex or concave surface is controlled by  $s$ , and the radial range in local coordinates is denoted by  $\rho$ . Aspheric surfaces are defined by  $-1 < k < 0$ . Table 1 contains the factors used in this investigation to determine the form of the processed micro-aspheric lenslet cell. The micro-aspheric MOA was created using STDM and traditional diamond milling, with the processing parameters reported in Table 2 for comparison.

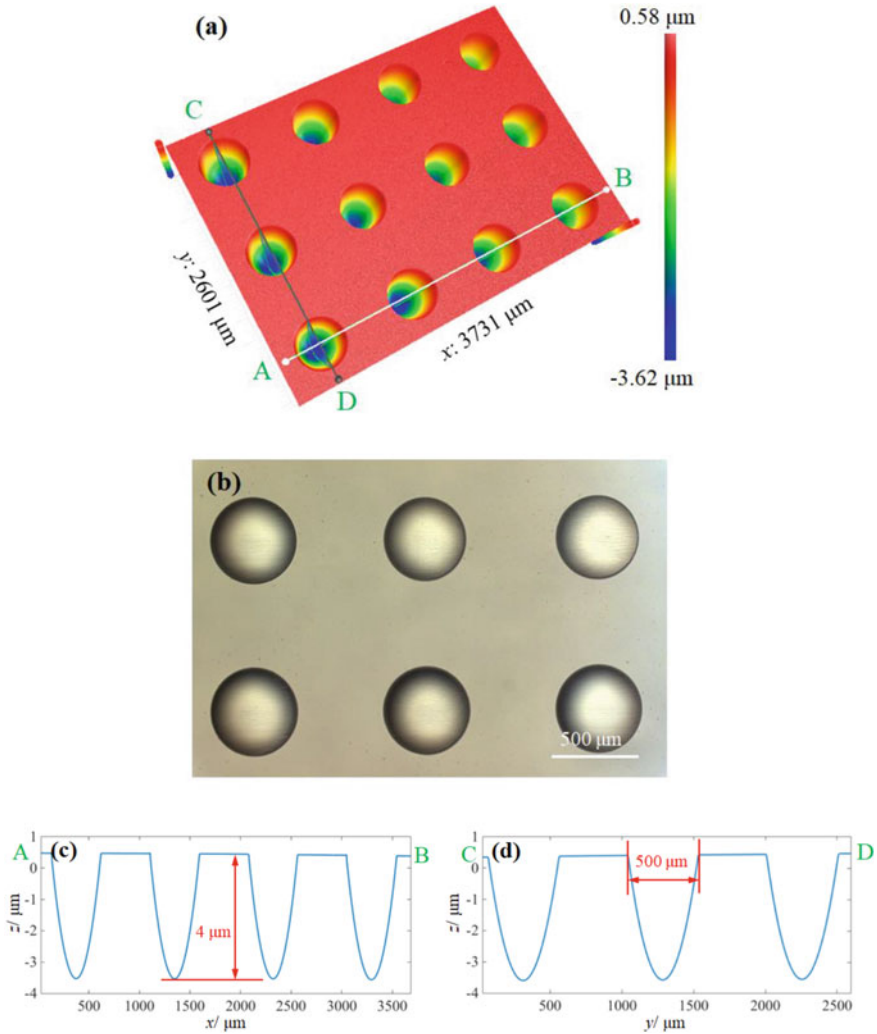
## 5 Results and Discussion

In order to verify the advantages of the proposed STDM technology in infrared MOAs manufacturing, the proposed STDM method is compared with the traditional raster milling method in micro aspheric MOAs milling on single crystal silicon wafer. Figure 7a depicts the  $4 \times 3$  MOAs' three-dimensional (3D) surface morphology, and Fig. 7b displays the matching microscope diagram of an extracted region. The entire microscope figure shows the mirror surface with no friable cracks or cracks, which

supports a fully malleable cutting pattern in the STDM of infrared MOAs even at continuously changing deepness of cutting and partial gradients. Additionally, it has been shown that each lenticle cell in the created MOAs has a consistent shape, size, and smoothness. The two-dimensional cross-sectional profiles crosses the centers of the lenticle along the feed direction and the grating direction, as illustrated in Fig. 7c, d, respectively, make it easier to see the homogenous properties. Along the feed and grating directions, a continuous spacing gap is seen between adjacent lenticle cells. Each lenticle has an aperture of 500  $\mu\text{m}$  and a height of 4  $\mu\text{m}$ , respectively, and the measured values are in good agreement with the intended values in Table 1.

In order to assess the form correctness of the created MOAs, enlarging the field of view of each lenticle cell 20 times, as shown in Fig. 8a. This was done because the shape distortion of the lenticle might significantly affect the optic performance of MOAs. Figures 8b, c compare the processed lenticle's two dimensional profiles of the cross-sectional along the  $x$ - and  $y$ -axes with the intended ones specified by Eq. (9). The form error is estimated to be less than  $\pm 60$  nm  $PV$  based on the fact that the measured contour (blue line) and the expected curve (orange line) are nearly completely intersecting in both directions. By deducting the aspheric surface from the lenticle cell, the micro-morphology of the lenticle cell is gained, as shown in Fig. 8d, and the lenticle's microscope image is presented in Fig. 8e to examine the homogeneity and smoothness of the surface quality. The microscopic morphology is described as homogeneous from the center to the edge field without cracks, and the surface roughness is very low, only 4 nm Sa, demonstrating the efficiency of the STDM processing in manufacturing smooth infrared MOAs and consistent the quality of surface. The intermittent cutting method of STDM [27] produces the ribbon-stripe graphics seen in Fig. 8d. Additionally, it confirms that the distinctive STDM cutting technique effectively ensures the form correctness and infrared MOAs homogeneity of surface with intricate micro-structures surfaces.

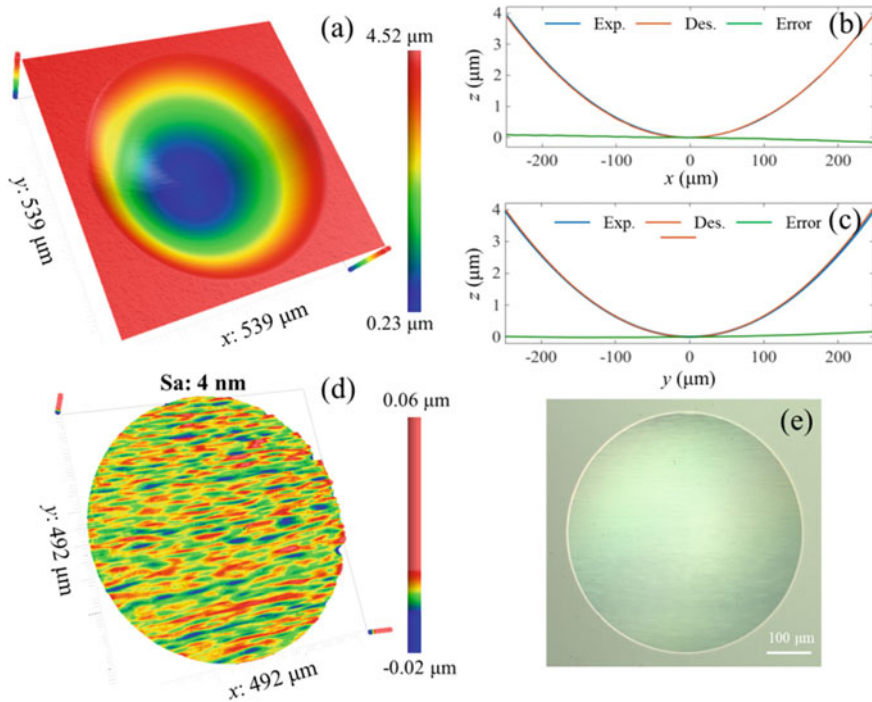
The proposed STDM's unique cutting mechanism, which uses a super-rapid servo movement along the direction of feed to adaptively match the maximum thickness of the chip for each tool rotation period with the critical DoC, is largely responsible for the even and smooth surface quality of the MOAs that are produced. Owing to the additional self-tuned movement, as stated in Sect. 2, the instant feed speed of the STDM constantly swings around the nominal one, despite the nominal speed of feed in STDM being 22 mm/min or the speed of movement of the spindle along the  $x$  axis. Therefore, even with constantly fluctuating partial gradients and the deepness of cutting, the maximum thickness of chip in micro-freeform surfaces's STDM is identical to the essential DoC of the infrared material, ensure consistency of process and removal of malleable material throughout the cutting area. To put it another way, the STDM is an adaptive approach of the cutting that takes into account both shape precision and material removal. Additionally, STDM processes the conventional benefits of diamond milling while cutting infrared materials, as opposed to the well-known FTS/STS diamond turning: (i) By producing very thin chips, the STDM's intermittent cutting method effectively reduces infrared material's surface damage [25];(ii) as shown in Fig. 7b, e, the unaltered direction of feed of STDM prevents the unfavorable radial-spoke markings and nonhomogeneous fractures that



**Fig. 7** **a** 3D morphology and **b** microscope of the processed MOAs, **c** and **d** the cross-sectional profiles along *x*- and *y*-axis, respectively

are frequently created in single-crystal infrared materials' s FTS/STS [11, 12]. This enhances the infrared optic scattering homogeneity.

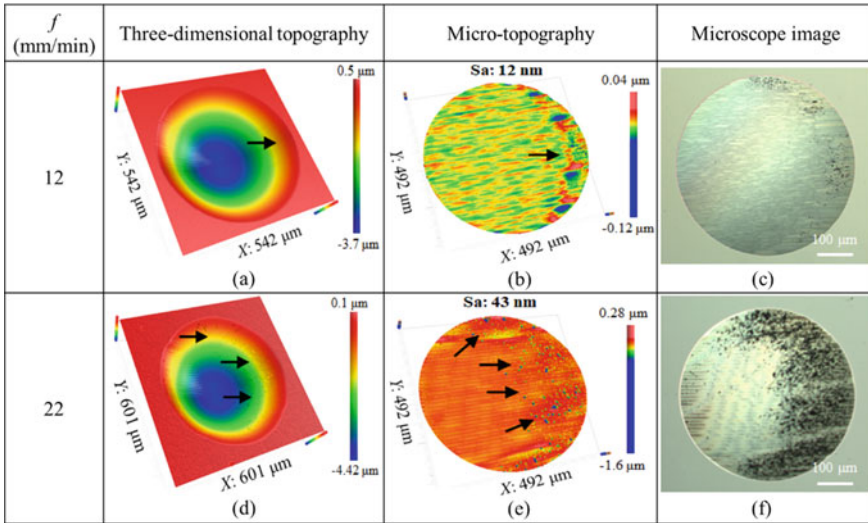
As shown in Fig. 9, conventional raster milling with a variety of feed speeds is also used to produce silicon MOAs to further demonstrate the particular advantages of the suggested STDM in improving surface homogeneity and processing efficiency in producing infrared MOAs. Even with a much lower speed of feed of 12 mm/min, distinct friable fractures are observed in the downward gradient of the lenticle produced by conventional raster milling, as compared with the STDM lenticle



**Fig. 8** **a** 3D morphology of the lenticle cell, **b** and **c** the corresponding cross-sectional profiles along x and y-axis, **d** micro-morphology and **e** microscope

as illustrated in Fig. 8. This leads to an uneven surface quality and a higher roughness of surface of 12, as illustrated in Fig. 9b, c. This is a result of traditional milling's fixed feed speed. When cutting micro-freeform surfaces with a typical grating mill, as shown in Fig. 2, the maximum thickness of the chip for every rotation cycle of the tool is different in different locations. For traditional raster milling, friable fracture is easy to occur in the area where the cutting deepness gradually increases because higher thickness of chip may be made in the gradient of decline compared with the gradient of rise [11]. Additionally, due to the non-homogenous cutting procedure of raster milling, a substantially more rough surface is produced for traditional raster milling compared to STD M, even if in the zone of the malleable cut, as seen by the microscopic graphics compared in Figs. 8e and 9c. In contrast, as shown in Fig. 5d, due to the additional servo movement in the STD M along the direction of feed, the instant feed speed in the downward sloping area is significantly lower than that in the upward sloping area to optimize the maximum chip thickness. The main factor underlying the more even and the smoother quality of surface produced by STD M is the adaptive modification of the feed speed.

As demonstrated in Fig. 9d–f, more intense friable fractures are created when a higher speed of feed rate of 22 mm/min is used for traditional milling. These



**Fig. 9** 3D surface topographies, micro-topographies and microscopes of the lenticle generated by raster milling under different feed speeds

fractures extend from the low gradient zone to the underside surface of the lenticle. As demonstrated in Fig. 9e, substantially higher roughness of the surface of 43 nm is attained. Therefore, the feed speed of traditional raster milling should be less than 12 mm/min, and the spindle speed should be 6000 rpm to produce infrared MOAs with a surface without cracks. In contrast, STDM can produce a smooth surface devoid of friable fractures even when employing the nominal speed of the feed of 22 mm/min, as illustrated in Fig. 8. As a result, STDM can reach processing efficiency approximately twice as high as the traditional one.

As is known to all that rough cutting is typically used to minimize severe tool vibrations at high deepness. When milling the free-form optic surface whose azimuthal height changes more than hundreds or even thousands of microns. When microstructured surfaces were cut by the diamond-cutting with a small azimuthal elevation change, like the MLAs in this manuscript, the one-step operation is typically used to increase processing efficiency. The reason for this is that the permissible deepness of the cutting for ultra-precision diamond cutting is typically between sub-micrometer and tens of micrometers. One-step cutting is more beneficial to guarantee the optic properties of infrared optics because, unlike when processing an optic mold out of copper or aluminum, where rough cutting can be used, repeat cutting will cause the expansion of microcracks in infrared materials, and ultimately reduce the surface quality of infrared materials [25]. Based on the local surface morphology, self-adaptive matching of the maximum chip thickness for each tool rotation cycle with the required deepness of cut of the infrared material, the proposed STDM may produce infrared MOAs in one step with the quality of the surface is homogenous without cracks.

According to Refs. [11, 16, 28], researchers largely accept total integrated scattering (*TIS*) as an Index for evaluating infrared optic properties. *TIS* can be determined by:

$$TIS \approx \left( \frac{4\pi\delta}{\lambda} \right)^2 \quad (10)$$

where  $\lambda$  is the wavelength of the incident light, which for single-crystal silicon ranges from 6 to 1.2  $\mu\text{m}$ , and  $\delta$  is the root mean square value of deviation of the surface, approximately equal to 1.25 times of the surface roughness. According to Harvey et al. [28], to ensure the best performance of most optical elements, *TIS* should be less than 0.01. Hence silicon infrared MOAs must have a surface roughness no greater than 9 nm. As a result, the surface roughness obtained by STDM is 4 nm, which meets the highest requirement of silicon based infrared MOAs covering the entire infrared region. The surface roughness obtained by traditional milling is 12 nm, which is not satisfactory even in the case of low feed speed. In addition to the roughness of surface, an optic element's form accuracy typically needs less than a quarter  $\lambda$  [29]. Therefore, silicon MOAs must have a form accuracy of less than 300 nm. The lenticle processed with STDM in the current study has a form accuracy of 60 nm, which also satisfies the requirements.

The primary geometrical characteristic of all micro-optic arrays, including convex micro-lens, concave micro-lens and micro pyramid array, it is the height and gradient of the constantly changing microstructure surface. The main advantage of the proposed STDM is its self-tuning property, which can self-adaptively fit the maximum thickness of the chip of each rotating tool cycle with the critical cutting deepness of infrared materials based on the local height and gradient of the processed micro-optic arrays. This is illustrated in the manuscript. Therefore, STDM may be used with any micro-optics array with continuously varying height and gradient.

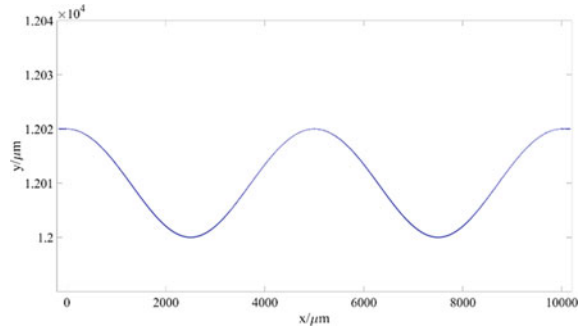
## 6 STDM for Sinusoidal Microgrooves

To further verify the uniqueness of self-tuned diamond milling, this section presents the simulation of tool trajectory and processing efficiency of sinusoidal microgrooves by processing sinusoidal microgrooves through self-tuned diamond milling and verifies its effectiveness through experiments [30].

### 6.1 Simulation of STDM for Sinusoidal Microgrooves

Finding the tool's centre of rotation is essential when using self-tuned diamond milling because the tool trajectory points of conventional diamond milling are homogeneously distributed. In contrast, SDTM is calculated based on the deepness of cut and gradient at various locations of the processed microstructure. The iterative

**Fig. 10** Diagram of cutting path center of rotation location



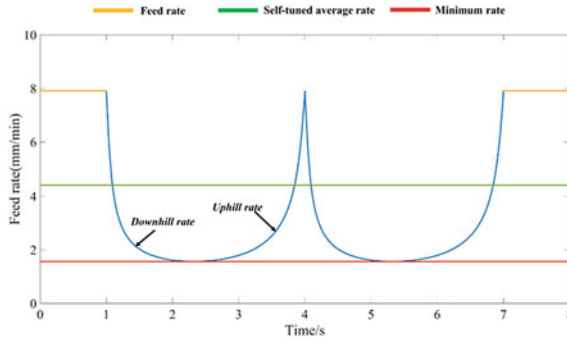
approach's origin is specified as the centre of rotation of the second tool in the right-angle coordinate system. The iterative approach is used to compute the location of the centre of rotation of the subsequent tool, and so on, during the whole sinusoidal microgroove processing process.

The computed tool center of rotation trajectory may be transformed into a feed speed, according to the SDTM system. The feed speed is derived by multiplying the separation between the centers of rotation of two adjacent tools by a predetermined time interval. Figure 10 depicts the tool trajectory locations along the feed direction during milling. The tool trajectory points of the downhill part are more intense than those of the uphill section because, given the same deepness of cut and gradient, the maximum chip thickness of the downhill section is larger than that of the downhill section. In comparison to the uphill phase, the tool trajectory points in the downhill section are more numerous. At various  $X$ -axis points, there are periodic fluctuations in the instant feed speed. According to Fig. 11, using a 1,000 r/min spindle speed as an assumption, the minimum feed speed for the SDTM is 1.67 mm/min and the average speed of the feed is 4.36 mm/min. The maximum feed speed permitted by conventional diamond milling is lower than that of the conventional diamond milling under the same cutting circumstances. In order to prevent friable fracture at the maximum chip thickness, maximum feed speed of the traditional diamond milling is less than 1.67 mm/min under the same cutting circumstances. As a result, the STDM is nearly 2.5 times as effective as traditional diamond milling.

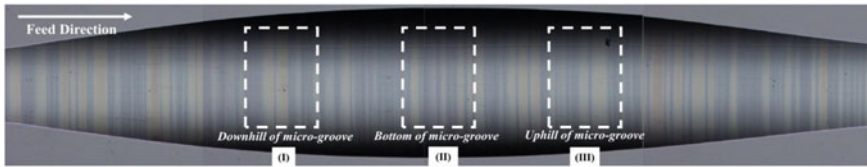
## 6.2 Results and Discussion of STDM for Sinusoidal Microgrooves

Experiments were done to compare the STDM with the traditional diamond milling for processing sinusoidal microgrooves on single-crystal silicon wafers to verify the benefits of the proposed STDM for processing infrared optic materials. Figure 12 depicts the morphology of the sinusoidal microgrooves created using the STDM. It is





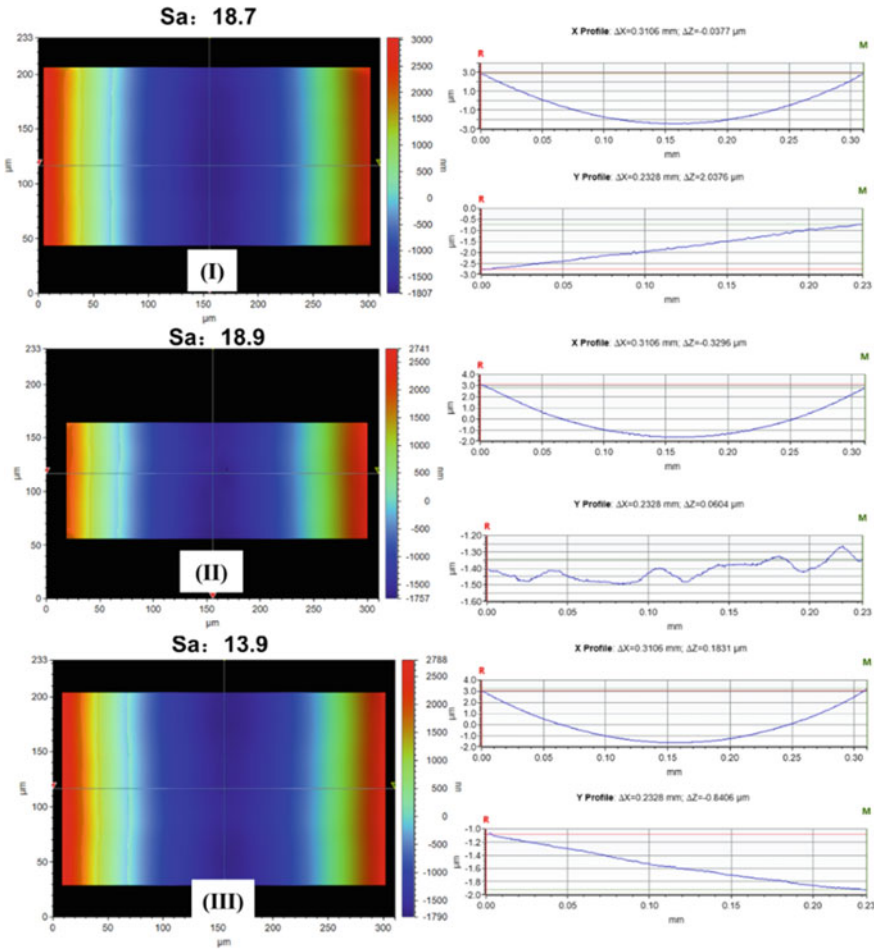
**Fig. 11** Schematic diagram of cutting speed comparison



**Fig. 12** Sinusoidal microgroove morphology for STDM under optic microscope

demonstrable that the STDM processes the microgrooves in a malleable way despite variations in cutting deepness and short gradient.

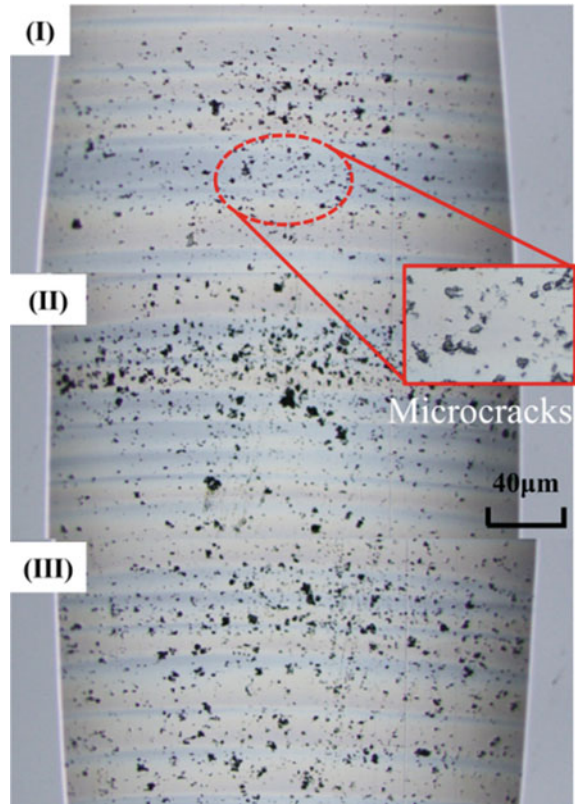
According to Fig. 13, the microgroove's surface quality is consistent and devoid of microcracks along the feed direction from the downhill part at the beginning to the uphill region at the conclusion. Only roughly 18 nm of surface roughness exists inside the microgroove. This shows that a surface with a consistent and smooth surface quality may be produced using the STDM. The STDM process results in stripes, that can be seen in Fig. 12. This further proves that the cutting process used by the ultra-precision diamond milling is unique and guarantees the correctness of shape and surface homogeneity of surfaces with complicated structures. Because of its distinct cutting mechanism, STDM can create micro-grooves with smooth and homogenous surface quality. This technique matches the maximum chip thickness to the instant deepness of cut and gradient to adaptively compute the location of each tool rotation cycle in the feed direction. Consequently, even though the theoretical feed speed setting for the STDM is the spindle's speed along the  $X$ -axis, its instant feed speed is constantly changing due to the additional adaptive speed regulation movement to meet its processing characteristics. Since the maximum thickness of the chip is absolutely equal to the critical deepness of cut for the ductile-friable transition of the single-crystal silicon, even though the instant local deepness of cut and gradient of the microgroove is constantly changing, the process is consistent throughout the cutting area, and the material is removed in a malleable way.



**Fig. 13** Surface roughness for STDM

The experiments were also set up to compare the conventional diamond milling microgrooves at various feed speeds, and the experimental results are shown in Fig. 14. This was done in order to further validate the STDM’s particular merits in terms of improving surface homogeneity and processing efficiency in processing and fabrication. Under an optic microscope, it is possible to see the microcracks and black-speckled friable fractures that run along the downhill in the feed direction of the microgrooves created by conventional diamond milling. The quality of surface and increased the roughness of surface of roughly 25 nm, as seen in Fig. 15. This results from conventional diamond milling’s inability to modify the feed speed. While cutting micro-grooves with conventional diamond milling, the maximum thickness of chip produced per tool rotation cycle varies with location. In areas where the deepness of cut progressively increases, the downhill part can develop a bigger chip

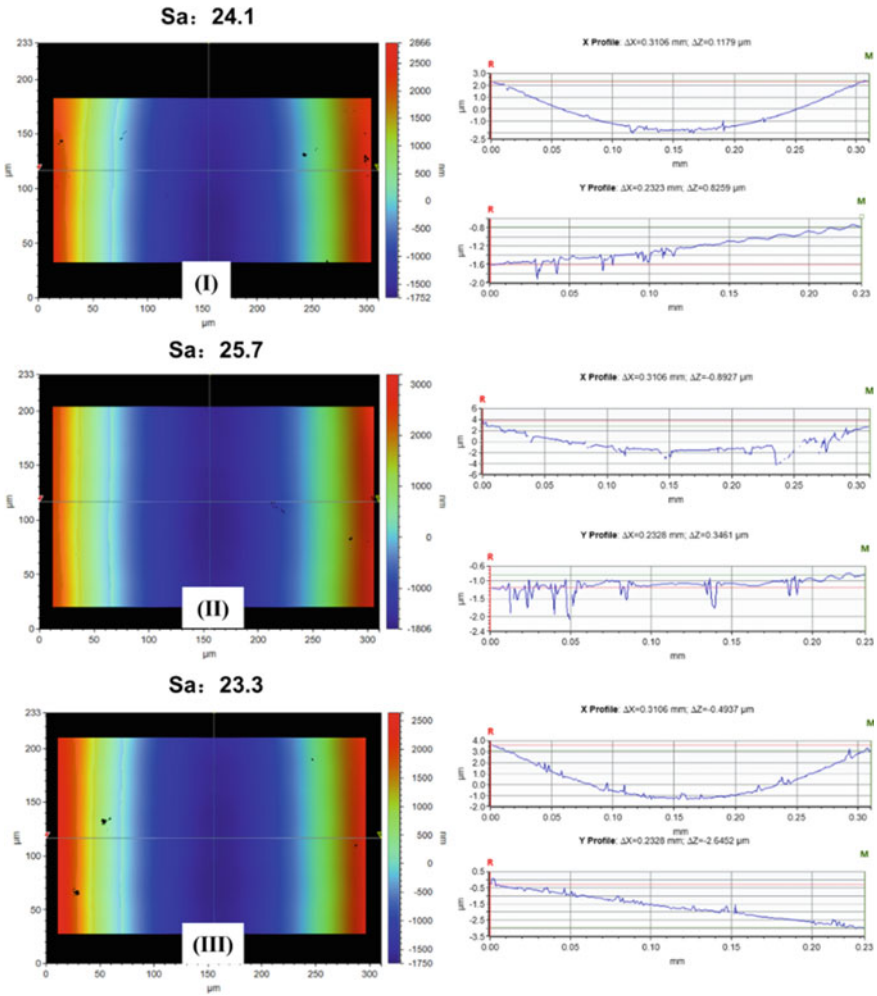
**Fig. 14** Structure of segmented optic microscope for conventional diamond milling



thickness than the uphill and is more vulnerable to friable fracture during conventional diamond milling. Even in malleable processing, conventional diamond milling results in a rougher surface than STDM.

## 7 Conclusions

In this chapter, a new type of self-tuning diamond milling (STDM) system is proposed, which integrates a double-axial rapid servo movement platform into a diamond raster milling system to realize the malleable cutting of infrared micro-optics arrays (MOA) with high surface homogeneity and enhanced processing efficiency. In the STDM, the maximum thickness of the chip per rotation tool cycle is self-adaptively adjusted so as to be exactly the same as the deepness of cut (DoC) of the infrared material at the same time as generating micro-freeform lenticle, both the smoothness and homogeneity of the whole MOAs are guaranteed and the processing efficiency is improved. This is accomplished by a two-axis rapid servo



**Fig. 15** Surface roughness for conventional flying cutting

movement in the direction of feed and deepness of cut (DoC). The appropriate tool-path programming method is also put out with fully consider the geometry of the tool, the STDM’s distinctive characteristic kinematics, and infrared material characteristic. In order to avoid local fractures and improve the speed of feed when milling micro-structured optics on the infrared materials, the suggested STDM effectively conquers the inherent limits of the current methods of diamond cutting. The following are the main conclusions:

- (1) The STDM tool path programming algorithm can take into account the shape precision of the desired MOAs as well as the infrared material removal method

- thanks to dual-axial rapid servo movements. Concerning the partial gradient and instant cutting deepness, the density of the swing center points (SCP) is altered.
- (2) In STD, the oscillations of the self-tuned rapid servo movements and the spindle's homogenous movement can be used to separate the relative movement of the SCP with the workpiece. The instant feed speed changes that ensue cause the maximum thickness of the chip and the critical DoC to self-tuned match.
  - (3) To verify the proposed STD, in order to validate the proposed STD, a microspheric MOAs without crack with a shape error of 60 nm have been successfully processed on single-crystal silicon. Due to the homogeneity of STD's processing, each lenticle has a more homogeneous and smoother surface quality than conventional milling, with the roughness of surface of only 4 nm.
  - (4) To prevent fractures created at the downgrade gradient and significant DoC areas, extremely low speeds of feed are typically needed for traditional milling. In contrast, STD's self-tuning capability greatly increases the average feed speed while maintaining smoothness, substantially doubling processing efficiency.
  - (5) STD creates a more consistent microgroove surface and less roughness than the conventional diamond milling. The average feed speed may be significantly increased while maintaining surface quality with STD, and the processing efficiency is 2.5 times more than conventional diamond milling.

**Acknowledgements** This work described in this chapter was supported by the National Natural Science Foundation of China (NSFC Project No. 52005110, No. 51975128), the Natural Science Foundation of Guangdong Province (Project No. 2022A1515011055) and Guangzhou Basic and Applied Basic Research Project (No. 202201010233).

## References

1. Hong Z, Liang R (2017) IR-laser assisted additive freeform optics manufacturing. *Sci Rep* 7(1):7145
2. Deng C, Kim H, Ki H (2019) Fabrication of a compound infrared microlens array with ultra-short focal length using femtosecond laser-assisted wet etching and dual-beam pulsed laser deposition. *Opt Express* 27(20):28679–28691
3. Zhu W, Duan F, Zhang X, Zhu Z, Ju B (2018) A new diamond machining approach for extendable fabrication of micro-freeform lens array. *Int J Mach Tools Manuf* 124:134–148
4. Yan G, Zhang Y, You K, Li Z, Yuan Y, Fang F (2019) Off-spindle-axis spiral grinding of aspheric microlens array mold inserts. *Opt Express* 27(8):10873–10889
5. Zhu Z, Zhou X, Luo D, Liu Q (2013) Development of pseudo-random diamond turning method for fabricating freeform optics with scattering homogenization. *Opt Express* 21(23):28469–28482

6. Krywonos A, Harvey JE, Choi N (2011) Linear systems formulation of scattering theory for rough surfaces with arbitrary incident and scattering angles. *J Opt Soc Am A-Opt Image Sci Vis* 28(6):1121–1138
7. Zuo H, Choi D-Y, Gai X, Luther-Davies B, Zhang B (2017) CMOS compatible fabrication of micro, nano convex silicon lens arrays by conformal chemical vapor deposition. *Opt Express* 25(4):3069–3076
8. Zhang Y, Luo J, Xiong Z, Liu H, Wang L, Gu Y, Lu Z, Li J, Huang J (2019) User-defined microstructures array fabricated by DMD based multistep lithography with dose modulation. *Opt Express* 27(22):31956–31966
9. Li Z, Fang F, Chen J, Zhang X (2017) Machining approach of freeform optics on infrared materials via ultra-precision turning. *Opt Express* 25(3):2051–2062
10. Li D, Wang B, Qiao Z, Jiang X (2019) Ultraprecision machining of microlens arrays with integrated on-machine surface metrology. *Opt Express* 27(1):212–224
11. Mukaida M, Yan J (2017) Ductile machining of single-crystal silicon for microlens arrays by ultraprecision diamond turning using a slow tool servo. *Int J Mach Tools Manuf* 115:2–14
12. Wang M, Wang W, Lu Z (2012) Anisotropy of machined surfaces involved in the ultra-precision turning of single-crystal silicon—a simulation and experimental study. *Int J Adv Manuf Technol* 60:473–485
13. Sun Z, To S, Zhang G, Zhang S (2019) Flexible fabrication of micro-optics arrays with high-aspect-ratio by an offset-tool-servo diamond machining system. *Opt Express* 27(7):9631–9646
14. Zhu Z, To S (2015) Adaptive tool servo diamond turning for enhancing machining efficiency and surface quality of freeform optics. *Opt Express* 23(16):20234–20248
15. Zhu Z, To S, Zhang S (2015) Large-scale fabrication of micro-lens array by novel end-fly-cutting-servo diamond machining. *Opt Express* 23(16):20593
16. Sun Z, To S, Yu K (2018) One-step generation of hybrid micro-optics with high-frequency diffractive structures on infrared materials by ultra-precision side milling. *Opt Express* 26(21):28161–28177
17. Dutterer BS, Lineberger JL, Smilie PJ, Hildebrand DS, Harriman TA, Davies MA, Suleski TJ, Lucca DA (2014) Diamond milling of an Alvarez lens in germanium. *Precis Eng* 38(2):398–408
18. Owen J, Troutman J, Harriman T, Zare A, Wang Y, Lucca D, Davies M (2016) The mechanics of milling of germanium for IR applications. *CIRP Ann* 65(1):109–112
19. Sun Z, To S, Zhang S (2018) A novel ductile machining model of single-crystal silicon for freeform surfaces with large azimuthal height variation by ultra-precision fly cutting. *Int J Mach Tools Manuf* 135:1–11
20. Sun Z, To S, Yu K (2019) An investigation in the ultra-precision fly cutting of freeform surfaces on brittle materials with high machining efficiency and low tool wear. *Int J Adv Manuf Technol* 101(5–8):1583–1593
21. Mir A, Luo X, Cheng K, Cox A (2018) Investigation of influence of tool rake angle in single point diamond turning of silicon. *Int J Adv Manuf Technol* 94(5–8):2343–2355
22. Zhu Z, To S, Xiao G, Ehmann KF, Zhang G (2016) Rotary spatial vibration-assisted diamond cutting of brittle materials. *Precis Eng* 44:211–219
23. Wang S, Wang J, Lei X, Liu Z, Zhang J, Xu Q (2019) Investigation of the laser-induced surface damage of KDP crystal by explosion simulation. *Opt Express* 27(11):15142–15158
24. Xiao G, To S, Jelenković E (2015) Effects of non-amorphizing hydrogen ion implantation on anisotropy in micro cutting of silicon. *J Mater Process Technol* 225:439–450
25. Sun Z, To S, Yu K (2019) Feasibility investigation on ductile machining of single-crystal silicon for deep micro-structures by ultra-precision fly cutting. *J Manuf Process* 45:176–187
26. Yu D, Wong Y, Hong G (2011) Ultraprecision machining of micro-structured functional surfaces on brittle materials. *J Micromech Microeng* 21:095011
27. Zhang S, To S (2013) The effects of spindle vibration on surface generation in ultra-precision raster milling. *Int J Mach Tools Manuf* 71:52–56

28. Harvey JE, Schröder S, Choi N, Duparré A (2012) Total integrated scatter from surfaces with arbitrary roughness, correlation widths, and incident angles. *Opt Eng* 51:013402-013401–013402-013411
29. Ottevaere H, Cox R, Herzig H-P, Miyashita T, Naessens K, Taghizadeh M, Völkel R, Woo H, Thienpont H (2006) Comparing glass and plastic refractive microlenses fabricated with different technologies. *J Opt A-Pure Appl Opt* 8:S407
30. Li P, D X, Sun Z, Wang S, Xu S (2022) Efficient adaptive flying cutting for infrared optics micro-structured surfaces. *Opt Precis Eng* 15(30):1845–1856

# Chapter 6

## Cutting Force and Energy Modelling in Ultra-Precision Machining of Micro-structures



ZeJia Zhao and Yiji Liang

**Abstract** Cutting force and energy are usually used as important criteria for the selection and optimization of the ultraprecision machining parameters. Effective strategies for minimizing the cutting force and energy are becoming increasingly vital to meet sustainable manufacturing requirements. This chapter focuses on the prediction and validation of cutting forces and energies in ultra-precision machining of micro-structural surfaces on difficult-to-cut materials such as titanium alloy and brittle silicon. In the introduction, the current technical status of cutting force and cutting energy models is reviewed and some critical issues are described in the machining process. Then, the evaluation of cutting forces for fabricating microgrooves on titanium alloys is discussed with respect to material constitutive models and geometrical relationships. The predicted cutting forces are in good agreement with the measured cutting forces at various cutting conditions within an error of about 3.53%, and the equivalent stress required to overcome the plastic deformation of the titanium alloys increases with the cutting speeds because of the high dislocation drag stress. Next, the cutting energy in ultraprecision machining of micro-lens arrays (MLAs) on single crystal silicon by slow tool servo is discussed in terms of material ductile and brittle removal processes. It is clarified that the total material removal energy decreases with the increasing of feedrates, but the maximum material removal energy increases with the feedrates. The formation mechanism of the surface damage and its effects on the cutting energies are also discussed concerning crystalline orientations and surface energy of the silicon.

## 1 Introduction

Micro-structured functional surfaces on components serving as the refractive or diffractive lenses are attracting considerable attention in recent years because of their

---

Z. Zhao (✉) · Y. Liang

Institute of Semiconductor Manufacturing Research, College of Mechatronics and Control Engineering, Shenzhen University, Nan-hai Ave 3688, Shenzhen 518060, Guangdong, People's Republic of China

e-mail: [zhaozejia@szu.edu.cn](mailto:zhaozejia@szu.edu.cn)



wide applications such as infrared imaging and detection, automatic driving, optical communication and biomedical analysis. Up to date, micro-structured surfaces could be obtained by injection molding [1], lithography [2], focused ion beam (FIB) [3], etching [4] and ultraprecision machining [5]. The ultraprecision machining, as one of mechanical machining approaches, is regarded as an efficient, low-cost and flexible method to directly generate different micro-structured surfaces on various materials in comparison to other techniques, which has developed rapidly as a very-promising method for fabrication of functional surfaces.

An evaluation of the cutting force and cutting energy in ultraprecision machining is one of the critical work to achieve sustainable manufacturing of micro-structured functional surfaces, especially for machining of difficult-to-cut materials. Prediction of cutting force evolution has attracted great attention for many years, and the most famous one is the Merchant's force model in orthogonal cutting [6], but the effects of material spring back and cutting tool edge radius are not considered in this model. Arcona and Dow [7] proposed an empirical force model considering the influence of material elastic deformation and verified their model by diamond turning of four types of metals. Similarly, Zhang et al. [8] reported a force model which considers the tool-workpiece contact area induced by the spring back in vibration-assisted machining. The cutting tool edge radius is another important factor to affect the cutting force, especially in ultraprecision machining with small depth of cut (DoC). The effective rake angle tends to be more negative as the depths of cut reach to be comparable to the edge radius [9]. It is generally accepted that materials would be removed by shear deformation if the DoC is larger than the critical chip thickness that is affected by the edge radius, while ploughing instead of cutting would occur if the depth is smaller than the critical chip thickness [10, 11]. Fang [12] predicted the cutting and ploughing forces with respect to the effect of tool edge roundness in machining with a round edge tool. Jin and Altintas [13] analyzed the stress distribution in the material deformation zone induced by the tool edge radius using the slip-line field model and verified by the cutting forces in micro-turning experiments. Zhu et al. [14] and Sun et al. [15] proposed an equivalent contact angle induced by the round cutting edge of the diamond tool to successfully predict the dynamic cutting force evolution in turning of the micro-structured surface. Therefore, the effects of spring back and round cutting edge should not be neglected when analyzing the cutting forces in machining metal and alloys.

The increasing sustainability and environmental consciousness have raised the awareness of saving energy in computer numerical control (CNC) machining [16]. Evaluation of energy consumption under different cutting parameters in the machining is very important because it could provide useful instructions for energy saving. The total required energy in the machining could be primarily divided into different stages based on manufacturing states [17], machine tool states [18], or machining levels [19]. Though the classification criterion of the energy consumption is different, the energy consumed by the actual material removal stage is an essential part of the overall demanded energy.

In this chapter, the prediction and validation of the cutting force and cutting energy are introduced and discussed in ultraprecision machining of micro-structured

surfaces, mainly including microgrooves on titanium alloys and micro-lens arrays (MLAs) on single crystal silicon.

## 2 Evaluation of Cutting Forces for Fabricating Microgrooves

### 2.1 Theoretical Models for Prediction of Cutting Forces

The prediction of cutting force evolution has a significant effect on the rational formulation of machining parameters and the study of the mechanism of ultra-precision machining. In this section, taking the cutting force when machining microgrooves on Ti6Al4V as an example, cutting force models which take into account the material spring back and other factors are developed.

The distribution of forces during the diamond cutting process is depicted schematically in Fig. 1a–c. To depict the frictional force  $f_1$  and the normal force  $F_n$  exerted on the tool, an equivalent coordinate system ( $x_e$ – $y_e$ ) is developed taking into account the diamond tool edge radius  $r_\beta$  and equivalent contact length  $l_c$  between the tool and cutting chip. To depict the inclined angle of the  $y_e$  axis from the vertical direction, an equivalent contact angle of  $\psi$  is employed. With consideration of spring back force  $F_s$ , frictional forces  $f_1$  between chip and the tool rake face, and  $f_2$  between work-piece and the tool flank face, the cutting force  $F_c$  and thrust force  $F_t$  are estimated to be:

$$\begin{cases} F_c = F_n \cos \psi - f_1 \sin \psi + f_2 \cos \theta \\ F_t = F_n \sin \psi + f_1 \cos \psi + f_2 \sin \theta + F_s \end{cases} \quad (1)$$

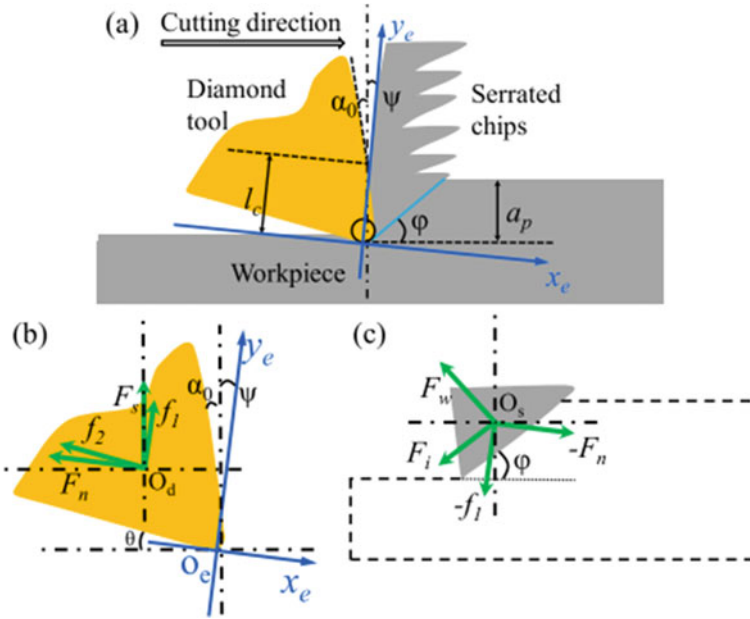
where  $\theta$  is the clearance angle. Given by Ref. [14], the corresponding contact angle  $\psi$  is as follow:

$$\psi = \begin{cases} \arccos\left(\frac{l_c}{2r_\beta}\right), l_c \leq l_e \\ \arcsin\left[\frac{r_\beta(1+\tan \alpha_0) \cos \alpha_0}{l_c}\right] - \alpha_0, l_c > l_e \end{cases} \quad (2)$$

$$l_e = \frac{\sqrt{2}r_\beta \cos \alpha_0}{\sqrt{1 - \sin \alpha_0}} \quad (3)$$

where  $\alpha_0$  is the rake angle of the diamond tool. The contact length  $l_c$  could be calculated using the slipline field based model as follows [20],

$$l_c = \frac{\sqrt{2}a_p \cos(\alpha_0 - \varphi)}{\sin \varphi} \quad (4)$$



**Fig. 1** Schematics of material removal in the ultraprecision groove cutting, **a** serrated chip formation and force distribution in **b** diamond tool and **c** workpiece

where the shear angle between the shear direction and the cutting speed direction is  $\varphi$ , and  $a_p$  is the DoC. The shear angle could be calculated by:

$$\varphi = \arctan \frac{\frac{a_p}{a_t} \cos \alpha_0}{1 - \frac{a_p}{a_t} \sin \alpha_0} \quad (5)$$

where  $a_t$  is the thickness of the chips. The force  $F_n$  applied to the workpiece causes it to produce shear deformation in the main cutting area, and the  $F_n$  might be expressed using the following equation in accordance with the geometric relationship shown in Fig. 1c.

$$F_n = \frac{F_i + f_1 \sin(\varphi + \psi)}{\cos(\varphi + \psi)} \quad (6)$$

where  $\psi$  is the shear angle between the shear direction and the direction of the cutting speed, and  $F_i$  is the internal force needed to resist workpiece plastic deformation. The normal force and thrust force, respectively, are proportional to the frictional forces  $f_1$  and  $f_2$ .

$$f_1 = \mu_1 F_n, f_2 = \mu_2 F_t \quad (7)$$

where the corresponding tool-chip and tool-workpiece friction coefficients are  $\mu_1$  and  $\mu_2$ , respectively. The two friction coefficients are given a reasonable value of 0.4. [21]. As a result, from Eqs. (1) and (7), the spring back force  $F_s$  is expressed by:

$$F_s = (1 - \mu_2 \sin \theta) F_t - (\sin \psi - \mu_1 \cos \psi) F_n \quad (8)$$

The internal force  $F_i$  causing the shear deformation can be calculated as follows:

$$F_i = \sigma_e A_i = \frac{\sigma_e w_c a_p}{\sin \varphi} \quad (9)$$

where  $A_i$  is the area of the shear deformation plane,  $w_c$  is the width of the cutting chips, and  $\sigma_e$  is the corresponding internal stress needed to overcome the plastic flow of the workpiece in the deformation zone. The corresponding internal stress is defined as follows using the von Mises criterion:

$$\sigma_e = \frac{\sigma_i}{\sqrt{3}} \quad (10)$$

where  $\sigma_i$ , the internal stress, is the result of the addition of the dislocation drag stress  $\sigma_d$  under high stress rates, the atmospheric stress  $\sigma_{ath}$ , and the thermal stress  $\sigma_{th}$  [19]:

$$\sigma_i = \sigma_{th} + \sigma_{ath} + \sigma_d \quad (11)$$

The Kocks-Mecking model is employed to evaluate thermal stress [22, 23]:

$$\sigma_{th} = \sigma_0 \left[ 1 - \left( \frac{RT_1}{\Delta G} \ln \frac{\dot{\varepsilon}_0}{\dot{\varepsilon}} \right)^{\frac{1}{q}} \right]^{\frac{1}{p}} \quad (12)$$

where  $\sigma_0$  represents the initial stress,  $\Delta G$  is the energy to activate deformation,  $\dot{\varepsilon}_0$  represents the reference strain rate,  $\dot{\varepsilon}$  is the strain rate at deformation,  $p$  and  $q$  are material constants, and  $T_1$  is the temperature at the main deformation zone. The strain rate is described as follows:

$$\dot{\varepsilon} = \frac{\varepsilon}{t} \quad (13)$$

where  $\varepsilon$  represents the shear strain in the main deformation zone, and  $t$  is the amount of time spent deforming. They are calculated as follows [24]:

$$\varepsilon = \frac{\cos \alpha_0}{2 \sin \varphi \cos(\varphi - \alpha_0)} \quad (14)$$

$$t = \frac{h_i}{2\pi r_i v_s} \quad (15)$$

where  $v_s$  and  $r_i$  are the spindle speed and the radius of  $i$ th groove, and  $h_i$  is the average height of the chip segment. The dislocations ( $\sigma_g$ ) and grain boundaries ( $\sigma_g$ ) that cause athermal stress are provided by [19]:

$$\sigma_{th} = \frac{\alpha_g \mu \sqrt{b}}{\sqrt{D}} + \alpha_\rho \mu b \sqrt{\rho} \quad (16)$$

where  $D$  is workpiece average grain size,  $\rho$  represents the dislocation density, While  $\alpha_g$  is the constant regarding grain boundaries and  $\alpha_\rho$  is the constant concerning dislocation forests. For  $\alpha$  phase and  $\beta$  phase, respectively, the Burgers vector  $b$  values  $2.95 \times 10^{-10}$  m and  $2.86 \times 10^{-10}$ . And,  $\mu$  is the shear modulus, a function of temperature that can be expressed by the following equation:

$$\mu = 48.66 - 0.32223T_1 \quad (17)$$

The dislocation drag stress  $\sigma_d$  might potentially become part of the internal stresses during metal cutting at high strain rates ( $>10^3 \text{ s}^{-1}$ ), as seen below [19]:

$$\sigma_d = \alpha_d \dot{\epsilon} \quad (18)$$

where  $\sigma_d$  is the dislocation drag coefficient ( $\sigma_d = 4.5 \text{ kPa}\cdot\text{s}$ ).

Given that both the  $\alpha$  and  $\beta$  phases have an impact on the deformation of the Ti6Al4V alloy, the total internal stress required is [25]:

$$\sigma_i = f_\alpha \sigma_{i,\alpha} + f_\beta \sigma_{i,\beta} + \sigma_d \quad (19)$$

where  $f_\alpha$  and  $f_\beta$  are the respective volume fractions of the  $\alpha$  and  $\beta$  phases. The sum of  $f_\alpha$  and  $f_\beta$  is 1. As the temperature rises, the amount of the  $\alpha$  phase decreases, as shown by [26]:

$$\begin{cases} f_\alpha = 0.82 \{1 - \exp[0.012(T_1 - T_\beta)]\}, T \leq T_\beta \\ f_\alpha = 0, T \geq T_\beta \end{cases} \quad (20)$$

where the  $\beta$  phase transition temperature  $T_\beta$  is 1268 K. The associated thermal and athermal stresses can be used to determine the internal stresses  $\sigma_{i,\alpha}$  and  $\sigma_{i,\beta}$  generated from the  $\alpha$  phase and  $\beta$  phase, respectively. However, because of the intensive recovery at high temperatures, just thermal stress is taken into account for the  $\beta$  phase with temperatures over  $T_\beta$ .

In accordance with the geometric relationship of the diamond tool, the following equation can be used to estimate the width of serrated cutting chips.

$$w_c = 2\sqrt{r_d^2 - (r_d - a_p)^2} = 2\sqrt{2r_d a_p - a_p^2} \quad (21)$$

The internal force  $F_i$  can be expressed as follows using Eqs. (9) through (11), (19), and (21):

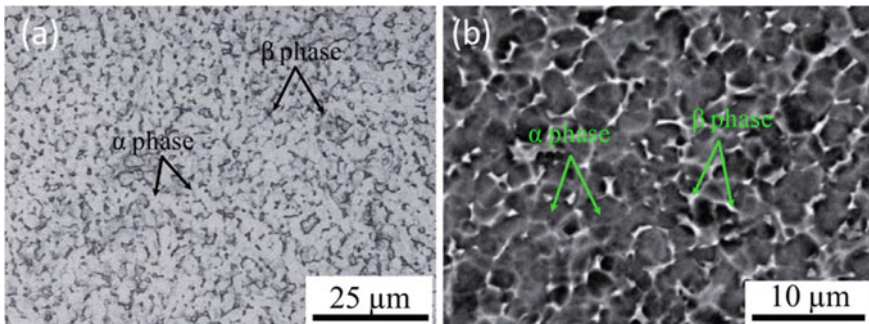
$$F_i = \frac{2a_p \sqrt{r_d^2 - (r_d - a_p)^2}}{\sqrt{3} \sin \varphi} [f_\alpha (\sigma_{i,\alpha}^{th} + \sigma_{i,\alpha}^{ath}) + (1 - f_\alpha) (\sigma_{i,\beta}^{th} + \sigma_{i,\beta}^{ath}) + \sigma_d] \quad (22)$$

## 2.2 Materials and Experimental Procedures

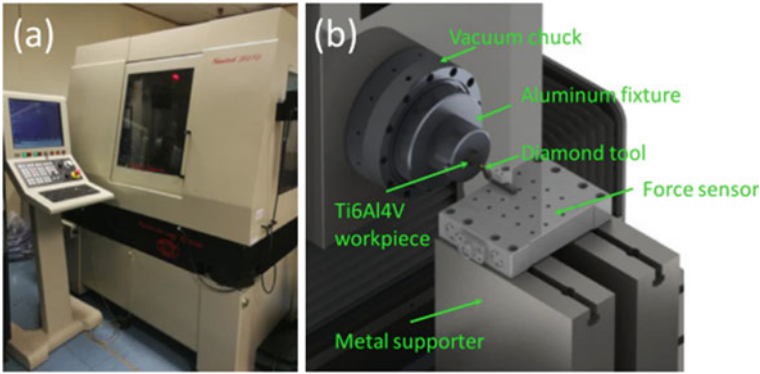
For microscopic structural study and microgroove cutting, Ti6Al4V alloys that had a diameter of roughly 16 mm were used. The optical and electronic microstructures under room temperature of the Ti6Al4V alloy having phases  $\alpha$  and  $\beta$  are shown in Fig. 2. The white and dark parts in Fig. 2a, b, respectively, demonstrate that the alloy is largely made up of the  $\alpha$  phase, having an average grain size of roughly 3  $\mu\text{m}$ . Between two adjacent  $\alpha$  phases,  $\beta$  particles are distributed.

Firstly, the alloy was divided into six samples using a wire electrical discharge machine, each covering approximately 18 mm in length. The samples were then mechanically ground using a succession of silicon carbide (SiC) papers and polished by a polishing cloth that contained SiC particles averaging approximately 0.5  $\mu\text{m}$  in size to achieve a comparatively flat surface. To observe the microstructure, 50 percent of the samples were etched chemically in a solution containing HF: HNO<sub>3</sub>: H<sub>2</sub>O = 1: 3: 5, while the other samples were used to carve microgrooves.

As shown in Fig. 3a, a 4-axis ultra-precision machine Moore Nanotech 350FG was used for both rough machining and microgroove cutting. The workpiece Ti6Al4V was fixed to an aluminium fixture, and the vacuum chuck of the ultra-precision machine sucked the fixture throughout. For the groove cutting, a brand-new diamond tool with the following specifications was used: edge radius of 0.25  $\mu\text{m}$ , rake angle of 0°,



**Fig. 2** Microstructures of Ti6Al4V alloys obtained from **a** optical microscope and **b** scanning electron microscope



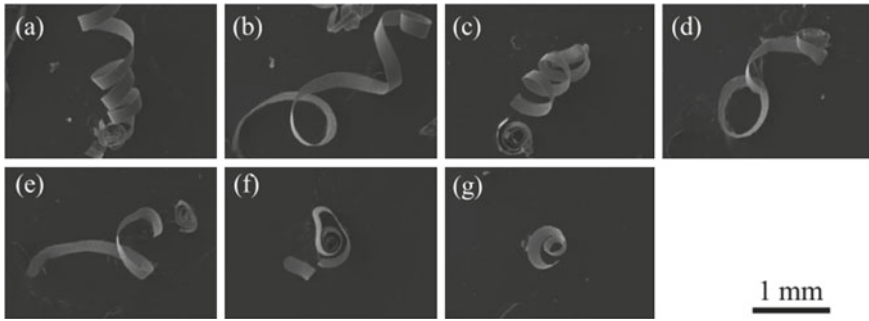
**Fig. 3** Ultraprecision machining set-up of **a** a physical image of the Moore Nanotech 350FG and **b** a schematic diagram

corner radius of 1.112 mm and front clearance angle of  $12.5^\circ$ . Under the tool holder, a Kistler 9256C1 force sensor was installed for tracking cutting and thrust forces. In order to obtain a flat surface, the workpiece was first processed using a different diamond tool with a rake angle of  $0^\circ$ , a corner radius of 1.0002 mm and a front clearance angle of  $12.5^\circ$ . Next, to ensure flatness, the surface was twice finished cut at a DoC of  $3 \mu\text{m}$ , a spindle speed of 1000 rpm and a feed rate of  $4 \mu\text{m/r}$ . The final step involved fabricating seven microgrooves with gradually rising DoC to  $5 \mu\text{m}$  at radiuses: 1 mm, 2 mm, 3 mm, 4 mm, 5 mm, 6 mm, and 7 mm of the workpiece. The corresponding cutting speeds  $v_c$  are 62.83 mm/s, 125.66 mm/s, 188.50 mm/s, 251.33 mm/s, 314.16 mm/s, 376.99 mm/s and 439.82 mm/s. The experiment set-up for groove cutting and finish machining is shown schematically in Fig. 3b. To assure reliability, the cutting experiment was carried out three times.

A LEICA DFC 450 optical microscope was employed to observe material microstructures. The morphologies of microgrooves, microstructures, and cutting chips were detected using a scanning electron microscope (SEM, Tescan VEGA3). A Nexview three-dimension (3D) optical surface profiler (Zygo) was utilized to obtain the surface topographies and groove profiles.

### 2.3 Serrated Chip Formation and Cutting Temperature Evolution

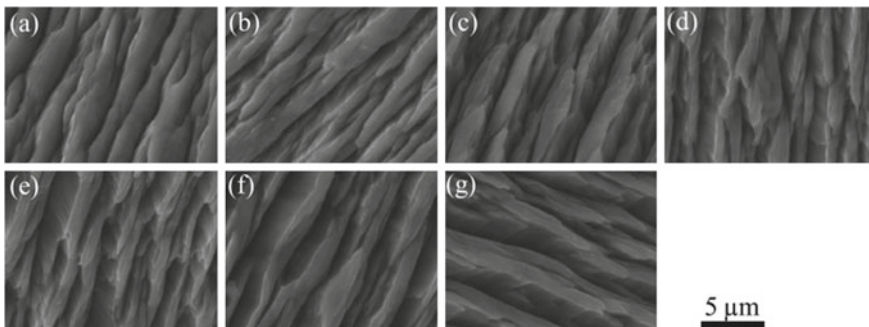
Figure 4 shows the morphologies of the chips at the seven grooves after machining. After the cutting procedure, continuous cutting chips could be obviously observed for each groove because of the low cutting speeds compared to the high-speed machining of Ti6Al4V, where the high-speed cutting speed exceeds a few tens of meters per second, a condition that may result in discontinuous chips being formed during machining [27].



**Fig. 4** Continuous cutting chips of the seven grooves at cutting speeds of **a** 439.82 mm/s, **b** 376.99 mm/s, **c** 314.16 mm/s, **d** 251.33 mm/s, **e** 188.50 mm/s, **f** 125.66 mm/s and **g** 62.83 mm/s

As seen in Fig. 5, a continuous cutting chip is often made up of numerous small, successive chip segments. Even at a very slow cutting speed of 62.83 mm/s, typical serrated chips could be seen for each groove. Nevertheless, the distance from one chip segment to another neighbouring chip segment changes with grooves. The distance between two adjacent segments is decreased as the cutting speed increases. Additionally, different cutting chips have variable segment heights  $h_i$  and contact widths  $w_i$  between the chip segment and the diamond tool, which is measurable using chip morphologies. Table 1 lists the average values of  $w_i$  and  $h_i$  at the DoC of 5  $\mu\text{m}$ , which were calculated using a minimum of twenty segments for every cutting chip. The table also includes the average measured thrust forces at various cutting speeds and a depth of 5  $\mu\text{m}$ .

It makes sense to measure the temperature as different grooves are being machined since the temperature has a substantial impact on the deformation of the workpiece. However, it is challenging to directly monitor the temperature of the deformation zone during the machining process. Hence, the temperature evolution is estimated



**Fig. 5** Serrated chip morphologies at cutting speeds of **a** 439.82 mm/s, **b** 376.99 mm/s, **c** 314.16 mm/s, **d** 251.33 mm/s, **e** 188.50 mm/s, **f** 125.66 mm/s and **g** 62.83 mm/s



**Table 1** Experimental parameters for various microgrooves

Grooves	1st	2nd	3rd	4th	5th	6th	7th
$v_c(mm/s)$	439.82	376.99	314.16	251.33	188.50	125.66	62.83
$w_i(\mu m)$	1.738	1.850	1.921	2.080	2.387	3.125	3.282
$h_i(\mu m)$	3.042	3.081	3.080	3.123	3.120	3.285	3.856
$\dot{\epsilon}_i \times 10^{-4}(s^{-1})$	9.398	7.909	6.594	5.171	3.883	2.407	0.973
$F_t(N)$	1.823	2.017	2.173	2.206	2.242	2.243	2.245

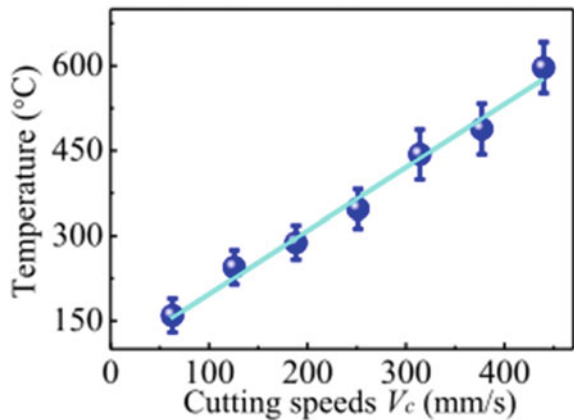
using the geometry and physical models described in Sect. 2.1 of this chapter. In Table 2, relevant data from previous research is summarized.

The estimated temperature in the primary deformation zone of the seven microgrooves is shown in Fig. 6. With an increase in cutting speeds from 62.83 to 439.82 mm/s, the average temperature roughly rises linearly from 150 to 600 °C.

The calculated maximum temperature is only about 641.78 °C, which is significantly lower than the phase change temperature of the Ti6Al4V alloy (which is about

**Table 2** Parameters for models calculation

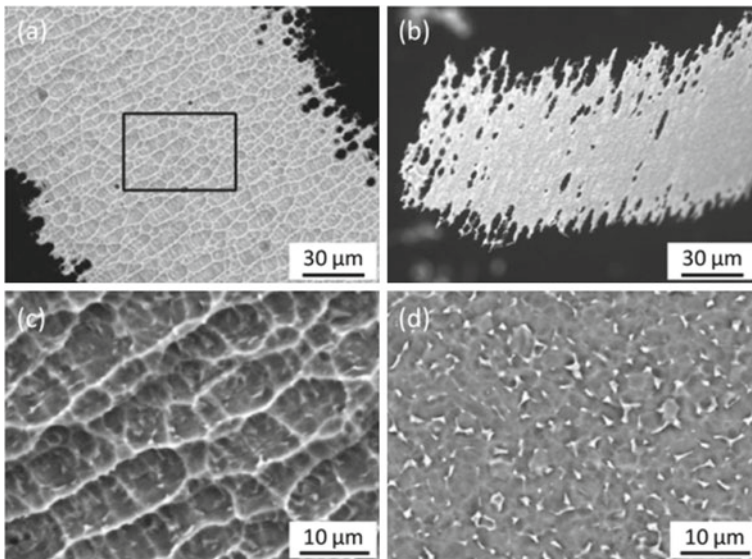
Parameter	Value	References	Parameter	Value	References
$\sigma_{0,\alpha}(MPa)$	1078.6451	[25]	$q_\beta$	1	[28]
$\dot{\epsilon}_{0,\alpha}(s^{-1})$	$10^{17}$	[25]	$p_\beta$	0.4	[28]
$\Delta G_\alpha(Kj \cdot mol^{-1})$	560.2436	[25]	$\alpha_g$	0.4544	[19]
$q_\alpha$	1.1131	[25]	$\alpha_\rho$	0.5	[19]
$p_\alpha$	0.3189	[25]	$\rho(m^{-2})$	$10^{12}$	[19]
$\sigma_{0,\beta}(MPa)$	1200	[28]	$k(W \cdot m^{-1} \cdot k^{-1})$	7.0	[29]
$\dot{\epsilon}_{0,\beta}(s^{-1})$	$2 \times 10^{13}$	[28]	$\alpha_a(W \cdot m^{-2} \cdot k^{-1})$	100	[30]
$\Delta G_\beta(Kj \cdot mol^{-1})$	200	[28]	$\rho_m(kg \cdot m^{-3})$	$4.42 \times 10^3$	[31]

**Fig. 6** Temperature evolution with cutting speed in the machining of Ti6Al4V alloys

994 °C), despite the fact that the temperature grows with cutting speed [26]. As a result,  $\beta$  grains may become coarser as temperature rises as a result of the energy gained, however, no phase transition from  $\alpha$  phase to  $\beta$  phase was anticipated to take place during the machining of each groove.

According to Fig. 7a–d, the microstructure derived from the microgroove of the seventh groove and serrated chip confirms that no phase transformation takes place in the machining procedure. The microstructures acquired from the magnifying morphology (rectangular mark) in Fig. 7a and the surface of the seventh groove, respectively, are shown in Fig. 7c, d. It can be seen that the  $\alpha$  phase and the  $\beta$  particles make up both microstructures. Furthermore, in the morphology, neither secondary  $\alpha$  phase nor lamellar  $\alpha$  phase that has transformed from the  $\beta$  phase is visible, proving that no phase transformation from the phase ( $\alpha + \beta$ ) to the single  $\beta$  phase has taken place in the procedure of groove machining. By contrasting Fig. 7a, b, it can be seen that multiple reticulate patterns may be seen on the free surface of serrated chips. The pattern is thought to be induced by the erosion of many serrated chip segments after chemical etching.

In addition, despite the fact that the  $\beta$  grains on the groove surface have been coarsened, the average size of the  $\beta$  particles in the serrated chips is significantly less than it was in the original microstructures. Chips are typically subjected to high strain and strain rate during the machining process, which increases the probability that the grains may be crushed into little grains [32]. Additionally, the serrated chips may contain a significant number of dislocations induced by the intense plastic



**Fig. 7** SEM morphologies of the **a** free surface and **b** machined surface of the 7th serrated chip after chemical etching; microstructures from **c** the magnifying free surface marked in **(a)** and **(d)** the surface of the 7th groove after machining

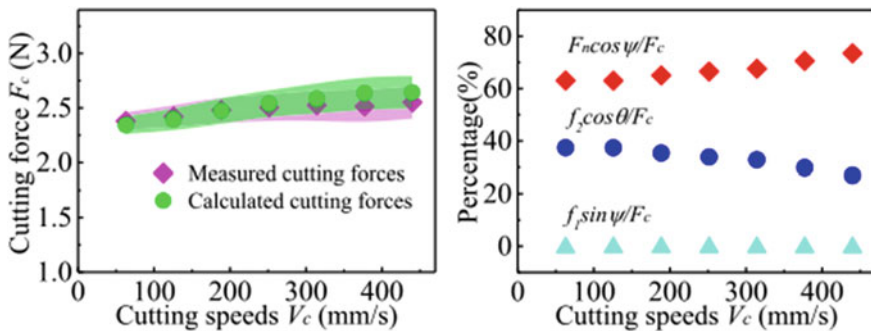
deformation, and the grains are prone to recrystallize as the cutting temperature rises. During the machining of titanium, aluminum, and copper alloys, grain refinement in the cutting chips has been observed [33–35]. Nevertheless, when the temperature rises, grain growth rather than refinement of  $\beta$  phase is observed on the groove surface. This is consistent with Eq. (20), which states that as the temperature rises, the volume fraction of the  $\alpha$  phase decreases while the  $\beta$  phase increases.

## 2.4 Cutting Force Validation

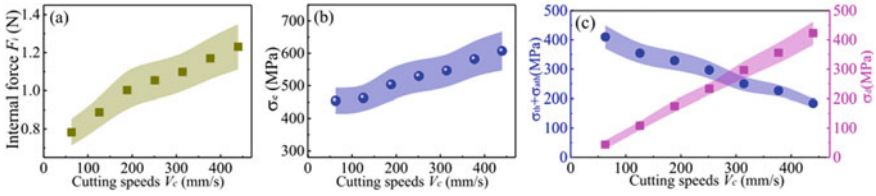
The cutting forces of the seven grooves based on the measurement and models are compared in Fig. 8a. The pink shadow area shows the error bands of measurement, while the green shadow area represents the error bands of calculation. According to both results, a slight rise in cutting force with an increase in cutting speed. For the measurement and calculation, respectively, the average forces increase from roughly 2.38 to 2.55 N and from roughly 2.34 to 2.64. As a result, the inaccuracy of the models is within a range of 3.53%. Additionally, at cutting speeds below 251.33 mm/s, the estimated forces from the model are well consistent with the experimental results, however, the higher cutting speeds, the calculated forces exhibit slightly large values.

Figure 8b displays the contribution to the cutting forces. As can be observed, over 60% of the cutting force for each groove comes from the normal force, which makes a major contribution to the cutting force. In particular, the percentage could go as high as 73.51% when the seventh groove is machined at a cutting speed of 439.82 mm/s. In contrast, the friction between the diamond tool and the serrated chips accounts for a small percentage of the cutting force during the machining of all grooves.

Figure 9 shows the evolution of the internal force and equivalent stress at various cutting speeds. The internal force exhibits an increasing trend with increasing of cutting speeds at the DoC of 5  $\mu\text{m}$ . As the cutting speed increases from 62.83 mm/s to 439.82 mm/s, the equivalent stress rises from around 410 MPa to 660 MPa. An



**Fig. 8** **a** Measured and calculated cutting forces at different cutting speeds and **b** contributions of normal and frictional forces to the cutting force at different cutting speeds



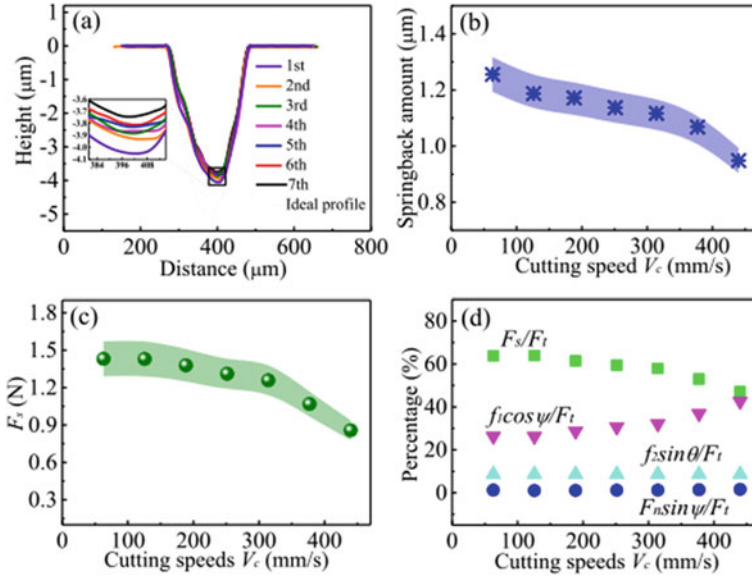
**Fig. 9** The evolution of **a** internal forces, **b** equivalent stresses and **c** stresses with cutting speeds

increase in temperature often causes a decrease of the resistance of plastic deformation. Since high cutting speed could result in high cutting temperature, the total amount of thermal and athermal stresses needed to overcome plastic deformation should decrease with the cutting speeds. However, the dislocation drag stress is also an important fraction of the equivalent stress according to the Eq. (11). In Fig. 9c, it is clearly seen that the dislocation drag stress gradually increases with cutting speeds due to the extremely high strain rates in the machining, while the total amount of thermal and athermal stress decreases as cutting speeds increase. Consequently, the equivalent stress shows an increasing trend with the cutting speeds.

## 2.5 Spring Back Force Analyses

The profiles of the seven measured grooves at different radii and an ideal profile are compared in Fig. 10. The measured profiles are not perfectly symmetrical along the curve center because of the tool setting error, but it does not impact on the analysis of material spring back behavior that can be seen from the depth difference between the ideal and measured curves. The measured depth steadily rises with radius, as seen in the magnified figure in Fig. 10a, indicating that the amount of spring back decreases as cutting speeds increase. The height disparities between the measured and desired depth of the seven microgrooves with different cutting speeds are shown in Fig. 10b. An increasing of cutting speed results in a small amount of spring back, and it is consistent with the fluctuation of material spring back forces with cutting speeds. In other words, a small spring back amount usually gives rise to a small spring back force.

According to Eq. (1), the thrust force is essentially determined by the normal force, the spring back force, the front clearance angle, two frictional forces, and the equivalent contact angle. The terms in Eq. (1) that affect the evolution of the thrust force are compared in Fig. 10d. It can be observed that the spring back force accounts for more than 45% of the thrust force, and the percentage rises as cutting speeds fall. When the cutting speed reduces to 62.83 mm/s, the proportion of the spring back force reaches approximately 63.74% of the total thrust force. The remaining force is from two frictional forces and a normal force by taking into account the front clearance angle and equivalent contact angle. Overall speaking, the spring back force is one of



**Fig. 10** a Cross-sectional profiles of seven cutting grooves and an ideal groove; cutting speeds effects on b spring back amount and c spring back forces; d four factors contributing to the thrust force at various cutting speeds

the key contributors to the thrust force in the ultraprecision machining of Ti6Al4V alloys.

### 3 Evaluation of Cutting Energy in Machining of MLAs

#### 3.1 Cutting Energy Models for Fabricating MLAs

With the increased importance of sustainable development, the study of energy consumption in ultra-precision machining has become necessary. In this section, material removal energy models are proposed in manufacturing of MLAs on single crystal silicon by the slow tool servo (STS) diamond turning. The total net energy  $E$  for the material removal is the sum of the energy consumption per revolution:

$$E = \sum_1^n E_n \quad (23)$$

where  $E_n$  is the removal energy of the  $n$ th revolution. It is equal to the work  $W_n$  induced by the cutting force, containing the main cutting force  $F_{c,n}$ , thrust force  $F_{t,n}$  and feeding force  $F_{f,n}$ . Accordingly, the energy  $E_n$  can be further represented by:

$$E_n = W_n = F_{c,n}L_{1,n} + F_{t,n}L_{2,n} + F_{f,n}L_{3,n} \tag{24}$$

where  $L_{1,n}$ ,  $L_{2,n}$ ,  $L_{3,n}$  are the lengths of the material removal in the main cutting, thrust and feeding direction at the  $n$ th rotation. The projected image of one microlens profile in the O-xy plane is shown in Fig. 11a, along with a portion of the shape at the  $n$ th revolution. The lengths at the  $n$ th revolution could be estimated to be:

$$L_{1,n} = 2L_{OK_n}\sin\theta = 2(L_{OM} - nf)\sin\theta \tag{25}$$

$$L_{2,n} = 2P_nD = 2\left(R - \sqrt{R^2 - [(L_{OM} - nf)\sin\theta]^2}\right) \tag{26}$$

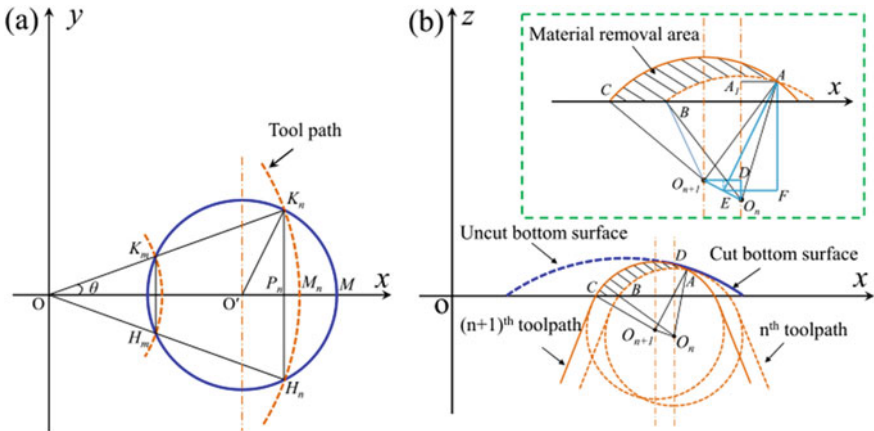
$$L_{3,n} = 2L_{P_nM_n} = 2(L_{OM} - nf)(1 - \cos\theta) \tag{27}$$

where  $L_{OM}$  is the lengths of line OM,  $f$  is the feedrate,  $R$  is the curvature radius of the micro-lens, and  $\theta$  is the angle of the sector  $\widehat{OK_nM_n}$ , which could be calculated in the triangle  $OO'K_n$  based on the Cosine law:

$$\theta = \arccos\frac{L_{OK_n}^2 + L_{OO'}^2 - L_{O'K_n}^2}{2L_{OK_n}L_{OO'}} \tag{28}$$

The specific cutting energy (SCE)  $U$  is another crucial indicator to assess the energy consumption in the machining, which is defined as [36]:

$$U = \frac{E_n}{V_n} \tag{29}$$



**Fig. 11** A schematic diagram of the STS diamond turning: **a** the lateral view and **b** the top view

where  $V_n$  is the material removal volume at the  $n$ th revolution, which could be calculated based on the numerical integration:

$$V_n = \sum_{i=1}^{m-1} \frac{S_{n,i} + S_{n,i+1}}{2} L_i = \frac{S_{n,i} + S_{n,i+1}}{2} \frac{\pi \theta_i}{180} (L_{OM} - nf) \quad (30)$$

where  $L_i$  is the arc length of the  $H_{n,i}K_{n,i}$ ,  $\theta_i = 0.25^\circ$ , and  $S_{n,i}$  is the region area at  $i$ th point. Based on the geometric relationship depicted in Fig. 11, the area  $S_{n,i}$  can be calculated by:

$$S_{n,i} = S_{O_{n+1}CA} + S_{O_{n+1}O_nA} - S_{O_nBA} + S_{O_{n+1}O_nBC} \quad (31)$$

where  $S_{O_{n+1}CA}$ ,  $S_{O_{n+1}O_nA}$ ,  $S_{O_nBA}$  and  $S_{O_{n+1}O_nBC}$  are area of the sector  $\widehat{O_{n+1}CA}$ , triangle  $O_{n+1}O_nA$ , sector  $\widehat{O_nBA}$  and quadrangle  $O_{n+1}O_nBC$ , respectively. They can be calculated as follows:

$$\begin{bmatrix} S_{O_{n+1}CA} \\ S_{O_{n+1}O_nA} \\ S_{O_nBA} \\ S_{O_{n+1}O_nBC} \end{bmatrix} = \begin{bmatrix} r_0^2 \arcsin \frac{D_{AC}}{r_0} \\ \frac{1}{2} D_1 \sqrt{r_0^2 - \left(\frac{1}{2} D_1\right)^2} \\ r_0^2 \arcsin \frac{D_{AB}}{r_0} \\ \sqrt{\frac{P_1}{2} (P_1 - r_0)(P_1 - D_1)(P_1 - D_2)} + \sqrt{\frac{P_2}{2} (P_2 - r_0)(P_2 - D_2)(P_2 - D_3)} \end{bmatrix} \quad (32)$$

where  $r_0$  is the radius of the diamond tool ( $r_0 = 1.145$  mm),  $D_{AC}$ ,  $D_{AB}$ ,  $D_1$ ,  $D_2$ ,  $D_3$  are the distance between points A and C, points A and B, points  $O_n$  and  $O_{n+1}$ , points  $O_{n+1}$  and B, points B and C, respectively.  $P_1$  and  $P_2$  are perimeters of the triangle  $\Delta O_{n+1}O_nB$  and  $\Delta O_nBC$ , respectively. In the material removal stage of STS diamond turning, the presented models can estimate the energy consumption and SCE caused by the material deformation but not include the energy used by the machine device. Since the volume is calculated utilizing numerical integration method using limit numbers when evaluating the SCE, the larger the sample number per revolution, the smaller the calculation error. In this experiment, a sampling size of 1440 points can ensure the precision of the calculations.

Material removal rate (MRR) can also be evaluated by the ratio of the material removal volume  $V$  to the cutting time:

$$MRR = \frac{V}{t} \quad (33)$$

where the time  $t$  is calculated to be as follows:

$$t = \frac{2\theta}{\theta_i} \cdot \frac{60}{1440v} \quad (34)$$

Furthermore, the hydrostatic stress has a significant impact on the deformation behaviour of the silicon workpiece. Goel et al. reported that phase transition from diamond cubic structure to metallic Si-II could enhance the ductile deformation of the brittle silicon [37]. In the STS turning of the MLAs, the hydrostatic stress at the  $n$ th revolution could be given by:

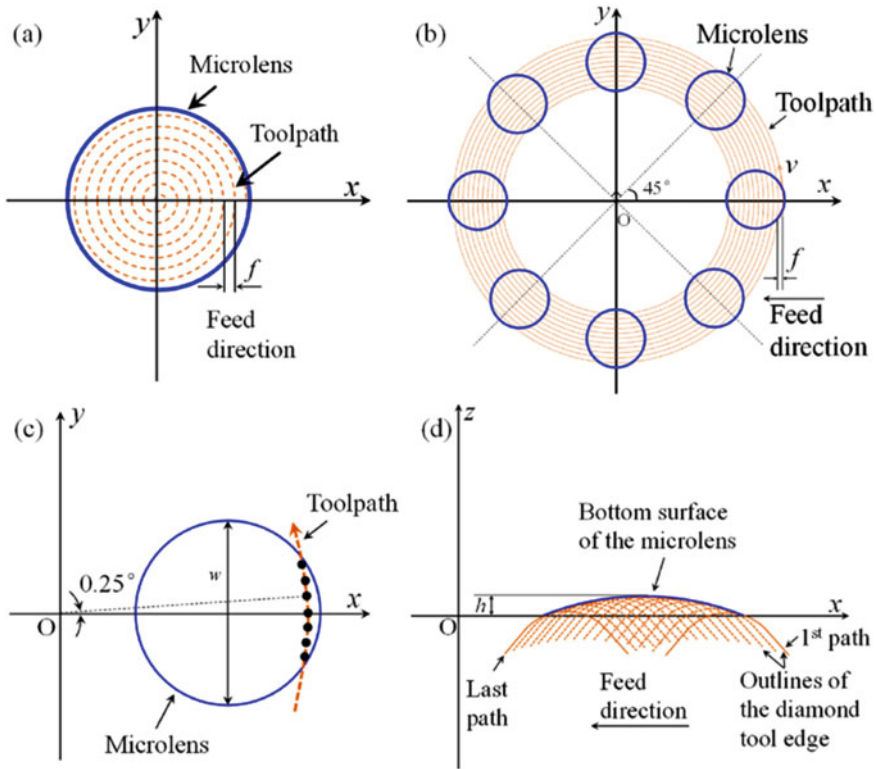
$$P_n = \frac{F_{c,n} \cos \alpha_{e,n} + F_{t,n} \sin \alpha_{e,n}}{S_n} \quad (35)$$

### 3.2 Materials and Experimental Procedures

The single crystal silicon (001) was used as the workpiece to fabricate the MLAs, and the workpiece dimension is 10 mm  $\times$  10 mm  $\times$  1 mm. The workpiece was firstly glued to the aluminium fixture by the aron alpha and the fixture was sucked on the vacuum chuck of the ultraprecision machine (Moore Nanotech 350FG). The roughing cutting was performed with a diamond cutter (nose radius: 1.495 mm, rake angle:  $-25^\circ$ , flank clearance angle:  $10^\circ$ ) to ensure a flat surface on the workpiece. Next, MLAs were fabricated the by the STS diamond turning using a fresh diamond tool (nose radius: 1.145 mm, rake angle:  $-25^\circ$ , flank clearance angle:  $12.5^\circ$ ). Under the fresh diamond tool, a force sensor was mounted (KISTLER 9256 C1) to measure the cutting forces.

One micro-lens was created in the center of the workpiece and eight in the position of 1 and 2 mm from the center of the Si workpiece, respectively. The angle between two adjacent lenses is  $45^\circ$  at the position of 1 mm and 2 mm. The tool trajectory is different for the center of the lens than for the outside of the lens. The trajectory in the process of machining the center lens is continuous and spiral, while the toolpath is discontinuous in the process of machining the outside lens, as compared in Fig. 12a, b. Figure 12c, d that demonstrate the lateral view and top view of the toolpath. The diameter  $d$  and height  $h$  of each micro-lens are 372  $\mu\text{m}$  and 4.5  $\mu\text{m}$ , respectively. The radius of curvature is about 3.85 mm. In the turning, the spindle speeds are 40 rpm, 20 rpm and 10 rpm at the center and positions of 1 mm and 2 mm, respectively. Feedrates of 1  $\mu\text{m}/\text{rev}$ , 2  $\mu\text{m}/\text{rev}$  and 3  $\mu\text{m}/\text{rev}$  are adopted in the turning. As shown in Fig. 2c, to ensure that the shape inaccuracy of the microlens is acceptable, the sample number of each revolution is 1440, so the angle between two adjacent points is  $0.25^\circ$ . Some relevant parameters used for the machining process are summarized in Table 3. The topographies and profiles of the MLAs were measured using an atomic force microscope (AFM, Park's XE-70) and a three-dimensional (3D) surface profiler (Nexview, Zygo). The morphologies of the surface damage were examined using a scanning electron microscope (SEM, Tescan VEGA3).





**Fig. 12** A schematic of toolpath in machining of **a** center lens and **b** outside lenses, **c** lateral view and **d** top view of the toolpath

**Table 3** Parameters in fabricating of micro-lens arrays

Parameters		
Diamond tool parameters	Nose radius	1.145 mm
	Rake angle	$-25^\circ$
	Flank clearance angle	$12.5^\circ$
Machining parameters	Spindle speeds	40, 20, 10 rpm
	Feedrates	1, 2, 3 $\mu\text{m}/\text{rev}$
	Sampling number	1440
Micro-lenses geometry	Radius	3.83 mm
	Height	4.5 $\mu\text{m}$

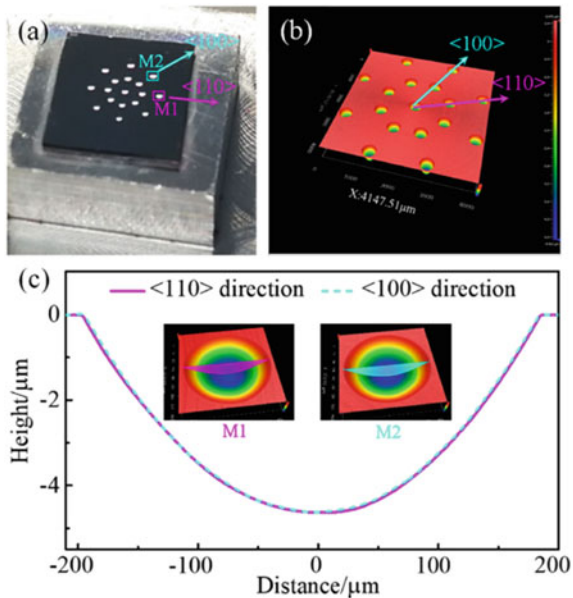
### 3.3 Surface Topographies of the MLAs

Figure 13a illustrates an example of MLAs fabricated on the workpiece in the  $\langle 100 \rangle$  and  $\langle 110 \rangle$  directions at a feedrate of  $2 \mu\text{m}/\text{rev}$  and the three-dimensional (3D) surface topography is shown in Fig. 13b. A total of 8 lenses were produced at the diameters of 1 mm and 2 mm, respectively. The morphologies and profiles of the lenses chosen from the two crystal directions indicated in Fig. 13a are shown in Fig. 13c. It can be seen that the profiles in the two directions almost overlap with each other, which means that the surface profile is not significantly impacted by the crystalline orientations. This is because the workpiece was almost removed in a ductile mode in the two directions since little fractures were discovered in all grooves.

The morphologies of the micro-lenses in the center of the workpiece at various feedrates are shown in Fig. 14a–c, and the corresponding surface quality are given in Fig. 14d–f. It can be seen that high surface quality with rare damage could be observed at the surface machined with a feedrate of  $1 \mu\text{m}/\text{rev}$ , and the surface roughness reaches nearly 4 nm. As the feedrate increased to 2 m/rev and 3 m/rev, the surface quality gradually degrades, which should be caused by the generation of surface damages on the lens, as indicated by the arrows in Fig. 14e, f. Damages are mostly generated in the  $\langle 100 \rangle$  crystal orientation, and they are obvious at the feedrate of  $3 \mu\text{m}/\text{rev}$ .

The topographies of the machined lenses at the diameters of 1 mm and 2 mm of the workpiece at various feedrates are compared in Fig. 15. At feedrates of  $1 \mu\text{m}/\text{rev}$  and  $2 \mu\text{m}/\text{rev}$ , it is discovered that few damages were observed on the lenses surface, but

**Fig. 13** a MLAs on the Si wafer, b 3D morphologies of the lenses in directions of  $\langle 100 \rangle$  and  $\langle 110 \rangle$  and c morphologies and profiles of the two lenses marked in (a)



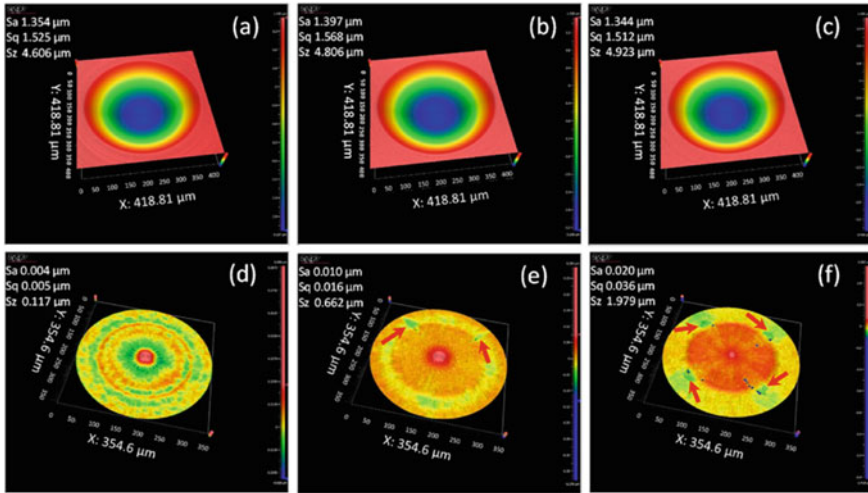


Fig. 14 Morphologies of the center lens generated at feedrates of a 1  $\mu\text{m}/\text{rev}$ , b 2  $\mu\text{m}/\text{rev}$ , c 3  $\mu\text{m}/\text{rev}$ , and d, e are corresponding surface qualities

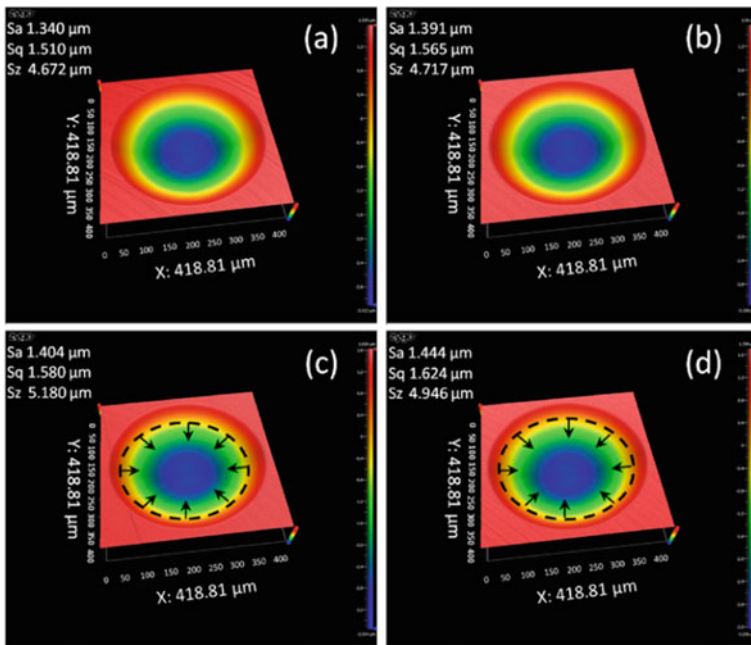
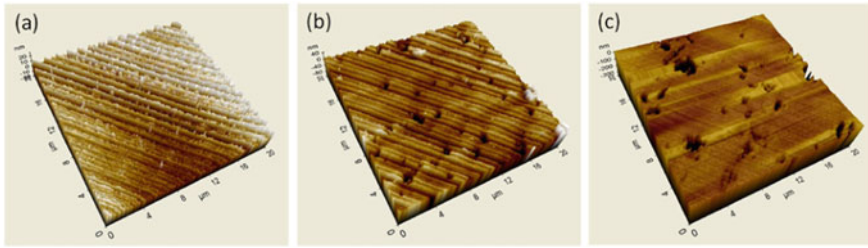


Fig. 15 Surface morphologies of the lenses at feedrates of a 1  $\mu\text{m}/\text{rev}$ , b 2  $\mu\text{m}/\text{rev}$ , c 3  $\mu\text{m}/\text{rev}$  at the diameter of 1 mm and d 3  $\mu\text{m}/\text{rev}$  at the diameter of 2 mm



**Fig. 16** AFM morphologies of one part of dimple surfaces at feedrates of **a** 1  $\mu\text{m}/\text{rev}$ , **b** 2  $\mu\text{m}/\text{rev}$  and **c** 3  $\mu\text{m}/\text{rev}$

numerous damages were found when the feedrate increased to 3  $\mu\text{m}/\text{rev}$ , especially in the area of the marked ellipse illustrated in Fig. 15c–d. The generation of the damages indicates that the brittle deformation occurs in the machining.

The surface quality of the dimples observed by the AFM at various feedrates are also compared in Fig. 16. At a feedrate of 1  $\mu\text{m}/\text{rev}$ , normal tool marks are generated on the machined surface and no damage is observed. However, some damages are discovered on the surface at feedrates of 2  $\mu\text{m}/\text{rev}$  and 3  $\mu\text{m}/\text{rev}$ . In detail, few surface damages are randomly generated and the tool marks are still visible at the feedrate of 2  $\mu\text{m}/\text{rev}$ . When the feedrate is increased to 3  $\mu\text{m}/\text{rev}$ , obvious surface damages are formed randomly and the tool marks cannot be seen clearly because of the formation of deep damages. According to Ref. [38], the formation of random fractures typically results in a decrease in cutting forces.

### 3.4 Evaluation of Material Removal Energies for Fabricating MLAs

Firstly, the energy consumption in diamond turning of the center micro-lens was analyzed. The primary cutting force and thrust force variation in producing of the center lenses with regard to varied feedrates is depicted in Fig. 17a. The cutting and thrust forces significantly increase when the feedrate is increased from 1  $\mu\text{m}/\text{rev}$  to 2  $\mu\text{m}/\text{rev}$ , however, there is a slight drop in forces when the feedrate is increased further to 3  $\mu\text{m}/\text{rev}$ . Additionally, the force fluctuation is more apparent with higher feedrates. This implies that cutting forces in ductile cutting are proportional to the amount of material removed but decrease as the brittle fracture increases in turning of the Si.

The average stresses perpendicular to the tool rake face are shown in Fig. 17b. At the beginning and ending stage of the turning, the average stresses of workpiece at the feedrate of 2  $\mu\text{m}/\text{rev}$  are nearly identical to those at the feedrate of 1  $\mu\text{m}/\text{rev}$ . However, a sudden reduction of the stresses is observed at the distance around 90  $\mu\text{m}$  for the cutting with the feedrate of 2  $\mu\text{m}/\text{rev}$ , which is in agreement with the region occurring surface damages in Fig. 14e. This indicates that the formation of surface

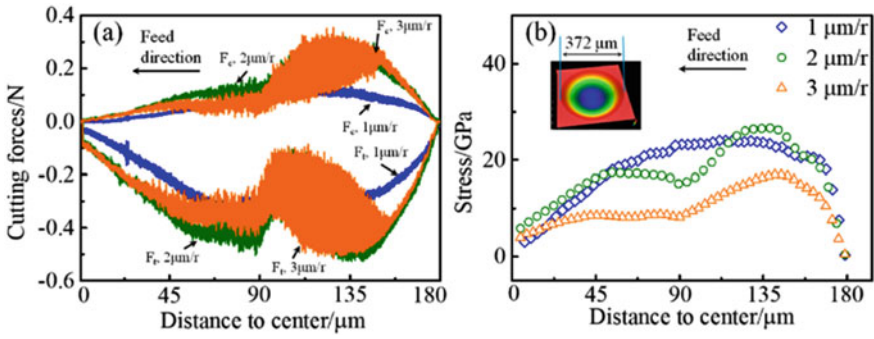


Fig. 17 Variation of **a** cutting forces and **b** average stresses perpendicular to the rake face in generation of center lenses with various feedrates

damages helps to reduce the average stresses needed to overcome material deformation. Furthermore, the average stresses to overcome material deformation is further decreased at the distance from 35 μm to 140 μm when the feedrate is increased to 3 μm/rev, which is also consistent with the area with surface damage shown in Fig. 14f. This suggests that the formation of the surface damages highly affects the required stress to overcome deformation. In ductile cutting mode, the required stress to overcome deformation is essentially independent of feedrates, but the stress decreases when the deformation transfers to brittle mode.

Figure 18 illustrates the variation of material removal energy and SCE in diamond turning of the center lens. A similar fluctuation trend is found for both of the material removal energy and SCE. They increase rapidly at the start of the cutting and then reduce gradually as the diamond cutter moves forward. Furthermore, increasing the feedrate from 1 μm/rev to 2 μm/rev leads to a large increase in material removal energy, but the energy increases slightly when the feedrate is further increased to 3 μm/rev. The maximum removal energy grows by about 90.67% when the feedrate increases from 1 μm/rev to 2 μm/rev, but the energy only increases by 6.25% as

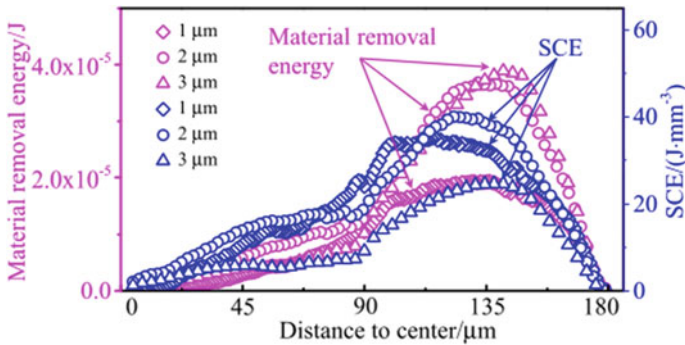


Fig. 18 Material removal energy and SCE in turning of the center lens with different feedrates

the feedrate rise from  $2 \mu\text{m}/\text{rev}$  to  $3 \mu\text{m}/\text{rev}$ . This difference of the energy change is mainly caused by the small change of cutting and thrust forces when the feedrate increases from  $2 \mu\text{m}/\text{rev}$  to  $3 \mu\text{m}/\text{rev}$ . However, the overall energy consumption of the cutting at the feedrate of  $1 \mu\text{m}/\text{rev}$  is higher than others since more revolutions are required at a low feedrate. Moreover, the evolution of SCE in the turning at feedrates of  $1 \mu\text{m}/\text{rev}$  and  $2 \mu\text{m}/\text{rev}$  exhibit a similar trend with the material removal energy and the values are close to each other, but the SCE in the turning with the feedrate of  $3 \mu\text{m}/\text{rev}$  is lower than others, especially at distances ranging from  $35 \mu\text{m}$  to  $140 \mu\text{m}$ . This is consistent with the evolution of stresses.

The creation of surface damages is considered to be responsible for the decrease in SCE at large feedrates. Figure 19 depicts the morphology of surface damages after machining at the feedrate of  $3 \mu\text{m}/\text{rev}$ . In the center of the dimple, the damage has an oval form. The damage begins to form at a distance of about  $140 \mu\text{m}$ , as shown in the center images. This corresponds to the stage depicted in Fig. 18 where material removal energy and SCE begin to decrease, implying that the emergence of surface damages reduces the material removal energy needed to overcome deformation. Additionally, the magnified images of the damage in Fig. 19 show an apparent cleavage characteristic, indicating that the deformation-induced surface damages are cleavage fractures. Furthermore, as indicated by the arrows, the cleavage fracture is more severe toward the start of the damage.

The latter part analyzes the energy consumption during the machining of micro-lens array at the diameters of 1 mm and 2 mm. Figures 20 and 21 demonstrate the

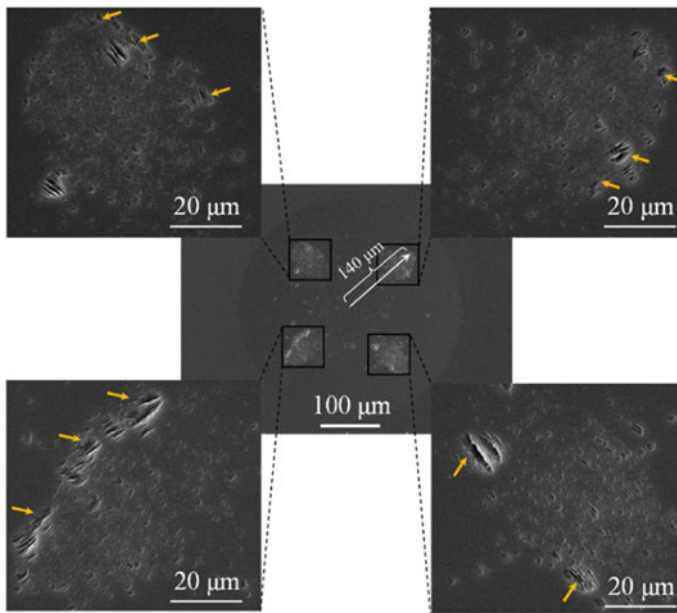
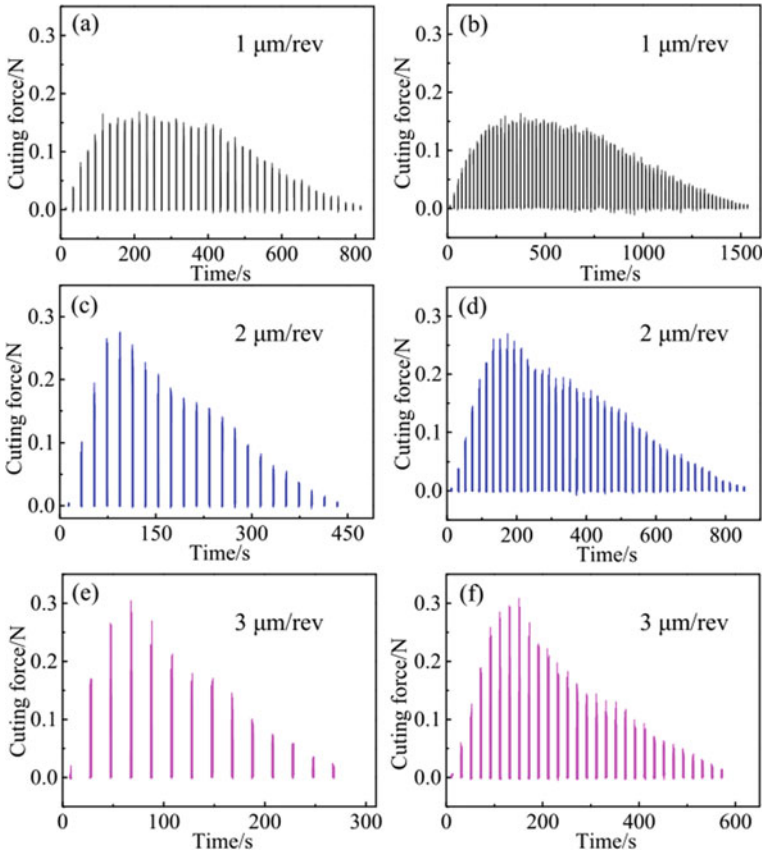


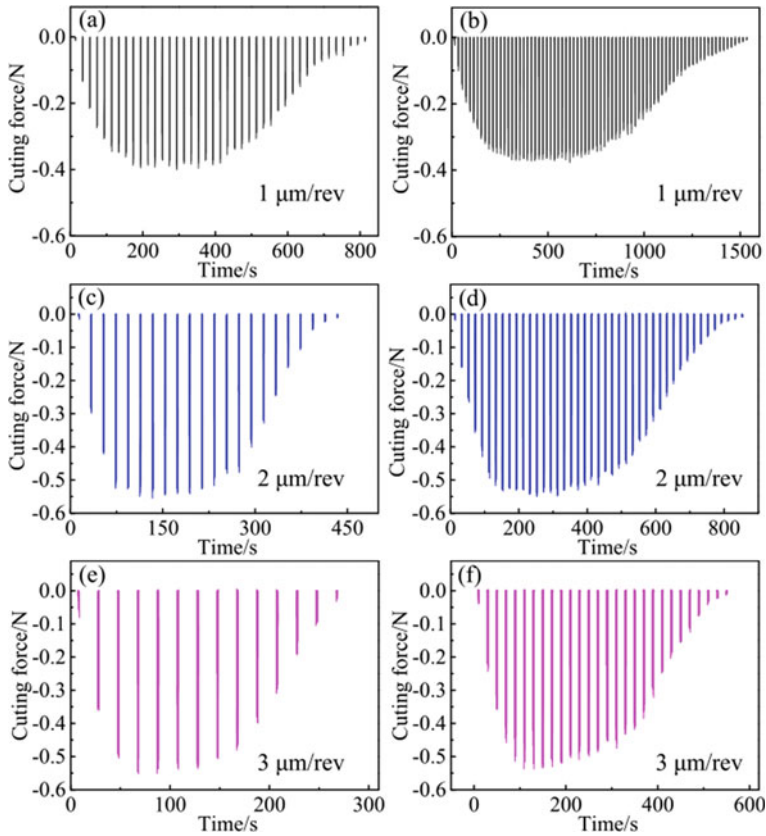
Fig. 19 SEM morphologies of the surface damages on the center dimple at the feedrate of  $3 \mu\text{m}/\text{rev}$



**Fig. 20** Cutting force evolution in generating of the dimples at the diameters of **a, c, e** 1 mm and **b, d, f** 2 mm at various feedrates

cutting and thrust forces in the machining of lenses with diameters of 1 mm and 2 mm, respectively, and an interval of 20 s is used to depict the force evolution. Cutting and thrust forces both increase fast at the start of the machining and gradually decrease with the forward motion of the diamond tool, and there is little difference between the values of the cutting and thrust forces at the two diameters since the cutting speeds are nearly identical.

However, during the entire process, the thrust forces are larger compared to the cutting forces. The negative rake angle of diamond cutter is supposed to induce the high thrust force. The maximum cutting forces during the turning process of silicon dimples could reach 0.16 N, 0.28 N, and 0.32 N at feedrates of 1  $\mu\text{m}/\text{rev}$ , 2  $\mu\text{m}/\text{rev}$ , and 3  $\mu\text{m}/\text{rev}$ , respectively. The maximum thrust forces at the corresponding feedrates might be as large as 0.39 N, 0.55 N, and 0.56 N. The highest resultant cutting forces rise by approximately 46.41% while the feedrate rise from 1  $\mu\text{m}/\text{rev}$  to 2  $\mu\text{m}/\text{rev}$ ; however, when the feedrate goes from 2  $\mu\text{m}/\text{rev}$  to 3  $\mu\text{m}/\text{rev}$ , the forces slightly

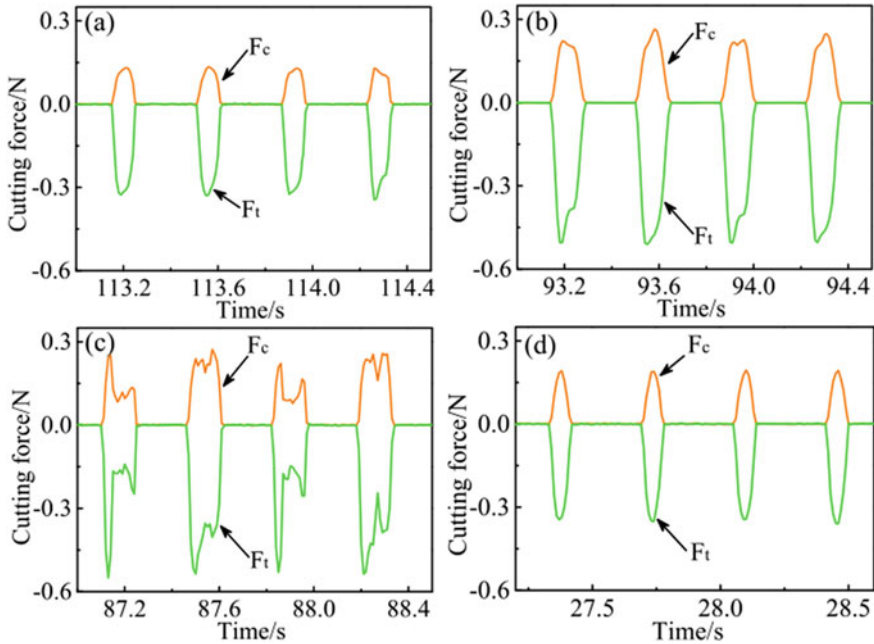


**Fig. 21** Thrust force evolution in generating of the dimples at the diameters of **a, c, e** 1 mm and **b, d, f** 2 mm at various feedrates

increase by roughly 4.51%. As a result, the increase in cutting forces is significant when the feedrate is increased from 1  $\mu\text{m}/\text{rev}$  to 2  $\mu\text{m}/\text{rev}$ .

Figure 22a–c show magnified views of the maximum cutting and thrust forces during the turning process of dimples at the diameter of 1 mm. The evolution of force during the machining of the outside dimples is discontinuous and exhibits a periodic change characteristic as a result of the change in the depth of cut, in contrast to the force evolution during the turning process of the center dimples. At feedrates of 1  $\mu\text{m}/\text{rev}$  and 2  $\mu\text{m}/\text{rev}$ , the largest cutting and thrust force waviness exhibits regular characteristics, meanwhile, at 3  $\mu\text{m}/\text{rev}$ , the force waviness is irregular. At small feedrates, a single peak force is shown at the center of each wave; however, at a feedrate of 3  $\mu\text{m}/\text{rev}$ , no peak force is seen. Instead, the cutting and thrust forces drop suddenly at the center of the per wave. The fluctuation of cutting and thrust forces at the high feedrate of 3  $\mu\text{m}/\text{rev}$  could be caused by the deformation of the silicon workpiece due to the force waviness remain regular when the turning process began,





**Fig. 22** Magnified images of the largest cutting and thrust forces at feedrates of **a**  $1 \mu\text{m}/\text{rev}$ , **b**  $2 \mu\text{m}/\text{rev}$ , **c**  $3 \mu\text{m}/\text{rev}$ , and the initial forces of **(c)**  $3 \mu\text{m}/\text{rev}$

as shown in Fig. 22d. Due to the little amount of material removed during the initial cutting step, the workpiece was machined in the ductile mode, as a result, the shape of force waviness is regular. The cutting depth grows gradually as the diamond tool continues to move, and once the undeformed chip thickness surpasses the critical cutting depth, the deformation behaviour of silicon workpiece changes from ductile mode to brittle mode. This causes the main cutting and thrust forces to fluctuate significantly.

The evolution of the typical stresses parallel to the rake face of the diamond tool during the machining of lenses at the 1 mm diameter is shown in Fig. 23. It is discovered that the average stress gradually reduces when feedrates are increased, which is primarily attributed to the occurrence of random fractures on the surface. This suggests that if brittle fractures were created on the surface, the required stress to overcome deformation would decrease.

Figure 24 compares the MRR and material removal energy during the machining of the lenses at the diameter of 1 mm. Even the feedrates are different, the MRR has a similar pattern, i.e., it rises with cutting and reaches its peak value at one-third of the cutting (point B), and then gradually falls with cutting time, as shown in Fig. 24a. This indicates that as the diamond cutter goes to the position of the one-third of the dimples, the amount of material removed reaches its maximum value.

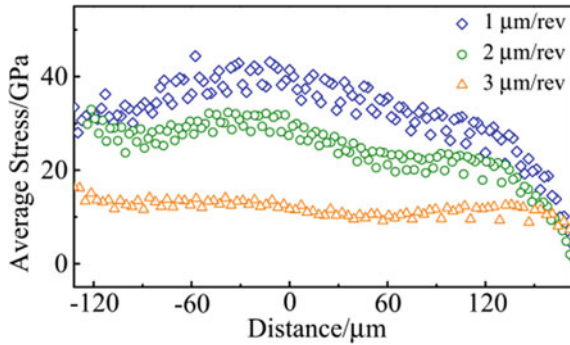


Fig. 23 Evolution of the stresses perpendicular to the rake face of the diamond tool

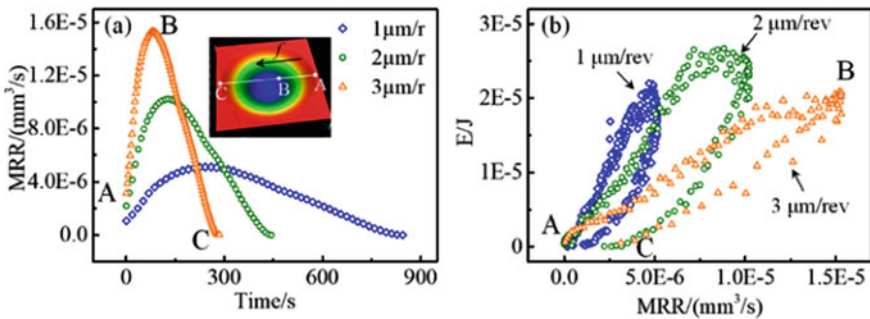
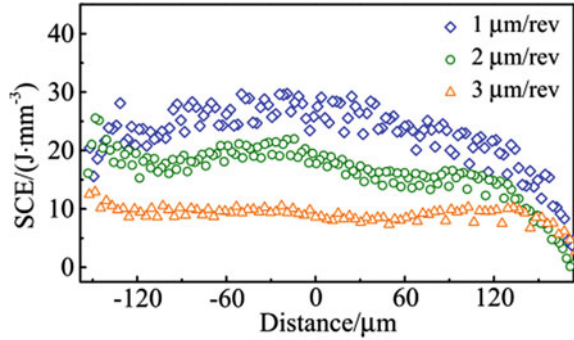


Fig. 24 The relationship of **a** MRR and time, **b** net material removal energy and MRR at various feedrates

The link between the net material removal energy and the MRR is depicted in Fig. 24b. The amount of energy needed to resist deformation at a particular feedrate increases as MRR increases, and then reaches the peak at maximum MRR, and then decreases as MRR reduces. It is interesting to find that the net material removal energy exhibits a hysteresis characteristic. For instance, in the cutting with a feedrate of 3  $\mu\text{m}/\text{rev}$ , the removal energy needed to overcome deformation at the region AB is constantly larger than that at the region BC, even though the MRR is the same. Additionally, although the maximum energy for material removal at the feedrate of 2  $\mu\text{m}/\text{rev}$  is higher than others, the total energy for material removal decreases as feedrates rise, achieving about 0.0031 J, 0.0021 J, and 0.0012 J for the machining of each lens at feedrates of 1  $\mu\text{m}/\text{rev}$ , 2  $\mu\text{m}/\text{rev}$ , and 3  $\mu\text{m}/\text{rev}$ , respectively. As a result, the increase in feedrates helps to reduce the amount of material removal energy needed to overcome deformation.

The evolution of the SCE during the machining of lenses with a 1 mm diameter is shown in Fig. 25. For all samples, the SCE gradually increases to stable values, but as feedrates increase, the SCE values decrease. The variation trend of SCE is identical to the average stress perpendicular to the diamond tool.

**Fig. 25** Evolution of the SCE in machining of dimples with various feedrates



### 3.5 Generation Mechanism of Surface Damages

The atomic behaviour of silicon ultimately determines the production of surface damage, particularly for the production of brittle fracture which needs atomical sharp crack tip [39]. Surface energy is a crucial characteristic when analyzing the brittle materials fracture. According to the Griffith criterion, cleavage planes are selected from crystallographic planes having low surface energy [40]. In addition, the orientations of the crystals affect the surface energy. The surface energy of the major planes of silicon single crystal are listed in Table 4. Table 4 shows that the surface energies of planes of  $\{110\}$  and  $\{100\}$  are higher than the surface energies of planes of  $\{111\}$ . In general, the single crystal silicon can be easily deformed along the orientation of  $\langle 110 \rangle$ , and the easiest crystallographic plane to cleave is  $\{111\}$ .

Cleavage damages are mainly created in the direction of  $\langle 100 \rangle$  during the machining of center lenses. The cleavage cracks of the center lens, which were machined at a feedrate of 3 m/rev, are displayed in detail in Fig. 26a. After machining, a number of parallel stripy microcracks are formed, and the inclination angle between the top surface plane (001) and the cleavage plane is measured to be between  $45^\circ$  and  $65^\circ$ , and roughly the same as the angle between the crystalline planes of  $\{100\}$  and  $\{111\}$ , which is around  $54.7$  degrees [44]. As a result, The most possible cleavage plane is  $\{111\}$ , and  $\langle 110 \rangle$  is the preferred direction for cleavage propagation due to

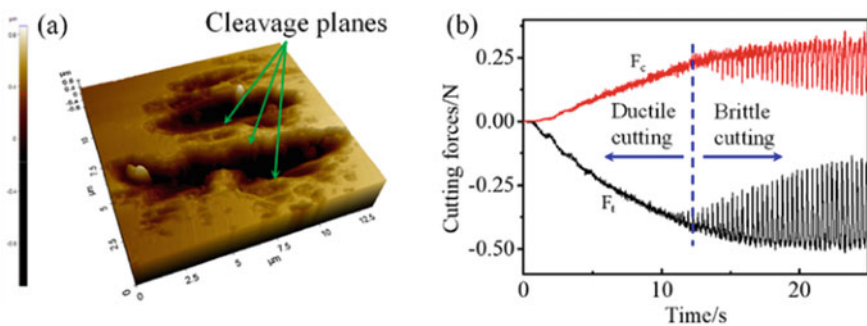
**Table 4** Surface energies of primary planes and orientations of the silicon

Planes	Surface energy ( $\text{J}\cdot\text{m}^{-2}$ )	References
$\{111\}$	1.19	[41]
	1.02	[42]
$\{110\}$	1.50	[41]
	1.48	[42]
	1.83	[43]
$\{100\}$	2.25	[41]
	2.16	[42]

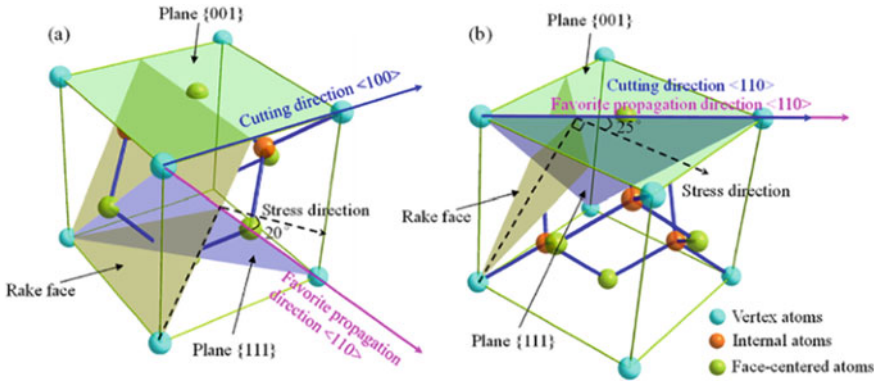
it has the lowest surface energy. One aspect of the cutting forces during the turning process of the center lenses is shown in Fig. 26b. The force evolution displays two unique characteristics that, respectively, correlate to brittle and ductile cutting. First, as the diamond cutter moves forward in the ductile cutting region, the primary cutting force and thrust force steadily increase and the forces fluctuate slightly. Then, during the brittle cutting, the forces change drastically. The machining energy could be used to evaluate the various material removal mode [45]. The major method to remove material at a small scale is ductile cutting because the energy needed to trigger the cleavage fracture should be greater than the energy needed to overcome plastic deformation [46]. Moreover, brittle cutting mode may be initiated if the undeformed chip thickness surpasses the critical value. It has been found that as the undeformed chip thickness increases, the specific cutting energy gradually decreases [47].

During the brittle cutting stage, it can be observed that the force evolution exhibits periodic characteristics; however, this is distinct from the periodic evolution of the cutting forces during the turning process of the exterior lens. The periodic change in cutting force of the former is caused by the cleavage damages that form in the direction of  $\langle 100 \rangle$ , while the periodic generation of 8 lenses at the 1 mm and 2 mm diameters of workpiece is responsible for the force evolution of latter. Additionally, as the amount of cleavage fracture increases, the cutting and thrust forces needed to overcome deformation gradually decrease, which is comparable to the force evolution during the machining of the outside lenses.

Figure 27a, b schematically depict the geometrical relationship of various planes and directions in the machining of the single crystal silicon (001) in directions of and, respectively. In the cutting direction of  $\langle 100 \rangle$ , the stress distribution is perpendicular to the rake face, and the minimum angle between the stress direction and favorite propagation direction  $\langle 110 \rangle$  is calculated to be  $20^\circ$ , while the minimum angle is  $25^\circ$  in the cutting direction of  $\langle 110 \rangle$ . This indicates that, under the same cutting conditions, the component stress of the cutting in the direction of  $\langle 100 \rangle$  is larger than that in  $\langle 110 \rangle$ . As a result, the stress in  $\langle 100 \rangle$  exceeds the critical stress to overcome cleavage deformation first, leading to the formation of cleavage fractures



**Fig. 26** **a** Morphologies of surface damages and **b** cutting forces evolution in machining of the center dimple at the feedrate of  $3 \mu\text{m}/\text{rev}$



**Fig. 27** Schematic diagram of geometrical relationship of crystalline structures in machining of the silicon in the direction of **a**  $\langle 100 \rangle$  and **b**  $\langle 110 \rangle$

in  $\langle 100 \rangle$  rather than  $\langle 110 \rangle$ . After the crack tip formed, the local stress concentration caused by the sidewall flaws around the crack tip could quickly dissipate, allowing the material to split along the preferred cleavage plane of  $\{111\}$  and lowering the amount of stress needed to resist deformation [48]. In addition, Weissgraeber et al. [49] noted that the creation of crystal fissures caused a release of stress concentration. As a result, in the brittle cutting mode, a clear decrease in cutting forces is seen.

## 4 Conclusions

In this chapter, the material cutting forces and spring back behaviour of the Ti6Al4V alloy are theoretically and experimentally investigated in ultraprecision machining of seven microgrooves with respect to material constitutive models and geometrical relationship with respect to material constitutive models and geometrical connections. The following conclusions are drawn:

- (1) The average cutting forces in the experiments and models rise from about 2.38 to 2.55 N and from around 2.34 to 2.64 N, respectively. Therefore, within an error of around 3.53%, the estimated cutting force values from models agree well with the experimental forces. The equivalent stress to overcome plastic deformation rises with the cutting speeds since the increased dislocation drag stress even though the temperature rising with the cutting speeds could decrease the thermal and athermal stresses.
- (2) Because of the evolution of the Young's modulus and spring back force during micro groove machining, an increase in DoC and a reduction in cutting speed would cause more material to spring back. Additionally, even though frictional forces, normal forces, and spring back forces all have an impact on thrust force, spring back force contributes to more than 45% of the thrust force.

Besides, the material removal energy, MRR, SCE, and stress distribution are investigated theoretically and experimentally using STS processing of MLA on single crystal silicon as an example. Evaluation of the energy consumption and SCE under various cutting parameters not only contributes to understanding the material removal process but also provides useful instruction for achieving sustainable fabrication of micro-structured surfaces. The following conclusions are possible:

- (1) When the feedrate is increased from  $1 \mu\text{m}/\text{rev}$  to  $2 \mu\text{m}/\text{rev}$ , the maximum cutting forces increase by about 46.41%, however, when the feedrate is increased from  $2 \mu\text{m}/\text{rev}$  to  $3 \mu\text{m}/\text{rev}$ , the forces only marginally increase by around 4.51%. This diversity is attributed to the formation of many damages at feedrate of  $3 \mu\text{m}/\text{rev}$ .
- (2) Damages are thought to be cleavage fractures, and they are most visible in the direction of  $\langle 100 \rangle$  in the center lens as a result of high component stress on the low surface energy plane of  $\{111\}$ . The initiation and propagation of the cleavages should be  $\{111\}$  planes along direction, and the number of cleavages increases with the increasing of feedrates.
- (3) The creation of cleavage fracture causes a decrease in the amount of required stress and specific cutting energy during the machining process. Additionally, the material removal energy exhibits a hysteresis characteristic with the MRR, meaning that even though the material removal rate is the same, more energy is needed to overcome deformation in the one-third region of the lens than that in the left.
- (4) Although large feedrates need high cutting energies every cycle, the total net material removal energy decreases as feedrates increase, so adopting higher feedrates could benefit for energy saving, however, surface degradation is another challenge with large feedrates. Therefore, in order to reduce energy consumption during the machining of micro lens arrays, large feedrates are advised under the premise of ductile cutting and accepted surface profiles.

**Acknowledgements** The work described in this chapter was supported by the National Natural Science Foundation of China (Grant No. 52205489), the Department of Education of Guangdong Province Research Project (2022KQNCX066) and the Shenzhen Natural Science Foundation University Stability Support Project (Grant No. 20220809212220001).

## References

1. Zhang H, Zhang N, Han W, Gilchrist MD, Fang F (2021) Precision replication of microlens arrays using variotherm-assisted microinjection moulding. *Precis Eng* 67:248–261
2. Zhu X, Fang W, Lei J, Li Z, Xie F, Cao Y, ... Li X (2020) Supercritical lens array in a centimeter scale patterned with maskless UV lithography. *Opt Lett* 45(7):1798–1801
3. Gorelick S, De Marco A (2018) Fabrication of glass microlenses using focused Xe beam. *Opt Express* 26(10):13647–13655

4. Bian H, Wei Y, Yang Q, Chen F, Zhang F, Du G, ... Hou X (2016). Direct fabrication of compound-eye microlens array on curved surfaces by a facile femtosecond laser enhanced wet etching process. *Appl Phys Lett*, 109(22):221109.
5. Tanikawa S, Yan J (2022) Fabrication of micro-structured surface with controllable randomness by using FTS-based diamond turning. *Precis Eng* 73:363–376
6. Merchant ME (1945) Mechanics of the metal cutting process. I. Orthogonal cutting and a type 2 chip. *J Appl Phys* 16(5):267–275
7. Arcona C, Dow TA (1998) An empirical tool force model for precision machining
8. Zhang X, Arif M, Liu K, Kumar AS, Rahman M (2013) A model to predict the critical undeformed chip thickness in vibration-assisted machining of brittle materials. *Int J Mach Tools Manuf* 69:57–66
9. Manjunathaiah J, Endres WJ (2000) A study of apparent negative rake angle and its effect on shear angle during orthogonal cutting with edge-radiused tools. *NAMRI SME*, 197–202
10. Ramos AC, Autenrieth H, Strauß T, Deuchert M, Hoffmeister J, Schulze V (2012) Characterization of the transition from ploughing to cutting in micro machining and evaluation of the minimum thickness of cut. *J Mater Process Technol* 212(3):594–600
11. Huang P, Lee WB (2016) Cutting force prediction for ultra-precision diamond turning by considering the effect of tool edge radius. *Int J Mach Tools Manuf* 109:1–7
12. Fang N (2003) Slip-line modeling of machining with a rounded-edge tool—Part I: new model and theory. *J Mech Phys Solids* 51(4):715–742
13. Jin X, Altintas Y (2011) Slip-line field model of micro-cutting process with round tool edge effect. *J Mater Process Technol* 211(3):339–355
14. Zhu Z, To S, Zhu WL, Huang P, Zhou X (2019) Cutting forces in fast-/slow tool servo diamond turning of micro-structured surfaces. *Int J Mach Tools Manuf* 136:62–75
15. Sun Z, To S, Wang S (2019) An analytical force model for ultra-precision diamond sculpturing of micro-grooves with textured surfaces. *Int J Mech Sci* 160:129–139
16. Zhong Q, Tang R, Peng T (2017) Decision rules for energy consumption minimization during material removal process in turning. *J Cleaner Prod* 140:1819–1827
17. Zhao GY, Liu ZY, He Y, Cao HJ, Guo YB (2017) Energy consumption in machining: classification, prediction, and reduction strategy. *Energy* 133:142–157
18. Sihag N, Sangwan KS (2020) A systematic literature review on machine tool energy consumption. *J Cleaner Prod* 275:123125
19. Melkote SN, Liu R, Fernandez-Zelaia P, Marusich T (2015) A physically based constitutive model for simulation of segmented chip formation in orthogonal cutting of commercially pure titanium. *CIRP Ann* 64(1):65–68
20. Toropov A, Ko SL (2003) Prediction of tool-chip contact length using a new slip-line solution for orthogonal cutting. *Int J Mach Tools Manuf* 43(12):1209–1215
21. Son SM, Lim HS, Ahn JH (2005) Effects of the friction coefficient on the minimum cutting thickness in micro cutting. *Int J Mach Tools Manuf* 45(4–5):529–535
22. Kocks UF (1976) Laws for work-hardening and low-temperature creep
23. Mecking H, Kocks UF (1981) Kinetics of flow and strain-hardening. *Acta metall* 29(11):1865–1875
24. Özel T, Zeren E (2006) A methodology to determine work material flow stress and tool-chip interfacial friction properties by using analysis of machining
25. Luo J, Li M, Li X, Shi Y (2010) Constitutive model for high temperature deformation of titanium alloys using internal state variables. *Mech Mater* 42(2):157–165
26. Fan XG, Yang H (2011) Internal-state-variable based self-consistent constitutive modeling for hot working of two-phase titanium alloys coupling microstructure evolution. *Int J Plast* 27(11):1833–1852
27. Sutter G, List G (2013) Very high speed cutting of Ti–6Al–4V titanium alloy—change in morphology and mechanism of chip formation. *Int J Mach Tools Manuf* 66:37–43
28. Picu RC, Majorell A (2002) Mechanical behavior of Ti–6Al–4V at high and moderate temperatures—Part II: constitutive modeling. *Mater Sci Eng A* 326(2):306–316

29. Umbrello D (2008) Finite element simulation of conventional and high speed machining of Ti6Al4V alloy. *J Mater Process Technol* 196(1–3):79–87
30. Howell JR, Mengüç MP, Daun K, Siegel R (2020) Thermal radiation heat transfer. CRC Press
31. Yang J, Sun S, Brandt M, Yan W (2010) Experimental investigation and 3D finite element prediction of the heat affected zone during laser assisted machining of Ti6Al4V alloy. *J Mater Process Technol* 210(15):2215–2222
32. Zhao Z, To S (2018) An investigation of resolved shear stress on activation of slip systems during ultraprecision rotary cutting of local anisotropic Ti-6Al-4V alloy: Models and experiments. *Int J Mach Tools Manuf* 134:69–78
33. Ding H, Shen N, Shin YC (2011) Modeling of grain refinement in aluminum and copper subjected to cutting. *Comput Mater Sci* 50(10):3016–3025
34. Swaminathan S, Brown TL, Chandrasekar S, McNelley TR, Compton WD (2007) Severe plastic deformation of copper by machining: microstructure refinement and nanostructure evolution with strain. *Scr mater* 56(12):1047–1050
35. Shi Q, Tse YY, Higginson RL (2016) Effects of processing parameters on relative density, microhardness and microstructure of recycled Ti–6Al–4V from machining chips produced by equal channel angular pressing. *Mater Sci Eng A* 651:248–258
36. Jamil M, Zhao W, He N, Gupta MK, Sarikaya M, Khan AM, ... Pimenov DY (2021) Sustainable milling of Ti–6Al–4V: a trade-off between energy efficiency, carbon emissions and machining characteristics under MQL and cryogenic environment. *J Cleaner Prod* 281:125374
37. Goel S, Kovalchenko A, Stukowski A, Cross G (2016) Influence of microstructure on the cutting behaviour of silicon. *Acta Mater* 105:464–478
38. Zhao Z, To S, Xiao G, Jelenković EV (2019) Effects of cutting angles on deformation of single crystal silicon in plunge cutting along  $\langle 1\ 0\ 0 \rangle$  direction. *Mater Lett* 253:234–237
39. Pérez R, Gumbsch P (2000) Directional anisotropy in the cleavage fracture of silicon. *Phys rev lett* 84(23):5347
40. Griffith AA (1921) VI. The phenomena of rupture and flow in solids. *Proc R Soc Lond A* 221(582–593):163–198
41. Tanaka M, Higashida K, Nakashima H, Takagi H, Fujiwara M (2006) Orientation dependence of fracture toughness measured by indentation methods and its relation to surface energy in single crystal silicon. *Int J Fract* 139(3):383–394
42. Masolin A, Bouchard PO, Martini R, Bernacki M (2013) Thermo-mechanical and fracture properties in single-crystal silicon. *J Mater Sci* 48(3):979–988
43. Huang K, Sumigawa T, Guo L, Yan Y, Kitamura T (2018) Unstable cracking behavior in nanoscale single crystal silicon: initiation, unstable propagation and arrest. *Eng Fract Mech* 196:113–122
44. Trempa M, Reimann C, Friedrich J, Müller G, Oriwol D (2012) Mono-crystalline growth in directional solidification of silicon with different orientation and splitting of seed crystals. *J Cryst Growth* 351(1):131–140
45. Wang JJJ, Liao YY (2008) Critical depth of cut and specific cutting energy of a microscribing process for hard and brittle materials. *J Eng Mater Technol* 130(1)
46. Arif M, Xinquan Z, Rahman M, Kumar S (2013) A predictive model of the critical undeformed chip thickness for ductile–brittle transition in nano-machining of brittle materials. *Int J Mach Tools Manuf* 64:114–122
47. Lee YJ, Kumar AS, Wang H (2021) Beneficial stress of a coating on ductile-mode cutting of single-crystal brittle material. *Int J Mach Tools Manuf* 168:103787
48. Ando T, Li X, Nakao S, Kasai T, Shikida M, Sato K (2004) Effect of crystal orientation on fracture strength and fracture toughness of single crystal silicon. In: 17th IEEE International Conference on Micro Electro Mechanical Systems. Maastricht MEMS 2004 Technical Digest. IEEE, pp 177–180
49. Weißgraeber P, Leguillon D, Becker W (2016) A review of Finite Fracture Mechanics: crack initiation at singular and non-singular stress raisers. *Arch Appl Mech* 86(1):375–401



**Part II**  
**Fabrication of Micro/Nano Structures**  
**via Electrical Discharge Machining (EDM)**

# Chapter 7

## Introduction to Electrical Discharge Machining Micro/Nano Structures



Weitong Liu, Yuping Li, and Bin Xu

**Abstract** Micro electrical discharge machining (micro-EDM) is a kind of micro-machining technology, which can process super hard, brittle materials (such as cemented carbide and quenched steel). Micro-EDM is suitable for the fabrication of micro-parts due to its very small cutting force. With the development of MEMS, functional 3D micro-structures have been widely used in the industrial field. At present, micro-EDM has been widely used for machining the 3D micro-structure. In this paper, the fabrication of micro-electrode and 3D micro-structure in 3D micro-EDM were introduced.

### 1 Introduction

In the mid-twentieth century, the former Soviet Union scientists studied the corrosion damage of spark discharge on switch contacts and they found that the instantaneous high temperature of electric spark can corrode the metal locally. Inspired by this phenomenon, the electrical discharge machining (EDM) was invented. At the beginning of EDM, the application scope of EDM was greatly limited because of its very slow processing speed and the need to use mineral oil with good insulation as processing medium. However, compared with traditional machining methods, EDM has the following advantages: (1) It can process super hard and brittle materials (such as cemented carbide and quenched steel, etc.); (3) it is very suitable for processing micro-parts due to its very small cutting force.

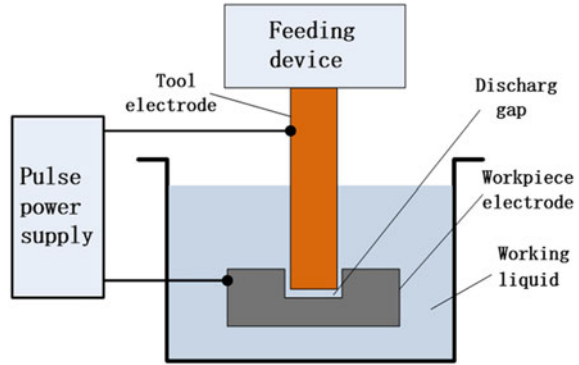
The schematic diagram of EDM was shown in Fig. 1 and its main technological process was described as follows. (1) The tool electrode and the workpiece were connected to the positive and negative of the pulse power supply respectively. (2) The pulse power supply was switched on and the tool electrode gradually closed to the workpiece through the feed movement of the feed device. When the gap between the tool electrode and the workpiece reached a certain distance, the pulse voltage

---

W. Liu · Y. Li · B. Xu (✉)

College of Mechatronics and Control Engineering, Shenzhen University, Shenzhen, Guangdong, China  
e-mail: [binxu@szu.edu.cn](mailto:binxu@szu.edu.cn)

**Fig. 1** The schematic diagram of EDM



applied can break down the working fluid, resulting in an electric spark discharge. At the moment of EDM discharge, a large amount of heat energy was concentrated between the tool electrode and the workpiece, resulting in a sharp rise of temperature and a sharp change of pressure in this area. As a result of these factors, the workpiece site hit by the electric spark immediately melted, vaporized, and explosively splashed into the working fluid. At this time, the surface of the workpiece will leave a tiny pit trace. (3) The above process was repeated, and the workpiece was finally processed by intermittent discharge of the tool electrode for thousands of times.

Because EDM has very small cutting force, it is suitable for machining micro-parts. In the late 1960s, people began to use EDM for the manufacture of micro-parts, and it was named as micro-EDM. For the micro-EDM technology, scholars from all over the world have carried out in-depth research and applied it in the machining of 3D microstructure.

## 2 Preparation of Micro Electrode for 3D Micro-EDM

The electrodes used in 3D micro-EDM include micro electrodes with simple cross section and micro electrodes with 3D structure characteristics. Because it is difficult to fabricate 3D micro-electrodes, micro-electrodes with simple cross section are usually used to fabricate 3D micro-structures by layer scanning and discharging in micro-EDM. Therefore, the preparation process of micro electrode with simple cross section shape was mainly summarized as follows.

### 2.1 Wire Electrical Discharge Grinding (WEDG)

WEDG was first proposed by Masuzawa in 1984 [1], and the schematic diagram of WEDG was shown in Fig. 2a. In the process, the wire electrode moved continuously to

the tool electrode under the action of the guide apparatus. Under the action of pulse power supply, the wire electrode performed electrical discharge grinding and the grinding of specific area of the tool electrode was completed. After the above process, the tool electrode was moved along its axial direction to complete the grinding of different areas of the tool electrode (Fig. 2b). Because the wire electrode moved in one direction, the adverse effect of wire electrode wear on the processing of tool electrode can be ignored.

Because of the on-line fabrication method, the geometric axis of the tool electrode and its axis of rotation were always coincident. Therefore, the machining error caused by the secondary clamping was avoided. In addition, the movement of wire electrode was continuous unidirectional, which can avoid centralized discharge and short circuit, thus effectively ensuring the stability of electrical discharge grinding. As electrical discharge grinding is non-contact machining, the influence of cutting force on tool electrode can be avoided and the tool electrode with very small size can be processed by this technology. According to relevant reference reports, the WEDG can be used to fabricate cylindrical electrodes with a diameter of only 2.5  $\mu\text{m}$ .

At present, WEDG is mainly used to process micro electrodes with simple cross section. Although the machining accuracy of this technology is high, the application scope of this technology in the industrial field is limited by the shortcomings of low machining efficiency and single electrode shape. In view of the shortcomings of WEDG, multi-mode WEDG technology was proposed [3]. Multi-mode WEDG can adjust the distance between grinding head 1 and grinding head 2 by changing the adjusting rod. At the same time, the stable wire running can be achieved by changing the tension of grinding wire. In addition, combined with the angle and speed control of the spindle of the machine tool, the multi-mode WEDG can complete the machining of variety of special-shaped tool electrodes. Multi-mode WEDG can achieve the fabrication efficiency of micro electrodes with complex structural characteristics, which is very suitable for the machining of array micro electrodes.

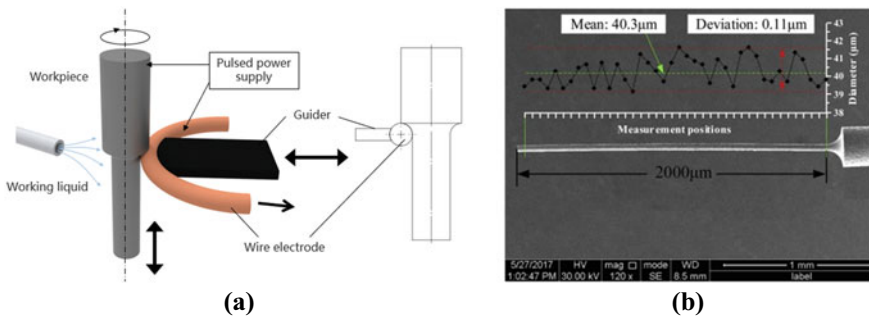
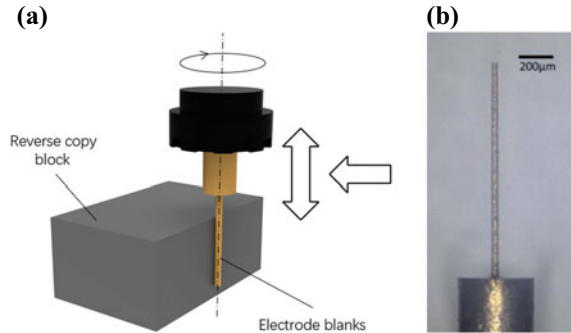


Fig. 2 a Schematic diagram of WEDG; b Micro electrode fabricated by WEDG [2]

**Fig. 3** **a** Schematic diagram of BEDG; **b** Micro electrode fabricated by BEDG [4]



## 2.2 Block Electrode Discharge Grinding (BEDG)

The schematic diagram of BEDG was shown in Fig. 3a. The tool electrode was mounted on the EDM machine spindle and the block electrode was mounted on the workbench. Under the action of the spindle of the machine tool, the tool electrode rotated and gradually approached to the block electrode. The tool electrode was ground by EDM discharge under the action of pulsed power supply. In the above process, the tool electrode can move up and down along the Z direction of the machine tool, and the block electrode can be fed laterally with the workbench. With the gradual progress of EDM grinding, the size of the tool electrode decreased continuously until the desired size of the micro electrode was obtained.

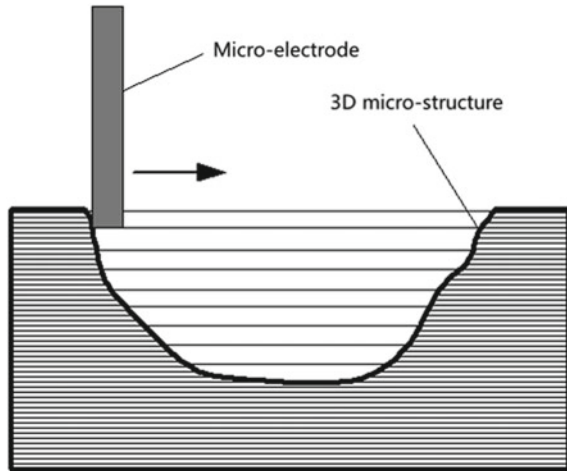
Compared with the WEDG, the BEDG has a larger processing range and thus it has higher processing efficiency. However, in the process of BEDG, the micro electrode was obtained by repeated discharge grinding between the block electrode and the tool electrode. In the above process, the shape, position and EDM wear of the block electrode will adversely affect the machining accuracy of the micro electrode, which can result the low stability of the dimensional accuracy of the micro electrode.

## 3 3D Micro-structures Fabricating by 3D Micro-EDM

Due to the difficulty in preparing 3D micro-electrodes, micro-electrodes with simple cross section are usually used in micro-EDM to process 3D micro-structures by layer scanning and discharging. The schematic diagram is shown in Fig. 4. In the above machining process, the electrode wear will adversely affect the shape accuracy of the 3D micro-structure, so it is necessary to compensate for the electrode wear.

To compensate the micro-electrode wear, T. Masuzawa et al. proposed the uniform wear method (UWM) and wear compensation model in the 3D micro-EDM [5]. In UWM, a micro-electrode with simple cross section was used for layer-by-layer scanning discharge and the discharge process was limited to the front end of the electrode through the micro-feed. After the completion of each layer of discharge

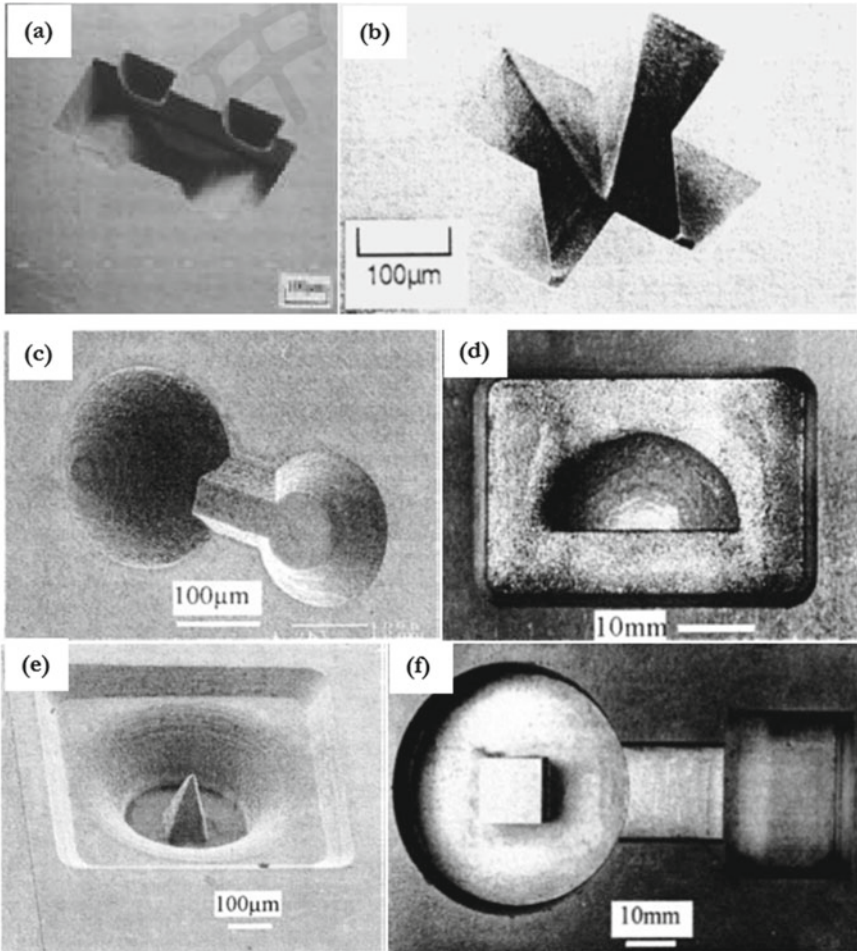
**Fig. 4** Schematic diagram of 3D micro-EDM



machining, the micro-electrode only produced the wear in the length direction and the shape of the front end of the micro-electrode was basically unchanged. Finally, according to the micro-electrode wear in the processing process, UWM compensated the wear at the initial point of each layer. This method can realize the uniform micro-electrode wear and keep the shape of the micro-electrode unchanged, so as to ensure the machining accuracy of the micro-EDM.

Through UWM, T. Masuzawa et al. used the micro-electrode to perform layer by layer micro-EDM on stainless steel materials and successfully fabricated a car model (Fig. 5a) with length, width and height of 500  $\mu\text{m}$ , 300  $\mu\text{m}$  and 200  $\mu\text{m}$  respectively. Based on the UWM, K.P. Rajurkar et al. combined with CAD/CAM system to prepare arbitrary complex 3D micro-structure (Fig. 5c–f) [6]. W. Meeusen et al. prepared a micro-electrode with a simple cross section through WEDG and applied it in micro-EDM [7]. Based on UWM, W. Mueusen et al. successfully prepared micro hemispheric cavity, micro square cavity and micro temple cavity. The above processing experiments again proved the superiority of UWM in fabricating complex 3D micro-structures.

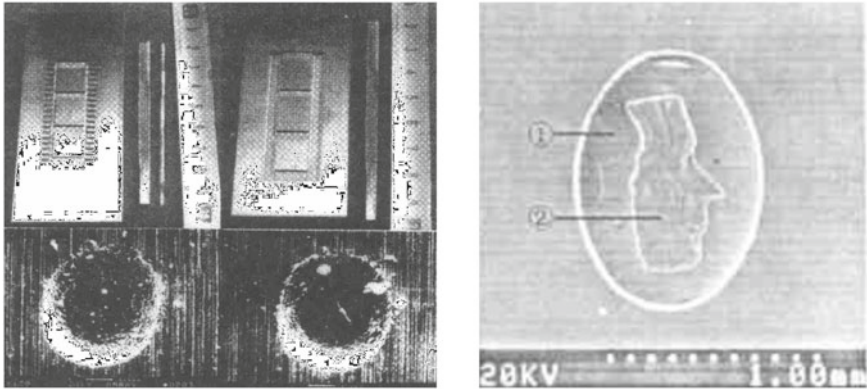
In the UWM method, the micro-electrode compensation only occurred at the initial position of each discharge machining layer and only one time electrode compensation was performed for each layer. Therefore, this compensation feature caused that the machining shape accuracy cannot be guaranteed, and the bottom surface contour of the micro-cavity was approximately a slanted straight line. In order to solve the above problems, Pei et al. proposed a fixed-length compensation method [8]. The method was based on the UWM, and the compensation times of electrode wear in each layer were increased from one time to multiple times. In the process of each layer, when the electrode wear reached a certain set value  $L_e$ , the fixed-length compensation method will compensate once and the compensation amount was  $\Delta L_e$ . Through the above methods, Pei et al. successfully prepared 3D micro-structure with high accuracy.



**Fig. 5** a, b 3D micro-structure prepared by UWM [5]; c, d, e, f 3D micro-structure prepared by combining UWM with CAD/CAM [6]

In order to eliminate the machining slope caused by electrode wear in the UWM, Wang et al. proposed that reciprocating motion should be adopted for the processing of the two adjacent layers. That is, the cutter should return along the original path at the next time [9]. Through the above method, Wang et al. successfully prepared IC socket, spherical crown and miniature face (Fig. 6).

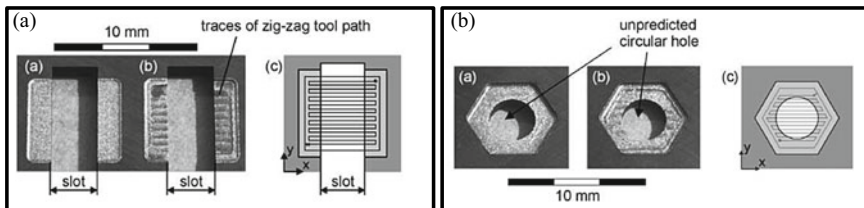
In order to improve the efficiency and accuracy of 3D micro-EDM, Li et al. proposed combination of linear compensation method with UWM (CLU) [10]. Based on the uniform wear method and linear compensation method, the total compensation amount of electrode wear between layers was determined by the UWM, and the total



**Fig. 6** IC socket, spherical crown and miniature face fabricated by micro-EDM [9]

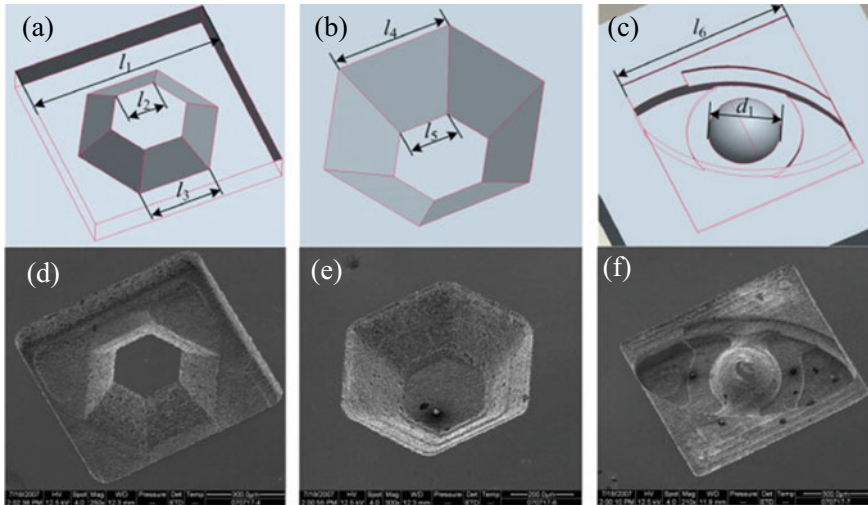
compensation amount of each layer was evenly distributed to the processing trajectory of each layer by the linear compensation method. CLU combined the advantages of UWM and linear compensation method, so that the machining efficiency and machining accuracy of 3D micro-EDM were significantly improved. Through the CLU method, Li et al. successfully prepared the 3D micro cavity structure with high accuracy.

In the process of micro-EDM, the single wear of electrode was proportional to the discharge energy. Therefore, the electrode wear can be predicted and compensated by detecting the number of effective discharge pulses. Based on the above principles, P. Bley et al. proposed a real-time electrode wear compensation method [11]. The method combined model prediction with real-time measurement. Before EDM, the compensation amount of electrode was predicted according to the volume and relative volume wear ratio of the workpiece material to be removed. In the machining process, the effective discharge pulse number in a certain time was counted, and the actual electrode wear was calculated and compared with the predicted value, so as to take the appropriate value to compensate the electrode wear. Through the above methods, P. Bley et al. successfully prepared the 3D micro cavity structure (Fig. 7).



**Fig. 7** Three-dimensional micro cavity structure prepared by P. Bley et al. [11]





**Fig. 8** Three-dimensional micro cavity structure prepared by 3D SSMEDM [12]

In order to improve the machining efficiency of 3D micro-EDM and thus promote the industrialization process of this technology, Li et al. proposed servo scanning 3D micro-EDM (3D SSMEDM) based on the discharge gap servo control real-time electrode wear compensation technology [12]. In this machining method, the discharge gap obtained by high-speed real-time acquisition was quantitatively compared with the gap during normal machining. The electrode wear was compensated by the longitudinal servo feed system of the electrode, so that the discharge gap was always kept within the normal discharge range. Through in-depth and detailed research on the processing method, Li et al. successfully prepared various complex 3D micro-structures (Fig. 8).

In order to obtain accurate electrode compensation, Yan et al. used the machine vision system to directly obtain the images of the electrode wear and edge wear [13]. Then, the images were processed through the image processing software to obtain the electrode wear and thus the electrode wear was compensated. Through the above methods, Yan et al. successfully prepared 3D micro-structure with high accuracy (Fig. 9).

In order to improve the machining accuracy of 3D micro-EDM, M.D Nguyen et al. analyzed the systematic errors micro-EDM [14]. It was found that the radius of the micro-electrode and the machining gap of the micro-EDM need to be compensated effectively. Through the above method, M.D Nguyen et al. processed a 3D micro cavity structure with high shape accuracy (Fig. 10).

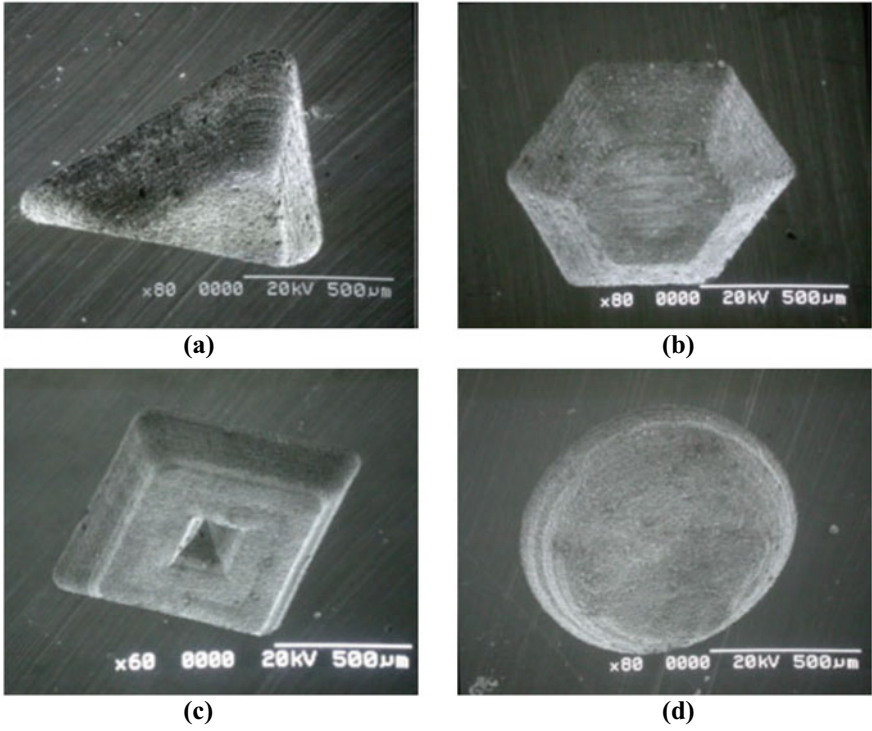


Fig. 9 Three-dimensional micro cavity structure prepared by Yan et al. [13]

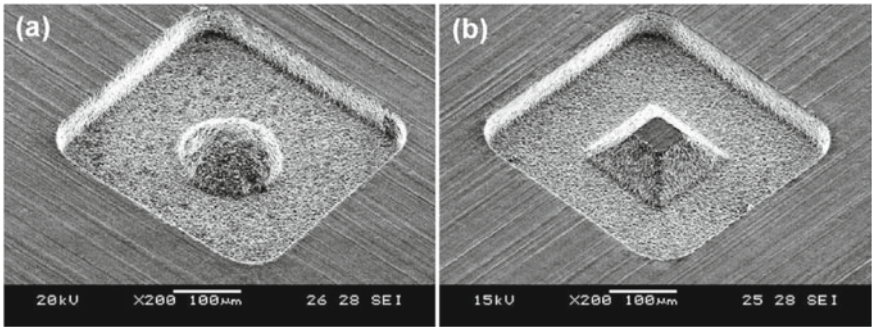


Fig. 10 Three-dimensional micro cavity structure prepared by M.D.Nguyen et al. [14]

## 4 Summary and Outlook

Functional 3D micro-structures have been widely used in microelectronics, precision machinery, biomedicine, aerospace, and so on. Because it is very difficult to fabricate the 3D micro-electrode, the micro-electrode with simple cross section is usually used to fabricate the 3D micro-structure through layer-by-layer scanning discharge in the micro-EDM. Although this machining method can process complex micro-structure, it also has some disadvantages, such as serious micro-electrode wear and low machining efficiency.

To solve these existing problems, this part mainly focuses on improving the machining efficiency and precision of using micro-EDM in 3D micro-structure machining. In Chap. 1, the application of micro-EDM in 3D micro-structure machining and the preparation technology of micro-electrode are introduced. In particular, the advantages and disadvantages of 3D micro-EDM are analyzed, which can help us better understand the development status and direction of this technology. In Chap. 2, the preparation method of 3D microelectrode and its application in 3D micro-EDM are introduced. The research content introduced in this chapter provides a new idea for improving the efficiency of 3D micro-EDM. In Chap. 3, the preparation method of 3D composite microelectrode and its application in 3D micro-EDM are introduced. The research content introduced in this chapter provides ideas for solving the defects in 3D micro-structure obtained from the micro-EDM of 3D micro-electrode. In Chaps. 4 and 5, fabrication of microgrooves obtained from the micro-EDM of laminated disc electrode is introduced. The research content of these chapter provides a reference for the efficient and economical acquisition of surface functional micro-groove structure. In Chap. 6, the numerical simulation of composite microelectrode for machining microstructure is introduced. The research content of this chapter provides a useful reference for the design and preparation of composite microelectrode.

**Acknowledgements** The work described in this chapter was supported by the National Natural Science Foundation of China (Grant No. 51405306), and the Shenzhen Natural Science Foundation University Stability Support Project (Grant No. JSGG20201102145402008).

## References

1. Masuzawa T, Fujino M, Kobayashi K (1985) Wire Electrodischarge Grinding for Micromachining. *Cirp Ann-Manuf Techn* 34(1):431–434
2. Li ZK, Bai JC, Yan C, Wang YQ, Zhu GZ (2019) Fabrication of microelectrode with large aspect ratio and precision machining of micro-hole array by micro-EDM. *J Mater Process Tech* 268:70–79
3. Zhang YB, He JG, Wu ZQ, Lei YH, Liu GM (2017) Technology on efficiency enhancement for micro-electrical discharge machining. *Mod Manuf Eng* 6:1–6

4. Yin QF, Wang XQ, Wang P, Qian ZQ, Zhou L, Zhang YB (2016) Fabrication of micro rod electrode by electrical discharge grinding using two block electrodes. *J Mater Process Tech* 234:143–149
5. Yu ZY, Masuzawa T, Fujino M (1998) Micro-EDM for three dimensional cavities-development of Uniform Wear Method. *Cirp Ann-Manuf Techn* 47(1):169–172
6. Rajurkar KP, Yu ZY (2000) 3D Micro-EDM using CAD/CAM. *Cirp Ann-Manuf Techn* 49(7):127–130
7. Meeusen W, Reynaerts D, Peirs J, Brussel HV, Driesen W (2001) The machining of freeform micro moulds by Micro EDM; work in progress. *Proc Micromech Eur Workshop Mme*
8. Pei JY, Deng R, Hu DJ (2009) Bottom Surface Profile of Single Slot and Fix-length Compensation Method in Micro-EDM Process. *J Shanghai Jiao Tong U* 43(1):42–46
9. Wang ZL, Zhao WS, Liu GZ (2002) Research on laminated removal micro-EDM. *Chin J Mech Eng-En* 38(2):22–26
10. Yu HL, Luan JJ, Li JZ, Zhang YS, Yu ZY, Guo DM (2010) A new electrode wear compensation method for improving performance in 3D micro EDM milling. *J Micromech Microeng* 20(5):055011
11. Bleys P, Kruth JP, Lauwers B (2004) Sensing and compensation of tool wear in milling EDM. *J Mater Process Tech* 149(1–3):139–146
12. Tong H, Li Y, Wang Y, Yu D (2008) Servo scanning 3D micro-EDM based on macro/micro-dual-feed spindle. *Int J Mach Tool Manu* 48(7–8):858–869
13. Yan MT, Lin SS (2011) Process planning and electrode wear compensation for 3D micro-EDM. *Int J Adv Manuf Tech* 53(1–4):209–219
14. Nguyen MD, Wong YS, Rahman M (2013) Profile error compensation in high precision 3D micro-EDM milling. *Precis Eng* 37(2):399–407

# Chapter 8

## Fabrication of 3D Micro-electrode and Its Application in Micro-EDM



Yangquan Liu, Weitong Liu, and Bin Xu

**Abstract** In micro-EDM, it is difficult to prepare the 3D microelectrodes through traditional methods. Therefore, micro-EDM usually adopts the method of layer by layer scanning discharge machining to prepare 3D microstructure by using micro-electrode with a simple cross section shape, which has the disadvantages of complicated process and low processing efficiency. Focus on the above problems, this paper used laminated object manufacturing (LOM) to superimpose multi-layer thin microstructures to fabricate 3D microelectrodes. Then, micro-EDM adopted the 3D microelectrode to machine 3D microstructure. The thin microstructures were fabricated through wire-EDM of copper foil and these copper foil 2D microstructures were welded together by using diffusion welding. Through the above process, the 3D microelectrode can be obtained. To improve the machining accuracy of 3D microstructure, 3D microelectrode array was fabricated and used to process the same 3D microstructure, which the rough machining and finish machining were carried out in sequence. Compared with the layer by layer scanning discharge machining, the 3D microstructure can be obtained by the up and down reciprocating method of the 3D microelectrode array, which is simple and efficient.

### 1 Introduction

At present, functional 3D microstructures have been widely applied in microelectronics, precision machinery, and so on. Micro electrical discharge machining (Micro-EDM) is a non-contact machining technology and thus it has little cutting force. Little cutting force can avoid the adverse effect on microstructures and thus micro-EDM is appropriate to machine of functional microstructures because it avoids the adverse effect of cutting force on microstructures.

---

Y. Liu · W. Liu · B. Xu (✉)

Shenzhen Key Laboratory of High Performance Nontraditional Manufacturing, College of Mechatronics and Control Engineering, Shenzhen University, Nan-Hai Ave 3688, Shenzhen 518061, Guangdong, PR China  
e-mail: [binxu@szu.edu.cn](mailto:binxu@szu.edu.cn)

Functional microstructures includes 3D micro cavity [1–3], micro part [4–6] and micro hole [7–9] which were machined by micro-EDM according to the research results of scholars from various countries. Because the preparation of 3D EDM micro-electrode is difficult to realize, micro-EDM usually adopts the method of layer by layer scanning discharge machining to prepare 3D microstructure by using microelectrode with a simple cross section shape [1]. microstructure with complex structural characteristics can be prepared through the above method. However, the disadvantages of complex process and low processing efficiency restrict the application of this method in the industrial field. In addition, the size of the adopted microelectrode is very small, so the electrode wear caused by EDM needs to be compensated to ensure the processing quality of the 3D microstructure.

To compensate the tool electrode wear and improve processing efficiency, the servo scanning 3D micro-EDM (3D SSMEDM) [2] were proposed to use in the EDM of 3D microstructure. An ultrasonic linear motor and a piezoelectric actuator were combined in 3D SSMEDM and the electrode wear was compensated [2, 10]. In addition, the machine vision system was also applied in micro-EDM for compensating the electrode wear [3]. The machine vision system can observe the shape of the tool electrode in real time and measure its wear. These data can provide the basis for compensating the electrode wear [11]. The application of 3D microelectrode in micro-ED can prepare 3D microstructure with up and down reciprocating machining method, which has higher the machining efficiency and simple process flow.

The author of this paper proposed to superimpose multiple layer of thin microstructures to prepare 3D micro-molds [12–15]. Inspired by the above process, this paper fabricated 3D microelectrodes through superposition of multi-layer of thin microstructures. We adopted the 3D microelectrodes in micro-EDM [16, 17] to efficiently prepare 3D microstructures.

## 2 The Preparation of 3D Microelectrode

### 2.1 Preparation Method

The proposed method included two work stations. Firstly, multi-layer thin microstructures were prepared through wire-EDM. Secondly, through diffusion welding (DFW), the multi-layer of thin microstructures were welded with each other and thus the 3D microelectrode was obtained. Figure 1 shows the preparation method of machining 3D microelectrode and Fig. 2 shows the experimental facilities used in the above process flow.

- (1) Through 3D design software, the required 3D microstructure model was firstly designed. Taking the 3D microstructure as a reference, the corresponding 3D microelectrode was then designed. The characteristic data of the multi-layer of thin microstructures was obtained through discrete slices along the height

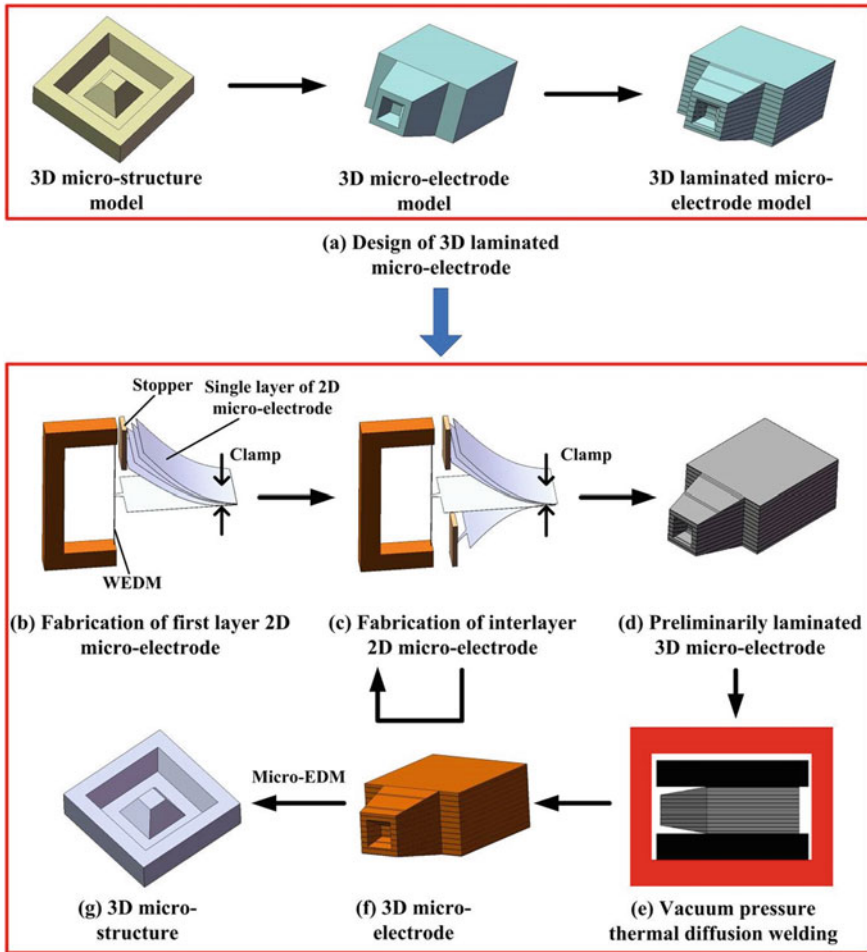
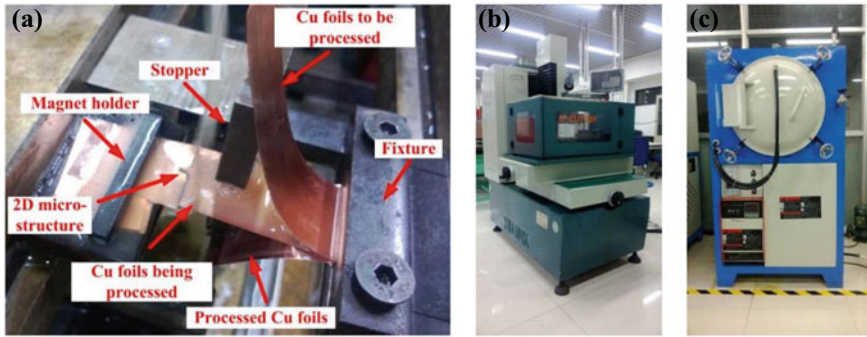


Fig. 1 Process sketch of fabricating 3D microelectrode

direction of the 3D microelectrode (Fig. 1a). Finally, the machining data of each layer of thin microstructure can be got in the above process.

- (2) Front end of the multi-layer copper foil was clamped. Each layer of copper foil was machined successively to obtain the thin microstructure according to the processing data. In the above process, for ensuring the machining quality of each layer of copper foil, it was necessary to separate the processed copper foil and the unprocessed copper foil from the processing copper foil to prevent the interference between the layers of copper foil (Figs. 1b, c and 2a). After that, the preliminarily laminated 3D microelectrode could be prepared from the above process (Fig. 1d).



**Fig. 2** The experimental facilities used for fabricating 3D microelectrode: **a** fixture; **b** wire cutting machine; **c** vacuum furnace

- (3) In the 3D microelectrodes obtained from procedure (2), multi-layer of the thin microstructure was not connected together. Therefore, the 3D microelectrodes with preliminary laminating need place in a vacuum furnace to undergo DFW (Fig. 1e). Under the effect of DFW, each layer of thin microstructures in the initial superimposed 3D microelectrodes can be fully connected. Then, the obtained 3D microelectrode was adopted by micro-EDM and the 3D microstructure was fabricated (Fig. 1g).

## 2.2 Wire-EDM of Cu Foil

Through wire-EDM, copper foils were machined and multi-layer of thin microstructures were obtained. After that, the 3D microelectrodes were prepared through superposition fitting of multi-layer of thin microstructures. Hence, the morphology and machining quality of 3D microelectrodes were significantly impacted by the machining quality of thin microstructure. Cutting current  $I_c$ , pulse width  $T_{on}$  and pulse interval  $T_{off}$  were main process parameters of WEDM, which had significant impact on the quality of thin microstructure. For obtaining appropriate technological parameters of wire cutting, different technological parameters were applied in the wire cutting of copper foil and Fig. 3 shows the experimental results.

For obtaining the applicable  $I_c$ , different  $I_c$  was used to cut the copper foil with other process parameters fixed.  $I_c$  was set to 0.42 A ~2.52 A, the voltage was set to 80 V, the  $T_{on}$  was set to 20  $\mu$ s, the  $T_{off}$  was set to 40  $\mu$ s. The molybdenum wire with diameter of 180  $\mu$ m was adopted as electrode. According to the experimental results, we found that with the increase of the  $I_c$ , the processing quality of copper foil slit became worse and worse. As the current increased from 0.42 to 2.52 A, the energy of the monopulse power supply became larger and larger. Therefore, under the influence of the above factors, the quality of copper foil slit was getting worse and worse. As shown in Fig. 3, when  $I_c$  was 0.42 A, the wire cutting edge was better.



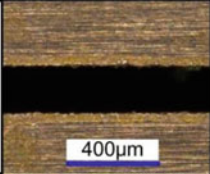
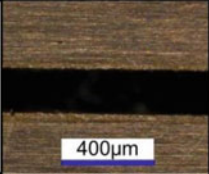
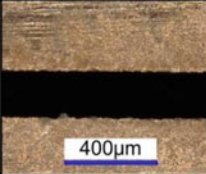
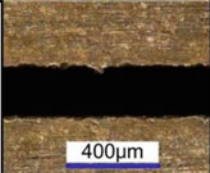
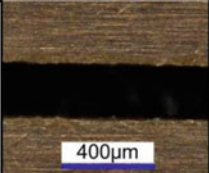
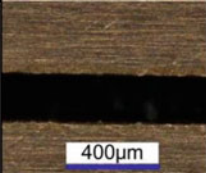

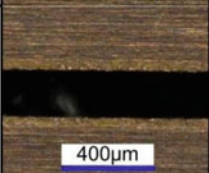
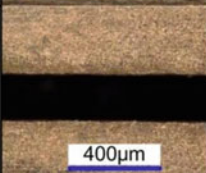
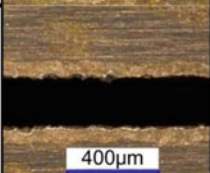
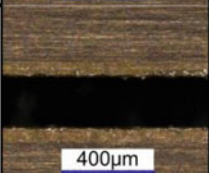
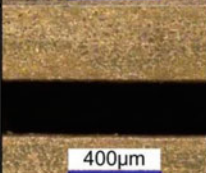
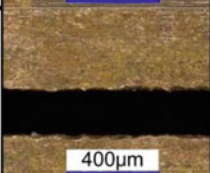
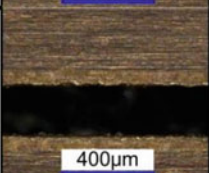

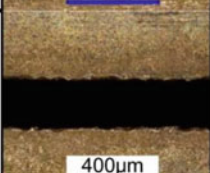
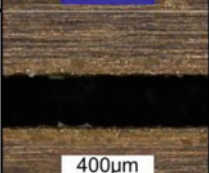
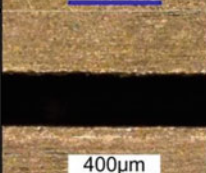
Impact of $I_e$ on WEDM quality		Impact of $T_{on}$ on WEDM quality		Impact of $T_{off}$ on WEDM quality	
$I_e$ /A	$T_{on} = 20 \mu s$ $T_{off} = 40 \mu s$	$T_{on}$ / $\mu s$	$I_e = 0.42 A$ $T_{off} = 40 \mu s$	$T_{ff}$ / $\mu s$	$I_e = 0.42 A$ $T_{on} = 10 \mu s$
0.42		10		10	
0.84		20		20	
1.26		30		30	
1.68		40		40	
2.1		50		50	
2.52		60		60	

Fig. 3 Impact of  $I_e$ ,  $T_{on}$  and  $T_{off}$  on the WEDM quality of copper foil

For obtaining the applicable  $T_{on}$ , different  $T_{on}$  was used to cut the copper foil on the premise of determining other process parameters.  $T_{on}$  was set to 10~60  $\mu$ s,  $I_c$  was set to 0.42 A, voltage was set to 80 V, and  $T_{off}$  was set to 40  $\mu$ s. It can be seen from the experimental results that with the increase of the  $T_{on}$ , the processing quality of copper foil slit became worse and worse. Pulse width  $T_{on}$  was proportional to the discharge energy of EDM. With  $T_{on}$  increased from 10 to 60  $\mu$ s, the energy of monopulse power supply became larger and larger. Therefore, under the influence of the above factors, the quality of copper foil slit was getting worse and worse. As shown in Fig. 3, when  $T_{on}$  was 10  $\mu$ s, the wire cutting edge was better.

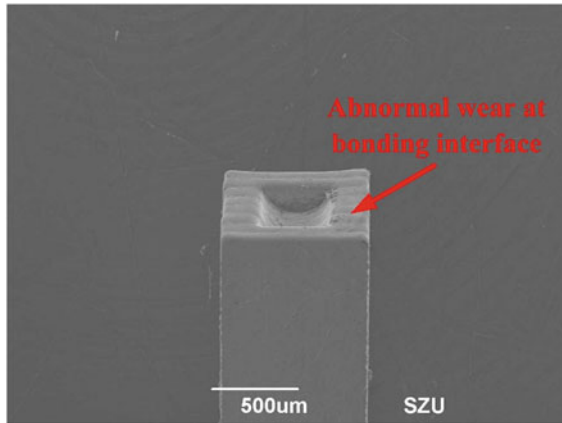
For obtaining the applicable  $T_{off}$ , the copper foil was cut with different pulse interval  $T_{off}$  with other process parameters fixed.  $T_{off}$  was set to 10~60  $\mu$ s,  $I_c$  was set to 0.42 A, voltage was set to 80 V and  $T_{on}$  was set to 10  $\mu$ s. If the corrosion products produced by EDM cannot be discharged in time, the stability of EDM will be affected. In order to ensure the normal process of EDM, there must be enough time interval between two discharges so that the electrical corrosion products can be fully eliminated, so as to restore the insulation of discharge channel. The above process is referred to as deionization of the working fluid. Therefore, the  $T_{off}$  cannot be too large or too small. Too large  $T_{off}$  will reduce the energy density, thus affecting the stability of EDM. Too small  $T_{off}$  will lead to insufficient desionization of the working fluid, and will also have adverse effects on the normal operation of EDM. As shown in Fig. 3, when the  $T_{off}$  was 40  $\mu$ s, the wire cutting edge was the smoothest.

### 2.3 DFW of 3D Microelectrode

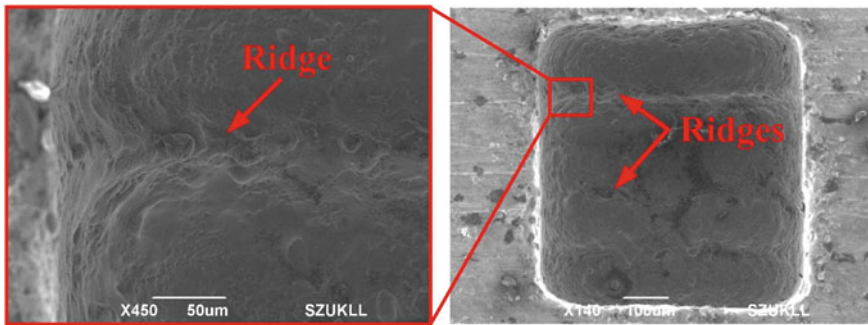
Multi-layer of thin microstructures composed the preliminarily laminated 3D microelectrode and each layer of the thin microstructure was not welded together. Therefore, the preliminarily laminated 3D microelectrode need to be underwent DFW and thus multi-layer of thin microstructures can be actually connected together.

The welding quality of 3D microelectrode had important influence on its application in micro-EDM. If the welding quality between the 2D microstructure was not good, then under the action of discharge energy, the abnormal wear on the bonding interface would appear (Fig. 4). Under the impact of abnormal wear on the bonding interface, the micro-EDMed surface may have ridges (Fig. 5). The ridges had adverse effect on the surface quality. In view of the above problems, this paper mainly adjusted the holding time to guarantee the welding quality of thin microstructure.

Under vacuum condition, DFW refers to the welding method that makes welding parts connect with each other through atomic diffusion. The temperature of DFW is usually set at 50 to 80% of the melting point of the welding material. Because the melting point of copper is 1083°C, its thermal diffusion temperature  $T$  is 542~867 °C. In DFW, the influence of thermal diffusion time  $t$  and thermal diffusion force  $F$  on the welding quality is very important. According to the results of previous experimental studies, the force and thermal diffusion temperature were set as 100 N and 850 °C respectively.



**Fig. 4** The abnormal wear on the bonding interface in 3D microelectrode after micro-EDM



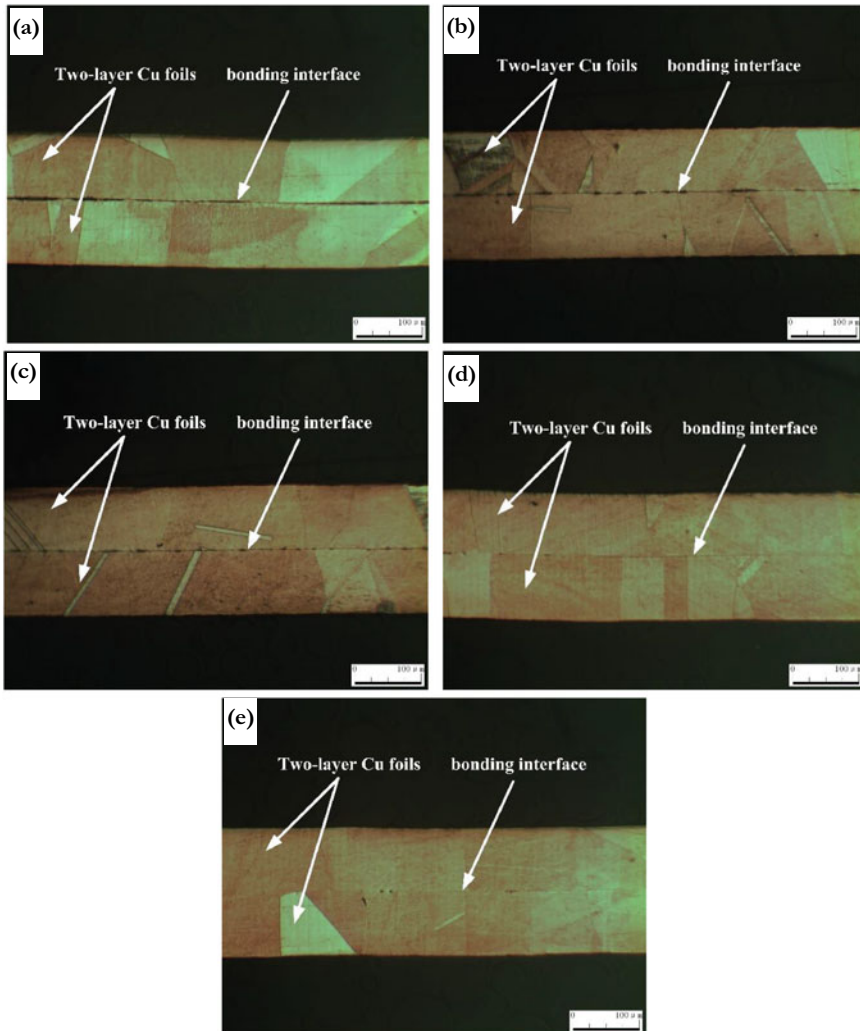
**Fig. 5** Ridges on the surface of 3D microstructure

For obtaining the appropriate thermal diffusion time, the paper successively used different thermal diffusion time to weld the 3D microelectrode. The  $t$  was set from 2~10 h with the  $T$  of 850 °C and the  $F$  of 100 N. The 3D microelectrode was carried out the DFW. After that, the 3D microelectrode was ground and polished. Then, ferric nitrate alcohol solution was used for corrosion, so as to observe the morphology of the bonding interface.

Based on the experimental results shown in Fig. 6a, when the thermal diffusion time was 2 h, the gap between Cu foil 2D microstructures was obvious. With the increase of  $t$ , the gap between thin microstructure gradually decreased and finally disappeared (Fig. 6e). When the  $t$  was equal to or less than 8 h, 3D laminated microelectrode had slightly deformation along its thickness direction. When the  $t$  was 10 h, the deformation of 3D laminated microelectrode was not obvious. With the increase of  $t$ , the atoms between the copper foil thin microstructure diffused with each other, so that the gaps between thin microstructure gradually disappeared. When the gaps

between thin microstructure disappeared, the overall rigidity was improved, which could effectively prevent deformation of the 3D microelectrode.

For investigating the influence of  $t$  on the dimensional accuracy of the 3D microelectrode in the thickness direction, this paper measured the thickness of the samples shown in Fig. 6, and the measurement results are shown in Table 1. Based on the experimental results in Table 1, with the gradual increase of  $t$ , the size of the sample in the thickness direction was closer and closer to the designed size.



**Fig. 6** Impact of thermal diffusion time on the welding quality of 3D microelectrode: **a**  $t = 2$  h; **b**  $t = 4$  h; **c**  $t = 6$  h; **d**  $t = 8$  h; **e**  $t = 10$  h

**Table 1** Impact of thermal diffusion time on the thickness of sample

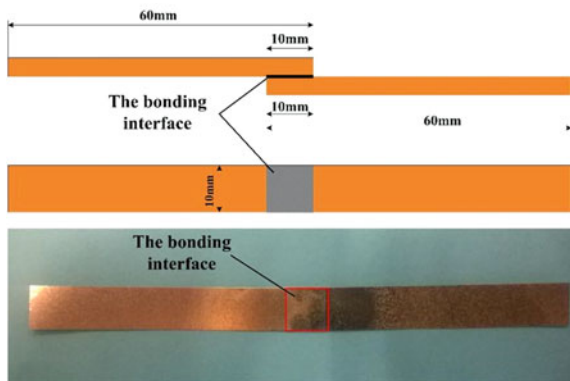
Thermal diffusion time (hour)	2	4	6	8	10
Thickness of each Cu foil before bonding ( $\mu\text{m}$ )	100				
Designed thickness of sample ( $\mu\text{m}$ )	200	200	200	200	200
Real thickness of sample ( $\mu\text{m}$ )	209.71	206.13	202.42	200.58	199.64

When the  $t$  was short, the atomic diffusion on the contact surface of each layer was not enough and there was a gap between the copper foil, so as to result in the poor dimensional accuracy in the thickness direction. As the increase of the  $t$ , the atomic diffusion on the contact surface became more and more sufficient, and the gaps between copper foil gradually disappeared. At this time, the dimensional accuracy in the thickness direction was better. Therefore, in order to guarantee the overall mechanical properties and dimensional accuracy of the 3D microelectrode, the parameters of DFW selected in this paper are as follows: thermal diffusion time of 10 h, thermal diffusion temperature of 850 °C and force of 100 N.

The shear resistance can reflect the connection strength of each layer of thin microstructure. The greater the ultimate shearing force of each layer of microstructure, the better the connection strength of each layer of microstructure. Consequently, the overall mechanical properties of the 3D microelectrode are better. For researching the effect of the  $t$  on welding quality, a shear test was carried out.

Two layers of copper foil were bonded in  $1000\ \mu\text{m} \times 1000\ \mu\text{m}$  area to make a shear test sample (Fig. 7), and then the shear test sample was manually mounted on the drawing machine for shear test. The loading force was exerted on the sample. When the loading force decreased, the sample broken and the displacement of the sample was measured. The preloading force was 2 N, the preloading speed was 10 mm/min, and the test speed was 4 mm/min. As shown in Fig. 8, with the increase of the  $t$  from 2 to 10 h, the shearing force of the sample gradually increased from 116.03N to 165.95N. Therefore, in this paper, the thermal diffusion time was set as 10 h and the thermal diffusion temperature was set as 850 °C.

**Fig. 7** The shearing test samples



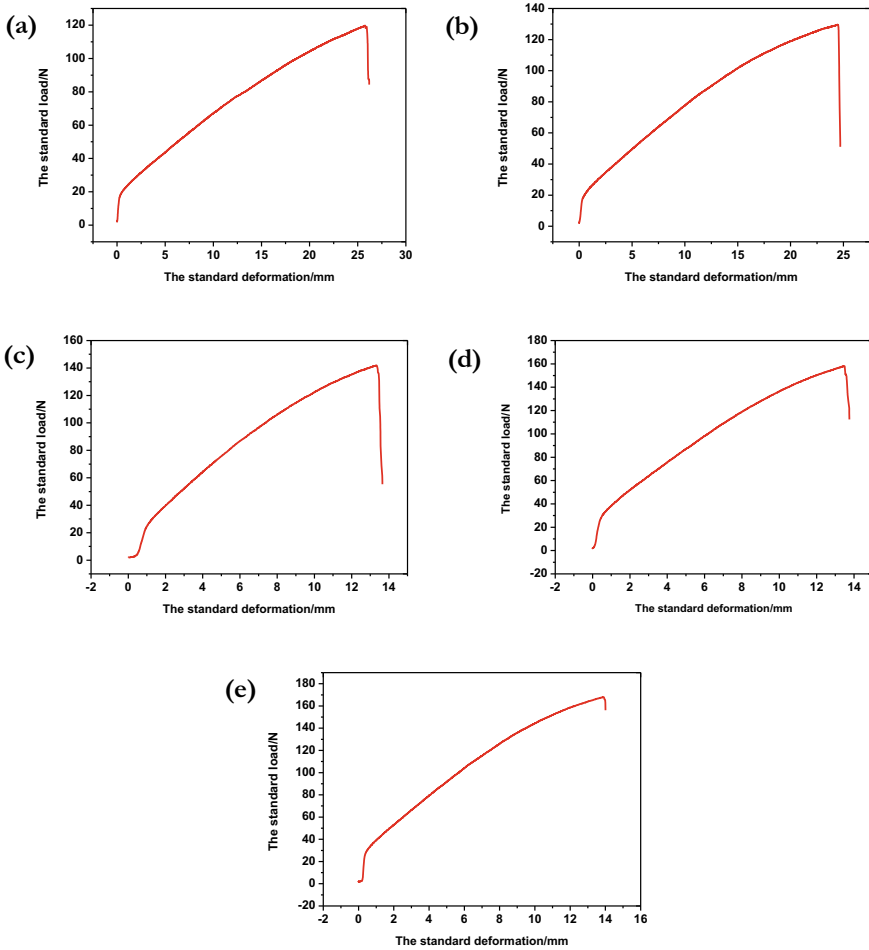


Fig. 8 The shearing test of sample under different thermal diffusion time  $t$ : a  $t = 2$  h; b  $t = 4$  h; c  $t = 6$  h; d  $t = 8$  h; e  $t = 10$  h

### 3 Preparation of 3D Microelectrode and Its Application in the Micro-EDM of 3D Microstructure

#### 3.1 Processing 3D Microstructure with Single 3D Microelectrode

Three kinds of 3D microstructure were designed in this paper, and their basic shapes are shown in Fig. 9. The 3D microelectrodes were designed based on the above 3D microstructures, and the 3D microelectrode models were discretised by slicing

software to obtain the number of copper foil layers and the machining path of each layer of thin microstructure.

Based on the above data, the 3D microelectrodes were prepared using 100  $\mu\text{m}$  thick copper foil by wire-EDM and DFW. The process parameters are as follows:  $I_c$  of 0.42 A, wire cutting voltage of 80 V,  $T_{on}$  of 10  $\mu\text{s}$ ,  $T_{off}$  of 40  $\mu\text{s}$ , T of 850  $^\circ\text{C}$ , t of 10 h and F of 100 N. The obtained 3D microelectrodes are shown in Fig. 10.

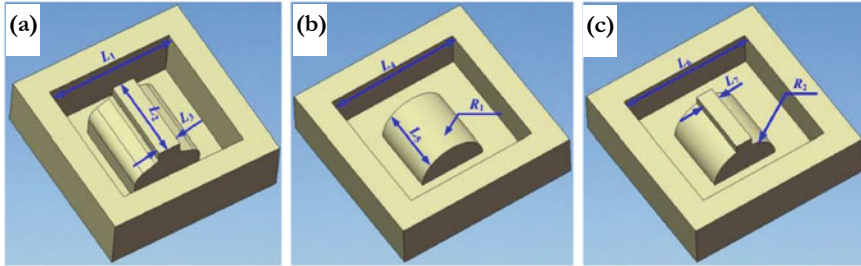


Fig. 9 The CAD models of 3D microstructure

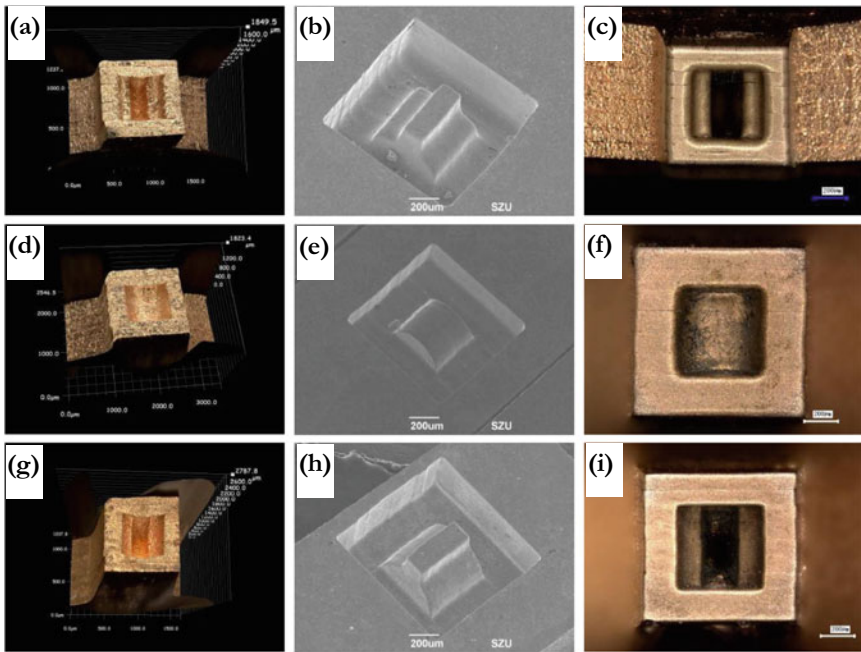


Fig. 10 3D microelectrode and its micro-EDM results: a, d, g 3D microelectrodes before micro-EDM; b, e, h 3D microstructures obtained by the micro-EDM of 3D microelectrodes; c, f, i 3D microelectrodes after micro-EDM

**Table 2** Dimensional comparison between CAD models and machined structures shown in Fig. 10

	Dimensional symbols	Dimensional values ( $\mu\text{m}$ )		
		CAD models	Machined structures	Errors
(a)	L1	800	788.7	11.3
	L2	400	391.6	8.4
	L3	150	138.3	11.7
	Depth	400	385.4	14.6
(b)	L4	900	890.6	9.4
	L5	500	489.1	10.9
	R1	200	191.2	8.8
	Depth	220	203.6	16.4
(c)	L6	900	890.5	9.5
	L7	200	189.9	10.1
	R2	250	240.8	9.2
	Depth	360	347.2	12.8

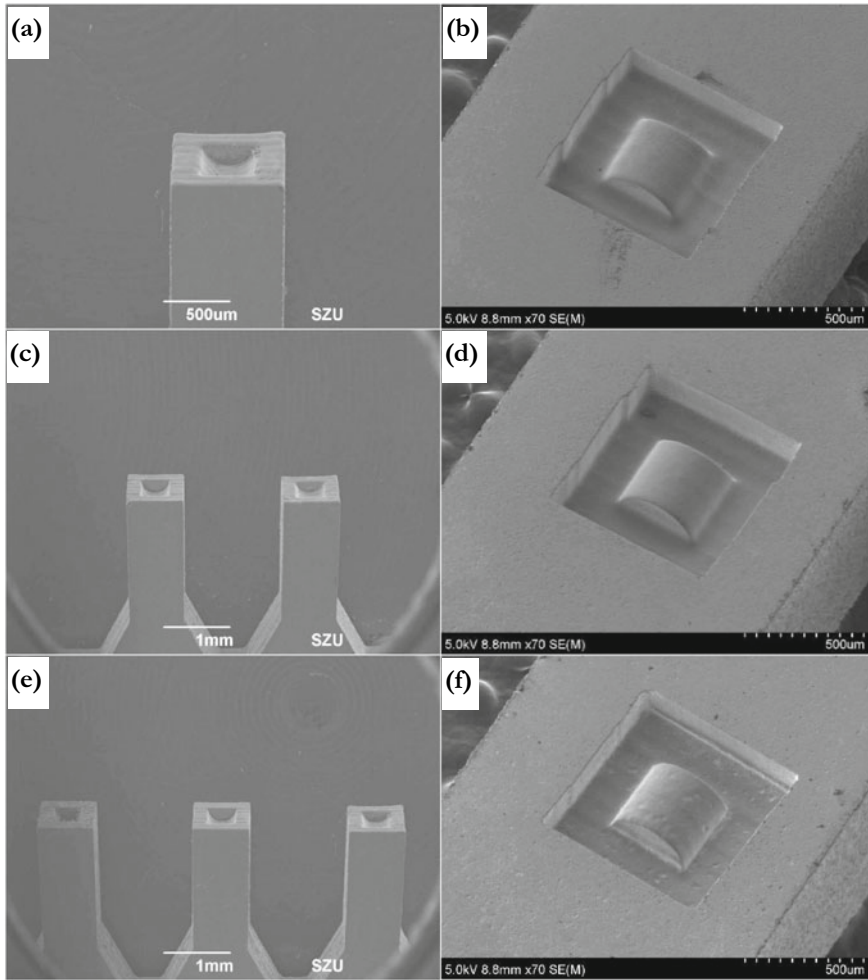
The 3D microstructure was obtained in 304# stainless steel by micro-EDM with 3D microelectrode. Micro-EDM process parameters are as follows: voltage of 80 V, pulse frequency of 0.2 MHz, pulse width  $T_{\text{on}}$  of 800 ns, pulse interval  $T_{\text{off}}$  of 4200 ns. To investigate the influence of 3D microelectrode wear on the dimensional accuracy of 3D microstructures, single 3D microelectrode was applied to process the 3D microstructures shown in Fig. 10b, e and h respectively.

The sizes of the 3D microstructures were measured, and the measurement results were compared with the designed size of the 3D microstructure. The comparison results are shown in Table 2 and it was found that the size error was from 8.4 to 16.4  $\mu\text{m}$  when the single 3D microelectrode was adopted to machine the 3D microstructure. The machining time of 3D microstructure shown in Fig. 10b, e and h was 85, 39 and 63 min. The surface roughness and section profile of 3D microstructure were also measured. It was found that the 3D microstructure was basically consistent with the design model, and the surface quality was good with surface roughness Ra of 0.48  $\mu\text{m}$ . The ridges on the 3D microstructure surface were not obvious.

### 3.2 3D Microstructure Machined by 3D Microelectrode Array

Through up and down reciprocating processing method, the 3D microelectrode can be applied in micro-EDM for obtaining the 3D microstructure, and the 3D microelectrode would have wear in the above process. The shape and dimension accuracy of 3D microstructure were adversely affect by the 3D microelectrode wear. In order to reduce the influence of 3D microelectrode wear on the machining accuracy of

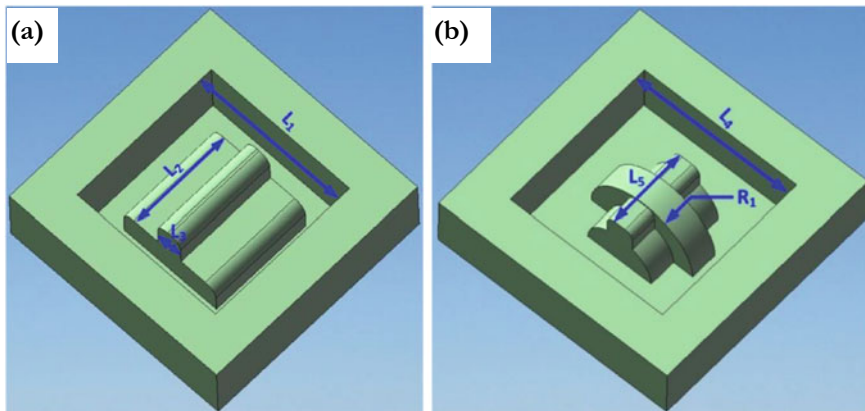




**Fig. 11** Impact of 3D microelectrode number on 3D micro-cavity: **a** the processed single microelectrode; **b** processing result of single microelectrode; **c** the processed microelectrode array with two electrodes; **d** processing result of microelectrode array with two electrodes; **e** the processed microelectrode array with three electrodes; **f** processing results of microelectrode array with three electrodes

3D microstructure, a group of 3D microelectrode array was prepared and adopted in micro-EDM in sequence for machining the same 3D microstructure.

In the 3D microelectrode array, the first 3D microelectrode was used for the rough machining and the subsequent 3D microelectrode was used for the finish machining of the same 3D microstructure, so as to reduce the influence of electrode wear on the machining accuracy of the 3D microstructure. Therefore, the more 3D microelectrodes involved in the machining of the 3D microstructure, the higher the



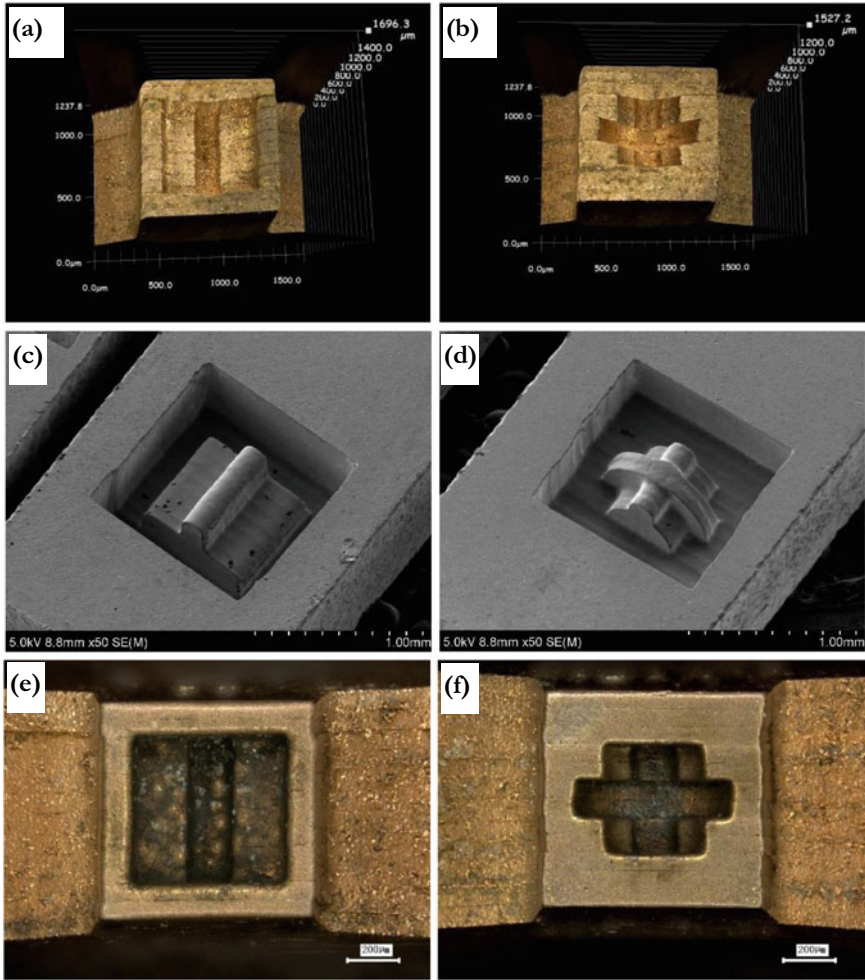
**Fig. 12** The CAD models of 3D micro-cavity molds

machining precision of the 3D microstructure, but the lower the machining efficiency of the 3D microstructure. Therefore, in order to obtain an appropriate number of microelectrodes, this paper used different numbers of microelectrodes to process the 3D microstructure, and the processing results are shown in Fig. 11.

The experimental object was a 3D micro-cavity with a half cylinder and the design depth of the micro-cavity was 250  $\mu\text{m}$ . According to the machining results shown in Fig. 11, the shape accuracy of the 3D micro-cavity machined by a single microelectrode was poor, but its surface quality was well (Fig. 11b). The shape accuracy and surface quality of the 3D micro-cavity machined by the microelectrode array containing two microelectrodes were better (Fig. 11d). The 3D micro-cavity machined by an electrode array containing three microelectrodes had good shape accuracy but poor surface quality (Fig. 11f). Joint discharge marks will appear inside the micro-cavity obtained in the above experiments, and the joint discharge marks are closely related to the welding quality of the 3D microelectrode. The better the welding quality of the 3D microelectrode, the less obvious the joint discharge marks.

The electrode wear will not only affect the shape accuracy of the 3D micro-cavity, but also affect the dimensional accuracy of the 3D micro-cavity. For investigating the effect of electrode wear on the dimensional accuracy of 3D micro-cavity, a stereomicroscope was used to measure the depth of the micro-cavity. The depth of the 3D micro-cavity shown in Fig. 11b was 235  $\mu\text{m}$ , the depth of the 3D micro-cavity shown in Fig. 11d was 246  $\mu\text{m}$ , and the depth of the 3D micro-cavity shown in Fig. 11f was 252  $\mu\text{m}$ . The shape accuracy and size accuracy of the 3D micro-cavity machined by the electrode array containing two and three microelectrodes had little differences. Therefore, considering the machining efficiency of 3D micro-cavity, electrode array containing two microelectrodes was selected in this paper to process 3D micro-cavity.

We also designed two kinds of micro-cavities, whose basic shapes are shown in Fig. 12. According to the micro-cavity, the 3D microelectrode array were designed and sliced to obtain the processing data. The 3D micro-cavity was machined in 304#



**Fig. 13** The 3D microelectrode array and the 3D micro-cavity: **a, b** 3D microelectrode array without micro-EDM; **c, d** the obtained 3D micro-cavities; **e, f** 3D microelectrode after processing

stainless steel through the micro-EDM of 3D microelectrode array including two microelectrode. The process parameters of micro-EDM are describe as follows: 80 V voltage, 0.2 MHz pulse frequency, 800 ns pulse width and 4200 ns pulse interval. The 3D micro-cavities were observed by the SEM and the results are shown in Fig. 13. Based on the experimental results, it can be seen that the 3D micro-cavity had a good surface morphology, and the joint discharge marks in the 3D micro-cavity mold were not obvious. The characteristic size of the 3D micro-cavity was measured and the measurement results are shown in Table 3. It can be seen from the data shown in Table 3 that the size error was from 2.5 to 8.4  $\mu\text{m}$  when the 3D microstructure

**Table 3** Dimensional comparison between CAD models and machined structures shown in Fig. 13

	Dimensional symbols	Dimensional values ( $\mu\text{m}$ )		
		CAD models	Machined structures	Errors
(a)	L1	1200	1203.7	3.7
	L2	800	806.8	6.8
	L3	200	203.7	3.7
	Depth	500	497.5	2.5
(b)	L3	1200	1206.3	6.3
	L4	600	608.4	8.4
	R1	425	428.2	3.2
	Depth	430	435.1	5.1

was processed with 3D microelectrode array. By comparing the data in Tables 2 and 3, the dimensional accuracy of the 3D micro-cavity processed by using the 3D microelectrode array was significantly improved.

## 4 Conclusions

In this paper, 3D microelectrodes were fabricated by superimposing multi-layer 2D microstructures, and the feasibility of this method were verified by the preparation of 3D microelectrodes.

3D microelectrodes with good surface quality were prepared using copper foil with thickness of 100  $\mu\text{m}$  under pulse width of 10  $\mu\text{s}$ , pulse interval of 40  $\mu\text{s}$ , wire cutting current of 0.42 A, voltage of 80 V, thermal diffusion temperature of 850  $^{\circ}\text{C}$ , thermal diffusion time of 10 h and force of 100 N.

Under the action of 80 V voltage, 0.2 MHz pulse frequency, 400 ns pulse width and 4600 ns pulse interval, the 3D microstructure with good surface quality was obtained by micro-EDM of 3D microelectrode in 304# stainless steel and the 3D microstructure was basically consistent with the design model. Compared with the layer by layer scanning discharge machining method, the 3D microstructure can be obtained by the up and down reciprocating method of 3D microelectrode array, which is simple and efficient.

**Acknowledgements** The work described in this chapter was supported by the National Natural Science Foundation of China (Grant No. 51405306), and the Shenzhen Natural Science Foundation University Stability Support Project (Grant No. JSGG20201102145402008).

## References

1. Yu ZY, Masuzawa T, Fujino M (1998) Micro-EDM for three-dimensional cavities-development of uniform wear method. *Cirp Ann-Manuf Techn* 47(1):169–172
2. Tong H, Li Y, Wang Y, Yu DW (2008) Servo scanning 3D micro-EDM based on macro/micro-dual-feed spindle. *Int J Mach Tool Manu* 48(7–8):858–869
3. Yan MT, Lin SS (2011) Process planning and electrode wear compensation for 3D micro-EDM. *Int J Adv Manuf Tech* 53:209–219
4. Richter C, Krah T, Büttgenbach S (2012) Novel 3D manufacturing method combining micro-electrical discharge machining and electrochemical polishing. *Microsyst Technol* 18:1109–1118
5. Sheu DY, Cheng CC (2013) Assembling ball-ended styli for CMM's tactile probing heads on micro EDM. *Int J Adv Manuf Tech* 65:485–492
6. Liu W, Jia ZY, Zou SB, Zhang LX (2014) A real-time predictive control method of discharge state for micro-EDM based on calamities grey prediction theory. *Int J Adv Manuf Tech* 72:135–144
7. Nguyen MD, Rahman M, Wong YS (2013) Transitions of micro-EDM/SEDCM/micro-ECM milling in low-resistivity deionized water. *Int J Mach Tool Manu* 69:48–56
8. D'Urso G, Maccarini G, Ravasio C (2014) Process performance of micro-EDM drilling of stainless steel. *Int J Adv Manuf Tech* 72:1287–1298
9. Liew PJ, Yan JW, Kuriyagawa T (2014) Fabrication of deep micro-holes in reaction-bonded SiC by ultrasonic cavitation assisted micro-EDM. *Int J Mach Tool Manu* 76:13–20
10. Tong H, Wang Y, Li Y (2008) Vibration-assisted servo scanning 3D micro EDM. *J Micromech Microeng* 18:025011
11. Yan MT, Lin SS (2010) Process planning and electrode wear compensation for 3D micro-EDM. *Int J Adv Manuf Tech* 53:209–219
12. Xu B, Wu XY, Lei JG, Luo F, Gong F, Du CL, Sun XQ, Ruan SC (2013) Research on micro-electric resistance slip welding of copper electrode during the fabrication of 3D metal micro-mold. *J Meter Process Tech* 213(12):2174–2183
13. Xu B, Wu XY, Ling SQ, Luo F, Gong F, Du CL, Ruan SC, Sun XQ (2012) Study on tungsten electrode deposition effect of 3D metal micro-mold during laminated slip welding. *Int J Adv Manuf Tech* 67:2529–2536
14. Xu B, Wu XY, Ling SQ, Luo F, Du CL, Sun XQ (2012) Fabrication of 3D metal micro-mold based on femtosecond laser cutting and micro-electric resistance slip welding. *Int J Adv Manuf Tech* 66:601–609
15. Xu B, Wu XY, Lei JG, Luo F, Du CL, Ruan SC, Wang ZL (2014) Study on the joining of 2D microstructure during the fabrication of 3D micro-mold. *Int J Precis Eng Man* 15:725–734
16. Xu B, Wu XY, Lei JG, Cheng R, Ruan SC, Wang ZL (2015) Laminated fabrication of 3D micro-electrode based on WEDM and thermal diffusion welding. *J Meter Process Tech* 221:56–65
17. Xu B, Wu XY, Lei JG, Cheng R, Ruan SC, Wang ZL (2015) Laminated fabrication of 3d queue micro-electrode and its application in micro-edm. *Int J Adv Manuf Tech* 80(9):1701–1711

# Chapter 9

## Fabrication of Micro-structures by Applying Cu-Sn 3D Micro-electrode



Zhaozhi Wu and Xiaoyu Wu

**Abstract** Laminated three-dimensional (3D) microelectrodes are fabricated via the thermal diffusion bonding process of two-dimensional (2D) microstructures of multi-layer Cu foils, and then applied to micro-electrical discharge machining (micro-EDM) to achieve 3D microstructures. The main difficulties are as follows. Firstly, the thermal diffusion bonding process is very time-consuming, reducing the 3D microelectrode preparation efficiency. Secondly, if the thermal diffusion bonding of the 3D microelectrode is unqualified, discharge ridges will be formed on the microstructure bottom surface. In this method, the 2D microstructures of multilayer Sn-plated Cu foils were clamped and fixed to fabricate a bundled 3D-laminated microelectrode, and a uniformly suspended EDM oil containing Cu (particle-size: 100 nm) and graphite (Gr, particle-size: 1  $\mu\text{m}$ ) powders was used as dielectric fluid to perform reverse-polarity powder-mixed EDM (PMEDM). Based on the matching process parameters, with the action of reverse-polarity spark discharge, self-welding was generated at the seams and its adjacent area of the interlayers in the bundled 3D-laminated microelectrode working surface. Meanwhile, a protective film was generated on the working surface of the laminated electrode. These factors leading to a favorable practicability of the bundled 3D-laminated microelectrode, improving the electrode preparation efficiency and surface quality, eliminating the discharge ridges on the microstructure bottom surface. To verify the feasibility of the aforementioned method, square-shaped blind microcavity, as well as 3D microstructures containing semi-cylindrical and rectangular features with a depth of nearly 800  $\mu\text{m}$ , were achieved on #304 stainless steel. The surface roughness of the microstructure was below Ra 0.5  $\mu\text{m}$ , and the wear of the bundled 3D-laminated microelectrode was significantly reduced.

---

Z. Wu (✉)

Guangdong Provincial Research Center of CNC Technology and Functional Component Engineering Technology, Guangdong Polytechnic Normal University, Zhongshan Ave West 293, Guangzhou 510665, Guangdong, China  
e-mail: [wuzhaozhi@gpnu.edu.cn](mailto:wuzhaozhi@gpnu.edu.cn)

X. Wu

Guangdong Provincial Key Laboratory of Micro/Nano Optomechanics Engineering, College of Mechatronics and Control Engineering, Shenzhen University, Nan-Hai Ave 3688, Shenzhen 518060, Guangdong, China

## 1 Introduction

Micro-fabrication technology is widely used in the fields of biomedical, aerospace and micro-electro-mechanical systems. One of which nonconventional machining technology of micro-electrical discharge machining (micro-EDM) through the high-density thermal energy to slightly remove the metallic material, with no need to consider the hardness of the workpiece [1, 2].

Comparing with traditional EDM, Micro-EDM with features include a lower discharge energy of single-pulse, smaller discharge gap and higher machining accuracy. These advantages yielding it has been widely used in the process of three-dimensional (3D) microstructures. In order to realise 3D micro-EDM, the means of uniform wear method (UWM) was proposed and used to fabricate complex 3D micro-cavities via the layer-by-layer discharge milling with a cylindrical microelectrode [3]. For realising the preparation of arbitrary 3D microstructures, researchers combined UWM with CAD/CAM systems to perform 3D micro-EDM [4]. With this method, complex 3D microstructures were prepared on #304 stainless steel by using a tungsten microelectrode with a diameter of 52  $\mu\text{m}$ . To determine and compensate for the wear of cylindrical microelectrode, the researchers proposed a method of real-time compensation for the electrode wear, and successfully fabricated a high-precision 3D microcavity via this method [5, 6].

In the process of 3D micro-EDM, the working end of cylindrical microelectrode is worn down to a cone, which is not conducive to the machining accuracy. To improve this problem, a mathematical model for a fixed-length compensation method for the cylindrical microelectrode wear in micro-EDM milling was established to predict the shape of the machined surface of the tool and the workpiece [7]. Researchers replaced a cylindrical tool with a tubular tool to develop an analytical model relating the truncated conic shape to fix-length compensation parameters for improving the machining precision [8]. Previous studies applied composite electrodes of tungsten carbide-polycrystalline diamond to alternately change the discharge energy, and established the principle and discharge model of electric spark discharge according to the relationship between discharge current and plasma channel expansion. Examination results revealed that the surface roughness and the recast layer thickness decreased obviously [9].

Cylindrical microelectrode discharge milling can manufacture various complex 3D microstructures, but with a poor anti-interference ability and a low machining efficiency. The application of 3D electrode to micro-EDM is an available method to overcome these matters. A means of thermal diffusion bonding technology was used to construct a laminated electrode containing microgrooves with several tens micron width and depth that were machined in a copper plate for jetting dielectric liquid over the working surface and it was applied to EDM [10, 11]. The products removing ability, machining time and machining precision were improved. On the basis, a 3D-laminated microelectrode that prepared by the thermal diffusion bonding process with two-dimensional (2D) microstructures of multilayer Cu foils was applied to

micro-EDM [12]. In the process, discharge ridges that copied by laminated micro-electrode were formed on the microstructure bottom surface, which significantly reduced the surface precision. To avoid discharge ridges, researchers used Sn-plated Cu foils to process 3D-laminated microelectrodes by increasing the time of thermal diffusion bonding process [13]. Not only a strong Cu/Sn alloy connection formed at the interlayer seams, but also the discharge ridges on the bottom surface of the 3D microcavities were effectively eliminated. However, the wear of Cu/Sn alloy electrode was obviously higher than that of the pure Cu electrode, and the former microelectrode manufacture process was time-consuming. To solve the difficulty of timely updating dielectric in the manufacturing process of large-depth 3D microstructure via 3D microelectrode, a 3D-laminated microelectrode with rectangular holes on both of its undersurfaces was fabricated by the means of bending-and-avoiding mode wire EDM combined with vacuum thermal diffusion bonding process was used for performing vibration-assisted micro-ECM to prepare deep 3D microcavities via a suspension containing  $B_4C$  particles [11]. The results indicated that the quality of the bottom surface and sidewall of the deep 3D microcavities were improved [14].

The processing performance with reverse-polarity EDM is significantly different from that with positive-polarity EDM. Previous studies confirmed that the electrode wear in normal polarity processing was much larger than that in reverse-polarity processing [15]. Moreover, it was revealed that the use of a negative electrode polarity in EDM is necessary to acquisition the mirror-finish condition [16]. Previous study examined that depositing a thicker carbon layer on the copper anode leads to a lower copper vapor density, conforming the hypothesis that the electrode surface carbon layer could protect the copper anode from wear [17]. And observed that many metal fragments were adhered to the working surface of the electrode after the reverse-polarity machining process. Some researchers used Cu and graphite (Gr) electrodes to conduct reverse-polarity EDM on a Ti-6Al-4 V alloy [18]. The results showed that the material removal rate (MRR) of the Cu electrode was high, and a suitable large pulse ON/OFF-time could generate a minimal tool wear. There some experiments of discharge milling researched the performance of tool polarity on the wear of electrode and the roughness of microstructure surface [19, 20].

Powder-mixed EDM (PMEDM) possessing significantly more spark discharge channels, thus reducing the discharge energy of a single pulse and resulting in small surface corrosion craters, which was beneficial for the quality improving of microstructure surfaces [21].  $Al_2O_3$  particles was added into kerosene for EDM of titanium alloy. Results suggested that the decomposition of dielectric fluids led to the formation of carbon, oxygen, surface oxides and carbides. The addition of powder yielding a decreased crack density and conductivity of the machined surface, resulting in lower deep cavities and uniformity PMEDM surface [22]. Various powders were separately added to the dielectric fluid for EDM experiments, the consequences revealed that the Gr powder was effective to yield a very fine finish surface and the narrowed breakdown voltage enable spark discharge to be carried out in a wider range of machining gap [16]. Although the pulse energy of a single spark discharge reduced during the PMEDM, a higher frequency of spark discharge could lead to a greater MRR [23]. To improve the material removal efficiency, the empirical formula



of MRR that according to the research analysis of powder-mixed near-dry EDM was established [24]. Some researchers used kerosene-containing Gr powder for micro-EDM to study the MRR and tool wear rate (TWR) [25]. The results suggested that the wear ratio of TWR/MRR was decreased by approximately 28%. Moreover, a study indicated that processing with Cu powder could generate the smallest MRR compared with other powders but also the smallest machining gap and TWR [26].

3D microelectrode can improve the preparation efficiency of micro-EDM. But the time-consuming fabrication process of 3D microelectrode limit the machining efficiency. The research proposed a method of abandoning the thermal diffusion bonding process to fabricate the bundled 3D-laminated microelectrodes with the foils of Sn-plated Cu. Reverse-polarity micro-PMEDM experiments were carried out via the bundled microelectrodes and a uniform suspension dielectric fluid adding both Gr and Cu powders. Under the action of reverse-polarity powder-mixed spark discharge, self-welding generated at the interlayer seams in the working surface of the bundled 3D-laminated microelectrode. Compared with the previous manufacturing technologies of 3D-laminated microelectrode, the fabrication procedure of the bundled 3D-laminated microelectrode was simplified and does not involve the vacuum pressure thermal diffusion bonding process, which effectively improved the fabrication efficiency of laminated microelectrode. Meanwhile, a protective film was generated on the laminated microelectrode working surface, which would significantly improve the electrode surface quality and wear, eliminating the discharge ridges on the bottom surface of the microstructure.

## 2 Experimental Materials and Equipment

Sn film with a thickness of 3  $\mu\text{m}$  was plated on the upper and lower surfaces of the copper foil matrix to produce a Sn-plated copper foil with a total thickness of 106  $\mu\text{m}$ , which was applied to prepare the bundled 3D-laminated microelectrode. 2 mm thickness #304 stainless steel was used as workpiece blank for processing typical 3D microstructures. Figure 1 shows the reverse-polarity micro-PMEDM platform. The EDM oil which contain both Gr (particle size, 1  $\mu\text{m}$ ) and Cu (particle size, 100 nm) powders was used as dielectric fluid.

A wire EDM (WEDM) machine (H-CUT-32F, HI-LINK) was used to cut the Sn-plated Cu foils layer-by-layer to achieve multilayer 2D microstructures. On this ground, preparing the bundled 3D-laminated microelectrode. A three-axis motion platform (M511.DD, PI) used for the feeding of bundled 3D-laminated microelectrode while on the reverse-polarity micro-PMEDM. All the preparing process of microstructure on the #304 workpiece were completed by the conventional means of Die-sink EDM. The tool electrode feed and back process with a travelling speed of 2 mm/s. A scanning electron microscope (Quanta FEG450, FEI) was applied to reconstruct the 3D morphology of the microstructure and measure the dimensions. A laser scanning confocal microscope (LSCM) (VK-X260K, Keyence) used for testing the surface roughness and 3D profile of the microstructures.

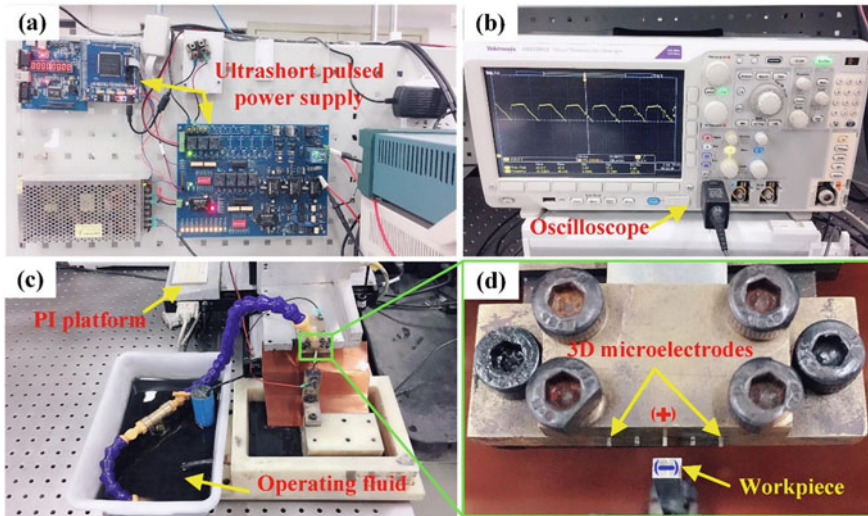


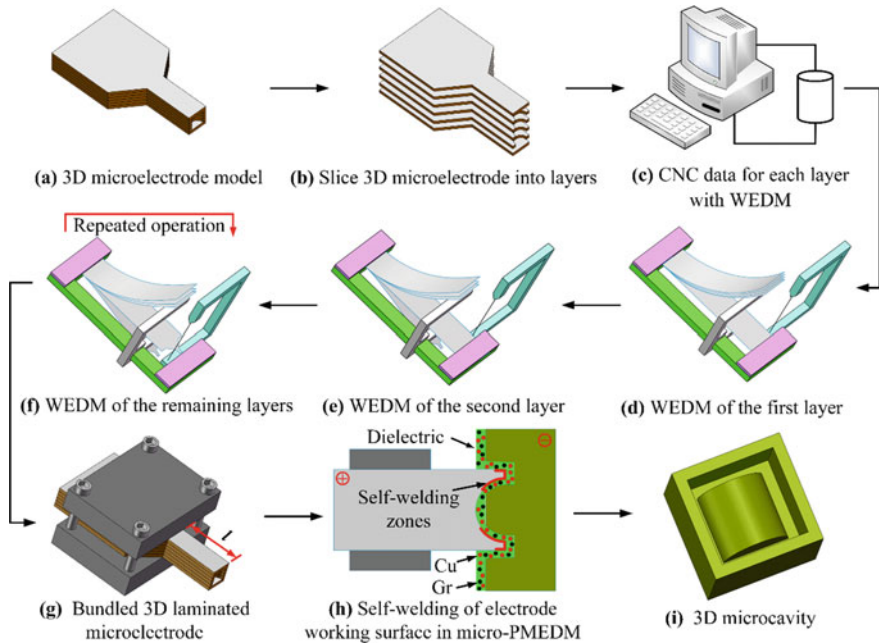
Fig. 1 Reverse-polarity micro-PMEDM platform

### 3 Principle of Reverse-Polarity Micro-PMEDM of Bundled 3D-Laminated Microelectrode

#### 3.1 Technological Process

The manufacturing procedure of the bundled 3D-laminated microelectrode and the process of reverse-polarity micro-PMEDM are as follow.

- (1) Based on the target 3D microstructure, the corresponding 3D microelectrode (Fig. 2a) was designed and divided into thin slices following the thickness direction, so that to achieve much information of each 2D layer of the designed microelectrode, including the number, thickness and processing data (Fig. 2b).
- (2) The total 2D layers processing data were introduced to the system of WEDM (Fig. 2c) for layer-by-layer cutting of the preliminary laminated Sn-plated Cu foil blanks, thus to achieve an initial laminated electrode composed of the multi-layer 2D microstructures. The detailed process of wire EDM cutting was as follows. Firstly, one end of the laminated Sn-plated Cu foils was welded through the micro-resistance welding and clamped with a fixture. Then, another end of the first layer was tiled and fixed upon the fixture (Fig. 2d). To avoid cutting interference, the rest of the Sn-plated Cu foils were elastically bent upward and fixed by a block. After the cutting of the first layer was completed, it was bent downward elastically and fixed through the block. Then, the second layer was tiled and fixed on the fixture to be cut (Fig. 2e). This process was repeated (Fig. 2f) until all the foils were cut.

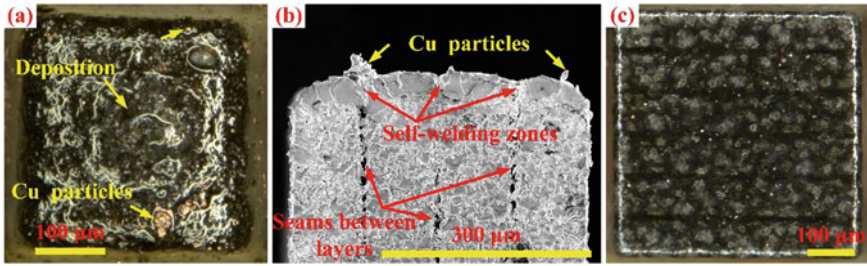


**Fig. 2** Reverse-polarity micro-PMEDM process for the bundled 3D-laminated microelectrode

(3) As shown in Fig. 2g, the bundled 3D-laminated microelectrode that fabricated by the multilayer 2D microstructures obtained from step (2) was installed on a special fixture to conduct reverse-polarity micro-PMEDM (Fig. 2h). Finally, the corresponding 3D microstructure was obtained on the workpiece (Fig. 2i). The time-consuming thermal diffusion bonding process was excluded from the bundled 3D-laminated microelectrode preparation process.

### 3.2 *Effects of Powder on the Working Surface of Laminated Electrode*

The dielectric fluid of the processed method was EDM oil, which contains Gr and Cu powders. For the purpose of ensuring the uniformity of the suspension fluid in the whole process of reverse-polarity micro-PMEDM, the dielectric fluid was stirred continuously. The Cu powder with a melting point of 1,083.4 °C was the same material with the bundled 3D-laminated microelectrode matrix, and its affinity with the Sn (melting point: 231.89 °C) film at the seams was appreciative. In the process of reverse-polarity micro-PMEDM, Cu powder is easily adhered to the working surface of the bundled microelectrode, so that to transfer high temperature to the Sn films. Under these factors, the interlayer seams on the working surface of the laminated electrode generated completed and continuous welds (Fig. 2h).



**Fig. 3** Effects of Cu and Gr powders on the working surface of bundled 3D-laminated microelectrode: **a** only adding Cu powder; **b** section view of (a); **c** both adding Cu and Gr powders

As shown in Fig. 3a, the results depicted that with the effect of the high-temperature channels during the EDM process, the added powder was easy to mutual collide and bond, generating larger size particles and adhering to the laminated electrode working surface, when the dielectric fluid only contain Cu powder. Figure 3b displays completely welded Sn films at the seams on the electrode working surface. The addition of Gr powder which with a significantly higher melting point of 3,652 °C could isolate, impact, and separate the Cu powder, thus preventing its mutual bonding in the high-temperature discharge channels. Suitable concentration of Cu and Gr powders was beneficial to generate a high-quality working surface of the bundled 3D-laminated electrode (Fig. 3c). Similar study has also shown, in the process of reverse-polarity EDM, a protective film of thicker carbon layer that generated on the working surface of the electrode could reduce the electrode from wear [17].

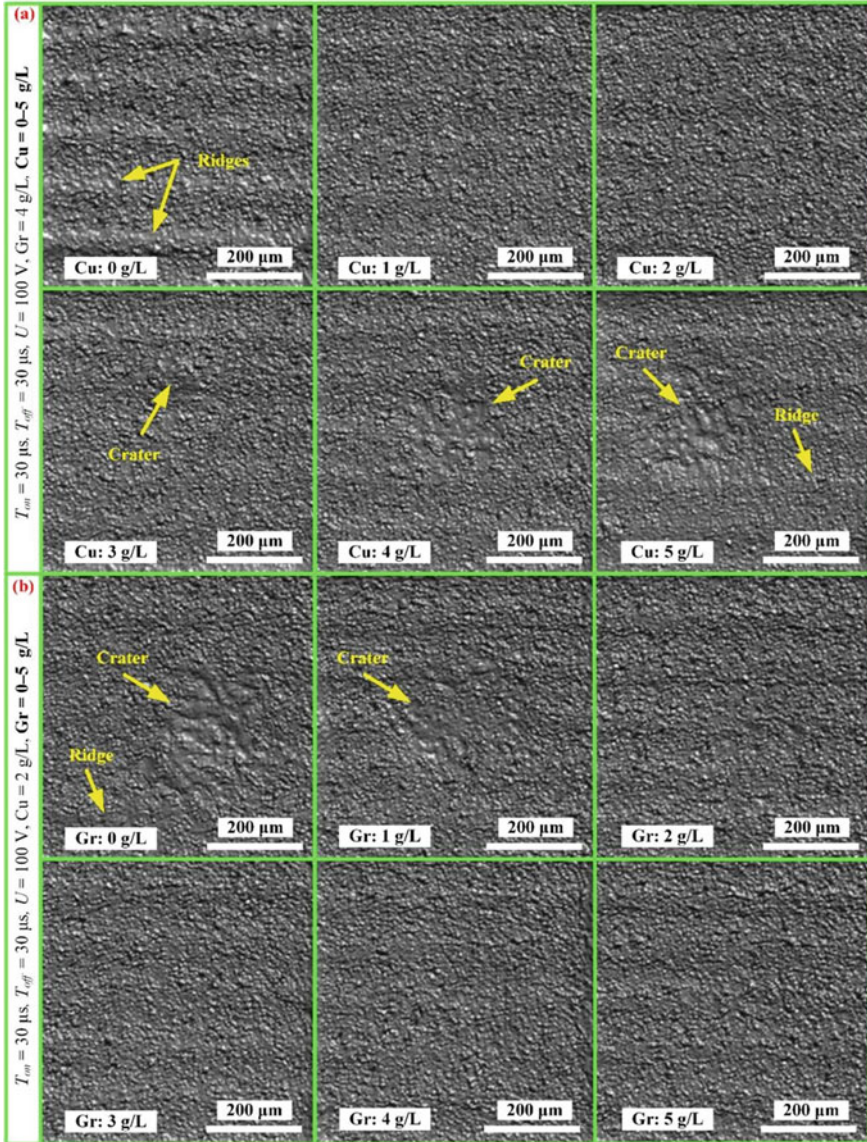
## 4 Elimination of Discharge Ridges on Microstructure Bottom Surface

### 4.1 Concentrations of Gr and Cu Powders

To reveal the influence of discharge ridges on the bottom surface of the microstructures by Gr (0–5 g/L) and Cu (0–5 g/L) powder concentrations, reverse-polarity micro-PMEDM was performed via the bundled 3D-laminated microelectrodes which fabricated with six Sn-plated Cu foils. The process parameter of voltage  $T_{on} = 30 \mu s$ , voltage  $T_{off} = 30 \mu s$  and machining voltage  $U = 100 V$ . The processing object was a 200- $\mu m$ -deep square-shaped blind cavity.

Figure 4 displays the results of reverse-polarity micro-PMEDM with different concentrations of Gr and Cu powders. Under the concentration of 4 g/L of Gr powder, the effect of different concentrations of Cu powder on the removal of discharge ridges on the bottom surface of the microstructures as shown in Fig. 4a. If the dielectric fluid only contained Gr powder without Cu powder (0 g/L), clear discharge ridges could be observed on the bottom surface. When the Cu powder with a concentration of 1 g/L,

the discharge ridges were weakened. When the concentration increased to 2 g/L, there were no obvious discharge ridge. However, if the concentration exceeded 2 g/L, more obvious and increasingly large micro-craters formed on the bottom surface of the microstructures.



**Fig. 4** Effect of the powder concentration on the removal of discharge ridges on the bottom surface of the machining results: **a**  $Gr = 4 g/L$ ,  $Cu = 0-5 g/L$ ; **b**  $Cu = 2 g/L$ ,  $Gr = 0-5 g/L$

The experimental results show that the Cu powder is easily melted and adhered to the bundled 3D-laminated microelectrode working surface and its interlayer seams, leading to a high temperature transfer to the Sn-plated Cu foil. The seams on the bundled 3D-laminated microelectrode working surface formed continuous welds. Under these favorable conditions, include the action of the uniform electric field contributed by the suspended Cu powder, the surface material was uniformly removed by uniform discharge, the bottom surface discharge ridges were effectively weakened and eventually eliminated. When the concentration of Cu powder increased above 2 g/L, the insulation effect of the dielectric fluid decreased. Redundant Cu powder was equivalent to metal debris particles, which easy to induce concentrated discharge. Therefore, frequent short circuits, arcing and an unstable process could occur [26], resulting in micro-craters in the middle of the machined surfaces and reducing the removal efficiency of discharge ridges. In addition, the presence of excessive powder particles in the discharge gap led to sedimentation and bridging effects, resulting in the surface deterioration of the machined result [27].

Figure 4b displays the effects of different concentrations of Gr powder on the removal of the discharge ridges on the microstructure bottom surface under the condition of Cu powder concentration was 2 g/L. If the dielectric fluid only contained Cu powder without Gr powder (0 g/L), there were slight discharge ridges on the bottom surface of the microstructure. As only with Cu powder, arc discharge easily occurred in the middle of the electrode, leading to a micro-crater in the corresponding position of the machining result. With the increase of Gr powder concentration, the micro-crater on the bottom surface of the machining result gradually weakened and disappeared.

The Gr powder with a high melting point could isolate and separate the Cu powder, reducing the bonding with each other and avoiding the generation of large Cu particles, which decreased the formation possibility of arc discharge. In addition, with the increase of Gr powder concentration, the discharge energy density of a single pulse was decreased and the gap explosions pressure weakened, which effectively decreased the generation of micro-crater. When the Gr powder concentration was 4 g/L, the discharge ridge and micro-crater on the bottom surface of the machining result were effectively eliminated. If the Gr powder concentration raised to 5 g/L, the frequently short circuits led to an inefficient machining process.

Therefore, considering the processing efficiency and surface quality of the machining results, the concentrations of Gr and Cu powders were set as 4 and 2 g/L, respectively.

## 4.2 Voltage $T_{on}$ and $T_{off}$

To achieve a suitable voltage  $T_{on}$  (10–60  $\mu$ s) and  $T_{off}$  (10–60  $\mu$ s), different combinations of  $T_{on}$  and  $T_{off}$  were applied to perform reverse-polarity micro-PMEDM. The other major factors of U was 100 V, concentrations of Gr and Cu powders was 4 and

2 g/L, respectively. The processing object was a 200- $\mu\text{m}$ -deep square-shaped blind cavity.

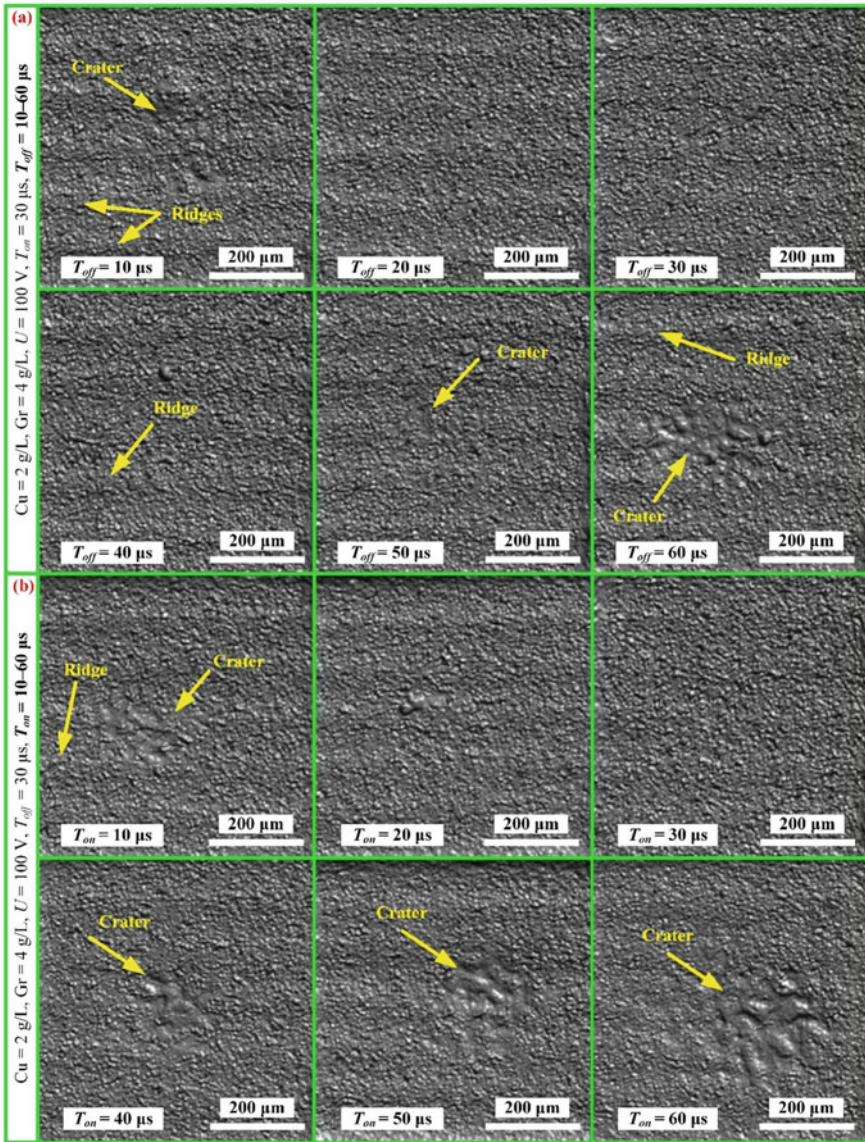
Figure 5a displays the effect of voltage  $T_{\text{off}}$  on the elimination of discharge ridges when the voltage  $T_{\text{on}}$  was 30  $\mu\text{s}$ . When the  $T_{\text{off}}$  was 10  $\mu\text{s}$ , micro-crater and obvious discharge ridges were generated on the bottom surface of the machining result. As the  $T_{\text{off}}$  increased, the micro-crater disappeared and the discharge ridges were weakened. When the  $T_{\text{off}}$  was 30  $\mu\text{s}$ , discharge ridges effectively were eliminated. As the  $T_{\text{off}}$  increased further, the discharge ridges and micro-craters became obvious, especially with a  $T_{\text{off}}$  of 60  $\mu\text{s}$ .

A small  $T_{\text{off}}$  means a too short time was applied for transferring the corrosion products that produced in the EDM process, which caused a trouble to renew the dielectric fluid in the limited time. The corrosion products that were unable to be transferred in a timely manner that were easily non-uniformly deposited on the electrode working surface, which induced some troubles include short circuits and arc discharge. Correspondingly, micro-crater was formed on the microstructure bottom surface. With the increase of  $T_{\text{off}}$ , the difficulty of the corrosion products transferring was gradually declined, and the quality of the bottom surface of the microstructure gradually improved. When the  $T_{\text{off}}$  reached to 30  $\mu\text{s}$ , defects such as discharge ridges and micro-crater were effectively disappeared. For the further increase of  $T_{\text{off}}$ , a too low pulse duty cycle decreased the processing energy. The phenomena of short circuits and arc discharge caused an unstable machining process, reducing the removal efficiency of discharge ridge, which led to the regeneration of micro-craters especially with a  $T_{\text{off}}$  of 60  $\mu\text{s}$ .

Figure 5b displays the effects of  $T_{\text{on}}$  on the elimination of discharge ridges when the  $T_{\text{off}}$  was 30  $\mu\text{s}$ . When the  $T_{\text{on}}$  was 10  $\mu\text{s}$ , the result surface generated clear micro-crater and discharge ridges. With the increase of  $T_{\text{on}}$ , the micro-crater and discharge ridges were gradually weakened. When it increased to 30  $\mu\text{s}$ , the smooth machined surface had no obvious defect. However, with the further increase of  $T_{\text{on}}$ , the micro-craters became increasingly visible. The crater was the most obvious when the  $T_{\text{on}}$  was 60  $\mu\text{s}$ .

The results showed that with a small  $T_{\text{on}}$  of 10  $\mu\text{s}$ , a low pulse duty cycle caused an unstable machining process and surface defects such as micro-crater and discharge ridges. With the increase of  $T_{\text{on}}$ , the duty cycle became reasonable and the quality of the bottom surface gradually improved. When the  $T_{\text{on}}$  increased up to 30  $\mu\text{s}$ , the microstructure with a smooth surface and without clear defect. With the further increase of  $T_{\text{on}}$ , the MRR also improved. Within a limited time, the redundant processing products were unable to be effectively transferred, leading to short circuits and arc discharge during the process. In summary, when the  $T_{\text{on}}$  is out of range, defects can be easily formed on the bottom surface.

Thus, with  $T_{\text{on}}$  and  $T_{\text{off}}$  both at 30  $\mu\text{s}$ , discharge ridges on the bottom surface of the machining result were effectively removed, and there were no micro-crater.



**Fig. 5** Effect of the voltage  $T_{off}$  and  $T_{on}$  on the elimination of defects on the bottom surface of the machining results: **a**  $T_{on} = 30 \text{ }\mu\text{s}$ ,  $T_{off} = 10\text{--}60 \text{ }\mu\text{s}$ ; **b**  $T_{off} = 30 \text{ }\mu\text{s}$ ,  $T_{on} = 10\text{--}60 \text{ }\mu\text{s}$



### 4.3 Machining Voltage $U$

To achieve a suitable machining voltage  $U$  (80–140 V), experiments of reverse-polarity micro-PMEDM were performed with different voltages. The other parameters, Gr powder concentration was 4 g/L, Cu powder concentration was 2 g/L. The  $T_{on}$  and  $T_{off}$  were both 30  $\mu$ s. The processing object was a 200- $\mu$ m-deep square-shaped blind cavity.

Figure 6 displays the bottom surfaces of the 3D microstructures obtained via the different machining voltages. With a low machining voltage of 80 V, the insufficient discharge energy and the unstable machining process went against the removal efficiency of discharge ridges, and resulted in the defects that generated on the surface of the machining result. With the increase of  $U$ , surface defect of discharge ridges was gradually weakened. When the  $U$  increased up to 100 V, the discharge ridge effectively eliminated. With the further increase of the  $U$ , the discharge ridges reappeared and the electrode wear increased accordingly.

In the machining process, when the protective film was fully destroyed by discharge and arc, the difference in resistivity between the electrode matrix and the interlayer seams yielding a non-uniform wear in the adjacent area on the working surface of the bundled 3D-laminated microelectrode. Under the action of this factor, the wavy wear gradually formed on the working surface of the microelectrode, leading to the generation of discharge ridges on the machined surface [11]. When the  $U$  reached up to 140 V, the removal rate of workpiece material was greatly improved, but redundant corrosion products that unable to be effectively transferred within a

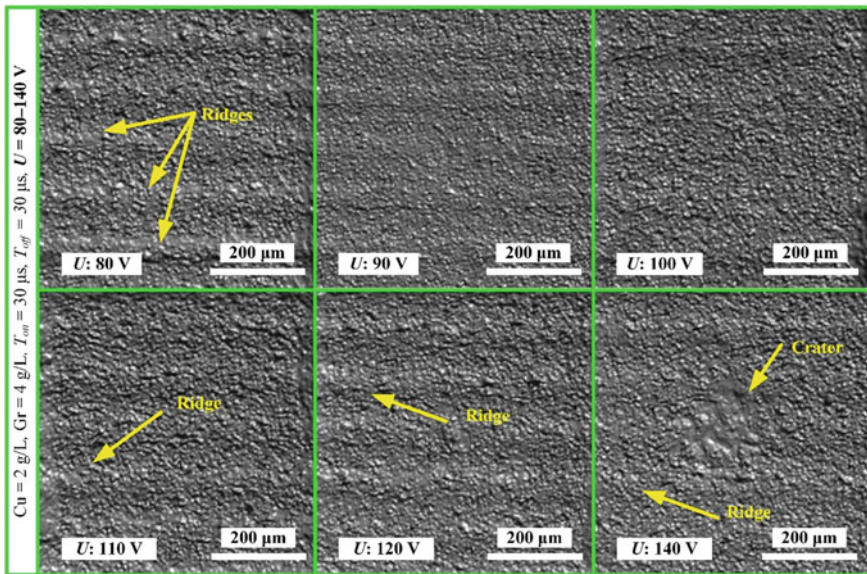


Fig. 6 Effect of the  $U$  (80–140 V) on the elimination of discharge ridges on the bottom surface

certain period of time, resulting in the short circuits and arc discharge in the machining process. Finally, the obvious discharge ridges and larger micro-crater generated on the microstructure surface. According, the  $U$  should be set to a reasonable value of 100 V.

According to the foregoing explore, when the key parameters were matched, including the Gr and Cu powders concentrations, the voltage  $T_{on}$  and  $T_{off}$  and the machining voltage  $U$ , defects such as discharge ridge and micro-crater on bottom surface of the machining results could be effectively avoided in reverse-polarity micro-PMEDM.

## 5 Fabrication of 3D Microstructure

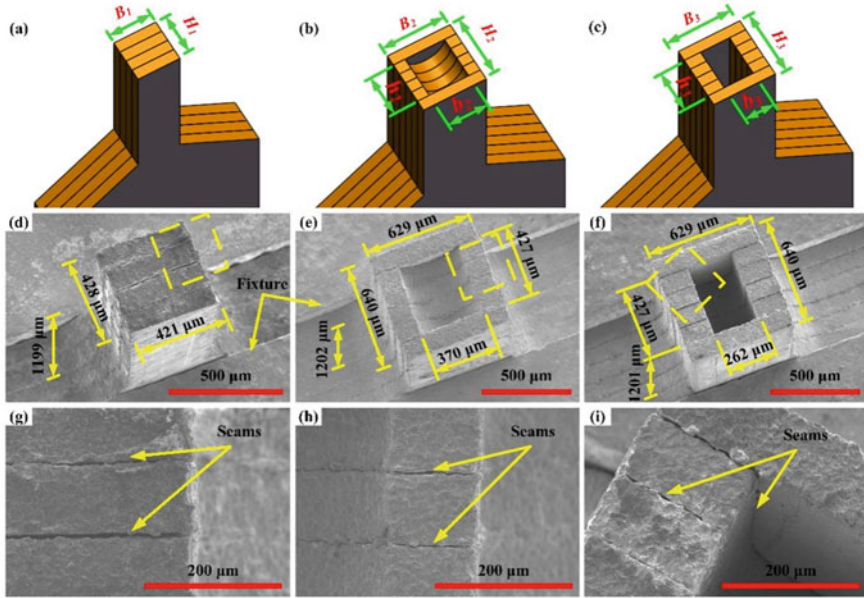
### 5.1 Typical 3D Microelectrodes

Three types of bundled 3D-laminated microelectrode models with rectangular solid, semi-cylindrical and rectangular cavities, as shown in Fig. 7a–c. The laminated microelectrodes were prepared by Sn-plated Cu foils with a thickness of 106  $\mu\text{m}$ . The main dimensions of 2D microstructures of the bundled microelectrodes are as follows:  $H_1 = 424 \mu\text{m}$  (4-layers),  $B_1 = 424 \mu\text{m}$ ,  $H_2 = 636 \mu\text{m}$  (6-layers),  $B_2 = 636 \mu\text{m}$ ,  $h_2 = 424 \mu\text{m}$ ,  $b_2 = 370 \mu\text{m}$  (R 185  $\mu\text{m}$ ),  $H_3 = 636 \mu\text{m}$  (6-layers),  $B_3 = 636 \mu\text{m}$ ,  $h_3 = 424 \mu\text{m}$  and  $b_3 = 260 \mu\text{m}$ .

Figure 7d–f display the bundled 3D-laminated microelectrodes which prepared by the method of bending-and-avoiding layer-by-layer WEDM. The actual dimensions of the three type microelectrodes corresponding to the design models as shown in Fig. 7d–f. The preparation method can be used to fabricate multiple laminated microelectrodes with the same specifications simultaneously on a set of laminated foils (Fig. 1d). The actual dimensions in Fig. 7d–f show that the dimension error of the bundled 3D-laminated microelectrode in the thickness direction was no larger than 4  $\mu\text{m}$ . The magnified images in Fig. 7g–i corresponding to the sections that marked by yellow dashed lines in Fig. 7d–f, respectively. The interlayers on the working surface of the bundled 3D-laminated microelectrode was better joined and with no obvious misalignment

### 5.2 Micro-EDM 3D Microstructure Without Powder

For the bundled 3D-laminated microelectrode, to verify the advantages of reverse-polarity micro-PMEDM on the machining result, the bundled laminated microelectrode was used for micro-EDM without powder. The process parameters were as follows. The concentrations of Gr and Cu powders were both 0 g/L, the voltage  $T_{on}$

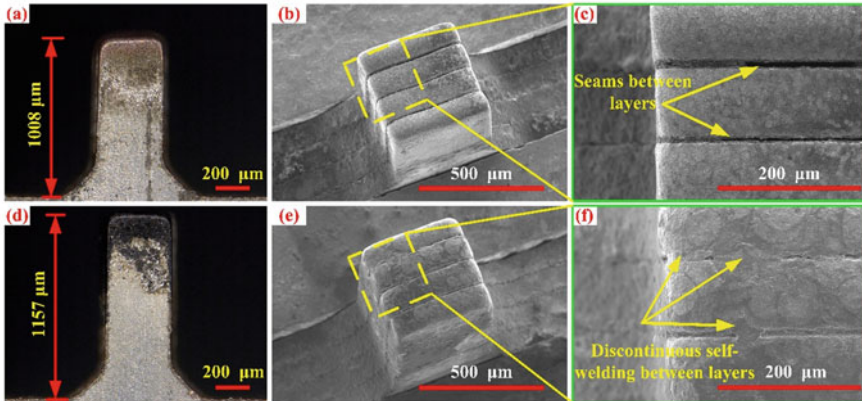


**Fig. 7** Bundled 3D-laminated microelectrodes: **a, d, g** solid microelectrode; **b, e, h** with a semi-cylindrical cavity; **c, f, i** with a rectangular cavity

and  $T_{off}$  were both  $30 \mu s$ , the  $U$  was  $100 V$ , the workpiece blank was #304 stainless steel, and the preset machining depth  $D$  was  $800 \mu m$ .

Before the micro-EDM, the height of the laminated microelectrode was  $1,199 \mu m$ . Figure 8a–c and d–f show the electrodes after machining to the preset depths via positive-polarity and reverse-polarity micro-EDM, respectively. As shown in Figs. 8a and d, the height of the machined microelectrodes decreased to  $1,008$  and  $1,157 \mu m$ , respectively. In other words, under the action of positive-polarity and reverse-polarity machining, the wear of the microelectrodes in the height direction was  $191$  and  $42 \mu m$ , respectively. Figure 8c and f show the magnified drawings of the sections marked by yellow dashed lines in Fig. 8b and e, respectively. Figure 8c shows that there were obvious seams between the electrode layers, and the discontinuous self-welding between the electrode layers is obvious in Fig. 8f.

Figure 9a–c and d–f show the square-shaped blind microcavities obtained via positive-polarity and reverse-polarity machining, respectively. Figures 9b and e show magnified images of the bottom faces in Fig. 9a and d, respectively. The measurement results obtained using the LSCM show that the surface roughness of the microstructure obtained via positive-polarity machining was low ( $R_a = 0.375 \mu m$ ), but there were obvious discharge ridges (Fig. 9c). The resistivity of the electrode Cu foil matrix was significantly lower than that of the Sn films at the seams, leading to an inconsistent machining wear between the electrode Cu foil matrix and the seams. Correspondingly, a wavy morphology on the electrode working surface was formed, resulting



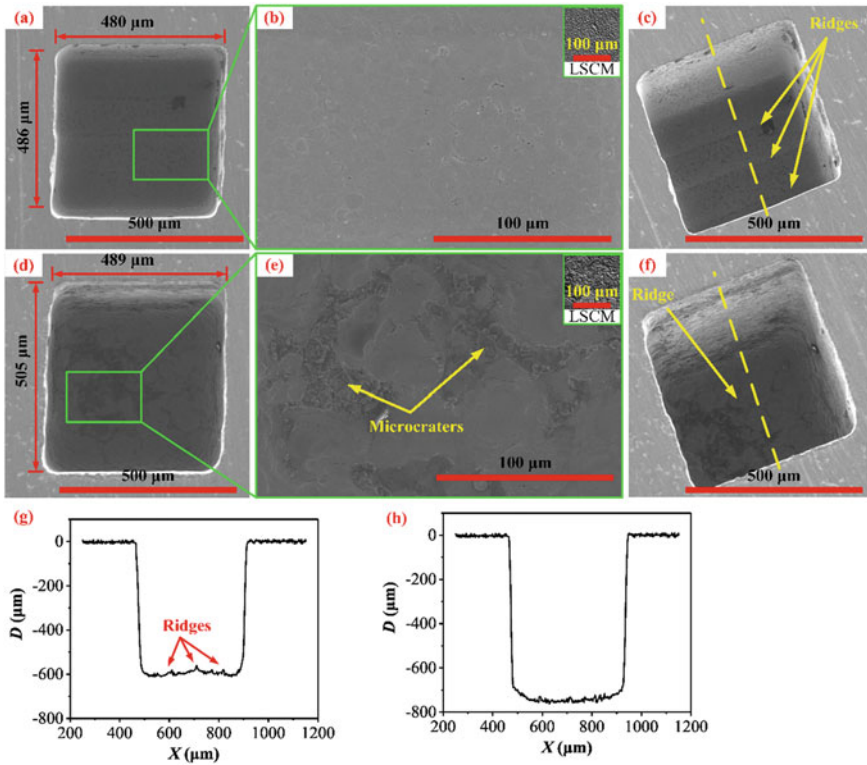
**Fig. 8** 3D microelectrodes after positive-polarity and reverse-polarity micro-EDM: **a–c** positive polarity; **d–f** reverse polarity

in obvious discharge ridges on the bottom surface of the machining result (Fig. 9g). The machining result obtained via the reverse-polarity machining had obvious micro-craters and high surface roughness ( $R_a = 1.344 \mu\text{m}$ ), but the discharge ridges were significantly weakened (Fig. 9h). Figure 9a and d that obtained by the aforementioned process parameters compared with Fig. 7d, revealing that the machining side gaps for positive-polarity and reverse-polarity machining were below 30 and 37  $\mu\text{m}$ , respectively.

### 5.3 Reverse-Polarity Micro-PMEDM 3D Microstructure

The bundled 3D-laminated microelectrodes in Fig. 7d–f were conducted to reverse-polarity micro-PMEDM via the EDM oil containing Gr and Cu powders with concentrations of 4 and 2 g/L, respectively. The other parameters were the same as the mentioned in Sect. 5.1.

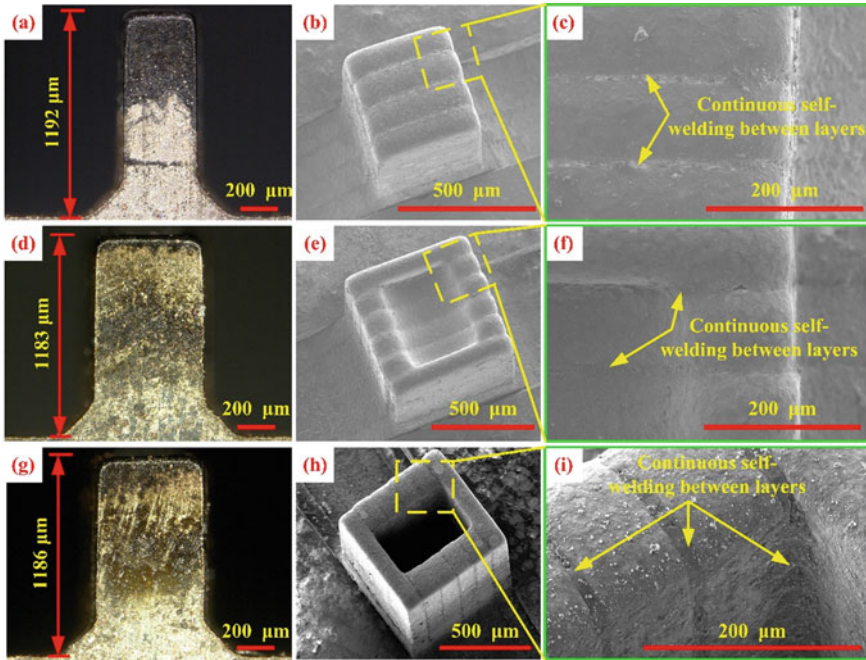
Figure 10 displays the bundled 3D-laminated microelectrodes after reverse-polarity micro-PMEDM. The heights of the machined electrode respectively decreased from 1199, 1202 and 1201  $\mu\text{m}$  to 1,192, 1,183, and 1,186  $\mu\text{m}$ , as shown in Fig. 10a, d, and g. It suggests that the wear of the three typical electrodes in the height direction were less than 20  $\mu\text{m}$ , which was greatly smaller than the wear of positive-polarity micro-EDM and reverse-polarity micro-EDM without powder. Figure 10c, f, and i exhibit magnified drawings corresponding to the sections that marked by the yellow dashed lines in Fig. 10b, e, and h, respectively. The interlayers on the working surface of the machined microelectrodes presented a better phenomenon of continuous self-welding, which was very advantageous for obtaining a high-quality machining surface.



**Fig. 9** Fabrication of square-shaped blind microcavities without powder: **a–c, g** positive polarity; **d–f, h** reverse polarity

Figure 11 displays the 3D microstructures which obtained by reverse-polarity micro-PMEDM with a peak current of 2 A. The corresponding process time of machining to the preset depth of 800 μm approximately was 3, 4 and 3 h, respectively. The results revealed that there were no clear discharge ridge on the bottom surfaces. The corresponding magnified drawings in Fig. 11d–f exhibit the roughness of the microstructure bottom surfaces respectively was  $R_a$  0.488, 0.492 and 0.486 μm, all of which were less than  $R_a$  0.5 μm. The machined sidewall surface roughness  $R_a$  of zones #4' (Fig. 11g), #5' (Fig. 11h) and #6' (Fig. 11i) which corresponding to the zones #4, #5 and #6 were 0.892, 0.904 and 0.886 μm, respectively.

For the entrance dimensions of the microstructure, the machining results in Fig. 11a–c suggested that the side gap could be maintained around 40 μm, approximately. The aim of this study was to avoid the time-consuming vacuum thermal diffusion bonding processing and efficiently fabricate the 3D microstructures that without discharge ridges on the bottom surface via the bundled 3D-laminated microelec-



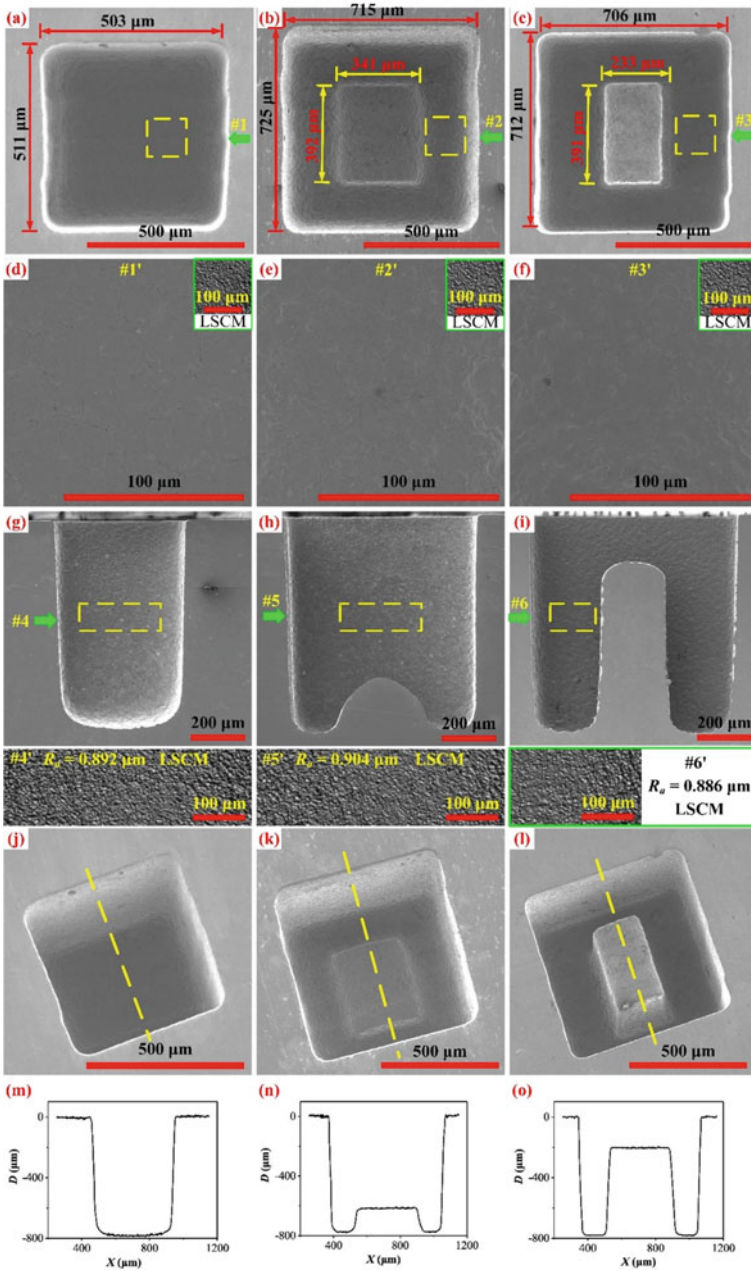
**Fig. 10** 3D microelectrode after reverse-polarity micro-PMEDM: **a–c** solid microelectrode; **d–f** with a semi-cylindrical cavity; **g–i** with a rectangular cavity

trodes. The application of the major parameters that matched by experiments possess a high discharge energy led the reverse-polarity micro-PMEDM itself increased the machining gap.

## 6 Conclusions

To improve the preparation efficiency of 3D-laminated microelectrode, a method for preparing a bundled 3D-laminated microelectrode was proposed. The bundled microelectrode was used to perform reverse-polarity micro-PMEDM to process 3D microstructures with high-quality surface. Patterns relating to the effects of the Gr and Cu powder concentrations, the voltage  $T_{on}$  and  $T_{off}$  and the U on the removal of discharge ridge on the bottom surface of the machining results were detail explored. The main conclusions are as follows.

- (1) Compared with the conventional fabrication technique for the 3D-laminated microelectrode, the bundled 3D-laminated microelectrode avoids the thermal diffusion bonding process, which makes the 3D microelectrode preparation procedure simple, highly efficient and inexpensive.



**Fig. 11** Microstructures of reverse-polarity micro-PMEDM: **a, d, g, j, m** square-shaped blind microcavity; **b, e, h, k, n** with a semi-cylindrical feature; **c, f, i, l, o** with a rectangular feature

- (2) Gr and Cu powders had different effects. To improve the self-welding performance of the bundled microelectrode working end between the Sn-plated Cu foils, Cu powder was added to the EDM oil. For improving the surface quality of the 3D microstructure, Gr power was also added to the EDM oil. Cu powder easily melted and adhered to the electrode, and facilitated transferring heat to the Sn films, to generate the continuous self-welding. The addition of Gr powder could prevent the mutual bonding of Cu particles to yield a high-quality working surface of the bundled 3D-laminated microelectrode.
- (3) Many experiments were performed and the matched process parameters were determined. When the concentrations of Gr powder was 4 g/L, Cu powder was 2 g/L, the voltage  $T_{on}$  was 30  $\mu$ s,  $T_{off}$  was 30  $\mu$ s, and the U was 100 V, defects include discharge ridges and micro-craters on microstructure bottom surfaces were eliminated, effectively.
- (4) With the matched process parameters, an approximately 800- $\mu$ m-deep square-shaped blind microcavity, 3D microstructures containing semi-cylindrical and rectangular features were fabricated. The bottom surface roughness of all the 3D microstructures was less than  $R_a$  0.5  $\mu$ m, the side surface roughness was around  $R_a$  0.9  $\mu$ m, and the electrode wear in the height direction was below 20  $\mu$ m. The discharge energy of the matched process parameters that aimed at eliminating the discharge ridges was high, and the micro-PMEDM itself would enlarge the machining gap, but the machining side gap could still be maintained at approximately 40  $\mu$ m.

**Acknowledgements** The work described in this chapter was supported by the National Natural Science Foundation of China (Grant No. 51975385), the Natural Science Foundation of Guangdong (Grant No. 2023A1515011785, 2022A1515011065), Science and Technology Program of Guangzhou (2023A04J0286), Talent Introduction Scientific Research Launch Project of GPNU (2023SDKYA009), Science and Technology Innovation Strategy Special Fund Project of Guangdong (Grant No. 2020A1414050064), Horizontal Topic (Grant No. 1746829). The authors are also grateful to the colleagues for their essential contribution to the work.

## References

1. Singh T, Dvivedi A (2016) Developments in electrochemical discharge machining: a review on electrochemical discharge machining, process variants and their hybrid methods. *Int J Mach Tool Manu* 105:1–13
2. Yue X, Yang X (2021) The role of discharge plasma on molten pool dynamics in EDM. *J Mater Process Technol* 293:117092
3. Yu ZY, Masuzawa T, Fujino M (1998) Micro-EDM for three-dimensional cavities-development of uniform wear method. *CIRP Ann Manuf Technol* 47(1):169–172
4. Rajurkar KP, Yu ZY (2000) 3D micro-EDM using CAD/CAM. *CIRP Ann Manuf Technol* 49(1):127–130
5. Bleys P, Kruth JP, Lauwers B, Zryd A, Delpretti R, Tricarico C (2002) Real-time tool wear compensation in milling EDM. *CIRP Ann Manuf Technol* 51(1):157–160



6. Bleys P, Kruth JP, Lauwers B (2004) Sensing and compensation of tool wear in milling EDM. *J Mater Process Technol* 149(1–3):139–146
7. Zhang L, Du J, Zhuang X, Wang Z, Pei J (2015) Geometric prediction of conic tool in micro-EDM milling with fix-length compensation using simulation. *Int J Mach Tool Manufact* 89:86–94
8. Pei J, Zhuang X, Zhang L, Zhu Y, Liu Y (2018) An improved fix-length compensation method for electrical discharge milling using tubular tools. *Int J Mach Tool Manufact* 124:22–32
9. Wang X, Li C, Guo H, Yi S, Kong L, Ding S (2020) Alternating energy electrical discharge machining of titanium alloy using a WC-PCD electrode. *J Mater Process* 60:37–47
10. Shibayama T, Kunieda M (2006) Diffusion bonded EDM electrode with micro holes for jetting dielectric liquid. *CIRP Ann Manuf Technol* 55(1):171–174
11. Shibayama T, Kunieda M (2010) Diffusion-bonded tool electrode for electrical discharge machining with microchannels for jetting dielectric liquid. *J Jpn Soc Electr Mach Eng* 44(105):12–16
12. Xu B, Wu XY, Lei JG, Cheng R, Ruan SC, Wang ZL (2015) Laminated fabrication of 3D micro-electrode based on WEDM and thermal diffusion welding. *J Mater Process Technol* 221:56–65
13. Lei J, Wu X, Xu B, Zhao Z, Ruan S, Cheng R (2015) Laminated fitting fabrication of Cu–Sn composite 3D microelectrodes and elimination of ridges on the machined surface of 3D micro-cavities. *J Mater Process Technol* 225:24–31
14. Wu ZZ, Wu XY, Lei JG, Xu B, Jiang K, Zhong JM, Diao DF, Ruan SC (2018) Vibration-assisted micro-ECM combined with polishing to machine 3D microcavities by using an electrolyte with suspended B<sub>4</sub>C particles. *J Mater Process Technol* 255:275–284
15. Uno Y, Nakajima T, Okada M (1991) The effect of electrode polarity on electrical discharge machining performance in water. *Memoirs Faculty Eng Okayama Univ* 26(1):9–20
16. Wong YS, Lim LC, Rahuman I, Tee WM (1998) Near-mirror-finish phenomenon in EDM using powder-mixed dielectric. *J Mater Process Technol* 79(1–3):30–40
17. Kunieda M, Kobayashi T (2004) Clarifying mechanism of determining tool electrode wear ratio in EDM using spectroscopic measurement of vapor density. *J Mater Process Technol* 149(1–3):284–288
18. Praveen L, Krishna PG, Venugopal L, Prasad NEC (2018) Effects of pulse ON and OFF time and electrode types on the material removal rate and tool wear rate of the Ti-6Al-4V Alloy using EDM machining with reverse polarity. In: *IOP Conference Series: Mater Sci Eng* (Vol. 330, No. 1, p. 012083). IOP Publishing
19. Ji R, Liu Y, Zhang Y, Cai B, Ma J, Li X (2012) Influence of dielectric and machining parameters on the process performance for electric discharge milling of SiC ceramic. *Int J Adv Manuf Technol* 59(1–4):127–136
20. Ji R, Liu Y, Zhang Y, Wang F (2011) Machining performance of silicon carbide ceramic in end electric discharge milling. *Int J Refract Met Hard Mater* 29(1):117–122
21. Jahan MP, Rahman M, San Wong Y (2011) Study on the nano-powder-mixed sinking and milling micro-EDM of WC-Co. *Int J Adv Manuf Technol* 53(1–4):167–180
22. Taherkhani A, Ilani MA, Ebrahimi F, Huu PN, Long BT, Van Dong P, Tam NC, Minh ND, Van Duc N (2021) Investigation of surface quality in Cost of Goods Manufactured (COGM) method of  $\mu$ -Al<sub>2</sub>O<sub>3</sub> Powder-Mixed-EDM process on machining of Ti-6Al-4V. *Int J Adv Manuf Technol* 116(5):1783–1799
23. Marashi H, Jafarlou DM, Sarhan AA, Hamdi M (2016) State of the art in powder mixed dielectric for EDM applications. *Precis Eng* 46:11–33
24. Bai X, Zhang QH, Yang TY, Zhang JH (2013) Research on material removal rate of powder mixed near dry electrical discharge machining. *Int J Adv Manuf Technol* 68(5–8):1757–1766
25. Jeswani ML (1981) Effect of the addition of graphite powder to kerosene used as the dielectric fluid in electrical discharge machining. *Wear* 70(2):133–139

26. Tzeng YF, Lee CY (2001) Effects of powder characteristics on electrodischarge machining efficiency. *Int J Adv Manuf Technol* 17(8):586–592
27. Tzeng YF, Chen FC (2005) Investigation into some surface characteristics of electrical discharge machined SKD-11 using powder-suspension dielectric oil. *J Mater Process Technol* 170(1–2):385–391

# Chapter 10

## Fabrication of Micro-grooves by Applying Laminated Disc Electrodes



Weijie Pan, Jianguo Lei, and Xiaoyu Wu

**Abstract** During the electrical discharge machining (EDM) process, the wear of tool electrodes is inevitable and varies from material to material, thus inevitably degrading the processing accuracy and quality of microstructures. In order to transform this disadvantage into a favourable process, a wear-variation EDM (WV-EDM) method was proposed to prepare a laminated disc electrode (LDE) with stable-profile microchannels on the outer edge surface; subsequently, the electrode was employed to fabricate microgrooves on the workpiece surfaces by EDM. In this study, the difference in wear between the single-disc foil electrodes and corresponding disc foils in the LDE, the formation of the LDE by WV-EDM, the relative volume wear rate of disc foils versus the processing depth, and the distribution of the flow field in the LDE machining gap during machining were investigated, respectively. The results indicate that the proposed approach in this paper could reliably yield LDEs with stable-profile microchannels on the outer edge surface, and then microgroove arrays of the same processing depth could be continuously machined on the workpiece surface of the same material using the EDM method, especially the LDEs did not need to be reshaped. Moreover, due to the protection between the foils, not all disc foils in LDE had the same wear pattern as the single disc foil. In addition, the “pump effect” of the vortex situated in the flow field between microchannels in the LDE and the machining surface facilitated debris removal. Finally, the microgroove arrays and columnar microstructures were produced successfully on Ti-6Al-4 V alloy workpieces using the proposed method.

---

W. Pan · J. Lei (✉) · X. Wu

Shenzhen Key Laboratory of High Performance Nontraditional Manufacturing, College of Mechatronics and Control Engineering, Shenzhen University, Nan-Hai Ave 3688, Shenzhen 518060, Guangdong, PR China  
e-mail: [ljj\\_sc111@163.com](mailto:ljj_sc111@163.com)

## 1 Introduction

Microgroove is an important surface microstructure, which can effectively diminish friction and resistance [1], enhance heat dissipation [2], and decrease noise [3]. It is widely used in various fields, such as micromechanical, electromunication and biomedical [4–6]. In these fields, materials to be used such as die steel, titanium alloys, tungsten carbide and other metals are very popular. Nevertheless, it is challenging to accurately create and manufacture microgrooves on the surfaces of these materials using conventional machining approaches. Micro electric discharge machining (micro-EDM), a non-conventional machining method, owns ignorable cutting forces and can produce a variety of microstructures on any conductive material without regard to its hardness. Much attention has been paid by researchers to the microgroove preparation.

Murali et al. [7] utilized a 100  $\mu\text{m}$  thick graphite foil electrode to replace the traditional pin shaped tool electrode in micro-EDM. The straight microgrooves of 20 mm in length and 2.3 in aspect ratio were successfully prepared on hardened tool steel. For obtaining microgrooves with various cross-sections, Yan et al. [8] prepared tool electrodes with different cross-sections for micro-EDM using the wire electro-discharge grinding (WEDG) technique. Microgrooves featuring triangular, circular, rectangular and semi-enclosed cross-sections were manufactured on stainless steel. In addition, the electrode wear greatly decreased by the use of high voltage and small capacitance. To reduce machining time and production cost, Hung et al. [9] used micro high-speed milling technique to fabricate tool electrodes with microstructures, and then fabricated microchannels with depth of 600  $\mu\text{m}$  and width of 500  $\mu\text{m}$  on a SUS316L stainless steel plate by micro-EDM. To alleviate the noise generated via friction, Wang et al. [3] used an EDM technique to prepare parallel regularly spaced microgrooves with a width of 250  $\mu\text{m}$  and a depth of 100  $\mu\text{m}$  on the compacted graphite iron material surface used for brake disc. Hsue et al. [10] machined spiral microchannels with a depth of 45  $\mu\text{m}$  and a pitch of 200  $\mu\text{m}$  on a 0.3 mm diameter tungsten carbide tool by WEDG. Subsequently, fine diamond abrasives of 6–12  $\mu\text{m}$  were deposited on the surface of the tool by electroplating. After that, the obtained object was employed as a tool electrode to process micro holes through the micro-EDM grinding process. The spiral-shaped microchannels facilitated debris removal and improved the stability of the manufacturing process. In addition, the machining surface was ground by the abrasive diamond grinds, thereby decreasing the recast layer thickness and improving the processed surface quality ( $R_a$  0.107  $\mu\text{m}$ ). Wan et al. [11] produced a series of layered microgroove structures on H62 brass surfaces using the wire electrical discharge machining (WEDM) technique. These surfaces with layered microgrooves had more pronounced hydrophilicity and higher mist collection efficiency compared to smooth surfaces. Using safflower oil as a working medium, Tamura et al. [12] machined microgrooves of width 2  $\mu\text{m}$  on the soft gelatin surfaces by micro EDM. The geometry of the microgrooves could be changed by controlling the gap, machining voltage, electrode diameter and type. Bangash et al. [13] created U-shaped, V-shaped and semi-circular microgrooves on the Ti-6Al-4 V

surface by micro EDM. Therefore, the adhesion and joint strength of the Ti-6Al-4 V surface were remarkably improved.

The debris concentration in the machining gap significantly affected the stability of the machining process. Murali et al. [7] innovatively used the gravitational effect to effectively remove the debris generated during the fabrication of microgrooves using micro EDM by placing the workpiece on top of the electrode. The aspect ratio of the microgrooves was increased to about 8. To facilitate debris removal, Chow et al. [4] performed micro EDM of microgrooves using a rotating disc electrode. A microgroove with a width of 42  $\mu\text{m}$  and a length of 400  $\mu\text{m}$  was manufactured successfully on a Ti-6Al-4 V workpiece. Yan et al. [14] used Cu disc of diameter 80 mm and thickness 0.5 mm as electrodes in EDM to fabricate microgrooves on Al<sub>2</sub>O<sub>3</sub>/6061Al composites and found that electrical factors such as pulse and peak current duration had a much greater effect on the machining characteristics than non-electrical factors. At 15 A peak current and 100  $\mu\text{s}$  pulse duration, the material removal rate could reached about 0.275 g/min. To increase the quality and efficiency of the workpiece surface modification, Furutani et al. [5] chose a rotating toothed disc as a tool electrode for EDM in a working fluid with titanium powder. The working fluid was dragged effectively into the processing gap, guaranteeing the concentration of titanium powder in the machining zone. Using pure water of resistivity 17 M $\Omega$  cm as the working fluid, Lin et al. [15] selected Cu disc as the tool electrode to prepare microgrooves on Ti-6Al-4 V alloy workpieces using negative polarity EDM. Microgrooves with a width of 75–80  $\mu\text{m}$  were fabricated successfully. Yan et al. [16] used Cu-nickel alloy disc electrodes for EDM micromachining on polycrystalline diamond workpieces. The diamond was graphitized due to the chemical interaction between diamond and nickel, and microgrooves with a depth of 200  $\mu\text{m}$  and a width of 200  $\mu\text{m}$  were manufactured. Kuo et al. [17] manufactured micro disc electrodes on metal raw pins by the WEDM technique and utilized them for rotary EDM to produce parallel microgrooves with a depth of about 30  $\mu\text{m}$  and a width of 25  $\mu\text{m}$  as the distinguishing lines of the micro die.

The use of rotating disc foil as an electrode in EDM effectively enhances the debris removal from the processing gap and keeps a good discharge state during the processing. Additionally, the outer edge surface of the disc electrode keeps a uniform wear rate and a long lifetime, which contributes to accuracy and is extremely well suited for long-term and continuous production of large-scale micro-grooves. Nevertheless, when processing deep and narrow microgrooves by EDM, the disc foil electrode mentioned above easily oscillates due to the lack of support, making it hard to guarantee machining stability. In addition, it can only process one micro-groove at a time, thus the processing efficiency is low.

To solve the above issue, a wear-variable EDM (WV-EDM) method was proposed in the paper to prepare a laminated disc electrode (LDE) possessing multiple microchannals of stable shape on the outer edge surface, which was then employed to fabricate an array of microgrooves of uniform depth and shape on the workpiece using the EDM technology. The paper studied the formation of the LDE by WV-EDM and the correlation between the relative volume wear rate of the disc foils and the processing depth, simulated the flow field of LDE in the machining gap in EDM

for revealing the influence of flow field distribution on the removal of the debris. Using the approach proposed, the adverse factor of tool electrode wear in EDM could be converted into a useful procedure, and microgroove arrays and columnar microstructures were machined successfully on Ti-6Al-4 V workpieces by EDM using the LDE.

## 2 Process of the LDE Fabrication

### 2.1 Method

The LED preparation procedure includes: (1) preparation of disc-shaped foils of various materials and the same inner and outer diameters by WEDM (2) WV-EDM of LDE blanks built on request to obtain LDEs. The process is shown in Fig. 1 and consists of the following key stages.

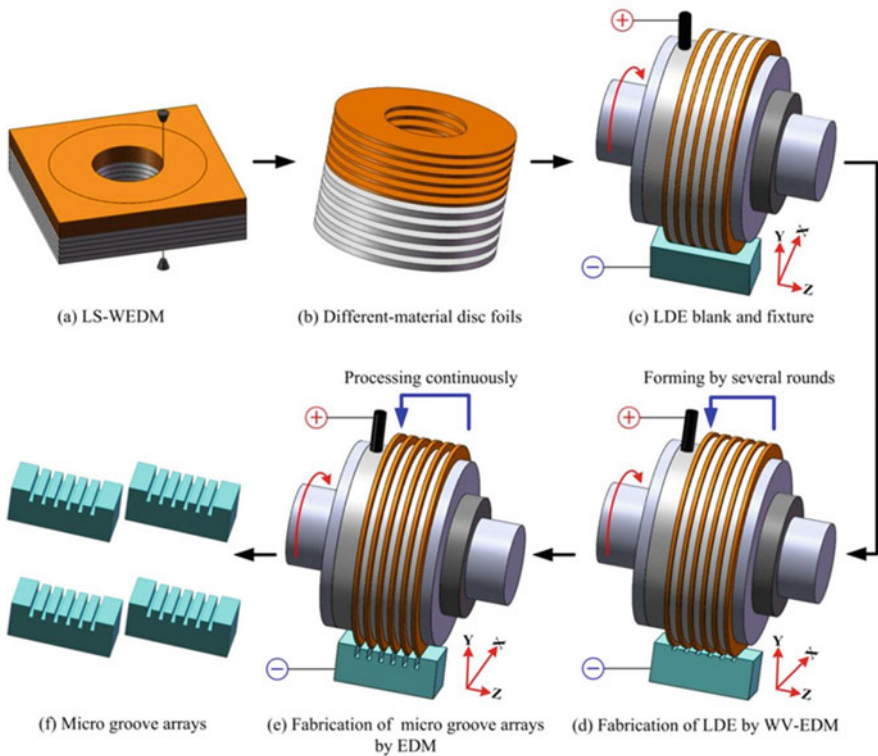


Fig. 1 Illustration of LDE and microgroove array fabrication

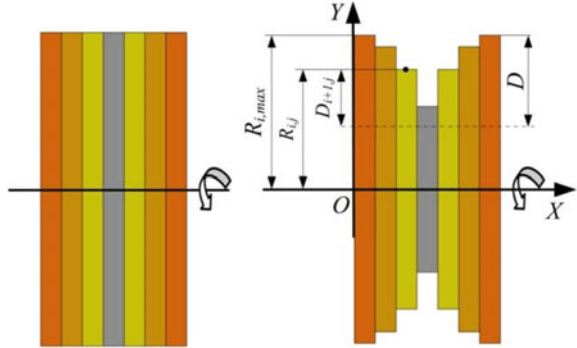
- (1) Fabrication of disc-shaped metal foils of different materials. According to the requirements of LDE fabrication, metal foils of various materials were laminated together and fixed on a fixture. These metal foils were processed along a given path by a low-speed wire EDM (LS-WEDM) to produce disc with the same inner and outer diameters, as shown in Fig. 1a and b, respectively.
- (2) Preparation of LDEs. Based on the cross-sectional profile of the microgroove to be processed, the pre-prepared disc foils were chosen and combined to create a LDE blank, which was fastened on a jig (Fig. 1c) and then installed on the rotating shaft of the precision grinding machine. The LDE blank and the workpiece were connected to the positive electrode and negative electrode of the pulse power supply, respectively. The workpiece is fixed on the grinding machine table, along the X direction at a certain speed reciprocating motion. Set the same process parameters and the processing depth  $D$ , WV-EDM was conducted on the workpiece surface at different positions. As a result, the LDE was obtained. Since disc foils of various materials exhibited various electrode wear rates in EDM, microchannels were gradually generated on the outer surface of the LDE blank. As the number of rounds of WV-EDM increased, the wear of each disc foil gradually stabilized, resulting in the formation of LDEs consisting of microchannels with stable cross-sectional profiles on their outer edge surfaces (Fig. 1d).
- (3) Preparation of microgrooves. Setting the same processing depth  $D$ , microgrooves were machined by EDM on workpieces of the same material using LDE, as illustrated in Fig. 1e and f. LDE could produce continuously microgrooves of the same size thanks to the stable wear of each disc. During this period, there was no need to modify the shape of the LDE until the diameter became very small due to wear and the LDE could not work anymore.

When deep and narrow microgrooves were machined on the workpiece via EDM, the related section of the LDE does not need to be lengthened separately to expand its diameter in this region. LDE has excellent anti-interference performance. In particular, the disc foil with higher wear rate has a supporting and stabilizing effect on the adjacent disc foils with lower wear rate, significantly improving processing accuracy. With this method, multiple microgrooves can be simultaneously machined, significantly improving the machining efficiency. This technology is particularly well suited for microstructure machining on the surfaces of difficult-to-machine materials (for instance, titanium alloy, etc.) and large stroke workpieces.

## 2.2 *Relative Volume Wear Ratio*

In this paper, a set of discs of various materials in specific combinations were used to construct an LDE. Due to the wear rate differences of the various material disc foils, microchannels on the outer edge surface of the LDE could be obtained in the following WV-EDM process. Specifically, multiple Cu, different ratios of CuSn

**Fig. 2** WV-EDM model of the LDE: **a** LDE blank; **b** LDE blank with a microchannel on the outer edge surface



alloy and Sn disc foils were alternately combined to regulate the wear rate at different positions of the electrode, and finally the corresponding microchannels on the outer edge of the electrode was formed by WV-EDM.

In this study, a universal geometric model was developed to better understand the mechanism of LDE formation by WV-EDM, as shown in Fig. 2. According to the profiles of the microgroove to be processed, different material disc foils with the same initial diameter were chosen to construct the LDE blank (Fig. 2a). The LDE blank with microchannels on its outer edge surface was obtained after *i* WV-EDM rounds, as shown in Fig. 2b.

In the EDM process, it is assumed that the outer edge surface of each disc foil in the LDE blank wears uniformly in the direction of thickness, and that the processing gap is zero. Depending on the disc foil radial wear and the actual depth of microgrooves on the workpiece, the volume of workpiece material removed  $V_w$  can be described by:

$$V_w = dl \tag{1}$$

where *l* and *d* represent the length of the microgroove and actual depth on the workpiece, respectively; *t* represents the disc foil thickness.

The volume loss of the disc foil  $V_t$  can be given by the following equation:

$$V_t = 2\pi R \Delta R t \tag{2}$$

where *R* represents the radius of the disc foil and  $\Delta R$  is the wear of the disc foil radius.

Here, the relative volume wear rate *T* of the disc foil is defined as:

$$T = \frac{V_t}{V_w} = \frac{2\pi R \Delta R}{dl} \tag{3}$$

Assuming  $R_{i,j}$  is the radius of the *j*th disc foil after the *i*th round of WV-EDM, the largest disc foil radius in the LDE after the *i*th round of WV-EDM is  $R_{i,max}$ .



When the processing depth  $D$  keeps constant, the disc foil radius wear corresponding to  $R_{i,\max}$  is minimal. During the  $(i + 1)$ th round of WV-EDM, the machining depth  $D_{i+1,j}$  of the  $j$ th disc foil is:

$$D_{i+1,j} = R_{i,j} - R_{i,\max} + D \quad (4)$$

where  $D$  is the processing depth of the LDE blank in each round.

Therefore, the actual depth  $d_{i+1,j}$  of the  $j$ th disc foil after the  $(i + 1)$ th round of WV-EDM is:

$$d_{i+1,j} = D_{i+1,j} - \Delta R_{i+1,j} = R_{i,j} - R_{i,\max} + D - \Delta R_{i+1,j} \quad (5)$$

where  $\Delta R_{i+1,j}$  is the radius wear of the  $j$ th disc foil after the  $(i + 1)$ th round of WV-EDM.

Based on Eq. (3),  $\Delta R_{i+1,j}$  can be given by the following equation:

$$\Delta R_{i+1,j} = \frac{T_{i+1,j}d_{i+1,j}l}{2\pi R_{i,j}} \quad (6)$$

where  $T_{i,j}$  is the relative volume wear rate of the  $j$ th disc foil after the  $i$ th round of WV-EDM.

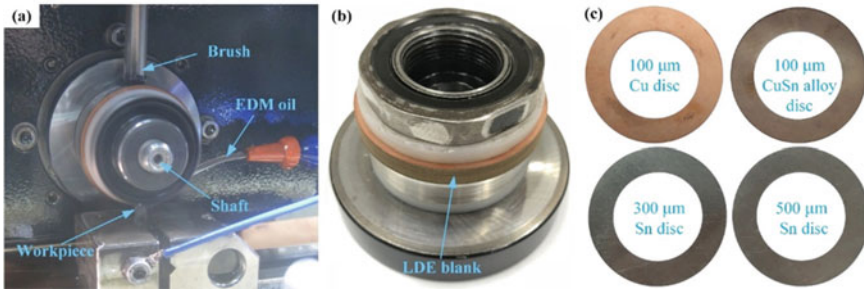
By substituting Eqs. (5) into (6), the radius wear  $\Delta R_{i+1,j}$  of the  $j$ th disc foil after the  $(i + 1)$ th round can be rewritten as the following expression:

$$\Delta R_{i+1,j} = \frac{T_{i+1,j}l}{2\pi R_{i,j} + T_{i+1,j}l} (D - R_{i,\max} + R_{i,j}) \quad (7)$$

### 3 Experiments

The main experimental equipment includes an LS-WEDM machine, a pulse power supply, a high-precision grinding machine, a vacuum furnace and an oscilloscope. Metal foils of various materials, including Cu, Sn and CuSn alloy foils were prepared by WEDM on the LS-WEDM machine (AP250L, Sodick Co., Ltd., Japan), obtaining disc foils of the same initial diameter. Subsequently, according to the profiles of the microgrooves to be processed, the disc-shaped metal foil was selected to construct the LDE blank. Vacuum furnace (ZK1-12-1200) was produced by Shenzhen Zhongda Electric Furnace Factory in China to fabricate CuSn alloy foils by thermal diffusion at the temperature of 800 °C for 15 h. Microgrooves were machined on Ti-6Al-4 V alloy plate by performing EDM experiments on a high-precision grinder (CHEVALIER Smart-B 818 III, CHEVALIER MACHINERY INC., China), as shown in Fig. 3a.

In addition, in order to fix the disc foil electrodes and LDEs, a special fixture was designed (Fig. 3b). Cu foils of 100 μm in thickness, CuSn alloy (3.85-vol % Sn) foils



**Fig. 3** a A precision grinder machine; b LDE blank and fixture; c Various material disc foils

of 100  $\mu\text{m}$  in thickness, Sn foils of 300  $\mu\text{m}$  and 500  $\mu\text{m}$  in thickness were selected to produce disc foils (Fig. 3c). A scanning electron microscope (Quanta FEG 450, FEI, USA) and a laser scanning confocal microscope (VK-X250, KEYENCE, Japan) were employed to collect the morphology and processing depth of the microgrooves. The experimental conditions are shown in Table 1.

**Table 1** Process parameters

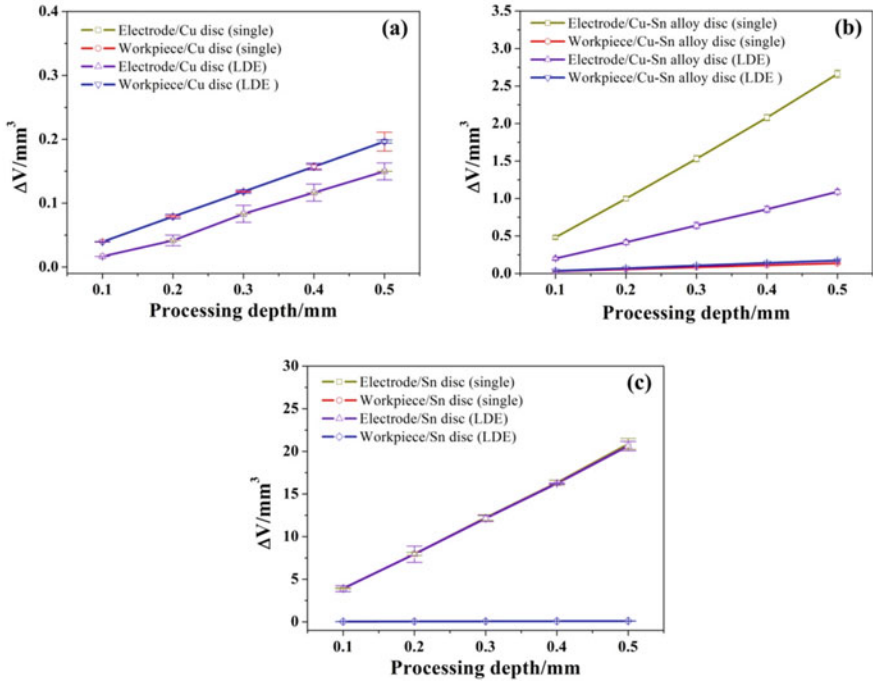
Parameters	Description	Unit
Machining voltage (U)	180	V
Rotational speed of electrode (n)	1000	rpm
Movement speed of workpiece (v)	200	mm/min
Scheduled machining depth of microgrooves (D)	100, 200, 300, 400, 500	$\mu\text{m}$
Length of microgrooves (l)	4	mm
Disc electrode initial radius ( $R_0$ )	26.5	mm
Pulse duration ( $t_{\text{on}}$ )	26	$\mu\text{s}$
Pulse interval ( $t_{\text{off}}$ )	11	$\mu\text{s}$
Disc foil material	Cu, CuSn alloy, Sn	
Workpiece material	Ti-6Al-4 V	
Polarity	+ (disc electrode) -(workpiece)	

## 4 EDM of Cu/CuSn/Sn/CuSn/Cu Structured LDE

### 4.1 *Wears of a Single Disc Foil Electrode and LDE During the EDM Process*

In EDM, a high-speed rotating disc foil was used as a tool electrode to fabricate a microgroove structure. This method not only effectively facilitated the discharge of debris and maintains a good discharge processing state, but also ensured the uniform wear of the outer surface of the disc foil electrode, thereby greatly improving the processing accuracy. However, in the process of EDM, with the increase of processing depth, the difficulty of debris discharge was also increasing. In order to study the effect of processing depth on the wear of the LDE and the single-disc foil electrode, and the difference in wear between single-disc foil electrode and the corresponding disc foil in LDE, a 100  $\mu\text{m}$  thick Cu disc foil electrode, a 100  $\mu\text{m}$  thick CuSn alloy disc foil electrode, a 300  $\mu\text{m}$  thick Sn disc foil electrode and a Cu/CuSn/Sn/CuSn/Cu structured LED were used to perform EDM experiments on titanium alloys. The experimental conditions are listed in Table 1.

Figure 4a–c show the relationship between the volume loss of the disc foil electrode, the workpiece removal and the processing depth for the single foil electrode and the corresponding foil in LDE with the same experimental conditions. Clearly, disc electrode volume loss increased as machining depth was increased for all electrodes. By comparing a single Cu foil electrode with a Cu foil in LDE, the volume loss was the same (Fig. 4a). Sn foil electrodes had a slightly larger loss than CuSn foil electrodes in LDE (Fig. 4c), while CuSn foil electrodes had a significantly greater loss (Fig. 4b). The analysis shows that the wear of Cu, CuSn alloy and Sn disc electrode increased sequentially during the whole EDM process under the same machining conditions. When using the above three kinds of disc foil made of LDE for EDM, because the disc foils adjacent to the Cu disc foil wear was relatively large, there was no other disc foil visible on the two sides of the outer edge surface of the Cu disc foil. Thus, in LDE, the Cu foil wear was comparable to that of a single Cu foil electrode. Sn disc electrodes underwent a lot of wear in EDM because of their high resistivity and low melting point. Even though the Sn disc foil in the LDE was protected by disc foils with a smaller wear rate, the overall wear resistance was not obvious, and the result was only slightly smaller than that of a single Sn foil electrode. However, the more pronounced volume loss difference occurred on the CuSn alloy disc electrode because in EDM the outer surface of a single CuSn alloy disc foil electrode was almost uniformly worn in the direction of thickness, with a cross-sectional view equivalent to region #1 in Fig. 5b. A considerable reduction in the wear of the CuSn alloy disc foil was observed in the LDE. This was because the side adjacent to the Cu foil had a strong protective effect, while the opposite side (the foil adjacent to Sn disc) was far away, leading to weakened protection and relatively large wear, which was smaller than the single CuSn alloy foil electrode even under the same processing conditions. Therefore, in the LDE, the CuSn alloy disc foil outer edge surface was



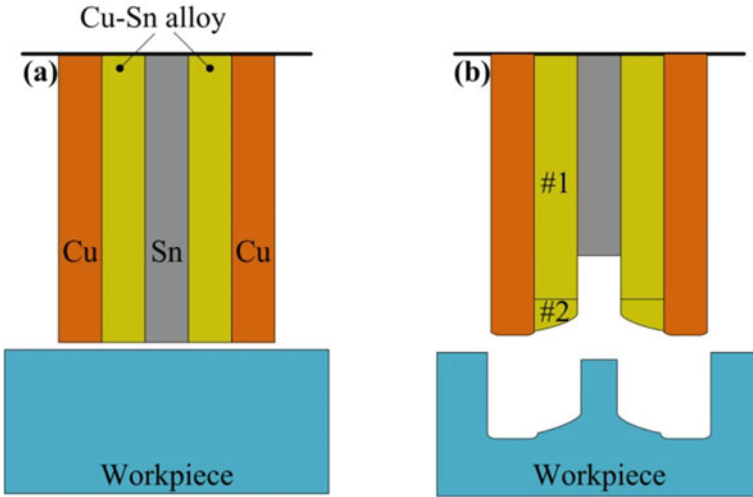
**Fig. 4** Relationship between the disc foil volume loss, workpiece removal and the processing depth: **a** Cu disc foil electrode; **b** CuSn alloy disc foil electrode; **c** Sn disc foil electrode

unevenly worn in thickness direction, and its cross section was equivalent to the region #1 + #2 in Fig. 5b.

According to the above analysis, although the LDE was composed of multiple disc foils of different materials, there was a difference in wear modes between the disc foil electrode in the LEDs and the single disc foil electrode because of the protection between the disc foils.

### 4.2 WV-EDM Formation of the LDE

In the process of EDM, the disc foils of different materials in LDE had different wear rates. At the same processing depth (D), the LDE performed several rounds EDM, thus generating a stable microchannel structure on the outer surface of LDE. In the process of microchannels from generation to stabilization, the radius wear of CuSn alloy disc-shaped foil electrode and Sn disc-shaped foil electrode gradually decreased until it was equal to the radius wear of Cu disc-shaped foil electrode. The processing depth (D) of CuSn alloy disc-shaped foil electrode and Sn disc-shaped foil electrode gradually decreased with the increase of rounds, and only the processing

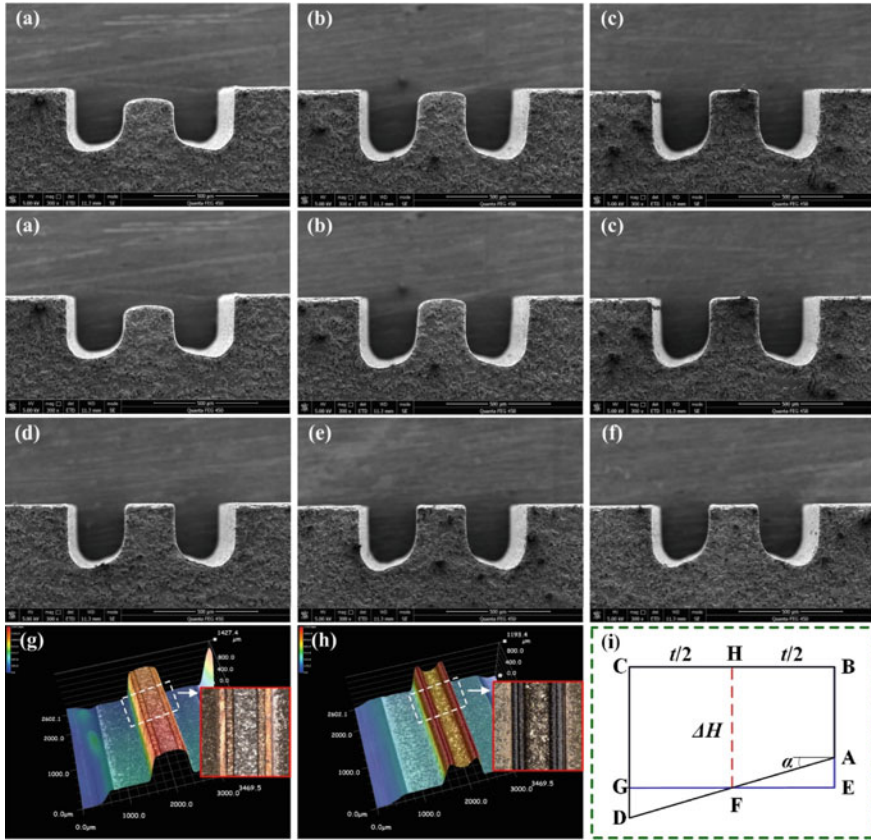


**Fig. 5** Illustration of LDE blank consisting of Cu, CuSn alloy and Sn disc foils by WV-EDM: **a** LDE blank; **b** LDE blank after one round of WV-EDM

depth ( $D$ ) of Cu disc-shaped electrode with the smallest wear rate remained the same. However, in the process of EDM, the processing depth and electrode shape had an important influence on the discharge of debris, and the discharge of debris affected the relative volume wear rate of the disc electrode.

In order to study the formation of the LDE by WV-EDM, in this section, Cu disc foils of thickness  $100\ \mu\text{m}$ , CuSn alloy disc foils of thickness  $100\ \mu\text{m}$  and Sn disc foils of thickness  $300\ \mu\text{m}$  were selected as laminated materials to construct an LDE blank with a Cu/CuSn/Sn/CuSn/Cu structure, and the partial view is shown in Fig. 6g. Then, using the parameters listed in Table 1 and setting processing depth of each round to  $300\ \mu\text{m}$ , the LDE blank performed six rounds WV-EDM. The LDE used is shown in Fig. 6h, and the microgrooves processed in each round on the workpiece are displayed in Fig. 6a–f. It could be clearly seen from the diagram that from the first round to the third round of WV-EDM, the cross-section of the microgrooves on the workpiece had changed significantly, indicating that the disc foils of different materials had significant wear differences. However, from the fourth round, the wear difference narrowed sharply. From the fifth round, the profile of the microgroove starts to stabilize.

Due to the different protective effects from adjacent Cu foils, there was a wear difference in the thickness direction on the outer surface of the CuSn alloy foil. After some analysis, it was found that the closer the distance to the Cu foil, the stronger the protection and the smaller the wear. Otherwise, the opposite will occur. Therefore, the protection and wear resistance of Cu foil with low wear rate to CuSn foil gradually decrease from near to far, so that a slope in the thickness direction was formed on the outer surface of CuSn foil (Fig. 6i). At the same time, the disc foil with relatively high wear rate played a supporting and stabilizing role for the adjacent disc foil with



**Fig. 6** **a** Partial view of the LDE blank; **b** Partial view of the LDE; **c** Cross-sectional diagram of CuSn alloy disc foil wear in LDE; **d–i** Microgrooves machined during the manufacture of LDE with WV-EDM

low wear rate. As shown in Fig. 7, Cu disc were supported by CuSn alloy disc, while CuSn alloy disc were supported by Sn disc.

On the basis of the analysis in Sect. 4.1, because of protection from adjacent Cu disc foil, the gradient wear of the outer edge surfaces of the CuSn alloy disc foils was obvious. The diagram of the wear zone was the right trapezoid ABCD, as displayed in Fig. 6i. The volume wear of the CuSn alloy disc foils can be represented as:

$$V = S_{ABCD} \times 2\pi R = \frac{AB + CD}{2} \times t \times 2\pi R \tag{8}$$

where  $t$  and  $R$  are the thickness and the radius of the CuSn alloy disc foil, respectively.

Selecting the midpoints  $F$  and  $H$  of side  $AD$  and side  $BC$ , respectively to form a median line  $FH$  of the right trapezoid  $ABCD$  and a rectangle  $BCGE$ , then

**Table 2** Experimental results of the radius wear ( $\Delta R/\mu\text{m}$ ) of each disc foil and corresponding microgroove depth ( $d/\mu\text{m}$ ) in each round during the LDE formation

Round	Cu disc foil		CuSn alloy disc foil		Sn disc foil	
	$\Delta R_{\text{Cu}}/\mu\text{m}$	$d_{\text{Cu}}/\mu\text{m}$	$\Delta R'_{\text{CuSn}}/\mu\text{m}$	$d'_{\text{CuSn}}/\mu\text{m}$	$\Delta R_{\text{Sn}}/\mu\text{m}$	$d_{\text{Sn}}/\mu\text{m}$
1	5.2	297.5	40.2	263.3	244.5	56.3
2	5.5	295.0	15.1	255.1	53.1	13.5
3	5.8	296.3	12.6	249.2	15.6	4.1
4	5.3	294.5	8.2	248.2	7.2	3.9
5	5.5	295.2	7.1	249.1	7.1	3.2
6	6.2	294.1	6.5	248.5	7.3	3.3

$$\Delta R' = FH = \frac{AB + CD}{2} \quad (9)$$

Equation (8) can be re-expressed as:

$$V = S_{\text{ABCD}} \times 2\pi R = \Delta R' \times t \times 2\pi R \quad (10)$$

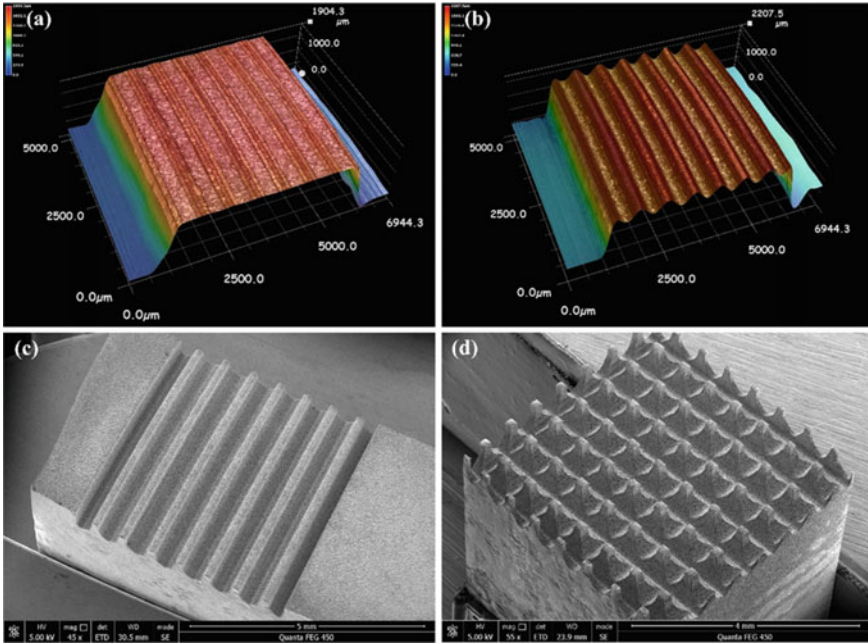
Therefore, during the measurement process, the radius wear of the CuSn alloy disc foil in LDE could be equated to the uniform wear of the radius  $\Delta R'$  of the disc electrode in the direction of thickness.

The radius wear of each disc foil and corresponding microgroove depth in each round during LDE formation are listed in Table 2. It can be observed that the difference in radius wear between CuSn alloy discs, Sn discs and Cu discs decreases with the increase of rounds. At the fifth round, the difference in radius wear between them was reduced to within  $2 \mu\text{m}$ . In this research, it could be considered that the wear of Cu, CuSn alloy and Sn disc foil came to a balance point where the outer surface profile of LDE remained stable.

### 4.3 Preparation of Surface Microgroove Structures

According to the research above, a Cu/CuSn/Sn/CuSn/Cu structured LDE blank was prepared, which consisted of  $100 \mu\text{m}$  thick Cu disc,  $100 \mu\text{m}$  thick CuSn alloy disc and  $300 \mu\text{m}$  thick Sn disc. The LDE blank was carried out five rounds of WV-EDM to obtain the LDE, which was then utilized to process microgroove arrays on Ti-6Al-4V alloy workpieces. The depth to be processed was  $500 \mu\text{m}$ , and other experimental conditions are listed in Table 1.

The partial image of the LDE blank and the LDE possessing a stable outer surface microchannels are displayed in Fig. 7a and b, respectively. Setting the same parameters and processing depth, the microgroove arrays and columnar microstructures in Fig. 7c and d were fabricated by EDM with the pre-fabricated LDE on Ti-6Al-4V



**Fig. 7** **a** Partial image of the LDE blank; **b** Partial image of the LDE; **c** Microgroove array; **d** Columnar microstructure array

alloy, respectively. The microgrooves depths in Fig. 7c and d were about  $490\ \mu\text{m}$ . The LDE could machine multiple microgrooves at one time compared to a single disc foil electrode, significantly improving the machining efficiency. In addition, microgrooves with complex shapes could be fabricated by regulating the wear in various areas of the LDE.

## 5 EDM of Cu/Sn/Cu Structured LDE

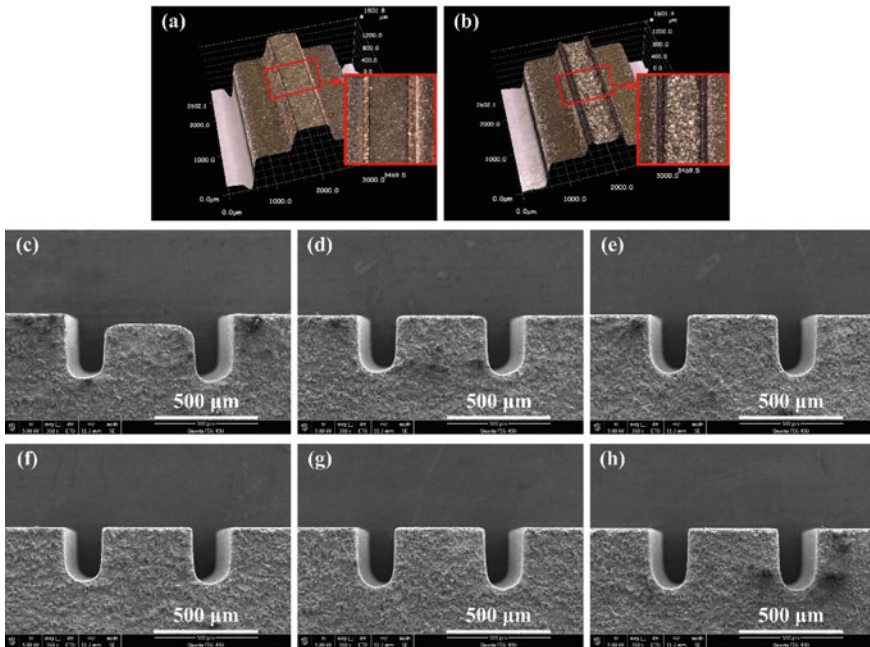
### 5.1 WV-EDM Formation of the LDE

According to the study in Sect. 4.1, the wear of single Cu and Sn disc was basically the same as that of Cu and Sn disc foils in LDE. In this section, a Cu/Sn/Cu structured LDE blank was established using  $100\ \mu\text{m}$  thick Cu disc foil and  $500\ \mu\text{m}$  thick Sn disc foil as laminated materials, which was used for WV-EDM to prepare LDE, and then utilized for performing EDM to produce straight wall microgroove structure. Processing depth was set to  $300\ \mu\text{m}$ , the experimental conditions are shown in Table 1.

Compared to Cu foil, Sn foil had experienced extremely tremendous wear in EDM due to the large wear rate. This facilitated the rapid formation of microchannels on



the outer surface. In addition, the Sn foil provided support and stability for the adjacent Cu foil, thereby improving the machining accuracy and stability. Figure 8a and b shows the LDE blank and the LDE after six rounds of WV-EDM, respectively. Figure 8c–h shows the corresponding microgrooves on the workpiece from the first round to the sixth round. The microgroove dimensions in Fig. 8c–h as well as each disc foil were measured by LSCM after each WV-EDM round. The machining gap for Cu disc foils was  $46 \pm 2 \mu\text{m}$ . This shows that the processing stability of LDE was very good due to the support and stabilization of adjacent Sn disc. As the number of WV-EDM rounds increased, the radius wear of Sn disc was progressively close to that of Cu disc. At the fourth round, the difference in radius wear between Cu and Sn foils was reduced to within  $2 \mu\text{m}$ . As a result, the LDE was obtained. After this, the LDE could be used continuously to fabricate microgrooves of the same size on workpieces of the same material, especially the LDE did not need to be reshaped. Since the LDE consisted only of Cu and Sn disc-shaped foils, there was no gradient wear along the thickness direction of the disc-shaped foil, so a straight-wall microgroove structure could be produced.



**Fig. 8** **a** Partial image of a Cu/Sn/Cu structured LDE blank; **b** Partial image of a Cu/Sn/Cu structured LDE; **c–h** microgrooves machined during the manufacture of LDE with WV-EDM

### 5.2 Relative Volume Wear Rate

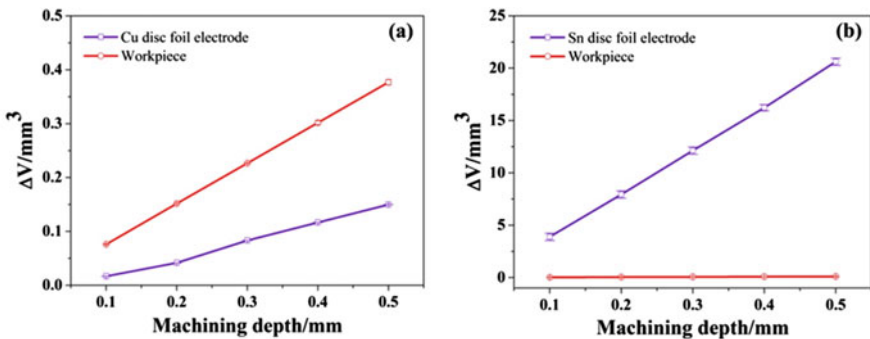
The relative volume wear rate  $T$  was defined as the ratio of electrode volume loss to workpiece removal volume. The electrode wear rate was closely dependent on the processing depth and the characteristics of the electrode material. Before the microgrooves on the outer edge surface of the LDE stabilize, the depth of the microgrooves on the workpiece machined by the disc foil with the higher wear rate gradually decreased as the number of forming rounds increased, which also made the wear of this disc electrode gradually decreased until the wear of each disc foil reached equilibrium.

In order to investigate the effect of processing depth on the disc foil electrode wear in EDM, Cu disc foils with a thickness of  $100\ \mu\text{m}$  and Sn disc foils with a thickness of  $500\ \mu\text{m}$  were used to process different depth microgrooves on Ti-6Al-4 V alloy workpieces. Machining depths ( $D$ ) varied from  $100$  to  $500\ \mu\text{m}$ . The experimental conditions are shown in Table 1.

Figure 9a and b show the relationship between the volume wear of Cu and Sn disc-shaped foil electrodes, workpiece removal, and microgroove machining depth ( $D$ ). It could be observed that the volume wear of the disc foil electrode increased as the processing depth increased. At the same processing depth, the electrode volume wear of Cu disc foil was significantly small than that of Sn disc foil, while the workpiece removal was much larger than that of Sn disc foil. This suggested that Sn foils processability was exceedingly weak, which was very favorable for the generation of microchannels on the outer surface of the LDE by EDM.

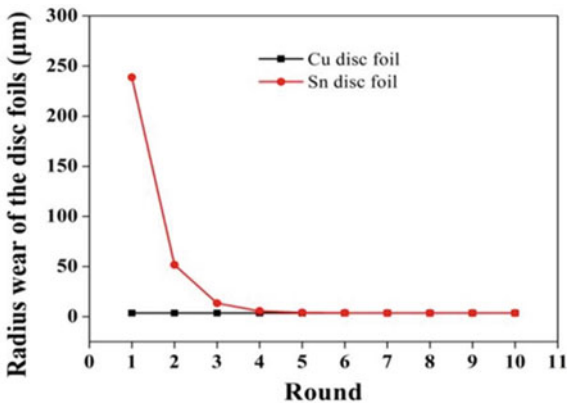
According to Sect. 4.2 and the experimental data in Fig. 9. The relationship between the relative volume wear ratio  $T$  of the Cu disc foils, Sn disc foils and the machining depth  $D$  can be described as follows:

$$T_{\text{Cu}} = 0.39371 + \frac{0.11586}{1 + e^{\frac{D-0.2258}{0.04269}}} \tag{11}$$



**Fig. 9** The relationship between the volume wear of the disc foil, the amount of workpiece removal and the processing depth: **a** Cu disc foil; **b** Sn disc foil

**Fig. 10** Relationship between radius wear of the Cu, Sn disc foils and rounds during the LDE fabrication



$$T_{Sn} = 337.56119 - \frac{5010.97999}{1 + e^{\frac{D+3.64497}{1.09878}}} \tag{12}$$

where  $T_{Cu}$  and  $T_{Sn}$  are relative volume wear rates of the Cu and Sn disc foil electrode, respectively.

The radial wear of each disc electrode in each round of WV-EDM and the number of forming rounds required for microchannels stabilization on the outer edge surface of the LDE could be obtained through the calculation of the Eqs. (7), (11), (12), thus providing a reliable reference for the experiment. The processing depth  $D$  was set to  $300 \mu\text{m}$ , other experimental conditions are listed in Table 1. MATLABs was used to perform the calculation. Figure 10 displays the relationship between radius wear of the Cu, Sn disc foils and formation rounds of the LDE. It shows that after five WV-EDM rounds the radius wear of the Cu and Sn disc foils was nearly equal when the processing depth  $D$  was  $300 \mu\text{m}$ , i.e., the each disc foil wear reached equilibrium. As compared to the experimental results in Table 2, the formation rounds of the LDE by the calculation were only larger than one. This was mainly due to the neglect of the lateral processing gap in Eq. (7). The experiments could be performed on the basis of the calculated rounds, which could ensure to obtain stable microchannels on the LDE.

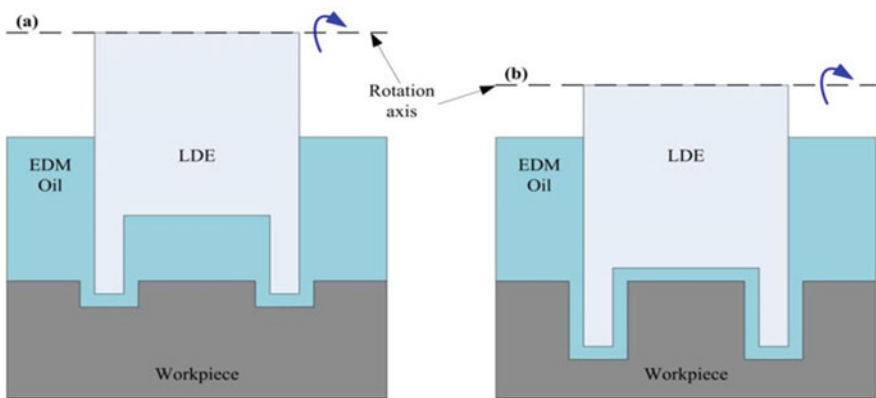
### 5.3 Simulation of Flow Field in the Machining Gap of the LDE During EDM

In the process of rotary EDM, despite a lot of debris were brought out by the disc electrode along the tangential direction, there were still some residues in the machining zone. The accumulation of debris directly affected the discharge state of EDM [18]. If the debris could not be discharged in time, it would not only cause abnormal discharge, leading to excessive electrode wear and low processing accuracy [19],

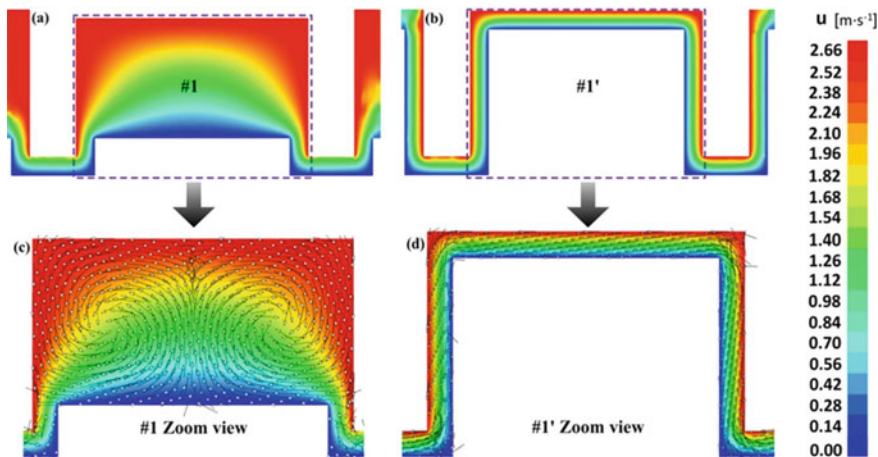
but also reduce the surface quality and increase the thickness of the heat affected zone [20]. The fluid flow distribution significantly affected debris movement in the machining gap. Proper fluid flow facilitated the timely debris removal, thus improving processing efficiency and accuracy. This paper employed a finite element simulation software to simulate the flow field distribution of the LDE in the process to clarify the movement of debris.

Flow field models of the Cu/Sn/Cu structured LDE in the initial and final machining stages were built according to the experimental results above, as shown in Fig. 11a and b, respectively. The front and side machining gaps  $\delta$  are both set to 46  $\mu\text{m}$ , the LDE rotates at 1000 rpm. In the initial machining stage of EDM, the distance between Sn foil and machining surface was much larger than  $\delta$ . As the machining depth increased, this distance decreased gradually and tended to  $\delta$ . Thus, the flow field of the processing gap was a dynamic process acting on the movement of debris.

Figure 12a and b displays the distribution of the flow field in the machining gap for the initial and final machining stages in EDM with LDE. For the sake of better seeing and analyzing the flow field structure, Fig. 12c and d displays zoom view corresponding to the zone between the Sn disc and the machining surface. In the initial stage, because the distance between the Sn disc foil of LDE and the workpiece was very large (#1), lots of working fluid passed through this microchannel and generated two large scale vortices (Fig. 12c), where mainly stored the energy of the moving fluid in the flow field. Because of the powerful “pump effect” of the large vortex, lots of debris was suctioned into this area and was discharged in time together with the working fluid. As a result, the processing efficiency was enhancing significantly. As the processing depth increased, the distance between the Sn disc of LDEs and the machining surface gradually decreased. When the distance was reduced to the machining gap  $\delta$  (Fig. 12b), the working fluid between the Sn foil and the processing surface was broken down and a spark discharge was generated,



**Fig. 11** Flow field model of a Cu/Sn/Cu structured LDE in the processing gap: **a** initial stage ( $D = 100 \mu\text{m}$ ); **b** final stage ( $D = 300 \mu\text{m}$ )

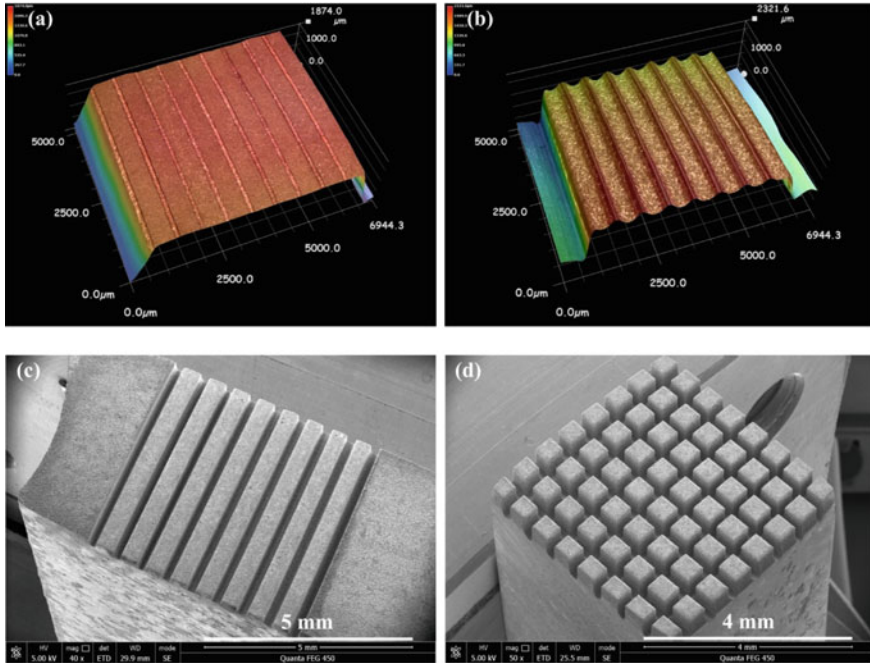


**Fig. 4.12** Simulation results of the flow field distribution in the machining gap of LDE in the initial and final machining stages of EDM

at which point the “pump effect” in the processing gap was weakest. Therefore, the microchannel on the outer surface of LDE was beneficial to further remove debris in the process of preparing microgrooves on the workpiece by EDM, so that the machining efficiency and stability were improved.

#### 5.4 Fabrication of Microstructures by EDM with the LDE

In order to validate the feasibility of LDE in processing microgrooves, LDE blanks consisting of alternating layers of 100  $\mu\text{m}$  thick Cu disc foils and 500  $\mu\text{m}$  thick Sn disc foils were prepared. A local image of the LDE blank is displayed in Fig. 13a. The process parameters listed in Table 1 were applied to EDM and the processing depth  $D$  was set to 500  $\mu\text{m}$ . According to Eqs. (7), (11) and (12), the number of forming rounds of WV-EDM was calculated and determined to be five. After that, the LDE blank performed five rounds WV-EDM, obtaining the LDE with stable microchannels on the outer surface. Figure 13b displays a local image of the LDE. Following this, microgroove arrays (Fig. 13c) and columnar microstructures (Fig. 13d) were successfully manufactured by EDM using LDE under the same processing depth and conditions. The depth of the microgrooves machined in Fig. 13c and d were about 490  $\mu\text{m}$ .



**Fig. 13** **a** Local image of the LDE blank made of Cu and Sn disc foils; **b** local image of the LDE made of Cu and Sn disc foils; **c** microgroove arrays machined by EDM with the LDE in **(b)**; **d** columnar microstructures machined by EDM with the LDE in **(b)**

## 6 Conclusions

In this study, a WV-EDM approach was proposed to produce the LDE with stable shape microchannels on the outer surface, and then the LDE was adopted to further machine the microgrooves on the workpiece surface by EDM. With the proposed method, the wear of tool electrode presented in EDM was converted into a useful process, in which Cu, CuSn alloy and Sn disc foils with distinct wear rates were utilized to create LDE blanks. After several rounds WV-EDM, microchannels with stable shapes could be generated. In addition, the study studied the WV-EDM formation of LDE, the relationship between relative volume wear rate and processing depth, the electrode wear relationship between a single disc foil electrode and the corresponding disc foil in LDE, and the flow field distribution in the machining gap. The conclusions drawn from the study are as follows.

- (1) With the machining voltage of 180 V, the pulse width of 26  $\mu\text{s}$ , the rotation speed of the disc electrode of 1000 rpm, the reciprocating speed of the workpiece of 200 mm/min, and the processing depth of 300  $\mu\text{m}$ , for the LDE blank with a Cu/Sn/Cu structure or a Cu/CuSn/Sn/CuSn/Cu structure, the LDE with stable microchannels on the outer surface could be obtained after less

than five rounds of WV-EDM. After that, under the same process parameters and processing depth, microgrooves with the same profile and size could be continuously manufactured on the workpiece by EDM without re-shaping the LDE.

- (2) The adjacent disc foils in LDE exhibited special protective wear and support instability effects, leading to different wear modes. In LDE, the Cu and Sn foil wear was comparable to the wear of a single Cu and Sn foil electrode. The CuSn alloy foil between the Cu and Sn foils changed considerably in the direction of thickness. Specifically, due to the strong protection of Cu foil, the adjacent Cu foil side of the wear was greatly reduced, and the other side of the adjacent Sn disc due to weak protection, wear was larger, but still less than that of a single CuSn alloy foil electrode.
- (3) Based on the relationship between the relative volume wear rate of the disc foil electrode and the processing depth, the WV-EDM forming round of the LDE could be determined. Based on this forming round, the LDE with stable microchannels on the outer edge surface could be prepared.
- (4) In the EDM of microgrooves on the workpiece with the LDE, the vortex of the flowing fluid formed in the zone between the microchannel on the LDE and the machining surface facilitated the removal of debris, and this vortex gradually decreased as the depth of the microgroove increased.
- (5) Cu disc with a thickness of 100  $\mu\text{m}$ , CuSn disc with a thickness of 100  $\mu\text{m}$ , and Sn disc with a thickness of 500 and 300  $\mu\text{m}$  were selected as laminated materials to create LDE blanks. Setting 500  $\mu\text{m}$  processing depth, stable microchannels were successfully yielded on the outer surface of the LEDs utilizing the WV-EDM technology. Subsequently, microgroove arrays and columnar microstructures were produced on Ti-6Al-4 V alloy workpieces by EDM with the LDEs and the same machining depth. The depth of the microgrooves was about 490  $\mu\text{m}$ .

**Acknowledgements** The work described in this chapter was supported by the National Natural Science Foundation of China (Grant Nos. 51805333, 51575360), and the Shenzhen Natural Science Foundation University Stability Support Project (Grant No. JCYJ20170817094310049).

## References

1. Wang Z, Li YB, Bai F, Wang CW, Zhao QZ (2016) Angle-dependent lubricated tribological properties of stainless steel by femtosecond laser surface texturing. *Opt Laser Technol* 81:60–66
2. Naqiuddin NH, Saw LH, Yew MC, Yusof F, Ng TC, Yew MK (2018) Overview of micro-channel design for high heat flux application. *Renew Sustain Energy Rev* 82:901–914
3. Wang DW, Mo JL, Wang ZG, Wang XC, Chen GX, Zhu MH (2013) Mechanism of the effect of groove-textured surface on the friction vibration and noise. *J Mech Eng* 49:112–116
4. Chow HM, Yan BH, Huang FY (1999) Micro slit machining using electro-discharge machining with a modified rotary disc electrode (RDE). *J Mater Process Technol* 91:161–166

5. Furutani K, Saneto A, Takezawa H, Mohri N, Miyake H (2001) Accretion of titanium carbide by electrical discharge machining with powder suspended in working fluid. *Precis Eng* 25:138–144
6. Hung JC, Yang TC, Li KC (2011) Studies on the fabrication of metallic bipolar plates—using micro electrical discharge machining milling. *J Power Sources* 196:2070–2074
7. Murali M, Yeo SH (2004) A novel spark erosion technique for the fabrication of high aspect ratio micro grooves. *Microsyst Technol* 10:628–632
8. Yan J, Kaneko T, Uchida K, Yoshihara N, Kuriyagawa T (2010) Fabricating micro grooves with varied cross-sections by electrodischarge machining. *Int J Adv Manuf Technol* 50:991–1002
9. Hung JC, Chang DH, Chuang Y (2012) The fabrication of high-aspect-ratio micro-flow channels on metallic bipolar plates using die-sinking micro-electrical discharge machining. *J Power Sources* 198:158–163
10. Hsue AWJ, Chang YF (2016) Toward synchronous hybrid micro-EDM grinding of micro-holes using helical taper tools formed by Ni-Co/diamond co-deposition. *J Mater Process Technol* 234:368–382
11. Wan Y, Xu J, Lian Z, Xu J (2021) Superhydrophilic surfaces with hierarchical groove structure for efficient fog collection. *Colloids Surf A* 628:127241
12. Tamura T, Akiyama R, Tanaka RI, Kawamoto H, Umezu S (2020) Groove fabrication on surface of soft gelatin gel utilizing micro-electrical discharge machining (Micro-EDM). *J Food Eng* 277:109919
13. Bangash MK, Casalegno V, Kumar Das A, De la Pierre des Ambrosis, Ferraris M (2020) Surface machining of Ti6Al4V by means of micro-electrical discharging to improve adhesive joining. *J Mater Process Technol* 286:1–9
14. Yan BH, Wang CC, Liu WD, Huang FY (2000) Machining characteristics of Al<sub>2</sub>O<sub>3</sub>/6061Al composite using rotary EDM with a dislike electrode. *Int J Adv Manuf Technol* 16:322–333
15. Lin CT, Chow HM, Yang LD, Chen YF (2007) Feasibility study of micro-slit EDM machining using pure water. *Int J Adv Manuf Technol* 34:104–110
16. Yan J, Watanabe K, Aoyama T (2014) Micro-electrical discharge machining of polycrystalline diamond using rotary cupronickel electrode. *CIRP Ann Manuf Technol* 63:209–212
17. Kuo CL, Huang JD (2004) Fabrication of series-pattern micro-disc electrode and its application in machining micro-slit of less than 10 μm. *Int J Mach Tool Manufact* 44:545–553
18. Wang J, Han F (2014) Simulation model of debris and bubble movement in consecutive-pulse discharge of electrical discharge machining. *Int J Mach Tool Manufact* 77:56–65
19. Yu ZY, Rajurkar KP, Shen H (2002) High aspect ratio and complex shaped blind micro holes by micro EDM. *CIRP Ann Manuf Technol* 51:359–362
20. Yeo SH, Tan LK (1999) Effects of ultrasonic vibrations in micro electro-discharge machining of microholes. *J Micromech Microeng* 9:345–352



# Chapter 11

## Fabrication of Blind Multi-microgrooves by Applying Long-Laminated Electrode



Huiyong Wu, Jianguo Lei, and Xiaoyu Wu

**Abstract** In this study, a combination of wire electrical discharge machining (WEDM), dry WEDM, and wear-variation EDM (WV-EDM) was proposed. This combined process allowed the cost-effective fabrication of Long-laminated electrodes (LLEs) with significant interference resistance and long service life, and subsequent stable large-scale production of deep and narrow micro-blind grooves by EDM on materials with difficult-to-cut/grind surface. The disadvantage of electrode wear in EDM was converted successfully into a critical technology for manufacturing LLEs and blind microgrooves. The remelting connection layer (RCL) formed on the LLE side wall was investigated, and the RCL was characterized and analyzed using energy dispersive X-ray spectroscopy and X-ray diffraction. The experimental results indicate that the prerequisite for the formation of RCL was dry WEDM, and the uniformity and thickness of RCL were mainly influenced by the removing thickness of dry WEDM. In addition, the impact of LLE EDM performance by electrode length and processing depth were also considered, and it was found that the above two parameters had no significant effect on the processing performance. Finally, the LLE was applied to the Ti-6Al-4 V alloy workpiece under the experimental conditions used. The blind multi-microgrooves with a depth of 250  $\mu\text{m}$  and a width of 74  $\mu\text{m}$  were generated, and the crisscross blind microgrooves were prepared. This study demonstrates that the proposed approach can be used to manufacture LLEs with long service life and strong anti-interference ability, and can also be used for successive large-scale manufacturing of deep-narrow blind multi-microgrooves through the EDM technology.

---

H. Wu · J. Lei (✉) · X. Wu

Shenzhen Key Laboratory of High Performance Nontraditional Manufacturing, College of Mechatronics and Control Engineering, Shenzhen University, Nan-Hai Ave 3688, Shenzhen 518060, Guangdong, PR China  
e-mail: [ljj\\_sc111@163.com](mailto:ljj_sc111@163.com)

## 1 Introduction

Microgrooves are an extremely important surface microstructure that can impart many special features to the surface, such as higher lubricity properties [1], enhanced heat dissipation [2, 3], better machining performance [4], and better self-cleaning behavior [5]. Therefore, it is used in a wide range of fields such as micromechanics, optoelectronics, biomedicine, and biochemistry. In recent years, the production of microgrooves has been intensively studied by scholars.

Based on the microturning technology, Egashira et al. successfully machined micro face grooves with a depth of 25  $\mu\text{m}$  in brass using cemented carbide tools with an external diameter of 25 to 50  $\mu\text{m}$  [6]. Micro-cutting experiments were performed on electroless-plated NiP surfaces by Yan et al. A microgroove array with a depth of 1–20  $\mu\text{m}$  was processed with a sharp diamond cutting tool. Subsequently, the processed microgroove arrays were employed as molds in hot-pressed glass molding assays, enabling the large-scale fabrication of precise micromechanical and optical elements [7]. Chen et al. successfully fabricated microgrooves with a deepness of 10  $\mu\text{m}$ , a breadth of less than 10  $\mu\text{m}$ , and a surface roughness of Ra 0.010  $\mu\text{m}$  on NAK80 die steel utilizing a high-speed and fast-shallow grinding process and a boron infiltrated poly-crystalline diamond wheel tool with an ultra-thin grinding edge of thickness 5  $\mu\text{m}$  [8]. Zhang et al. machined microgrooves on cylindrical surfaces using ultrasonic elliptical vibration-assisted turning and developed a machining process simulation algorithm to prediction and optimization of the processing operation [9]. In order to enhance the machining performance of the tool, preparing microgrooves on the leading edge surface of the tool is a very effective method [10, 11]. Xie et al. created a variety of microgrooves with depths ranging from 7 to 149  $\mu\text{m}$  and aspect ratios of 0.14 to 0.50 on the leading edge surface of the tool by microgrinding, which reduced the temperature of the tool during cutting by 103  $^{\circ}\text{C}$  and improved the tool cutting performance [12].

Nevertheless, the successful production of surface microstructures using traditional processing methods on materials that are hard to cut/grind has rarely been demonstrated, such as titanium alloys [13]. Electrical discharge machining (EDM), a non-traditional processing technology, is a non-contact processing with no cutting forces and can be utilized to produce a variety of microstructures on any conducting material, independent of the material stiffness [14–17]. Therefore, EDM can be the best choice for fabricating microstructures on surfaces of the materials that are hard to cut/grind.

Wire EDM (WEDM), as a technology for EDM, is a prospective processing method that allows the machining of precise and complex microstructures [18, 19]. The surface microstructures were manufactured using WEDM on Ti-6Al-4 V alloy by Gao et al. [20]. As a result, the surface demonstrated ultra hydrophobicity. Zhou et al. used a low-speed WEDM to machine the  $\text{Ti}_3\text{SiC}_2$  surface with microgrooves of 63.2  $\mu\text{m}$  in width and 33.8  $\mu\text{m}$  in depth [21]. A near ultra hydrophobic surface was obtained when the parallel contact angle reached 142.7 $^{\circ}$ . A rotating microgroove was produced by Wang et al. on cemented carbide and bearing steel workpieces using

WEDM [22]. Processing errors were less than  $1.4\ \mu\text{m}$  and  $2.3\ \mu\text{m}$  along the axial and radial directions, respectively. Using the WEDG technology, Hsue et al. fabricated a spiral microgroove with a depth of dozens of microns on a  $0.3\ \text{mm}$  diameter cemented carbide tool electrode, which effectively improved the debris discharge during the machining process [23]. Yan et al. used WEDG-formed electrodes with different cross sections of tungsten tools and various microgrooves were machined by EDM on stainless steel, which consisted of circular, triangular, rectangular and semi-enclosed cross sections [24].

The timely clearing of debris in the processing gap during EDM of microgrooves can improve the machining stability and decrease the arc, which can improve the machining efficiency and surface quality. In order to improve debris clearing from the processing gap, the EDM of microgrooves was performed on a  $450\ \mu\text{m}$  thick Ti-6Al-4 V workpiece with a  $25\ \mu\text{m}$  thick electrode of rotating disc by Chow et al. [25]. The microgrooves with a width of  $42\ \mu\text{m}$  were prepared successfully. The microgrooves were effectively manufactured on Al<sub>2</sub>O<sub>3</sub>/6061Al composite workpieces by applying a Cu disc foil electrode in rotary EDM using it as a heat sink by Yan et al. [26]. For improving the processing efficiency, Lin et al. used a Cu disc with  $25\text{--}50\ \mu\text{m}$  thickness and  $42\ \text{mm}$  diameter as a tool electrode and pure water as the dielectric to machine microgrooves by EDM on Ti-6Al-4 V alloy [27]. By choosing copper-nickel alloy that was the raw material, the disc electrodes with different cross section types were manufactured and the EDM was applied on poly-crystalline diamond which produced microgroove structures with high surface quality ( $R_a\ 0.1\ \mu\text{m}$ ) and high accuracy by Yan et al. [28]. Based on the characteristics of the different wear rates for tool electrodes of different materials in EDM, Lei et al. assembled Sn and Cu discs of initially the same outside diameter into laminated disc electrode (LDE) blanks and performed multiple rounds of wear variation EDM (WV-EDM) to generate LDEs on LDE blanks that have stable microchannels on the outside edge surface [29]. Subsequently, microgrooves were processed on Ti-6Al-4 V alloy using LDE by EDM. This method shows high processing efficiency and stability, and allows the preparation of several microgrooves at once. In order to speed up the working fluid renewal in the processing gaps, Wu et al. suggested rotary micro EDM with toothed disc foil electrodes in emulsified liquid and manufactured deep and narrow microgrooves with a width of about  $78\ \mu\text{m}$  and length–width ratio of 6.4 on a 304 stainless steel workpiece [30].

As we all know, in the rotary EDM process of disc electrode, the high-speed rotating electrode will generate centrifugal force, which will prompt the electrode to self clean and drive the dielectric fluid to scour the processing surface, thereby removing debris and keeping a well EDM condition. Nevertheless, rotary EDM is unable to produce blind microgrooves. Currently, blind microgroove for EDM is mainly achieved by layer-by-layer scanning using micro-column electrodes [31] or by reciprocating up and down using foil electrodes [32]. Hung et al. applied micro EDM milling using a  $480\ \mu\text{m}$  diameter tungsten carbide tool. The microgrooves of  $500\ \mu\text{m}$  in depth and rib width, and  $300\ \mu\text{m}$ ,  $600\ \mu\text{m}$  in height (width to length ratio of 0.6 and 1.2), respectively, were manufactured on SUS316L stainless steel [33]. The development of a micro EDM machine with a creeping micro-feed mechanism and

using a scanning EDM method to fabricate blind microgrooves on single crystal silicon with microelectrodes of circular cross section was performed by Li et al. [34]. Lim et al. used an on-machine manufactured high aspect ratio thin electrode to fabricate triangular-shaped blind microgrooves of width under 150  $\mu\text{m}$  on aluminum workpieces by micro scanning EDM [35]. An approximately 79  $\mu\text{m}$  wide blind microgroove was manufactured by layer by layer scanning Micro-EDM by Zou et al. using a 65  $\mu\text{m}$  diameter tungsten wire as the tool electrode and a plasma jet of nitrogen as the medium [36]. Song et al. performed spray micro discharge milling using a bipolar pulsed power supply and deionized water. Blind microgrooves 200  $\mu\text{m}$  long and 50  $\mu\text{m}$  deep on WC-Co workpieces were machined by using an 80  $\mu\text{m}$  diameter micropillar electrode [37]. A MOSFET was introduced in a common RC type pulse generator for microelectronic discharge milling to improve the geometric precision of microgrooves by Cheong et al. [38]. In order to enhance the processing efficiency, Wei et al. introduced a novel method of interpolation with flexible cycle and step length on the basis of square constraints in Micro-EDM, and a variety of microgrooves were machined using a 100  $\mu\text{m}$  diameter electrode [39]. Yeo and Murali performed up-and-down reciprocating micro EDM using stainless steel foil of 10  $\mu\text{m}$  thickness for the tool electrode. Microgrooves of width about 50  $\mu\text{m}$  and depth of 7 to 69  $\mu\text{m}$  were prepared successfully on the Cu plate [32]. The micro EDM of a graphite foil electrode with the thickness of 100  $\mu\text{m}$  was selected by Murali and Yeo for reciprocating up and down on the tool steel. As a result, a 200  $\mu\text{m}$  wide microgroove was successfully manufactured [40].

It is known that the wear of the tool electrode is inevitable during EDM. In particular, there is tremendous wear and diminished resistance to interference when the ultra-thin tool electrode is chosen, which makes it unavailable for continuous large-scale production of narrow and deep blind microgrooves. Therefore, if deep and narrow blind microgrooves are consistently produced in large quantities with a microelectrode, it can increase the tool electrode length and theoretically extended the service life; nevertheless, once the length is increased, its apparently small cross section size drastically weakens the resistance of the micro-pillar electrode or foil electrode to interference, thus reducing processing accuracy and stability. Furthermore, the research on producing deep and narrow blind multi-microgrooves through EDM in one time is scarce.

In order to resolve the above problems and decrease the electrode manufacturing cost, through combining WEDM, dry WEDM and WV-EDM, the paper proposed to produce the long-laminated electrode (LLE) with exceptionally high interference resistance and long service life, which was then used for up and down reciprocating EDM for continuous large production of narrow and deep blind multi-microgrooves of the same size. There was no need to make shape modifications to the LLE in the interim, until the length became sufficient short, so that the LLE could no longer work because of wear. The technology transformed the disadvantage of the electrode wear during EDM into a favorable method for manufacturing LLE and blind microgrooves, totally reversing the view about electrode wear as a disadvantage of EDM. In addition, the EDM using LLE could machine multiple blind microgrooves of several tens of microns in width on a large surface area of the workpiece. This study investigated

the formation of remelting connection layers (RCLs) on the LLE sidewalls and the influence of processing polarity, processing depth and electrode length to the EDM performance of LLEs. In addition, LLEs with lengths of tens of millimeters were produced and applied to the EDM of multiple blind microgrooves.

## 2 Experiments

### 2.1 Methods

The procedure for the preparation of LLE and blind microgrooves is illustrated in Fig. 1. And the critical steps are described as follows:

- (1) Several layers of Sn and Cu foil were laminated alternatively (Fig. 1a), and clamped between two cemented carbide plates, which were then fixed in a fixture. The LLE blanks are produced using WEDM following a defined path (Fig. 1(b)). As a whole, the size of the carbide plate is approximately 1 mm narrower than the dimension of the LLE blank.
- (2) The dry WEDM process was performed on the LLE blank's sidewalls using electric parameters identical to the WEDM process applied in step 1 (Fig. 1(c)).

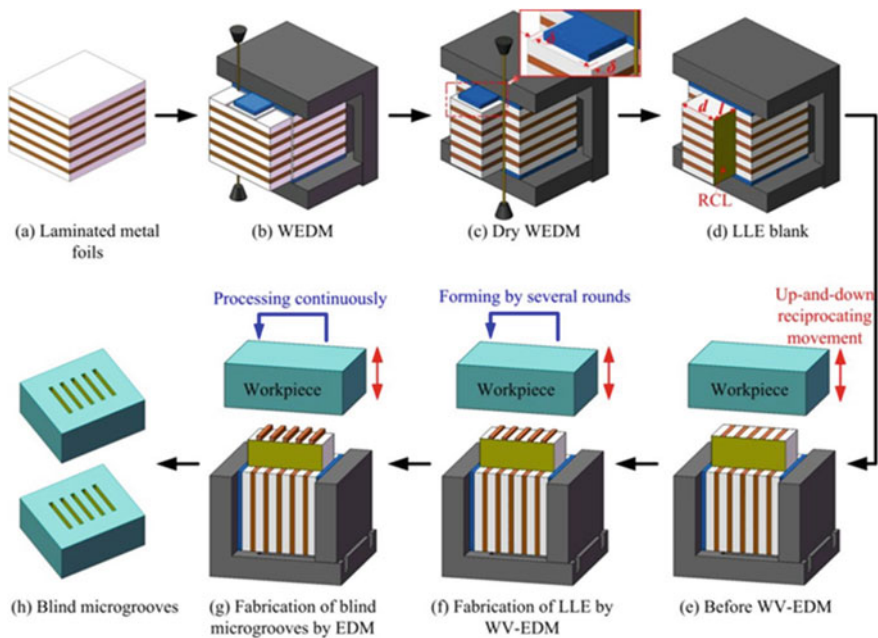


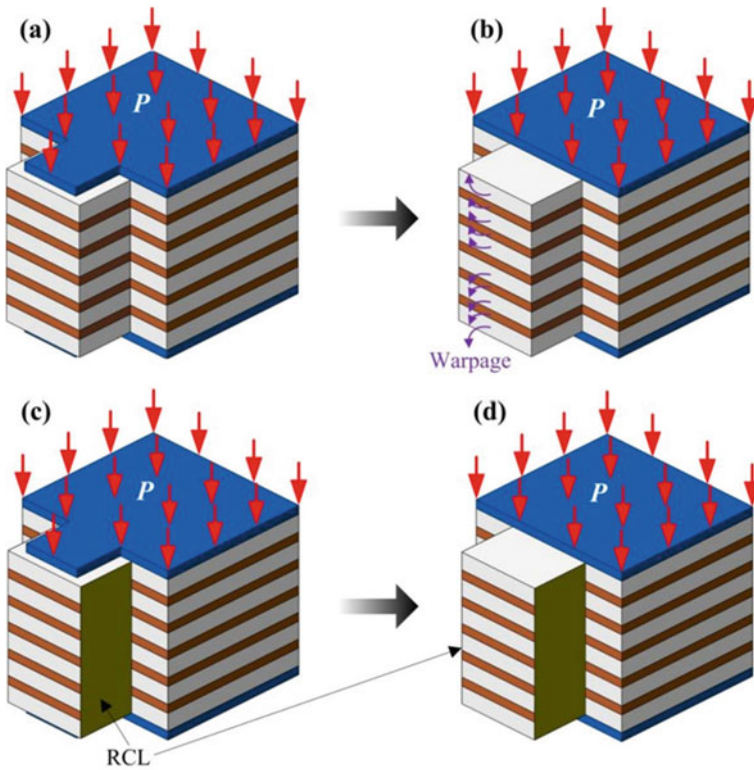
Fig. 1 Illustration of manufacturing the LLE and blind microgrooves

Thickness of removal was set to  $\delta$ . In addition, the transient high temperature produced by the spark discharge formed RCL on the side walls of the LLE blank, which securely bonded the tin and Cu foils together. Then, with removal of the cemented carbide board by WEDM, a solid LLE blank was produced in length (l) and width (d) (Fig. 1d).

- (3) On the EDM table, the LLE blank and fixture were mounted, and the workpiece was clamped on the Z axis for up and down reciprocating motion (Fig. 1e). Setting a uniform processing depth (D) and process parameters, several rounds of WV-EDM were performed at different locations of the workpiece to fabricate the LLE (Fig. 1f). The Sn foil electrode exhibited remarkably weaker EDM capability compared to the Cu foil electrode and drastically wore out during the EDM process. Afterward, the Cu foil was progressively visible on the working surface of the LLE blank. As the number of WV-EDM cycles increased, the difference in height between the Sn and Cu foil on the working surface progressively reached stability, resulting in the LLE (Fig. 1g). The low-wear Cu foil was the actual tool electrode, producing a blind multi-microgroove, while the high-wear Sn foil sacrificed self to provide the neighboring Cu foil with support in real time.
- (4) The LLE was formally applied to EDM for preparing blind multi-microgrooves under the same experimental conditions (Fig. 1g–h). Despite the continuous wear of the metal foil in the LLE during the EDM process, the LLE work surface profile remained consistently stable without shape change because of the consistent wear balance between the metal foils. Compared to foil electrodes and micropillar, the LLE had a wider cross section, so the electrode length could reach several tens of millimeters. Thus, LLE could be used to continuously large scale production of blind multi-microgrooves before it become too short to be used no longer.

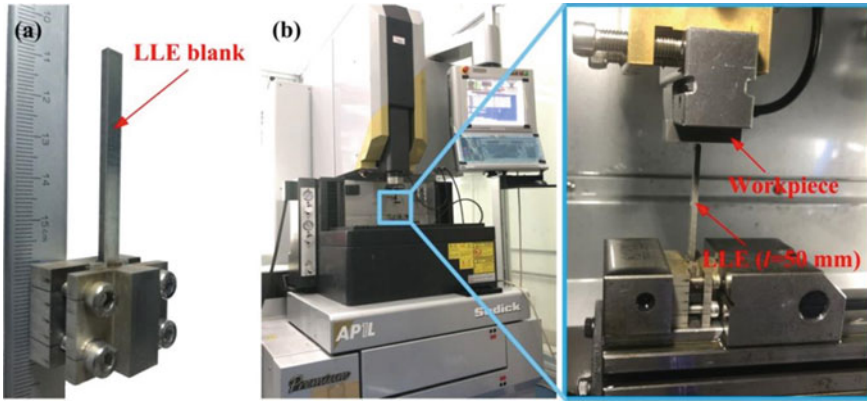
## 2.2 Process of Manufacturing RCLs

In this research, it was shown that the LLE blanks was manufactured from Sn and Cu foils, that were stacked and sandwiched with physical contact between the foils and without metallurgical reactions. The Sn foil served for a sacrificial layer which only had to be in close contact with these two layers to obtain the tool electrode ideally. The Sn and Cu foils were easily in mutual contact with each other by the pressure (P) of the cemented carbide board on each side when the LLE blank was only manufactured by WEDM (Fig. 2a). Nevertheless, even the position of the electrode clamp was still fixed on the fixture, the Sn and Cu foils in the LLE blank were readily detached from each other once the cemented carbide boards were taken away and bended toward the sides of the cemented carbide boards because of the weak rigidity of the Sn and Cu foils, which was demonstrated by the purple arrow in Fig. 2b. Especially the foil warping became more obvious as the electrode was long enough. The process was applied only to laminated electrodes under 1 mm in length.



**Fig. 2** a, b Illustration of LLE blanks processed by WEDM before and after removal of cemented carbide plates; c, d illustration of LLE blanks processed by WEDM and dry WEDM before and after removal of cemented carbide plates

Nevertheless, the short electrode cannot be applied for large-scale production of microgrooves because of the continuous wear of tool electrodes in the EDM. In order to resolve the problem, a combination of WEDM and dry WEDM was used in the experiment. At first, WEDM was applied to machine LLE blanks, then the dry WEDM was used to machine the side walls of the LLE blanks. Because of the extreme softness and the low melting point (231.2 °C) of the Sn foil, a part of the melted Sn remained on the machined surface and resulted in the formation of the RCL when machining the electrode side wall, which made the electrode side wall a single unit, thereby ensuring tight layer-to-layer contact, as shown in Fig. 2c. When the cemented carbide plates had been removed, the Sn and Cu foils were still joined together because of the RCLs on both side walls, as shown in Fig. 2d. This assured the manufacturing accuracy of tool electrodes in the lamination direction, producing a passable LLE which could be applied for large-scale production of microgrooves for EDM.



**Fig. 3** a LLE blank; b machining platform

### 2.3 Experimental Materials and Setup

Cu foil with a 50  $\mu\text{m}$  thickness and Sn foil with a 300  $\mu\text{m}$  thickness were selected to manufacture the LLE blanks via WEDM and dry WEDM (Fig. 3a). Ti-6Al-4 V sheets were applied as the workpiece for processing the blind microgrooves. The cemented carbide boards were chosen to provide assistance in preparing the LLE blanks.

A WEDM machine (Model: H-CUT 32F) fabricated by HI-LINK Precision Machinery Co. Ltd. of China was modified for forming LLE blanks. The maximum travels of X, Y and Z axis were 400 mm, 320 mm and 400 mm respectively. The positioning accuracy of all axes was 1  $\mu\text{m}$ . An EDM machine (model: AP1L) manufactured by Sodick Co. Ltd. was used for shaping the LLE and machining the blind multi-microgrooves. The maximum travels of the X, Y and Z axes were 200 mm, 120 mm and 200 mm, respectively. The positioning accuracy of all axes was 0.1  $\mu\text{m}$ . The used the machining table is shown in Fig. 3b. The workpiece was positioned on top of the LLE, and this facilitated debris removal. To observe and characterize the workpiece, the WEDM was used to cut blind microgrooves, which were polished afterwards. Using a laser scanning confocal microscope (VK-X250, KEYENCE, Japan), the size of the blind microgrooves were measured. Every microgroove were measured three times. The microgroove morphology was gathered with a scanning electron microscope (SEM) (Quanta FEG 450, FEI, USA).

### 2.4 Experimental Conditions

In order to research the RCL of the LLE side walls and the influence of the parameters on the processing performance for fabrication of blind microgrooves with



**Table 1** Process parameters for WEDM, dry WEDM and WV-EDM/EDM

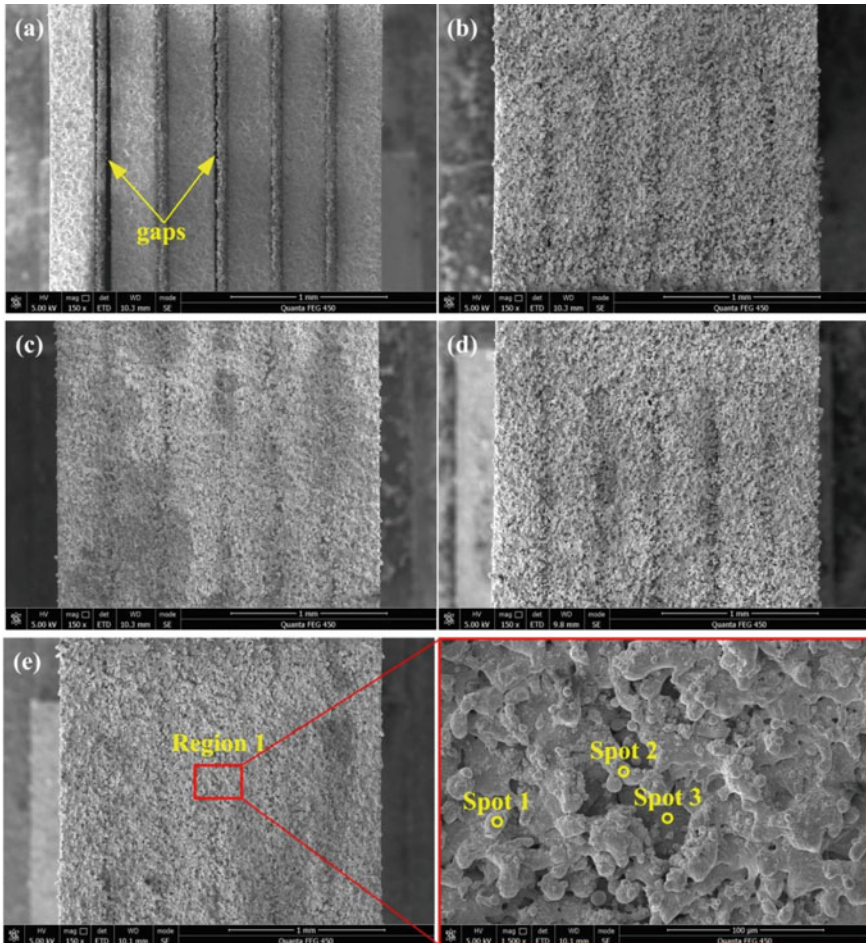
Parameters	WEDM	Dry WEDM	WV-EDM/EDM
Machining current (A)	0.42	0.42	–
Machining voltage (V)	80	80	200
Pulse width ( $\mu\text{s}$ )	10	10	1
Pulse interval ( $\mu\text{s}$ )	40	40	10
Processing speed (mm/min)	3	3, 3.5, 4, 4.5	–
Dielectric fluid	Emulsion	Air	EDM oil
Removal thickness ( $\mu\text{m}$ )	–	20, 30, 40, 50	–
Electrode length (mm)	–	–	5, 10, 15, 20, 25
Machining depth ( $\mu\text{m}$ )	–	–	100, 200, 300, 400, 500

LLE and single Cu foil electrodes, a sequence of experiments were conducted with each parameter setting repeated three times. The processing conditions are listed in Table 1.

### 3 Results and Discussion

#### 3.1 RCL on the Sidewalls of the LLE

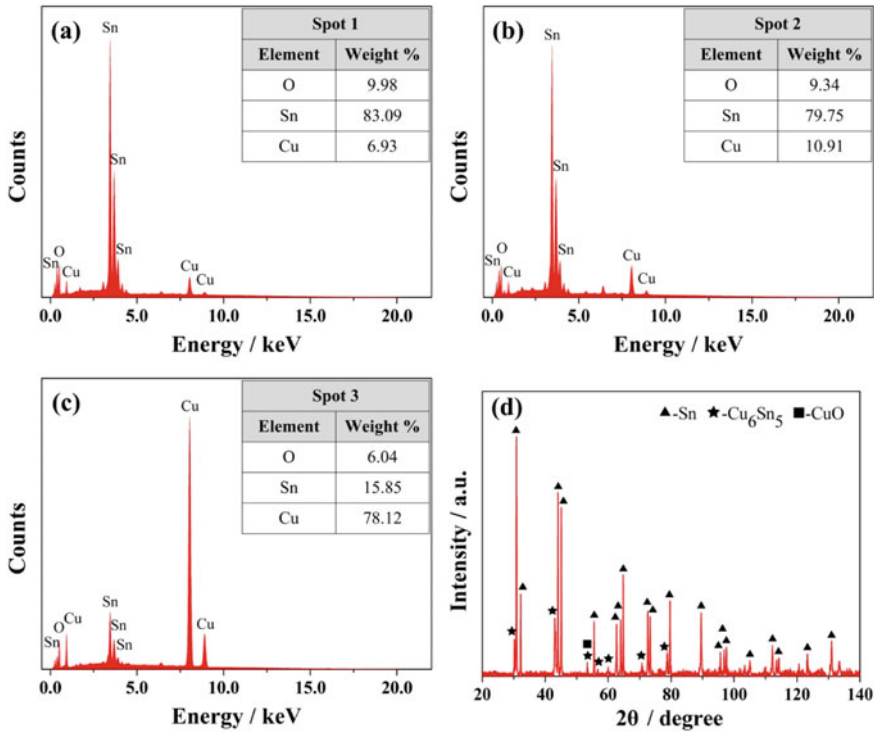
The side walls of the LLE blanks manufactured by combination of WEDM and dry WEDM machining at various machining speeds were shown in Fig. 4. Based on our previous study, the following parameters were applied: 0.42 A processing current, 80 V processing voltage, 10  $\mu\text{s}$  pulse width, and 40  $\mu\text{s}$  pulse interval [41]. When only WEDM was selected, a large quantity of Sn eroded by the EDM discharge was removed because of the flushing and immediate cooling by the dielectric fluid, thus failing to produce the RCL on the side wall. Consequently, after removal of the cemented carbide board, a large gap developed between the Cu and Sn foil (Fig. 4a), which negatively affected subsequently the EDM processing of the blind microgrooves. Figure 4b–e displays the side walls of the LLE blanks manufactured by WEDM and then dry WEDM at machining speeds of 3.0, 3.5, 4.0 and 4.5 mm/min, respectively. The thickness removed by dry WEDM was 50  $\mu\text{m}$ . In Fig. 4b–e, it can be shown that after dry WEDM, the side walls of the electrodes were covered with RCL, which was tightly attached to the foil in the LLE blank. Nevertheless, the machining speed had no significant effect on the RCL. Thus, in order to obtain



**Fig. 4** SEM images of the LLD sidewalls prepared by a combination of WEDM and dry WEDM with different processing speeds: **a** 3.0 mm/min WEDM; **b** 3.0 mm/min WEDM + 3.0 mm/min dry WEDM; **c** 3.0 mm/min WEDM + 3.5 mm/min dry WEDM; **d** 3.0 mm/min WEDM + 4.0 mm/min dry WEDM; **e** 3.0 mm/min WEDM + 4.5 mm/min dry WEDM

high electrode manufacturing effectiveness, a combination of 3.0 mm/min WEDM + 4.5 mm/min dry WEDM was selected to fabricate the LLE blanks in the experiment.

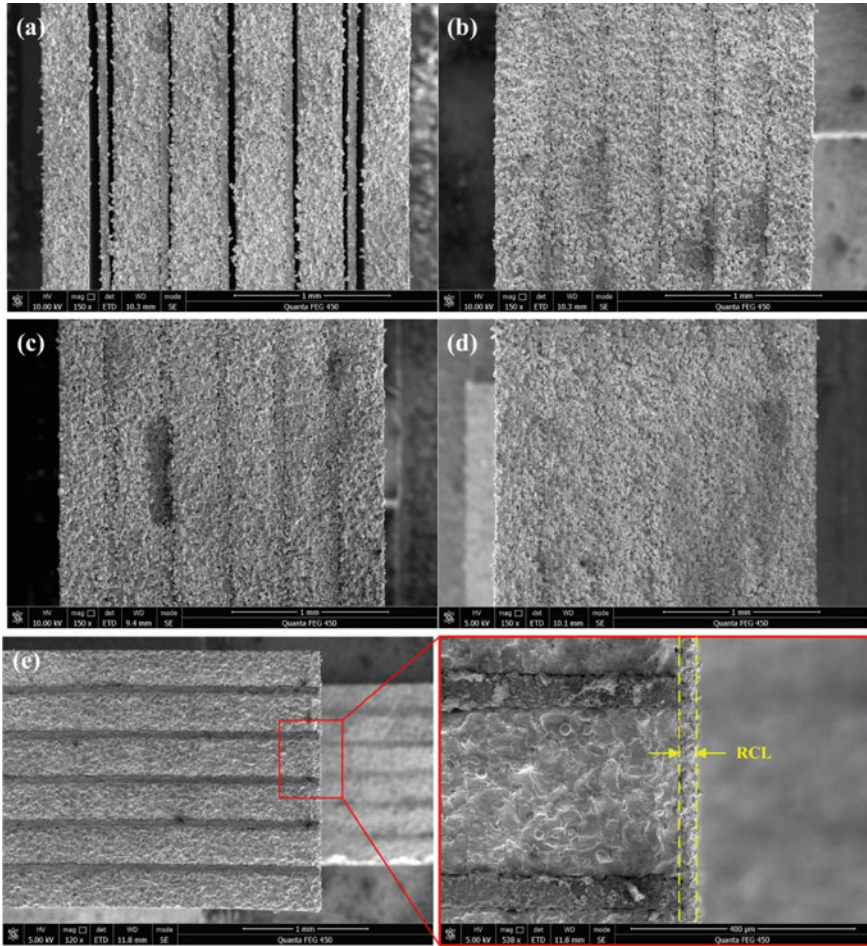
In order to investigate further the RCL on the side walls, a point analysis of energy dispersive X-ray spectroscopy (EDS) was performed at different positions in area 1, as shown in Fig. 4e. Points 1 and 3 were situated on the Sn and Cu foil, respectively, whereas point 2 was situated at the intersection of Sn and Cu foil. In addition, points 1 and 2 were situated on the RCL surface, whereas point 3 was situated at the underside of a crater in the RCL. The analysis results are illustrated in Fig. 5a–c. It is observed that points 1 and 2 have the highest Sn content, which indicates the RCL contains



**Fig. 5** a EDS of spot 1 shown in Fig. 4e; b EDS of spot 2 shown in Fig. 4e; c EDS of spot 3 shown in Fig. 4e and d XRD of the surface shown in Fig. 4e

mainly Sn. In addition, in point 3 the maximum Cu content was noticed, which was situated on the Cu foil, at the base of one of the craters of the RCL. In addition, the surfaces of the RCL was characterized by X-ray diffraction (XRD). The results illustrated in Fig. 5d show the RCL contained primarily Sn, as well as small amounts of Cu-Sn alloy and CuO. These materials had significantly higher resistivity than the Cu, which caused significant wear in EDM. In addition, it was noticed that the RCL was very thin and therefore had negligible effect on the machining accuracy of the microgrooves.

The removal thickness during dry WEDM had a significant influence on the uniformity and thickness of the RCL. In order to acquire a particularly thin RCL with the presence of a close connection between the foils of the LLE blank, the influence of various removal thicknesses on the RCL was investigated. Figure 6a–d shows the surface of dry WEDMed for removal of 20, 30, 40 and 50 μm thicknesses. It is observed that at a removal thickness of 20 μm, the foils were separated due to the retention of too little molten Sn on the sidewalls, thus failing to produce a reliable RCL on the machined surface. In addition, with increasing removal thickness, more and more molten Sn was observed, which led to a gradual homogenization of the



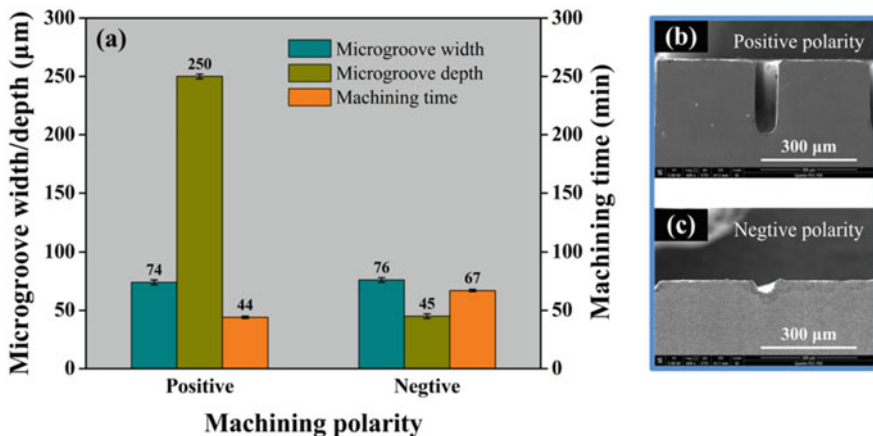
**Fig. 6** SEM images of the LLD sidewalls processed by dry WEDM with diverse removal thicknesses: **a** 20  $\mu\text{m}$ ; **b** 30  $\mu\text{m}$ ; **c** 40  $\mu\text{m}$ ; **d** 50  $\mu\text{m}$  and **e** working surface of the electrode shown in (d)

RCL on the machined surface. Furthermore, as the removing thickness was increased to 50  $\mu\text{m}$ , the machined surface was totally coated by RCL, thereby assuring a tight connection between the foils of the LLE blanks. Figure 6e is the SEM image of the working surface of the LLE shown in Fig. 6d. Based on the measured data, the RCL thickness was about 30  $\mu\text{m}$ .

### 3.2 Machining Polarity

During the EDM operation, the machining pole had a great influence on the ratio of energy distribution and therefore the direct affected on the workpiece material removal. The machining pole was classified into positive pole (tool electrode: negative; workpiece: positive) and negative pole (tool electrode: positive; workpiece: negative). Experiments with positive and negative polarities were conducted to obtain reasonable machining pole. Using the process parameters were: 1  $\mu$ s pulse width, 10  $\mu$ s pulse interval, 200 V machining voltage, 300  $\mu$ m machining depth, and 10 mm electrode length.

Figure 7a displays the influences of machining polarity on the depth, width and processing time of the microgrooves machined by LLE. It was clear that the microgrooves produced by both processing methods had similar width, although the positive polarity produced significantly deeper microgrooves and shorter processing times than those produced by the negative polarity. The reason for this was that positive polarity was bombarded by electrons in the presence of an electric field, whereas negative polarity was ballasted by positive ions. Nevertheless, because the electrons had smaller quality and inertance than the positive ions, the electrons attained a significantly higher velocity and bombarded the positive electrode in a very brief period of time. For positive ions, just a small fraction reaches the negative electrode. As a result, the bombardment energy of electrons to the workpiece as positive electrode was significantly higher than the bombardment energy of positive ions to the tool electrode as negative electrode. Therefore, in the next experiments, the positive electrode was used for EDM. Figures 7b, c display the cross section of the microgrooves generated by the positive and negative electrode EDM, respectively.



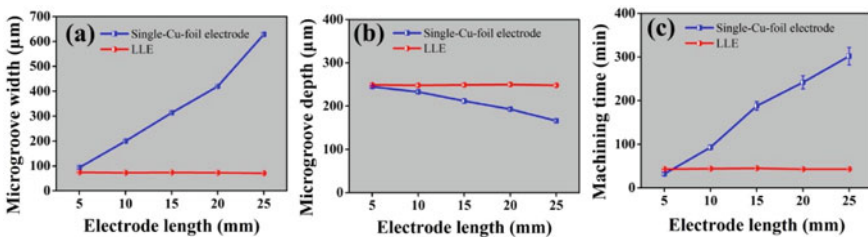
**Fig. 7** a Influence of machining polarity on the width, depth and machining time of the microgrooves; b microgrooves fabricated by positive polarity; c microgrooves fabricated by negative polarity

### 3.3 Electrode Length

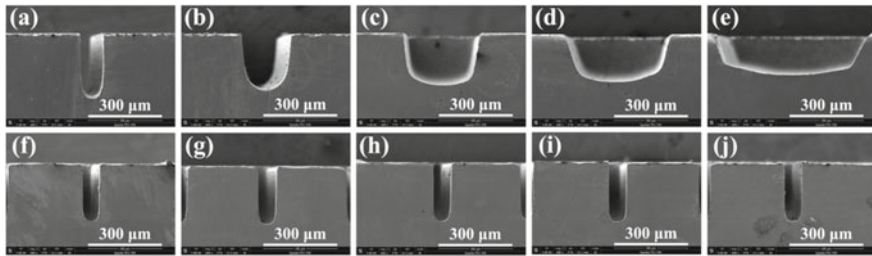
In order to decrease the cost of fabrication and extend the electrode service life, a viable approach would be to prolong the length of the electrode for continuous large-scale production of microgrooves. Nevertheless, for foil electrodes, the prolongation of electrode length unavoidably causes a drastic decrease in electrode rigidity, which affects the stability and accuracy of the process. To investigate the variation between foil electrodes and the LLE when processing microgrooves with different lengths of electrodes, the experiments were performed with a Cu foil electrode and an LLE made up of six Sn foils and five Cu foils. Using a 1  $\mu\text{s}$  pulse width, a 10  $\mu\text{s}$  pulse interval, a 200 V processing voltage, a 5 mm electrode width, and a 300  $\mu\text{m}$  machining depth, microgrooves were machined by EDM with positive polarity using foil electrodes and LLEs with lengths of 5, 10, 15, 20, and 25 mm. Figure 8a–c displays the influences of various electrode lengths ( $l$ ) on the width, depth and machining time of the microgrooves.

As can be seen from Fig. 8a–c, when the length of the electrode ( $l$ ) was 5 mm and other processing parameters were kept constant, the two types of electrodes produced essentially the same depth of microgrooves, however, the microgrooves produced by the LLE were smaller in width than those produced by the single Cu foil electrode. That was attributed to the Sn foil supporting the neighboring Cu foil, which improved the process stability of the Cu foil in the LLE. Furthermore, one microgroove could be produced in approximately 32 min using a single Cu foil electrode. In contrast, it took about 43 min to produce five microgrooves at a time using LLE, so it took about 8.6 min to produce one microgroove using LLE. Compared to the single Cu foil electrode, the machining efficiency of the LLE was improved by about 73.1%.

With increasing electrode length, the resistance to interference as well as the processing stability of the single Cu foil electrode decreases sharply, thus greatly increasing the width and processing time of the microgrooves with gradually reducing the depth. The microgroove produced with the single Cu foil electrode had a 629  $\mu\text{m}$  width and 166  $\mu\text{m}$  depth with a processing time of 302 min when the electrode length was 25 mm. Nevertheless, because LLE was apparently highly resistance to interference, it was very stable in its processing. The microgroove width (43  $\mu\text{m}$ ),



**Fig. 8** Influence of electrode length on **a** the width, **b** depth, and **c** machining time of the blind microgrooves machined via EDM with the foil electrode and LLE, respectively



**Fig. 9** Microgrooves prepared using the single Cu foil electrodes of different lengths: **a** 5 mm; **b** 10 mm; **c** 15 mm; **d** 20 mm; **e** 25 mm; microgrooves prepared using the LLEs of different lengths: **f** 5 mm; **g** 10 mm; **h** 15 mm; **i** 20 mm; **j** 25 mm

depth ( $248\ \mu\text{m}$ ) and machining time (43 min) were essentially unaffected. Figure 9a–j displays the microgrooves machined with a single Cu foil electrode and different lengths of LLEs. Because of the presence of RCL on the side walls of the LLE, the processing accuracy remained unaffected even when a LLE of 50 mm was used in the experiments. Based on the experiments, the wear caused by the production machining of multiple microgrooves with a depth of  $500\ \mu\text{m}$  was  $100\ \mu\text{m}$ , while the 50 mm length LLE could process continuously at least 490 groups of such multiple microgrooves. Thus, the LLE is regarded as usable for mass production of microgrooves.

### 3.4 Machining Depth

In EDM, it became more and more challenging to refresh the working fluid and clear the debris from the processing gap as the machining depth increases, resulting in a dramatic decrease in processing stability, which was particularly obvious in blind hole and blind microgroove machining. In this research, an efficient approach was employed to manufacture blind microgrooves by placing the workpiece above the LLE and performing an up-and-down reciprocating motion. Under the combined gravity effect of the debris and the up and down reciprocating motion of the workpiece, the debris were effectively cleared from the processing gap, thus avoiding the deposition of debris on the workpiece surface, enhancing the efficiency and stability of the process. Figure 10 displays the width, depth and machining time of the microgrooves generated by EDM using LLEs for different depths. It was observed that microgrooves depth fluctuates in the range of several micrometers as machining depth increased, which was mainly attributed to the secondary discharge during chip evacuation, thus affecting the machining gap [42, 43]. In addition, the relationship between microgroove depth ( $d$ ), machining time ( $t$ ) and machining depth ( $D$ ) when the processing depth was smaller than  $500\ \mu\text{m}$  can be depicted as follows:

$$d = 0.783D + 10.5 \quad (1)$$

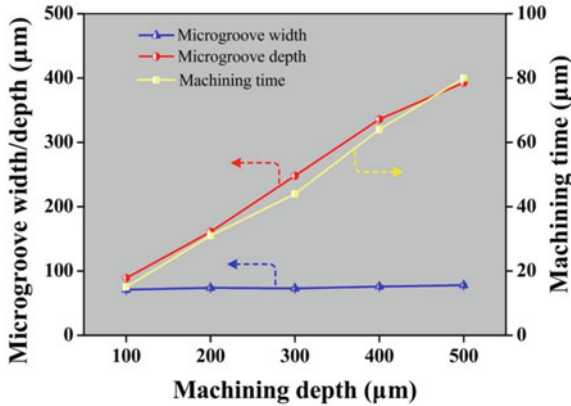


Fig. 10 Influence of the machining depth on the microgroove width, depth, and machining time

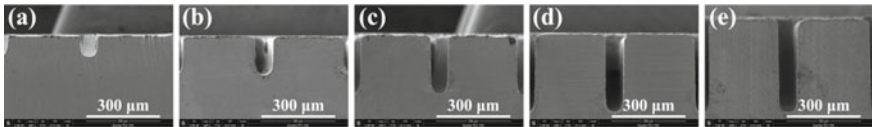


Fig. 11 Blind microgrooves prepared with different machining depths: a 100 μm; b 200 μm; c 300 μm; d 400 μm; e 500 μm

$$t = 0.163D - 2.1 \tag{2}$$

It indicates that the machining process exhibits extremely high stability when machining microgrooves by EDM with LLE. The first reason was that the Cu foil in the LLE possessed a strong resistance to interference supported by the adjacent Sn foil. The second reason was that a good EDM process was maintained by the workpiece placed on the LLE and the up and down reciprocating motion and the gravity of the debris, which discharged the debris in time. Figure 11 displays the corresponding microgrooves on the workpiece.

#### 4 LLE Forming and Blind Microgroove Structure Production

The LLE blanks of 10 mm in length and 5 mm in width were fabricated by WEDM and dry WEDM sequentially on the basis of the method proposed by stacking six Sn foils of thickness 300 μm and five Cu foils of thickness 50 μm alternately. Afterwards, under the processing conditions of 1 μs pulse width, 10 μs pulse interval, 200 V processing voltage, positive pole of the workpiece, and 300 μm processing depth,



WV-EDM was conducted at different locations on the Ti-6Al-4 V alloy workpiece surface. Due to the different wear rates exhibited by tool electrodes of different materials, after several WV-EDM rounds using the same process parameters, Cu foils appeared progressively on the working surface of the LLE blank, at the same time, the Sn foils with a higher wear rate provided immediate support for the adjacent Cu foils. As more rounds were processed, a relative wear balance between the Cu and Sn foils was achieved on the working surface of the LLE blank, resulting in the LLE. Figure 12a, b displays the LLE blank and the LLE manufactured after six WV-EDM rounds, and Figs. 12c–h displays the cross-sectional profiles of the microgrooves on the workpiece from the first round to the sixth round.

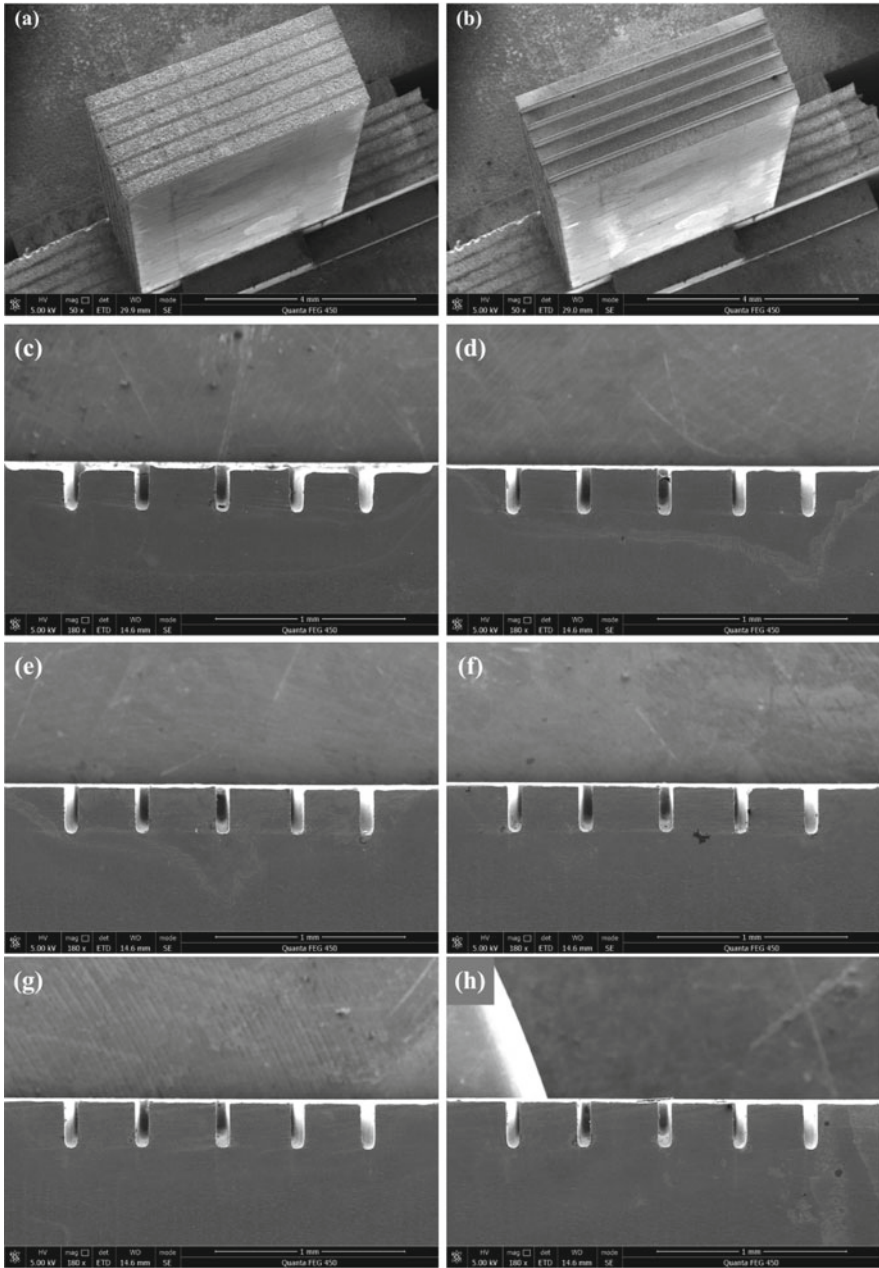
In order to reduce measurement error, the microgrooves shown in Fig. 12c–h were repeatedly measured three times with the laser scanning confocal microscope, and the average values were calculated, as listed in Table 2. The reference point to measure the depth of the microgrooves chose the the workpiece surface.  $d_{Cu}$  and  $d_{Sn}$  represent the depths of the microgrooves processed with Cu and Sn foils, respectively.  $w_{Cu}$  represents the width of the microgrooves processed with Cu foils. Clearly, the depth of the microgrooves machined with Cu foils following each round was  $249 \pm 2 \mu\text{m}$  and the width was  $74 \pm 2 \mu\text{m}$ . Meanwhile, the depth of the microgrooves machined with Sn foils decreased gradually with the number of rounds, remaining at a depth of  $7.5 \pm 1 \mu\text{m}$  from the fourth round. It showed that the microgrooves dimensions on the workpiece stabilized from this round, which meant that the profile of the corresponding LLE's working surface was also stabilized.

The manufactured LLE was applied to machine blind microgroove structures on Ti-6Al-4 V alloy using the same process parameters and processing depth as described above. The produced blind microgrooves were displayed in Fig. 13a. The depth and width of the microgrooves were about  $250 \mu\text{m}$  and  $74 \mu\text{m}$ , respectively. After the machining was completed, the microgroove workpiece was turned horizontally by 90 degrees and the process was duplicated to produce a longitudinal and horizontal microgroove structure as shown in Fig. 13b.

## 5 Conclusions

In this study, a combined process of WEDM, dry WEDM and WV-EDM was proposed to produce LLE with long service life effectively, and then the LLE was used for machining multiple blind microgrooves by EDM. The method successfully transformed wear of the electrode, an adverse feature in the EDM process, into a favorable process and extended the electrode life by prolonging the tool electrode length, enabling sustainable mass manufacturing of blind microgrooves. The following conclusions are drawn from the experimental studies:

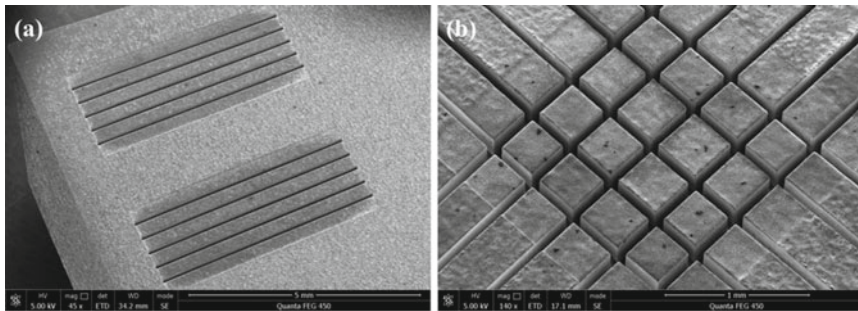
- (1) It was the prerequisite for generating the RCL and was an essential process for the manufacture of the LLE. In contrast, the removal thickness had a greater effect than the processing speed on the RCL. Under the processing conditions



**Fig. 12** a LLE blank; b LLE after six rounds of WV-EDM; c–h cross-sectional profiles of the blind microgrooves processed during the LLE manufacturing by WV-EDM

**Table 2** Dimensions of the blind microgrooves prepared from the first to sixth round in the manufacture of the LLE with WV-EDM

Round	Microgroove depth for the Cn foil ( $d_{cu}$ )/ $\mu\text{m}$	Microgroove width for the Cn foil ( $w_{cu}$ )/ $\mu\text{m}$	Microgroove depth for the Sn foil ( $d_{sn}$ )/ $\mu\text{m}$
1st	250.6	74.2	35.4
2nd	250.4	75.1	12.9
3rd	249.5	73.6	8.8
4th	250.3	74.8	7.5
5th	248.8	76.0	7.8
6th	249.6	74.9	7.6



**Fig. 13** a Blind microgroove structures; b crisscross blind microgrooves

of 0.42 A machining current, 80 V machining voltage, 10  $\mu\text{s}$  pulse width, 40  $\mu\text{s}$  pulse interval, 50  $\mu\text{m}$  removal thickness, and 4.5 mm/min machining speed, a uniformly distributed RCL with a thickness of approximately 30  $\mu\text{m}$  was generated on the sidewalls of the LLE. The RCL contained mainly Sn, as well as a small amounts of Cu-Sn alloy and CuO.

- (2) It was found that the effect of length of electrode on LLE processing performance was significantly smaller than that of the single Cu foil electrode. For machining one microgroove, under the processing conditions of 5 mm electrode length and 300  $\mu\text{m}$  processing depth, the LLE consisting of five Cu foils of 50  $\mu\text{m}$  in thickness and six Sn foils of 300  $\mu\text{m}$  in thickness exhibited a processing efficiency about 73.1% higher than the single Cu foil electrode of 50  $\mu\text{m}$  in thickness. With increasing electrode length, the LLE exhibited significantly higher processing accuracy and efficiency than the single Cu foil electrode due to its high interference resistance.
- (3) It was found that the machining depth had an apparently smaller effect on the performance of EDM with the LLE. Meanwhile, the machining depth barely affects the width of the microgrooves produced by LLE when the machining depth was between 0 and 500  $\mu\text{m}$ . In addition, the depth and processing time of microgrooves increased nearly linearly with increasing processing depth.

- (4) Using Cu foils with the thickness of 50  $\mu\text{m}$  and Sn foils with the thickness of 300  $\mu\text{m}$ , LLE blanks were manufactured by WEDM and dry WEDM. By performing four rounds WV-EDM, LLE with stable working surface profile was obtained using the following parameters: processing voltage 200 V, machining depth 300  $\mu\text{m}$ , pulse width 1  $\mu\text{s}$ , and positive polarity of the workpiece. The above process parameters were applied to EDM on the surface of Ti-6Al-4 V alloy, blind microgrooves as well as crisscross blind microgroove structures were achieved. The depth and width of the microgrooves were about 250  $\mu\text{m}$  and 74  $\mu\text{m}$ , respectively.

**Acknowledgements** The work described in this chapter was supported by the National Natural Science Foundation of China (Grant Nos. 51805333, 51975385), and the Shenzhen Natural Science Foundation University Stability Support Project (Grant No. JCYJ20190808143017070, JCYJ20170817094310049).

## References

- Gong J, Jin Y, Liu Z, Jiang H, Xiao M (2019) Study on influencing factors of lubrication performance of water-lubricated micro-groove bearing. *Tribol Int* 129:390–397
- Naqiuddin NH, Saw LH, Yew MC, Yusoff F, Ng TC, Yew MK (2018) Overview of micro-channel design for high heat flux application. *Renew Sust Energ Rev* 82:901–914
- Tang H, Tang Y, Yuan W, Peng R, Lu L, Wan Z (2018) Fabrication and capillary characterization of axially micro-grooved wicks for aluminium flat-plate heat pipes. *Appl Therm Eng* 129:907–915
- Yan H, Bakadiasa Kabongo D, Yan Z, Han F, Chen Z (2020) Sustainable production of high-uniformity workpiece surface quality in wire electrical discharge machining by fabricating surface microstructure on wire electrode. *J Clean Prod* 259:120881
- Liu P, Gao Y, Wang F, Yang J, Yu X, Zhang W, Yang L (2017) Superhydrophobic and self-cleaning behavior of Portland cement with lotus-leaf-like microstructure. *J Clean Prod* 156:775–785
- Egashira K, Iwata M, Nomura Y (2011) Boring and face grooving using micro turning tools. *CIRP Ann Manuf Technol* 60:81–84
- Yan J, Oowada T, Zhou T, Kuriyagawa T (2009) Precision machining of microstructures on electroless-plated NiP surface for molding glass components. *J Mater Process Technol* 209:4802–4808
- Chen ST, Chang CH (2013) Development of an ultrathin BD-PCD wheel-tool for in situ microgroove generation on NAK80 mold steel. *J Mater Process Technol* 213:740–751
- Zhang C, Shi G, Ehmann KF, Li Y (2016) Modeling and simulation of micro-groove topography on cylindrical surface by elliptical vibration-assisted turning. *Int J Adv Manuf Technol* 86:1407–1424
- Sharma V, Pandey PM (2016) Recent advances in turning with textured cutting tools: A review. *J Clean Prod* 137:701–715
- Peña-Parás L, Maldonado-Cortés D, Rodríguez-Villalobos M, Romero-Cantú AG, Montemayor OE (2020) Enhancing tool life, and reducing power consumption and surface roughness in milling processes by nanolubricants and laser surface texturing. *J Clean Prod* 253:119836
- Xie J, Luo MJ, Wu KK, Yang LF, Li DH (2013) Experimental study on cutting temperature and cutting force in dry turning of titanium alloy using a non-coated micro-grooved tool. *Int J Mach Tools Manuf* 73:25–36

13. Huang P, Li H, Zhu WL, Wang H, Zhang G, Wu X, To S, Zhu Z (2020) Effects of eco-friendly cooling strategy on machining performance in micro-scale diamond turning of Ti-6Al-4V. *J Clean Prod* 118:526
14. Garg A, Lam JSL (2016) Modeling multiple-response environmental and manufacturing characteristics of EDM process. *J Clean Prod* 137:1588–1601
15. Gamage JR, DeSilva AKM, Chantzis D, Antar M (2017) Sustainable machining: Process energy optimisation of wire electrodischarge machining of Inconel and titanium superalloys. *J Clean Prod* 164:642–651
16. Kou Z, Han F (2018) On sustainable manufacturing titanium alloy by high-speed EDM milling with moving electric arcs while using water-based dielectric. *J Clean Prod* 189:78–87
17. Zhang Z, Yu H, Zhang Y, Yang K, Li W, Chen Z, Zhang G (2018) Analysis and optimization of process energy consumption and environmental impact in electrical discharge machining of titanium superalloys. *J Clean Prod* 198:833–846
18. Chen ST, Yang SW (2017) A high-density, super-high-aspect-ratio microprobe array realized by high-frequency vibration assisted inverse micro w-EDM. *J Mater Process Technol* 250:144–155
19. Pramanik A, Basak AK (2018) Sustainability in wire electrical discharge machining of titanium alloy: Understanding wire rupture. *J Clean Prod* 198:472–479
20. Gao D, Cao J, Guo Z (2019) Underwater manipulation of oil droplets and bubbles on superhydrophobic surfaces via switchable adhesion. *Chem Comm* 55:3394–3397
21. Zhou CL, Wu XY, Lu YJ, Wu W, Zhao H, Li LJ (2018) Fabrication of hydrophobic Ti<sub>3</sub>SiC<sub>2</sub> surface with micro-grooved structures by wire electrical discharge machining. *Ceram Int* 44:18227–18234
22. Wang YK, Chen X, Wang ZL, Li HC, Liu HZ (2016) Fabrication of micro-rotating structure by micro reciprocated wire-EDM. *J Micromech Microeng* 26(11):1–10
23. Hsue AWJ, Chang YF (2016) Toward synchronous hybrid micro-EDM grinding of micro-holes using helical taper tools formed by Ni-Co/diamond Co-deposition. *J Mater Process Technol* 234:368–382
24. Yan J, Kaneko T, Uchida K, Yoshihara N, Kuriyagawa T (2010) Fabricating microgrooves with varied cross-sections by electrodischarge machining. *Int J Adv Manuf Technol* 50(9–12):991–1002
25. Chow HM, Yan BH, Huang FY (1999) Micro slit machining using electro-discharge machining with a modified rotary disk electrode (RDE). *J Mater Process Technol* 91:161–166
26. Yan BH, Wang CC, Liu WD, Huang FY (2000) Machining characteristics of Al<sub>2</sub>O<sub>3</sub>/6061Al composite using rotary EDM with a disklike electrode. *Int J Adv Manuf Technol* 16:322–333
27. Lin CT, Chow HM, Yang LD, Chen YF (2007) Feasibility study of micro-slit EDM machining using pure water. *Int J Adv Manuf Technol* 34:104–110
28. Yan J, Watanabe K, Aoyama T (2014) Micro-electrical discharge machining of polycrystalline diamond using rotary cupronickel electrode. *CIRP Ann Manuf Technol* 63:209–212
29. Lei JG, Wu XY, Wang ZL, Xu B, Zhu LK, Wu W (2019) Electrical discharge machining of micro grooves using laminated disc electrodes made of Cu and Sn foils. *J Mater Process Technol* 271:455–462
30. Wu W, Wu XY, Lei JG, Xu B, Jiang K, Wu ZZ, Yin HM, Li W (2019) Fabrication of deep-narrow microgrooves by micro-EDM using rotary dentate disc foil electrodes in emulsion. *J Micromech Microeng* 29:035014
31. Bleys P, Kruth JP, Lauwers B (2004) Sensing and compensation of tool wear in milling EDM. *J Mater Process Technol* 149:139–146
32. Yeo SH, Murali M (2003) A new technology using foil electrodes for the electro-discharge machining of micro grooves. *J Micromech Microeng* 13:N1–N5
33. Hung JC, Yang TC, Li KC (2011) Studies on the fabrication of metallic bipolar plates-Using micro electrical discharge machining milling. *J Power Sources* 196:2070–2074
34. Li Y, Guo M, Zhou Z, Hu M (2002) Micro electro discharge machine with an inchworm type of micro feed mechanism. *Precis Eng* 26:7–14
35. Lim HS, Wong YS, Rahman M, Edwin Lee MK (2003) A study on the machining of high-aspect ratio micro-structures using micro-EDM. *J Mater Process Technol* 140:318–325

36. Zou R, Yu Z, Yan C, Li J, Liu X, Xu W (2018) Micro electrical discharge machining in nitrogen plasma jet. *Precis Eng* 51:198–207
37. Song KY, Chung DK, Park MS, Chu CN (2010) Micro electrical discharge milling of WC-Co using a deionized water spray and a bipolar pulse. *J Micromech Microeng* 20:045022
38. Cheong HG, Kim YS, Chu CN (2019) Effect of reverse current on tool wear in micro-electrical discharge milling. *Precis Eng* 55:484–490
39. Wei L, Zhang L, Liu W, Jia Z, Li A (2012) A new interpolation method of variable period and step size in micro-EDM milling based on square constraint. *Int J Adv Manuf Technol* 63:621–629
40. Murali M, Yeo SH (2004) A novel spark erosion technology for the fabrication of high aspect ratio micro-grooves. *Microsyst Technol* 10:628–632
41. Xu B, Wu XY, Lei JG, Cheng R, Ruan SC, Wang ZL (2015) Laminated fabrication of 3D micro-electrode based on WEDM and thermal diffusion welding. *J Mater Process Technol* 221:56–65
42. Li Z, Bai J, Cao Y, Wang Y, Zhu G (2019) Fabrication of microelectrode with large aspect ratio and precision machining of micro-hole array by micro-EDM. *J Mater Process Technol* 268:70–79
43. Kumar R, Singh I (2019) A modified electrode design for improving process performance of electric discharge drilling. *J Mater Process Technol* 264:211–219

# Chapter 12

## Geometric Evolution of Microstructures in EDM with Composite Laminated Electrode



Kai Jiang, Xiaoyu Wu, Jianguo Lei, and Bin Xu

**Abstract** Wear-variation electrical discharge machining makes the best use of the advantages of the characteristics of electrode wear, which has been considered as one shortcoming in previous research work, and utilizes the differences in physical properties of different metal materials in fabricating microstructure through electrical discharge machining (EDM), especially in creating continuous large-scale processing of surface microstructures provides favorable conditions. However, for tungsten EDM electrode wear device is not clear, indicating that the process of exploring the optimal processing parameters and the principle of electrode wear laws requires the majority of experiments, which inevitably this process will waste a lot of experimental materials, facilities, and labor costs. Reducing the quantity of EDM experiments to realize low carbon and healthy production and energy conservation is based on guaranteeing research quality and production demands. Due to the diversity of electrode materials, this paper proposed a unique erosion strategy for composite laminated electrode in EDM and studied the differences in the removal of material in single pulse EDM. Following this, a simulation model based on the two-dimensional was established, so the geometric variation of the electrode and workpiece during EDM could be investigated and predicted. Finally, the precision of the model proposed in this paper can be evaluated by differences between simulation results and experimental results. By comparing the data, the relative statistical error of the this model is less than 5%, while means that the simulation model can be used to predict the experimental processing results in the following experiments, thus significantly reducing the number of experiments, effectively saving experimental resources, and improving the experimental conditions to a certain extent.

---

K. Jiang (✉)

School of Software Engineering, Shenzhen Institute of Information Technology,  
Shenzhen 518172, Guangdong, China  
e-mail: [jiangkai@szit.edu.cn](mailto:jiangkai@szit.edu.cn)

X. Wu · J. Lei · B. Xu

College of Mechatronics and Control Engineering, Shenzhen University, Shenzhen 518060,  
Guangdong, China

## 1 Introduction

It was well known that surface functional microstructures play a part in lots of industrial fields, such as decreasing rubbing [1], improving lubricating conditions [2], enhancing heat dissipation [3], and self-cleaning surfaces [4]. The strength and firmness of materials did not limit EDM, and they can machine complex surface microstructures on conductive materials with high accuracy. Therefore, EDM has been considered as one primary methods for processing surface microstructures.

The materials of the electrode and the workpiece are eliminated together due to the high temperature generated by electric spark machining during EDM. Electrode wear is the main factor an essential factor restricting the accuracy of EDM [5]. Improving processing conditions is an effective way to reduce electrode wear in EDM. In the early research process, Yeo presented a method for using stainless steel foil as an electrode in manufacturing microgrooves on brass. Compared with the conventional micro cylindrical electrode micro EDM, the new method could significantly improve the workpiece's material removal rate, but also promote the processing efficiency to a certain extent [6]. Chow used the centrifugal force generated by the copper disk electrode in the process of high-speed rotation to accelerate the flow of working fluid in the EDM gap and improve the removal rate of machining debris. Finally, The machining efficiency is obviously improved, and at the same time, the electrode wear can be reduced [7]. Yan prepared disc electrodes with different cross-section shapes using copper-nickel alloy and then used the electrode to perform EDM on the multi-grain diamond. From the experiments, it is known that the removal efficiency of the material of this method is many times higher than that of the conventional electrode materials [8]. Wu.W effectively prepared microstructures on 304 stainless steel [9], using high-speed amorphous rotating tooth disc foil electrodes with emulsion as the medium and EDM with rotary to change electrode wear. Kou.Z performed dynamic arc high-speed EDM using water-based dielectrics to fabricate titanium alloys. This method remarkably improves the removal efficiency of the material during processing and decreases the electrode wear rate [10]. Dong presented novel oil-in-water nano-scale emulsion medium for high-speed composite settling treatment. Compared with traditional water-based dielectrics, the material removal rate and the relative electrode both change to the direction favourable to machining [11]. Zhang proposed a new machining mode that combines magnetic field with electric discharge. The discharge channels take shape from the magnetic field acceleration and promote the removal of the production of the discharge. Thus, electrode wear can be reduced by 18.3% [12]. Compensating the wear of electrode is another effective method to improve the precision of EDM. Many researchers have carried out much research in this field. Yu proposed a method based on layer-by-layer uniform abrasion, which maintains the primitive form of the micro-cylinder electrode by linearly compensating the electrode wear and finally realizes efficient and precise manufacturing of complex microstructures [13]. A method proposed by Bleys.P is the method of compensation of real-time wear sensing as base. This strategy does not need to establish geometric model of the blank but through the feedback of sensor measurement results to reduce



the machining error caused by electrode wear [14]. Schulze This method can give full play to the two sensors' advantages and control the processing depth error to 2  $\mu\text{m}$  [15]. Li analysed the relationship between the scanning area of each layer and electrode wear in micro EDM and established a compensation model between processing area and electrode loss [16]. By focusing on the compensation of electrode wear, the above method has made a crucial donation to improving the accuracy of EDM. However, the optimization of the machining parameters requires extensive experimental processing, which means that the experimental efficiency is low.

Establishing a reliable mathematical model for the EDM process has assisted much help for researchers to predict the electrode wear, and researchers can set reasonable compensation values according to the simulation results. Heo studied the Z-map algorithm and modified it to establish a micro EDM milling model, which can produce a precision forecast of the shape variation of the electrode. Therefore, the compensation value of cutter wear during machining can be set according to the simulation results [17]. Jeong established a simulation model of the cylindrical tool EDM in two-dimensional space. They utilized the model into the off-line recompense of cutter wear during micro-hole machining, making it feasible to control the machining error in the range of 2.9% [18]. Zhang proposed a fixed-length compensation mathematical model for electrode wear in micro EDM milling. When the thickness of each layer is less than 85.5  $\mu\text{m}$ , the proportional error remains below 4% [19]. Pei used tubular tools instead of cylindrical tools to establish a fixed-length compensation mathematical model, and finally verified the model by processing double reference 3D cavities. In most situations, the simulation results indicate that the proportional error can control within 2%, and the fluctuation of the surface is below 4  $\mu\text{m}$  [20, 21]. Garg adopted a multiresponse model for the EDM environment and manufacturing characteristics to process the optimization of the machining parameters and predict and compensate for electrode wear [22].

The above studies show that the EDM efficiency and machining accuracy can be effectively improved by improving the machining process or establishing a mathematical model to compensate electrode wear. Researchers are committed to reducing or recompensing electrode wastage to enhance EDM's dimensional resizing accuracy and have achieved some important results. However, the above studies did not fundamentally remove the limitations of EDM. Electrode wastage is still one of the factors that could be more conducive to processing accuracy. Lei proposed a new method to alleviate the above problems by using a rotating EDM with Cu/Sn foil laminated electrode to process microgrooves [23]. By adjusting the material composition of the electrode, and making use of the differences in wear rates of different materials during EDM, the electrode was gradually worn down to a stable structure and then the electrode was repeatedly used without reshaping to machine the same type of microstructure. Until the electrode was worn out, the machined microstructures have good consistency. Subsequently, Lei.J proposed a combined technique of wire EDM, dry wire EDM, and wear change EDM. The long laminated electrode was prepared by this method and applied to the continuous batch production of deep and narrow blind hole micro grooves by EDM [24]. Both methods can convert the unfavorable factors of electrode abrasion in EDM into crucial processes.

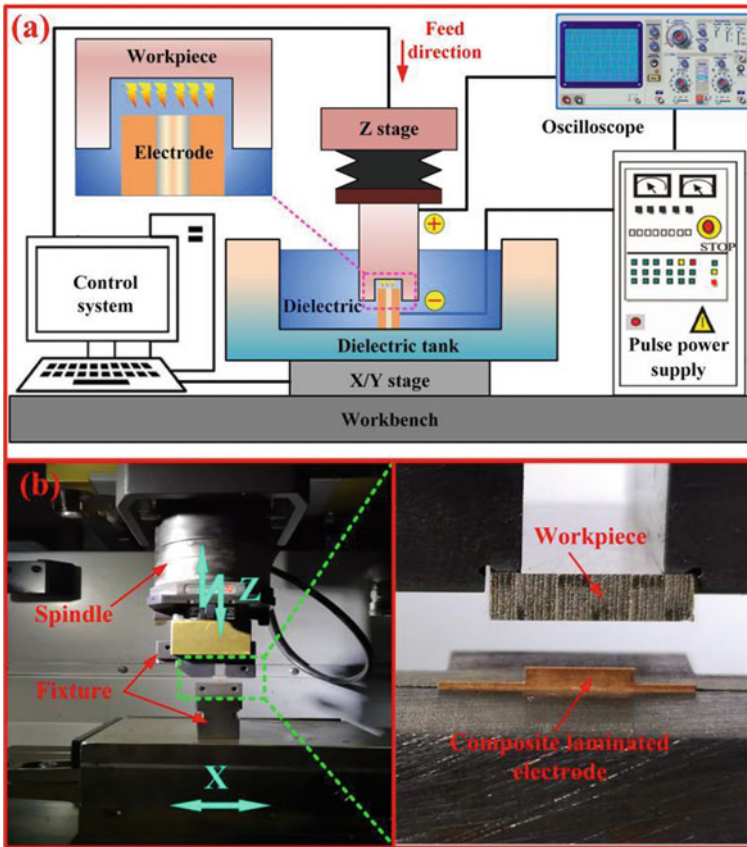
There needs to be more research on electrode wear mechanism and microstructure evolution in the published studies, which require a large number of experiments to process the machining parameters and acquire the electrode wear regulation. Many experiments using different composite electrodes has to be conducted to get the best process microstructures and help re-grasp the electrode to get the wear law. However, this will necessarily lead to a large waste of experimental materials, facilities, and human resources. To further study the mechanism of electrode wear in the process of continuous volume production of microstructure by EDM, this paper introduced the CuSn composite materials to construct more complex laminated electrodes for EDM. A 2D simulation model and the strategy of discharge erosion for EDM with CuSn composite laminated electrodes were established, and the evolution of electrode morphology and workpiece microstructure was predicted. Furthermore, the validity of the emulation model was validated by typical experiments, which provides critical guidance of theory for the batch production of the surface microstructure of composite laminated electrode EDM. It dramatically reduces the workload of EDM experiments, the production of waste oil, waste gas, waste materials and other harmful substances can be significantly reduced. It also reduces the effect on enhancing the environment and operator health.

## 2 Experimental Equipment and Materials

Figure 1 shows the CuSn composite laminated electrode EDM experimental device. Wherein, the Fig. 1b is the EDM machine, which was used in the experiment to process the microstructure. The experiment selected 304 stainless steel to be as the workpiece. The preparation of the composite laminated electrode blanks using metal foils, such as Cu, Sn, and gradient material of CuSn foil. The thickness of each foil was 100  $\mu\text{m}$ . A low-speed wire-cut EDM was used to cut the electrode blank to a predetermined size. Then fixing the electrode on the specific fixture of the workbench, and the workpiece was mounted on the moving spindle of the EDM. The microstructure was manufactured by gravity-assisted EDM, that is, the workpiece is on the top and the electrode is on the bottom. After processing, microstructures on the electrodes and workpiece are observed and characterized using a laser scanning confocal microscope and a scanning electron microscope.

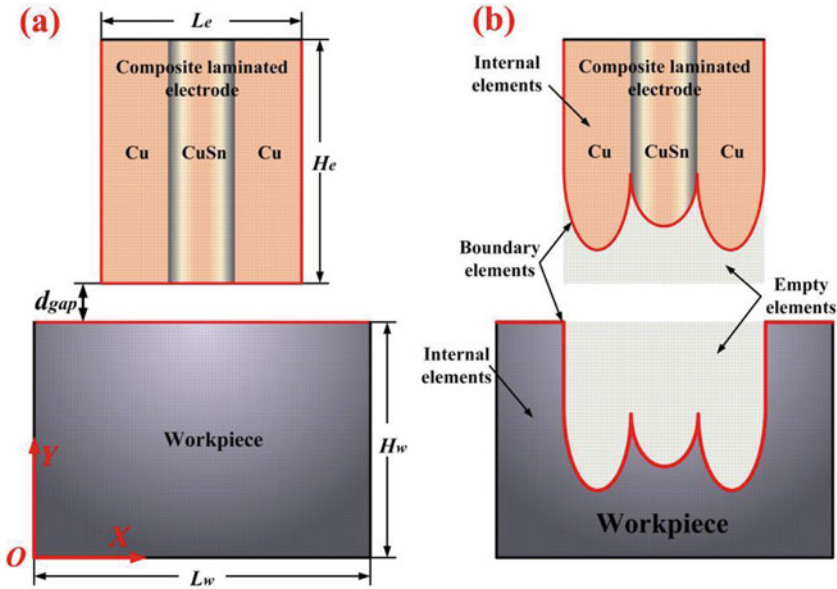
## 3 Modeling of EDM with the CuSn Composite Laminated Electrode

As shown in Fig. 2, in order to make the numeration simple, the EDM microstructure process was streamlined to a two-dimensional model, and the crucial hypotheses have to be made:



**Fig. 1** a Schematic diagram of EDM experimental device with composite laminated electrode; b Gravity assisted edm platform

- (1) It is considered to be an ideal debris removal method during the simulation. At the same time, the change of motion form caused by the reciprocating motion and short circuit of the electrode were ignored. The model of this simulation is considered as a simple one-way feeding movement mode.
- (2) In each pulse discharge, only one single spark is generated between the electrode and the workpiece [25]. In addition, the percentage of the discharge energy distributed between electrode and workpiece is constant per pulse discharge.
- (3) There is no interaction between the spark discharges. The electrode and workpiece can be considered completely deionized and cooled after each discharge.
- (4) The element center distance between the electrode and the workpiece is less than or equal to the discharge distance is a necessary condition for discharge operation [26]. Search for all border elements in the present procedures, combine



**Fig. 2** a Geometric model of the CuSn composite laminated electrode and the workpiece in simulation; b Profiles of the electrode and workpiece after simulation, and schematic diagram of marking boundary elements, internal elements, and empty elements

elements that meet the discharge conditions into a group of element pairs, and randomly select a group of element pair for discharge erosion.

- (5) In the current step, all component pairs that meet the discharge conditions are discharged to remove the empty component, which is considered as a necessary condition for the electrode to get to the next position.
- (6) The discharge pit simulated by EDM is a semisphere [18] and removed the elements of which center coordinates are inside the discharge crater, and there is no residual material.

### 3.1 Modeling of the Composite Laminated Electrode

As shown in Fig. 2a, for the purpose of calculating the coordinate positions of various elements in the EDM, it is necessary to establish the absolute coordinates XOY. Therefore, the center coordinate of the element  $W_{m,n}$  in the  $n$ -th row and  $m$ -th column on the workpiece can be got from the following equation:

$$x_{m,n} = \frac{l_{grid}}{2} + (m - 1)l_{grid}; \quad m = 1, 2, 3, 4, \dots, \left[ \frac{L_w}{l_{grid}} \right] + 1 \quad (1)$$

$$y_{m,n} = \frac{l_{\text{grid}}}{2} + (n-1)l_{\text{grid}}; \quad n = 1, 2, 3, 4, \dots, \left[ \frac{H_w}{l_{\text{grid}}} \right] + 1 \quad (2)$$

where  $(x_{m,n}, y_{m,n})$  is the position of the element  $W_{m,n}$  in the  $n$ -th row and  $m$ -th column on the workpiece;  $L_w$  is the length of the workpiece, and  $H_w$  is the height of the workpiece; the number of the  $l_{\text{grid}}$  is square element size.

Based on the dimensions of the workpiece, the center coordinates of the element  $E_{i,j}$  in the  $i$ -th column and  $j$ -th row on the electrode can be calculated as follows:

$$x_{i,j} = \frac{l_{\text{grid}}}{2} + (i-1)l_{\text{grid}} + \frac{L_w - L_e}{2}; \quad i = 1, 2, 3, 4, \dots, \left[ \frac{L_e}{l_{\text{grid}}} \right] + 1 \quad (3)$$

$$y_{i,j} = \frac{l_{\text{grid}}}{2} + (j-1)l_{\text{grid}} + H_w + d_{\text{gap}}; \quad j = 1, 2, 3, 4, \dots, \left[ \frac{H_e}{l_{\text{grid}}} \right] + 1 \quad (4)$$

where  $(x_i, j, y_i, j)$  is the position of the element  $E_{i,j}$  in the  $i$ -th column and  $j$ -th row on the electrode;  $L_e$  and  $H_e$  are the length and height of the electrode, respectively;  $d_{\text{gap}}$  is the incipient machining gap before process, and the  $l_{\text{grid}}$  is the size of each element.

In the simulation model, the electrodes need to be gradually given after removing all elements that meet the discharge conditions. So it can be calculated the center coordinate of the element  $E^t_{i,j}$  on the electrode as follows:

$$x^t_{i,j} = \frac{l_{\text{grid}}}{2} + (i-1)l_{\text{grid}} + \frac{L_w - L_e}{2}; \quad i = 1, 2, 3, 4, \dots, \left[ \frac{L_e}{l_{\text{grid}}} \right] + 1 \quad (5)$$

$$y^t_{i,j} = \frac{l_{\text{grid}}}{2} + (j-1)l_{\text{grid}} + H_w + d_{\text{gap}} - t \Delta s; \quad j = 1, 2, 3, 4, \dots, \left[ \frac{H_e}{l_{\text{grid}}} \right] + 1 \quad (6)$$

where  $(x^t_i, j, y^t_i, j)$  is the location of the element  $E^t_{i,j}$ ;  $t$  and  $\Delta s$  are the feed times and feed step of the electrode, respectively.

After the  $t$ -th admission electrode, the centroid distance of two arbitrary elements  $W_{m,n}$ , and  $E^t_{i,j}$  between the electrode and the workpiece can be calculated by the following formula:

$$D_t = \sqrt{\left(x^t_{i,j}, x_{m,n}\right)^2 + \left(y^t_{i,j}, y_{m,n}\right)^2} \quad (7)$$

The electrode and the workpiece will be corroded by the high temperature generated by the spark discharge after each spark discharge. The eroded unit will be updated as an empty element during the simulation process, and the empty element will no longer take part in the analog computation. The newly generated boundary after the electrode and workpiece are eroded set as the boundary element and the other elements are defined as internal elements, as shown in Fig. 2b.

### 3.2 The Radius of the Discharge Crater

During EDM, part of the energy was applied to exenterate electrode and workpiece materials [27]; after the medium was decomposed, the discharge channel was used to release electric energy and convert it into other types of energy. The formula can calculate the accumulative energy of the single-pulse discharge:

$$W_0 \int_0^{t_0} U(t)I(t)dt = U_0I_0t_0 \tag{8}$$

where  $W_0$ ,  $U(t)$ ,  $I(t)$  are the general energy of monopulse discharge, momentary discharge voltage and discharge circuit respectively;  $U_0$ ,  $I_0$  are the mean discharge tension and discharge circuit respectively;  $t_0$  is the pulse breadth.

As shown in Fig. 3a, the general energy of monopulse discharge wasted to the workpiece, electrode, and electrical medium. Only a tiny portion of the discharge energy transferred to the workpiece was consumed during the evaporation and melting of the material. Moreover, the remainder of the energy was dissipated in the modality of heat transmission (Fig. 3b). The spark energy delivery on the electrode was also dissipated in an identical manner.

In accordance with the thermal theory [28], the volumetric of the material removal during EDM monopulse discharge can be calculated as follows:

$$V_1 = \frac{F_v W_0}{\rho[C(T_v - T_v) + L_m + L_v]} + \frac{F_m W_0}{\rho[C(T_m - T_0) + L_m]} \tag{9}$$

here, the  $F_v$  and  $F_m$  are the ratios of spark energy used up by evaporation and melting material in EDM, respectively;  $T_v$  and  $T_m$  are the boiling point and melting point

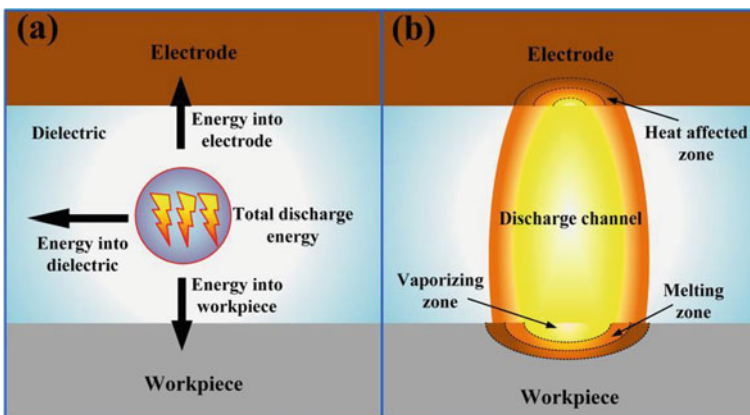


Fig. 3 a Distribution of the discharge energy in EDM; b Mechanism of material removal

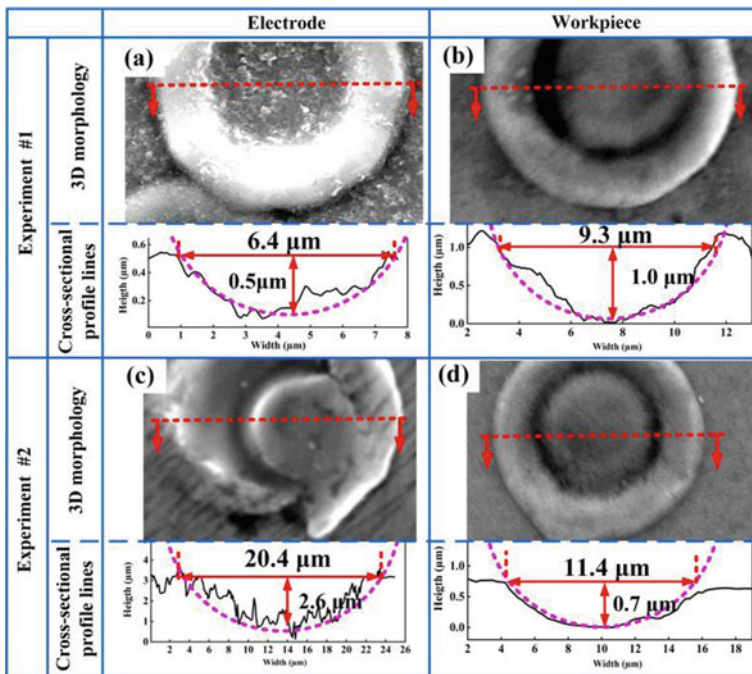
of the material, respectively;  $L_v$  and  $L_m$  are the heat of evaporation and melting, respectively;  $T_0$  is the temperature of material before discharge;  $C$  is the heat capacity;  $\rho$  is the matter density.

Therefore, the values of  $F_v$  and  $F_m$  is crucial in determining the volume of removed material in a single pulse discharge process. It is also essential data to establish the simulation model.

As shown in Fig. 4a, b, when Cu is the electrode and 304 stainless steel is the workpiece, the three-dimensional shape and cross-section profile of the discharge pit can be obtained by single pulse discharge. While Fig. 4c, d shows that Sn is electrode and stainless steel is workpiece. It can be seen from the figure that the discharge pit can become approximately part of the spherical. Using the following formula, the volume of material removed using the discharge pit in the experiment can be calculated.

$$V_2 = \frac{\pi}{6} D \left( \frac{3H^2}{4} + D^2 \right) \tag{10}$$

where  $D$  and  $H$  are the depth and width of the discharge crater, respectively.



**Fig. 4** Three dimensional morphologies and cross-sectional profiles of discharge craters generated by single-pulse discharge; **a** Cu electrode; **c** Sn electrode; **b, d** 304 stainless steel workpiece

In EDM, mainly material removal methods are gasification and melting. Assuming that the material during gasification and melting can be removed entirely from the electrical medium and not left behind, the volume of the corroded material is equal to the volume of the discharge pit. According to Eqs. (9) and (10), it can be got:

$$\frac{F_v W_0}{\rho[C(T_v - T_0) + L_m + L_v]} + \frac{F_m W_0}{\rho[C(T_m - T_0) + L_m]} = \frac{\pi}{0} D \left( \frac{3H^2}{4} + D^2 \right) \quad (11)$$

In EDM experiments using positive polarity, Cu and 304 stainless steel were used as electrodes and workpieces to gain the values of  $F_v$  and  $F_m$ . The values of  $F_v$  and  $F_m$  can be obtained by combining Eq. (8)–(11) and surveying the volume of discharge crater. After that, the machining parameters were changed to gain the distribution of  $F_v$  and  $F_m$  of the workpiece and electrode, as shown in Fig. 5. As can be seen from the picture that although the values of  $F_v$  and  $F_m$  under different process parameters are different, the overall difference is small. Therefore,  $F_v$  and  $F_m$  are invariable regardless of the processing parameters. Under different processing parameters, the average values of  $F_v$  and  $F_m$  of electrode are 2.13% and 3.11% respectively, and the average values of  $F_v$  and  $F_m$  of workpiece are 4.32% and 6.36% respectively. Using Sn as the electrode and 304 stainless steel as the workpiece (for workpiece  $F_v = 4.08\%$ ,  $F_m = 6.6\%$ ),  $F_v$  and  $F_m$  were obtained in the same way; (for electrode  $F_v = 1.03\%$ ,  $F_m = 4.21\%$ ).

Based on the Hypothesis 6, the discharge crater produced by a spark is semispherical (Jeong et al. 2007). In the simulation experiment, the radius of the discharge crater  $R$  can be expressed as follows:

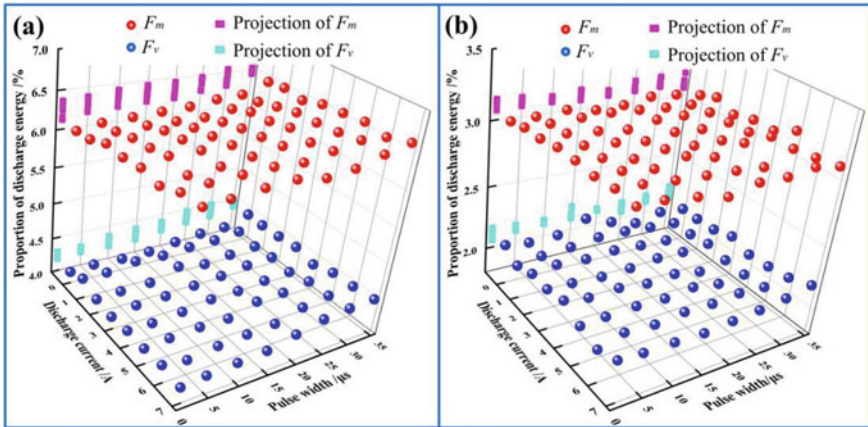


Fig. 5 Distribution of the  $F_v$  and  $F_m$  of the workpiece and electrode under different processing parameters: **a** workpiece (304 stainless steel); **b** electrode (Cu)



$$R = \sqrt[3]{\frac{3W_0}{2\pi\rho} \left[ \frac{F_v}{C(T_v - T_0) + L_m + L_v} + \frac{F_m}{C(T_m - T_0) + L_m} \right]} \quad (12)$$

### 3.3 Discharge Distance

Distance between the electrodes for reference to the distance between the workpiece and the electrode where the dielectric is broken down under a specific voltage to produce spark discharge. Because the runner size produced by discharge is much less than the electrode size, the size effect of electrode and discharge channel can be ignored. Therefore, it can be regarded that the electric field between the electrode and the workpiece is uniform, and the discharge distance can be expressed as follows:

$$D_{kp} = \frac{U_{kp}}{E_{kp}} \quad (13)$$

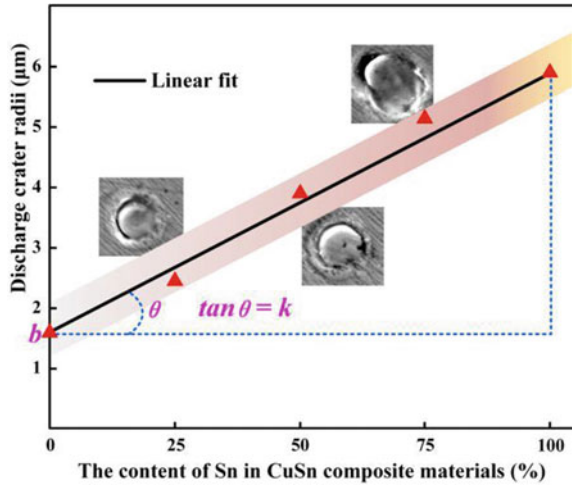
where  $D_{kp}$  is the discharge distance;  $U_{kp}$  is the discharge voltage;  $E_{kp}$  is the breakdown strength of the dielectric.

The EDM oil was regarded as the dielectric in the process of experiments, and the breakdown strength was  $2.8 \times 10^5$  V/cm according to its composition. In this study, the discharge energy is small, and the discharge distance is commonly smaller than 10  $\mu\text{m}$ . The results indicate that the discharge distance difference between the two electrodes is less than 1  $\mu\text{m}$ , which has minimal influence on the processing. The discharge distance can be calculated based on the machining parameters without considering the influence of the electrode material on the discharge distance.

### 3.4 The Discharge Erosion Strategy of the Simulation Model

Because the electrode was made up of composite material, the difference of physical characteristics of different electrode materials will inevitably lead to differences in the discharge crater. Therefore, CuSn gradient material must be the primary consideration. At the same time, the homogenous CuSn alloy can be perceptible as the gradient material with a gradient of 0. By the way, Cu and Sn can be looked upon as particular kinds of CuSn gradient material. It can be seen from Fig. 6 that the radius of discharge pits versus tin content for several typical homogeneous CuSn alloy electrodes. It can be seen that the discharge pit radius of the CuSn alloy electrode aggrandizement with the increase of the Sn content, which essentially satisfies the linear change trend. Therefore, it can be considered that the discharge pit radius of the CuSn alloy electrode is proportional to Sn content through the linear fitting.

**Fig. 6** Relationship between the discharge crater radii and Sn content of CuSn electrodes



In the simulation model proposed in this model, it can be considered that there is no difference in the vertical direction of the constituent electrode materials, and only the change of material composition in the horizontal direction can be studied. Therefore, the Sn content from the bilateralism of the CuSn gradient material can be surveyed as C1 and C2 through EDS. However, due to the linear change of Sn content in CuSn composite laminating electrode, a single pulse discharge experiment is not required for each content electrode. Therefore, several kinds of typical CuSn composite electrodes were chosen to measure the size of the discharge chamber in a single pulse discharge experiment. The experimental results are shown in Fig. 6. It is clear from the figure that the radius of the discharge pit on the CuSn electrode and the Sn content has a linear relation. The relationship between the radius of the discharge crater,  $R_{\alpha,\beta}$ , and the Sn content of the element in the  $\alpha$ -th column and  $\beta$ -th row,  $C_{\alpha,\beta}$ , on the CuSn gradient electrode can be calculated as following:

$$R_{\alpha,\beta} = kC_{\alpha,\beta} + b \tag{14}$$

$$C_{\alpha,\beta} = \frac{(C_2 - C_1)}{G - 1}(\alpha - 1) + C_1; \quad G = \left[ \frac{L}{l_{grid}} \right] + 1 \tag{15}$$

where  $C_1$  and  $C_2$  are the quantity of Sn on bilateral of the CuSn gradient material;  $l_{grid}$  is the size of element;  $L$  is the thickness of the CuSn gradient material;  $k$  and  $b$  are the straight line's slopes and the line's cutoff distance as shown in Fig. 6, respectively.

According to Eqs. (14) and (15), when  $C_1 = C_2 = 0$ , it indicated that the electrode is made of Cu, so the value of  $b$  can be calculated as  $R_{Cu}$ , and when  $C_1 = C_2 = 100\%$ , it indicated that the electrode is made of Sn, based on  $k + b = R_{Sn}$ ; therefore,  $b = R_{Cu}$  and  $k = R_{Sn} - R_{Cu}$ .  $R_{Cu}$  and  $R_{Sn}$  are the radius of discharge craters of Cu and Sn electrodes, respectively.

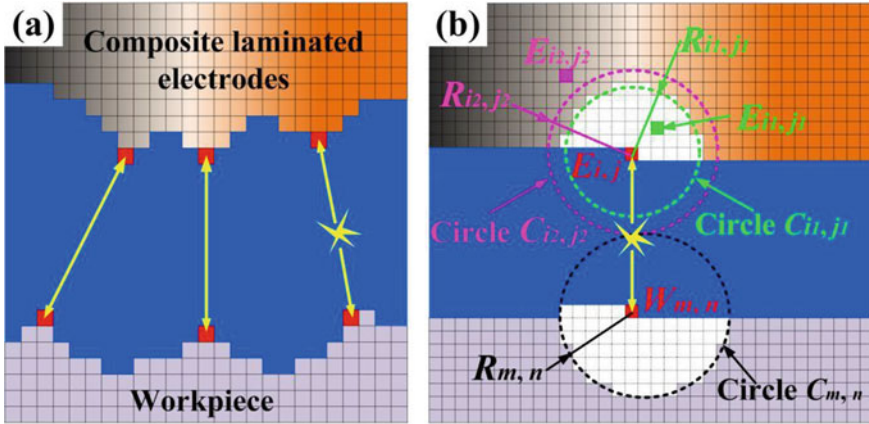
When the paired elements  $E_{i,j}$  on the electrode are eroded, the elements  $E_{\alpha,\beta}$  around the electrode will also be eroded. The center distance  $D_{\alpha,\beta}$  between the recognition element  $E_{\alpha,\beta}$  and the paired element  $E_{i,j}$  can be obtained as follows:

$$D_{\alpha,\beta} = \sqrt{(|\alpha - i|l_{\text{grid}})^2 + (|\beta - j|l_{\text{grid}})^2} \quad (16)$$

If the center distance  $D_{\alpha,\beta}$  between brand identify elements  $E_{\alpha,\beta}$  and the matching element  $E_{i,j}$  is less than or equal to the radius  $R_{\alpha,\beta}$  of the discharge pit of the identifying element, the center of identified element  $E_{\alpha,\beta}$  will be removed and marked as an empty element; on the contrary, it will be retained.

As shown in Fig. 7a, in accordance with the assumption (4) of the simulation model, it was considered that this pair of elements satisfied the spark discharge conditions when the center distance between the electrode element and workpiece element was less than or equal to the discharge distance. At this time, the electrode element and workpiece element formed an element pair (the red element pair connected by a yellow line in Fig. 7a), and the spark discharge was only took place between the element pair. If the number of element pairs  $>0$ , an element pair would be stochastically selected for discharge erosion (the red element pair connected by a yellow line with discharge marks in Fig. 7a). The removed element would be marked as an empty element at the end of each discharge. Then the center distance between the electrode element and the workpiece element within the frontier is calculated and the set of element pairs satisfying the discharge criterion is updated. When the number of components  $= 0$ , there was no component pair that could produce spark discharge. The electrode needed to be stepped, and the center distances between the electrode and all the boundary elements of the workpiece needed to be recalculated. The set of element pairs was formed through finding the element pairs satisfying the spark discharge conditions, and an element pair was randomly selected for discharge erosion. Repeat this process usque, ad the processing reaches the specified depth. This round of processing simulation is completed.

As the electrodes were composite materials, the different types of electrode materials lead to different elemental pits. Therefore, when determining whether an element on the electrode has been removed, the center of the paired element on the electrode should be used as the center of the circle, and the crater circle should be established based on the discharge crater radius of the identified element material. If the center of the identified element is located in the crater, the element will be removed and marked as an empty element. As shown in Fig. 7b, the pair of discharge elements on the electrode and workpiece is given by  $E_{i,j}$  and  $W_{m,n}$ , respectively. To determine whether the element  $E_{i_1,j_1}$  on the electrode has been removed, the center of the element  $E_{i,j}$  needs to be considered as the center of the circle, and the discharge crater radius  $R_{i_1,j_1}$  of the  $E_{i_1,j_1}$  material needs to be used to establish the crater circle  $C_{i_1,j_1}$ . As the center of the element  $E_{i_1,j_1}$  is located inside the crater circle  $C_{i_1,j_1}$ , it was removed and marked as an empty element. The center of the element  $E_{i_2,j_2}$  is located outside its own crater circle  $C_{i_2,j_2}$ , and hence, the element is retained. After



**Fig. 7** The strategy of discharge erosion during simulation: **a** set up a set of paired element satisfying discharge conditions (the red element pair connected by a yellow line) and select an element pair for discharge erosion by randomly (the red element pair connected by a yellow line with discharge marks); **b** the law of discharge erosion: taking the center of the paired element as the center and the discharge crater radius of the identified element as radius to establish erosion circle, if the center of the identified element is located in the circle, the element will be removed and marked as an empty element. For example, the center of the  $E_{i1,j1}$  is inside the circle  $C_{i1,j1}$ , it is removed and marked as empty element. The  $E_{i2,j2}$  is outside its own crater circle  $C_{i1,j1}$ , and hence, the element is retained. The material of the workpiece is the same, and it only needs to be removed by fixed circle  $C_{m,n}$

sequential inspection and labeling of all elements on the electrode, the electrode erosion process of this element pair was completed.

Use the same material for the workpiece. Create a crater circle  $C_{m,n}$  centered on the paired elements  $W_{m,n}$  and an empty crater radius  $R_{m,n}$ . Remove all elements centered on the crater circle and mark them as empty elements (white elements).

### 3.5 The Flowchart of the Simulation Model

Figure 8 shows the laminated composite electrode EDM simulation model flow chart. Through the computer program, the main geometric parameters and processing parameters are repeatedly measured, scoured, and fed until the predetermined depth is reached and the simulation is completed. This round of simulation was then completed. If the simulation requires multiple rounds of processing, the program can automatically read the electrode profile data of the previous round to complete the continuous multi-round simulation calculation.

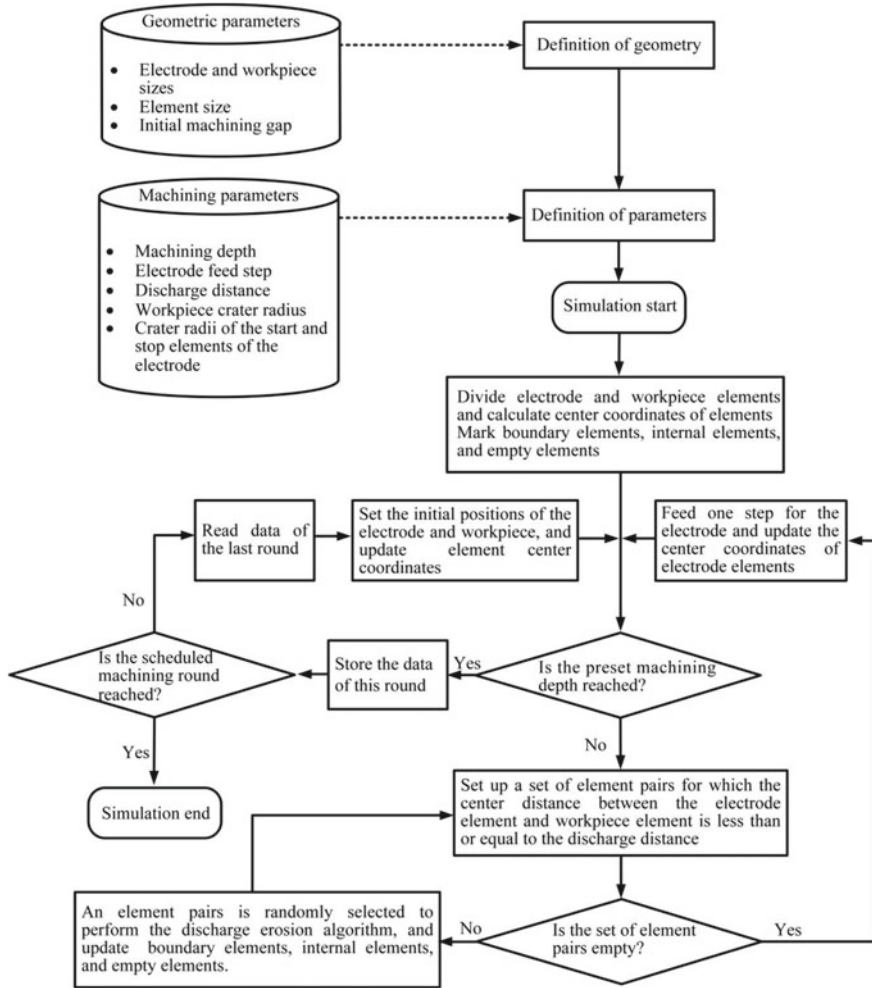


Fig. 8 Flowchart of the simulation model of EDM with the CuSn composite laminated electrode

## 4 Examples and Experimental Verification

### 4.1 Calculation of the Model Error

The relative error is used to measure the difference between experimental and simulation results and to validate the model's accuracy. using a laser scanning confocal microscope to measure the machined micro grooves for several times, so we can calculate the average values of the microstructure profile data. after that, the relative error  $\delta$  between the simulation model and experimental results can be obtained based

on the experimental profile data and simulation prediction.

$$up\delta = \frac{\sum_1^N \left| \frac{Y_i - Y'_i}{Y_i} \right|}{N} \times 100\% \tag{17}$$

where  $Y_i$  and  $Y'_i$  represent the actual profile values and simulated prediction values of the  $i$ -th position point, respectively, and  $N$  is the total number of position points.

### 4.2 The Simulation and Experimental of Cu/Sn/Cu Laminated Electrode

Multiple rounds of EDM are used to prepare Cu/Sn/Cu composite electrodes with 100  $\mu\text{m}$  thick Cu and Sn foils and 304 stainless steel. Table 1 shows the experimental parameters for EDM using composite laminated electrodes. During the machining process, the average discharge voltage and discharge current during EDM are 25 V and 0.1A, respectively. Therefore, the discharge pit radius of different materials can be calculated based on Eq. (12) that  $R_{Cu} = 1.6 \mu\text{m}$ ,  $R_{Sn} = 4.3 \mu\text{m}$ ,  $R_{304} = 2.5 \mu\text{m}$ . The discharge distance  $D_{kp} = 7.14 \mu\text{m}$  is obtained by the calculation of the Eq. (13). In the simulation process, the element size is 0.5  $\mu\text{m}$ , the electrode feed step is 1  $\mu\text{m}$ , the machining depth is 200  $\mu\text{m}$ , and the initial machining gap is 50  $\mu\text{m}$ .

Multiple rounds of EDM are used to prepare Cu/Sn/Cu composite electrodes with 100  $\mu\text{m}$  thick Cu and Sn foils and 304 stainless steel. The machining process is simulated by using the model proposed in this paper. The radius of the discharge pits of the laminated electrodes needs to be set in different areas due to the different size of the discharge pits of various materials.

According to Eqs. (14) and (15), the schematic diagram of the discharge crater radius on the Cu/Sn/Cu laminated electrode is shown in Fig. 9.

Figure 10a–e show the simulation prediction curves of microgrooves and electrodes of Cu/Sn/Cu laminated electrodes and experimental results during the first to fifth EDM cycles. The critical feature dimension diagram is shown in Fig. 10f, and

**Table 1** Experimental parameters

Parameters	Value
Workpiece material	304 stainless steel
Dielectric	EDM oil
Machining polarity	Positive polarity
Machining voltage	200 V
Pulse width	1 $\mu\text{s}$
Pulse interval	10 $\mu\text{s}$
Initial machining gap	50 $\mu\text{m}$
Machining depth	200 $\mu\text{m}$

**Fig. 9** Schematic diagram of crater radius on the Cu/Sn/Cu laminated electrode during simulation

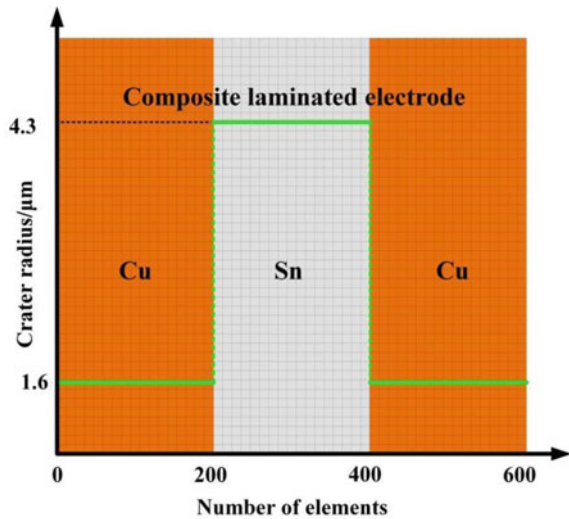
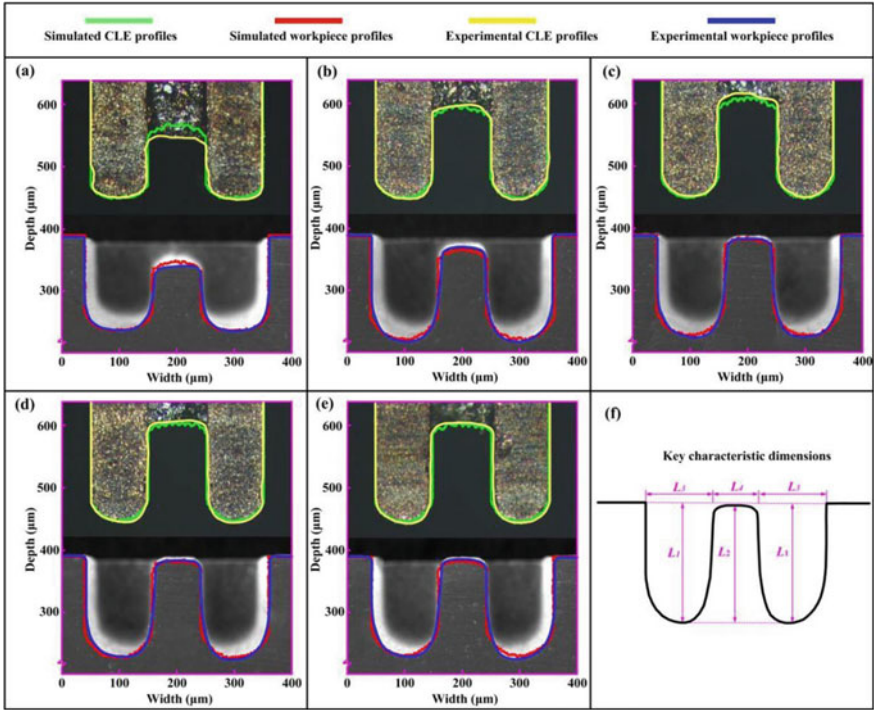


Table 2 show the statistical results of each essential characteristic dimension. From the pictures and table, it can be seen that the Sn electrode needs to be continuously exhausted during the first round of processing until the end of the processing. The amount of workpiece processed is significant, resulting in a bulge of about  $110 \mu\text{m}$  in the middle of the microgroove (Fig. 10a). The Sn electrode is in the state of suspension in the initial period of the 2nd machining. After processing, the Sn electrode shows a small amount of wear as the processing depth increases, and the bulge in the middle of the microgroove is almost equal to the processing depth (Fig. 10b). The wear of the Sn electrode gradually stabilized from the 3rd round. The Sn electrode was almost always suspended in each round of processing. Only a tiny amount of processing was conducted in the last stage, which plays a specific role in dividing the microgrooves and increasing the stiffness of the laminated electrode. Starting from the 3rd round of processing, the critical feature size deviation of the processed microgrooves is less than  $4 \mu\text{m}$ . At this moment, it could be considered that the working surface of the laminated electrode was worn into a stable profile. Subsequently, the electrode could reused and processed to the same depth for the same workpiece material. The processing results also have excellent consistency. Overall, the simulation results are basically in agreement with the experimental results, at the same time the relative errors were basically can be controlled within 5%.



**Fig. 10** Comparison of experimental and simulation results of Cu/Sn/Cu laminated electrode and workpiece in multiple rounds of EDM: **a** 1st round; **b** 2nd round; **c** 3rd round; **d** 4th round; **e** 5th round; **f** key characteristic sizes

**Table 2** Key characteristic sizes of micro grooves and relative errors between experiment and simulation

Round	Experimental results ( $\mu\text{m}$ )				Simulation results ( $\mu\text{m}$ )				Relative errors $\delta$ (%)
	L1	L2	L3	L4	L1	L2	L3	L4	
1st	155.5	108.4	123.5	82.8	161.0	110.5	117.0	84.0	4.53
2nd	169.0	152.2	128.0	78.0	163.5	141.5	118.0	82.0	5.26
3rd	163.0	158.5	128.0	77.6	161.5	156.0	117.0	83.0	3.08
4th	162.5	162.1	127.5	78.0	162.0	157.5	116.0	82.5	3.24
5th	162.5	161.4	127.0	77.3	162.5	157.0	117.5	82.0	3.47

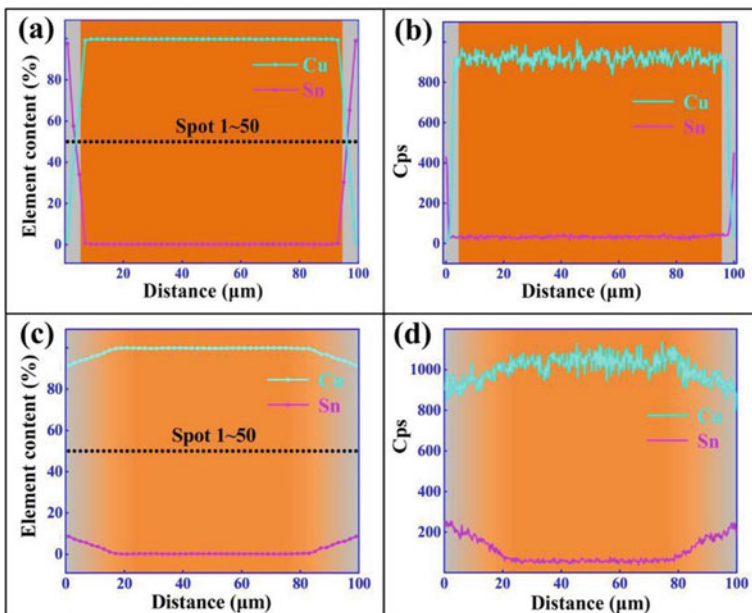


### 4.3 The Simulation and Experimental of Cu/CuSn/Cu Laminated Electrode

The Cu/CuSn/Cu laminated electrode was made of Cu foils and CuSn gradient material with a thickness of 100  $\mu\text{m}$ . After thermal diffusion in vacuum at 500  $^{\circ}\text{C}$  for 10 h, the Cu foil with a thickness of 3  $\mu\text{m}$  Sn film will be made into CuSn gradient material. The wear rate of electrode in EDM is determined by the mass fraction of Sn in CuSn foil; hence, it is necessary to analyze the composition of the CuSn gradient material quantitatively.

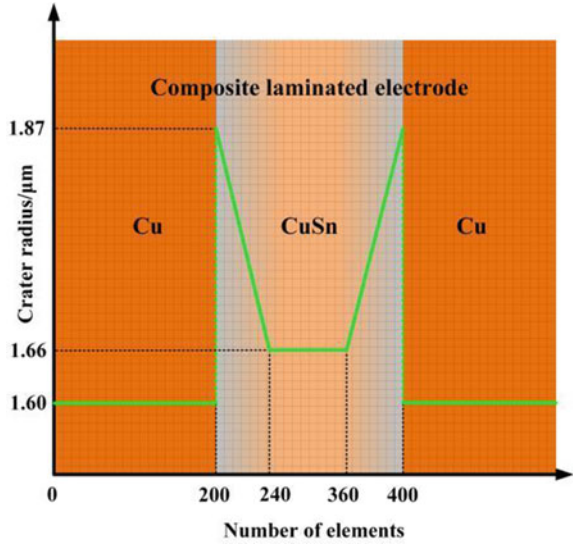
In the thickness direction of the tinned copper foil, the distribution of Cu and Sn before and after the heat treatment can be seen in Fig. 11, including point-scan energy spectra (Fig. 11a and c) and line-scan energy spectra (Fig. 11b and d). Sn and Cu elements spread significantly to generate CuSn gradient material after heat treatment. Measurement results show that the Sn content decreased linearly from 10 to 2% from foil surface to the depth of 20  $\mu\text{m}$ , while the content of Cu shows the opposite trend.

Assuming that the size of the discharge crater varies linearly with the Sn content, based on the Eq. (14) and (15), the discharge crater of electrode can be calculated. Figure 12 shows the schematic diagram of the radius of the discharge crater on the Cu/CuSn/Cu laminated electrode.



**Fig. 11** Distributions of Cu and Sn along the thickness direction of composite laminated electrodes: **a, b** raw material of Sn-coated Cu foil; **c, d** gradient material foil after heat treatment **a** and **c** the point-scanning energy spectrum, **b** and **d** the line-scanning energy spectrum)

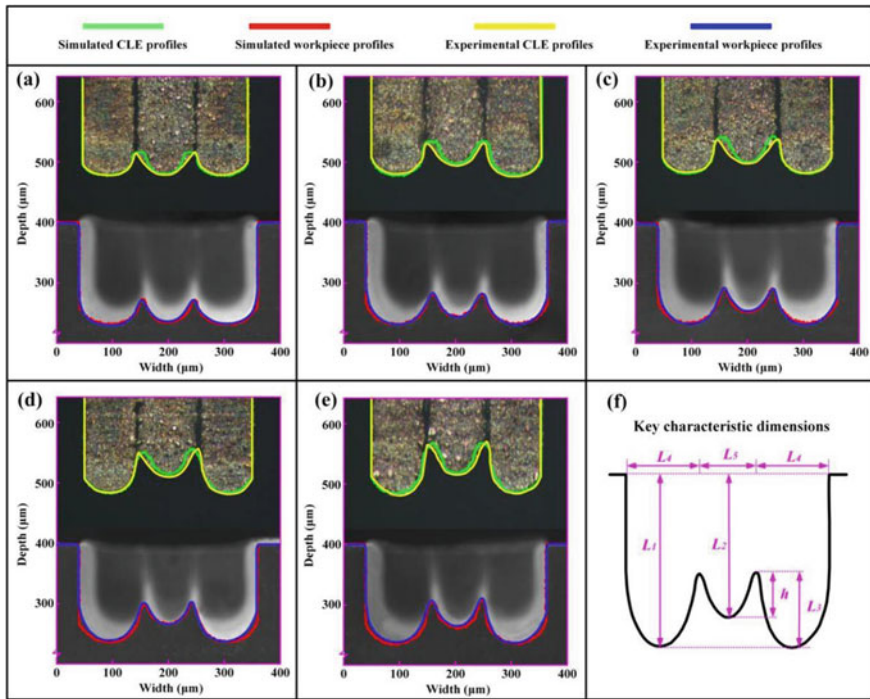
**Fig. 12** Schematic diagram of crater radius on laminated electrode during simulation



The experimental pictures, the profile of simulation and key sizes of microgrooves and electrodes during the first to fifth rounds of EDM are shown in Fig. 13. The Table 3 shows the statistical results of each key characteristic size. The microstructure tended to stabilize. Each round’s critical feature size difference is less than 3 μm from the fourth round of processing, and the secondary microstructure with a prosperous appearance was produced in the microgrooves with height  $h = L_{3-}(L_1-L_2)$ . The number of processing required to form a stable structure is slightly larger than the Cu/Sn/Cu laminated electrode, which maybe due to the presence of CuSn gradient material. In the comparative analysis of each round of simulation results, each round relative error between the simulation and experimental results of was less than 5%.

## 5 Conclusions

The use of composite laminated electrodes in EDM overthrew the traditional concept that electrode wear was an adverse phenomenon and converted electrode wear into a beneficial process, achieving the preparation of the required microstructure by precisely controlling the electrode wear. At this stage of the research, the simulation model of CuSn composite laminated electrode EDM was developed. The evolution process of electrode wear during continuous batch production of CuSn composite laminated electrode was studied, and the geometric evolution of CuSn composite laminated electrode and workpiece was predicted. The following conclusions can be drawn:



**Fig. 13** The profiles of Cu/CuSn/Cu laminated electrode and workpiece in multiple rounds of EDM, and the schematic diagram of key characteristic sizes of microstructures: **a** first round; **b** second round; **c** third round; **d** fourth round; **e** fifth round; **f** key characteristic sizes of microstructures

**Table 3** The relative errors and key characteristic sizes of micro grooves

Round	Experimental results (μm)					Simulation results (μm)					Relative errors $\delta$ (%)
	L1	L2	L3	L4	L5	L1	L2	L3	L4	L5	
1st	165.5	164.0	40.0	124.0	97.0	168.5	163.5	43.0	126.5	93.5	2.72
2nd	170.0	157.0	50.0	127.5	96.0	169.0	154.0	48.5	128.5	95.5	2.94
3rd	166.0	144.0	57.5	131.0	93.0	167.5	143.0	59.5	127.0	93.0	3.16
4th	165.0	137.0	67.0	132.0	95.0	165.0	134.5	62.0	129.5	94.0	3.35
5th	164.0	136.0	69.0	130.5	98.0	166.0	135.5	65.0	127.5	94.5	3.56

- (1) The fraction of energy exhausted by the electrode and the workpiece to evaporate the molten material is approximately constant for the same material for different processing parameters. According to theoretical calculations and experimental research, it can be concluded that the  $F_v$  and  $F_m$  of the electrode and workpiece were 2.13%, 3.11% and 4.32%, 6.36% when the electrode and workpiece were made of Cu and 304 stainless steel, respectively. When the Sn was used as the electrode, while and 304 stainless steel were used as workpiece materials, the

number of  $F_v$  and  $F_m$  on the electrode were 1.03%, 4.21%, and the values of  $F_v$  and  $F_m$  on the workpiece 4.08%, 6.6%, respectively. Therefore, it was assumed that the discharge crater was semi-spherical, the dielectric was EDM oil, the pulse-width was 1  $\mu\text{s}$ , the pulse-interval was 10  $\mu\text{s}$ , and that the processing voltage was 200 V. According to the numbers of  $F_v$  and  $F_m$  on the electrode and workpiece, the radii of discharge crater on the Cu and Sn electrodes in simulation model were 1.6 and 4.3  $\mu\text{m}$ , respectively, and the radius of discharge crater on the workpiece was 2.5  $\mu\text{m}$ . In the case of electrodes made of CuSn gradient material, the radius of the discharge points at different locations in the gradient material can be calculated linearly from the Sn content.

- (2) In EDM simulation, this paper established a new strategy of the discharge erosion for CuSn composite electrode. This means that a set of paired elements on the electrodes were removed, and the crater radius must be calculated based on the material composition of the identified elements to determine whether the surrounding elements need to be removed. Then the center distance between the identified electrode element and the paired elements is compared, and once the center distance is less than the erosion crater radius, the identified element is eroded, and vice versa is preserved. A simulation model of erosion by CuSn composite electrodes was developed and typical experiments was verified based on the strategy described above. After repeated experiments, the simulation model error can be limited within 5%, which indicating that the evolution of the microstructure profile of the electrode and workpiece in EDM with the CuSn composite laminated electrode can be accurately predicted by the model. In this way, the model can serve as a theoretical guide for EDM processing, thus significantly reducing the number of tests. That effectively economizing the resources and manufacturing costs, in addition reducing the production of poisonous gases, oil residues, and other harmful substances, reducing pollution and damage to users' health.

**Acknowledgements** This work was supported by Foundation of State Key Laboratory of Public Big Data under No. PBD2022-14, the Science and Technology Ph.D. Research Startup Project under No. Grant SZIIT2022KJ017. This work was also supported by the funding of the Guangdong Provincial Research Platform and Project (2022KQNCX231).

## References

1. Wang Z, Li YB, Bai F, Wang CW, Zhao QZ (2016) Angle-dependent lubricated tribological properties of stainless steel by femtosecond laser surface texturing. *Opt Laser Technol* 81:60–66
2. Gong J, Jin Y, Liu Z, Jiang H, Xiao M (2018) Study on influencing factors of lubrication performance of water-lubricated micro-groove bearing. *Tribol Int* 129:390–397

3. Tang H, Tang Y, Yuan W, Peng R, Lu L, Wan Z (2018) Fabrication and capillary characterization of axially micro-grooved wicks for aluminium flat-plate heat pipes. *Appl Thermal Eng* 129:907–915
4. Liu P, Gao Y, Wang F, Yang J, Yu X, Zhang W, Yang L (2017) Superhydrophobic and self-cleaning behavior of Portland cement with lotus-leaf-like microstructure. *J Clean Prod* 156:775–785
5. Mohri N, Suzuki M, Furuya M, Saito N, Kobayashi A (1995) Electrode wear process in electrical discharge machining. *CIRP Ann Manuf Technol* 44:165–168
6. Yeo SH, Murali M (2003) A new technique using foil electrodes for the electro-discharge machining of micro grooves. *J Micromech Microeng* 13:N1–N5
7. Chow HM, Yan BH, Huang FY (1999) Micro slit machining using electro-discharge machining with a modified rotary disk electrode (RDE). *J Mater Process Technol* 91:161–166
8. Yan J, Watanabe K, Aoyama T (2014) Micro-electrical discharge machining of polycrystalline diamond using rotary cupronickel electrode. *CIRP Ann Manuf Technol* 63:209–212
9. Wu W, Wu XY, Lei JG, Xu B, Jiang K, Wu ZZ, Yin HM, Li W (2019) Fabrication of deep narrow microgrooves by micro-EDM using rotary dentate disc foil electrodes in emulsion. *J Micromech Microeng* 29:035014
10. Kou Z, Han F (2018) On sustainable manufacturing titanium alloy by high-speed EDM milling with moving electric arcs while using water-based dielectric. *J Clean Prod* 189:78–87
11. Dong H, Liu Y, Li M, Liu T, Zhou Y, Li D, Shen Y (2019) High-speed compound sinking machining of Inconel 718 using water in oil nanoemulsion. *J Mater Process Technol* 274:116271
12. Zhang Z, Yu H, Zhang Y, Yang K, Li W, Chen Z, Zhang G (2018) Analysis and optimization of process energy consumption and environmental impact in electrical discharge machining of titanium superalloys. *J Clean Prod* 198:833–846
13. Yu ZY, Masuzawa T, Fujino M (1998) Micro-EDM for three dimensional cavities development of uniform wear method. *CIRP Ann Manuf Technol* 47:169–172
14. Bleys P, Kruth JP, Lauwers B (2004) Sensing and compensation of tool wear in milling EDM. *J Mater Process Technol* 149:139–146
15. Schulze V, Weber P, Ruhs C (2012) Increase of process reliability in the micro-machining processes EDM-milling and laser ablation using on-machine sensors. *J Mater Process Technol* 212:625–632
16. Li JZ, Xiao L, Wang H, Yu HL, Yu ZY (2013) Tool wear compensation in 3D micro EDM based on the scanned area. *Precis Eng* 37:753–757
17. Heo S, Jeong YH, Min BK, Lee SJ (2009) Virtual EDM simulator: three-dimensional geometric simulation of micro-EDM milling processes. *Int J Mach Tools Manuf* 49:1029–1034
18. Jeong YH, Min BK (2007) Geometry prediction of EDM-drilled holes and tool electrode shapes of micro-EDM process using simulation. *Int J Mach Tools Manuf* 47:1817–1826
19. Zhang L, Du J, Zhuang X, Wang Z, Pei J (2015) Geometric prediction of conic tool in micro-EDM milling with fix-length compensation using simulation. *Int J Mach Tools Manuf* 89:86–94
20. Pei J, Zhuang X, Zhang L, Zhu Y, Liu Y (2018) An improved fix-length compensation method for electrical discharge milling using tubular tools. *Int J Mach Tools Manuf* 124:22–32
21. Pei J, Zhou Z, Zhang L, Zhuang X, Wu S, Zhu Y, Qian J (2016) Research on the equivalent plane machining with fix-length compensation method in micro-EDM. *Proc CIRP* 42:644–649
22. Garg A, Lam JSL (2016) Modeling multiple-response environmental and manufacturing characteristics of EDM process. *J Clean Prod* 137:1588–1601
23. Lei J, Wu X, Wang Z, Xu B, Zhu L, Wu W (2019) Electrical discharge machining of micro grooves using laminated disc electrodes made of Cu and Sn foils. *J Mater Process Technol* 271:455–462
24. Lei J, Wu X, Zhou Z, Xu B, Zhu L, Tang Y (2021) Sustainable mass production of blind multi-microgrooves by EDM with a long-laminated electrode. *J Clean Prod* 279:123492
25. Zhao Y, Zhang X, Liu X, Yamazaki K (2004) Geometric modeling of the linear motor driven electrical discharge machining (EDM) die-sinking process. *Int J Mach Tools Manuf* 44:1–9
26. Jameson EC (2001) Electrical discharge machining. Society of Manufacturing Engineers, Dearborn

27. Ming W, Zhang Z, Wang S, Zhang Y, Shen F, Zhang G (2019) Comparative study of energy efficiency and environmental impact in magnetic field assisted and conventional electrical discharge machining. *J Clean Prod* 214:12–28
28. Zhang R, Zhang Y, Liu Y, Shen Y, Li Z, Wang X (2017) Energy distribution and material removal of electric arc machining (EAM). *J Mater Process Technol* 242:110–116

**Part III**  
**Fabrication of Micro/Nano Structures**  
**via Precision Grinding and Injection**  
**Molding**

# Chapter 13

## Introduction to Precision Grinding and Injection Molding Micro/Nano Structures



Yanjun Lu, Yuming Huang, and Jiangxiu Ouyang

**Abstract** Microarray structures with high form accuracy and low surface roughness can be machined on the surface of polymer and high performance components including single crystal silicon carbide, ceramics and mold steel to produce new functional characteristics such as surface hydrophobicity and light efficiency enhancing. However, laser, etching, cutting and other methods are difficult to assure the 3D form accuracy and surface quality at micron scale. The technical bottleneck of micro-structure machining on the surface of hard and brittle materials is the truing and dressing of micro-tip of ultra-hard diamond grinding wheel. In consequence, a dry pulse discharge truing and dressing method of diamond grinding wheel is innovatively proposed. Firstly, the dry contact discharge dressing technology was used to dress the diamond grinding wheel into a V-shaped tip, and then the V-tip diamond grinding wheel was used to process smooth and regular micro-grooves or micro-pyramid array structures on the surface of hard and brittle materials such as ceramics, sapphire, single crystal silicon carbide or mold steel. After that the micro-structured mold steel mold core was precisely polished by water jet polishing technology to improve the surface quality. Finally, the micro-structure rapid prototyping of the mold core surface is copied to the polymer surface by micro injection molding technology, so that the mass production and manufacture of V-structured polymeric LED light guide plate can be realized.

### 1 Machining Technique of Micro-structure

The micro-structure with controllable and regular shape was manufactured on high performance material surfaces such as single crystal silicon carbide, silicon carbide reinforced aluminum (SiCp/Al), ceramics and carbide alloy, which may produce new functional characteristics such as surface hydrophobicity and light efficiency

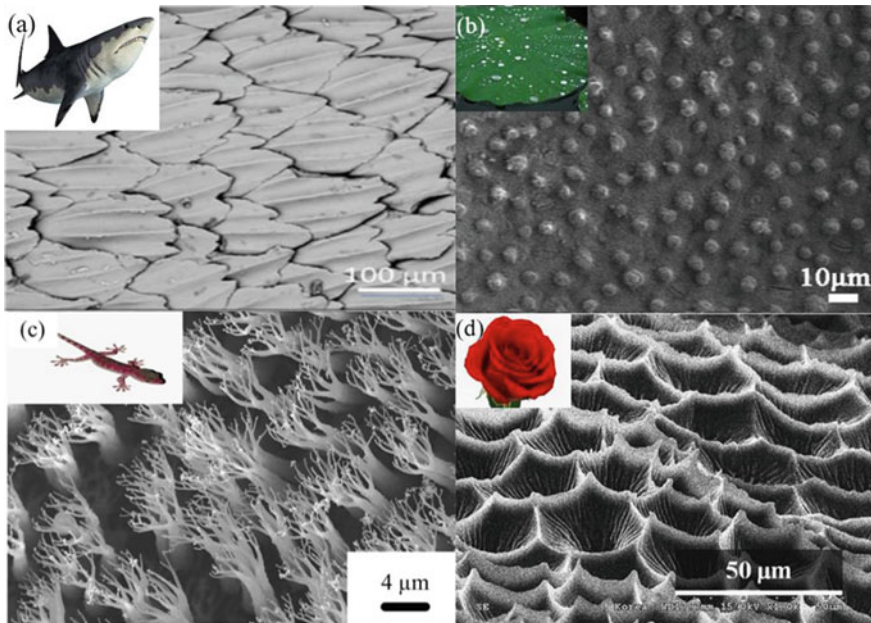
---

Y. Lu (✉) · Y. Huang · J. Ouyang  
Guangdong Provincial Key Laboratory of Micro/Nano Optomechanics Engineering,  
College of Mechatronics and Control Engineering, Shenzhen University, Nan-hai Ave 3688,  
Shenzhen 518060, Guangdong, PR China  
e-mail: [luyanjun@szu.edu.cn](mailto:luyanjun@szu.edu.cn)

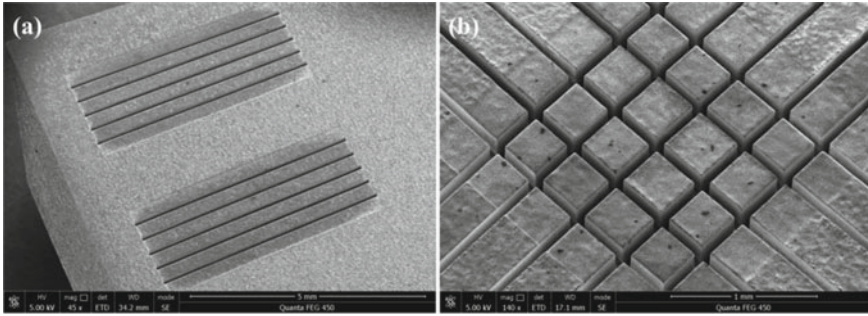


enhancing [1, 2]. The surface of plants and animals has relatively regular shape structure, which can make them acquire corresponding physical and chemical characteristics. For example, it has been observed that the skin of sharks looks smoother than that of whales, mainly because the micro-groove structure on the surface of shark skin (as shown in Fig. 1a [3]) makes it have good drag reduction effect and anti-adhesion performance, so as to avoid the attachment of microorganisms in seawater. Lotus leaf has super hydrophobic properties because of its surface array microstructure, as shown in Fig. 1b. Some scholars fabricated mastoid structures on the surface of lotus leaf on the electrode surface to reduce the tissue adhesion on the electrode surface [4]. The reason that geckos can freely climb walls is that the bristle structure of their feet is shown in Fig. 1c. Sethi Set al. prepared the nanoarray structure of gecko-like feet to make it have the function of adhesion and desorption [5]. Choo et al. replicated the rose-petal surface structure (as shown in Fig. 1d), which obtained high hydrophobicity [6]. The physical properties of object surface can be improved effectively by fabricating structures with different scales, dimensions and morphologies.

However, micro-structure machining of hard and brittle materials is the technical bottleneck of micro-fine and precision machining. At present, the main problem to be solved is how to improve the 3D microstructured form accuracy and surface quality of the mold at micron scale, and the quality of the microstructure polymer microinjection molding, so as to realize the mass manufacturing and application of



**Fig. 1** SEM images of functional microstructures of animal and plant surfaces: **a** Drag reduction of shark skin surface [3]; **b** Lotus leaf surface hydrophobic [4]; **c** foot surface adhesion and desorption of gecko [5]; **d** Hydrophobic surface of rose petals [6]



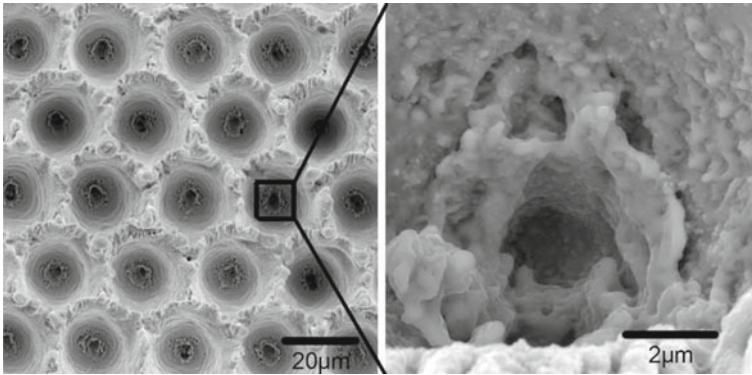
**Fig. 2** Micro array structure machined by micro electrical discharge machining (EDM) [7]

surface functional microstructure polymer components. The traditional machining methods of mold core microstructure mainly include precision grinding, precision cutting, micro electrical discharge machining (EDM), laser processing, ion beam processing, etc.

Discharge machining uses pulse power to form pulse discharge effect between tool and workpiece. The melting and gasification phenomenon of workpiece materials caused by instantaneous high temperature is removed, so as to achieve the purpose of material processing. Micro-structure machining of conductive materials can be realized by discharge machining including electrical discharge machining (EDM) and wire electrical discharge machining (WEDM) [7, 8]. Lei et al. [7] from Shenzhen University used EDM to fabricate the Ti-6Al-4 V alloy workpiece with the depth and width of about 250  $\mu\text{m}$  and 74  $\mu\text{m}$ , respectively, as well as the criss-crossed micro-groove structure, as shown in Fig. 2. Kamal et al. [8] proposed a method for evaluating the performance of carbide die-cast die cores made by WEDM. The results showed that larger workpiece thickness and smaller cone angle would lead to smaller geometric deviation, which is conducive to better core performance.

Ultrafast laser processing principle is to use ultra-high energy density beam in a very short time to produce melting and even gasification of workpiece materials to achieve the removal of workpiece materials. Ultrafast laser machining has the advantages of high precision, small damage and small heat affected zone in microstructure machining. According to the surface microstructure of lotus leaves, Gong et al. [9] processed micropore regular arrays with submicron structure on high-strength steel substrate by picosecond laser processing, as shown in Fig. 3, and found that PTFE films printed by hot stamping using this mold also showed superhydrophobicity. Zhang et al. [10] from Hunan University used the light speed wavelength of 1030 nm, the maximum repetition frequency of 20 MHz, and the pulse width <400 fs; It is found that the tungsten carbide mold with the optimal experimental processing parameters can be molded into glass micro-grooves, and the surface roughness can reach 0.164  $\mu\text{m}$ .

Different from laser processing, the principle of ion beam processing is to use the huge impact kinetic energy of the accelerated focusing ion beam to produce impact

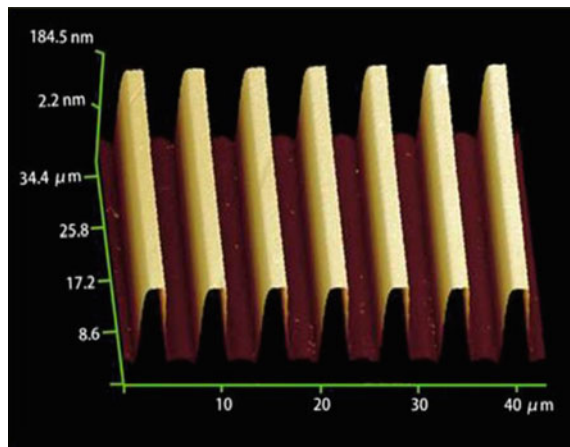


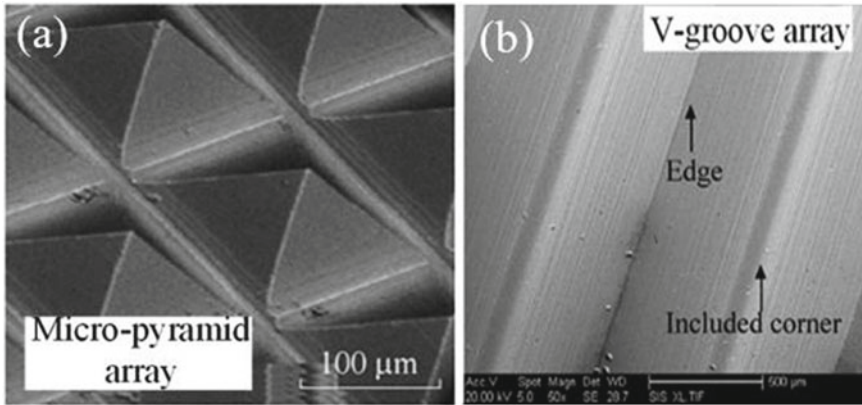
**Fig. 3** The microporous structure array of die steel surface processed by picosecond laser machining [9]

effect, sputtering effect and injection effect on the workpiece surface material to achieve the purpose of material processing, the processing principle determines that the ion beam processing has a very high processing precision. Wang et al. [11] used scanning ion beam etching to etch groove-array microstructure substrate with surface roughness up to 0.4 nm in aspect ratio, as shown in Fig. 4.

Studies have shown that microarray structures with controllable shape accuracy can be manufactured on the surface of the mold by using micro-grinding [12, 13], and the processing cost is low and the operation process is simple. The precision machining of those high performance materials with macroscopic size and microscopic structure depended on grinding machining of superhard diamond grinding wheel. Micro-structure/micro-lens structure with suitable form accuracy can be machined on the curved surface of hard and brittle materials by using micro-fine and precision grinding technology [14]. For example, Brunswick University of Technology from

**Fig. 4** The 3D topography with micro-grooved array structure processed by scanning ion beam etching machining [11]





**Fig. 5** Micro-grinding machined surfaces: **a** Micro-pyramid array structure [15] and **b** V-groove array structure [16]

Germany was able to process the structural surface of micro-pyramid array with the ratio of height to width through precision grinding with disc diamond grinding wheel [15], as shown in Fig. 5a. Guo and Zhao et al. from Harbin Institute of Technology used a diamond wheel with V-shaped tip to grind the V-shaped groove array structure on the surface of tungsten carbide alloy [16], as shown in Fig. 5b. From Fig. 5, it can be concluded that precision grinding technology is used to obtain a microarray structured surface with complete and undamaged edges with high quality.

## 2 Truing Technique of Diamond Grinding Wheel

However, the difficult problem at present is how to dress and true the diamond grinding wheel efficiently and how to delay the wear of the cutting edge tip of the diamond grinding wheel tool. Therefore, this topic proposes to use the metal-bonded diamond grinding wheel tool with good control and high grinding wheel strength and stiffness, and use the micro-abrasive cutting edge tip on the working surface of the diamond wheel to process the micro-array structure with suitable shape accuracy on the complex curved surface of the high hardness material. However, the cutting tool of metal-bonded diamond grinding wheel is extremely difficult to be dressed and trued.

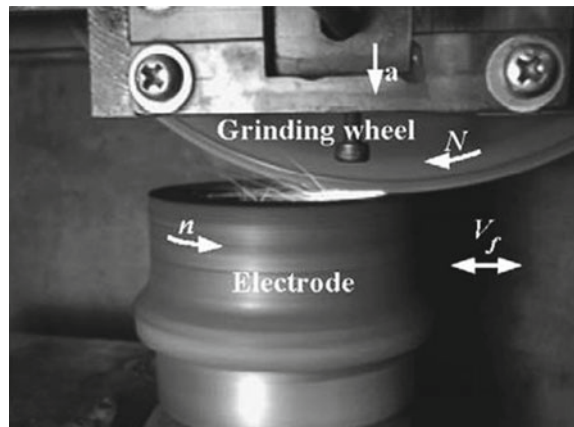
Precision dressing technology is an important factor affecting the grinding performance of the grinding wheel. The grinding wheel with good morphology and sharpened cutting edge can carry out the micro-grinding with high surface quality requirements. The purpose of truing is to make the grinding wheel obtain a specific geometric shape, remove the surface defects of the grinding wheel and ensure its shape accuracy. During truing, abrasive and bonding agents of the excess parts of the grinding wheel are generally removed. The purpose of dressing is to make the exposed cutting

tool on the surface of the grinding wheel have an appropriate cutting edge height, and ensure sufficient bonding strength and sufficient chip space, and increase the number of effective grinding grains per unit area of the grinding wheel surface. It is an ideal condition to remove only the adhesive of grinding wheel without causing the grinding particle to fall off and collapse. The traditional wheel dressing and truing technologies include mechanical dressing [17], electrolytic in-process dressing (ELID) [18], electrical discharge dressing (EDD) [19], laser dressing [20], etc.

Electro-Contact Discharge (ECD) is a new electrical discharge dressing method first put forward by J. Tamaki and Kondoh in 1999 [21]. The working principle of ECD is that after diamond abrasive cutting electrodes, pulse discharge occurs between conductive chips and metal bond to etch the metal binder, so that the diamond abrasive is removed from the edge, so as to realize the purpose of dressing and truing. ECD can obtain a higher material removal rate and enhance the dressing efficiency of grinding wheel, and the dressing electrode loss is very small. Xie et al. used ECD technology to carry out dressing test on diamond grinding wheel [22]. The dry ECD dressing device and the dressing principle diagram are shown in Fig. 6. The experimental results show that the peak pulse current and pulse duration have great influence on the edge height and surface morphology of diamond abrasive grains. Tonshoff et al. [23] also conducted a comparative experimental study on online ECD technology, and the research results showed that ECD online dressing technology could reduce the grinding force of the grinding wheel as well as it was an environmentally friendly dressing method with no pollution, simple operation and low cost. Therefore, the dry ECD dressing method was proposed to enhance the dressing efficiency of diamond grinding wheel. By controlling the cutting edge parameters of the micro-tip of the micro-abrasive, the shape of the micro-abrasive tip was copied to the curved surface of the parts, and the micro-nano structure machining of the curved surface of hard and brittle materials with the controllable shape accuracy may be realized.

The precision dressing technology of diamond grinding wheel used for micro-structure surface grinding mainly adopts discharge dressing, roller dressing or

**Fig. 6** The dry ECD dressing setup [22]



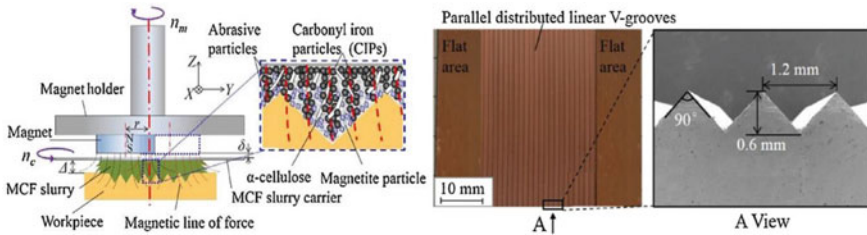
composite dressing technology combining them. The discharge dressing efficiency is high, the grinding wheel surface grout edge height is large, the working face sharpness is good, and it can be used for complex grinding wheel shape precision dressing, but the implementation is complicated, the shape accuracy of grinding wheel is not very high. Recently, the dressing and truing technology of diamond grinding wheel micro-tip has been developed [24, 25], which can obtain high-quality and high-precision microstructure on hard and brittle surfaces such as monocrystalline silicon, tungsten carbide and quartz glass. But up to now, it has not solved the problem that the cutting edge tip of diamond grinding wheel tool wears fast in the process of machining. Therefore, the micro-abrasive cutting edge tip of diamond grinding wheel was applied to fabricate the complex curved surface of the workpiece with high hardness.

In summary, ECD dressing method can effectively make diamond grinding wheel grind out the edge, and obtain good surface topography and shape and dimension accuracy of grinding wheel. Moreover, it is an environmentally friendly dressing method with no pollution and simple operation.

### 3 Polishing Technique of Micro-structured Mold Core

The further improvement of the surface quality requirements of the micro-structured mold core surface promotes the emergence of a variety of polishing methods, such as copying tool polishing, magnetic field assisted polishing, vibration assisted polishing, etc. The key is to improve the surface roughness without reducing the accuracy of the characteristic structure shape. As proposed by scholars Brinksmeier et al. [26, 27] and Riemer et al. [28], the use of copying tools to polish structural surfaces refers to tools with the same or similar geometric shapes as the characteristic structures of structured surfaces. Brinksmeier et al. [26] proposed the method of polishing structural array on die steel (X40Cr13) and electroless nickel plating steel by using pen and wheel copy tools, and the surface roughness after polishing reached 4.5 nm. Suzuki et al. [29] used a metal-alloy-shaped imitation diamond wheel to grind the unbonded tungsten carbide Fresnel die, and obtained a shape accuracy of 0.8  $\mu\text{m}$  and a surface roughness of 14 nm with PV value.

The magnetic field assisted polishing method includes a variety of polishing techniques such as magnetic abrasive polishing. Guo et al. [30] proposed a local vibration-assisted magnetic lapping polishing for micro-feature polishing, and successfully improved the surface quality of rectangular micro-features on the die surface, which can be used for mass production of microfluid components. Wu et al. [31] studied the process of magnetic abrasive nano polishing on the surface of micro grooves by low frequency alternating magnetic field. The surface roughness  $R_a$  of glass and alloy steel samples changed from 123.38 nm, 130.71 nm, 136.08 nm and 129.39 nm to 55.18 nm, 50.92 nm, 65.62 nm and 62.42 nm, respectively. The surface roughness  $R_a$  of alloy steel was reduced from 192.48 to 68.70 nm, and the surface quality of groove



**Fig. 7** Magnetic composite fluid slurry polishing of V-grooved structure [33]

and the burr phenomenon of groove edge were improved effectively. The magnetorheological polishing technology is to use a magnetorheological liquid mixed with nano-polishing abrasives which can be transformed into viscoelastic solid under the action of magnetic field as polishing medium to polish the structural surface. Kim et al. [32] carried out magnetorheological polishing on the micro-structure slot array on the silicon surface of copper plating. After polishing, the surface roughness of the tetrahedral structure was reduced to one tenth of the initial value, and the bottom roughness reached 11.1 nm and the side roughness reached 18.1 nm. Wang et al. [33] conducted a feasibility study on polishing the surface of V-groove structure with magnetic composite fluid slurry, and the surface roughness decreased from 350 nm to 15–50 nm after 150 min of polishing, as shown in Fig. 7. Therefore, the magnetic field assisted polishing method can achieve nanometer or subnanometer surface roughness, but maintaining the shape of the characteristic structure, especially the surface structure with aspect ratio, is still a big challenge.

Vibration-assisted polishing is a polishing method in which abrasive particles are hammered to the workpiece to achieve material removal by applying tangential, longitudinal or elliptical ultrasonic vibration to the workpiece or polishing tool. Suzuki et al. [34] proposed to use magnetic induction ultrasonic assisted vibration polishing to polish the surface of micro-aspherical structure. Zhao et al. [35] added vibration-assisted polishing on the basis of chemical mechanical polishing to obtain better surface quality than non-vibration-assisted polishing. Guo et al. [36] used circular vibration with a frequency of 9.2 kHz and a radius of 30  $\mu\text{m}$  to polish spherical glass, as shown in Fig. 8. After vibration-assisted polishing, PV value of surface profile of spherical glass lens was reduced to less than 100 nm, and its surface roughness  $R_z$  reached 3.3 nm.

Abrasive water jet polishing method is a polishing method that realizes material removal in the process of fluid jet polishing by using the erosion process that the micron/nano level abrasive, which is evenly mixed with water, is pumped out of the nozzle and impinges on the target surface. Fluid jets are highly flexible and highly adaptable to surfaces with complex geometric shapes, and have been widely used in polishing optical lenses and molds. Chen et al. [37] proposed a low pressure abrasive flow polishing (LAFP) technology and carried out polishing experiments on rectangular microchannels of copper and SUS304 materials. Through numerical simulation, the distribution of turbulence intensity and shear force in the polishing

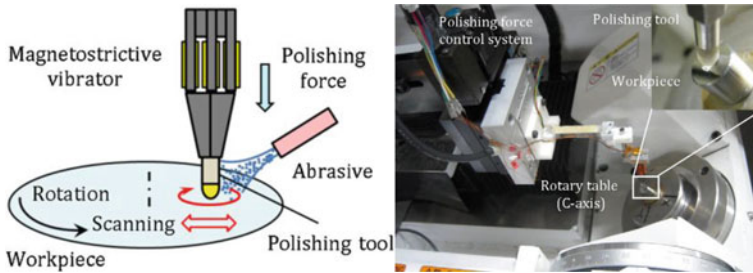


Fig. 8 Vibration assisted polishing technique [36]

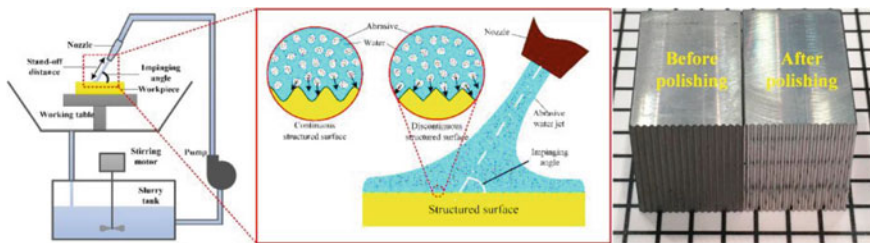


Fig. 9 Low pressure micro abrasive water jet polishing technology for sinusoidal surface [38]

microchannel was analyzed, and it was found that the material removal rate increased with the increase of polishing particle size, polishing pressure and polishing particle concentration. The microstructure with high quality surface was finally prepared in copper and SUS304 with surface roughness of  $R_a$  4.8 nm and  $R_a$  12.7 nm, respectively. Wang et al. [38] used low-pressure micro-abrasive water jet polishing technology to achieve mask-free polishing of sinusoidal and V-groove structural surfaces, as shown in Fig. 9, and revealed fluid flow motion and material removal characteristics through computational fluid dynamics (CFD) model. The results show that the low pressure micro-abrasive water jet polishing technology can significantly improve the surface quality of the optical structured surface while ensuring the shape accuracy. Therefore, the water jet polishing technology was applied to improve the micro-ground surface quality of micro-structured mold core in this section.

## 4 Summary and Outlook

Overall, at present, the industrialization of micro/nano structures functional surface of hard and brittle materials is faced with the problem that the grinding wheel dressing is difficult in the grinding, which leads to the limited machining accuracy of micro/nano structures, followed by the low efficiency and high cost of large-scale production in the injection molding. To breakthrough the technical bottleneck of the truing



and dressing of micro-tip of ultra-hard diamond grinding wheel in micro-structures machining, this section proposed a novel dry pulse discharge truing and dressing method of diamond grinding wheel with in depth theoretical research. Also focusing on the efficiency improvement and consumption reducing in injection molding using novel methods and design.

This part contains a total of six chapters, the general contents of each chapter are briefly introduced as follows:

Chapter 1 briefly reviewed the machining technique of micro-structure, dressing and truing technique of diamond grinding wheel and polishing technique of micro-structured mold core. As a result, the precision grinding technology was used to machine micro array structures on the surfaces of hard-brittle materials and die steel mold core. The dry ECD dressing and truing technology was proposed to efficiently and precisely true the metal-bonded diamond wheel to obtain sharp micro grain cutting edge and good shape topography. The water jet polishing technology was applied to improve the micro-ground surface quality of micro-structured mold core.

Chapter 2 introduced the precision dressing and truing of #600 and #1200 metal-bonded diamond grinding wheel with V-tip using dry ECD truing. The influences of discharge parameters, such as impulse frequency, duty cycle and open-circuit voltage on the form accuracy of the V-tip diamond wheel were investigated. To achieve high truing accuracy, the V-tip angle and radius were analyzed under different pulse discharge parameters. As a typical hard-brittle material, the tungsten carbide was used to perform the micro-grinding experiments to test the truing accuracy of diamond wheel V-tip.

Chapter 3 introduced the precision grinding of micro-structures of hard and brittle material surfaces. The micro-grinding technology is used to fabricate micro-grooves and micro-pyramid array structures on the surface of single crystal silicon, aluminum-based silicon carbide, reaction sintered silicon carbide, crystallite glass ceramics and die steel with high strength. The V-groove tip angle, tip arc radius and form accuracy were comparatively investigated after micro-grinding machining for different hard and brittle materials.

Chapter 4 introduced the precision grinding and polishing of optical micro-structured die steel surface. In this chapter, Maskless fluid Jet Polishing (MFJP) is used for precision polishing of optical micro-structured die steel mold core surfaces and can provide a turnkey method for precision machining of complex optical structural surfaces with high precision. On the basis of the analysis of surface roughness, surface smoothness, and form maintainability, experimental investigations on the polishing of sinusoidal structured surface and V-groove structured surface were performed to achieve the technical feasibility of MFJP on structured surface.

Chapter 5 introduced the fabrication of micro-structured polymer via. precision grinding and injection molding. In order to achieve the mass production and manufacture of micro-structured polymer components by micro injection molding, precise micro-grinding machining was proposed to fabricate regular and suitable micro-grooved array structures on the surface of mold cores. By micro-grinding the mold

core, micro-structured polymers are produced with high efficiency and high precision using micro-injection molding technology. It enables cost-effective large-scale production of micro-structured polymer parts.

Chapter 6 introduced the manufacture of micro-structured LED diffusion plate via. precision grinding and injection molding. In this chapter, a new micro-structured diffusion sheet for LED (light-emitting diode) was developed by combining efficient and accurate hybrid machining methods with micro-injection molding and micro-grinding, enabling cost-effective large-scale production of LED lamps with excellent light output. An efficient micro injection molding technique is used for the rapid fabrication of micro-structured diffusion plate with high shape accuracy. The raised hybrid production method enables the large-scale production and fabrication of micro-structured LED diffusion sheets through low production cost.

**Acknowledgements** The work described in this chapter was supported by the National Natural Science Foundation of China (Grant No. 51805334), the International Science and Technology Cooperation Project of Shenzhen City (Grant No. GJHZ20190822091805371), and the Science and Technology Planning Project of Guangdong Province (Grant No. 2017A010102003).

## References

1. Maghsoudi K, Jafari R, Momen G, Farzaneh M (2017) Micro-nanostructured polymer surfaces using injection molding: a review. *Mater Today Commun* 13:126–143
2. Gao S, Qiu Z, Ma Z, Ma Z, Yang YJ (2017) Development of high efficiency infrared-heating-assisted micro-injection molding for fabricating micro-needle array. *Int J Adv Manuf Technol* 92:831–838
3. Chien H, Chen X, Tsai W, Lee M (2020) Inhibition of biofilm formation by rough shark skin-patterned surfaces. *Colloids Surf B* 186:110738
4. Li X, Gong F, Liu D, He S, Yuan H, Dai L, Cai X, Liu J, Guo J, Jin Y, Sang F (2019) A lotus leaf based random laser. *Org Electron* 69:216–219
5. Sethi S, Ge L, Ci L, Ajayan PM, Ali D (2008) Gecko-inspired carbon nanotube-based self-cleaning adhesives. *Nano Lett* 8:822–825
6. Choo S, Choi H, Lee H (2014) Replication of rose-petal surface structure using UV-nanoimprint lithography. *Mater Lett* 121:170–173
7. Lei JG, Wu XY, Zhou ZW, Xu B, Zhu LK, Tang Y (2021) Sustainable mass production of blind multi-microgrooves by EDM with a long-laminated electrode. *J Clean Prod* 279:123492
8. Jangra K, Grover S, Aggarwal A (2011) Digraph and matrix method for the performance evaluation of carbide compacting die manufactured by wire EDM. *Int J Adv Manuf Technol* 54:579–591
9. Gong DW, Long JY, Fan PX, Jiang DF, Zhang HJ, Zhong ML (2015) Thermal stability of micro–nano structures and superhydrophobicity of polytetrafluoroethylene films formed by hot embossing via a picosecond laser ablated template. *Appl Surf Sci* 331:437–443
10. Zhang HJ, Yin SH, Jia HP, Huang S, Liu X, Li JX, Chen FJ (2019) Femtosecond laser machining process of tungsten carbide die for microfluidic grooves molding. *Surf Technol* 48:93–99
11. Wang RQ, Zhang ZY, Bai YY, Wang YC, Yin XL, Kong LS, Deng WJ, Xue DL, Zhang XJ (2021) Scanning ion beam etching: a method for the fabrication of computer-generated hologram with nanometric accuracy for aspherical testing. *Opt Lasers Eng* 139:106503

12. Xie J, Zhuo YW, Tan TW (2011) Experimental study on fabrication and evaluation of micro pyramid-structured silicon surface using a V-tip of diamond grinding wheel. *Precis Eng* 35:173–182
13. Xie J, Luo MJ, He JL, He JL, Liu XR, Tan TW (2012) Micro-grinding of micro-groove array on tool rake surface for dry cutting of titanium alloy. *Int J Precis Eng Manuf* 13:1845–1852
14. Xie J, Luo MJ, Wu KK, Yang LF, Li DH (2013) Experimental study on cutting temperature and cutting force in dry turning of titanium alloy using a non-coated micro-grooved tool. *Int J Mach Tools Manuf* 73:25–36
15. Xie J, Liu XR, Wu KK, Lu YJ, Li P (2013) Evaluation on 3D micro-ground profile accuracy of micro-pyramid-structured Si surface using an adaptive-orientation WLI measurement. *Precis Eng* 37:918–923
16. Guo B, Zhao QL (2015) On-machine dry electric discharge truing of diamond wheels for micro-structured surfaces grinding. *Int J Mach Tools Manuf* 88:62–70
17. Chen B, Li SC, Deng ZH, Guo B, Zhao QL (2017) Grinding marks on ultra-precision grinding spherical and aspheric surfaces. *Int J Precis Eng Manuf Green Technol* 4:419–429
18. Ohmori H, Takahashi I, Bandyopadhyay BP (1996) Ultra-precision grinding of structural ceramics by electrolytic in-process dressing (ELID) grinding. *J Mater Process Technol* 57:272–277
19. Weingärtner E, Roth R, Kuster F, Boccadoro M, Fiebelkorn F (2012) Electrical discharge dressing and its influence on metal bonded diamond wheels. *CIRP Ann Manuf Technol* 61:183–186
20. Ramesh BN, Radhakrishnan V (1989) Investigations on laser dressing of grinding wheels—part ii: grinding performance of a laser dressed aluminum oxide wheel. *J Eng Ind* 111:253–261
21. Tamaki J, Kondoh K, Iyama T (1999) Electrocontact discharge dressing of metal-bonded diamond grinding wheel utilizing a hybrid electrode. *J Jpn Soc Precis Eng* 65:1628–1632
22. Xie J, Tamaki J (2006) In-process evaluation of grit protrusion feature for fine diamond grinding wheel by means of electro-contact discharge dressing. *J Mater Process Technol* 180:83–90
23. Tönshoff HK, Friemuth T (2000) In-process dressing of fine diamond wheels for tool grinding. *Precis Eng* 24:58–61
24. Wegener K, Hoffmeister HW, Karpuschewski B, Kuster F, Hahmann WC, Rabiey M (2011) Conditioning and monitoring of grinding wheels. *CIRP Ann Manuf Technol* 60:757–777
25. Xie J, Xie HF, Luo MJ, Tan TW, Li P (2012) Dry electro-contact discharge mutual-wear truing of micro diamond wheel V-tip for precision micro-grinding. *Int J Mach Tools Manuf* 60:44–51
26. Brinksmeier E, Riemer O, Gessenharter A, Autschbach L (2004) Polishing of structured molds. *CIRP Ann* 53:247–250
27. Brinksmeier E, Riemer O, Gessenharter A (2006) Finishing of structured surfaces by abrasive polishing. *Precis Eng* 30:325–336
28. Riemer O (2008) A review on machining of micro-structured optical molds. *Key Eng Mater* 364:13–18
29. Suzuki H, Okada M, Yamagata Y, Morita S, Higuchi T (2012) Precision grinding of structured ceramic molds by diamond wheel trued with alloy metal. *CIRP Ann* 61:283–286
30. Guo J, Liu K, Wang Z, Wang ZF, Tnay GL (2017) Magnetic field-assisted finishing of a mold insert with curved microstructures for injection molding of microfluidic chips. *Tribol Int* 114:306–314
31. Wu JZ, Yin SH, Xing BJ, Zou YH (2019) Effect of magnetic pole on finishing characteristics in low-frequency alternating magnetic field for micro-groove surface. *Int J Adv Manuf Technol* 104:4745–4755
32. Kim W, Lee S, Min B (2004) Surface finishing and evaluation of three-dimensional silicon microchannel using magnetorheological fluid. *J Manuf Sci Eng* 126:772–778
33. Wang Y, Wu Y, Nomura M (2016) Feasibility study on surface finishing of miniature V-grooves with magnetic compound fluid slurry. *Precis Eng* 45:67–78
34. Suzuki H, Hamada S, Okino T, Kondo M, Yamagata Y, Higuchi T (2010) Ultraprecision finishing of micro-aspheric surface by ultrasonic two-axis vibration assisted polishing. *CIRP Ann* 59:347–350

35. Zhao Q, Sun Z, Guo B (2016) Material removal mechanism in ultrasonic vibration assisted polishing of micro cylindrical surface on SiC. *Int J Mach Tools Manuf* 103:28–39
36. Guo J, Morita S, Hara M, Yamagata Y, Higuchi T (2012) Ultra-precision finishing of micro-spheric mold using a magnetostrictive vibrating polisher. *CIRP Ann* 61:371–374
37. Chen FJ, Hao SM, Miao XL, Yin SH, Huang S (2018) Numerical and experimental study on low-pressure abrasive flow polishing of rectangular microgroove. *Powder Technol* 327:215–222
38. Wang CJ, Zhang ZL, Cheung CF, Luo W, Loh YM, Lu YJ, Kong LB, Wang SX (2022) Maskless fluid jet polishing of optical structured surfaces. *Precis Eng* 73:270–283

# Chapter 14

## Precision Dressing and Truing of Diamond Grinding Wheel with V-tip



YanJun Lu, Jiangxiu Ouyang, and Yuming Huang

**Abstract** Due to low efficiency and environmental pollution in the traditional mechanical or EDM truing of the metal-bonded wheel, a novel method termed dry ECD (electro-contact discharge) truing was proposed to truing of V-tip diamond wheel with grain sizes of #600 and #1200 in this chapter. The effects of discharge parameters, such as pulse frequency, duty cycle, and open-circuit voltage, on the shape accuracy of the V-tip diamond wheel were investigated. The relationship between the V-tip angle/radius and discharge parameters was analyzed. The parameters were then optimized to obtain a high shape accuracy. On the other hand, to evaluate the grinding performances of the V-tip wheel after truing, a micro-grinding test was also conducted on cemented carbide to grinding grooves. The depth error, arc error and surface roughness of the ground groove were measured to evaluate the grinding performances of the V-tip wheel trued with the optimal parameters. The results revealed that the highest shape accuracy was obtained at pulse frequency of 4000 Hz, duty cycle of 50%, and open-circuit voltage of 25 V. As a result, the V-tip wheel obtained the minimum tip angle of  $62.4^\circ$  and the minimum tip radius of  $15\ \mu\text{m}$ . Simultaneously, the groove had the minimum depth error of  $2.6\ \mu\text{m}$  and the minimum arc radius of  $3.2\ \mu\text{m}$  on the surface of cemented carbide ground with the trued V-tip wheel. The surface roughness was  $0.31\ \mu\text{m}$  on the surface of the ground groove.

---

Y. Lu (✉) · J. Ouyang · Y. Huang  
Shenzhen Key Laboratory of High Performance Nontraditional Manufacturing, College of  
Mechatronics and Control Engineering, Shenzhen University, Nan-Hai Ave 3688,  
Shenzhen 518060, Guangdong, PR China  
e-mail: [luyanjun@szu.edu.cn](mailto:luyanjun@szu.edu.cn)

## 1 Introduction

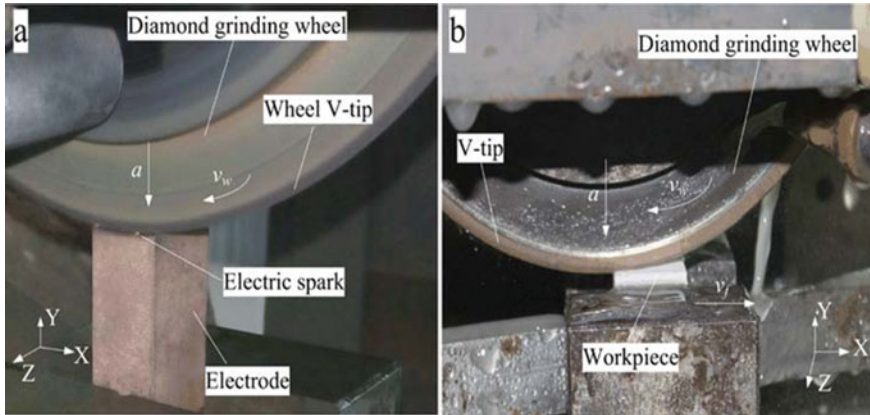
The regular micro array structure at micron scale can now be fabricated on the surface of hard-brittle materials to achieve new levels of functionality [1]. However, surface machining of micro structures in difficult-to-machine materials is challenging. Precision grinding with diamond grinding wheel is known to be the most valid micro fabrication technique [2]. However, the dressing and truing of diamond grinding wheel is very significant. The efficiency and accuracy of truing are technical obstacles in industrialization.

It is very difficult to process the V-groove structure on the surfaces of hard and brittle materials because of its high melting point and fragility, so at present, in addition to precision grinding, there are other precision machining methods such as laser machining, ion beam, chemical etching and so on. For example, Zheng et al. used the high-energy laser to process micro-grooves on cemented carbide tools to explore their tribological properties [3]. Liu et al. used femtosecond laser equipment to process grooves at  $45^\circ$  to the main cutting edge on the carbide tool surface, latter cut  $\text{Al}_2\text{O}_3$ -based ceramics by using it [4]. Lian proposed inductively coupled plasma etching cemented carbide to process micro-grooves and other micro-structures [5]. However, the energy consumption of laser processing and ion beam processing is several times that of grinding processing, which is complicated and the equipment expensive as well, the latter will also cause pollution problems of chemical waste liquid and other problems, while the precision grinding technology with V-shaped tip grinding wheel can ensure the shape precision and the surface quality of grooves simultaneously. The shape accuracy of the grooves after machining depends largely on the shape accuracy of the V-tip grinding wheel when grinding hard alloy grooves with v-tip grinding wheel, therefore, the grinding wheel needs to be carefully trued for several times before machining in order to better ensure the shape accuracy of the V-shaped grooves on the workpiece surface after machining.

Presently, methods of grinding wheel truing are mainly divided into three categories. The first category is traditional mechanical truing method, the second type is special truing method represented by discharge truing, electrolytic truing and laser pulse truing, and the third kind is the complementary truing method of traditional mechanical truing method and special truing method [6]. The traditional mechanical truing method is the most developed and mature truing method of them. Zhou et al. [7] realized the truing of arc diamond grinding wheel through three-axis coupling control, and pointing out it were significantly reduced that the arc error, radial runout error and radius fluctuation of the diamond grinding wheel after truing, especially the shape error of the processed aspheric lens was less than  $4\ \mu\text{m}$ . The traditional mechanical truing method has its advantages of simple process, mature technology and stable truing accuracy, but it as well has such defects as easy wear of truing tool, low truing efficiency, difficult tool measurement and compensation [8], moreover cause mechanical damage to diamond particles of grinding wheel. In order to solve the truing problem of metal bonded grinding wheels, Suzuki K applied electric discharge machining (EDM) [9] to the grinding field for the first time and proposed the

concept of electric discharge dressing (EDD) [10]. In principle, the discharge truing method is to take the machining tool as the negative pole while the workpiece as the positive pole, and make use of momentary and localized high temperature produced by the discharge between the two electrodes, which causes the fusion or evaporation of the metal bond of the grinding wheel, thus forming overlapping discharge pits on the surface of the grinding wheel to achieve the function of binding agent removal. As EDD avoids the vibration phenomenon that the traditional mechanical contact truing process, which greatly improves the truing accuracy and the integrity of grinding wheel grains [11]. Electrolytic in-process (ELID) truing [12] can effectively solve the sharpening problem of metal bond grinding wheel. According to its principle, adding an electrolyte between the electrode and the trued grinding wheel to make it dissolve under the action of electric current, at the same time, it produces a layer of oxide film on the surface of the grinding wheel to avoid its transition reaction. In the truing process, ELID can produce the truing amount that it is suitable for the wear of the grinding wheel in time to maintain a good grinding performance of it [13, 14]. Wu et al. [15] used ELID to make the dull abrasive particles fall off so timely that the grinding wheel always keeps its sharpness. Both ELID and EDD can be a solution to deal with the problem of metal bonded grinding wheel truing, but they requires the processing object is conductive material when using these two truing methods, and they cannot achieve the precision truing of the coarse-grained super-abrasive grinding wheels, need to be equipped with special power, the maintenance equipment is expensive as well [16]. In addition, the dielectric fluids and electrolytes will cause the problems of environmental contamination and equipment corrosion [17, 18]. For the shortcomings of traditional mechanical truing method and electrolytic truing method, Wang [19] proposed a new truing method, namely dry non-contact discharge assisted truing method, which can achieve high truing efficiency and good truing quality, but it has the disadvantages of poor multi-controllability and high processing cost due to the need to adjust discharge gap for many times in non-contact mode.

In view of various problems existed in the grinding wheel truing method mentioned above, an environmentally friendly and pollution-free dry electrical contact discharge (ECD) truing method [20, 21] is adopted in this chapter. Therefore, the ECD truing process was developed to achieve high efficiency and accuracy in grinding diamond V-tip. There is no need to take cutting fluid or waste liquid discharge and require expensive discharge gap control equipment because of the contact characteristics of it. Dry ECD truing not only allows the fine diamond abrasive grains to protrude without damaging the metal bond of the wheel, but also removes the bond tail behind the protruding abrasive grains. By adjusting discharge parameters, the angle and radius of V-shaped tip under different pulse discharge parameters were analyzed to achieve the highest shape accuracy. In order to test the effectiveness of V-shaped tip truing, micro-grinding experiments were carried out with cemented carbide materials, meanwhile, the grinding performance of trued diamond wheel was verified by observing the ground surface topography.



**Fig. 1** Dry electro-contact discharge (ECD) truing and micro-grinding of V-tip diamond grinding wheel: **a** image of V-tip truing and **b** micro-grinding photo of trued V-tip diamond wheel

## 2 V-tip Truing of #600 Diamond Grinding Wheel Using Dry ECD

### 2.1 Experimental Setup of Dry ECD for #600 Diamond Grinding Wheel

The V-tip diamond wheel was used for grinding micro microcrystallite glass ceramics and SiC reinforced Al (Al/SiCp) composites. Micro-grinding machining technology were applied to create the micro-groove array structures and micro-pyramid array structures on the surfaces of these three materials. Figure 1b shows a picture of the micro-grinding with SD600 V-tip diamond wheel. The depth and space of the processed V-groove was  $500\ \mu\text{m}$  and  $570\ \mu\text{m}$ , respectively. The detailed micro-grinding machining conditions of the SD600 diamond inserts were shown in Tables 1 and 2.

### 2.2 Results and Discussions

As shown in Fig. 2, the state of the protruding part of the micro grain. on the V-side surface of the diamond wheel were in very good condition. However, the micro tip of grinding wheel was dull. This is due to the excessive truing time of the ECD diamond wheels. There were a great number of protrusive diamond grains on the surface of the metal bond. As a result, V-shape tip on diamond grinding wheel can be produced during when ECD truing. A sharp micro-grain cutting edge was created on the surface



**Table 1** The ECD truing conditions of SD600 diamond grinding wheel V-tip

CNC grinder	SMART B818
Diamond grinding wheel	SD600, metal bond, diameter $D = 160$ mm, width $B = 2$ mm
Tool truing path	Crossed V-shape interpolation path
Truing electrode	Hybrid electrode of Cu and SiC (#600); Size: $20 \times 50 \times 15$ mm
Discharge parameters	Pulse power supply, open-circuit voltage $E = 10 \sim 25$ V, pulse frequency $f = 1000 \sim 5000$ Hz, duty cycle $dc = 10 \sim 50\%$
Truing parameters	Wheel speed $v_w = 12.6 \sim 20.9$ m/s, feed speed $vf = 200 \sim 500$ mm/min, depth of cut $a = 1 \sim 10$ $\mu\text{m}$ , cumulative feed depth $a = 0.05 \sim 0.1$ mm
Coolant	No

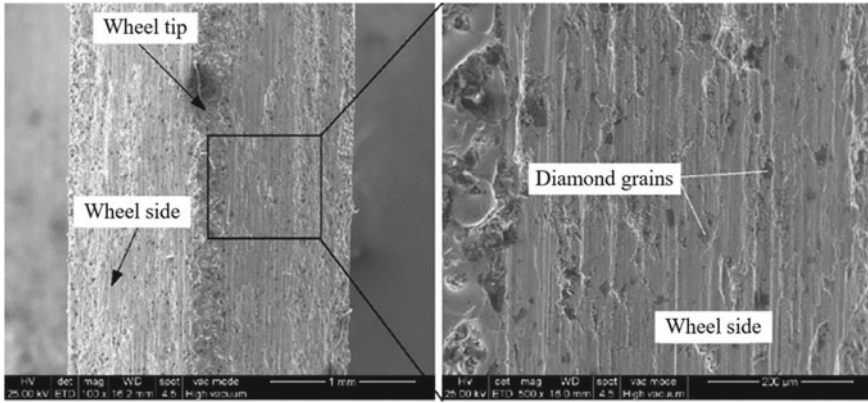
**Table 2** Micro-grinding machining conditions of SD600 diamond grinding wheel

CNC grinder	SMART B818
Diamond grinding wheel	SD600, metal bond, diameter $D = 160$ mm, width $B = 2$ mm, wheel speed $v_w = 25.1$ m/s
Tool path	Horizontal reciprocating and crossed interpolation path
Rough machining	Feed speed $v_f = 600$ mm/min, depth of cut $a = 10$ $\mu\text{m}$ , cumulative feed depth $a = 490$ $\mu\text{m}$
Finish machining	Feed speed $v_f = 300$ mm/min, depth of cut $a = 2$ $\mu\text{m}$ , cumulative feed depth $a = 10$ $\mu\text{m}$
Workpieces	Microcrystallite glass ceramics ( $30 \times 15$ mm); SiC reinforced Al (Al/SiCp) composites ( $10 \times 10$ mm)
Coolant	Water

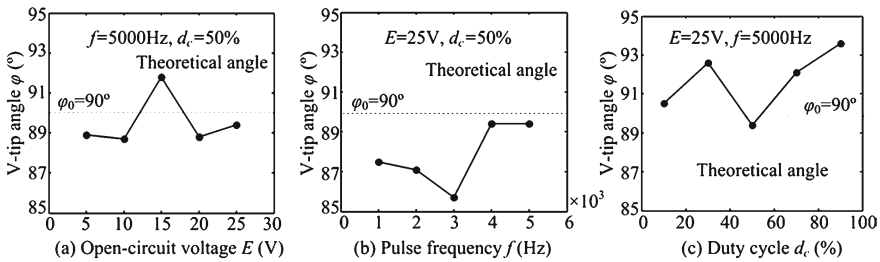
of the grinding wheel in the V-cut direction. Diamond grinding wheels with a trued V-tip can be used for micro-grinding of machining hard and brittle materials.

Figure 3 shows the effect of different pulse field parameters on V-tip angle  $\varphi$  of SD600 diamond grinding wheel. The matching V-tip angle  $\varphi$  were  $88.9^\circ$  and  $89.4^\circ$  for open-circuit voltages  $E$  of 5 V and 25 V, respectively. Compared to the setting theoretical angle of  $90^\circ$ , the errors of angles V-tip were only  $1.1^\circ$  and  $0.6^\circ$  (see Fig. 3a). As the pulse frequency  $f$  increases. the maximum angle  $\varphi$  of V first gradually decreases and then increases (see Fig. 3b), this is caused by arc discharge while excessive truing on the V-tip on the surface of the diamond grinding wheel. At pulse frequencies  $f$  of 4000–5000 Hz and duty cycle  $dc$  of 50%, the V-tip angle error realized a minimum value of  $0.6^\circ$  (see Fig. 3c).

Figure 4 shows the effect of different pulse discharge parameters on V-tip radius  $r_v$  of SD600 diamond grinding wheel. The V-tip radius  $r_v$  increases as the open-circuit voltage  $E$  increases (see Fig. 4a). When the open-circuit voltage  $E$  was 5 V, the trued V-tip radius of diamond wheel reached a minimum value of 33  $\mu\text{m}$ . The V-tip radius  $r_v$  was 44  $\mu\text{m}$  and 78  $\mu\text{m}$  respectively when the pulse frequency  $f$  is 4000 Hz and 5000 Hz (see Fig. 4b). Due to the inhomogenous electrical spark discharge caused



**Fig. 2** V-shape tip and its protrusion topographies of SD600 diamond wheel after dry ECD truing

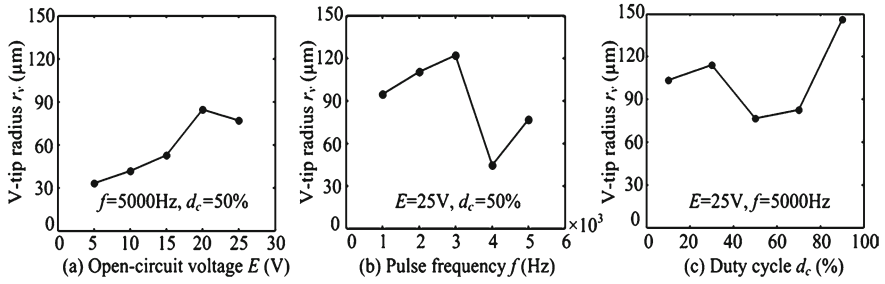


**Fig. 3** The V-tip angles  $\phi$  of SD600 diamond grinding wheel versus different pulse discharge parameters: **a** open-circuit voltage  $E$ , **b** pulse frequency  $f$  and **c** duty cycle  $dc$

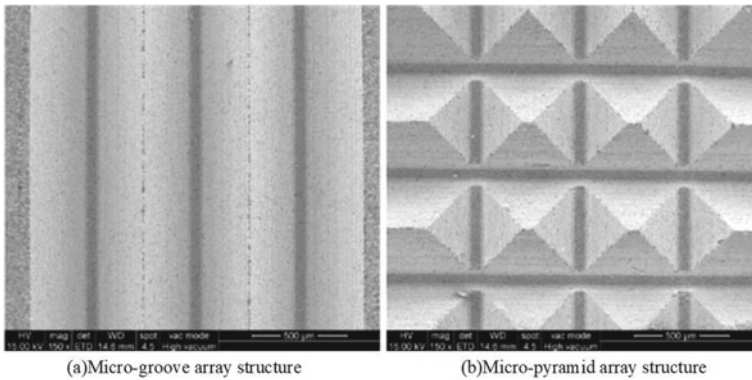
by large and little duty cycle, the V-tip radius  $r_v$  first decreased gradually and then boosted with the increase of duty cycle  $dc$  (see Fig. 4c). The peak radius  $V$  reaches a minimum value of  $78 \mu\text{m}$  when the duty cycle  $dc$  was 50%. As a result, at the optimal parameters of the pulse discharge ( $E = 5 \text{ V}$ ,  $f = 4000 \text{ Hz}$ ,  $dc = 50\%$ ), the minimum errors of V-tip angle and radius of SD600 diamond grinding wheel after ECD truing was  $1.1^\circ$  and  $33 \mu\text{m}$ , respectively.

Figure 5 shows the ground surface topography of microcrystallite glass ceramics after micro-grinding with the trued SD600 V-diamond grinding wheel. It can be concluded that after grinding, the surface of micro-groove and micro-pyramid structured surfaces were very smooth as well as the edges are undamaged. In addition, the V-tip shape at the ends of the micro-grooves and micro-pyramids spire was also very intact. However, the surface of microcrystallite glass ceramics contained many microscopic holes. This is due to the high fragility of microcrystalline glass ceramics.

Figure 6 shows the ground surface topography of SiC-reinforced Al composites (Al/SiCp) after micro-grinding with an SD600 V-tip diamond grinding wheel. In contrast to the surface of microcrystalline glass and reaction sintered SiC ceramics,



**Fig. 4** Shows the V-tip radius  $r_v$  of SD600 diamond grinding wheel versus different pulse discharge parameters: **a** open-circuit voltage  $E$ , **b** pulse frequency  $f$  and **c** duty cycle  $d_c$



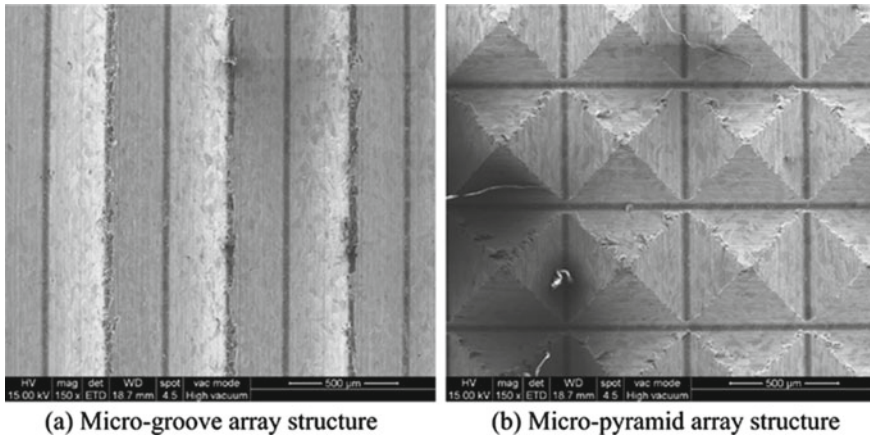
**Fig. 5** The ground surface topography of microcrystallite glass ceramics after micro-grinding: **a** micro-groove array structure and **b** micro-pyramid array structure

the SiC-reinforced Al composites had the worst surface machining quality. In addition, the crack of micro-groove tip was very severe, with several burrs at the edge of micro-pyramid. This is due to the fact that the aluminum substrate contained SiC particles. In the grinding process of Al/SiCp composites, collision or brittle rupture occurred very easily. This made the processing of Al/SiCp composites very difficult.

### 3 V-tip Truing of #1200 Diamond Grinding Wheel Using Dry ECD

#### 3.1 Experimental Setup

The experiments were performed on a CNC grinder (SMART-B818) in air, as shown in Fig. 7. The V-tip truing schematic diagram and setup of diamond grinding wheel

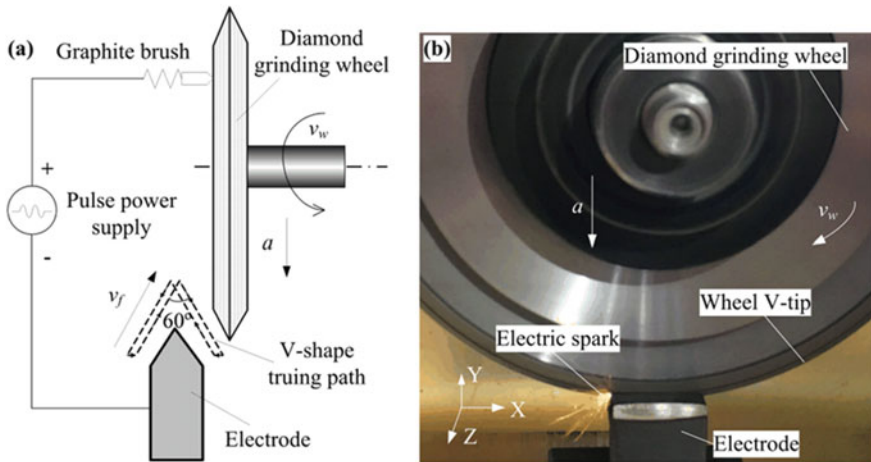


**Fig. 6** The ground surface topography of SiC reinforced Al composites after micro-grinding: **a** micro-groove array structure and **b** micro-pyramid array structure

based on dry electro-contact discharge (ECD), the pulse power supply was linked between hybrid electrode (Cu and SiC) and metal-bonded diamond grinding wheel through conductive graphite brush (see Fig. 7a), and the cut machining along with electrical spark discharge was produced when the rotating grinding wheel was driven to grind electrode along a defined V-shape truing path, gradually, the V-shape tip of diamond grinding wheel was produced (see Fig. 7b). After truing and forming the V-shape tip of diamond grinding wheel, the precision truing experiments of SD1200 diamond grinding wheel using dry ECD were conducted by changing the pulse discharge parameters, including open-circuit voltage  $E$ , pulse frequency  $f$  and duty cycle  $dc$  derived from pulse power supply. Certain discharge energy levels were considered by adjusting the pulsed discharge parameters to explore their effect on material removal modes, as described in Table 3. They were shown in Table 1 that the detail dry ECD truing conditions of SD1200 diamond grinding wheel V-tip. Table 3

### 3.2 Experimental of Dry Micro-grinding

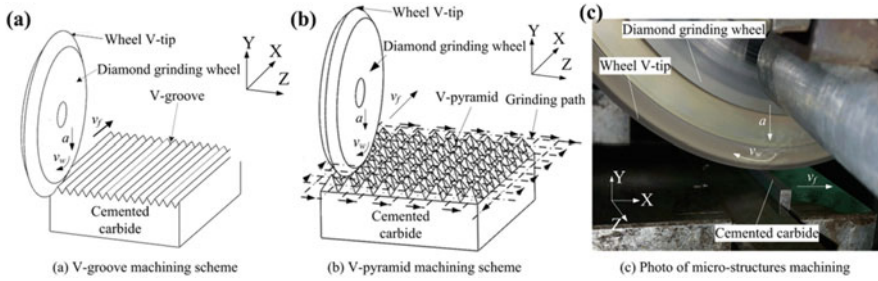
Using trued diamond grinding wheel for experimental of dry micro-grinding on the surfaces of cemented carbide, as Fig. 8 shows dry micro-grinding machining schemes and photo of cemented carbide using trued V-tip diamond grinding wheel. The trued diamond grinding wheel with V-tip was employed to process micro-groove and micro-pyramid array structures on the surfaces of cemented carbide using micro-grinding machining technology (see Fig. 8a, b). The dry micro-grinding photo of cemented carbide without any coolant using trued SD1200 V-tip diamond wheel was shown in Fig. 8c, which uses 200  $\mu\text{m}$  as the ground V-groove depth of trued



**Fig. 7** Dry electro-contact discharge (ECD) truing of diamond grinding wheel V-tip: **a** V-tip truing scheme of diamond wheel and **b** V-tip truing image

**Table 3** The ECD truing conditions of SD1200 diamond grinding wheel V-tip

CNC grinder	SMART B818	
Diamond grinding wheel	SD1200, metal bond, diameter $D = 150$ mm, width $B = 2.5$ mm	
Tool truing path	Crossed V-shape interpolation path	
Truing electrode	Hybrid electrode of Cu and SiC (#1200); Size: $L \times B \times H = 20 \times 50 \times 15$ mm	
Discharge parameters	Pulse power supply, open-circuit voltage $E = 5 \sim 25$ V, pulse frequency $f = 1000 \sim 5000$ Hz, duty cycle $d_c = 10 \sim 80\%$	
Truing parameters	Wheel speed $v_w = 18.8$ m/s, feed speed $v_f = 200$ mm/min, depth of cut $a = 1 \mu\text{m}$	
Coolant	No	
Pulse discharge parameters	1	$E = 25$ V, $f = 5000$ Hz, $d_c = 50\%$
	2	$E = 15$ V, $f = 5000$ Hz, $d_c = 50\%$
	3	$E = 5$ V, $f = 5000$ Hz, $d_c = 50\%$
	4	$E = 25$ V, $f = 4000$ Hz, $d_c = 50\%$
	5	$E = 25$ V, $f = 1000$ Hz, $d_c = 50\%$
	6	$E = 25$ V, $f = 5000$ Hz, $d_c = 10\%$
	7	$E = 25$ V, $f = 5000$ Hz, $d_c = 80\%$



**Fig. 8** Dry micro-grinding machining schemes and photo of cemented carbide: **a** V-groove machining scheme, **b** V-pyramid machining scheme and **c** micro-grinding image

**Table 4** Dry micro-grinding conditions of cemented carbide using trued V-tip diamond grinding wheel

CNC grinder	SMART B818
Diamond grinding wheel	SD1200, metal bond, diameter $D = 150$ mm, width $B = 2.5$ mm; Wheel speed $v_w = 18.8$ m/s
Workpiece	Cemented carbide
Rough grinding	depth of cut $a = 5$ $\mu\text{m}$ , cumulative feed depth $\Sigma a = 190$ $\mu\text{m}$ ; feed speed $v_f = 50$ mm/min
Finish grinding	depth of cut $a = 1$ , cumulative feed depth $\Sigma a = 10$ $\mu\text{m}$ ; feed speed $v_f = 10$ mm/min
Coolant	No

V-tip diamond wheel. The detail micro-grinding machining conditions of SD1200 diamond grinding wheel were shown in, Tables 3 and 4.

### 3.3 Measurements

To obtain the V-tip profiles of trued diamond grinding wheel, the surface profiler (TALYSURF CLI 1000) and white light interferometer (WLI, BMT SMS Expert 3D) were used to measure the V-groove profiles by replicating the V-tip profile on the surface of the graphite plate, in the meanwhile, the surface topographies of trued diamond grinding wheel and ground cemented carbide workpieces were presented by scanning electron microscope (SEM, FEI Quanta 200) and 3D laser scanning microscope (VK-250, Keyence).

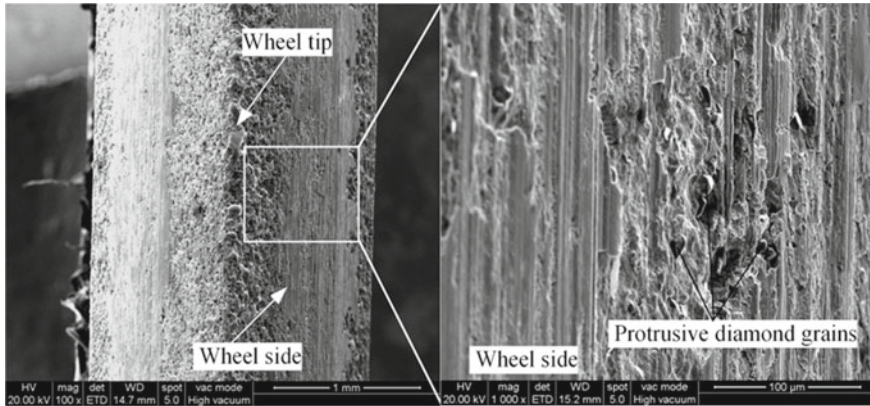


Fig. 9 SEM images of rough trued SD1200 V-tip diamond grinding wheel

### 3.4 Results and Discussions

#### 3.4.1 Morphology of Rough Trued Tip Diamond Grinding Wheel

Figure 9 shows the SEM photos of rough trued SD1200 V-tip diamond grinding wheel after dry ECD. It is shown that the micro tip of diamond grinding wheel was roughly trued into the V-shape with a large V-tip radius, which is caused by the uneven roundness of the grinding wheel, the cutting edges of diamond grains on the side of grinding wheel were protruded out of the metal bond, however, the scratch on the side of grinding wheel was relatively serious. It may be because that the short circuit occurred when processing electrical discharge truing, resulting in the mutual scratch between the silicon carbide particles derived from hybrid electrode and metal bond on the surface of grinding wheel.

#### 3.5 Morphology of Fine Trued Tip Diamond Grinding Wheel

As shown in Fig. 10, the SEM photos of fine trued SD1200 V-tip diamond grinding wheel after dry ECD is presented. In comparison with Fig. 9, as seen from Fig. 10, the V-shape tip of diamond grinding wheel become more sharp and the V-tip arc radius significantly decreased. Besides, due the micro-discharge can remove the metal binder around the abrasive particles, there is no binder tail, the wheel surface was relatively smooth and there were also many protrusive diamond micro-grains on the surface of the grinding wheel, which were beneficial for conducting precise micro-grinding machining.

As shown in Fig. 11, the section profiles of SD1200 diamond grinding wheel before and after truing forming is presented. As shown in Fig. 11a, the section contour

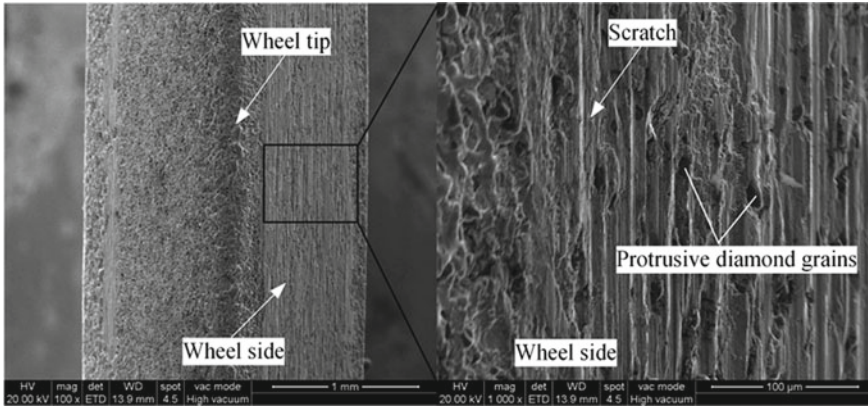


Fig. 10 SEM images of fine trued SD1200 V-tip diamond grinding wheel

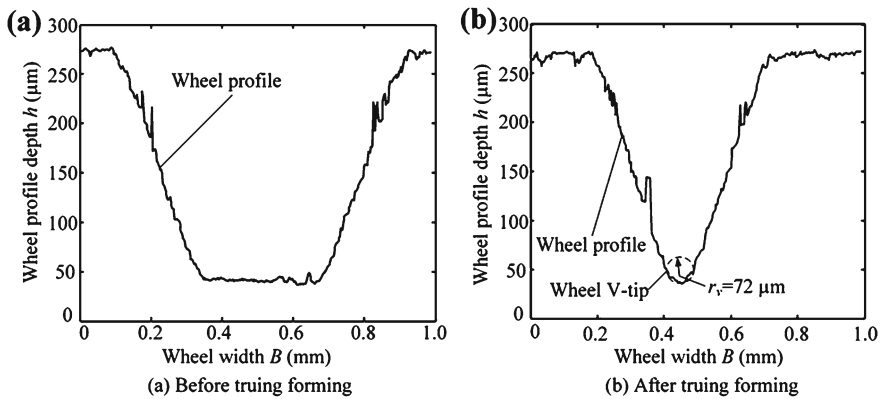


Fig. 11 The section profiles of SD1200 V-tip diamond grinding wheel before and after truing forming: **a** before truing forming and **b** after truing forming

of the diamond grinding wheel micro tip was trapezoidal before truing forming, while the V-shaped section contour of the diamond grinding wheel micro tip was presented after truing forming, and the V-tip radius  $r_v$  of the diamond grinding wheel was about 72 μm.

### 3.6 Influences of Impulse Discharge Parameters on V-tip Profiles of Diamond Grinding Wheel

Figure 12 shows the trued V tip profiles of SD1200 diamond grinding wheel under various pulse discharge parameters. It is shown that the V-tip contour shape



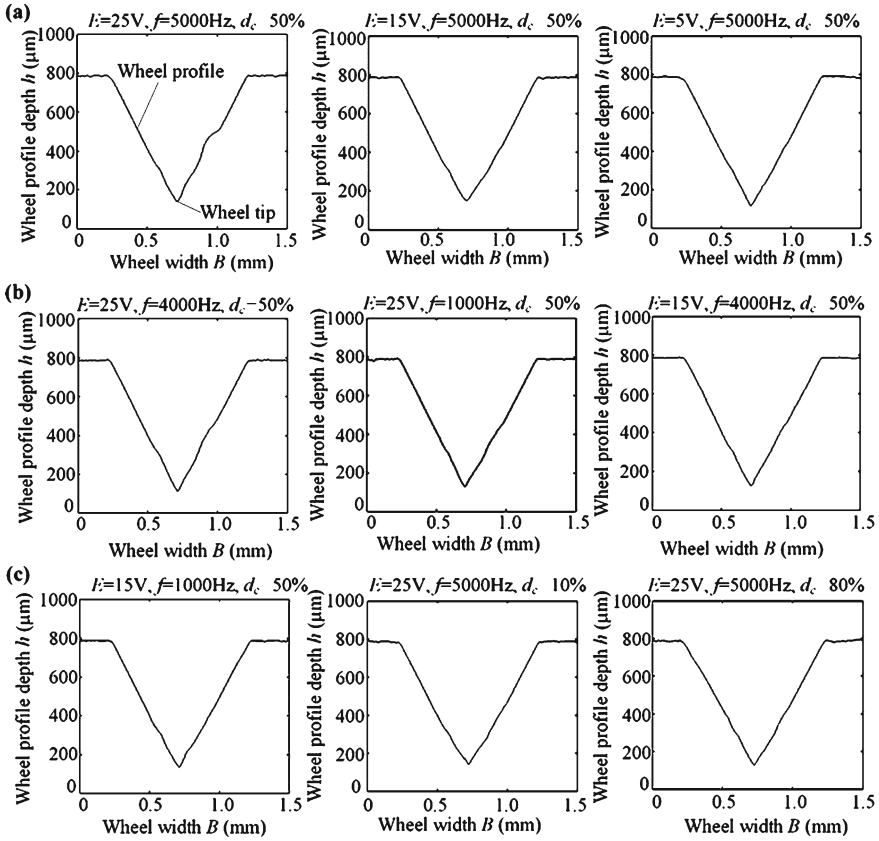
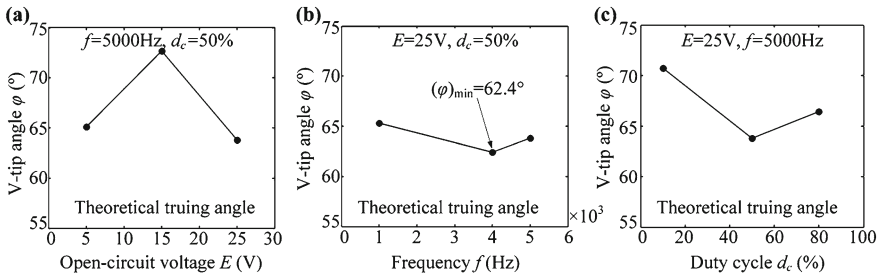


Fig. 12 The V-tip profiles of trued SD1200 diamond grinding wheel under different pulse discharge parameters: **a** open-circuit voltage  $E$ , **b** pulse frequency  $f$  and **c** duty cycle  $d_c$

of diamond grinding wheel after truing under various pulse discharge parameters conditions was basically similar, nonetheless the V-tip angle and V-tip radius were different.

### 3.7 Influences of Impulse Discharge Parameters on V-tip Angle of Diamond Grinding Wheel

Figure 13 shows the influences of impulse discharge parameters on V-tip angle of SD1200 diamond grinding wheel. As shown in Fig. 13a, with the rise of open-circuit voltage  $E$ , the V tip angle  $\varphi$  first increased and then decreases, when the open-circuit voltage  $E$  was 25 V, the trued V tip angle reached a minimum value of  $62.4^\circ$ , and with the increase of pulse frequency  $f$ , the V tip angle  $\varphi$  first decreased and then increased



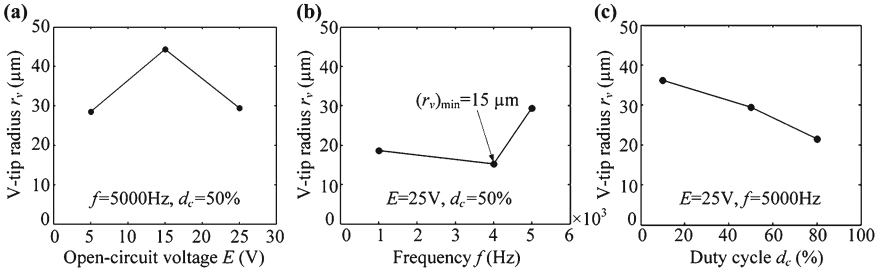
**Fig. 13** The V-tip angles  $\phi$  of trued SD1200 diamond grinding wheel under different pulse discharge parameters: **a** open-circuit voltage  $E$ , **b** pulse frequency  $f$  and **c** duty cycle  $d_c$

(see Fig. 13b). This is because Low frequency leads to low energy, and the main truing process is machine grinding, the wheel with V-tip would be easily burned in high impulse discharge power and high pulse frequency. Either too high or too low discharge frequency increases the tip angle to some extent. In the other hand, when frequency  $f$  was 4000 Hz, the trued V tip angle also realized the minimum value of  $62.4^\circ$ , and with the increase of duty cycle  $d_c$ , the V tip angle  $\phi$  first decreased and then increased (see Fig. 13c)., when duty cycle  $d_c$  was 50%, the trued V tip angle also reached the minimum value of  $62.4^\circ$ . This is because when the duty cycle is small or large, it will lead to uneven discharge. In contrast with the theoretical V-tip angle of  $60^\circ$  according to the setting truing path, the angle error of the trued V-tip was  $2.4^\circ$ .

### 3.8 Influences of Impulse Discharge Parameters on V-tip Radius of Diamond Grinding Wheel

As shown in Fig. 14, the influences of pulse discharge parameters on the V-tip radius  $r_v$  of trued SD1200 diamond grinding wheel is presented. With the increase of open-circuit voltage  $E$ , the V-tip radius  $r_v$  first increased and then decreased (see Fig. 14a). As the open-circuit voltage  $E$  were 5 V and 25 V, the trued V-tip radius  $r_v$  were  $28\ \mu\text{m}$  and  $29\ \mu\text{m}$ , respectively. With the increase of pulse frequency  $f$ , V-tip radius  $r_v$  first decreased and then increased (see Fig. 14b).

When pulse frequency  $f$  was 4000 Hz, the trued V-tip radius  $r_v$  realized a minimum value of  $15\ \mu\text{m}$ . The V-tip radius  $r_v$  decreased with the increase of duty cycle  $d_c$  (see Fig. 14c), this is because the larger duty cycle was, the longer pulse discharge duration time and micro spark discharge time were and more fully dressed the grinding wheel is. When duty cycle  $d_c$  was 80%, the trued V-tip radius  $r_v$  reached a minimum value of  $21\ \mu\text{m}$ . However, too large duty cycle will cause the angle of V-tip to become larger. Therefore, in the V-tip truing process of SD1200 diamond grinding wheel, the better pulse discharge parameters including open-circuit voltage  $E$ , pulse frequency  $f$  and duty cycle  $d_c$  were 25 V, 4000 Hz and 50%, respectively, under the optimal pulse discharge parameters, namely, the open-circuit voltage  $E$  of 25 V, pulse frequency  $f$



**Fig. 14** The V-tip radius  $r_v$  of trued SD1200 diamond grinding wheel under different pulse discharge parameters: **a** open-circuit voltage  $E$ , **b** pulse frequency  $f$  and **c** duty cycle  $d_c$

of 4000 Hz and duty cycle  $d_c$  of 50%, the minimum V-tip radius of trued SD1200 diamond grinding wheel was 15  $\mu\text{m}$ .

### 3.9 Micro-topography and Form-Accuracy of Ground Micro-structured Cemented Carbide Surface

Figure 15 shows the V-groove morphologies of micro-ground cemented carbide before and after the V-tip truing forming of SD1200 diamond grinding wheel. The section contour of diamond grinding wheel was trapezoidal before V-tip truing forming, therefore, the section contour of micro-ground V-groove was also trapezoidal and the trued angle was  $121^\circ$  (see Fig. 15a), and in contrast with the theoretical truing angle of  $120^\circ$ , the angle error was only  $1^\circ$ . After the V-tip truing forming, the section contour of diamond grinding wheel was V-shaped so that the section contour of micro-ground V-groove was also V-shaped. The measured V-tip angle  $\varphi$  and V-tip radius  $r_v$  was  $64.2^\circ$  and  $78 \mu\text{m}$ , respectively, then compared with the theoretical V-groove angle of  $60^\circ$ , the micro-ground V-tip angle error was  $4.2^\circ$ . Since the V-tip arc radius of grinding wheel section contour before machining cemented carbide was  $72 \mu\text{m}$ , it indicates that the V-tip of grinding wheel was worn.

Figure 16 shows the surface morphologies of micro-ground cemented carbide. As shown in Fig. 16, the tip and bottom of V-groove can be clearly seen. The bottom of V-groove had a tiny arc, which indicates that the grinding wheel tip was worn in the grinding process of cemented carbide.

Figure 17 shows the V-groove profile on the cemented carbide surface. From the figure, it can be observed that the minimum error between the groove depth and the theoretical depth of  $200 \mu\text{m}$  is only  $2.6 \mu\text{m}$ , and the maximum depth error is  $11.7 \mu\text{m}$ . Compared with the grinding wheel tip radius of  $15 \mu\text{m}$ , the minimum error of the bottom arc radius is  $3.2 \mu\text{m}$ , and the maximum error is  $7.3 \mu\text{m}$ . As the grinding progresses, the error of the bottom arc radius of the groove gradually increases, which indicates that the grinding wheel tip is worn and the V groove is worn. The difference between the groove angle and the theoretical angle of  $60^\circ$  is

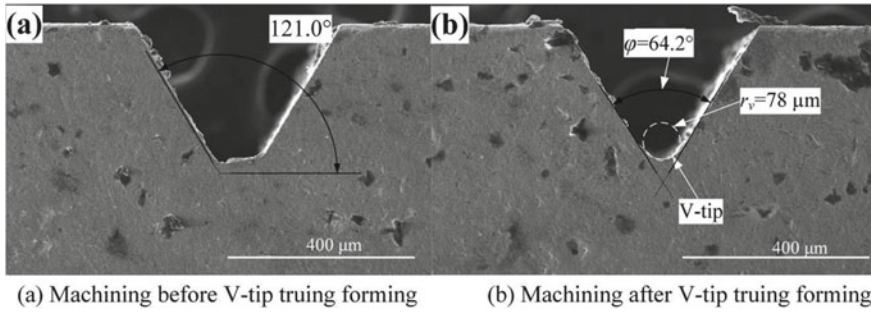


Fig. 15 SEM photos of micro-ground V-groove on the surfaces of cemented carbide before and after V-tip truing forming: **a** before V-tip truing forming and **b** after V-tip truing forming

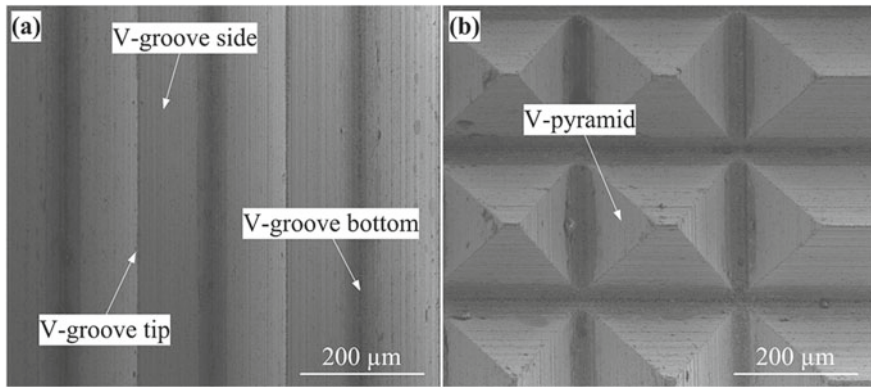
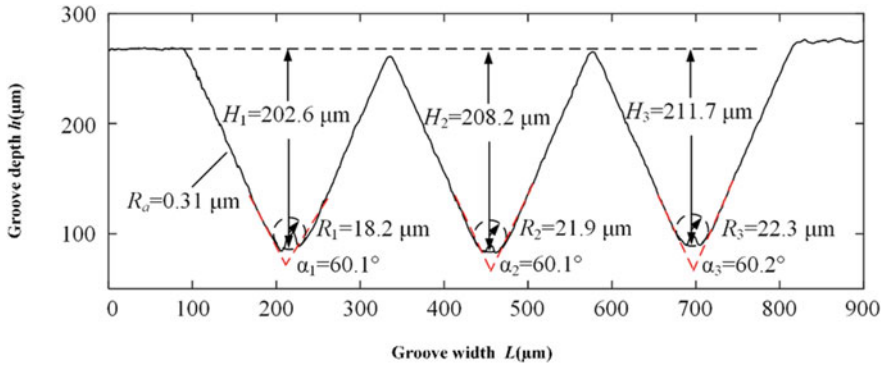


Fig. 16 SEM photos of micro-ground micro-structured cemented carbide surface: **a** V-grooved array structures surface and **b** V-pyramid array structures surface

very small, indicating that grinding in the plastic domain of the micro-structure of the cemented carbide surface can ensure a better shape error.

### 4 Conclusions

The ECD dry truing method can achieve the V-tip truing of diamond with high efficient and precise. The pulse field parameters were optimized in repeated V-tip truing test. The optimal parameters for pulse trimming were open-circuit voltage of 5 V, pulse frequency of 4000 Hz and duty cycle of 50%. After ECD cutting, sharp micro grain cutting edges were formed on the surface of the wheel. The minimum V-tip angle error and radius of trued SD600 V-tip diamond grinding wheel reached 1.1° and 33 μm, respectively. The trued V-tip diamond wheel can be used to fabricate regular and smooth micro-groove and micro-pyramid array structures on the surfaces



**Fig. 17** Cemented carbide surface V-groove profile curve

of hard and brittle materials such as microcrystalline glass ceramics and Al/SiCp composites.

The truing technology of grinding wheel V-tip with dry contact discharge (ECD) is put forward in this chapter, the influence of pulse discharge parameters on the truing effect of metal base grinding wheel tip is studied to achieve efficient and precise truing of grinding wheel, whose conclusion is of guiding significance to the truing process optimization of diamond grinding wheel used in cemented carbide microstructure manufacturing. The specific conclusions are shown as follows:

- (1) The ECD truing technology, which can settle several issues concerning low truing efficiency of metal fund diamond grinding wheel, uncertainty of accuracy and special structure truing requirements, to obtain diamond grinding wheel with good cutting edge effect and high shape accuracy.
- (2) The precise truing of V tip of #1200 diamond grinding wheel can be achieved by applying ECD technology, whose optimal truing pulse discharge parameters are  $E = 25$  V,  $f = 4000$  Hz,  $d_c = 50\%$ . Under those parameters it can realize the minimum radius of arc of grinding wheel tip after truing and the minimum angle error of grinding wheel tip, which are  $15 \mu\text{m}$  and  $2.4^\circ$  respectively.
- (3) It is beneficial to realize plastic domain machining of hard alloy surface microstructure, obtain surface microstructure with high shape precision and low error and high surface quality by adapting diamond grinding wheel with good cutting edge effect. The minimum error of groove depth and the minimum error of bottom arc radius are respectively  $2.6 \mu\text{m}$ ,  $3.2 \mu\text{m}$ , additionally the average roughness of groove side is  $0.31 \mu\text{m}$  as the results show.

**Acknowledgements** The work described in this chapter was supported by the National Natural Science Foundation of China (Grant No. 51805334), the China Postdoctoral Science Foundation [Grant No. 2016M602460], the Science and Technology Planning Project of Guangdong Province [Grant Nos. 2016A040403043 and 2017A010102003] and the International Science and Technology Cooperation Project of Shenzhen City (Grant No. GJHZ20190822091805371).

## References

1. Egashira K, Hosono S, Takemoto S, Masao Y (2011) Fabrication and cutting performance of cemented tungsten carbide micro-cutting tools. *Precis Eng* 35:547–553
2. Zhao QL, Guo B (2011) Ultraprecision grinding technology of microstructured optical functional molds. *J Mech Eng* 47:177–185
3. Zheng G, Lin Y (2021) Tribological properties of micro-groove cemented carbide by laser processing. *Micromachines* 12:486
4. Tan JH, Wong WLE, Dalgarno KW (2017) An overview of powder granulometry on feedstock and part performance in the selective laser melting process. *Addit Manuf* 18:228–255
5. Lian Y, Mu C, Xie C, Yao B (2019) Experimental investigation of inductively coupled plasma etching on cemented carbides. *Vacuum* 162:101–109
6. Deng H, Xu Z (2019) Dressing methods of superabrasive grinding wheels: a review. *J Manuf Process* 45:46–69
7. Zhou L, Wei Q, Zheng N et al (2019) Dressing technology of arc diamond wheel by roll abrading in aspheric parallel grinding. *Int J Adv Manufact Technol* 105:2699–2706
8. Chen B, Guo B, Zhao Q (2018) Online monitoring of truing arc-shaped diamond wheel by acoustic emission signal. *Proc Inst Mech Eng Part B J Eng Manufact* 232:1484–1490
9. Wang X, Ying B, Liu W (1996) EDM dressing of fine grain super abrasive grinding wheel. *J Mater Process Technol* 62:299–302
10. Yu J, He L, Huang S et al (2015) State-of-the-art of electrical discharge dressing technology for superabrasive grinding wheel. *China Mech Eng* 26:2254
11. Zhang FH, Kang GW, Yang YS et al (2006) EDM dressing for metal-bond super hard arc-forming wheel. In: *Key Engineering Materials*. Trans Tech Publ, pp 99–103
12. Kuai J, Zhang H (2019) Research on generation and polishing mechanisms of nano grain  $\alpha$ -Fe<sub>2</sub>O<sub>3</sub> in precision electrolytic in process dressing (ELID) grinding. *Proc Manufact* 37:425–430
13. Mao C, Zhou F, Hu Y et al (2019) Tribological behavior of cBN-WC-10Co composites for dry reciprocating sliding wear. *Ceram Int* 45:6447–6458
14. Mao C, Lu J, Zhao Z et al (2018) Simulation and experiment of cutting characteristics for single cBN-WC-10Co fiber. *Precis Eng* 52:170–182
15. Wu Q, Ouyang Z, Wang Y et al (2019) Precision grinding of engineering ceramic based on the electrolytic dressing of a multi-layer brazed diamond wheel. *Diam Relat Mater* 100:107552
16. Xxx DH, Xu Z (2019) Dressing methods of superabrasive grinding wheels: A review. *J Manuf Process* 45:46–69
17. Wu Q, Wang Y, Qu W, Deng Z (2017) Research status and perspectives of ELID grinding fluid. *China Mech Eng* 28:1118
18. Wegener K, Hoffmeister H-W, Karpuschewski B et al (2011) Conditioning and monitoring of grinding wheels. *CIRP Ann* 60:757–777
19. Wang Y, Zhou X, Hu D (2006) An experimental investigation of dry-electrical discharge assisted truing and dressing of metal bonded diamond wheel. *Int J Mach Tools Manuf* 46:333–342
20. Lu YJ, Li LJ, Xie J, et al (2017) Dry electrical discharge dressing and truing of diamond grinding wheel V-tip for micro-grinding. In: *2017 5th International conference on mechatronics, materials, chemistry and computer engineering (ICMMCCE 2017)*. Atlantis Press, pp 548–552
21. He Q, Xie J, Lu K, Yang H (2020) Study on in-air electro-contact discharge (ECD) truncating of coarse diamond grinding wheel for the dry smooth grinding of hardened steel. *J Mater Process Technol* 276:116402

# Chapter 15

## Precision Grinding of Micro-structures of Hard-Brittle Material Surfaces



Yanjun Lu, Yuming Huang, Haojun Huang, and Long Zhang

**Abstract** In this chapter, in view of the low processing efficiency and accuracy of hard-brittle material, a precision-trued V-tip diamond grinding wheel is proposed as the means to fabricate regular micro array structures with high surface quality and controllable form accuracy on the surfaces of those difficult-to-machine materials. First, a V-shaped tip diamond grinding wheel with sharp micro-grain cutting edges was obtained by mechanical truing along V-shaped cross interpolation trajectories. Four typical hard-brittle ceramics and ceramic-matrix composite materials including monocrystalline silicon carbide, aluminum-based silicon carbide, reaction sintered silicon carbide, glass ceramics were selected as the workpiece materials. The trued V-tip diamond grinding wheel was employed to machine the micro-groove and micro-pyramid array structures on the surfaces of ceramics and ceramic-matrix composite materials. Finally, the micro-ground surface and 3D topographies, micro-groove profile, tip arc radius, tip angle and form accuracy were analyzed and investigated for four different materials. The experimental results show that the arc radius at the bottom of micro-groove on the surface of monocrystalline silicon carbide, aluminum-based silicon carbide, sintered silicon carbide and three kinds of silicon-carbide ceramics is close to  $21\ \mu\text{m}$  while the difference is less than  $1\ \mu\text{m}$ , the difference between the tip angle and the theoretical angle of  $60^\circ$  is less than  $1^\circ$ , and the shape-accuracy error can be controlled within  $15\ \mu\text{m}$ . It can be seen that micro-grinding hard-brittle material such as ceramics and ceramic-matrix composite can ensure high machining accuracy.

---

Y. Lu (✉) · Y. Huang · H. Huang

Shenzhen Key Laboratory of High Performance Nontraditional Manufacturing, College of Mechatronics and Control Engineering, Shenzhen University, Nan-Hai Ave 3688, Shenzhen 518060, Guangdong, PR China  
e-mail: [luyanjun@szu.edu.cn](mailto:luyanjun@szu.edu.cn)

L. Zhang

State Key Laboratory of Mechanical System and Vibration, School of Mechanical Engineering, Shanghai Jiao Tong University, 800 Dongchuan RD. Minhang District, Shanghai 200240, PR China

## 1 Introduction

The high mechanical strength, fracture toughness, elastic modulus, low thermal expansion, and many other advantages of structural ceramic that as a kind of hard-brittle material, as well as its excellent mechanical properties and excellent corrosion resistance and high temperature resistance merit thorough consideration. Ceramic and its composite matrix materials with special micro-structure have very important application value and extremely broad application prospect in the fields of photoelectric imaging, optical fiber communication, information processing, biomedicine, fuel cell and microelectronic packaging due to their excellent chemical, physical, optical and mechanical properties [1, 2]. Single crystal silicon carbide is used as a semiconductor support material and conductive material, as well as be commonly used in the semiconductor field to manufacture high-frequency, high-temperature, high-power devices and optoelectronic power devices [3]. Aluminum-based silicon carbide and aluminum-based composite materials have been widely used in the field of aerospace, as well as components such as fighter jet fins and aero-engine guide blades [4]. Reaction sintered SiC is used to manufacture SiC micro-rotors with diameters of 5 and 10 mm for micromachining gas turbines [5]. Kyocera uses glass ceramics as the substrate for electronic component installation and the wiring board for built-in capacitors [6]. With the wide application of functional structural ceramics, the importance of its machining accuracy and efficiency is increasingly prominent. However, due to the hardness and brittleness of ceramic materials themselves, cracks and edge breakage are easy to occur in the processing process [7], which has a great impact on the processing cost, service performance and effective life, and restricts the wide application of ceramic materials [8, 9].

More common micromachining methods such as micro-turning [10], micro-milling, micro-EDM [11] (Electrical Discharge Machining), laser micro-machining, 3D printing and special composite machining [12, 13]. Liu et al. [14] used micro-milling to process lime glass, analyzed the micro-milling mechanism of glass materials, and obtained critical brittle and ductile transition conditions taking into account the size effect. Plastic machining of lime glass was achieved by changing machining parameters and tool parameters to obtain microstructure with good surface quality. However, the efficiency of this method is low on the premise of guaranteeing the machining quality. Grigor'ev [15, 16] used EDM to process small diameter holes on the surface of high density ceramic materials. The effect of EDM on the precision of small diameter holes of high density ceramic parts was studied. The results showed that high pulse frequency and pulse width would increase the size error and shape deviation of micro holes. Some scholars [17, 18] use laser machining technology in ceramic cutting tool surface micro-structure, determination of micro-structure of ceramic cutting tool abrasion curve and hardness, found that after laser processing ceramic cutting tool hardness is markedly reduced, wear resistance curve has obvious improvement, visible laser processing can effectively improve wear resistance of ceramic cutting tool and quality stability, However, the thermal stress in laser processing can easily crack the ceramic. Zhang et al. [19] developed two



processing methods of laser composite irradiation, and successfully processed crack-free microstructure on the surface of silicon nitride ceramics. Johannes [20] used 3D printing technology to print ceramic parts with hexagonal honeycomb structure. The part exhibits extremely high specific strength under compression load, and the density of ceramic parts is reduced by about 2–3 times without losing mechanical strength. Zhai et al. [21] investigated the effect of laser-assisted turning and conventional turning on the machining properties of 2024 aluminum matrix composites reinforced by 45% sic particles (45 vol.% SiCp/2024A1). The experimental results showed that, under the same cutting parameters, The surface roughness value after laser-assisted turning is reduced by 81.73%, which can produce more residual compressive stress, and no microcracks appear on the workpiece surface after processing. Wu et al. [22] used square micro-structured diamond grinding wheel to grind the surface of WC ceramics and BK7 optical glass, and produced a square micro-structure with a depth of 150  $\mu\text{m}$ , an edge radius of 5.9  $\mu\text{m}$  and a side wall inclination Angle of 4.8°. Heungkil et al. [23] prepared microdiamond grinding head by electroless Ni–P process, and processed square micro-structure on silicon surface under the process parameters of 2.4 mm/min feed rate and 11.3 m/min grinding rate. It was found that the edge of the micro-structure did not collapse, and the edge sharpness was maintained well. The channel has good surface quality and morphology. It can be seen that grinding can realize the machining of micron-level microstructure of ceramics and other materials, and can obtain relatively ideal surface microstructure. However, there are few reports about the machining of V-shaped array microstructure on ceramic surface and the dressing technology of V-shaped tip grinding wheel. Few scholars have reported the shape accuracy and structural parameter error rate of the surface microstructure of the same ceramic material.

In this chapter, micro-grinding technology is introduced to fabricate microarray grooves and microarray cones on the surface of ceramic and ceramic composite materials. After truing and dressing, the diamond grinding wheel with good cutting edge effect can easily process ceramics and ceramic composite materials in plastic domain under lower grinding depth and appropriate grinding parameters, and obtain surface microarray structure with lower roughness and excellent shape precision [24, 25]. This article will from the tip modification and ceramic grinding wheel V-groove structure processing part two experiments, and then to the grinding wheel surface topography and ceramic workpiece surface topography, etc. The results were analyzed, and the observation of material removal mechanism in the process of fine grinding, study the tip Angle of four kinds of materials and cutting-edge arc radius parameters and the theory of error rate, The superiority of micro grinding technology in ceramic microstructure machining was demonstrated.

## 2 Experimental

The precision dressing of diamond grinding wheel is the key point in the high value-added precision micro-grinding process. For the diamond grinding wheel with metal bonding agent, the SD600 diamond grinding wheel with precision dressing and V-shaped tip is used to process the micro-groove structure on the surfaces of four materials, namely monocrystalline silicon-carbide ceramic, aluminum-based silicon carbide, reactive sintered silicon carbide and microcrystalline ceramics. The angles and tip radius of the four materials were compared.

### 2.1 V-Tip-Dressing Experiment of Grinding Wheel

Figure 1 shows the mechanical dressing path of the V-tip of diamond grinding wheel. The V-tip numerical control grinding dressing technology of diamond grinding wheel is used. The diamond grinding wheel follows the V-tip CNC interpolation track, and the V-tip cross angle is 60 degrees. The diamond grinding wheel continuously feeds vertically downward at feed depth until the grinding wheel tip is trued into a V-tip. The mechanical dressing process conditions of the V-tip of the SD600 diamond grinding wheel are shown in Table 1. The picture of mechanical CNC dressing of the SD600 diamond grinding wheel is shown in Fig. 1a.

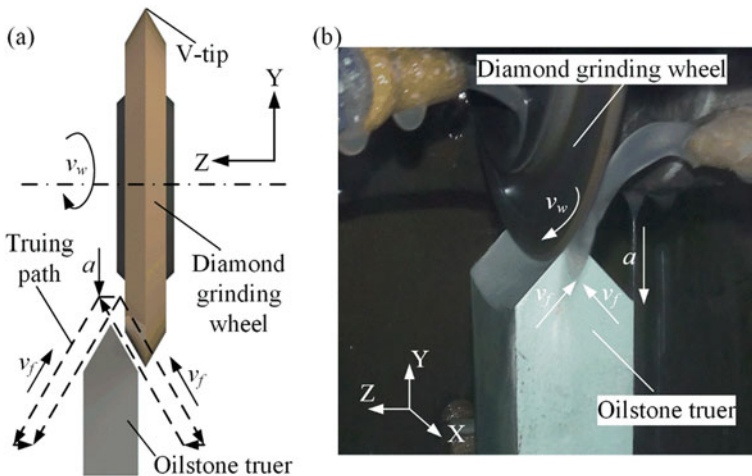


Fig. 1 Photos and schematic diagram of grinding wheel using mechanical dressing

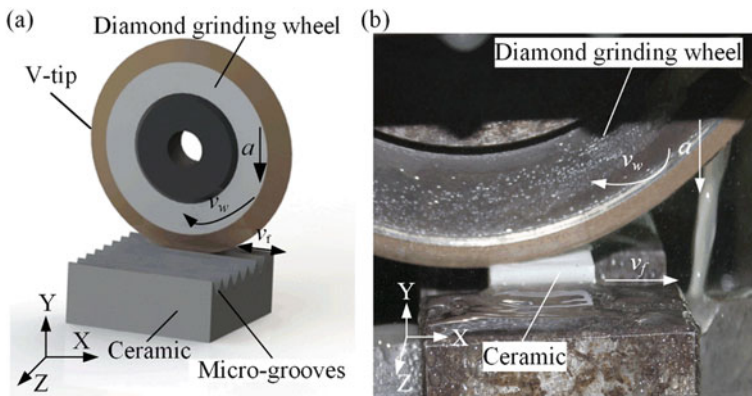
**Table 1** Mechanical dressing process conditions of V-tip of SD600 diamond grinding wheel

CNC grinding machine	SMART B818
Diamond wheel	SD600 Diamond wheel, Metal binder; D = 160 mm; B = 2 mm
Cutting tool path	V-shaped CNC interpolation trajectory
Dressing parameters	$N = 1500 \sim 2500$ r/min; $v_f = 200 \sim 500$ mm/min; $a = 1 \sim 10$ $\mu\text{m}$ , $\Sigma a = 0.05 \sim 0.1$ mm
Cooling fluid	–

## 2.2 Experiment of V-Groove Structure Machining of Ceramics

Figure 2a shows the schematic diagram of machining ceramics with V-shape diamond grinding wheel. The rotated diamond grinding wheel feeds vertically downward at the feed depth  $a$ , and sets the machining depth and groove spacing of V-grooves. The micro-groove array structure can be processed by using the V-tip of the diamond grinding wheel to reciprocate horizontally along the surface of the workpiece.

Figure 2b shows the site of micro-grinding of the SD600 micro-pointed diamond wheel. The diamond grinding wheel dressed into a V-tip moves horizontally on the surface of the workpiece, with a micro-groove processing depth of 500  $\mu\text{m}$  and groove spacing of 570  $\mu\text{m}$ . Micro-groove array structures were machined on four ceramic surfaces such as microcrystalline glass ceramics, monocrystalline silicon carbide, react-sintered silicon carbide and aluminum-based silicon carbide (SiC-Al) through the use of the V-tip diamond wheel. The micro-grinding conditions of the SD600 diamond wheel are shown in Table 2.



**Fig. 2** V-groove structure processing experiment of ceramic and its schematic diagram

**Table 2** Micro-grinding conditions of the SD600 diamond grinding wheel

CNC grinding machine	SMART B818
Diamond grinding wheel	SD600 grinding wheel, metal binder, D = 160 mm, B = 4 mm, N = 3000 r/min
Tool path	Track of horizontal reciprocating motion
Rough machining	Feed speed $v_f = 600$ mm/min.; cutting depth $a = 10$ $\mu$ m; cumulative cutting depth $\Sigma a = 490$ $\mu$ m
Finishing machining	Feed speed $v_f = 300$ mm/min.; cutting depth $a = 2$ $\mu$ m; cumulative cutting depth $\Sigma a = 10$ $\mu$ m
Workpiece	Glass ceramics (30 $\times$ 15 mm); aluminum-based silicon carbide (10 $\times$ 10 mm); monocrystalline silicon carbide (20 $\times$ 10 mm); sintered silicon carbide (15 $\times$ 15 mm)
Cooling fluid	Water

### 3 Micro-structure Grinding of Ceramics and Ceramic Matrix Composites

Figure 3 shows the V-shape tip and surface blade morphology of the SD600 diamond wheel after mechanical dressing. It can be seen from the Fig. that the whole shape of the grinding wheel has been trimmed into a V-shape, but there is still a small part at the tip of the grinding wheel that has not come to a point, and there is a certain degree of arc, which is caused by the uneven roundness of the grinding wheel. The V-shape side of the grinding wheel can see many diamond grains with micro cutting edges, which indicates that the surface of the grinding wheel has achieved a good sharpening effect. V-shaped CNC machine dressing process can trim diamond grinding wheel into V-tip, so that the micro diamond grinding grains on the surface of the grinding wheel can be edged out, forming sharp grinding grain cutting edges along the V-shape cutting direction, and the V-tip after dressing can achieve highly precise grinding on the surfaces of hard and brittle materials.

Figure 4 shows the surface morphology of monocrystalline silicon carbide after micro-grinding. As can be seen in Fig. 4, the surface of monocrystalline silicon carbide is very smooth with good surface processing quality. There is a small amount of damage on the micro-groove tip, and the shape of the micro cone tip is complete. In the 3D morphology diagram, it can be seen that the depth of the monocrystalline silicon carbide micro-groove is as much as 478.35  $\mu$ m. The height of the micro-pyramid is up to 475.78  $\mu$ m. Moreover, the monocrystalline silicon carbide microstructural parts have complete morphology and good processing quality.

Figure 5 shows the surface morphology of aluminum-based silicon carbide micro-grinding. It can be seen from Fig. 5, the surface processing quality of aluminum-based silicon carbide ceramic is very poor, with serious damage at the micro-groove tip and more burr at the edge of the micro pyramid. The reason is that there are silicon carbide

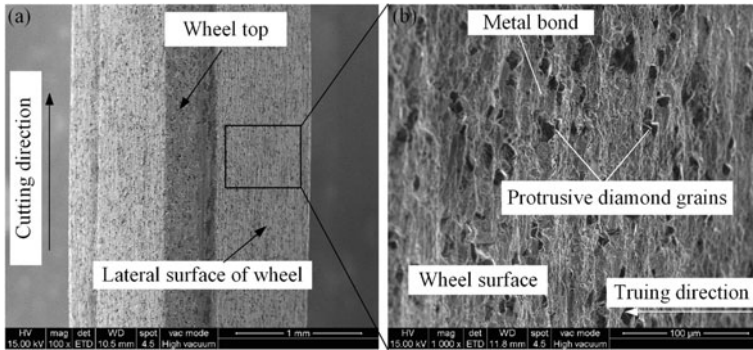


Fig. 3 SEM morphology of dressed grinding wheel surface

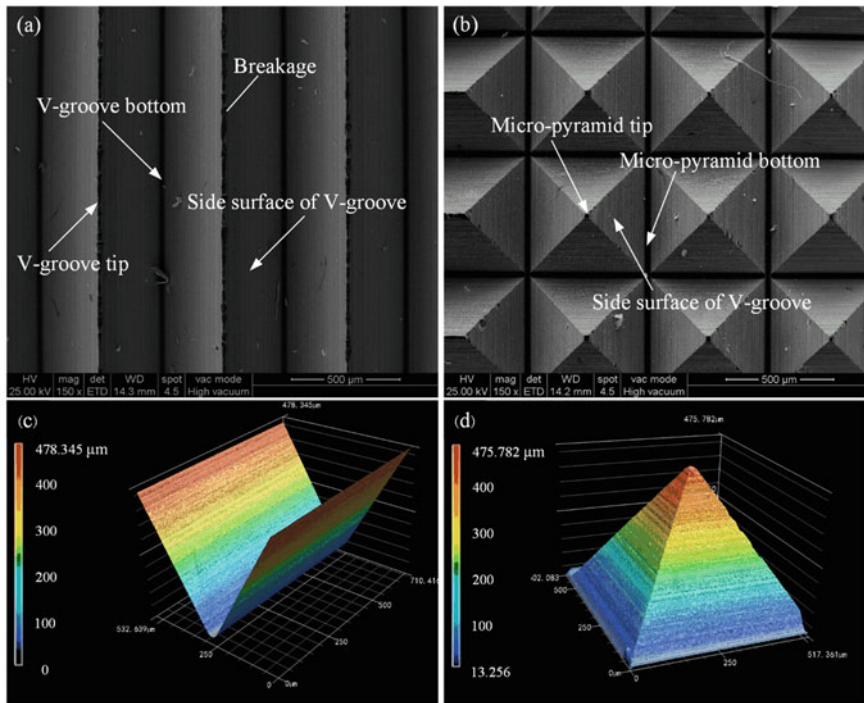
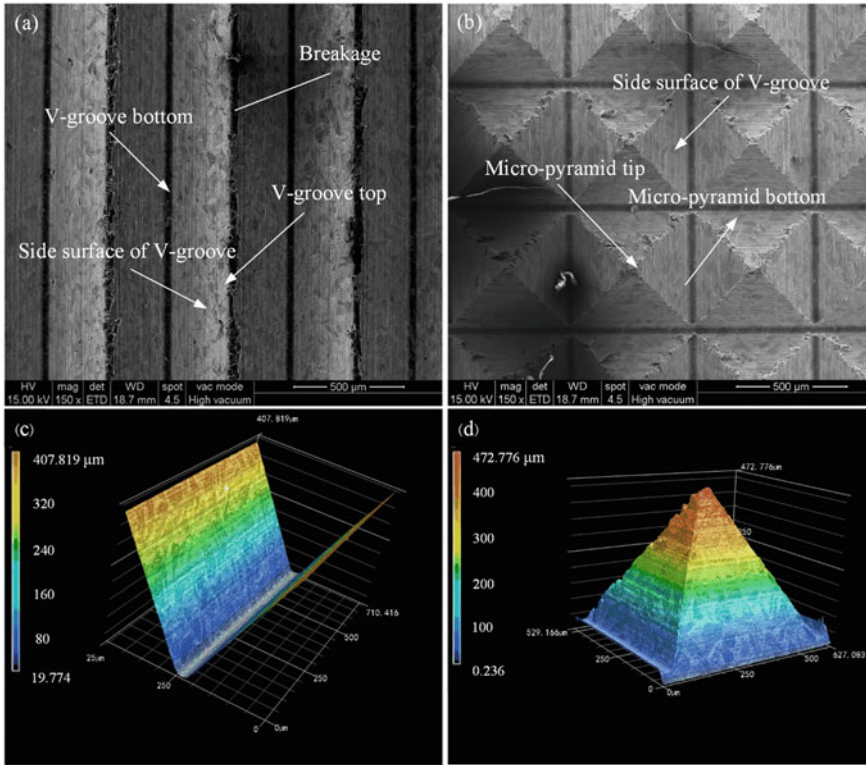


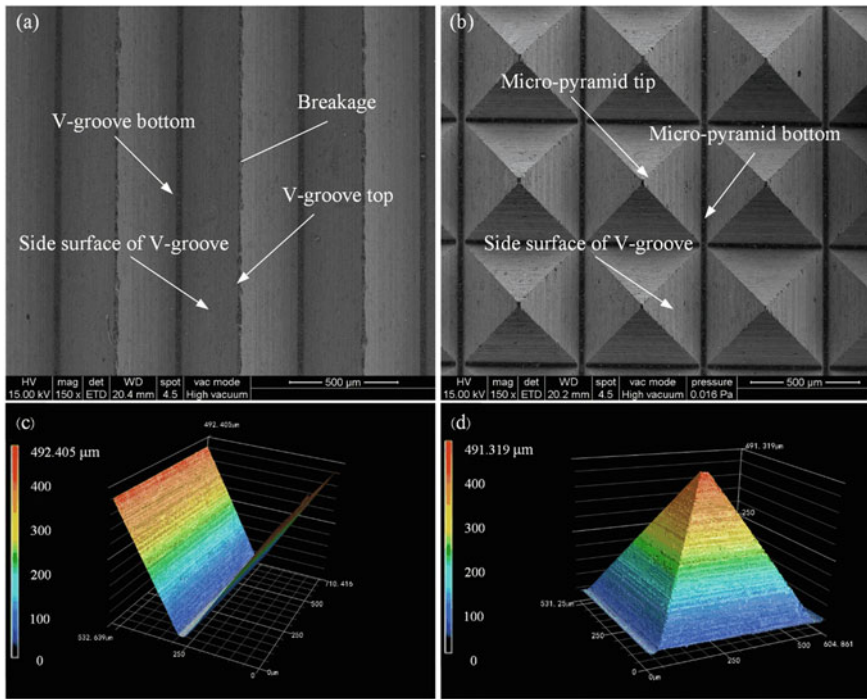
Fig. 4 SEM and 3D morphologies of V-groove and micro-pyramid on monocrystalline silicon carbide surface: a SEM morphology of V-groove; b SEM of micro-pyramid; c 3D morphology of V-groove; d 3D morphology of micro-pyramid



**Fig. 5** SEM and 3D morphologies of V-groove and micro-pyramid on aluminum-based silicon carbide surface: **a** SEM morphology of V-groove; **b** SEM morphology of micro-pyramid; **c** 3D morphology of V-groove; **d** 3D morphology of micro-pyramid

particles in the aluminum matrix, which are prone to collision or brittle fracture in the processing process, making it difficult to process aluminum-based silicon carbide. It can be seen from the 3D morphology that the depth of the aluminum-based silicon carbide micro-groove is as much as 407.82 μm. The height of the micro-pyramid is up to 472.78 μm. The damage of micro-pyramid is serious.

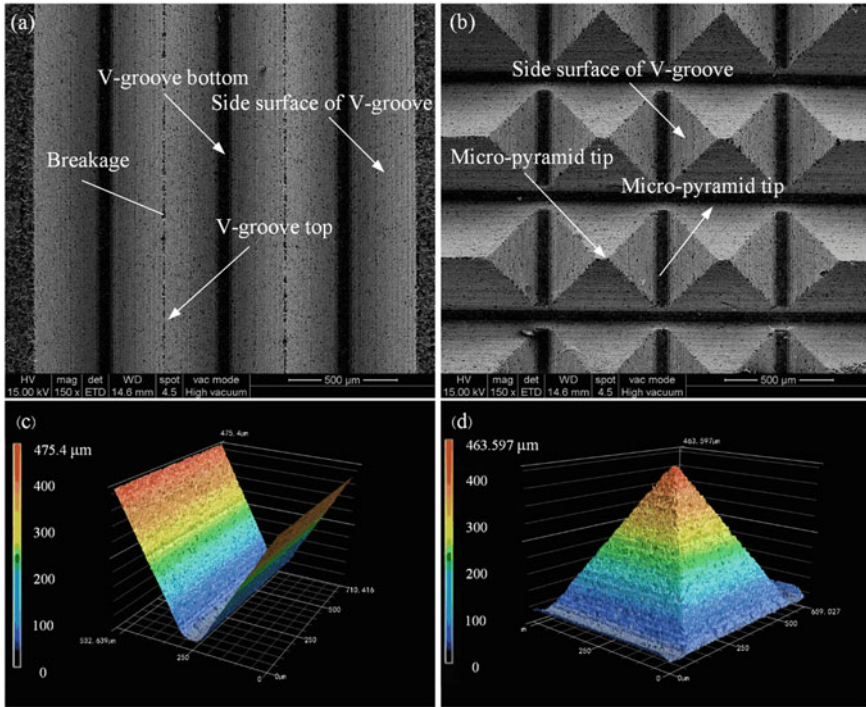
Figure 6 shows the micro-ground surface morphology of reaction sintered silicon carbide. As can be seen in Fig. 6, the surface of reprocessed reaction sintered silicon carbide is also relatively smooth with good surface processing quality. However, many tiny scratches can be seen, indicating that the material has undergone plastic deformation in the process of abrasive cutting, and the tip shapes of micro-grooves and micro-pyramid are also relatively complete. It can be seen from the 3D morphology diagram that the depth of the reaction sintered silicon carbide micro-groove is as much as 492.41 μm. The height of the micro-pyramid was up to 491.32 μm.



**Fig. 6** SEM and 3D morphologies of V-groove and micro-pyramid on reaction sintered silicon carbide surface: **a** SEM morphology of V-groove; **b** SEM morphology of micro-pyramid; **c** 3D morphology of V-groove; **d** 3D morphology of micro-pyramid

Figure 7 shows the surface morphology of reactive glass ceramics after micro-grinding. As can be seen in the same Fig., there are numerous tiny holes on the surface of glass ceramics, and the material at the bottom of the groove has a large radian removal, which is because the glass ceramics are of high brittleness. References [26–29] However, the surface of the V-groove and the micro-pyramid tower are relatively smooth, with no damage to the edges and basically no burrs. The shapes of the micro-groove and micro-pyramid spire are also very complete. It can be seen from the 3D morphology diagram that the depth of the ceramic micro-groove of glass ceramic is as much as 475.40 μm. The height of the micro-pyramid reached 463.60 μm.

Figure 8 shows the profile of micro-grooves in four ceramic micro-grinding processes. As can be seen in the same Fig., the contour curves of monocrystalline silicon carbide, aluminum-based silicon carbide and sintered silicon carbide are relatively complete. Among them, the grinding contour of aluminum-based silicon carbide is relatively flat, and the bottom of the groove has few protrusions. It is the material with the best processing effect among the four types of ceramics. Figure 8d shows that the material at the bottom of the ceramic groove of glass ceramic has a higher degree of radian removal, which is because of the brittleness of glass ceramics. However, the surface of the V-groove is relatively smooth, and the edges are not

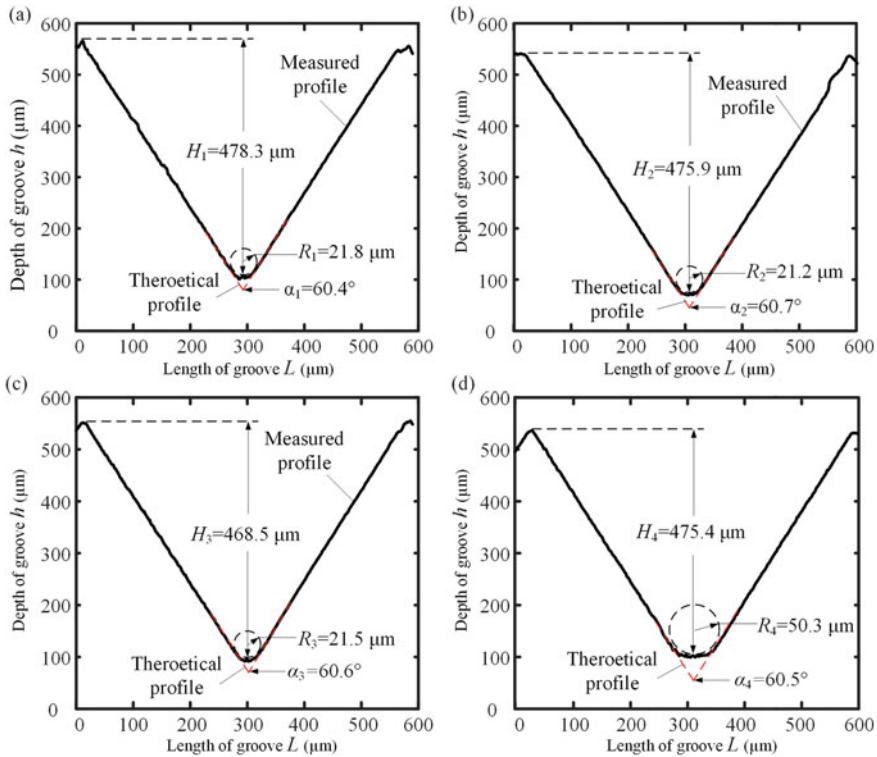


**Fig. 7** SEM and 3D morphologies of V-groove and micro-pyramid on glass ceramic surface: **a** SEM morphology of V-groove; **b** SEM morphology of micro-pyramid; **c** 3D morphology of V-groove; **d** 3D morphology of micro-pyramid

damaged, there is basically no burr, and the shape of the micro-groove is also very complete. It can also be seen in Fig. 8 that the micro-grooves of the four types of ceramics have different degrees of fracture at the top. This is because the brittle material of ceramics breaks under the action of grinding force in the process of machining, resulting in brittle deformation, and therefore its structure is out of order. Figure 8 also shows the profile angle of the bottom of the micro-groove in four ceramic micro-grinding processes. As can be seen in Fig. 8, monocrystalline silicon carbide, aluminum silicon carbide and sintering of silicon carbide, microcrystalline glass ceramic material profile at the bottom of the four angles of diamond grinding wheel dressed at an angle approaching 60°, whereby it can be seen that grinding-wheel mechanical correction is very precise, and value difference is small, high degree of precision grinding process.

Figure 8 shows the profile radius of the bottom of the micro-groove in four ceramic micro-grinding processes. As can be seen in Fig. 8, the bottom contour radii of the three kinds of silicon carbide ceramics are 21.795 μm, 21.273 μm and 21.518 μm, respectively, and the bottom contour radii of the three ceramic grooves of the same

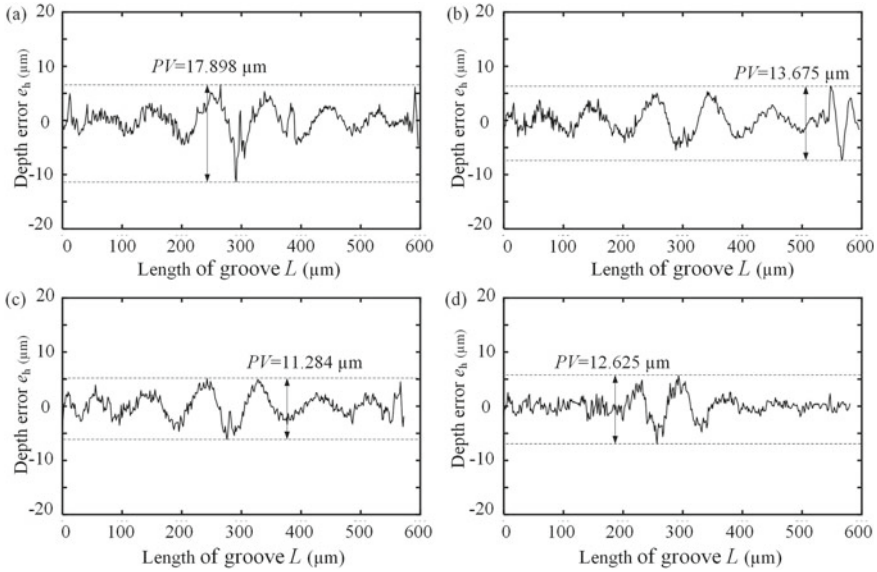




**Fig. 8** Outline of four materials (micro-groove outline) **a** monocrystalline silicon carbide **b** aluminum-based silicon carbide **c** reaction sintered silicon carbide **d** glass ceramics

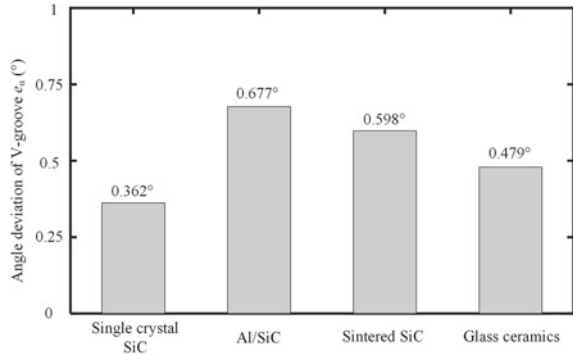
type are approximately similar. Radius of the bottom profile of glass–ceramic micro-groove is 50.311  $\mu\text{m}$ . This is because the brittleness of glass ceramic is relatively large, and therefore its lower material removal degree is higher.

Figures 8 and 9 show the profile curve and shape error distribution diagram of V-groove of ceramic workpiece. The profile of the V-tip of the grinding wheel was copied to the graphite plate, and then the V-groove profile on the surface of the graphite plate was measured to obtain the profile curve of the section of the V-tip grinding wheel after dressing. By comparing the theoretical V-shape contour of the original design with the V-groove contour curve on the surface of the ceramic workpiece (as shown in Fig. 8), the shape error distribution of the V-groove structure on the surface of the ceramic workpiece can be calculated. Figure 9 shows the distribution diagram of the shape error of V-groove of four types of ceramics, which shows the distribution of the absolute difference between the cross-section profile of the grinding wheel tip and the cross-section profile of the V-groove of the ceramic workpiece. As can be seen in Fig. 10, the shape error of grinding mainly focuses on the tip of the V-groove. The shape error of the ceramic workpiece can be controlled within 15  $\mu\text{m}$ . The absolute difference between the maximum wave peak value and



**Fig. 9** Comparison of shape accuracies of four materials: **a** monocrystalline silicon carbide **b** aluminum-based silicon carbide **c** reaction sintered silicon carbide **d** glass ceramics

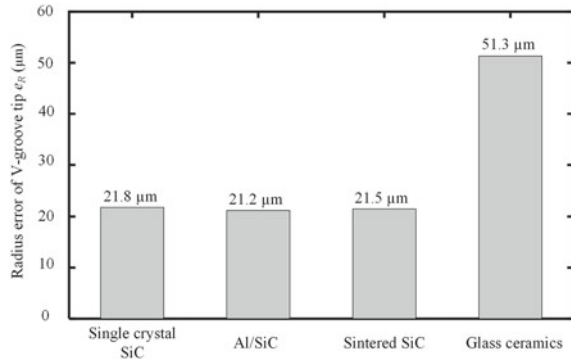
**Fig. 10** Tip-angle deviation of four materials: **a** Monocrystalline silicon carbide; **b** Aluminum-based silicon carbide; **c** Reaction sintered silicon carbide; **d** Microcrystalline glass



the minimum trough value of the shape error distribution curve is defined as the machining shape accuracy. The results show that the machining quality of ceramic and its composite base workpiece is better and the grinding precision is higher by the micro-grinding technology. Thus, the workpiece with complete shape and high precision can be machined.

Figure 10 to the tip of the four materials angular deviation histogram, diamond grinding wheel dressing set theory angle 60°, after processing finished work measuring the tip of the four types of materials available angular deviation is very small, and the theoretical angle is less than 1°, while a 60° difference visible fine-grinding technology in grinding of ceramic microstructure can guarantee higher

**Fig. 11** Bottom arc radius of four materials: **a** Monocrystalline silicon carbide; **b** Aluminum-based silicon carbide; **c** Reaction-sintered silicon carbide; **d** Microcrystalline glass



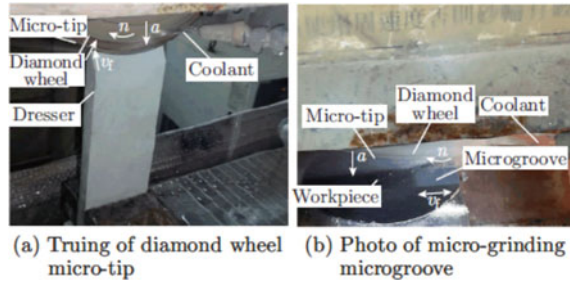
accuracy and has broad application prospects in regard to the microstructure of ceramic processing.

Figure 11 shows the bottom radius of the four materials, as shown in Fig. 11, the bottom radius of monocrystalline silicon carbide, aluminum-based silicon carbide and reaction-sintered silicon carbide are 21.8  $\mu\text{m}$ , 21.2  $\mu\text{m}$  and 21.5  $\mu\text{m}$ , respectively. The performance of silicon carbide matrix ceramics is similar in the processing process, and the degree of fracture damage is similar in the processing, whereby the arc radius at the bottom is approximately equal. The bottom arc radius of glass ceramic is 51.3  $\mu\text{m}$ . Compared with silicon carbide, glass ceramics has greater brittleness. Therefore, the bottom damage and collapse of glass ceramic are more serious in the material-removal process, and consequently the bottom arc radius is larger.

#### 4 Micro-structure Grinding of Single Crystal Silicon Carbide and Sapphire

The surface microstructure of single crystal silicon carbide and sapphire can produce special optical functions and features. Therefore, it is very necessary to study the high efficiency and precision grinding technology of single crystal silicon carbide and sapphire. Micro-grinding using diamond grinding wheel V-tip is an effective method to process the microstructure of hard and brittle chip materials such as single crystal silicon carbide and sapphire [30]. The microstructure on the surface of single crystal silicon carbide and sapphire were micro ground with a trued #600 V-tip diamond grinding wheel. Because of the high hardness of diamond grinding wheel, it is difficult to obtain micro-tips. The diamond grinding wheel was trued by whetstone, and the micro-tips of diamond grinding wheel were dressed by mutual wear between diamond grinding wheel and whetstone, as shown in Fig. 12a. The designed angle of diamond grinding wheel micro-tips was 60°. Then the micro-tip of the diamond

**Fig. 12** Microstructure grinding experiment of single crystal silicon carbide [30]



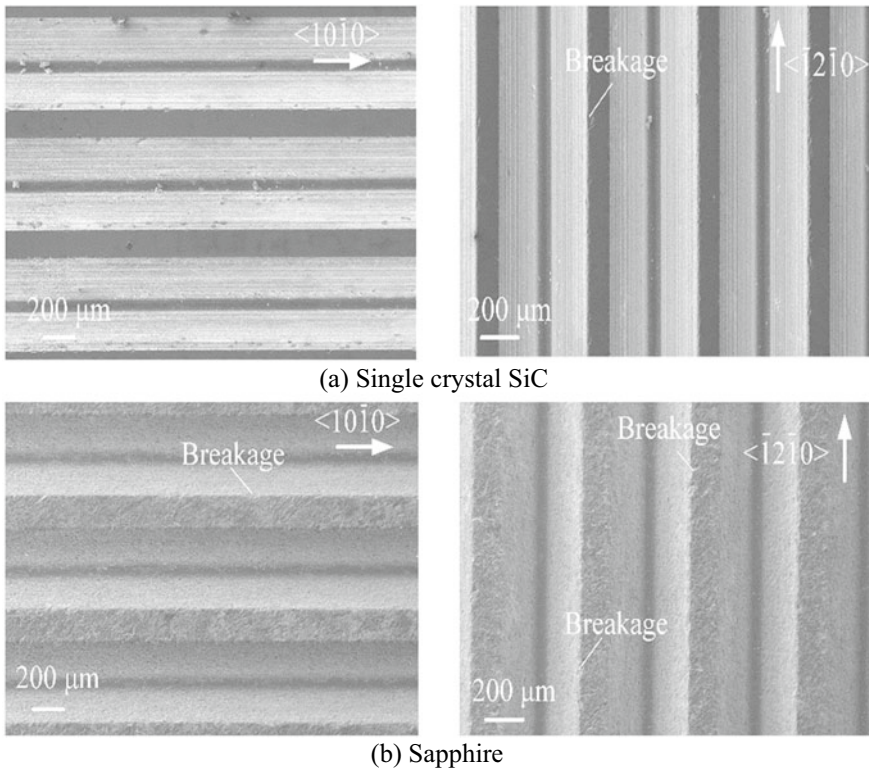
grinding wheel was used to grind the micro-groove and micro-pyramid array structures on the workpiece surface, as shown in Fig. 12b. The total depth of the micro-groove was 300  $\mu\text{m}$ . Single crystal silicon carbide and sapphire were regarded as the workpiece materials. The micro-groove grinding experiments were carried out along two different directions of the workpiece, and water was selected as the coolant.

The geometrical dimensions of microstructures (microgroove depth  $h_v$ , angle  $\beta_v$ , width  $b$  and tip radius  $r_v$ ) and roughness  $R_a$  of microgroove on the surface of single crystal silicon carbide and sapphire were measured by 3D optical profilometer, and the morphology of microgroove on the workpiece was measured by scanning electron microscope (SEM). For single crystal silicon carbide and sapphire,  $R_a$  values are 150 and 250 nm, respectively. The micro-grooves in different grinding directions were measured. The measurement results are shown in Table 3. The tip radius of the micro-grooves was 32–51  $\mu\text{m}$ , the angle error of the micro-grooves was  $0.2^\circ$ – $2.8^\circ$ , and the depth error was 7.6–62  $\mu\text{m}$ . The angle error and the depth error may be affected by the dressing error of the diamond grinding wheel micro-tip, the wear of the diamond grinding wheel micro-tip and the tool error respectively.

According to the SEM photos of the micro-grooves, it can be seen that the micro-grooves are regular, as shown in Fig. 13, but the edge of the micro-grooves on the workpiece was fractured, which indicates that under the set parameters, the material removal mode of micro-grinding was brittle removal. In addition, there was a little damage on the edge of microgroove on the surface of single crystal silicon carbide and sapphire with surface roughness values of 150 nm and 250 nm, respectively. This indicates that the micro-grinding performance of single crystal silicon carbide is stronger than that of sapphire, which is consistent with the sequence of microcrack propagation resistance. Materials with stronger microcrack propagation resistance can obtain better microgroove quality through the micro-grinding process.

**Table 3** Measurement results of micro groove geometry on workpiece surface

Workpiece	$h_v(\mu\text{m})$	$\beta_v(^{\circ})$	$r_v(\mu\text{m})$	$b(\mu\text{m})$
Single crystal SiC <1010>	316.8	60.2°	34	471.4
Single crystal SiC <1210>	292.4	58.4°	51	475.4
Sapphire <1010>	238	62.8°	32	424.6
Sapphire <1210>	266	57.5°	49	434.8



**Fig. 13** SEM photos of micro-ground workpiece surfaces: **a** Single crystal SiC; **b** Sapphire [30]

## 5 Conclusions

In this chapter, the experiment is conducted by controlling the micro abrasive cutting edge parameters of diamond wheel micro tip. The micro grinding technology are developed and used to process regular micro grooves and micro cone array structures on the surfaces of single crystal silicon, aluminum-based silicon carbide, reaction sintered silicon carbide, crystallite glass ceramics and other hard materials with high strength and high surface processing shape. Then the SEM and laser confocal microarray analysis are used to capture the surface morphology and structure parameters of sapphire glass ceramic. The above materials in grinding material removal in the process of form and the results show that the precision of grinding machining technology is suitable for most of the hard brittle material surface microstructure, and can obtain high shape accuracy and high surface quality of microstructure. The conclusions are as follows:

- (1) The surface microstructure of ceramic and ceramic composite materials can be obtained with high quality and low error rate after grinding with precision trued V-tip diamond grinding wheel. Theoretical design depth of ceramic surface microstructure  $h = 500 \mu\text{m}$ , theoretical design angle  $A = 60^\circ$ , theoretical bottom arc radius  $R = 20 \mu\text{m}$  (i.e. the radius of grinding wheel tip after truing). After processing, the depth of single crystal silicon carbide, aluminum-based silicon carbide, reaction sintered silicon carbide, glass microcrystalline surface microstructure is  $478.3 \mu\text{m}$ ,  $475.9 \mu\text{m}$ ,  $468.5 \mu\text{m}$ ,  $475.4 \mu\text{m}$ , respectively. The groove angle error is  $0.362^\circ$ ,  $0.677^\circ$ ,  $0.598^\circ$ ,  $0.479^\circ$ , respectively. The radius of the bottom arc is  $21.8 \mu\text{m}$ ,  $21.2 \mu\text{m}$ ,  $21.5 \mu\text{m}$  and  $51.3 \mu\text{m}$ , respectively.
- (2) The shape accuracy PV value of single crystal SiC, aluminum-based SiC, reaction sintered SiC and glass ceramics surface microstructure is  $12.6 \mu\text{m}$ ,  $13.7 \mu\text{m}$ ,  $11.3 \mu\text{m}$  and  $17.9 \mu\text{m}$ , respectively.
- (3) Micro-grinding technology can obtain good surface quality, high shape accuracy, smooth surface and neat edge microstructure in the micro-grinding of ceramics and ceramic matrix composite materials.

**Acknowledgements** The work described in this chapter was supported by the National Natural Science Foundation of China (Grant No. 51805334), the China Postdoctoral Science Foundation [Grant No. 2016M602460], the Science and Technology Planning Project of Guangdong Province [Grant Nos. 2016A040403043 and 2017A010102003] and the International Science and Technology Cooperation Project of Shenzhen City (Grant No. GJHZ20190822091805371).

## References

1. Liu HT, Sun YZ, De BS (2013) Experimental research of brittle-ductile transition conditions and tool wear for micro-milling of glass material. *Int J Adv Manuf Technol* 68:1901–1909
2. Xiao Y, Chen MJ, Yang YT, Cheng J (2015) Research on the critical condition of Brittle-Ductile Transition about Micro-milling of KDP crystal and experimental verification. *Int J Precis Eng Manuf* 16:351–359
3. Wang M, Zhao G, He N, Xia H, Li L (2019) Experimental study on laser-induced oxidation assist micro-milling of TiB<sub>2</sub>-based ceramic composite tool engineering 53:8–13
4. Qu S, Gong Y, Yang Y, Xu Y, Pang S (2020) Mechanical model and removal mechanism of unidirectional carbon fiber-reinforced ceramic composites. *Int J Mech Sci* 173:105465
5. Shen JY, Wang JQ, Jiang B (2015) Study on wear of diamond wheel in ultrasonic vibration-assisted grinding ceramic. *Wear* 332–333:788–793
6. Juan D, Zhan JL, Hu G (2013) Study on the mechanisms and control method of edge chipping fracture in the machining of brittle and hard materials. *Mech Sci Technol Aerosp Eng* 32:1451–1455
7. Niihara K (2010) New design concept of structural ceramics. *J Ceramic Soc Jpn* 99:974–982
8. Palmero P (2015) Structural ceramic nanocomposites: a review of properties and powders' synthesis methods. *Nanomaterials* 5:656–696
9. Kargin YF, Akhmadullina NS, Solntsev KA (2014) Ceramic materials and phosphors based on silicon nitride and sialon. *Inorg Mater* 50:1325–1342
10. Cheng X, Liu J, Zheng G, Yang X, Tian Y (2017) Study of microcutting fundamentals for peripheral and end cutting edges in micro-end-milling. *J Micromech Microeng* 28:015011

11. Tong H, Pu Y, Yang J (2019) A special process of 3D servo scanning micro EDM for machining pierced micro structures of TiNi alloy tube *J Micromech Microeng* 29:0960–1317
12. Zhang C , Song Y, Ehmann KF (2020) Design and experimental investigation of a parallel flexure hinge-based 3D elliptical vibration-assisted cutting mechanism. *J Micromech Microeng* 30:085008 (16pp)
13. Chen W, Zheng L, Huo D, Chen Y (2018) Surface texture formation by non-resonant vibration assisted micro milling. *J Micromech Microeng* 28:025006
14. Liu HT, Sun YZ, Shan DB (2013) Experimental research of brittle-ductile transition conditions and tool wear for micromilling of glass material. *Int J Adv Manufact Technol* 68:1901–1909
15. Grigor Ev SN, Kuzin VV, Fedorov SY (2014) Technological aspects of the electrical-discharge machining of small-diameter holes in a high-density ceramic: part 1. *Refract Ind Ceram* 55:330–334
16. Grigor Ev SN, Kuzin VV, Fedorov SY (2015) Technological aspects of the electrical-discharge machining of small-diameter holes in a high-density ceramic: part 21. *Refract Ind Ceram* 55:469–472
17. Islam MU, Campbell G (1993) Laser machining of ceramics: a review. *Mater Manufact Process* 8:611–630
18. Nagimova A, Perveen A (2019) A review on laser machining of hard to cut materials. *Mater Today Proc* 18:2440–2447
19. Zhang S, Kang S (1995) Experimental studies of laser processing of constructional ceramics. *Chin J Lasers* 22:797
20. Maurath J, Willenbacher N (2017) 3D printing of open-porous cellular ceramics with high specific strength. *J Eur Ceram Soc* 37:4833–4842
21. Zhai C, Xu J, Li Y (2020) The study on surface integrity on laser-assisted turning of SiCp/2024Al. *Int J Optomechatronics* 14:29–43
22. Wu M, Guo B, Zhao Q (2018) Precision grinding of a microstructured surface on hard and brittle materials by a microstructured coarse-grained diamond grinding wheel. *Ceram Int* 44:8026–8034
23. Park H, Onikura H, Ohnishi O (2010) Development of micro-diamond tools through electroless composite plating and investigation into micro-machining characteristics. *Precis Eng* 34:376–386
24. Zhou Y, Gong Y, Ming C, Zhu Z, Wen X (2017) Study on surface quality and subsurface recrystallization of nickel-based monocrystalline superalloy in micro-grinding. *Int J Adv Manuf Technol* 55:1749–1768
25. Kirsch B, Bohley M, Arrabiyeh PA, Aurich JC, Kirsch B (2017) Application of ultra-small micro grinding and micro milling tools: possibilities and limitations. *Micromachines* 8:261
26. Herczog (2010) Microcrystalline BaTiO<sub>3</sub> by Crystallization from Glass. *J Am Ceram Soc* 47:1151–2916
27. Wang Y, Gui Y, Song C, Xie C, Zhao J (2018) Research progress in glass ceramics with the blast furnace slag. *Multipurpose Utilization Mineral Resour* 2:1–6
28. Chen K, Li Y, Meng X, Meng L and Guo Z (2019) New integrated method to recover the TiO<sub>2</sub> component and prepare glass ceramics from molten titanium-bearing blast-furnace slag. *Ceram Int* 45:24236–24243
29. Gao HT, Liu XH, Chen JQ, Qi JL, Wang YB, Ai ZR (2018) Preparation of glass-ceramics with low density and high strength using blast furnace slag, glass fiber and water glass. *Ceram Int* 44:6044–6053
30. Zhang L, Xie J, Zhu LM, Lu YJ (2018) Micro-grinding performance of hard-brittle chip materials in precision micro-grinding microgroove. *J Shanghai Jiao Tong Univ (Science)* 23:70–76

# Chapter 16

## Precision Grinding and Polishing of Optical Micro-structured Surface



Chunjin Wang, Xingyu Mou, Wang Luo, and Yanjun Lu

**Abstract** In fields like imaging and illumination, different types of optical structured surface have been used in a wide variety of applications. However, defects such as tool marks, burs and debris are normally left on the structured surface during the machining process. How to remove aforesaid defects, and furtherly improve the surface quality with a higher efficient, so as to reach better functional performance is still a challenging problem. This chapter presents an advanced method, maskless fluid jet polishing (MFJP), to solve this problem. In MFJP, without using a mask, material can be removed in a tiny scale by low pressure micro abrasive water jet slurry impinged on the structured surface. On the basis of the analysis of surface roughness, form maintainability, and surface smoothness, experimental investigations on the polishing of sinusoidal structured surface and V-groove structured surface were performed to achieve the technical feasibility of MFJP on structured surface. In order to prove the fluid flow movement and material removal characteristics and to achieve a simulation of the MFJP process on V-groove surface, a computational fluid dynamics (CFD) model was also developed. Additionally, the influence of the key polishing parameters was also researched and discussed. The results indicate that MFJP can observably improve the surface quality of optical structured surface, while achieving high form maintainability under defined conditions. As a potentially competitive method for the precision polishing on optical structured surfaces, MFJP can also hold promise for polishing other surfaces with small or micro-meter sized cavities or channels, such as microfluidic chips, etc.

---

C. Wang

State Key Laboratory of Ultra-Precision Machining Technology, Department of Industrial and Systems Engineering, The Hong Kong Polytechnic University, Hong Kong, China

X. Mou · W. Luo · Y. Lu (✉)

Guangdong Provincial Key Laboratory of Micro/Nano Optomechanics Engineering, College of Mechatronics and Control Engineering, Shenzhen University, Nan-Hai Ave 3688, Shenzhen 518060, Guangdong, PR China

e-mail: [luyanjun@szu.edu.cn](mailto:luyanjun@szu.edu.cn)



## 1 Introduction

Structured surface has a regular and periodic pattern and can perform certain functions such as optical, physical, and biological [1]. In recent years, with the rapid development of industries such as optical fiber communication and imaging technology, components with structured optical functional surfaces are in a trend of a smaller size, lighter weight, and higher integration to reach the increasing needs in various fields such as optoelectronics and communication products, biomedical, automotive lighting. [2] Typical optical structured surfaces are widely used and divided into several kinds, such as optical micro lens arrays, Fresnel lens structures, artificial optical compound eyes, V-shaped or cylindrical groove structured arrays, reflective prism arrays, etc. [3, 4]. Due to the large demand and high processing costs for single components, mass production of structured surface components by high-precision injection molding is booming [5]. In order to boost the replication stability and extend the mold life, the difficult-to-machine material such as stainless steel, tungsten carbide, or silicon carbide, are used as the mold material.

Several methods have been developed to generate structured surfaces, including milling [6], turning [7], grinding [8], chiseling [9], electrical discharge machining [10], laser machining [11], abrasive jet machining [12], etc. Nevertheless, tool marks, burs, debris and defects are often left on the surface during process by these machining methods. In most instances, the surface quality after direct machining can't meet the practical and functional requirements, where subsequent polishing is demanded.

As the demand for high-precision optical structured surfaces is constantly increasing, several different kinds of polishing methods have been developed to improve the quality of the structured surface, such as copying tool polishing, magnetic field-assisted polishing, vibration or vibration-assisted polishing, etc. The purpose of polishing of optical structured surface is to improve the surface roughness without degrading the form accuracy of the featured structure. Brinksmeier et al. [13] presented the pen-shaped and wheel-shaped copying tools to polish a structured array on mold steel (X40Cr13) and electroless nickel-plated steel. After polishing, the surface roughness can reach 4.5 nm. Other researchers also successfully used the similar tool for the polishing of structures such as v-groove array [14, 15], cylindrical structure array [16, 17], Fresnel surface [18], etc.

However, the similar tool polishing method is limited in aspects like tool wear, specific design of tool for various kinds of structures, and high demand about the motion accuracy of the polishing machine. In recent years, researchers have also developed different kinds of magnetic field-assisted finishing methods for the polishing of structured surface, by which nanometer or sub-nanometer sized surface roughness of the structured surface can be successfully achieved, such as magnetic abrasive polishing [19–21], magnetorheological fluid polishing [22–25], and magnetic compound finishing [26–28]. Nevertheless, a big difficulty how to maintain the form of the featured structure still remains to be solved, especially for surface structures with a high aspect ratio. In addition, materials are limited when adopting the magnetic field-assisted polishing method. To achieve the polishing

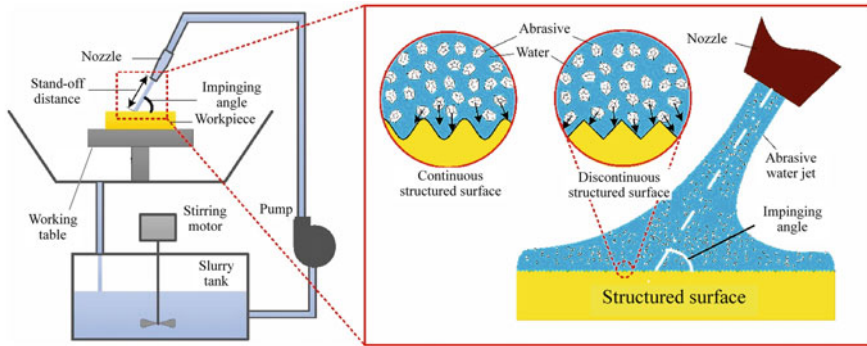
of structured surfaces, various kinds of vibration or vibration-assisted polishing have also been proposed [29–34], while these methods still have the limitations as mentioned of the copying tool polishing method. Matsumura et al. [35] attempted the abrasive water jet polishing of the V-groove adopting relatively high pressure (15–35 MPa) with the help of mask. In addition, the shape of the mask was purposely designed to obtain a larger stagnation zone to increase the size of the crack-free zone when polishing. The surface roughness of the groove was successfully enhanced from 46 to 25 nm in  $R_a$ . Nonetheless, it is difficult to make a purposely designed mask for structured array surface, and it will largely increase the polishing cost. Moreover, the surface roughness is poor because of the brittle fracture which can be easily generated by high-pressure abrasive water jets.

All in all, most of the existing structured polishing methods are technically limited in certain aspects, such as structure form maintainability, material limitation, and shape limitation. Additionally, conventional mechanical polishing methods can hardly adapt to the structured surface form. Therefore, in order to meet the increasing demand for ultra-precision optical structured surfaces, a mature and generic polishing method is still greatly required. In this chapter, an advanced maskless fluid jet polishing (MFJP) method is proposed which attempts to solve the problems mentioned above. In MFJP, without using a mask, material can be removed in a tiny scale by low pressure (normally less than 15 bar) micro abrasive water jet slurry impinging on the structured surface. The working principle of the process is proposed in Sect. 2. The design of the experiments so as to research the polishing performance on sinusoidal structured surface and V-groove structured surface is presented in Sect. 3. The experimental results, as well as the discussion which is based on the computational fluidic dynamics (CFD) simulation model built for the MFJP process are pursued in Sect. 4. Finally, the research work is concluded and summarized in Sect. 5.

## 2 Maskless Fluid Jet Polishing Methods

Proposed by Fahnle et al. [36], an abrasive water jet polishing method under relatively low pressure (also called ‘fluid jet polishing (FJP)’), has been widely applied in the polishing of optical lenses and molds, including spherical/aspherical or freeform surfaces. In the FJP process, micro/nano abrasives are uniformly mixed with water supplied from the nozzle and applied to the target surface to achieve material removal through an erosion process. Due to high flexibility, the fluid jet can easily adapt to surface with complicated geometry, and can be used for the polishing of ceramic, metal, glass, and most kinds of materials. Hence, why not try polishing the surface of optical structure with FJP? Considering that using a high-pressure water jet requires a mask, using a low-pressure water jet eliminates the need for a mask, which not only significantly reduces polishing costs, but also simplifies the procedure.

Hence, this study conducted a series of experimental and theoretical investigations of the polishing performance of maskless fluid jet polishing (MFJP) on optical

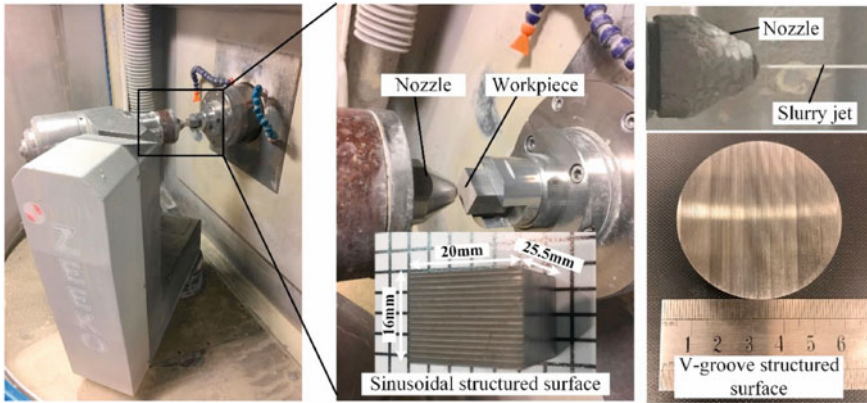


**Fig. 1** Schematic diagram of the maskless fluid jet polishing (MFJP) of structured surface

structured surface. MFJP generally uses fluid pressures below 15 bar and does not use a mask. It is shown a schematic diagram of MFJP on structured surface in Fig. 1. In this study, the structured surfaces were divided into continuous structured surface and discontinuous structured surface. The continuous structure are those with no sharp edge (e.g., wavy structure, sinusoidal structure, etc.), while the others are the discontinuous structured surface (e.g., V-groove structure array, lenticular lens array, etc.) as shown in Fig. 1.

### 3 Experimental Procedures

The experiments were performed on a ZEEKO IRP200 polishing machine as shown in Fig. 1. There are two kinds of structured surfaces which respectively represent the polishing performance on continuous structured surface and discontinuous structured surface tested in this study. One of the workpieces, a sinusoidal structured surface made of S136 mold steel, is the mold of the flood lighting component, implementing the function of transforming a surface source to a line source. The sinusoidal structured surface was machined by electrical discharge machining (EDM) and has arithmetic surface roughness ( $R_a$ ) between 400 and 700 nm. The other one was V-groove structured surface made of S136H mold steel as shown in the right bottom part of Fig. 2, where the mold for the LED diffuser plate was machined with a V-groove wheel with a surface roughness between 90 and 170 nm, as reported by Lu et al. [37]. A sapphire nozzle with a diameter of 0.5 mm was used, and the polishing slurry consisted of silicon carbide abrasive (average particle size of 11.9  $\mu\text{m}$ , GC 1000#, FUJIMI, Corp.) mixed with 10% pure water. The polishing conditions for surfaces with sinusoidal structure are summarized in Table 1. In order to prove the polishing performance, the entire surface was polished thoroughly in three passes of polishing. The polishing experiment on the V-groove surface was divided into four groups to



**Fig. 2** Experimental setup

**Table 1** Polishing conditions for the sinusoidal structured surface

Conditions	Value
Fluid pressure	10 bar
Impinging angle	90°
Stand-off distance (SOD)	2 mm
Feed rate	50 mm/min
Tool path	Raster path with 0.2 mm scan interval
Polishing time	3 passes of polishing, 32.4 min for each pass

study the polishing performance and the influence of several key polishing parameters, including feed rate, fluid pressure, impinging angle and stand-off distance. The polishing conditions are summarized in Table 2. The material used for the V-groove mold surface was S136H with a hardness of 30-35HRC. In each condition, two areas with a size of 3 mm × 3 mm on the V-groove surface were polished.

**Table 2** Polishing conditions for the V-groove structured surface

Conditions	Group 1	Group 2	Group 3	Group 4
Feed rate (mm/min)	10,20,30,40,60,80,100	30	30	30
Fluid pressure (bar)	8	6,8,10,12	8	8
Impinging angle (°)	90	90	45,60,75,90	90
Stand-off distance (mm)	4	4	4	2,4,6,8,10
Tool path	Raster path with 0.1 mm scan interval			
Polishing time (min)	1 pass of 9.3, 4.7, 3.1, 2.4, 1.6, 1.2, 1.0 min	1 pass of 3.1 min		

By a Hitachi Electron Microscope TM3000 with magnifications of 150, 1000, and 5000, the surface topography of the sinusoidal structured surface before and after polishing was characterized. The surface roughness was measured by a Zygo Nexview white light 3D interferometer. The magnification of the object lens was 40. The lateral and vertical resolutions of the measurement were 208.8 nm and 0.1 nm, respectively. The arithmetic average surface roughness ( $S_a$ ) was defined according to ISO25178 standard. The surface roughness was analysed by the software MX. A nine-order polynomial filter was used, and other parameters were the default settings of the software. Because of the small effective area of the lower part of the sinusoidal surface to measure surface roughness, an area of approximately  $50 \mu\text{m} \times 50 \mu\text{m}$  was used as the measurement area for the lower and upper parts of the structured sinusoidal surface. The 3D surface form of the sinusoidal structured surface was measured using a Form Talysurf PGI 1240 profilometer. A tapered diamond needle with a arm of 60 mm and a radius of  $2 \mu\text{m}$  was used. The vertical and lateral resolutions were 0.8 nm and  $0.25 \mu\text{m}$ , respectively.

## 4 Results and Discussion

### 4.1 Polishing Performance on the Sinusoidal Structured Array Surface

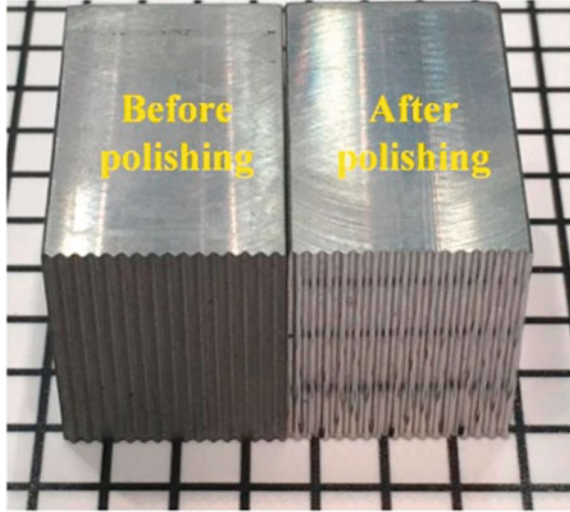
#### 4.1.1 Analysis of Surface Topography

Figure 3 shows snapshots of the sinusoidal surface before and after polishing. Compared to the initial surface, the surface becomes much shinier after polishing. The SEM measurement results were obtained on the top, side, and bottom surfaces of the sinusoidal surface under three different magnifications. As shown in Fig. 4, typical discharge craters could be clearly found on the initial surface after EDM [38]. These defects were completely removed after polishing. After that, it only left tiny abrasive erosion marks. SEM photos of the edge were also made a comparison as shown in Fig. 5. And after polishing the surface was much smoother than the original surface. At the same time, the shape of the sharp edges was well preserved. Figure 6 shows the results of the surface roughness measurements. Before polishing, the  $S_a$  of the top and bottom surface were 642.1 nm and 458.9 nm, respectively. After polishing, the  $S_a$  of the top and bottom surface decreased to 18.8 nm and 14.4 nm, respectively. The convergence rate of the surface roughness is defined as

$$\eta_{S_a} = \frac{S_{a_{initial}} - S_{a_{after\_polishing}}}{S_{a_{initial}}} \times 100\% \quad (1)$$

where  $S_{a_{initial}}$  is the  $S_a$  of the initial surface, while  $S_{a_{after\_polishing}}$  is the  $S_a$  after polishing. The  $\eta_{S_a}$  reached over 96%, proving the effectiveness of MFJP in

**Fig. 3** Snapshots of the sinusoidal structured surface before and after polishing



reducing the roughness of sinusoidal surfaces and demonstrating the possibility of the polishing on other kinds of continuous structured surfaces. In addition, the polishing efficiency could be much improved by using multi-jet polishing [39] or fluid line jet polishing [40].

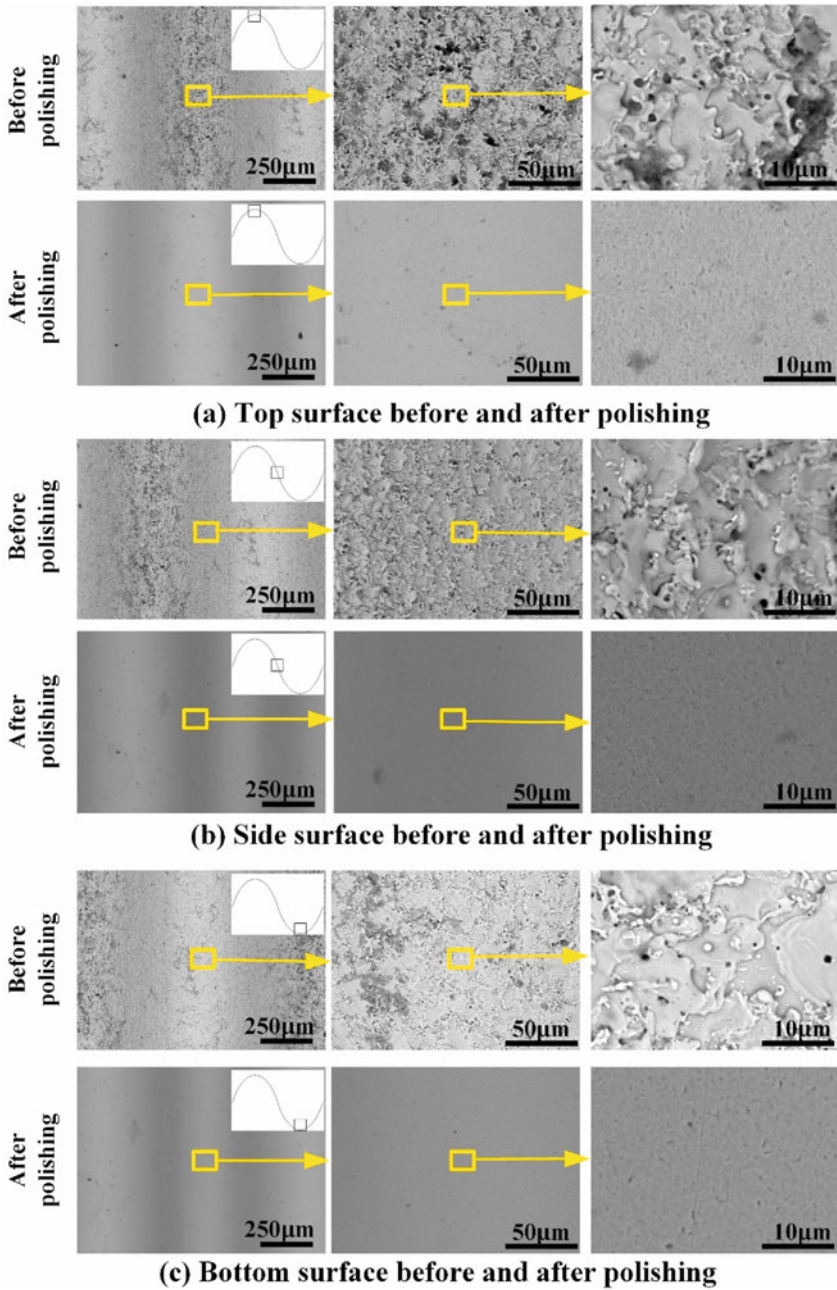
#### 4.1.2 Analysis of Surface Form Maintainability

In addition to surface topography, the maintainability of the surface profile is also an important evaluation criterion for the structured polishing of surfaces. The surface profile before and after polishing were measured on a Form Talysurf PGI1240. From Fig. 7a and b, it show the measured surface profile before and after polishing, respectively. For better analysis, they were matched based on the any DOF registration algorithm [41], and compared as shown in Fig. 7c, d. It is obvious that the surface profile was maintained well as shown in the sectional profile comparison results. Furthermore, the smoothing of the surface can also be clearly observed in Fig. 7c.

To make a comparison quantitatively, the maintenance ratio  $\eta$  is defined here for better comparison, which is expressed as

$$\begin{aligned} \eta &= \left[ 1 - \left| \frac{H_{before\_polishing} - H_{after\_polishing}}{H_{before\_polishing}} \right| \right] \times 100\% \\ &= \left[ 1 - \left| \frac{(h_{peak} - h_{bottom}) - (h_{0\_peak} - h_{0\_bottom})}{h_{0\_peak} - h_{0\_bottom}} \right| \right] \times 100\% \end{aligned} \quad (2)$$

where  $H_{before\_polishing}$  and  $H_{after\_polishing}$  are the height between the peak and bottom of the structure feature before and after polishing, respectively.



**Fig. 4** SEM photos of the sinusoidal structured surface before and after polishing under three different magnifications

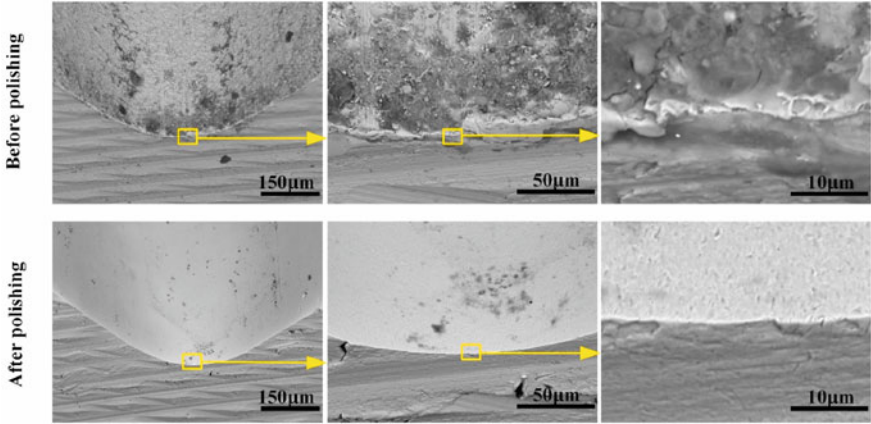


Fig. 5 SEM photos of the edge surface before and after polishing

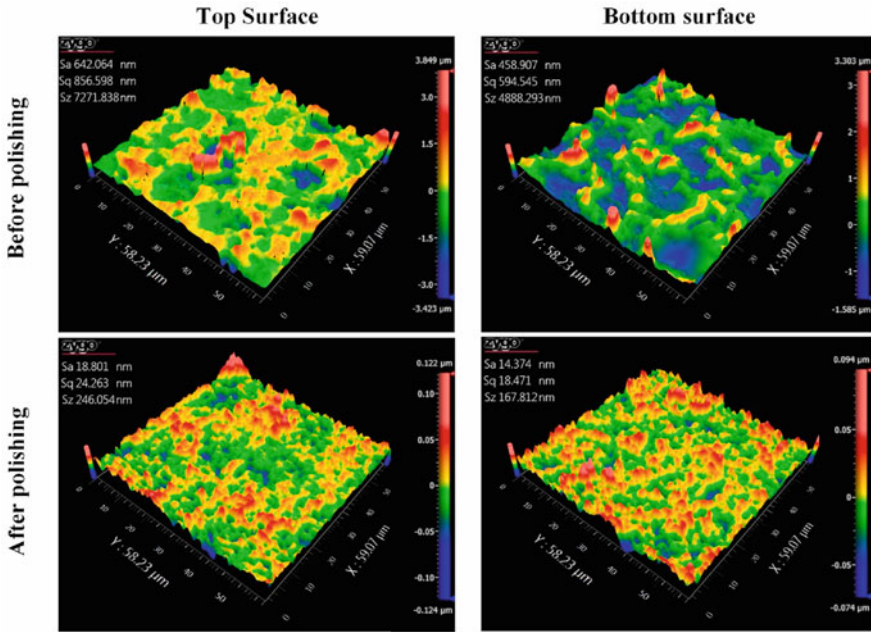


Fig. 6 Surface roughness comparison of the sinusoidal structured surface before and after polishing

$h_{0\_peak}$  and  $h_{0\_bottom}$  are the height of the peak and bottom before polishing, while  $h_{peak}$  and  $h_{bottom}$  are the height of the peak and bottom after polishing. After MFJP, The form maintenance ratio  $\eta$  of the sinusoidal structured surface reached 99.2%, indicating a high degree of form maintainability.



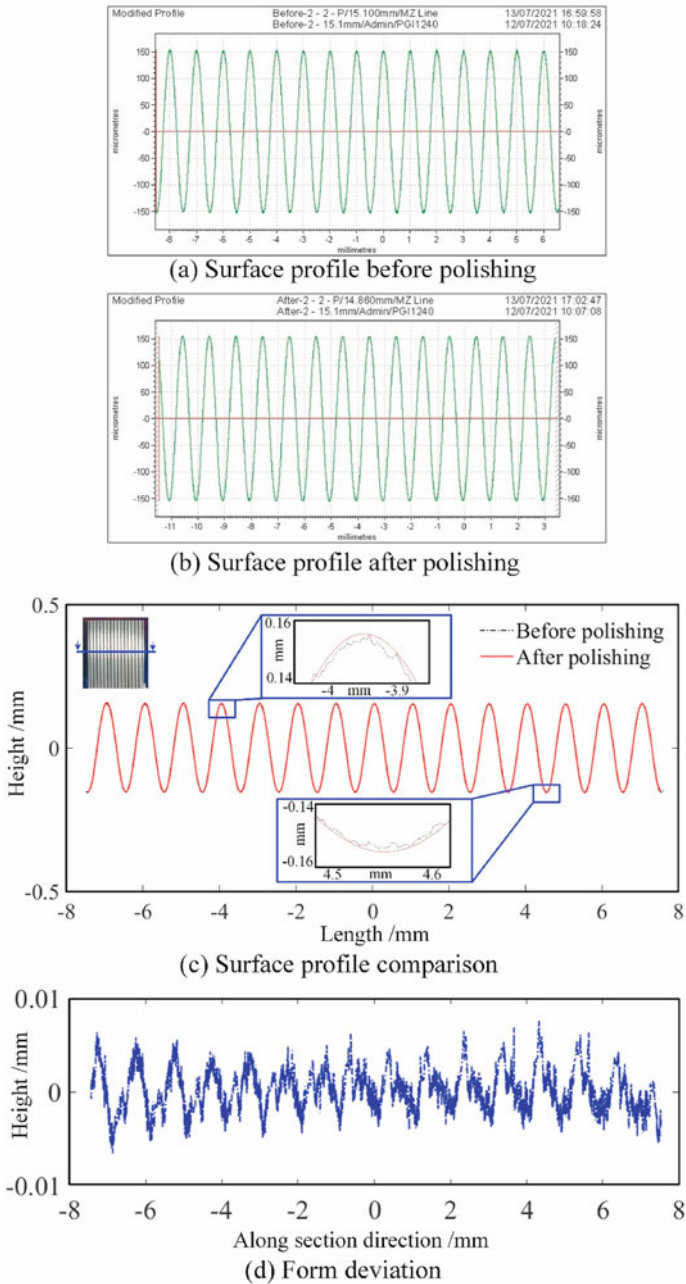


Fig. 7 Analysis of the sinusoidal structured surface profile before and after polishing

## 4.2 Polishing Performance on V-groove Structured Array Surface

After polishing, The surface roughness of the V-groove surface at different feed rates is shown in Fig. 8 Based on the data measured on the Alpha-Step D300 profiler (KLA-Tencor, California, USA), the surface arithmetic roughness Ra was calculated according to Eq. (3) [42], Meanwhile, the limited measurement depth and surface gradient of the Zygo Nexview white light 3D interferometer was considered.

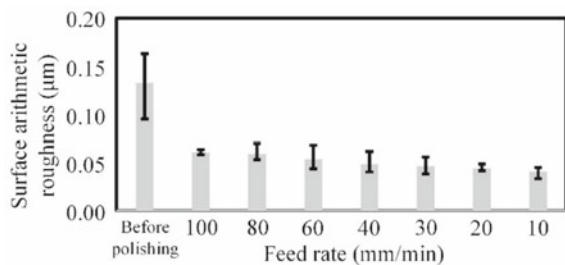
$$Ra = \frac{1}{L} \int_0^L |h| dx \quad (3)$$

where L is the sample length which was 50  $\mu\text{m}$  in this study, h is the profile height at each position. The data were collected in each condition at three different locations on each V-groove surface. It can found that the surface roughness was significantly reduced after a single fluid jet polishing, even under the feed rate of 100 mm/min ( $\sim 1$  min of the polishing time). With slower feed rates, it will be resulted in lower surface roughness and longer polishing times. At the feed rate of 10 mm/min, the average surface roughness was reduced from 132.5 nm to 40.6 nm after one pass of polishing ( $\sim 9.3$  min of polishing time). Selected SEM photos of the polished surface at different feed rates are also shown in Fig. 9 in order to compare the surface quality after polishing. It is found that with a slower feed rate, severe grinding marks on the V-groove surface were gradually removed. This is due to the fact that a slower feed rate results in longer polishing time and hence larger material removal.

In addition, at the feed rate below 30 mm/min, the grinding marks were mostly removed. This result show that MFJP is also effective in enhancing the surface roughness of V-groove structured surface, a typical type of discontinuous structured surface.

As shown in Fig. 10, the characteristic of the V-groove shape profile was also measured to evaluate the form maintainability of MFJP. When the feed rates was more than 30 mm/min, the MFJP maintains its shape well ( $\eta > 88\%$ ). When the feed rate reached 100 mm/min, the form maintainability ratio  $\eta$  was 95.3%, while  $\eta$  was 69.7% at a feed rate of 10 mm/min. Therefore, to achieve good form maintainability,

**Fig. 8** Measured surface roughness varies with the feed rate



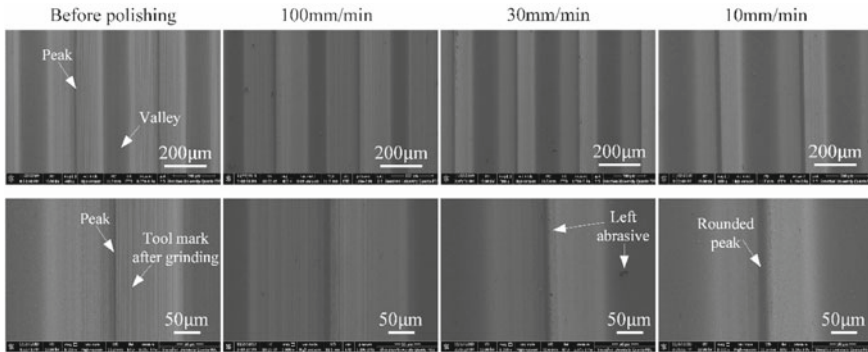


Fig. 9 Selected SEM photographs under different feed rates

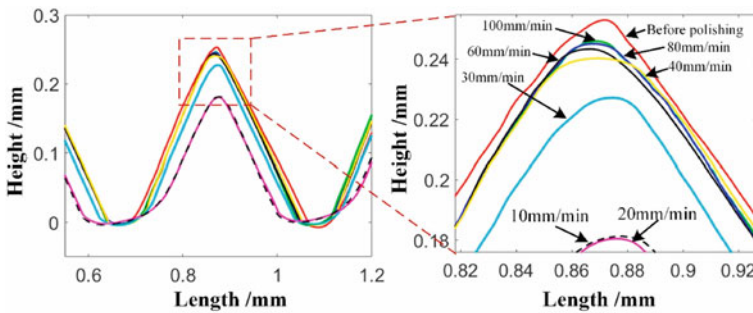
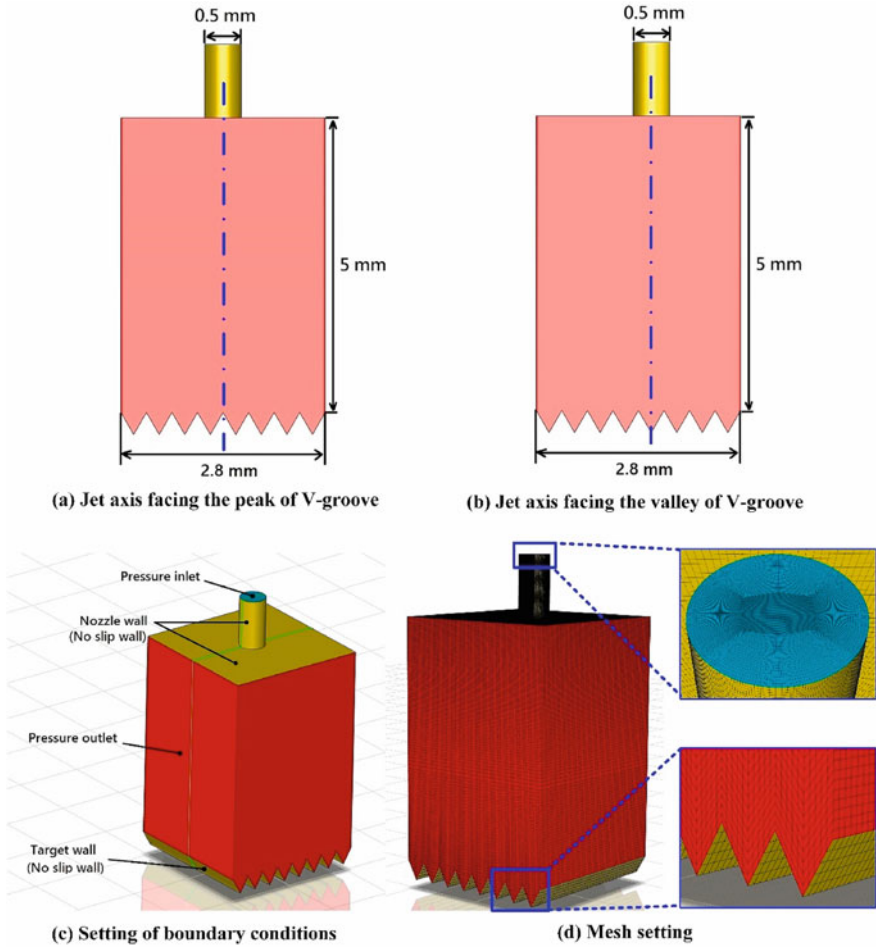


Fig. 10 Structured surface profile comparison after polishing under different feed rates

high feed rates and short polishing times are preferable for polishing MFJP surfaces with V-grooves, which is also applicable to other types of discontinuous structured surfaces.

### 4.3 Computational Fluidic Dynamics (CFD) Simulation

CFD simulations of FJP have been performed in the past by various researchers to demonstrate the fluid field distribution and material removal properties of the FJP process. Beaucamp et al. [43] used the CFD model to optimize the configuration of the slurry circulation system to achieve better polishing performance. Wang et al. [44] used the CFD model to simulate material removal of FJP under in vertical and inclined impact modes. Cheung et al. [45] used the CFD model to analyze the influence of the target surface curvature on the material removal and obtained a database of tool influence functions for different kinds of surfaces with different curvatures. Therefore, the CFD method was also used in this study to research the



**Fig. 11** Computational fluidic dynamic model of maskless fluid jet polishing V-groove surface

flow field distribution and material removal characteristics during FJP of V-grooved surface. The CFD simulation model was built using the ANSYS FLUENT software package.

Figure 11 shows two demonstrations of the developed model by using FLUENT, showing the peak and valley of the jet axis with respect to the V-groove surface. A Eulerian–Lagrangian method was used in this model to simulate the multiphase flow with liquid water, air, and abrasive particles. The water and air were treated as Eulerian phases, while the abrasive particle was treated as the Lagrangian phase. In addition, the Navier–Stokes equation are used in incompressible form to solve the fluid velocity field. Considering the effect of turbulence on the flow field, Shear-Stress Transport (SST) based on the blending of the  $k$ - $\omega$  and  $k$ - $\epsilon$  turbulence models

was used to express the turbulent fluid flow inside and outside the boundary layer for a wide range of the Reynolds number.

In order to describe the multiphase systems, a coupled algorithm and Volume of Fluid (VOF) model were employed to solve the pressure–velocity coupling and model the continuous multiphase, respectively. A random walk model and two-way coupling method were used to simulate the interaction between the discrete phase and continuum phase. Oka’s erosion model was used to determine the material erosion caused by the abrasive impact. The fluid pressure of the inlet was 8 bar. Further details on the structure are available in a previous publication by the authors [44].

Figure 12 shows the simulation result, and it is interesting to note that the velocity distribution in MFJP for V-groove surface is significantly different from the case of FJP on flat or curved surfaces as proposed by Wang et al. [44]. As can be seen from the velocity distribution in Fig. 12, the fluid is concentrated in the direction parallel to the groove during impact, while the fluid flow is blocked perpendicular to the groove direction. Therefore, the material removal distribution is not rotationally symmetric. Furthermore, in both cases, the shapes of the material removal distributions differ from each other and are caused by different fluid movements. It is also noted that the material removal on the peak surface was larger than the valley position in these two cases, indicating that the form change of the peak is the main reason for form deviation as shown in Sect. 4.2.

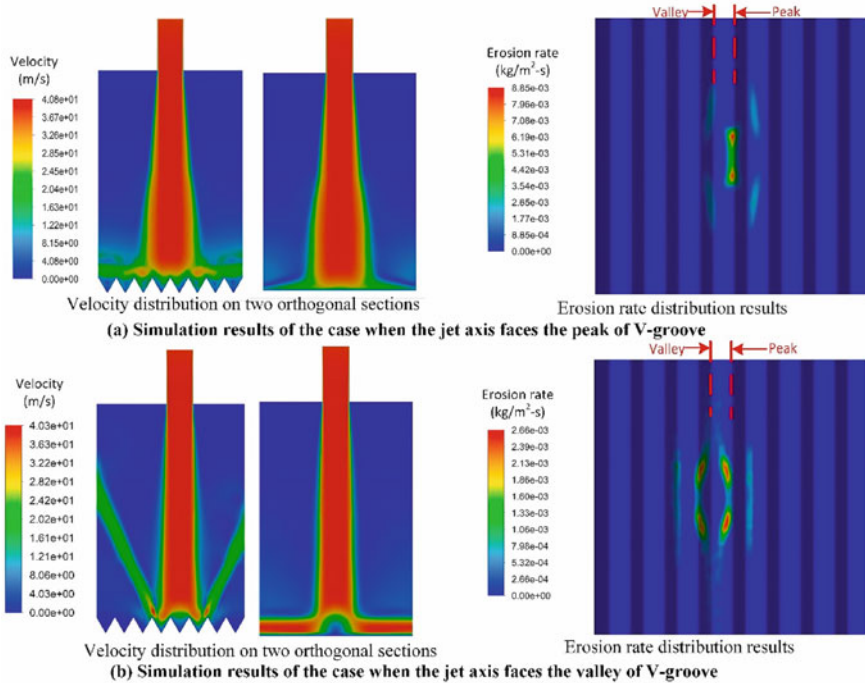


Fig. 12 Simulation results of the velocity and erosion rate distribution

## 4.4 Analysis of the Effect of Key Polishing Parameters

### 4.4.1 Effect of Fluid Pressure

Fluid pressure is a key parameter in FJP. It can directly determine the impinging velocity of the fluid jet, which can have a significant effect on the polishing performance. Figure 13 shows the surface roughness after polishing at different pressure, and when the fluid pressure was 8 bar, it is found that the minimum surface roughness was obtained. When the fluid pressure was higher than 8 bar, the surface roughness is higher. This is because the abrasives in the fluid jet can reach higher impact velocities at higher fluid pressures, resulting in deeper indentation in the target surface for each abrasive and thus a higher surface roughness. According to the material removal model of FJP developed by Cao and Cheung [46], the volume of material removal by a single abrasive  $V$  can be expressed as

$$V = k \left( \frac{1}{2} m_p v_t^2 \right) \left( \frac{1}{2} m_p v_n^2 \right)^{\frac{2(1-b)}{3}} \quad (4)$$

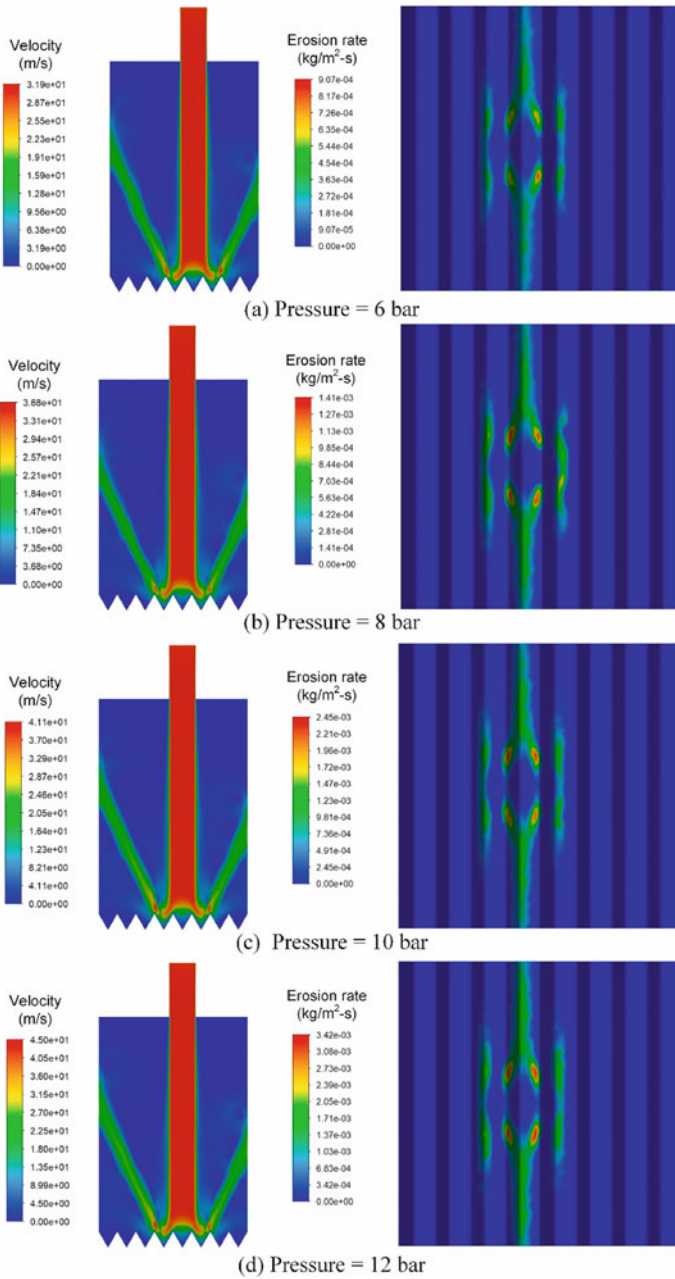
where  $k$  is a material dependent coefficient,  $m_p$  is the mass of abrasive particle,  $v_t$  is the tangential velocity at the target surface,  $v_n$  is the normal velocity to the target surface, and  $b$  is a material dependent exponent of the cross-section area of abrasive indentation. Higher fluid pressure can lead to a higher value of  $v_t$  and  $v_n$ , generating a larger material removal amount by a single abrasive particle, which can also be reflected in the simulation results for velocity and erosion rate as shown in Fig. 13.

The reason for the higher surface roughness at 6 bar of fluid pressure can be attributed to the low material removal in this case, which can also be explained by Eq. (4) (see Fig. 14). As shown in the SEM images at different fluid pressure in Fig. 15, the lack of material removal at low fluid pressure is also confirmed by the fact that most of the grinding tool marks on the V-groove surface are still present when the fluid pressure is 6 bar.

The form profile at different fluid pressure is also shown in Fig. 16. It is interesting to note that high fluid pressure can result in low form maintenance. At a fluid pressure of 8 bar, the form maintenance ratio was 91.9% after polishing, while  $\eta$  was 84.0% when the fluid pressure was 12 bar.

### 4.4.2 Effect of Impinging Angle

The impinging angle ( $0^\circ < \alpha \leq 90^\circ$ ) is the angle between the fluid jet and the target surface plane, which determines the impinging direction of the abrasive particles. Therefore, an appropriate impinging angle should be considered before MFJP of structured surface. In this study, impinging angles of  $45^\circ$ ,  $60^\circ$ ,  $75^\circ$  and  $90^\circ$  were compared. An impinging angle of less than  $45^\circ$  was not considered in this study due to the interference between the nozzle and the target surface during polishing.



**Fig. 13** Simulation results of velocity and erosion rate distribution in fluid jet polishing of V-groove surface under different pressure

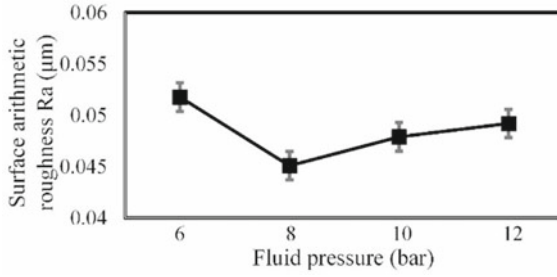


Fig. 14 Measured surface arithmetic roughness under different fluid pressure

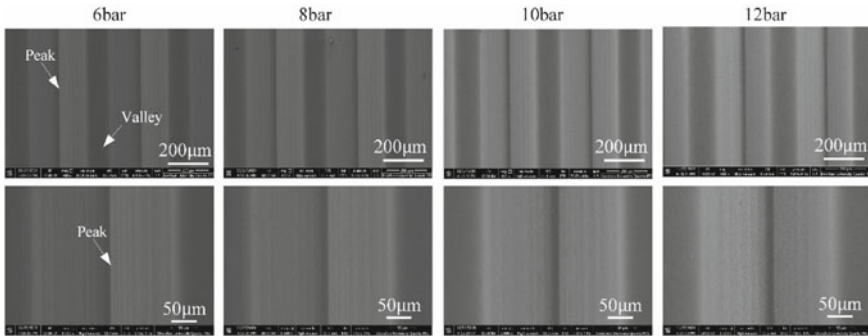


Fig. 15 SEM images at different fluid pressure

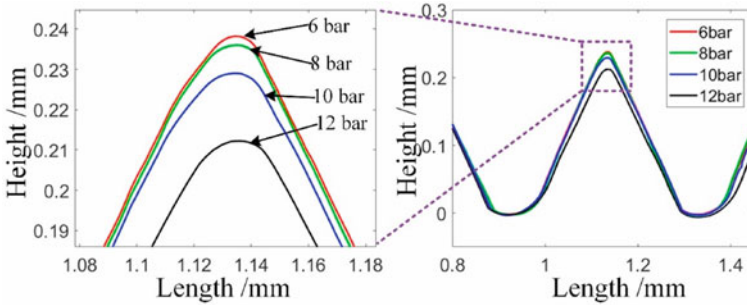
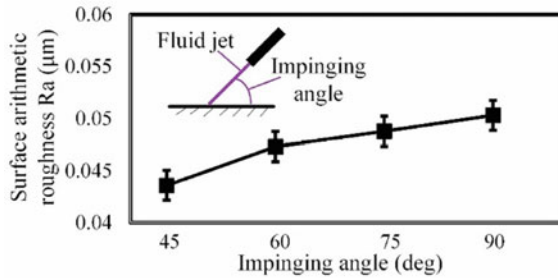


Fig. 16 Structured surface profile comparison after polishing under different fluid pressure

Figure 17 shows the surface roughness of the V-groove surface after polishing at different impinging angles. It is noted that a large impinging angle have a negative effect on achieving low surface roughness. Figure 17 shows that MFJP with an impinging angle of 45° can achieve the lowest surface roughness, which is 43.6 nm on average.





**Fig. 17** Measured surface arithmetic roughness under different impinging angles

The surface roughness is directly correlated with the amount of material removal by a single abrasive particle. As described in Cao and Cheung's model [46], the amount of removal by a single abrasive particle can be decomposed into the sum of normal and tangential components. The normal component of the volume removal  $V_N$  is essential for determining surface roughness, which can be expressed as

$$V_N = k \frac{m_p^{1+n} v_0^{2(1+n)} \sin^{2(1+n)} \alpha}{p_n} \quad (5)$$

where  $k$  and  $n$  are experimentally determined positive constants,  $v_0$  is the initial velocity of the particle before impinging, and  $p_n$  is the normal component of the contact pressure between the particle and target surface. Therefore, Eq. (5) shows that  $V_N$  is positively correlated with the impinging angle  $\alpha$ , which explains the phenomenon where a larger impinging angle leads to higher surface roughness.

Figure 18 shows SEM images of the V-groove surface after polishing at different impinging angles, and the form profile of them are made a comparison in Fig. 19. It is interesting to note that a lower impinging angle also contributes to form maintenance, which can also be explained by the lower removal volume in the normal direction of a single abrasive particle as shown in Eq. (4).

#### 4.4.3 Effect of Stand-Off Distance

For a normal FJP, the distance between the stand off distance (SOD) is not exceed 20 times the jet diameter. Therefore, SODs of 2 mm, 4 mm, 6 mm, 8 mm, and 10 mm were investigated in this study. Figure 20 shows the surface roughness results of the V-groove surface after polishing at different SODs. The result shows that in the relevant SOD range, the effect of SOD on the final surface roughness is negligible, which is consistent with the performance when polishing other kinds of surfaces as reported by Wang et al. [47]. However, the SOD cannot be too small, because some abrasive particles in the fluid jet cannot reach the same velocity as the jet due to collisions on the way to the nozzle outlet, resulting in insufficient impact for

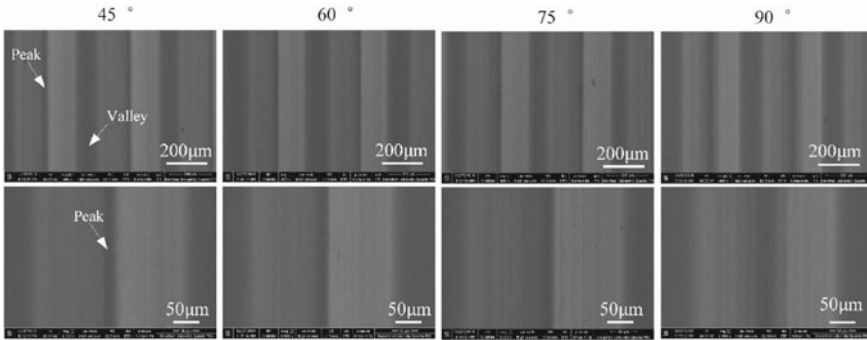


Fig. 18 SEM images at different impinging angles

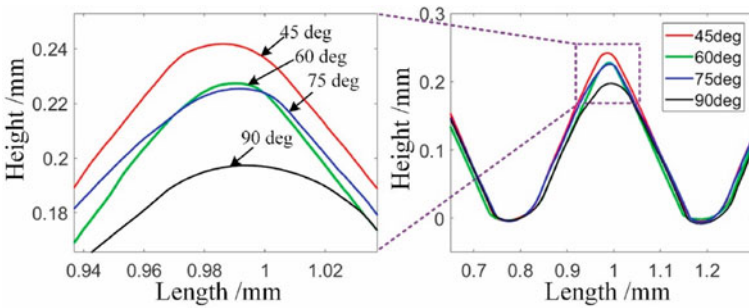


Fig. 19 Structured surface profile comparison after polishing under different impinging angles

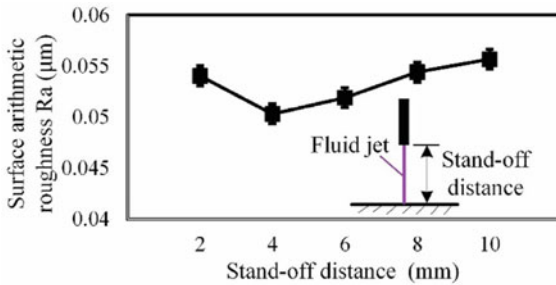


Fig. 20 Measured surface arithmetic roughness under different stand-off distances

material removal or a low material removal rate. As can be seen in Fig. 21, the lowest material removal rate is achieved when the SOD was 2 mm. When the SOD was in the range of 4 mm–8 mm, the material removal rate of them was close to each other. In addition, the effect of SOD on surface topography and form maintenance is also negligible, as shown in the SEM images and form profile comparison results in Figs. 22 and 23, respectively. The SOD can affect the impinging velocity of the

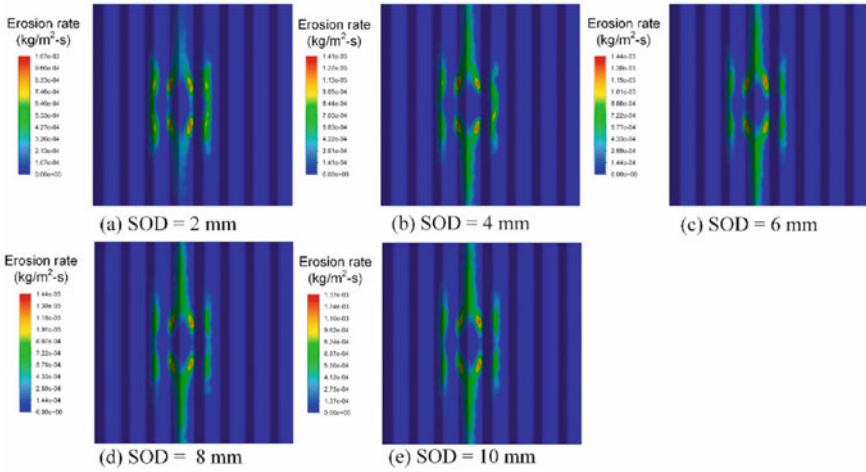


Fig. 21 Simulation results for the erosion rate distribution under different stand-off distances

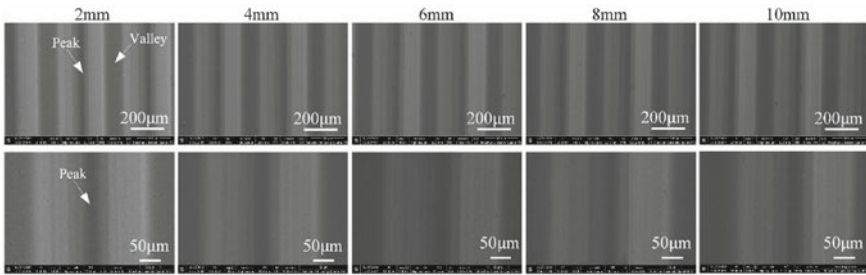


Fig. 22 SEM images at different stand-off distances

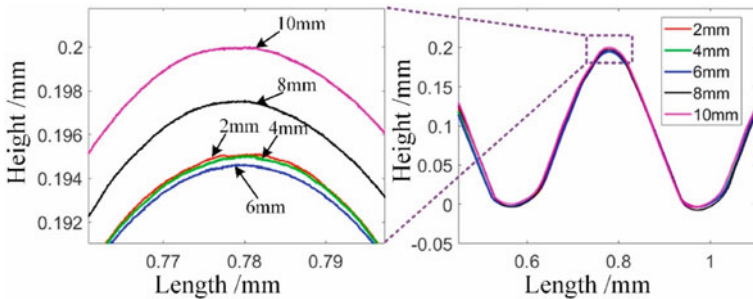


Fig. 23 Structured surface profile comparison after polishing under different stand-off distances

abrasive in the fluid jet, but in the operating range of SOD, the change in velocity is small, resulting in a small change in material removal rate according to Eq. (4).

## 5 Conclusions

Maskless fluid Jet Polishing (MFJP) is put forward for precision polishing of optical structural surfaces and can provide a turnkey solution for precision manufacturing of complex optical structural surfaces with high precision. Masks are not required due to the lower fluid pressure. The feasibility of continuous (sinusoidal structure surfaces) and discontinuous (V-groove structure surfaces) structure surfaces was investigated and the effects of key parameters were systematically studied.

The main conclusions can be summarized as follows:

- (1) Surface defects of the sinusoidal structure caused by wire EDM were significantly reduced with FJP, resulting in a very smooth surface. The surface roughness at the top and bottom positions was decreased from 642.1 nm and 458.9 nm to 18.8 nm and 14.4 nm, respectively. Meanwhile, the shape retention factor of the surface reached 99.8%, indicating a high shape retention capacity. This presents the excellent polishing performance of MFJP on surfaces with sinusoidal structure. In addition, it also highlights the good polishing performance of other continuous structure surfaces.
- (2) Grinding marks on textured surfaces with V-grooves can be completely removed with MFJP. The average surface roughness can be reduced from 132.5 nm to 40.6 nm after a single polishing pass, with a shape retention factor of over 95% under certain conditions. This demonstrates that MFJP is also suitable for polishing surfaces with a V-groove structure under appropriate polishing conditions.
- (3) High fluid pressure is unfavorable for good shape retention. In addition, a small impact angle is an advantage for achieving good surface roughness. The influence of distance is not clear, which is also the case with MFJP in other applications.

MFJP is suitable for polishing optically textured surfaces in applications without strict requirements for structural shape accuracy, such as lighting grids. This study also highlights the application of MFJP for finishing other components with small or micrometric cavities or channels, such as microfluidic channels, etc. In addition, nano-sized polishing abrasives or even colloidal polishing abrasives can be used for surfaces with stringent roughness requirements.

Nevertheless, it is interesting to note that the shape retention of MFJP on the discontinuous structured surface is low for long polishing times. Therefore, the roughness of the discontinuous structured surface must be good enough to reduce the polishing time on MFJP to ensure high shape retention. In addition, the polishing efficiency of MFJP is lower than that of the mechanical polishing method, resulting

in long polishing times when polishing large areas. And it should be improved in the future.

**Acknowledgements** The work described in this chapter was supported by the National Natural Science Foundation of China (Grant No. 51805334), the International Science and Technology Cooperation Project of Shenzhen City (Grant No. GJHZ20190822091805371), and the Science and Technology Planning Project of Guangdong Province (Grant No. 2017A010102003), the Research Grants Council of the Government of the Hong Kong Special Administrative Region, China (Project No. 15200119) and the financial support from the Guangdong Natural Science Foundation Program 2019–2020 (Project No. 2019A1515012015).

## References

1. Evans CJ, Bryan JB (1999) Structured”, “textured” or “engineered surfaces. *CIRP Ann Manuf Technol* 48(2):541–556
2. Zhang S, Zhou Y, Zhang H, Xiong Z, To S (2019) Advances in ultra-precision machining of micro-structured functional surfaces and their typical applications. *Int J Mach Tools Manuf* 142:16–41
3. Yan G, Zhang Y, You K, Li Z, Yuan Y, Fang F (2019) Off-spindle-axis spiral grinding of aspheric microlens array mold inserts. *Opt Express* 27(8):10873–10889
4. Zhu WL, Duan F, Zhang X, Zhu Z, Ju BF (2018) A new diamond machining approach for extendable fabrication of micro-freeform lens array. *Int J Mach Tools Manuf* 124:134–148
5. Jiang D, Fan P, Gong D, Long J, Zhang H, Zhong M (2016) High-temperature imprinting and superhydrophobicity of micro/nano surface structures on metals using molds fabricated by ultrafast laser ablation. *J Mater Process Technol* 236:56–63
6. Sun Z, To S, Wang S, Du J (2020) Development of self-tuned diamond milling system for fabricating infrared micro-optics arrays with enhanced surface uniformity and machining efficiency. *Opt Express* 28(2):2221–2237
7. Zhu Z, To S, Zhang S (2015) Theoretical and experimental investigation on the novel end-fly-cutting-servo diamond machining of hierarchical micro-nanostructures. *Int J Mach Tools Manuf* 94:15–25
8. Guo B, Zhao Q (2017) Ultrasonic vibration assisted grinding of hard and brittle linear micro-structured surfaces. *Precis Eng* 48:98–106
9. Brinksmeier E, Schönemann L (2014) Generation of discontinuous microstructures by diamond micro chiseling. *CIRP Ann* 63(1):49–52
10. He ZR, Luo ST, Liu CS, Jie XH, Lian WQ (2019) Hierarchical micro/nano structure surface fabricated by electrical discharge machining for anti-fouling application. *J Market Res* 8(5):3878–3890
11. Temmler A, Liu DM, Drinck S, Luo JB, Poprawe R (2020) Experimental investigation on a new hybrid laser process for surface structuring by vapor pressure on Ti6Al4V. *J Mater Process Technol* 277:116450
12. Park DS, Cho MW, Lee H, Cho WS (2004) Micro-grooving of glass using micro-abrasive jet machining. *J Mater Process Technol* 146:234–240
13. Brinksmeier E, Riemer O, Gessenharter A, Autschbach L (2004) Polishing of structured molds. *CIRP Ann* 53(1):247–250
14. Brinksmeier E, Riemer O, Gessenharter A (2006) Finishing of structured surfaces by abrasive polishing. *Precis Eng* 30(3):325–336
15. Riemer O (2008) A review on machining of micro-structured optical molds. *Key Eng Mater* 364:13–18

16. Klocke F, Brinksmeier E, Riemer O, Klink A, Schulte H, Sarikaya H (2007) Manufacturing structured tool inserts for precision glass moulding with a combination of diamond grinding and abrasive polishing. *Ind Diamond Rev* 67:65–69
17. Zhao Q, Sun Z, Guo B (2016) Material removal mechanism in ultrasonic vibration assisted polishing of micro cylindrical surface on SiC. *Int J Mach Tools Manuf* 103:28–39
18. Suzuki H, Okada M, Yamagata Y, Morita S, Higuchi T (2012) Precision grinding of structured ceramic molds by diamond wheel trued with alloy metal. *CIRP Ann* 61(1):283–286
19. Kawakubo H, Yomogida T (2006) Finishing characteristics of R-groove using magnetic field assisted machining method. In: Proceedings of JSPE semestrial meeting. The Japan Society for Precision Engineering, pp 733–734
20. Takebayashi Y, Hirogaki T, Aoyama E, Ogawa K, Melkote SN (2013) Development of magnetic polishing for micro channel with a ball-nose-shaped tool. In: ASME 2013 International mechanical engineering congress and exposition. American Society of Mechanical Engineers Digital Collection
21. Guo J, Liu K, Wang Z, Tnay GL (2017) Magnetic field-assisted finishing of a mold insert with curved microstructures for injection molding of microfluidic chips. *Tribol Int* 114:306–314
22. Kim WB, Lee SH, Min BK (2004) Surface finishing and evaluation of three-dimensional silicon microchannel using magnetorheological fluid. *J Manuf Sci Eng* 126:772–778
23. Yamaguchi H, Riveros RE, Mitsuishi I, Takagi U, Ezoe Y, Yamasaki N, Mitsuda K, Hashimoto F (2010) Magnetic field-assisted finishing for micropore X-ray focusing mirrors fabricated by deep reactive ion etching. *CIRP Ann* 59(1):351–354
24. Riveros RE, Yamaguchi H, Boggs T, Mitsuishi I, Mitsuda K, Takagi U, Ezoe Y, Ishizu K, Moriyama T (2012) Magnetic field-assisted finishing of silicon microelectromechanical systems micropore X-Ray optics. *J Manufact Sci Eng* 134(5)
25. Suzuki H, Okada M, Lin W, Morita S, Yamagata Y, Hanada H, Araki H, Kashima S (2014) Fine finishing of ground DOE lens of synthetic silica by magnetic field-assisted polishing. *CIRP Ann* 63:313–316
26. Shimada K, Wu Y, Wong YC (2003) Effect of magnetic cluster and magnetic field on polishing using magnetic compound fluid (MCF). *J Magn Magn Mater* 262(2):242–247
27. Guo H, Wu Y, Lu D, Fujimoto M, Nomura M (2014) Effects of pressure and shear stress on material removal rate in ultra-fine polishing of optical glass with magnetic compound fluid slurry. *J Mater Process Technol* 214:2759–2769
28. Wang Y, Wu Y, Nomura M (2016) Feasibility study on surface finishing of miniature V-grooves with magnetic compound fluid slurry. *Precis Eng* 45:67–78
29. Zhang C, Rentsch R, Brinksmeier E (2005) Advances in micro ultrasonic assisted lapping of microstructures in hard–brittle materials: a brief review and outlook. *Int J Mach Tools Manuf* 45(7–8):881–890
30. Suzuki H, Hamada S, Okino T, Kondo M, Yamagata Y, Higuchi T (2010) Ultraprecision finishing of micro-aspheric surface by ultrasonic two-axis vibration assisted polishing. *CIRP Ann* 59(1):347–350
31. Guo J, Morita SY, Hara M, Yamagata Y, Higuchi T (2012) Ultra-precision finishing of micro-aspheric mold using a magnetostrictive vibrating polisher. *CIRP Ann* 61:371–374
32. Wang G, Lv B, Zheng Q, Zhou H, Liu Z (2019) Polishing trajectory planning of three-dimensional vibration assisted finishing the structured surface. *AIP Adv* 9(1):015012
33. Guo J, Jong HJH, Kang R, Guo D (2018) Novel localized vibration-assisted magnetic abrasive polishing method using loose abrasives for V-groove and Fresnel optics finishing. *Opt Express* 26:11608–11619
34. Guo J, Feng W, Jong HJH, Suzuki H, Kang R (2020) Finishing of rectangular microfeatures by localized vibration-assisted magnetic abrasive polishing method. *J Manuf Process* 49:204–213
35. Matsumura T, Muramatsu T, Fueki S (2011) Abrasive water jet machining of glass with stagnation effect. *CIRP Ann* 60:355–358
36. Föhnle OW, Van Brug H, Frankena HJ (1998) Fluid jet polishing of optical surfaces. *Appl Opt* 37:6771–6773

37. Lu Y, Luo W, Wu X, Xu B, Wang C, Li J, Li L (2020) Fabrication of micro-structured LED diffusion plate using efficient micro injection molding and micro-ground mold core. *Polymers* 12(6):1307
38. Bisaria H, Shandilya P (2019) Experimental investigation on wire electric discharge machining (WEDM) of Nimonic C-263 superalloy. *Mater Manuf Processes* 34(1):83–92
39. Wang CJ, Cheung CF, Ho LT, Liu MY, Lee WB (2017) A novel multi-jet polishing process and tool for high-efficiency polishing. *Int J Mach Tools Manuf* 115:60–73
40. Wang CJ, Cheung CF, Ho LT, Loh YM (2021) Development of a fluid line-jet polishing process for rotational axisymmetric surfaces. *J Manuf Process* 61:15–24
41. Liu MY, Cheung CF, Feng X, Wang CJ, Cao ZC (2020) Any-degrees-of-freedom (anyDOF) registration for the characterization of freeform surfaces. *Precis Eng* 62:170–180
42. Whitehouse DJ (2002) *Surfaces and their measurement*. CRC Press
43. Beaucamp A, Namba Y, Freeman R (2012) Dynamic multiphase modeling and optimization of fluid jet polishing process. *CIRP Ann* 61(1):315–318
44. Wang CJ, Cheung CF, Liu MY (2017) Numerical modeling and experimentation of three dimensional material removal characteristics in fluid jet polishing. *Int J Mech Sci* 133:568–577
45. Cheung CF, Wang CJ, Ho LT, Chen J (2018) Curvature-adaptive multi-jet polishing of freeform surfaces. *CIRP Ann* 67(1):357–360
46. Cao ZC, Cheung CF (2014) Theoretical modelling and analysis of the material removal characteristics in fluid jet polishing. *Int J Mech Sci* 89:158–166
47. Wang CJ, Cheung CF, Ho LT, Loh YM (2020) An investigation of effect of stand-off distance on the material removal characteristics and surface generation in fluid jet polishing. *Nanomanuf Metrol*:1–11

# Chapter 17

## Fabrication of Micro-structured Polymer Via Precision Grinding and Injection Molding



YanJun Lu, Xingyu Mou, and Fumin Chen

**Abstract** In this chapter, precise micro-grinding machining was proposed to create regular and controllable micro-grooved array structures on the surface of mold cores for the mass production and fabrication of micro-structured polymer components by micro injection molding. First, the 3D topology and cross-sectional profiles of a micro-ground mold cores and micro-formed polymer with various microstructural parameters are presented. The surface roughness of the mold cores and polymers is then compared. Secondly, the relationship between the accuracy of the microbead-treated mould core and the fillability of the micro-structured injection polymer is investigated. Finally, the effect of micro injection molding parameters on the filling rate of micro-structures polymer were investigated. The results show that micro-structured polymers can be produced efficiently and rapidly using the proposed method. The experimental results show that the highest shape accuracy and filler level of the micro-structured polymer can be achieved at  $4.05\ \mu\text{m}$  and 99.30% respectively for a mold core with micro-grooves. It was found that the degree of filling of the micro-structured polymer increased approximately with the accuracy of the core processing. Injection pressure has the greatest influence on the degree of filling of the molded polymer, while melt temperature has the least effect.

### 1 Introduction

Micro-structured polymer devices have been applied in many fields such as optical, biomedical, electronic and microelectro-mechanical systems (MEMS) [1–3]. Currently, the main microforming techniques for micro-structured polymers are microinjection molding, microthermal compression molding, and injection and pressure molding [4, 5]. Microinjection molding has become an alternative method for mass production and fabrication of micro-structured polymer products due to its short

---

Y. Lu (✉) · X. Mou · F. Chen

Guangdong Provincial Key Laboratory of Micro/Nano Optomechanics Engineering, College of Mechatronics and Control Engineering, Shenzhen University, Nan-Hai Ave 3688, Shenzhen 518060, Guangdong, PR China  
e-mail: [luyanjun@szu.edu.cn](mailto:luyanjun@szu.edu.cn)



molding cycle time, high efficiency, and low production cost [6, 7]. For example, superhydrophobic polymer surfaces with a layered structure of micro- and nanocylinders have been successfully produced by microinjection molding [8]. It has been shown that droplets on layered micro- and nanopolymer surfaces reach a contact angle of about  $163^\circ$ , which gives them self-cleaning properties. An amorphous polymer surface with a high aspect ratio microstructure was fabricated by microinjection molding for erythrocyte depletion in bioelectromechanical systems [9]. The temperature of the mold proved to have the greatest influence on the degree of replication of microfeatures compared to other major process parameters. Microinjection molding has been used to produce microinjected polymer surfaces by replicating the microscopic features of molded inserts with microcavity structures [10]. Experimental results have shown that small cavity thickness and high mold temperature have a positive influence on the level of replication of micro features.

However, high-precision machining of the mold core surface to produce micro-nanostructures is very difficult, which directly determines the quality of micro-forming of micro-structured polymer products. Many advanced processing techniques have emerged for microscale machining of mold core microstructure surfaces, such as chemical etching [11], laser processing [12], electrical discharge machining (EDM) [13], and fluid jet array parallel machining (FJAPM) [14]. Although chemical etching and laser processing techniques can produce nanoscale microtextured structures, they are difficult to use to ensure the accuracy of the three-dimensional morphology of micron-scale microstructures. Although electrical discharge machining (EDM) can effectively fabricate complex 3D microstructures, it is difficult to achieve smooth microstructure surfaces. Parallel processing using fluid jet arrays (FJAPM) can produce smooth microstructure surfaces, but requires significant processing time. It was found that a dressed superhard diamond grinding wheel can perform precision micromachining of wire drawing mold cores to obtain smooth micro-structured surfaces [15–17]. To achieve high shape accuracy and surface quality of microstructures in the micron range, this study proposes an efficient and precise micro-ground technique to produce micron-sized slotted mesh structures with controlled shape accuracy on the mold core surface. In addition, the micro-ground process is very simple and the production cost is relatively low.

In this chapter, the regular and controlled micro-grooved array structures on the surface of mold core were machined by micro-grinding machining with a trued V-tip diamond grinding wheel. Micro injection molding technology rapidly produces micro-structured polymer parts by replicating microscopic features on the surface of the mold core. The surface morphology and V-groove profile of mold cores and micro-structured polymers are presented, and the shape accuracy of micro-grinding and the filling degree of micro-injection molding are analyzed. The surface roughness of the micro-ground mold cores and the micro-formed polymers are compared. In addition, the relationship between the shape accuracy of the micro-ground core and the degree of filling of the micro-structured polymer was revealed. The effect of microinjection molding parameters on the degree of filling of micro-structured polymers was also analyzed.

## 2 Materials and Methods

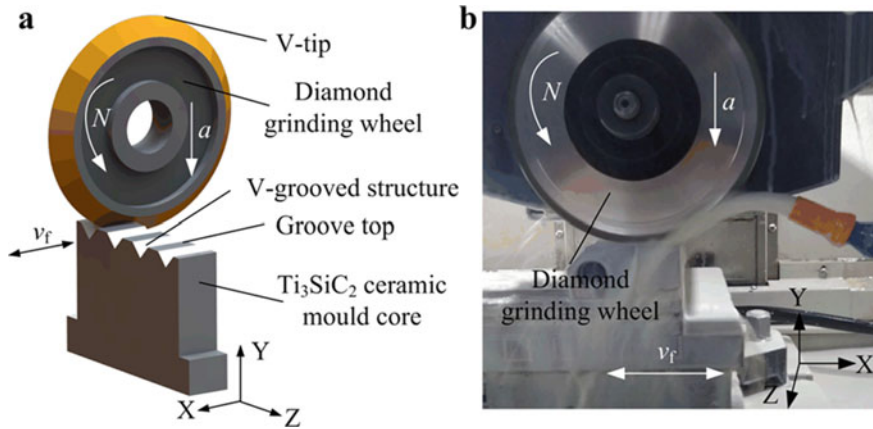
### 2.1 *Micro-grinding of Mold Core with V-Grooved Array Structures*

Titanium carbide ( $\text{Ti}_3\text{SiC}_2$ ) has both metallic and ceramic properties, which is compared to conventional mold core materials, such as excellent machinability, good electrical conductivity, high wear resistance and good self-lubrication [18, 19]. In this experiment,  $\text{Ti}_3\text{SiC}_2$  ceramic was chosen as the mold core material because of its good lubrication and self-lubrication properties.

Figure 1 shows a schematic diagram and photographs of microfabrication of the V-groove structure on the  $\text{Ti}_3\text{SiC}_2$  mold core surface using a computer-controlled precision grinder (CNC). First, the V-groove grinding head of the diamond wheel was mechanically ground using a CNC interpolation path [20] to straighten it out. The  $\text{Ti}_3\text{SiC}_2$  ceramic substrate was then installed on the horizontal table of the grinding machine. The machined V-shaped diamond wheel is driven by the CNC for grinding the  $\text{Ti}_3\text{SiC}_2$  tool core (see Fig. 1a). By mimicking the V-shape of the diamond wheel, V-grooves are gradually formed on the surface of the  $\text{Ti}_3\text{SiC}_2$  core. When one V-groove is completed, the diamond wheel is moved in the specified space in the Z-axis direction to carry out the grinding process for the second V-groove. Finally, a micro-groove structure is formed on the surface of the toolholder according to the specified machining path. Figure 1b shows a picture of the machining of the mold core. As  $\text{Ti}_3\text{SiC}_2$  is a ceramic material, the conditions for micro-grinding the mold core with a V-shaped diamond wheel were chosen based on previous machining experience (see Table 1). Six sets of well-developed V-grooves were ground on the surface of the substrate core under the same grinding conditions. The V-groove parameters developed include the V-groove angle  $\alpha$ , the V-groove depth  $h$  and the V-groove space  $b$ , as shown in Table 2. The corresponding mold cores with various V-grooved array structures are called as  $A_m$ ,  $B_m$ ,  $C_m$ ,  $D_m$ ,  $E_m$  and  $F_m$  sections respectively.

### 2.2 *Micro Injection Molding of Micro-structured Polymers*

With the micro injection molding machine (Babyplast 6/10P, Cronoplast SI, Barcelona, Spain), the V-groove array structure of the mold core surface can be reproduced on the part surface, as shown in Fig. 2a. With its metal ball plasticizing system and piston injection system, this efficient and precise micro injection molding machine is ideal for mass production and processing of all thermoplastic micro precision parts. Figure 2b shows the operation of the micro injection molding machine. For this experiment, polypropylene (PP) pellets (B310, Lotte Chemical Corporation, Seoul, Korea) were selected as the material for the polymer part and placed in the hopper. The flow rate, density, heat deflection temperature and melting point of the polymer material were 0.5 g/10 min, 0.9 g/cm<sup>3</sup>, 110 °C and 167 °C, respectively. The



**Fig. 1** Micro-grinding machining scheme and image of mold core: **a** Schematic diagram of V-grooved structures machining; **b** Image of micro-grinding

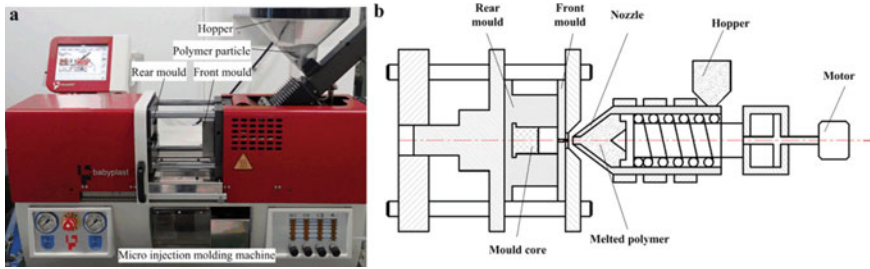
**Table 1** Micro-grinding conditions of mold core using a V-tip diamond grinding wheel

CNC grinder	SMART B818 III
Diamond grinding wheel	SD3000, resin bond, diameter $D = 150$ mm, width $B = 4$ mm, Wheel speed $N = 3000$ r/min
Workpiece	$Ti_3SiC_2$ ceramic mold core
Rough machining	Feed speed $v_f = 1000$ mm/min, depth of cut $a = 5$ $\mu$ m
Finish machining	Feed speed $v_f = 100$ mm/min, depth of cut $a = 1$ , $\Sigma a = 10$ $\mu$ m
Coolant	Emulsion

**Table 2** The designed V-grooved structure parameters of mold cores

Sample	V-groove angle $\alpha$ ( $^\circ$ )	V-groove depth $h$ ( $\mu$ m)	V-groove space $b$ ( $\mu$ m)
$A_m$	90	100	400
$B_m$	90	100	500
$C_m$	90	100	600
$D_m$	90	150	400
$E_m$	90	150	500
$F_m$	90	150	600

counter mold has a core shape with a V-grooved array structure. Polymer particles are first heated and plasticized, then melted by an electric piston and injected into the front cavity of the mold through a nozzle. The cavity is then cooled while maintaining a certain pressure. Finally, the micro-structured polymer is produced when the front and back side of the mold are simultaneously demolded.

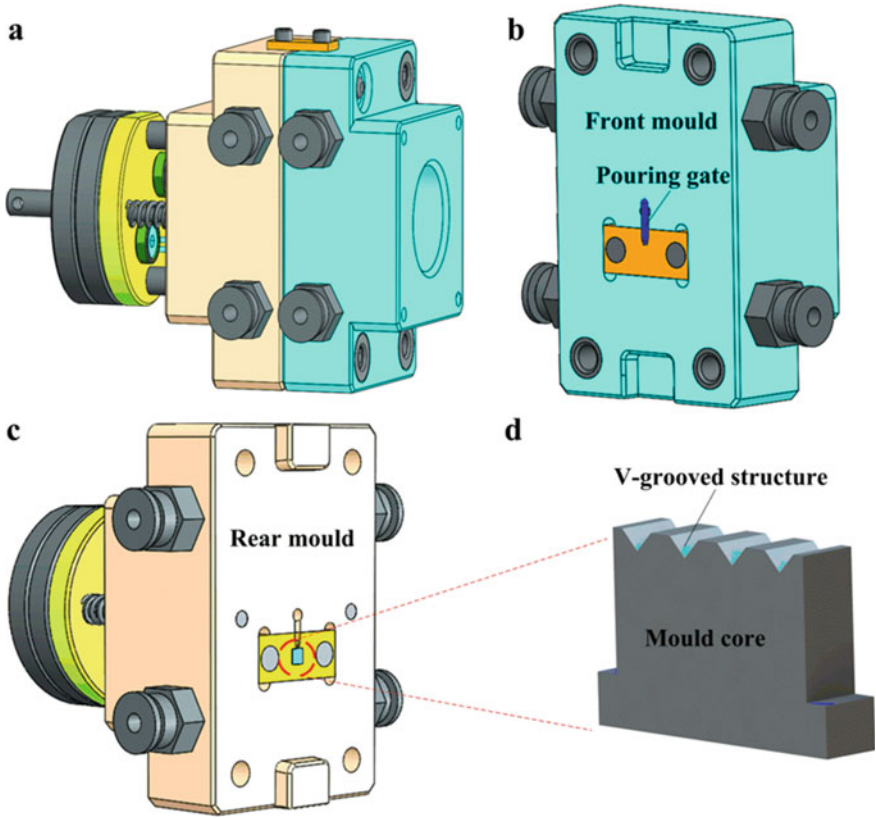


**Fig. 2** Photograph and working principle of the micro injection molding machine: **a** photograph; **b** working principle

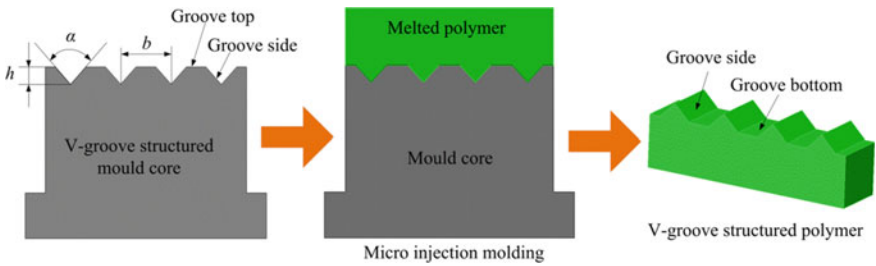
Figure 3 shows a sketch of the mold frame and mold core design. Figure 3a shows the whole mold frame. Figure 3b shows a schematic of the front side of the mold. The polymer material which is melted and plasticized is injected into the front mold cavity through the pouring port. Figure 3c shows a schematic view of the rear mold, which is equipped with a core. Figure 3d shows a schematic view of a mold core with V-grooves obtained by microfabrication.

Figure 4 shows the microinjection molding process of a micro-structured polymer. The V-groove of the mold core is repeated on the polymer surface to create an inverted V-groove structure after micro injection molding. The V-groove parameters of the micro-ground mold core are characterized as V-groove angle  $\alpha_1$ , V-groove depth  $h_1$  and V-groove space  $b_1$ . The V-groove parameters of the micro-structured polymer are characterized as V-groove angle  $\alpha_2$ , V-groove depth  $h_2$  and V-groove space  $b_2$ . The surface quality of the micro-structured polymer at the edge of the groove and at the bottom of the groove depends on the quality of the groove edge and the quality of the top edge of the core groove. Under the same conditions, six sets of micro-ground mold cores were used for micro-injection experiments. According to the preliminary tests, the melting temperature was set at 210 °C, the injection speed was 40 mm/s, the injection pressure was 7 MPa, and the holding pressure and pressure retention time were 5 s. After microinjection molding, the corresponding micro-structured polymer samples were defined as  $A_w$ ,  $B_w$ ,  $C_w$ ,  $D_w$ ,  $E_w$  and  $F_w$ .

In order to investigate the effects of melt temperature  $T$ , injection rate  $v$ , injection pressure  $P$  and residence time  $t$  on the degree of filling of micro-structured polymers, the experimental parameters listed in Table 3 were developed. Thirty micro-structured polymer samples were prepared under each process parameter condition, and five random samples were selected for testing and averaging.



**Fig. 3** The design sketches of mold frame and mold core: **a** the whole mold frame; **b** the front mold; **c** the rear mold; **d** the mold core



**Fig. 4** Principle of micro injection molding of the micro-structured polymer

**Table 3** Experimental parameter lists of micro injection molding

No	Melt temperature T (°C)	Injection speed v (mm/s)	Injection pressure P (MPa)	Holding time t (s)
1	200	40	7	3
2	205	40	7	3
3	210	40	7	3
4	215	40	7	3
5	220	40	7	3
6	210	30	7	3
7	210	35	7	3
8	210	45	7	3
9	210	50	7	3
10	210	40	5	3
11	210	40	6	3
12	210	40	8	3
13	210	40	9	3
14	210	40	7	1
15	210	40	7	2
16	210	40	7	4
17	210	40	7	5

### **2.3 Measurement of Micro-grooved Mold Cores and Polymers**

High-resolution scanning electron microscopy (SEM, FEI Quanta 450FEG and Apreo S, FEI Corporation, Hillsboro, OR, USA) was used to research the surface morphology of micro-structured mold cores. A 3D laser scanning microscope (VK-250, Keyence, Osaka, Japan) was used to measure the 3D morphology and cross-sectional profile of the micro-structured form bars. A probe stepper (D-300, KLA-Tencor, Milpitas, CA, USA) was used to measure the cross-sectional profile of the micro-structured polymer. Using data analysis software, the cross-sectional profiles were used to determine the surface roughness and V-curvature angle. The results presented are the average of five measurements.

### 3 Results and Discussions

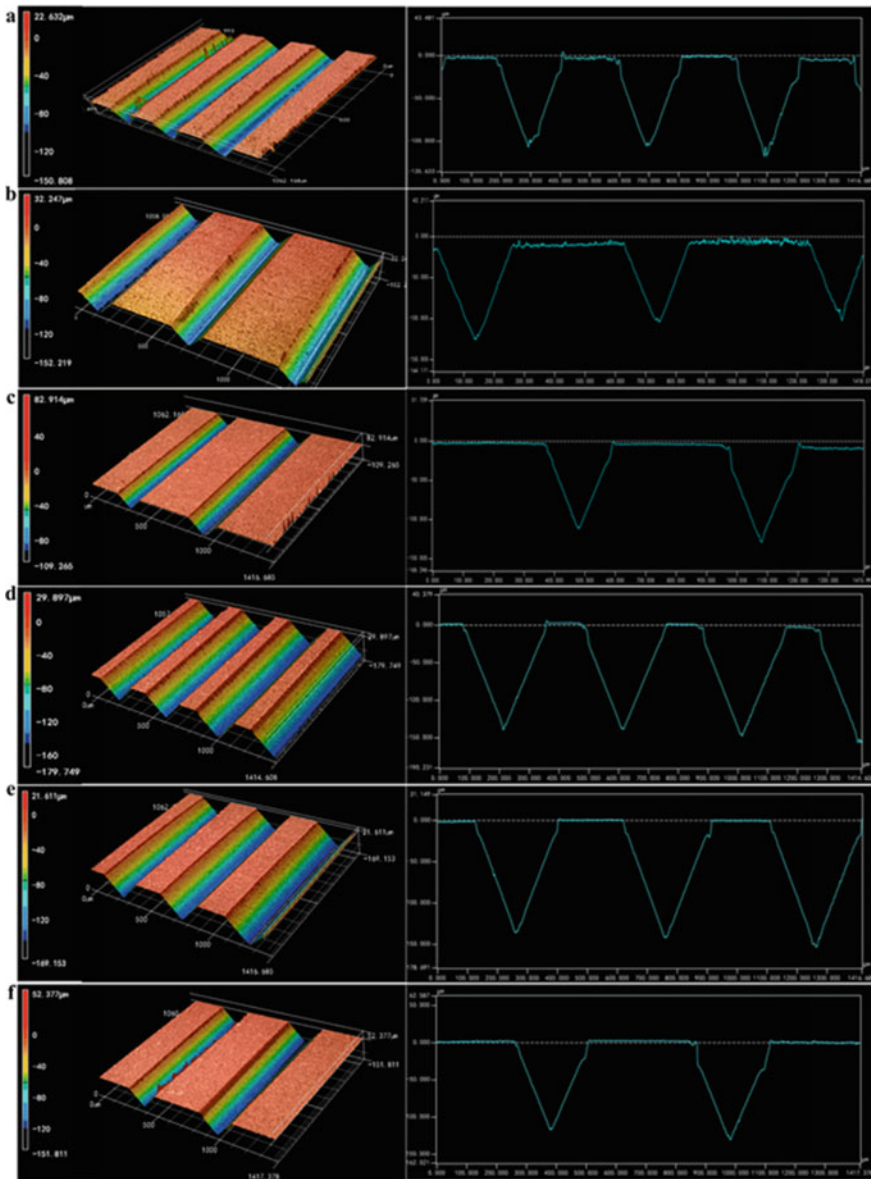
#### 3.1 Surface Topographies and Profiles of Micro-ground Mold Core

Figure 5 shows the 3D topographies and section profiles of the mold core with micro-grooved array structures after micro-grinding. It can be seen from the figure that a regular and uniform V-groove array structure is completely created on the surface of the mold core. The parameters of the micromachined V-groove structure are given in Table 4, which are approximately the same as those given in Table 2. the V-groove angle  $\alpha$  was obtained from the V-groove profile measured by a 3D laser scanning microscope. the angular error of the V-shaped micro-grooves varied from  $0.88^\circ$  to  $1.87^\circ$ , with an average angular error of  $1.38^\circ$ . The average errors of micro-groove depth and V-groove spacing were  $2.62\ \mu\text{m}$  and  $2.73\ \mu\text{m}$ , respectively. The actual distance of the V-groove in the cast bar was slightly larger than the theoretical value, which was mainly influenced by the non-circular surface of the diamond grinding wheel.

Figure 6 shows an SEM photograph of the surface of the micro-ground mold core. the SEM observation shows that the morphological characteristics of the V-groove surface are generally consistent with the 3D morphological measurements in Fig. 5. It can also be found that the surface on one side of the V-groove is smoother than the surface above the groove (the unground surface). The surface of the V-groove of sample  $D_m$  is the smoothest and most uniform compared to the other samples.

#### 3.2 Surface Topographies and Profiles of Micro-structured Polymers

Figure 7 shows the SEM topography of the micro-structured polymer after microinjection molding. It can be found from the SEM image that the V-shaped structure of the mold core is preferentially repeated on the polymer, forming an inverted V-shaped structure. It can be seen that the surface of the  $D_w$  microstructure is the smoothest, with a roughness  $R_a$  of  $0.052\ \mu\text{m}$  on the groove side. It can also be found that the V-groove side of the microinjected polymer is smoother than the V-groove side of the mold core (see Figs. 6d and 7d). The microinjected surfaces of samples  $B_w$ ,  $C_w$  and  $F_w$  show many cracks and melted polymer. This was attributed to the poor quality of the bead blasted surfaces of the respective mold sticks, which led to difficulties in demolding during the microinjection process. For all the micro-formed polymers, the sides of the V-groove were smoother than the bottom of the V-groove. This is due to the fact that the surface quality of the bottom of the polymer groove depends on the unpolished top surface of the mold core groove.

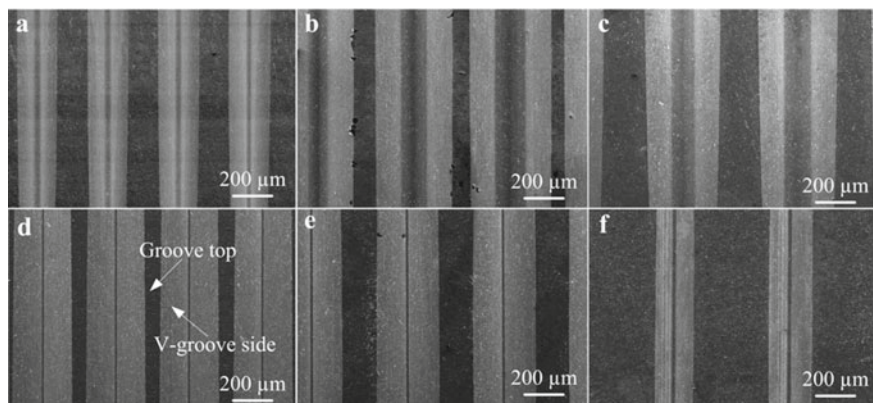


**Fig. 5** 3D topographies and profiles of micro-ground mold cores: **a** Sample A<sub>m</sub>; **b** Sample B<sub>m</sub>; **c** Sample C<sub>m</sub>; **d** Sample D<sub>m</sub>; **e** Sample E<sub>m</sub>; **f** Sample F<sub>m</sub>

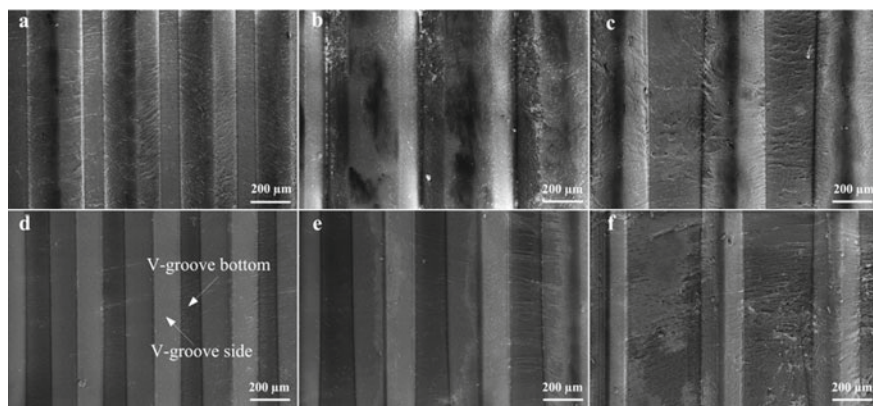


**Table 4** The V-grooved structure parameters of micro-ground mold cores

Sample	V-groove angle $\alpha_1$ ( $^\circ$ )	V-groove depth $h_1$ ( $\mu\text{m}$ )	V-groove space $b_1$ ( $\mu\text{m}$ )
A <sub>m</sub>	90.88	99.72	400.43
B <sub>m</sub>	91.87	106.64	503.17
C <sub>m</sub>	91.80	100.37	604.17
D <sub>m</sub>	91.17	148.10	401.97
E <sub>m</sub>	91.19	152.61	506.52
F <sub>m</sub>	91.35	153.93	599.86

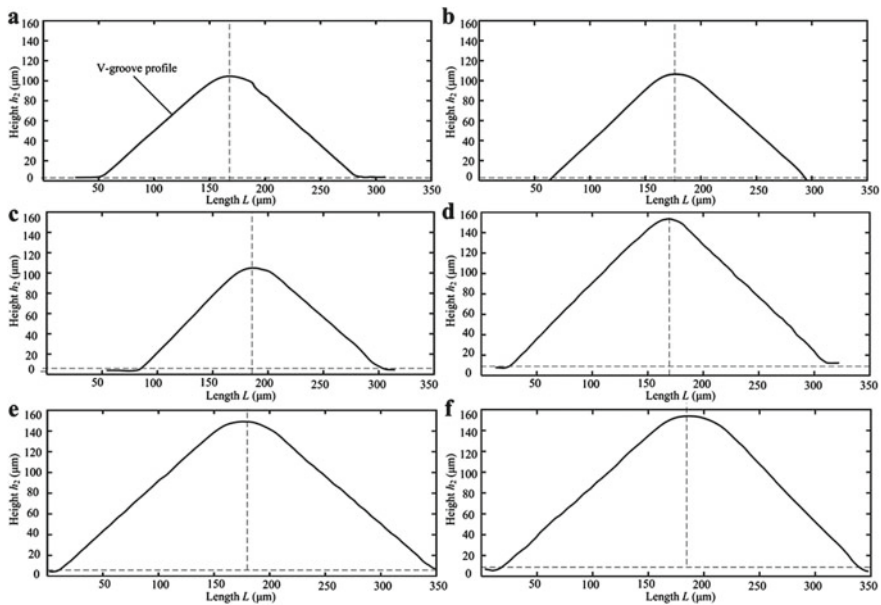


**Fig. 6** SEM photographs of micro-ground mold cores: **a** Sample A<sub>m</sub>; **b** Sample B<sub>m</sub>; **c** Sample C<sub>m</sub>; **d** Sample D<sub>m</sub>; **e** Sample E<sub>m</sub>; **f** Sample F<sub>m</sub>



**Fig. 7** SEM photographs of micro-structured polymers: **a** Sample A<sub>w</sub>; **b** Sample B<sub>w</sub>; **c** Sample C<sub>w</sub>; **d** Sample D<sub>w</sub>; **e** Sample E<sub>w</sub>; **f** Sample F<sub>w</sub>

Since the polymer is nonopaque, the cross-sectional profile of the micro-structured polymer surface is recorded using a contact profiler. Figure 8 shows the cross-sectional profile of the V-groove of the micro-structured polymer after micro injection molding. Table 5 shows the structural parameters of the V-groove polymer. The V-groove profile is circular due to the core radius of the V-groove shape and the diamond grinding wheel used for grinding. Compared to the calculated V-groove parameters shown in Table 2, the angular error on the micro-structured polymer surface of the V-groove ranged from 0.02 to 0.88° with an average angular error of only 0.46°. The average micromachining depth of the V-groove was 2.42 μm with a spatial error of 1.12 μm. The D<sub>w</sub> sample showed the highest micromachining accuracy compared to the V-groove profile. This result also agrees with the SEM image shown in Fig. 7.



**Fig. 8** The profiles of micro-structured polymers: **a** Sample A<sub>w</sub>; **b** Sample B<sub>w</sub>; **c** Sample C<sub>w</sub>; **d** Sample D<sub>w</sub>; **e** Sample E<sub>w</sub>; **f** Sample F<sub>w</sub>

**Table 5** The V-grooved structure parameters of micro-structured polymers

Sample	V-groove angle $\alpha_2$ (°)	V-groove depth $h_2$ (μm)	V-groove space $b_2$ (μm)
A <sub>w</sub>	89.98	98.74	400.40
B <sub>w</sub>	89.98	106.50	500.40
C <sub>w</sub>	89.12	98.43	600.50
D <sub>w</sub>	90.81	147.15	398.00
E <sub>w</sub>	89.26	150.77	501.40
F <sub>w</sub>	90.26	151.55	598.00

### 3.3 Machining Accuracy of Micro-ground Mold Core and Filling Rate of Micro-formed Polymer

Although the equipment used to measure the contours of the mold core and the polymer are different, the experience gained so far using both devices shows that the results are essentially the same. By comparing the contours of the V-groove of the mold core and the micro-tip of the grinding wheel tool, it can obtain the contour error distribution and the angular error profile. The profile error  $e_m$  is defined as the height difference between the V-groove profile of the mold core and the microtip profile of the diamond grinding wheel. The relative angular error  $\alpha_m$  of the V-groove of the mold core can be calculated according to the following equation:

$$\alpha_m = \frac{|\alpha - \alpha_1|}{\alpha} \times 100\% \quad (1)$$

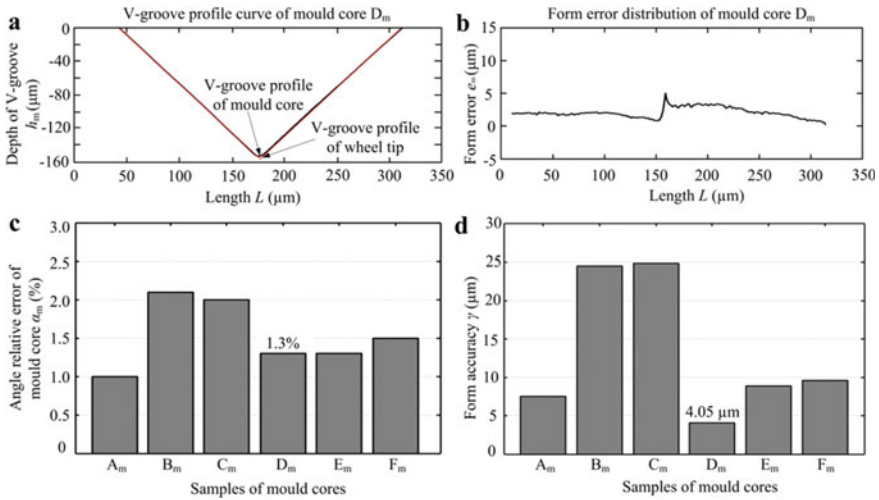
where  $\alpha$  is the V-groove angle of the wheel tool tip and  $\alpha_1$  is the V-groove angle of micro-structured mold core. Due to the offset of the end face of the diamond grinding wheel, the V-tip angle of mold core surface was commonly larger than that of the wheel tool tip. The morphological accuracy  $\gamma$  of the mold core can be defined as the difference between the tip and the valley of the contour error curve [21].

Figure 9 shows the relative angular error  $\alpha_m$  and the shape accuracy  $\gamma$  of the mold core. Based on the curves of the V-groove profile of mold core and wheel tool tip which is shown in Fig. 9a, the distribution curve for mold defects in the mold core can be determined as shown in Fig. 9b. It shows that the largest shape defect occurs at the tip of the V-groove. This is because the tip of the micromachined V-groove has been a technical bottleneck, so the radius of the circle has been present. It turns out that the contour error of the V-tip can be controlled to within 5  $\mu\text{m}$  using the micro-sharpened mold core. Figure 9c shows the relative angular error  $\alpha_m$  for all mold cores, which ranged between 1.0 and 2.1%. The average relative angular error of the finely ground cores is only 1.53%. The shape accuracy  $\gamma$  is determined by the shape error distribution curve shown in Fig. 9b. Figure 9d shows that the lowest shape accuracy of 4.05  $\mu\text{m}$  is obtained for the molded core  $D_m$ . The micro-grinding accuracy is below 10  $\mu\text{m}$  for all types of cores except for the  $B_m$  and  $C_m$  type cores.

By comparing the profile of the V-groove with the profile of the mold core and the polymer, the profile defect distribution and the angular defect can be determined. Thus, the relative defect  $\alpha_w$  of the V-groove angle of the polymer can be calculated as follows:

$$\alpha_w = \frac{|\alpha_1 - \alpha_2|}{\alpha_1} \times 100\% \quad (2)$$

where  $\alpha_2$  is the V-groove angle of the micro-structured polymer. The filling ratio  $\eta$  of injection molding can be calculated according to the following equation:



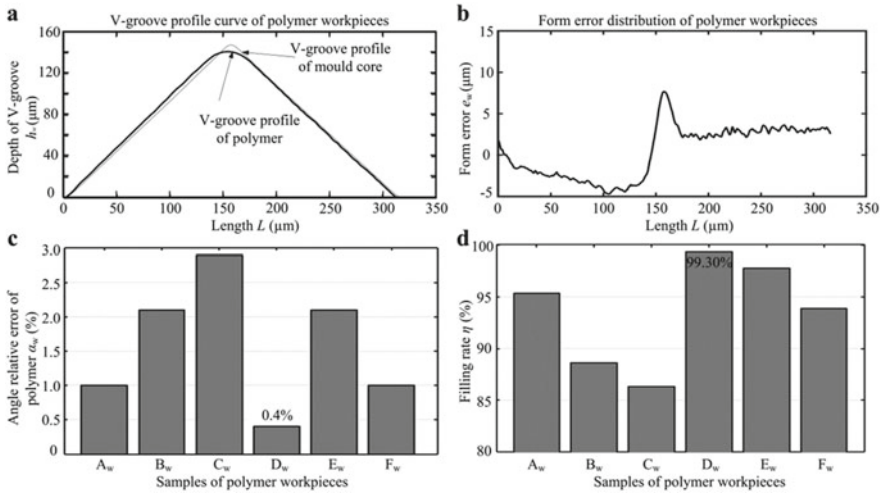
**Fig. 9** The angle relative error  $\alpha_m$  and form accuracy  $\gamma$  of mold core: **a** V-groove profile curves of wheel tip and mold core D<sub>m</sub>; **b** form error distribution of mold core D<sub>m</sub>; **c** angle relative error  $\alpha_m$ ; **d** form accuracy  $\gamma$

$$\eta = 1 - \frac{1}{N} \sum \frac{|h_1 - h_2|}{h_1} \times 100\% \quad (3)$$

where  $h_1$  is the V-groove depth value of the mold core,  $h_2$  is the V-groove depth of the polymer workpiece, and  $N$  is the data point of the measured V-groove profile.

Figure 10 shows the relative angular error  $\alpha_w$  and the filling factor  $\eta$  for the micro-structured polymers. Figure 10c shows the relative angular error  $\alpha_w$  for all micro-structured polymers, which ranges from 0.4 to 2.9%. The average relative angular error of the micro-structured polymers is only 1.58%. The results show that D<sub>w</sub> polymers have the lowest relative angular error of 0.4%. It was also found that the V-vertex of the micro-structured polymers.

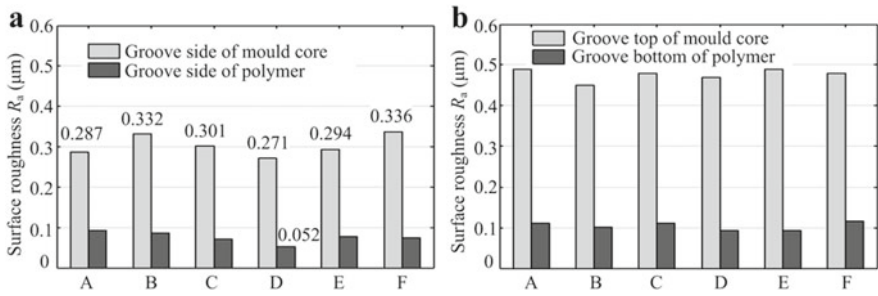
The angle was smaller than the V-groove angle of the mold core. The reason is that the shrinkage of the injection molded polypropylene (PP) during the cooling process, which leads to the reduction of the V-groove angle. As can be seen from Fig. 10c, the larger the space of the V-groove, the larger the relative angle error. The reason for this may be that the larger the space of the V-groove, the faster the micro-formed polymer shrinks, leading to a rise in the V-groove angle. Figure 10d shows the degree of filling  $\eta$  for all micro-structured polymers. It can be found that the blank D<sub>w</sub> has the highest degree of filling with 99.30%. By comparing with Figs. 9d and 10d, it can be concluded that the higher the mold accuracy of the core processing, the higher the degree of filling of the micro-structured polymer. It was also found that the greater the depth or depth-to-width ratio of the V-groove, the higher the filling rate.



**Fig. 10** The angle relative error  $\alpha_w$  and filling rate  $\eta$  of micro-structured polymer: **a** V-groove profile curves of polymer  $D_w$  and mold core  $D_m$ ; **b** form error distribution of polymer  $D_w$ ; **c** angle relative errors  $\alpha_w$ ; **d** filling rates  $\eta$

### 3.4 Surface Quality Analysis of Mold Core and Injection Molded Polymers

Based on the micro-forming principle of micro-structured polymers in microinjection molding, the surface roughness of the polymer on the side of the groove and the bottom of the groove depend on the side of the micro-ground groove and the top of the unground core groove, respectively, as shown in Fig. 4. Figure 11a shows the surface roughness  $R_a$  on the side of the mold core and polymer groove. Figure 11b shows a comparison of the surface roughness  $R_a$  on the top side of the mold core groove and the bottom side of the polymer groove. It can be seen that the surface roughness  $R_a$  of the groove sides of the micro-ground mold core and the micro-formed polymer are in the range of 0.271–0.336  $\mu\text{m}$  and 0.052–0.092  $\mu\text{m}$ , respectively, which indicates that the surface quality of the molded polymer is better than the quality of the molded core. The surface roughness  $R_a$  on the groove side of the microporous core  $D_m$  was the lowest at 0.271  $\mu\text{m}$ , while the corresponding polymer  $D_w$  reached the lowest value of 0.052  $\mu\text{m}$ . The surface roughness  $R_a$  on the groove side of the micro-ground polymer remained below 0.1  $\mu\text{m}$ . It was also shown that the upper surface of the grooves of the cast core was unpolished and much rougher than the surface of the micro-formed grooves, which resulted in a poorer surface quality at the bottom of the grooves of the micro-structured polymers.

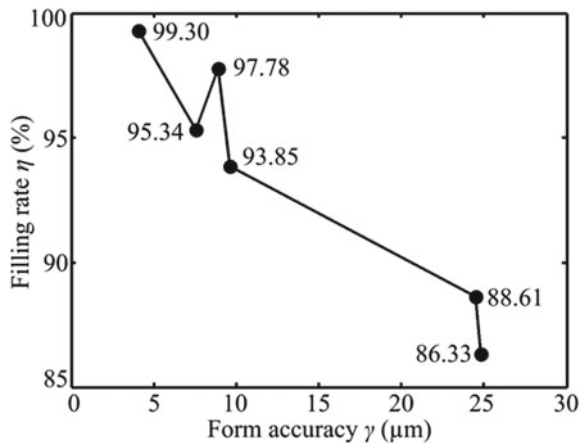


**Fig. 11** Comparisons of surface roughness  $R_a$  of micro-structured mold cores and polymers: **a** groove sides of mold core and polymer; **b** groove top of mold core and groove bottom of the polymer

### 3.5 Relationship Between the Filling Ratio of Micro-structured Polymer and the Form Accuracy of Micro-ground Mold Core

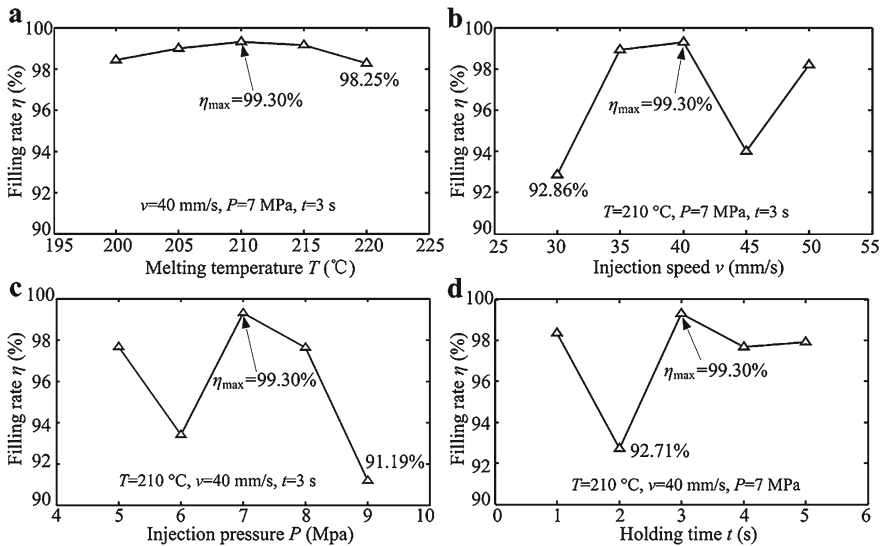
Figure 12 shows the relationship between the filling ratio  $\eta$  of the micro-structured polymer and the form accuracy  $\gamma$  of the microfine matrix rods. The form accuracies of the six matrix cores were 7.53  $\mu\text{m}$ , 24.5  $\mu\text{m}$ , 24.84  $\mu\text{m}$ , 4.05  $\mu\text{m}$ , 8.87  $\mu\text{m}$ , and 9.59  $\mu\text{m}$ , respectively. The corresponding fill rates of the micro-formed polymers were 86.33%, 95.34%, 88.61%, 93.85%, 97.78%, and 99.45%, respectively. The results showed that the accuracy of the mold core shape of the micro-ground mold core had a positive effect on the filling degree of microinjection molding. The degree of filling of micro-structured polymers tended to increase as the shape accuracy of the microform core decreased. This indicates that the higher the machining accuracy of the mold core, the higher the degree of filling in microinjection molding.

**Fig. 12** The relationship between the filling ratio of micro-structured polymer  $\eta$  and form accuracy of micro-ground mold core  $\gamma$



### 3.6 Effects of Micro Injection Molding Parameters on the Filling Rate of Micro-structured Polymer

As shown in Fig. 13, the filling factor  $\eta$  of the micro-structured polymers in relation to the microinjection parameters is presented, including melt temperature  $T$ , injection rate  $v$ , injection pressure  $P$  and residence time  $t$ . As shown in Fig. 10a, b, the filling factor  $\eta$  of the micro-structured polymers increased significantly with the increment of melt temperature  $T$  and injection rate  $v$ , and then decreased. The filling coefficients of micro-structured polymers were 98.25–99.30% and 92.86–99.30%, respectively. The results in Fig. 10c, d show that the filling coefficients varied between 91.19–99.30% and 92.71–99.30%, respectively, depending on the injection pressure  $P$  and residence time  $t$ . Thus, the results from experimenting indicate that the injection pressure has the dominant influence on the degree of filling of the mold polymer, while the melt temperature has the least effect. In general, the highest value of 99.30% filling of micro-structured polymers can be achieved when the melt temperature, injection velocity, injection pressure and residence time are 210 °C, 40 mm/s, 7 MPa and 5 s, respectively.



**Fig. 13** The filling rate of micro-structured polymer  $\eta$  versus micro injection molding parameters: **a** Melting temperature  $T$ ; **b** injection speed  $v$ ; **c** injection pressure  $P$ ; **d** holding time  $t$

## 4 Conclusions

A micro-grinding method with a V-tip diamond wheel is presented to form regular and precise micro-grooved structures on the mold core surface. By micro-grinding the mold core, micro-structured polymers are produced efficiently and accurately by micro-injection molding technology. It enables cost-effective large-scale production of micro-structured polymer parts. The main results can be summarized as follows.

- (1) The highest molding accuracy and filler degree of  $4.05\ \mu\text{m}$  and 99.30% of micro-structured polymer can be achieved by micro-milled mold cores, respectively. The minimum relative angular error of the micro-structured polymer is only 0.4%.
- (2) The surface roughness  $R_a$  on the micro-structured polymer side can be as low as  $0.1\ \mu\text{m}$ . A minimum  $R_a$  of 0.271 microns is achieved on the core side of the micro-milled polymer, while a minimum  $R_a$  of  $0.052\ \mu\text{m}$  can be achieved for the corresponding micro-formed polymer.
- (3) The core shape accuracy of the micro-ground mold core has a positive effect on the filling ratio of the micro-formed polymer. The fill rate of micro-formed polymers increases considerably as the shape accuracy of the core increases.
- (4) Injection pressure has the dominant influence on the fill rate of micro-structured polymers. However, melt temperature has the least effect.

**Acknowledgements** The work described in this chapter was supported by the National Natural Science Foundation of China (Grant No. 51805334), the International Science and Technology Cooperation Project of Shenzhen City (Grant No. GJHZ20190822091805371), and the Science and Technology Planning Project of Guangdong Province (Grant No. 2017A010102003).

## References

1. Maghsoudi K, Jafari R, Momen G, Farzaneh M (2017) Micro-nanostructured polymer surfaces using injection molding: a review. *Mater. Today Commun* 13:126–143
2. Gao S, Qiu ZJ, Ma Z, Yang YJ (2017) Development of high efficiency infrared-heating-assisted micro-injection molding for fabricating micro-needle array. *Int J Adv Manuf Technol* 92:831–838
3. Guarino V, Causa F, Salerno A, Ambrosio L, Netti PA (2008) Design and manufacture of microporous polymeric materials with hierarchal complex structure for biomedical application. *Mater Sci Tech* 24:1111–1117
4. Giboz J, Copponnex T, Mélé P (2007) Microinjection molding of thermoplastic polymers: a review. *J Micromech Microeng* 17:R96–R109
5. Loaldi D, Quagliotti D, Calaon M, Parenti P, Annoni M, Tosello G (2018) Manufacturing signatures of injection molding and injection compression molding for micro-structured polymer fresnel lens production. *Micromachines* 9:653–674
6. Bellantone V, Surace R, Trotta G, Fassi I (2013) Replication capability of micro injection molding process for polymeric parts manufacturing. *Int J Adv Manuf Technol* 67:1407–1421



7. Lu Z, Zhang KF (2009) Morphology and mechanical properties of polypropylene micro-arrays by micro-injection molding. *Int J Adv Manuf Technol* 40:490–496
8. Weng C, Wang F, Zhou MY, Yang DJ, Jiang BY (2018) Fabrication of hierarchical polymer surfaces with superhydrophobicity by injection molding from nature and function-oriented design. *Appl Surf Sci* 436:224–233
9. Lucchetta G, Sorgato M, Carmignato S, Savio E (2014) Investigating the technological limits of micro-injection molding in replicating high aspect ratio micro-structured surfaces. *CIRP J Manuf Sci Technol* 63:521–524
10. Masato D, Sorgato M, Lucchetta G (2016) Analysis of the influence of part thickness on the replication of micro-structured surfaces by injection molding. *Mater. Design* 95:219–224
11. Niewerth F, Necker M, Rösler J (2015) Influence of chromium on microstructure and etching behaviour of new Ni–Fe–Al based alloy. *Mater Sci Tech* 31:349–354
12. Zhou CL, Ngai TWL, Li LJ (2016) Wetting behaviour of laser textured Ti<sub>3</sub>SiC<sub>2</sub> surface with micro-grooved structures. *Mater Sci Tech* 32:805–812
13. Debnath T, Patowari PK (2019) Fabrication of an array of micro fins using wire EDM and its parametric analysis. *Mater Manuf Process* 34:580–589
14. Wang CJ, Cheung CF, Liu MY, Lee WB (2017) Fluid jet-array parallel machining of optical microstructure array surfaces. *Opt Express* 25:22710–22725
15. Lu YJ, Xie J, Si XH (2015) Study on micro-topographical removals of diamond grain and metal bond in dry electro-contact discharge dressing of coarse diamond grinding wheel. *Int J Mach Tool Manu* 88:118–130
16. Zhang L, Xie J, Guo AD (2018) Study on micro-crack induced precision severing of quartz glass chips. *Micromachines* 9:224–238
17. Li ZP, Zhang FH, Luo XC, Guo XG, Cai YK, Chang WL, Sun JN (2018) A new grinding force model for micro grinding RB-SiC ceramic with grinding wheel topography as an input. *Micromachines* 9:368–386
18. Zhou CL, Wu XY, Lu YJ, Wu W, Zhao H, Li LJ (2018) Fabrication of hydrophobic Ti<sub>3</sub>SiC<sub>2</sub> surface with micro-grooved structures by wire electrical discharge machining. *Ceram Int* 44:18227–18234
19. Zhou CL, Wu XY, Ngai TWL, Li LJ, Ngai SL, Chen ZM (2018) Al alloy/Ti<sub>3</sub>SiC<sub>2</sub> composites fabricated by pressureless infiltration with melt-spun Al alloy ribbons. *Ceram Int* 44:6026–6032
20. Xie J, Luo MJ, Wu KK, Yang LF, Li DH (2013) Experimental study on cutting temperature and cutting force in dry turning of titanium alloy using a non-coated micro-grooved tool. *Int J Mach Tool Manu* 73:25–36
21. Xie J, Xie HF, Luo MJ, Tan TW, Li P (2012) Dry electro-contact discharge mutual-wear truing of micro diamond wheel V-tip for precision micro-grinding. *Int J Mach Tool Manu* 60:44–51

# Chapter 18

## Fabrication of Micro-structured LED Diffusion Plate Via Precision Grinding and Injection Molding



Yanjun Lu, Xingyu Mou, Wang Luo, and Chunjin Wang

**Abstract** In this chapter, a new micro-structured diffusion sheet for LED (light-emitting diode) was developed by combining efficient and precise hybrid processing methods with micro-injection molding and micro-grinding, enabling cost-effective large-scale production of LED lamps with excellent light output. First, the mold core of the microstructure is machined to a controlled shape and surface quality using a precision V-shaped grinding wheel. Secondly, the micro-structured LED diffusion plates were rapidly processed by micro-injection molding technology. Finally, the effect of microinjection molding process parameters on the illumination of the micro-structured diffuser plate was investigated. According to the simulated optical results the illumination of the micro-structured diffuser plate can reach the highest value when the V-groove depth and V-groove angle are calculated as 300  $\mu\text{m}$  and 60°, respectively. The experimental results show that the developed micro-structured diffuser plate can enhance the illuminance by about 40.82% compared to the conventional diffuser plate. The prediction accuracy of the developed illumination efficiency simulation method is 90.33%.

### 1 Introduction

LED luminaires are widely used in the lighting industry because they are energy efficient, environmentally friendly, and provide uniform and soft light. [1, 2]. In order to enhance the luminous efficiency of LED lamps and lower their production and manufacturing costs, a great number of researchers are interested in fabricating micro-mesh structures on the diffusion shield of LED lamps [3, 4], which can reduce

---

Y. Lu (✉) · X. Mou · W. Luo

Guangdong Provincial Key Laboratory of Micro/Nano Optomechanics Engineering, College of Mechatronics and Control Engineering, Shenzhen University, Nan-Hai Ave 3688, Shenzhen 518060, Guangdong, PR China  
e-mail: [luyanjun@szu.edu.cn](mailto:luyanjun@szu.edu.cn)

C. Wang

State Key Laboratory of Ultra-Precision Machining Technology, Department of Industrial and Systems Engineering, The Hong Kong Polytechnic University, Hong Kong, PR China

the scattering and dispersion of light and thus improve the efficiency of light energy utilization.

Currently, the production process of micro-structured diffusion panels mainly includes screen printing, hot pressing and microinjection molding. Screen printing can be used to directly manufacture diffusion plates, which has the advantages of low cost and high production efficiency. Uniform macroscopic dot-like structures can be printed to obtain uniform illumination. Nevertheless, the silk-screen printing process is very complicated and the generated ink discoloration can pollute the environment [5]. Previous studies have shown that in order to rapidly processed micro-structured polymer diffusion sheets by hot pressing or microinjection [6, 7], in order to achieve mass production and fabrication of micro-structured diffusion sheets, microstructures are first processed on the surface of the mold and then replicated on the surface of the polymer blank. Microinjection molding is suitable for mass production and fabrication of micro-structured polymers due to the simplicity and low cost of the production process. In addition, there are almost no restrictions on the geometry of plastic parts. Hence, the micro injection molding technology has been recognized as the most important procedure for forming micro-structured polymer products [8, 9]. For instance, the correlation between mold micro-manufacturing and microinjection molding has been investigated in order to optimize the demolding step [10]. In order to prove the quality of 3D micro-molded parts, a hybrid method which combines optical micro metrology and injection molding process monitoring, has been presented [11]. The influences of grinding strategies and cutting parameters on the mold core were investigated to show the relationship between mold morphology and injection forces in microinjection molding [12]. To describe the frictional behavior of the polymer-mold interface, the correlation between various surface morphology parameters and injection force in microinjection molding was analyzed [13].

The forming quality of micro-structured polymer production is largely dependent on the quality of processing and the shape accuracy of the micro-structured mold cores. Typical micromachining techniques for micro-structured mold cores include electrochemical etching [14], laser processing [15], electrical discharge machining (EDM) [16] and mechanical micro-cutting [17, 18]. While chemical etching can provide the shape accuracy of nanoscale structures [14], it is not yet possible to create three-dimensional microstructures efficiently and accurately at the microscopic scale. To improve the accuracy of etched shapes, production costs would have to increase significantly. In addition, chemical etching solutions can pollute the environment. Efficient laser processing is environmentally friendly [15], but equipment costs are quite high and it is difficult to control the accuracy of 3D microstructure shapes. micro-EDM techniques can create microstructures smaller than 100  $\mu\text{m}$  [16], but are limited by conductive moulding materials. Unfortunately, the surface quality of the 3D microstructures is not satisfactory and the oil produced during the EDM process pollutes the environment. Microstructures with high surface quality can be achieved using mechanical diamond cutting [17, 18], but this method is limited to soft metal materials with low hardness. In addition, the depth to width ratio of the processed microstructures is relatively low. Therefore, it is difficult to produce microstructures with high shape accuracy and surface quality in the micron range for environmental

and efficiency reasons. With the currently developed micro-milling technology, it is possible to machine high-quality microstructures with controlled shape accuracy on the surface of hard and brittle moulded materials [19, 20]. This environmentally friendly and non-polluting machining process is also characterised by low cost and ease of operation. Currently, no relevant studies have been reported on the production of micro-structured scattering LED panels by means of micro-injection and micro-moulding. Therefore, in order to process microstructures with high surface quality and shape accuracy on the mould core surface, a precision grinding tool is first proposed. The three-dimensional microstructure obtained on the mould core surface is then replicated on an acrylic polymer screen by microinjection to rapidly produce LED diffusion panels with high quality microstructures, allowing for improved light output from LED lamps.

In this chapter, a hybrid processing method which combines micro-grinding and micro injection molding is presented to effectively process micro-structured LED scattering plates with high surface quality and shape accuracy. First, an optical simulation method is developed to simulate the light intensity distribution in the micro-structured scattering plate and to obtain the optimal parameters for the microstructure dimensions. Then, a V-groove structure with high shape accuracy was processed by performing precision micromachining on the surface of the forming steel. Finally, the V-groove structure on the surface of the molding strip is rapidly transferred to the surface of the acrylic polymer diffuser plate in the microinjection molding process, resulting in the efficient production of a new micro-structured LED diffuser plate. The effects of microinjection molding process parameters on the light intensity of the LED diffusion plate were examined to determine the appropriate parameters for the injection molding procedure.

## 2 The Optical Design and Light Efficiency Simulation of the Micro-structured LED Diffusion Plate

The commonly used material for LED diffusion panels is polymethyl methacrylate (PMMA), which has excellent optical properties such as high white light penetration, high refractive index, and high light transmittance. Its Mohs hardness and refractive index are 95 kg/cm<sup>2</sup> and 1.49, respectively. Based on the previous studies [21, 22], the optical properties can be effectively improved by creating microstructures on the surface of scattering LED panels. To effectively fabricate the optical structure of the scattering LED panel, TracePro software was used to simulate the luminous flux and illumination on the surface of conventional and micro-structured scattering LED panels to evaluate their optical performance.

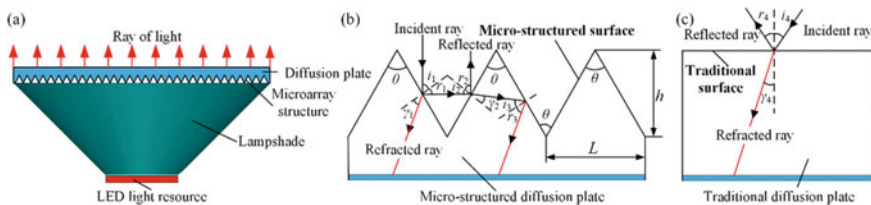
Based on the principle that light is emitted through the scattering panel, a microstructure with a V-groove shape is very suitable. A conventional LED lamp consists of an LED light source, a lampshade and a diffusion panel (see Fig. 1a). The light beam from the light source is refracted to the surface as it passes through the

diffusion plate. The diffusion plate sample has an outer diameter and thickness of 50 mm and 1.3 mm, respectively. An incandescent lamp with a nominal wattage of 3 W and a diameter of 10 mm and a thickness of 1 mm was used as the LED light source. The distance between the light source and the diffuser plate was 18 mm, and the simulated beam was visible light with a wavelength of 400–700 nm. The wavelength of the simulated beam was set to 450 nm and the number of experimental beams was 10 000. As shown in Fig. 1a, the side of the diffusion plate with a regular micro-grid structure was considered as the incident surface and the opposite side was considered as the exit surface. The angle of the V-groove, the depth of the V-groove and the width of the micro-grid structure on the surface of the diffusion plate sample were denoted by  $\theta$ ,  $h$  and  $L$ , respectively (Fig. 1b). Refraction and reflection occur when the incident beam passes through the diffuser plate. The incident, reflected and refracted beams are denoted by  $i$ ,  $r$  and  $\gamma$ , respectively. Figures 1b and c illustrate the optical displacement principle of the micro-structured plate and the conventional scattering plate. As shown in Figs. 1b, c, the micro-structured surface can fabricate more refracted and reflected light compared to the conventional surface, enhancing the light output of the LED lamp. The simulated luminous flux and the illumination produced by the diffuser plate are recorded to evaluate the luminous efficiency.

A V-groove depth  $h$  of 100–400  $\mu\text{m}$  and a V-groove angle  $\theta$  of 60–150° were developed to obtain the optimal microchannel size and modified to calculate the theoretical illuminance  $E$  (see Table 1). As shown in Table 1 the simulated illuminance of the LED diffuser plate for different microstructure parameters is presented.

Figure 2 shows the effect of the developed V-groove angle  $\theta$  on the irradiance and illuminance of the micro-structured LED diffuser plate. Brighter colour means the more intensive light. The diffuser plate has a diameter of 50 mm and the light source is positioned directly below the diffuser plate. The images of the irradiance and luminance of the diffuser plate show that the area of lower light intensity is farther from the center of the light source, resulting in a darker image. It can also be seen that the more intensive light is in the central region. If the depth  $h$  of the V-groove is kept constant, then the light intensity decreases as the V-groove angle  $\theta$  increases. The light intensity is highest at a V-groove angle of 60°, with a maximum illumination  $E$  of 138.07 Klux.

As shown in Fig. 3, the effect of the parameters of the V-groove structure on the simulated luminance is proposed. It can be seen that the V-groove angle has a greater



**Fig. 1** a Schematic diagram of the LED lamp. b Optical travel principle of the micro-structured diffusion plate. c Optical travel principle of the traditional diffusion plate

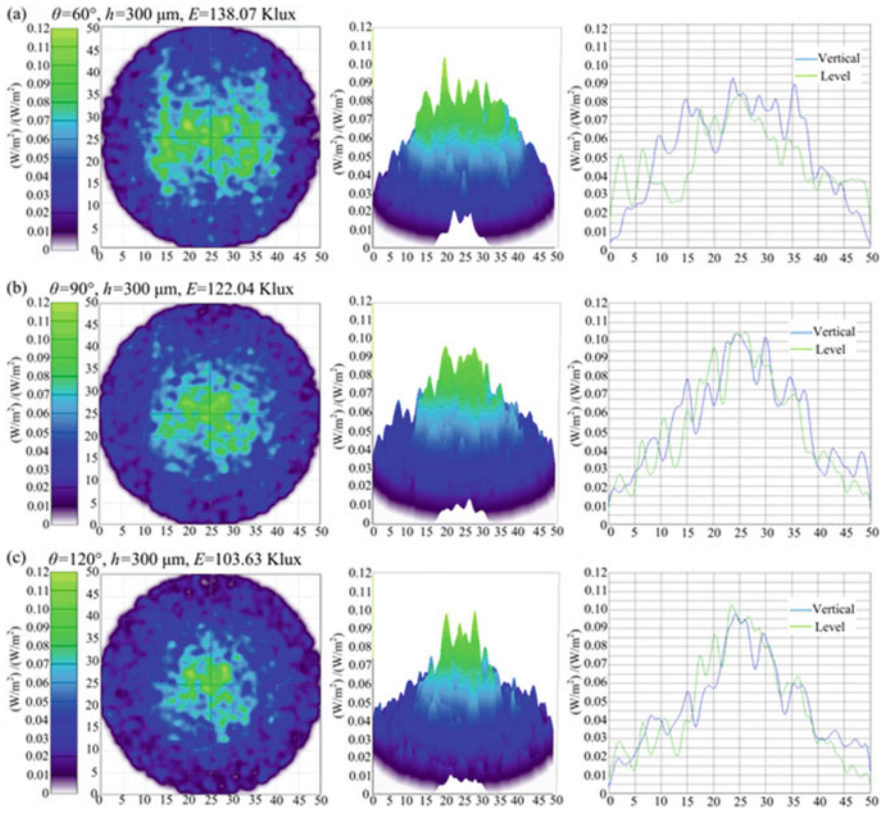
**Table 1** Simulated illuminances of LED diffusion plates under different V-groove structure parameters

No	V-groove depth h ( $\mu\text{m}$ )	V-groove angle $\theta$ ( $^\circ$ )	Illuminance E (Klux)
1	0	0	94.42
2	100	60	134.29
3	100	90	121.64
4	100	120	103.56
5	100	150	95.49
6	200	60	132.82
7	200	90	123.42
8	200	120	102.55
9	200	150	95.22
10	300	60	138.07
11	300	90	122.04
12	300	120	103.63
13	300	150	94.49
14	400	60	132.79
15	400	90	122.02
16	400	120	102.07
17	400	150	94.45

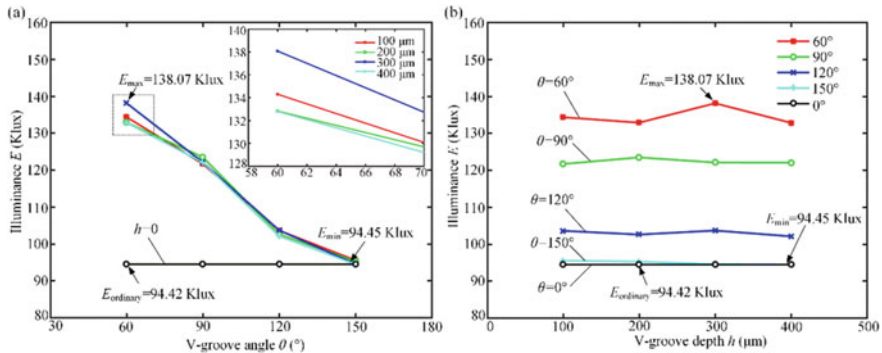
effect on the luminous flux than the V-groove depth. In the V-groove angle range of 60–150°, smaller V-groove angles lead to higher brightness (see Fig. 3a). It shows that for V-groove depths between 100 and 400  $\mu\text{m}$ , the illumination intensity does not change significantly with increasing V-groove depth (see Fig. 3b). By applying a special V-groove structure on the surface of the diffuser plate, the illumination intensity is significantly improved. Compared with the simulated  $E_{\text{traditional}}$  illumination of 94.42 kW for the conventional diffuser plate, the maximum  $E_{\text{max}}$  illumination of 138.07 kW for the micro-structured diffuser plate can be theoretically increased by about 46.23%. Larger groove depths can lead to faster wear of the grinding wheel, which requires frequent machining and calibration. Taking the actual machining conditions and simulation results into consideration, the optimal parameters for the microgroove were therefore chosen for the experiments: a V-groove depth of 300  $\mu\text{m}$  and a V-groove angle of 60°.

### 3 Experimental Details

The surface quality and shape accuracy of the V-groove machining on the mold core surface depend mainly on the precision machining and grinding of the V-tip of the CBN (cubic boron nitride) grinding wheel. Hence, before starting the grinding

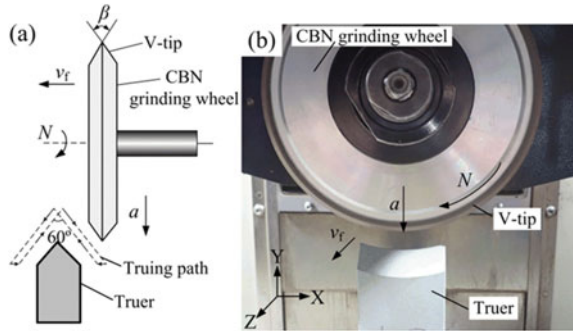


**Fig. 2** The simulated irradiances and illuminances of micro-structured LED diffusion plates depending on the designed V-groove angle  $\theta$ : **a**  $\theta = 60^\circ$ ; **b**  $\theta = 90^\circ$ ; **c**  $\theta = 120^\circ$



**Fig. 3** The simulated illuminance  $E$  as influenced by the designed V-groove structure parameters: **a** V-groove angle  $\theta$ ; **b** V-groove depth  $h$

**Fig. 4** The precision truing of the V-tip CBN grinding wheel: **a** V-tip truing principle; **b** truing image



experiments, a previously developed precision dressing and truing technique [23, 24] was firstly applied to manufacture a V-shaped wheel with a  $60^\circ$  tip angle. Then, a regular V-groove with a depth of  $300\ \mu\text{m}$  was produced on the mold core surface using a #600 resin-bonded CBN grinding wheel. Micro-structured LED diffusion panels were then fabricated using a micro-insertion method with the micro-ground mold core. Finally, the luminous fluxes of conventional and micro-structured LED diffusion plates were experimented for comparison.

### 3.1 Precision Truing of the V-Tip CBN Grinding Wheel

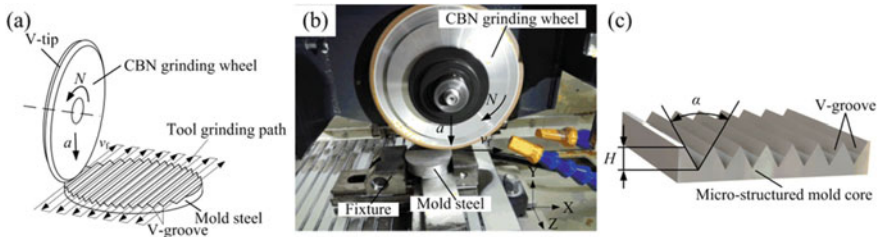
Figure 4 shows the principle of V-tip truing and a picture of the cubic boron nitride (CBN) grinding wheel. The machine is a three-axis precision CNC plane grinder (SMART-B818 III, Chevalier, Taiwan, China) under a minimum feed of  $1\ \mu\text{m}$ . First, a macroscopic V-shaped tip grinding wheel was rapidly processed through rough truing along a V-shape interpolation truing path with the #80 coarse oilstone truer (green SiC) (see Fig. 4a). Then fine truing was performed with a #600 oilstone to produce a V-shaped point with high shape accuracy and a microparticle cutting edge. The theoretical angle of the V-tip truing was set to  $60^\circ$  and the V-tip angle of the trued grinding wheel was set as  $\beta$ .

### 3.2 Precision Grinding of the Micro-structured Mold Core

In this study, the mold steel S136H using a hardness of 30–35 HRC was selected as the material for the mold cores because it has good wear resistance and machinability, and was polished to a mirror-like surface before grinding the microstructure. Figure 5 shows the principle of grinding the V-groove array structure and an experimental image of the mold core. The precision trued V-tip CBN grinding wheel was driven by the CNC system to grind the mold steel, which is mounted on the horizontal



worktable by the fixture (see Fig. 5a). The V-groove is processed on the surface of the mold steel by replicating the V-tip shape of the CBN grinding wheel along the defined horizontal reciprocating cutting path. When the V-groove was processed, the grinding wheel is moved along the Z-axis at a certain speed to machine a second V-groove. Finally, a micro-structured mold core with a regular and controlled V-groove structure was produced (see Fig. 5b). Based on the basic experimental parameters determined previously, the conditions for precision grinding of the micro-structured mold core, including the grinding wheel speed  $N$ , depth of cut  $a$  and feed rate  $v_f$ , were selected to assure the grinding quality and productivity, which are listed in Table 2. the angle  $\theta$  of the V-groove and the depth  $h$  of the V-groove were set to  $60^\circ$  and  $300\ \mu\text{m}$ , respectively. The V-groove angle and V-groove depth on the surface of the ground microstructure mold core are denoted by  $\alpha$  and  $h$ , respectively (see Fig. 5c).



**Fig. 5** The precision grinding of the micro-structured mold core: **a** grinding principle and path; **b** experimental image; **c** schematic diagram of the V-groove structure

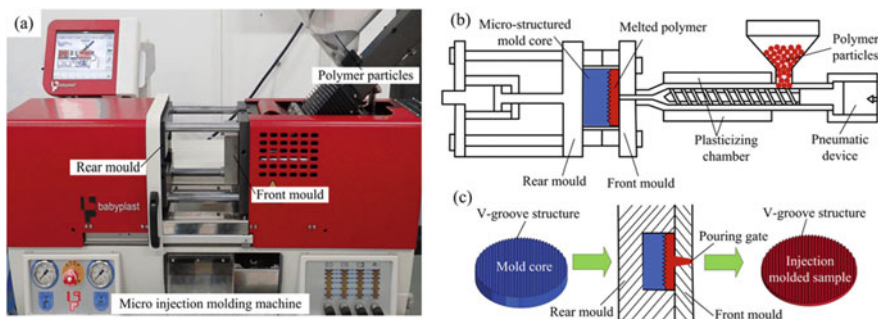
**Table 2** The precision grinding conditions of the micro-structured mold core

CNC grinding machine	SMART B818 III
Grinding wheel	#600 CBN resin-bonded grinding wheel Wheel speed $N = 3000\ \text{r/min}$
Workpiece	Super-mirror mold steel (S136H)
Rough grinding	$v_f = 1000\ \text{mm/min}$ ; $a = 5\ \mu\text{m}$ , $\Sigma a = 290\ \mu\text{m}$
Fine grinding	$v_f = 1000\ \text{mm/min}$ ; $a = 1\ \mu\text{m}$ , $\Sigma a = 10\ \mu\text{m}$
Cooling fluid	Water-soluble coolant
V-groove machining parameters	V-groove angle $\alpha = 60^\circ$ , V-groove depth $H = 300\ \mu\text{m}$

### 3.3 Micro Injection Molding of the Micro-structured LED Diffusion Plate

An efficient micro injection technique has been developed to form precise micro-structured diffuser panel samples by replicating the V-groove structure of the mold core surface to the PMMA surface using a micro injection machine (6/10P, Babyplast, Hospitalet Llobregat, Spain). As shown in Fig. 6, a picture of the micro injection and the molding principle of the micro-structured LED diffuser panel is presented. Firstly, the ground V-groove array structured mold core was mounted on the rear mold, and the PMMA (8817, Degussa, Frankfurt, Germany) polymer particles were put into the hopper (see Fig. 6a). A pneumatic device is then used to drive the polymer particles into the plasticizing chamber. The plasticized and melted polymer then enters the front mold through the pouring gate. Finally, after cooling and holding pressure the close-fitting rear mold and front mold were divided (see Fig. 6b). In this way, the V-groove structure on the core surface is reproduced on the surface of the polymer workpiece, forming a V-shaped injection molded sample (see Fig. 6c).

The quality of micro-forming on injection molded diffusion plate sample affects the light efficiency of LED luminaires. Hence, it is essential to determine the optimal parameters of the micro injection molding process to maximize the light efficiency on the micro-structured diffusion plates. For this purpose, the effects of micro injection molding process parameters on the molding accuracy and surface quality of micro-structured polymer samples were investigated. In general injection molding conditions, the ideal temperature for PMMA injection molding is in the range of 40–70 °C. Based on previous experiments [19], the molding quality of the micro-structured polymers in this experiment was satisfactory at room temperature. Therefore, in this work, the mold temperature was not regarded as a parameter of the injection molding process. In the experiments of this work, general parameters of the microinjection molding procedure, such as melt temperature, injection speed, injection pressure, holding pressure and holding time, were selected and calculated



**Fig. 6** The micro injection molding of the micro-structured diffusion plate: **a** experimental image; **b** schematic diagram of micro injection molding; **c** molding principle of the injection molded sample

**Table 3** Micro injection molding procedure parameters

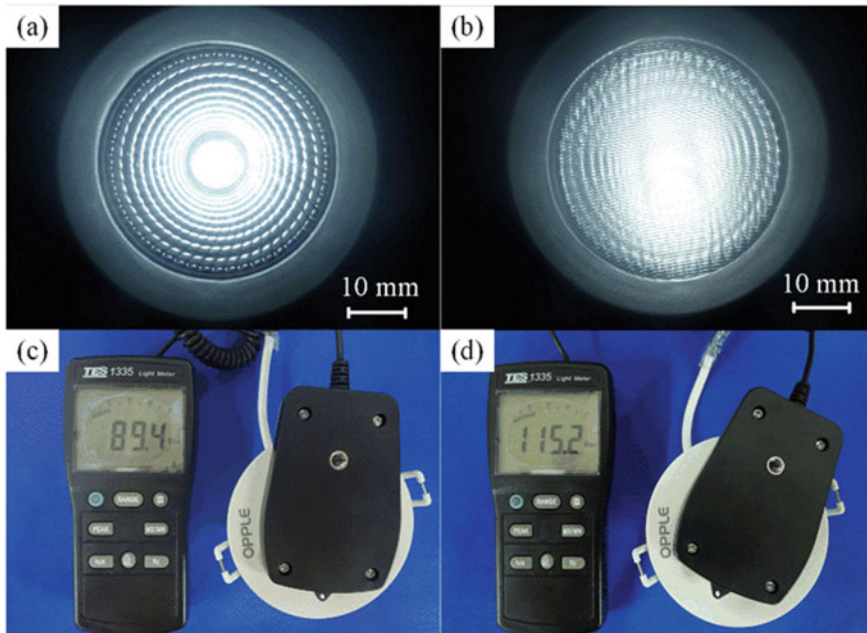
Process parameters	Level
Melt temperature T (°C)	240, 245, 250, 255, 260
Injection speed V (mm/s)	40, 44, 48, 52, 56
Injection pressure P <sub>i</sub> (MPa)	8.0, 8.5, 9.0, 9.5, 10.0
Holding pressure P <sub>h</sub> (MPa)	5.0, 5.5, 6.0, 6.5, 7.0
Holding time T (s)	1.5, 2.5, 3.5, 4.5, 5.5

(see Table 3). To reduce experimental errors, ten microinjection molding samples were selected and tested for each process parameter.

### 3.4 *Light Efficiency Testing of the Micro-structured LED Diffusion Plate*

In order to achieve maximum light efficiency, a digital illuminator (1335, TES, Taiwan, China) with a measurement resolution of 0.01–0.1 Klux was used to examine the illuminance of the micro-structured LED scattering panels with various parameters of the micro injection molding process. The average of the five measured illuminance values was considered as the average illuminance E. The light source was a commercially available LED recessed lamp (LEH0103010, OPPL, Shanghai, China) with a rated power of 3 W, a rated voltage of 220 V and a rated current of 0.025 A. As shown in Fig. 7, the images of the luminous efficacy tests of the conventional and micro-structured LED diffusion panels are presented. It can be seen that the injection process parameters: melt temperature, injection speed, injection pressure and dwell time are 245 °C, 40 mm/s, 8 MPa, 5 MPa and 2.5 s, respectively. The illuminance values of 89.4 and 115.2 Klux for conventional and micro-structured LED scattered light panels, respectively, were shown. It can be concluded that the illuminance of micro-structured diffusion panels can be improved by about 28.8% compared to conventional panels.

A probe stepper (D-300, KLA-Tencor, CA, USA) was used to evaluate the processing quality of the micromachined mold cores and the micro-forming quality of the injection molded diffusion plate samples to obtain the cross-sectional profiles of the micro-structured mold cores and polymer blanks. Three-dimensional laser scanning microscopy (VK-X250K, Keyence, Osaka, Japan) was used to study the 3D topography of micro-structured mold cores and micro-formed polymer samples. High-resolution scanning electron microscopy (SEM, FEI Quanta 450 FEG and Apreo S, FEI Corporation, Hillsboro, USA) was used to determine the surface topography of the micro-structured cores of molded and mold-cast polymer samples. From the measured cross-sectional profiles, the structural parameters of the V-grooves of the micro-milled cores of the molds and the micro-molded diffusion plate samples can be derived. The structural parameters of the V-groove of the micro-milled mold



**Fig. 7** The light efficiency testing images of the LED diffusion plates: **a** traditional diffusion plate; **b** micro-structured diffusion plate; **c** Light intensity of traditional diffusion plate; **d** Light intensity of micro-structured diffusion plate

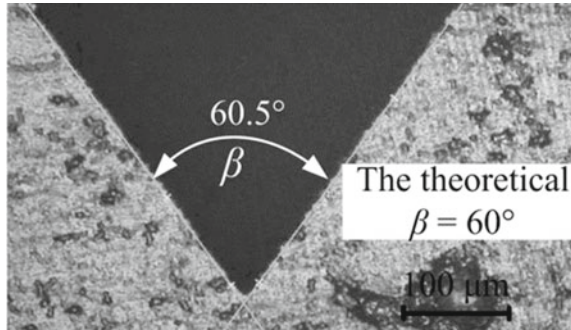
core are characterized by the angle  $\alpha$  of the V-groove width, the V-groove depth  $H$ , and the radius  $R$  of the V-tip. The structural parameters of the V-groove of the micro-structured scattering plate sample are described by the angle  $\theta$  of the V-groove, the depth  $h$  of the V-groove, and the radius  $r$  of the V-tip. The displayed results are the average of the three measured values.

## 4 Results and Discussion

### 4.1 Truing Accuracy of the Grinding Wheel V-Tip

Generally speaking, the tip of the grinding wheel will slightly wear during the grinding procedure. However, the angle of the grinding wheel will not change macroscopically. During V-groove machining, the grinding wheel is regularly dressed to reduce wear and improve shape accuracy to ensure machining quality and efficiency. Figure 8 shows the cross-sectional shape of the V-groove after precision dressing with a 600 CBN grinding wheel. The cross-sectional shape of the V-tip of the ground wheel can be achieved by cutting and replicating the V-tip on the surface

**Fig. 8** The V-tip section shape of trued grinding wheel

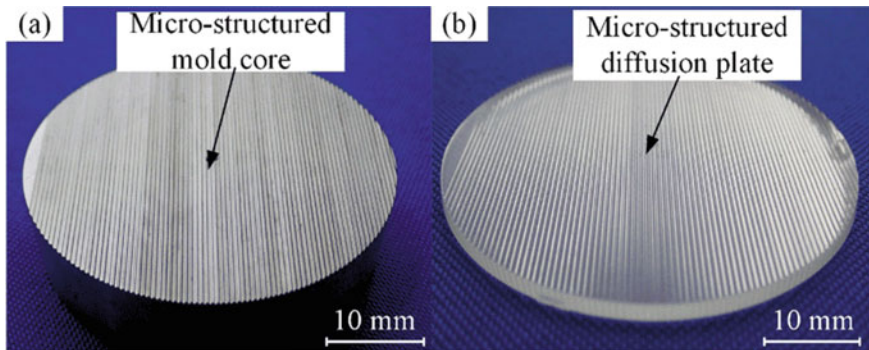


of the carbon graphite plate [25]. Based on the results, the trued V-tip angle  $\beta$  is about  $60.5^\circ$ . Compared with the theoretical V-groove angle of  $60^\circ$ , the error in the V-tip truing angle is only  $0.5^\circ$ . Thus, the previously developed method for trimming the V-tip [19] can provide shape accuracy during microstructure grinding and contribute to the microform accuracy of micro-structured polymer diffusion plates during microinjection molding.

#### ***4.2 Photos and Surface Topographies of the Micro-ground Mold Core and the Injection Molded Micro-structured Diffusion Plate***

As shown in Fig. 9, a photograph of the micro-ground mold core and the injection molded micro-structured LED diffusion plate are presented. The photograph shows a regular and smooth V-groove array structure incorporated on the surface of the mold steel mold core (see Fig. 9a). After micro injection molding, an inverted V-groove array structure was formed on the surface of the PMMA polymer and a micro-structured diffusion plate was formed by replicating the microstructural features obtained from the mold core. The surface roughness values  $R_a$  measured on the V-groove surfaces of the mold core and diffuser plate were  $0.42 \mu\text{m}$  and  $0.148 \mu\text{m}$ , respectively. Therefore, it can be summarized that the surface quality of the micro-structured diffuser plate produced by the injection molded method was clearly superior than that of the mold core. In the case of injection molding, this is due to the shrinkage of the molten polymer after a period of compression and cooling during the microinjection process, which results in a dense and smooth surface. Hence, the presented precision grinding and micro injection technique has the possibility to produce and manufacture micro-structured LED diffusion panels on a large scale.

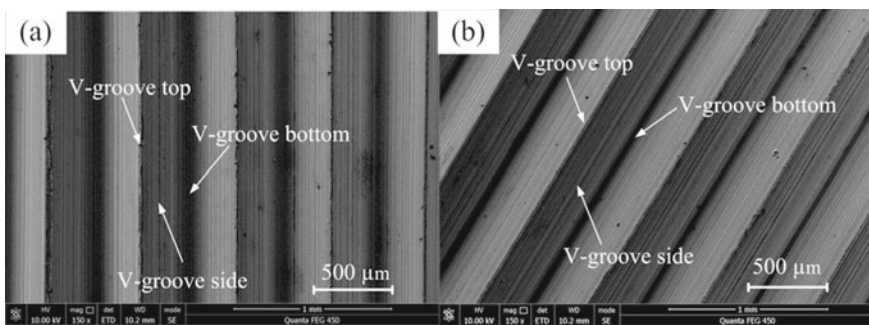
As shown in Fig. 10, the SEM photographs of the microstructure of the mold core in the vertical and oblique directions. Examination of the surface morphology of the mold core in the vertical and oblique directions shows that the microstructure of the



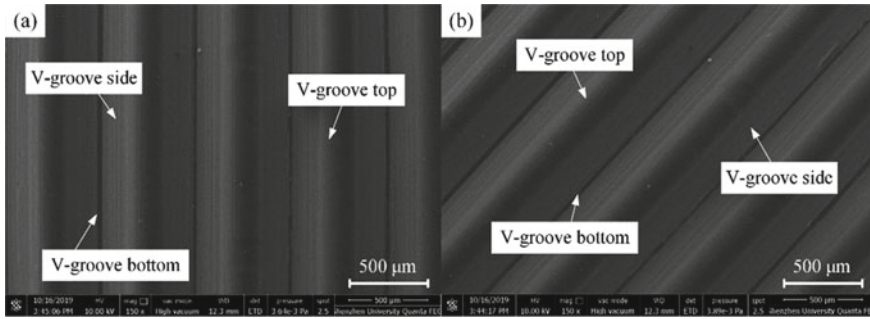
**Fig. 9** Images of the micro-structured mold core and diffusion plate: **a** micro-ground mold core; **b** injection molded diffusion plate sample

V-groove is quite regular and complete. In particular, the upper part of the V-groove is almost intact and the contour of the lower part of the V-groove is clearly discernible. Because the inevitable truing error and micro-grinding error are emerged at the end of the V-groove, there is a curved radius at the bottom of the V-groove. In this way, a V-groove structure with correct shape and controlled accuracy can be processed on the steel core surface of the mold using precision micro-grinding technology.

Because of the large number of diffusion plate samples, it is not essential to show all SEM images. Hence, the diffusion plate samples prepared under certain process parameters were selected for SEM imaging. The injection process parameters, i.e., melt temperature, injection speed, injection pressure, and dwell time were 250 °C, 40 mm/s, 8.0 MPa, 5.0 MPa, and 2.5 s. Figure 11 shows SEM photographs of the microstructure of the mold-cast diffusion plate samples in the vertical and inclined directions. Based on the images, the surface of the injection molded polymer sample is quite smooth and the micro-formed V-groove array structure is very regular and complete. In addition, there are no burrs or damages on the top and bottom of the V-grooves. This indicates that it is possible to produce high-quality micro-structured



**Fig. 10** SEM images of the micro-structured mold core in various orientations: **a** vertical; **b** inclined



**Fig. 11** SEM images of the injection molded micro-structured diffusion plate sample in various orientations: **a** vertical; **b** inclined

polymer samples for injection molding using the proposed microinjection molding technique and a micro-structured mold core with high molding accuracy. Compared with the SEM morphology of the mold core which is shown in Fig. 10, it was observed that the side surfaces of the V-grooves of the micro-structured polymer diffusion plate were smoother. The viscosity of the PMMA melt depends mainly on the pressure. Therefore, increasing the injection pressure reduces the viscosity and increases the flowability, resulting in good flow and shrinkage of the polymer melt, which facilitates the fabrication of smooth micro-structured diffusion plates.

### 4.3 The Section Profiles of the Micro-structured Mold Core and Diffusion Plate

The probe stepper was used to capture the cross-sectional profile of the microparticle die core and Fig. 12 shows the diffuser plate samples. As can be seen in Fig. 12a, the measured average V-groove depth  $H$  and V-groove angle  $\alpha$  of the microparticle die core were  $293.8 \mu\text{m}$  and  $60.11^\circ$ , respectively. Compared with the theoretically calculated V-groove depth of  $300 \mu\text{m}$  and V-groove angle of  $60^\circ$ , the micromachining errors of V-groove depth and V-groove angle are only  $6.2 \mu\text{m}$  and  $0.57^\circ$ , respectively. The average V-tip radius  $R$  of the ground V-groove structure is  $3.22 \mu\text{m}$ . Comparing the theoretical and actual V-groove profile curves of the form center, the shape error of the microstructure processing can be calculated. Due to the constant radius of the V-groove, the shape error of the microstructure mold core is mainly concentrated in the upper part of the V-groove. The absolute difference between the peak and valley values of the V-groove profile curve is defined as the shape accuracy [19, 25]. Therefore, the shape accuracy of the micro-manipulated shape bar was  $9.2 \mu\text{m}$ . The results show that micro-grinding allows the production of highly accurate micro-ground mold cores, which is useful for producing molded diffusion plates with high molding quality. The depth, angle and end radius of the three V-grooves

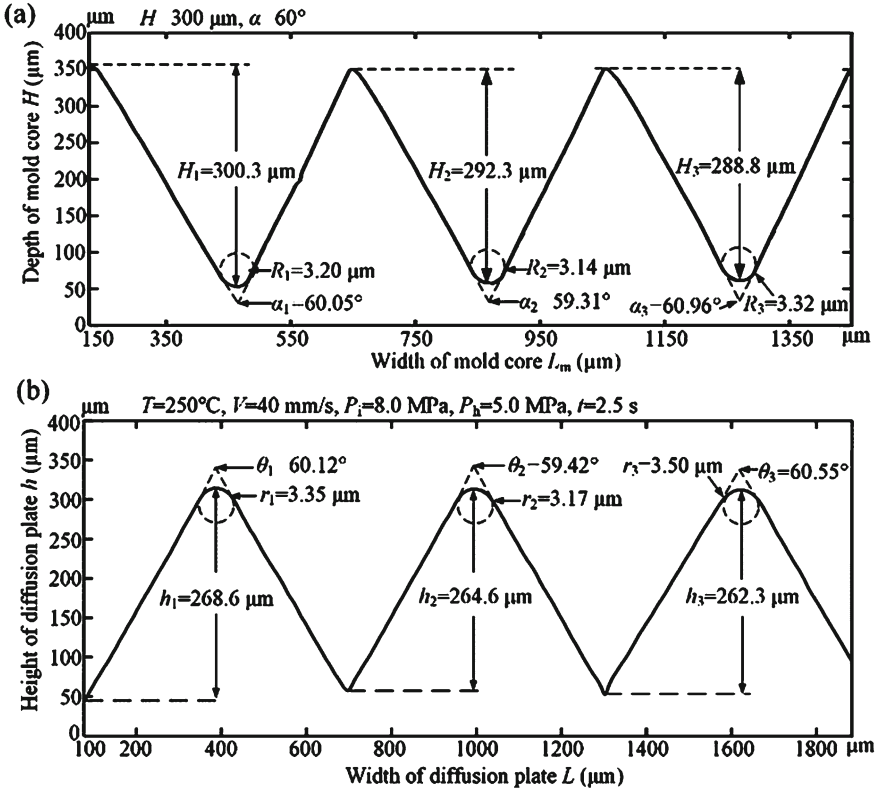


Fig. 12 The section profile curves of the micro-structured mold core and injection molded part were measured and the average value was calculated to evaluate the accuracy of the mold. Figure 12b shows the profile curves of the diffusion plate specimen, whose microstructure was obtained by injection molding. In this step, the parameters of the microinjection molding process, i.e., melt temperature, injection speed, injection pressure, holding pressure and holding time, were 250 °C, 40 mm/s, 8.0 MPa, 5.0 MPa and 2.5 s. The average depth  $h$  and angle  $\theta$  of the V-groove measured for the mold-cast diffusion microstructure wafer sample were 265.2  $\mu\text{m}$  and 60.03°, respectively, as shown in Fig. 12b. Compared with the depth and angle of the V-groove of the micro-structured diffusion plate shown in Fig. 12a, the microscopic formation errors of the depth and angle of the V-groove of the micro-structured diffusion plate were 28.6  $\mu\text{m}$  and 0.08°, respectively. The average radius  $r$  of the V-groove of the micro-structured diffuser plate is 3.34  $\mu\text{m}$ . Therefore, the microformation error of the radius of the V-groove of the micro-structured diffusion plate was 0.12  $\mu\text{m}$  compared to the radius of the V-groove of the mold core. Therefore, micro injection molding developed with a micro-abrasive mold core can accurately process micro-structured diffusion

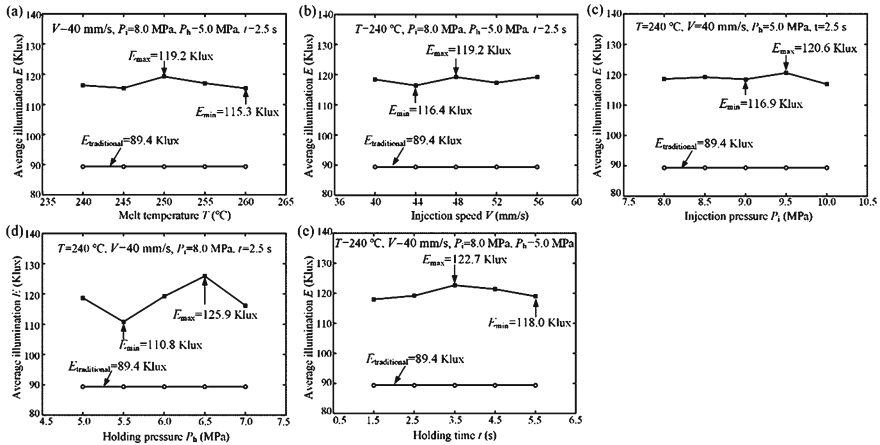
on the front surface of the mold core and injection molded part were measured and the average value was calculated to evaluate the accuracy of the mold. Figure 12b shows the profile curves of the diffusion plate specimen, whose microstructure was obtained by injection molding. In this step, the parameters of the microinjection molding process, i.e., melt temperature, injection speed, injection pressure, holding pressure and holding time, were 250 °C, 40 mm/s, 8.0 MPa, 5.0 MPa and 2.5 s. The average depth  $h$  and angle  $\theta$  of the V-groove measured for the mold-cast diffusion microstructure wafer sample were 265.2  $\mu\text{m}$  and 60.03°, respectively, as shown in Fig. 12b. Compared with the depth and angle of the V-groove of the micro-structured diffusion plate shown in Fig. 12a, the microscopic formation errors of the depth and angle of the V-groove of the micro-structured diffusion plate were 28.6  $\mu\text{m}$  and 0.08°, respectively. The average radius  $r$  of the V-groove of the micro-structured diffuser plate is 3.34  $\mu\text{m}$ . Therefore, the microformation error of the radius of the V-groove of the micro-structured diffusion plate was 0.12  $\mu\text{m}$  compared to the radius of the V-groove of the mold core. Therefore, micro injection molding developed with a micro-abrasive mold core can accurately process micro-structured diffusion



plates with high molding accuracy. The replication rate is defined as the ratio of the microstructure depth of the microinjection molded part to the microstructure depth of the mold core [26, 27]. Hence, the replication rate of polymer samples produced by microinjection molding was about 90.26% based on the average V-groove depth of the micro-structured mold core and diffusion plate samples. The mean standard deviations of V-groove depth, V-tip depth, and V-tip radius of the mold core were 5.89  $\mu\text{m}$ , 0.83  $\mu\text{m}$ , and 0.09  $\mu\text{m}$ , respectively. The mean standard deviations of V-groove depth, V-tip angle, and V-tip radius of the diffusion plate were 2.82  $\mu\text{m}$ , 0.57  $\mu\text{m}$ , and 0.17  $\mu\text{m}$ , respectively. It can be concluded that the standard deviations of the micro-structured diffusion plate relative to that of the mold rod were smaller.

#### **4.4 Light Efficiency Analysis of the Micro-structured LED Diffusion Plate**

In order to investigate the effects of melting temperature, injection speed, injection pressure, holding pressure and holding pressure time on the luminous efficiency of micro-structured LED diffusion plates, the relationship between the average illuminance  $E$  of micro-structured LED diffusion plates and various microinjection process parameters was determined, as described in Fig. 13. The figure shows that the measured average illuminance  $E_{\text{traditional}}$  for a conventional diffusion plate block is 89.4 Klux. Figure 13 shows that as the melting temperature, injection rate, injection pressure and retention time vary, the average illuminance  $E$  varies from 115.3 to 119.2 Klux, 116.4 to 119.2 Klux, 116.9 to 120.6 Klux and 118.0 to 122.7 Klux vary (see Fig. 13a–c, e). The variation in optical properties is about 13%. This is mainly due to the repetition of the V-groove geometry, which is controlled by the parameters of the microinjection molding process. Since the V-groove has a vertex arc, the difference in the reproduction of the groove geometry eventually leads to the difference in the optical properties. When the melt temperature, injection rate, injection pressure or dwell time are increased, the average illumination does not change significantly. The average illumination  $E$  varied between 110.8 and 125.9 Klux when the holding pressure was changed (see Fig. 13d). This indicates that the average illumination changes significantly with the change in holding pressure. The average illuminance  $E$  of diffusion plates with injection molded microstructures achieved a maximum value of 125.9 Klux at the optimum parameters of the microinjection process, i.e., melting temperature, injection speed, injection pressure, holding pressure and holding time of 240 °C, 40 mm/s, 8.0 MPa, 6.5 MPa and 2.5 s. As shown in the experimental results, the polymerization pressure had the greatest influence on the light production rate of the micro-structured diffusion plates. However, the effects of other parameters, i.e., microinjection process parameters, are negligible. Since the luminous efficiency of the conventional diffusion plate is 89.4 Klux, the maximum luminous efficiency of the micro-structured diffusion plate can be increased by about 40.82%. For the micro-structured diffuser plate, the experimentally measured illuminance is between



**Fig. 13** The average illuminations  $E$  of LED diffusion plates depending on micro injection molding process parameters: **a** melt temperature  $T$ ; **b** injection speed  $V$ ; **c** injection pressure  $P_i$ ; **d** holding pressure  $P_h$ ; **e** holding time  $t$

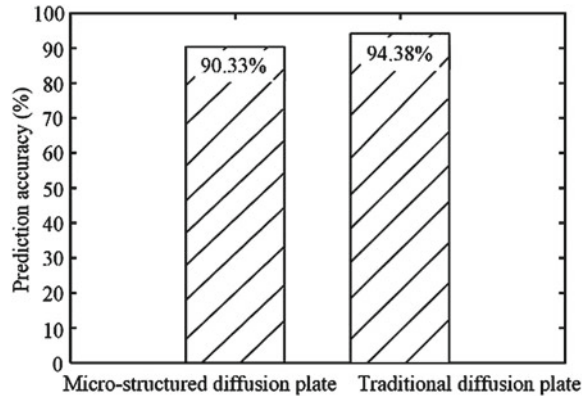
110.8 and 125.9 Klux, which is very close to the modeled theoretical illuminance of 138.07 Klux. Hence, it is possible to develop micro-structured LED scattered light panels using the light efficiency modeling approach.

Figure 14 shows the predicted accuracy of the conventional and micro-structured diffuser plates. As the V-groove depth  $h$  and V-groove angle  $\theta$  are defined to be  $300\ \mu\text{m}$  and  $60^\circ$ , respectively, the illuminance value of the micro-structured scattering plate obtained by the optical simulation method is 138.07 Klux. The maximum experimental illuminance value of the injection-molded micro-structured diffusion plate is 125.9 Klux. Hence, the prediction accuracy of the micro-structured scattering plate is about 90.33%. The simulated and experimentally measured illuminance values of the conventional diffusion plate are 94.42 and 89.4 Klux, respectively, so the prediction accuracy of the conventional diffusion plate is about 94.38%. Therefore, the developed luminous efficiency simulation method can be used for the structural design of micro-structured LED diffuser plates with high prediction accuracy. The presented microfabrication injection molding technology with high efficiency based on micro-fabrication die cores can achieve the large-scale production and manufacturing of micro-structured LED diffusion plate products with high shape accuracy.

## 5 Conclusions

In this chapter, a method for simulating light efficiency is developed to achieve optimal microstructure parameters for micro-structured LED diffusion plates. A high-precision micro-grinding technique is presented for generating regular and

**Fig. 14** The prediction accuracies of conventional and micro-structured diffusion plates



controllable micro-grooved array structures on the surface of mold core. An efficient micro injection molding technique is used for the rapid fabrication of micro-structured diffusion plate with high shape accuracy. The presented hybrid production method enables the large-scale production and fabrication of micro-structured LED diffusion sheets through low production cost. The main findings are briefly summarized as follows:

- (1) The optimal parameters of the micro-groove were developed using the optical output simulation method, i.e., the depth and angle of the V-groove were  $300\ \mu\text{m}$  and  $60^\circ$ , respectively.
- (2) The machining errors of the V-groove depth and V-groove angle of the micro-ground mold core were  $6.2\ \mu\text{m}$  and  $0.57^\circ$ , respectively. The micro-forming errors of V-groove angle and V-tip radius of the micro-structured diffusion plate were  $0.08^\circ$  and  $0.12\ \mu\text{m}$ , respectively. The shape accuracy of the micro-ground mold core and the repetition rate of the micro injection molded diffusion plate were  $9.2\ \mu\text{m}$  and  $90.26\%$ , respectively.
- (3) The holding pressure has the greatest influence on the light efficiency of the micro-structured diffusion plate. The measured illumination of the micro-structured diffusion plate reached a maximum value of  $125.9\ \text{Klux}$  at  $240\ ^\circ\text{C}$ ,  $40\ \text{mm/s}$ ,  $8.0\ \text{MPa}$ ,  $6.5\ \text{MPa}$  and  $2.5\ \text{s}$  of melt temperature, injection speed, injection pressure and dwell time respectively, which was about  $40.82\%$  higher than that of the conventional diffusion plate.
- (4) The prediction accuracies of the defined light efficiency simulation method for the traditional and micro-structured diffusion plates are  $94.38\%$  and  $90.33\%$ , respectively.

**Acknowledgements** The work described in this chapter was supported by the National Natural Science Foundation of China (Grant No. 51805334), the International Science and Technology Cooperation Project of Shenzhen City (Grant No. GJHZ20190822091805371), and the Science and Technology Planning Project of Guangdong Province (Grant No. 2017A010102003).

## References

1. Ramírez MG, Sirvent D, Morales-Vidal M, Ortuño M, Martínez-Guardiola FJ, Francés J, Pascual I (2019) LED-cured reflection gratings stored in an acrylate-based photopolymer. *Polymers* 11:632
2. Lu LB, Zhang Z, Guan YC, Zheng HY (2018) Enhancement of heat dissipation by laser micro structuring for LED module. *Polymers* 10:886
3. Chien CH, Chen CC, Chen T, Lin YM, Liu YC (2016) Thermal deformation of microstructure diffuser plate in LED backlight unit. *J Soc Inf Display* 24:99–109
4. Chien CH, Chen ZP (2009) The study of integrated LED-backlight plate fabricated by micromachining technique. *Microsyst Technol* 15:383–389
5. Pardo DA, Jabbour GE, Peyghambarian N (2020) Application of screen printing in the fabrication of organic light-emitting devices. *Adv Mater* 12:1249–1252
6. Weng C, Wang F, Zhou M, Yang D, Jiang B (2018) Fabrication of hierarchical polymer surfaces with super hydrophobicity by injection molding from nature and function-oriented design. *Appl Surf Sci* 436:224–233
7. Liao QH, Zhou CL, Lu YJ, Wu XY, Chen FM, Lou Y (2019) Efficient and precise micro-injection molding of micro-structured polymer parts using micro-machined mold core by WEDM. *Polymers* 11:1591
8. Maghsoudi K, Jafari R, Momen G, Farzaneh M (2017) Micro-nanostructured polymer surfaces using injection molding: a review. *Mater Today Commun* 13:126–143
9. Masato D, Sorgato M, Lucchetta G (2016) Analysis of the influence of part thickness on the replication of micro-structured surfaces by injection molding. *Mater Design* 95:219–224
10. Masato D, Sorgato M, Parenti P, Annoni M, Lucchetta G (2017) Impact of deep cores surface topography generated by micro milling on the demolding force in micro injection molding. *J Mater Process Tech* 246:211–223
11. Baruffi F, Calao M, Tosello G (2018) Micro-injection moulding in-line quality assurance based on product and process fingerprints. *Micromachines* 9:293
12. Parenti P, Masato D, Sorgato M, Lucchetta G, Annoni M (2017) Surface footprint in molds micromilling and effect on part demoldability in micro injection molding. *J Manuf Process* 29:160–174
13. Sorgato M, Masato D, Lucchetta G (2017) Effects of machined cavity texture on ejection force in micro injection molding. *Precis Eng* 50:440–448
14. Kim JH, Mirzaei A, Kim HW, Kim SS (2018) Facile fabrication of superhydrophobic surfaces from austenitic stainless steel (AISI 304) by chemical etching. *Appl Surf Sci* 439:598–604
15. Zhou CL, Ngai TWL, Li LJ (2016) Wetting behaviour of laser textured Ti<sub>3</sub>SiC<sub>2</sub> surface with micro-grooved structures. *J Mater Sci Technol* 32:805–812
16. Zhou CL, Wu XY, Lu YJ, Wu W, Zhao H, Li LJ (2018) Fabrication of hydrophobic Ti<sub>3</sub>SiC<sub>2</sub> surface with micro-grooved structures by wire electrical discharge machining. *Ceram Int* 44:18227–18234
17. Xu SL, Shimada K, Mizutani M, Kuriyagawa T (2014) Fabrication of Hybrid micro/nano-textured surfaces using rotary ultrasonic machining with one-point diamond tool. *Int J Mach Tools Manuf* 86:12–17
18. Wang JS, Zhang XD, Fang FZ, Chen RT (2019) Diamond cutting of micro-structure array on brittle material assisted by multi-ion implantation. *Int J Mach Tools Manuf* 137:58–66
19. Lu YJ, Chen FM, Wu XY, Zhou CL, Lou Y, Li LJ (2019) Fabrication of micro-structured polymer by micro injection molding based on precise micro-ground mold core. *Micromachines* 10:253
20. Lu YJ, Li LJ, Xie J, Zhou CL, Guo RB (2017) Dry electrical discharge dressing and truing of diamond grinding wheel V-tip for micro-grinding. The 5th international conference on mechatronics, materials, chemistry and computer engineering (ICMMCCE 2017). Atlantis Press
21. Li P, Xie J, Cheng J, Jiang YN (2015) Study on weak-light photovoltaic characteristics of solar cell with a microgroove lens array on glass substrate. *Opt Express* 23:192–203

22. Kim DS, Kim DH, Jang JH (2013) A nanoscale conical polymethyl methacrylate (PMMA) sub-wavelength structure with a high aspect ratio realized by a stamping method. *Opt Express* 21:8450–8459
23. Lu YJ, Xie J, Si XH (2015) Study on micro-topographical removals of diamond grain and metal bond in dry electro-contact discharge dressing of coarse diamond grinding wheel. *Int J Mach Tools Manuf* 88:118–130
24. Xie J, Xie HF, Luo MJ (2012) Dry electro-contact discharge mutual-wear truing of micro diamond wheel V-tip for precision micro-grinding. *Int J Mach Tools Manuf* 60:44–51
25. Xie J, Zhuo YW, Tan TW (2011) Experimental study on fabrication and evaluation of micro pyramid-structured silicon surface using a V-tip of diamond grinding wheel. *Precis Eng* 35:173–182
26. Seo YS, Park K (2012) Direct patterning of micro-features on a polymer substrate using ultrasonic vibration. *Microsyst Technol* 18:2053–2061
27. Lu YJ, Chen FM, Wu XY, Zhou CL, Zhao H, Li LJ, Tang Y (2019) Precise WEDM of micro-textured mould for micro-injection molding of hydrophobic polymer surface. *Mater Manuf Process* 34:1342–1351